University of Stuttgart
Germany

Elten
Polukhov

Multiscale Modeling and Stability Analysis of Soft Active Materials – from Electro- and Magneto-Active Elastomers to Polymeric Hydrogels

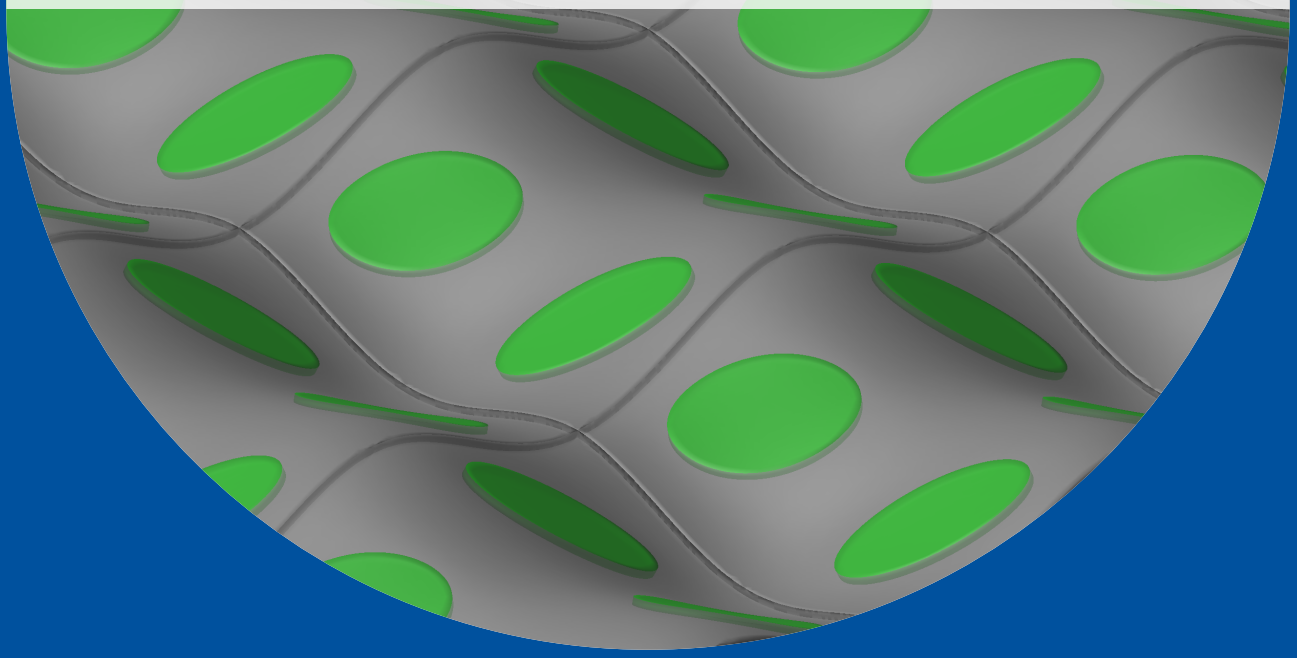

15

Publication series of the
Institute of Applied Mechanics (IAM)

Multiscale modeling and stability analysis of soft active materials – from electro- and magneto-active elastomers to polymeric hydrogels

Von der Fakultät Bau- und Umweltingenieurwissenschaften der Universität Stuttgart
zur Erlangung der Würde eines Doktor-Ingenieurs (Dr.-Ing.)
genehmigte Abhandlung

Vorgelegt von

Elten Polukhov

aus Marneuli, Georgien

Hauptberichter:	Prof. Dr.-Ing. Marc-André Keip
1. Mitberichter:	Prof. Oscar Lopez-Pamies, Ph.D.
2. Mitberichter:	Prof. Dr.-Ing. habil. Paul Steinmann

Tag der mündlichen Prüfung: 4. August 2023

Institut für Mechanik (Bauwesen) der Universität Stuttgart

2023

Publication series of the Institute of Applied Mechanics (IAM), Volume 15
Institute of Applied Mechanics
University of Stuttgart, Germany, 2023

Organisation und Verwaltung:

Institut für Mechanik (Bauwesen)
Lehrstuhl für Materialtheorie
Universität Stuttgart
Pfaffenwaldring 7
70569 Stuttgart
Tel.: +49 (0)711 685-66378
Fax: +49 (0)711 685-66347

ISBN 978-3-937399-63-8 (D 93 Stuttgart)

Acknowledgements

This dissertation is the outcome of my research work as a research associate at the Institute of Applied Mechanics (Civil Engineering) of the University of Stuttgart. Although my name stands alone as the author of this work, it could not have been possible without the support of many others. Therefore, I want to thank all the people for their contributions and support in various ways throughout my doctoral studies.

First of all, I want to thank my adviser, Professor Marc-André Keip, for providing me the opportunity to do my doctorate at his chair, regardless of many uncertainties that existed at the chair during my starting time. I am very thankful for his supervision, constant support on professional and personal matters, as well as extremely valuable inputs.

I thank Professor Paul Steinmann and Professor Oscar Lopez-Pamies for their interest in the present work and for accepting to be the co-referees of the dissertation. The discussions with them have been very insightful.

I am very grateful to my former and current colleagues for the pleasant atmosphere at the institute. I thank Daniel Vallicotti, Siddharth Sriram, Laura Pytel, and Hamza Khurshid for the fruitful collaborations and related discussions. I appreciate very much the discussions with Daniel Kienle, Felix Göküzüm, Aref Nateghi, and Stephan Teichtmesiter, whom I could approach quite often with any questions. A heartfelt thanks go to my former colleagues, Matthias Rambausek, Omkar Nadgiri, Harikrishnan Vijayakumaran, Khiem Nguyen, Ashish Sridhar, Fadi Aldakheel, Shreeraman Swamynathan, and my current colleagues, Basavesh Yaraguntappa, Linda Werneck, Claudius Haag, and Andreas Krischok. I am also very grateful to Jan Lukas Eurich, Arndt Wagner, David Krach, Matthias Ruf, Alixa Sonntag, and all the colleagues from the institute. Moreover, the support of our secretaries, first Nadine Steinecke, then Leonie Fischer, and now Christine Witke, cannot be appreciated enough. Thank you for being always so kind and ready to help.

Furthermore, I am thankful to Professor Michael Kaliske for inviting me for one-month research stay at his institute, Institute for Structural Analysis, at the TU Dresden. I also want to thank Anas Kanan for our collaboration during his research stay in Stuttgart and mine in Dresden.

I also want to gratefully acknowledge the financial support of DFG (German Research Foundation) through the SimTech and SFB1313 projects at the University of Stuttgart as well as the finanical support through the Course Director position of the international master program COMMAS at the University of Stuttgart. Along these lines, I also want to acknowledge the support of DAAD (German Academic Exchange Program) during my master's studies, which played an essential role in my subsequent decision to continue my doctorate studies.

For the pleasant times we have spent together outside work and for checking on my progress, I am much obliged to my friends, in particular, Parvin Garayev, Elmir Khalilov, Fikrat Talibli, and many others.

My deepest gratitude goes to my parents, sister, and late grandparents for their trust in me, their continuous support, and the many sacrifices they have made.

Stuttgart, September 2023 Elten Polukhov

Table of Contents

Abstract

This work is dedicated to modeling and stability analysis of stimuli-responsive, soft active materials within a multiscale variational framework. In particular, composite electro- and magneto-active polymers and polymeric hydrogels are under consideration. When electro- and magneto-active polymers (EAP and MAP) are fabricated in the form of composites, they comprise at least two phases: a polymeric matrix and embedded electric or magnetic particles. As a result, the obtained composite is soft, highly stretchable, and fracture resistant like polymer and undergoes stimuli-induced deformation due to the interaction of particles. By designing the microstructure of EAP or MAP composites, a compressive or a tensile deformation can be induced under electric or magnetic fields, and also coupling response of the composite can be enhanced. Hence, these materials have found applications as sensors, actuators, energy harvesters, absorbers, and soft, programmable, smart devices in various areas of engineering.

Similarly, polymeric hydrogels are also stimuli-responsive materials. They undergo large volumetric deformations due to the diffusion of a solvent into the polymer network of hydrogels. In this case, the obtained material shows the characteristic behavior of polymer and solvent. Therefore, these materials can also be considered in the form of composites to enhance the response further. Since hydrogels are biocompatible materials, they have found applications as contact lenses, wound dressings, drug encapsulators and carriers in bio-medicine, among other similar applications of electro- and magneto-active polymers.

All above mentioned favorable features of these materials, as well as their application possibilities, make it necessary to develop mathematical models and numerical tools to simulate the response of them in order to design pertinent microstructures for particular applications as well as understand the observed complex patterns such as wrinkling, creasing, snapping, localization or pattern transformations, among others. These instabilities are often considered as failure points of materials. However, many recent works take advantage of instabilities for smart applications.

Investigation of these instabilities and prediction of their onset and mode are some of the main goals of this work. In this sense, the thesis is organized into three main parts.

The first part is devoted to the state of the art in the development, fabrication, and modeling of soft active materials as well as the continuum mechanical description of the magneto-electro-elasticity.

The second part is dedicated to multiscale instabilities in electro- and magneto-active polymer composites within a minimization-type variational homogenization setting. This means that the highly heterogeneous problem is not resolved on one scale due to computational inefficiency but is replaced by an equivalent homogeneous problem. The effective response of the macroscopic homogeneous problem is determined by solving a micro-

scopic representative volume element which includes all the geometrical and material non-linearities. To bridge these two scales, the Hill-Mandel macro-homogeneity condition is utilized. Within this framework, we investigate both macroscopic and microscopic instabilities. The former are important not only from a physical point of view but also from a computational point of view since the macroscopic stability (strong ellipticity) is necessary for the existence of minimizers at the macroscopic scale. Similarly, the investigation of the latter instabilities are also important to determine the pattern transformations at the microscale due to external action. Thereby the critical domain of homogenization is also determined for computation of accurate effective results. Both investigations are carried out for various composite microstructures and it is found that they play a crucial role in the response of the materials. Therefore, they must be considered for designing EAP and MAP composites as well as for providing reliable computations.

The third part of the thesis is dedicated to polymeric hydrogels. Here, we develop a minimization-based homogenization framework to determine the response of transient periodic hydrogel systems. We demonstrate the prevailing size effect as a result of a transient microscopic problem, which has been investigated for various microstructures. Exploiting the elements of the proposed framework, we explore the material and structural instabilities in single and two-phase hydrogel systems. Here, we have observed complex experimentally observed and novel 2D pattern transformations such as diamond-plate patterns coupled with and without wrinkling of internal surfaces for perforated microstructures and 3D pattern transformations in thin reinforced hydrogel composites. The results indicate that the obtained patterns can be controlled by tuning the material and geometrical parameters of the composite.

Zusammenfassung*

Diese Arbeit widmet sich der Modellierung und Stabilitätsanalyse von stimuli-responsiven, weichen, aktiven Materialien innerhalb eines multiskaligen Variationsrahmens. Dabei werden insbesondere Kompositmaterialien aus elektro- und magnetoaktiven Polymeren und polymeren Hydrogelen betrachtet. Wenn elektro- und magnetoaktive Polymere (EAP und MAP) in Form von Kompositmaterialien hergestellt werden, bestehen sie aus mindestens zwei Phasen: einer polymeren Matrix und eingebetteten elektrischen oder magnetischen Partikeln. Das Resultat ist ein weiches, hoch dehnbares und bruchfestes Kompositmaterial entsprechend seiner polymeren Eigenschaften, das darüber hinaus durch die Wechselwirkung der Partikel eine stimulationsinduzierte Verformung erfährt. Durch die Gestaltung der Mikrostruktur von EAP- oder MAP-Kompositmaterialien kann eine Druck- oder Zugverformung unter elektrischen oder magnetischen Feldern induziert und das Kopplungsverhalten des Kompositmaterials verbessert werden. Daher werden diese Materialien als Sensoren, Aktuatoren, Energieabsorber, Dämpfungselemente, oder als weiche, programmierbare und intelligente Systeme in verschiedenen Bereichen der Technik eingesetzt.

In ähnlicher Weise sind auch polymere Hydrogele stimulierungsfähige Materialien. Sie erfahren große volumetrische Verformungen aufgrund der Diffusion eines Lösungsmittels in das Polymernetzwerk von Hydrogelen. In diesem Fall zeigt das Material ein charakteristisches Verhalten von Polymer und Lösungsmittel. In diesem Sinne können Hydrogele auch als Kompositmaterialien angesehen werden, deren Eigenschaften durch Anpassung ihrer Zusammensetzung verbessert werden können. Ferner handelt es sich bei Hydrogelen um biokompatible Materialien, werden sie unter anderem als Kontaktlinsen, Wundauflagen, Medikamentenkapseln und -träger in der Biomedizin eingesetzt, aber auch für ähnliche Anwendungen elektro- und magnetoaktiver Polymere.

Die oben genannten vorteilhaften Eigenschaften dieser Materialien sowie ihre Anwendungsmöglichkeiten machen es notwendig, mathematische Modelle und numerische Werkzeuge zu entwickeln, um die Antwort dieser Materialien zu simulieren, um geeignete Mikrostrukturen für bestimmte Anwendungen zu entwerfen und die beobachteten komplexen Muster wie Faltenbildung, Einreißen, Lokalisierung oder Mustertransformationen u.a. zu verstehen. Diese Instabilitäten werden oft als Versagenspunkte von Werkstoffen angesehen. Viele neuere Arbeiten nutzen jedoch die Vorteile von Instabilitäten für intelligente Anwendungen.

Die Untersuchung dieser Instabilitäten, die Vorhersage ihres Auftretens und ihrer Funktionsweise sind einige der Hauptziele dieser Arbeit. In diesem Sinne ist diese Arbeit in drei Hauptteile gegliedert.

*The help of DeepL Translator for the initial translation of the abstract into German is greatly acknowledged. The abstract was afterward read and corrected by my colleagues, for whom I am very grateful.

Der erste Teil ist dem Stand der Forschung bei der Entwicklung, Herstellung und Modellierung von weichen aktiven Materialien sowie der kontinuumsmechanischen Beschreibung der Magneto-Elektro-Elastizität gewidmet.

Der zweite Teil widmet sich Multiskaleninstabilitäten in elektro- und magnetoaktiven Kompositmaterialien im Rahmen einer variationellen Homogenisierung basierend auf Minimierungsprinzipien. Das bedeutet, dass das hochgradig heterogene Problem aufgrund von Recheneffizienz nicht auf einer Skala gelöst wird, sondern durch ein äquivalentes homogenes Problem ersetzt wird. Die effektive Antwort des makroskopischen homogenen Problems wird durch die Lösung eines mikroskopischen repräsentativen Volumenelements bestimmt, das alle geometrischen und materiellen Nichtlinearitäten enthält. Um die beiden Skalen zu überbrücken, wird die Hill-Mandel-Bedingung der Makrohomogenität verwendet. In diesem Rahmen untersuchen wir sowohl makroskopische als auch mikroskopische Instabilitäten. Erstere sind nicht nur aus physikalischer Sicht wichtig, sondern auch aus mathematischer Sicht, da die makroskopische Stabilität (starke Elliptizität) für die Existenz von Minimierern auf der makroskopischen Skala notwendig ist. Ebenso ist die Untersuchung der letztgenannten Instabilitäten wichtig, um Transformationen von Mikrostrukturen aufgrund externer Einwirkungen zu bestimmen. Dadurch wird auch der kritische Bereich der Homogenisierung für die Berechnung der genauen effektiven Ergebnisse bestimmt. Beide Untersuchungen werden für verschiedenartige Mikrostrukturen von Kompositmaterialien durchgeführt und es wird festgestellt, dass sie eine entscheidende Rolle für die Antwort der Materialien spielen. Daher müssen sie bei der Entwicklung von EAP- und MAP-Kompositmaterialien sowie bei der Erstellung zuverlässiger Berechnungen berücksichtigt werden.

Der dritte Teil der Arbeit ist den polymeren Hydrogelen gewidmet. Hier entwickeln wir einen auf einem Minimierungsprinzip basierenden Homogenisierungsrahmen, um die Reaktion von transienten periodischen Hydrogelsystemen zu bestimmen. Wir zeigen den vorherrschenden Größeneffekt als Ergebnis des transienten mikroskopischen Problems, welches für verschiedene Mikrostrukturen untersucht wurde. Unter Ausnutzung der Elemente des vorgeschlagenen Rahmens erforschen wir die materiellen und strukturellen Instabilitäten in ein- und zweiphasigen Hydrogelsystemen. Hier haben wir komplexe, experimentell beobachtete und neuartige 2D-Mustertransformationen betrachtet, wie z.B. Diamantplattenmuster, die mit und ohne Faltenbildung der inneren Oberflächen für perforierte Mikrostrukturen gekoppelt sind, sowie 3D-Mustertransformationen in dünnen, verstärkten Hydrogelen. Die Ergebnisse zeigen, dass die erhaltenen Muster durch die Abstimmung des Materials und der geometrischen Parameter von Kompositmaterialien gesteuert werden können.

Chapter 1

Soft-Active Materials: State of the Art

Over the last several decades, so-called smart or multifunctional materials have attracted a lot of attention because of their favorable and tailor-made properties. These materials are suitable for various applications in fields ranging from engineering, computer technology, and robotics to biomimetics, biomedicine, and agriculture. Some examples include shape-memory alloys, electro- and magneto-active materials (e.g., ferroelectric and ferromagnetic ceramics, liquid-crystal and dielectric elastomers), and polymeric hydrogels.

The characteristic behavior of all these materials is their coupling response. The coupling can manifest itself in the form of stimuli-induced behavior, such as a change in stiffness, electric and magnetic permittivity, or diffusivity of a material under an externally applied field. Causes for a coupling response are usually rooted in the microstructure of these materials. Many of them possess naturally heterogeneous microstructures. Such as, shape-memory alloys develop intricate patterns at length scales measured by micro- or nanometers, ferroelectric and ferromagnetic ceramics have a polycrystalline structure with unit-cell dimensions measured by angstroms, and polymeric hydrogels can be inhomogeneous as a result of clustered regions of crosslinks and swellings as well as due to defects in their polymer networks.

By virtue of complex fabrication techniques and 3D printing technology, many of the materials are also manufactured in the form of composites. The microstructures of these composites can range from millimeter to nanometer length scales. Careful design of the microstructures allows the development of materials with superior macroscopic behavior from favorable characteristics of underlying ingredients. For these materials, multiscale homogenization techniques have been applied successfully to predict the response due to structural and material nonlinearities, to aid with the design of microstructures for specific applications, or to develop micro-mechanically motivated phenomenological models to describe the macroscopic response.

Homogenization techniques are also extensively exploited to understand material and structural instabilities of heterogeneous materials, which have fascinating implications not only from the mathematical but also from the physical viewpoint. On the one hand, material and structural stability guarantees the existence and uniqueness of a converged solution, and it can have implications for the validity of the domain of a considered representative volume element within a homogenization setting. On the other hand, instabilities can be exploited for further advanced applications such as energy harvesting or dissipation, developing sensors and actuators, building morphing and deployable structures, and obtaining controlled and tunable responses.

In light of the above-mentioned facts, in the following, we give an introduction and motivation to soft-active materials and characterization of their response, modeling, and stability analysis in more detail. In particular, we concentrate on electro-active and magneto-active polymers as well as polymeric hydrogels. Furthermore, the goal and the outline of the thesis are discussed. Finally, the short summaries of the associated publications are also provided.

1.1 Electro-active polymers

An essential class of electro-active materials is given by dielectrics, which are exploited for developing sensors, actuators, and capacitors, among many other applications. Piezoelectric ceramics and electro-active polymers are dielectric materials that show electromechanical coupling. Prominent examples of piezoelectric ceramics are barium titanate ($BaTiO_3$) and lead zirconate titanate (PZT), which have been known since the 1940s [82, 67] and found a wide range of applications [159, 5]. Their favorable properties include lightweight, low power requirements, and fast response time. However, since these materials are mechanically stiff and brittle, they show low actuation strains.

Conversely, soft dielectrics, such as electro-active polymers (EAPs) are capable of undergoing large actuation strains under an external electric field. Depending on the actuation mechanism of EAPs, two main types are distinguished, i.e., ionic EAPs and electronic EAPs, as discussed in [7] and summarized in [195]; see also Fig. 1.1. Actuation in the ionic EAPs is driven by the diffusion of electrolyte ions in a polymer skeleton. Although these materials operate under low voltage (up to 5 V in ionic polymer-metal composites [195]) and can show fast actuation response, they undergo relatively low actuation strains (up to max. $\sim 40\%$ in conducting polymers [142] and in ionic polymer-metal composites [125]). Furthermore, the encapsulation of electrolytes generates complications.

In contrast to ionic EAPs, the actutation mechanism of electronic EAPs is based on Coulomb forces generated through an applied electric field. Depending on constituents and their properties, electronic EAPs can be classified further as ferroelectric EAPs, electrostrictive graft elastomers, liquid-crystal elastomers, and dielectric elastomers, see [7, 195] and Fig. 1.1. For example, ferroelectric polymers are made of semicrystalline polymers such as poly(vinylidene fluoride) (PVDF), and hence these types of EAPs can show permanent polarization and piezoelectric behavior, see [97]. Their responses depend on a critical applied temperature threshold – the Curie temperature. Applying a temperature above the Curie temperature can remove the permanent polarization and induce a transition to paraelectric behavior. Similarly, liquid-crystal elastomers merge the directional characteristics of liquid crystals and elasticity of elastomers, see, e.g., [42, 207, 116] for characterization, and related applications, as well as [19, 99, 254] for modeling.

Among the electronic EAPs, the dielectric elastomers (DEs) are capable of manifesting the highest actuation strains, which can be as high as several hundred percents [7]. DEs are made of a thin dielectric and soft electrodes attached on the top and bottom surfaces [175]. The actuation mechanism of DEs is based on the Coulomb forces. Under electric loading, opposite charges in electrodes attract each other and induce the thinning of the dielectric medium in the thickness direction and extension in the lateral directions. As a dielectric medium natural rubber (NR), poly(dimethylsiloxane) (PDMS), acrylic elastomers (e.g., 3M VHB 4905) can be considered, see [110, 175, 111, 174, 241, 195, 144, 145] and references

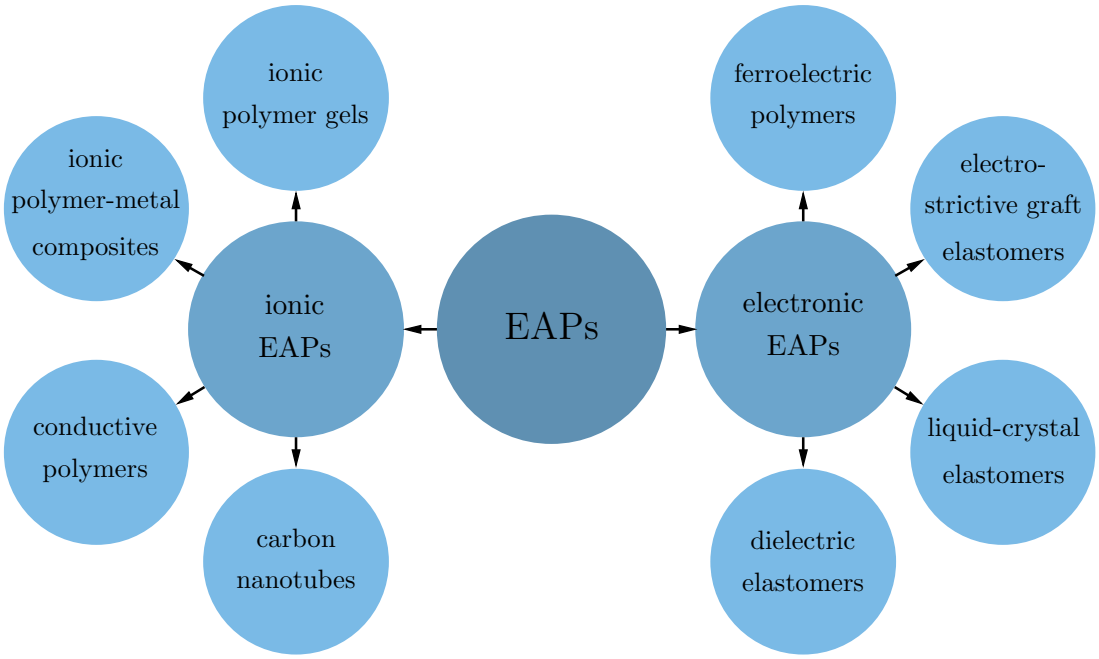

Figure 1.1: *Classification of Electroactive Polymers (EAPs).* Based on their actuation mechanism EAPs are classified as ionic and electronic according to [7], see also [195]. In ionic EAPs, the actuation is a result of the diffusion of electrolyte ions in a polymer network. On the other hand, in electronic EAPs, the main actuation mechanism is a result of Coulomb forces.

therein. DEs are lightweight, fracture-resistant, inexpensive and show strong electro-mechanical coupling. Therefore, they are considered suitable for developing actuators, transducers, grippers, and energy harvesters, which can be utilized as artificial muscles and mimicking biological structures [7, 8, 87, 213].

The main parameters of DEs that affect their electro-mechanical coupling and energy conversion are (voltage and deformation) boundary conditions as well as geometrical and material parameters such as thickness, dielectric constant, stiffness and dielectric strength of the dielectric medium [195]. The properties of DEs change depending on the considered dielectric medium. As given in [28], Table 1.2, Young's modulus of various dielectric media can be in the range of $E \approx \{0.007 - 3.0\}$ MPa and dielectric constant in a range of $\epsilon_r \approx \{1.8 - 12.7\}$ at 1 kHz for various elastomers. In this category, the commercially available 3M VHB 4910 films have nearly two times higher dielectric constant ($\epsilon_r \approx 4.8$) than the silicone-based (PDMS) films ($\epsilon_r \approx 2.8$). Hence they exhibit larger actuation under the same electric field than PDMS. Nevertheless, the former elastomers are also prone to viscous energy loss, while PDMS show unpronounced viscoelastic behavior. Another limiting factor to the actuation of DEs is their electric breakdown due to pull-in instabilities, which can result in the destruction of actuators. In order to increase the actuation performance of DEs, geometrical and material parameters can be modified; see Fig. 1.2. According to [195], the actuation strain can be improved via *(i)* reducing the thickness of the DE film, *(ii)* reducing the elastomer's stiffness and *(iii)* increasing the dielectric permittivity. It has been shown that equi-biaxial pre-stretching improves the electric breakdown field in acrylic elastomers and suppresses pull-in instabilities [174, 109, 179, 232, 232] due to the reduced mobility of electric dipoles. Nevertheless, the pre-stretching can also reduce dielectric permittivity in the acrylic elastomers in contrast to natural rubber (NR), which

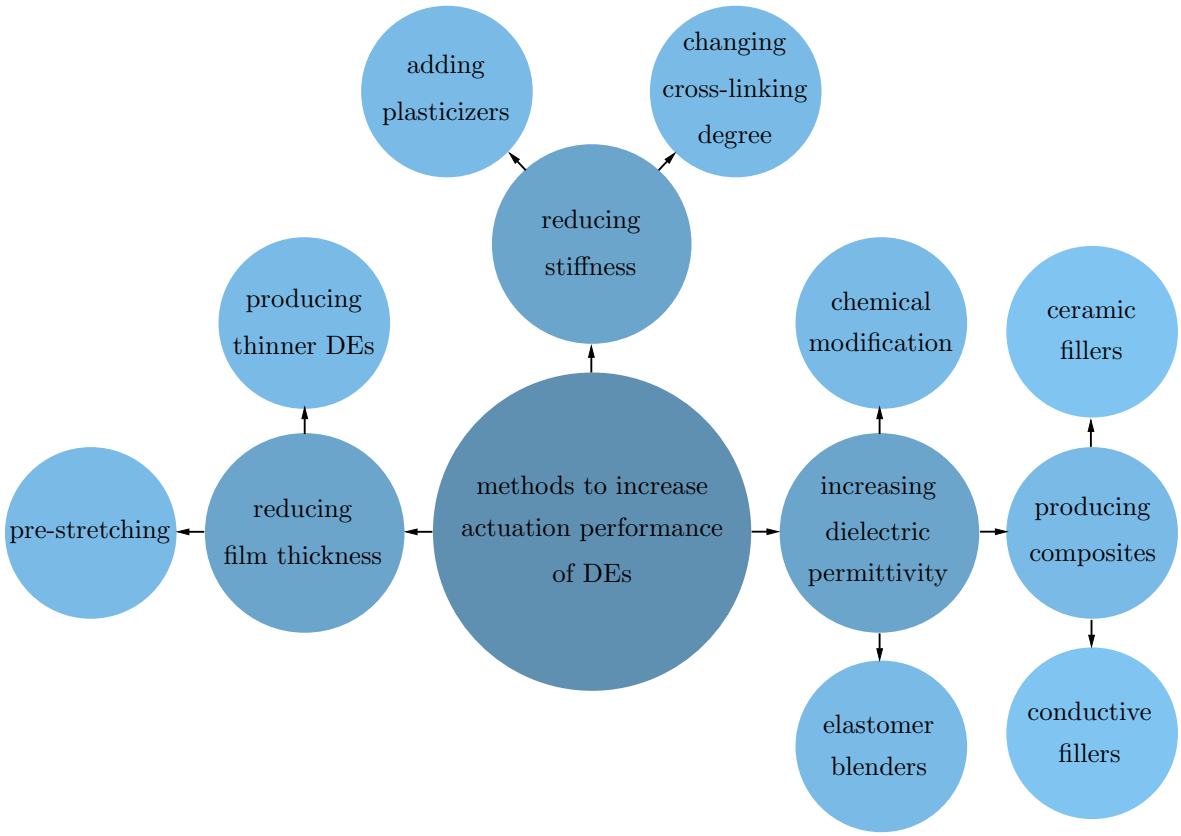

Figure 1.2: *Methods to increase actuation performance of dielectric elastomers (DEs) from Romasanta et al. [195].*

is found to be not responsive to the stretching; see [232]. It is important to note that the pre-stretching can harm the fatigue strength [195].

Another approach to enhance the actuation strain is the consideration of composites, i.e., embedding conductive or ceramic fillers into a polymer matrix. As it has been discussed in [195] in detail that special care must also be taken in this case to achieve improved electro-mechanical coupling without having the stiffness increased, and the dielectric permittivity of DEs reduced; see also [228, 133, 128]. In [193], it has been shown that conductive graphene layers in the PDMS matrix improve DE's permittivity ten times at low frequencies. Similar trends have been recorded for the composites made of ceramic fillers such as titanium dioxide (TiO_2), barium titanate ($BaTiO_3$), lead zirconate titanate (PZT). In [194], it is observed that ceramic calcium copper titanate ($CaCu_3Ti_4O_{12}$) in the PDMS matrix yields improvement of actuation strain by 100% and induces larger strains at the same electric field compared to single-phase PDMS DEs.

Considering all the above facts, we can conclude that the nonlinear response of electro-active polymers depends on many factors. In addition to their loading state, their intrigue and heterogenous microstructures play a critical role in determining their responses. To predict the response of composite DEs, phenomenological and multiscale continuum mechanical theories have been established and successfully applied, which we discuss in detail in Section 1.5 and 2.2.

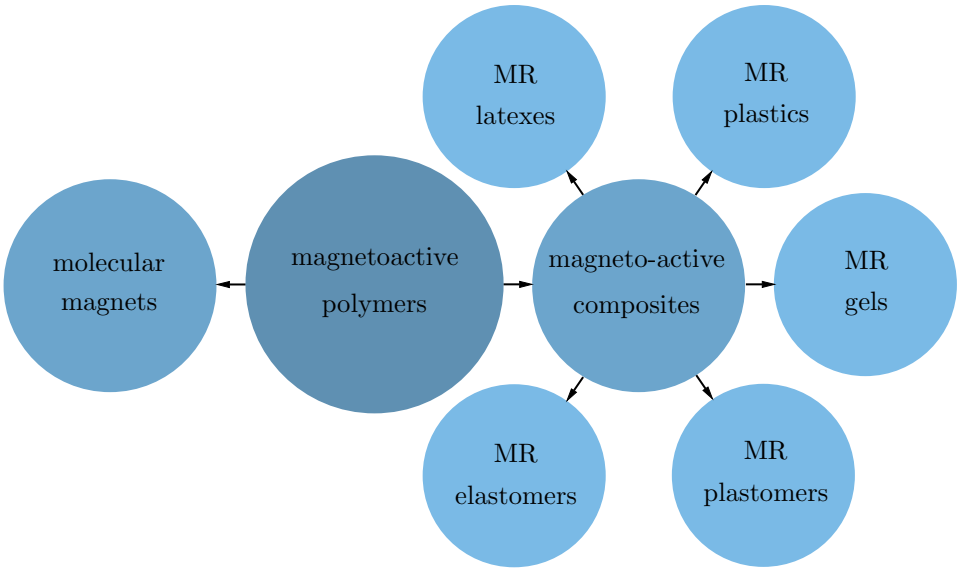

Figure 1.3: *Cassifications of magnetorheological polymers (adapted from Filipcsei et al. [54]).*

1.2 Magnetorheological elastomers

In the present section, we consider another emerging class of smart materials, namely magneto-active polymers. Like electro-mechanical coupling in EAPs, magneto-active polymers exhibit magneto-mechanical coupling response; they can manifest changes in their stiffness, damping, viscosity, storage, and loss moduli in a magnetic field [86, 237, 238, 41, 240]. Hence, these materials have found various applications, such as artificial muscles, actuators, vibration absorbers, dampers, and stiffness-tunable devices; see [62, 52, 223, 2] for more examples.

A possible classification for magneto-active polymers is given in Fig. 1.3; see also [54, 3]. In the present thesis, we focus on magnetorheological elastomers (MREs), which belong to the class of soft magneto-active composites. The magneto-mechanical response of an MRE is highly dependent on its microstructure, which is made of a highly compliant elastomeric matrix, stiff magnetic particles, and additives; see [176, 3, 11, 12] as well as Fig 1.4. The elastomeric matrix is non-magnetic in nature, and it characterizes the MRE's viscoelastic behavior and off-field stiffness. Examples of the matrix materials can be natural rubber (NR), silicone-based elastomers (PDMS), polyurethane, and polybutadiene, among others [212, 3, 11]. The silicone-based elastomers are common among these materials because of their negligible viscosity and reversible response [212, 3].

Furthermore, magnetic particles are responsible for the magneto-mechanical coupling effects in MREs. The magnetorheological (MR) effects and actuation strain are significantly influenced by particle-particle interactions in MREs. Such interactions are characterized by geometrical and material parameters of particles as well as their distribution in MREs [41, 240, 21]. Important material parameters of magnetic particles are their saturation magnetization m_s, magnetic coercivity h_c, and remanent magnetization m_r; see Fig. 1.5 and also [64, 113, 219]. As we see in the figure, some magnetic materials show pronounced hysteresis, which is reflected in the high values of remanent magnetization and coercivity [219]. The magnetic coercivity characterizes the required magnetic

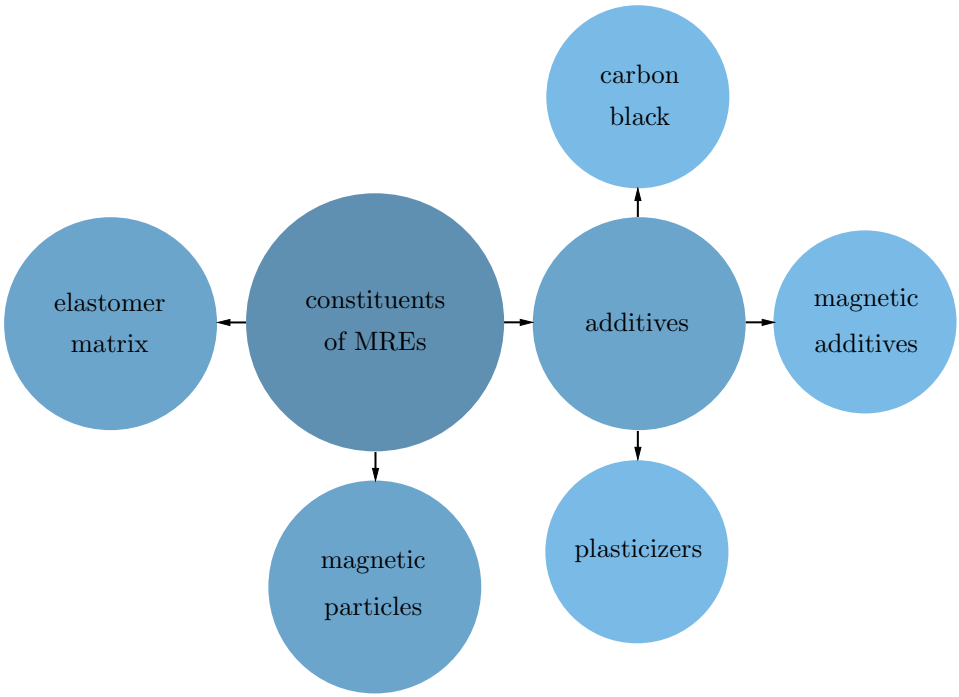

Figure 1.4: *Constituents of magnetorheological elastomers (MREs).* MREs are made of elastomer matrix, magnetic particles, and additives. As a matrix material, natural rubber, silicone rubber, polybutadiene, and polyurethane are usually considered. Examples of magnetic particles include carbonyl iron powders, cobalt, nickel, and iron oxides; see the review papers [3, 11] and references therein.

field to bring the magnetization to zero. Depending on the hysteresis, we distinguish magnetically *soft* and *hard* materials. Soft magnetic materials yield a lower hysteresis and a lower remanent magnetization. Carbonyl iron particles (CIP) are one of the most considered soft magnetic particles in MREs [223, 176]. Furthermore, CIPs also possess high saturation magnetization $\mu_0 m_s \approx 2\,\mathrm{T}$ [212]. Other materials such as magnetit (Fe_3O_4), nickel, cobalt and Nd-Fe-B alloys have also been deployed as the particles in MREs [114, 208, 218, 90, 212, 3]. The latter belongs to the category of hard magnetic particles [219]. These particles are capable of showing rotation in MREs and have been investigated in, e.g., [114, 158].

Not only the material parameters but also the geometrical parameters of particles play a critical role in the response of MREs. In particular, the volume fraction of particles, particle shape and size, and their topology can significantly influence the MR effects and the actuation strain. The volume fraction of magnetic particles in MREs can be up to 40%; see [240, 11] and the references therein. As the volume fraction increases, the magneto-mechanical interaction of particles increases, improving the MR effects. Nevertheless, MREs are also becoming stiffer, which above a critical value of the volume fractions, can result in reduced mobility of particles, and hence a lower actuation strain [40]. On the contrary, low particle concentrations can reduce particle-particle interactions.

The size and shape of the magnetic particles in MREs are other important geometrical parameters. The particle size can range from $\sim 2\,\mu\mathrm{m}$ up to $\sim 200\,\mu\mathrm{m}$ [203, 124, 11]. Magnetically soft iron and magnetite particles are, in general, spherical [212], however considering elliptic-shaped particles can further enhance the MR effects since the rotation of elliptic particles in a compliant matrix can induce larger actuation strains than the

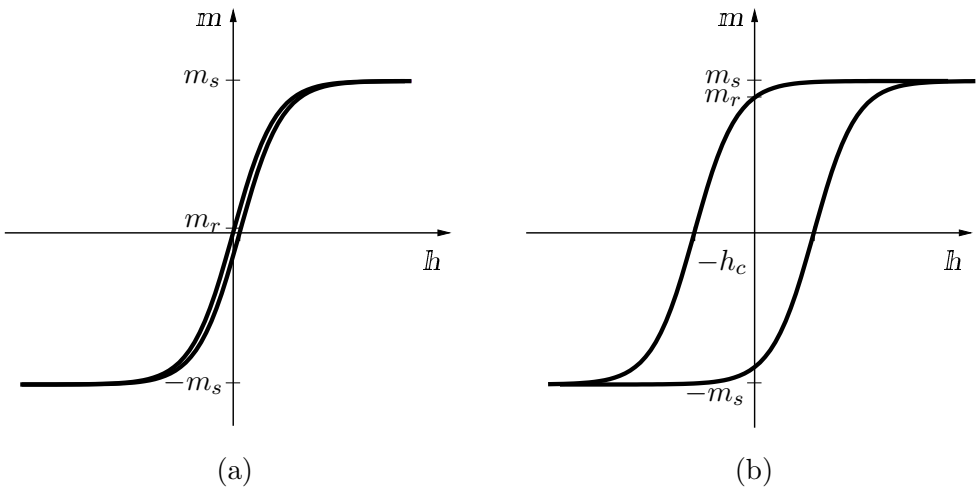

Figure 1.5: *Qualitative response of magnetically (**a**) soft and (**b**) hard materials.*

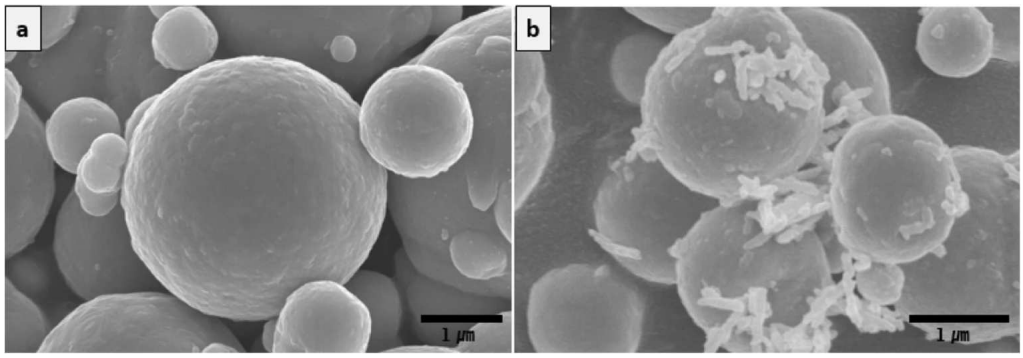

Figure 1.6: *SEM image of magnethorheological elastomer (MREs) from [124] (reproduced with permission from Springer Nature).* (**a**) MRE microstructure with carbonyl iron particles and (**b**) MRE microstructure with carbonyl iron particles and rod-shaped γ-Fe_2O_3 magnetic additives.

spherical ones. Such MRE microstructures have been investigated, for example, in [57]. By designing the microstructure of MREs and the shape of the magnetic particles, MREs can show not only tensile but also compressive and shear actuation strains; see, for example, [57, 41, 100, 40] and [183], Fig. 4.

In order to further enhance the magneto-mechanical coupling and improve the particle-particle and particle-matrix interactions, MREs can also contain magnetic and non-magnetic additives. In particular, we distinguish three types of additives: plasticizers, carbon black, and magnetic nanoadditives. While plasticizers are utilized to reduce the stiffness of the elastomeric matrix, carbon-based additives help to improve the mechanical properties of the matrix. Similarly, magnetic nanoadditives can enhance the actuation strain. Examples of these materials can be rod-like γ-Fe_2O_3 (see Fig. 1.6) and chromium dioxide (CrO_2) particles; see [124, 172, 120]. For a detailed description of the influence of additives on MREs, we refer to the review articles [3, 212].

With the advancement of fabrication techniques and 3D printing technology, MREs with complex microstructures and tailored macroscopic responses become more accessible; see [147, 9, 10, 188, 30]. Thus, mathematical models and homogenization techniques are useful for predicting the response of additively manufactured MREs and can also be deployed to guide the fabrication process.

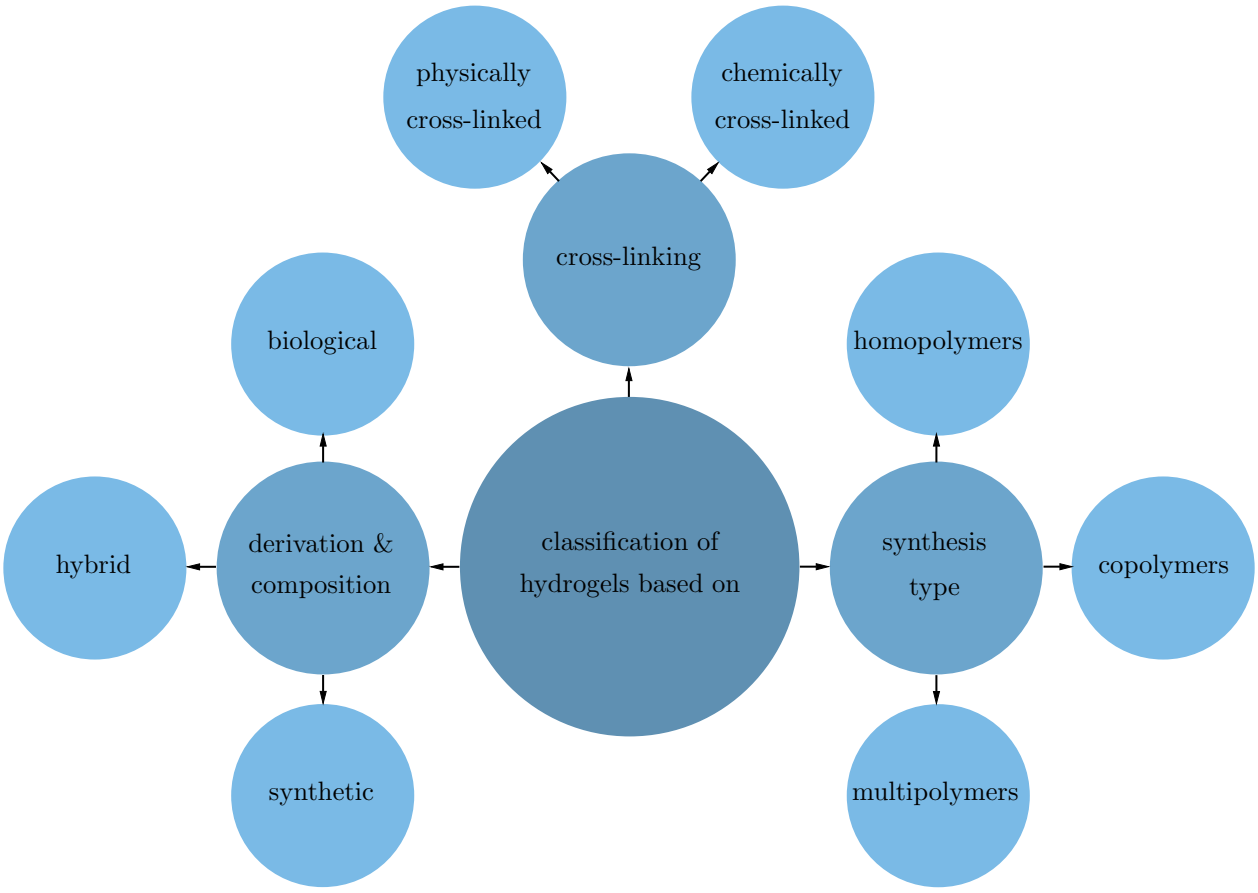

Figure 1.7: *A classification of hydrogels adapted from [119, 31, 4, 236, 138].*

1.3 Polymeric hydrogels

In addition to electro- and magneto-active polymers, the present thesis also deals with the modeling and stability analysis of polymeric hydrogels, which belong to the class of smart materials, too. Similar to electro- and magneto-active materials, hydrogels have favorable properties; they can be prepared as soft, biocompatible, biodegradable materials [178, 177, 73, 74, 236, 138]. Therefore, they have found applications in bio-medicine, agriculture, tissue engineering, and robotics [198, 93, 18, 17, 32]. When hydrogels are immersed in water or a biological fluid, they undergo swelling, resulting in large volumetric deformation. Activation deformation of hydrogels and release of biological fluid from the polymer network can be controlled by means of light, temperature, pH as well as electric and magnetic fields. These types of hydrogels belong to the class of multi-stimuli responsive hydrogels [119, 31]. However, in the present work, we focus on conventional hydrogels, where deformation is induced by the diffusion of a solvent into the polymer network [74, 4]. The capillary, osmotic, and hydration forces generated by the polymer-polymer and polymer-solvent interactions are considered responsible for the diffusion of the solvent, which is acting against the retractive forces of crosslinked polymer chains [196, 31].

The swelling behavior and diffusion phenomenon in hydrogels and their response to external stimuli are highly dependent on their polymer networks and the type of solvent. The polymer network is characterized by polymer volume fraction as well as molecular

weight and distance of chains between two neighboring crosslinks [196, 177, 24]. While the polymer volume fraction of the swollen hydrogel determines the amount of solvent in the hydrogel, the molecular weight of chains between two neighboring crosslinks characterizes the degree of crosslinking. The latter parameter, also known as the network mesh size, is the measure of available space between molecular chains. The polymerization method is one of the main factors that influences the mesh size. It is known that the polymerization in an aqueous solution yields a small mesh size that is measured by nanometers in poly(2-hydroxyethyl methacrylate) (pHEMA) gels [196]. By considering a freeze-thaw polymerization technique for these polymers, the mesh size can be increased [68, 31] and thus allow also delivery of macromolecular solvents [31]; also refer to [137] for detailed discussions on the fabrication techniques. The polymer network is also responsible for elastic response and initial stiffness of hydrogels. Moreover, the viscosity can also be influenced by the solvent's viscosity.

Hydrogels can be classified depending on constituting polymer, crosslinking, and synthesis type; refer to Fig. 1.7. The chemical composition, polymer network, and crosslinking can significantly influence the response of hydrogel. The polymer network of hydrogels can be crosslinked chemically, physically, or by the combination of both [31]. Early hydrogels, which were based on poly(2-hydroxyethyl methacrylate) (pHEMA) gels, were synthetic and had chemically crosslinked polymer networks [245]. These homopolymer hydrogels have found applications as contact lenses and drug delivery systems, among others. Other synthetic polymers often used in hydrogels are poly(vinyl alcohol) (PVA), poly(ethylene glycol) (PEG), and poly(acrylamide) (PAM) [177, 31]. In order to improve the properties of these polymers, their polymer network can also be co- or multi-polymerized. In contrast to chemically crosslinked hydrogels, physically crosslinked hydrogels utilize non-covalent interactions such as entanglements of polymer chains and hydrophobic or ionic interactions. This type of crosslinking is encountered in responsive hydrogels such as temperature- and pH-sensitive hydrogels [31]. Further detailed classifications and discussions can be found in the review articles [177, 119, 31, 4, 236, 138].

Furthermore, hydrogels are also manufactured with composite or cellular microstructures to tune their responses further and obtain controllable buckling patterns and deformation states [137, 131, 136, 243]. Similar to the electro- and magneto-active polymer composites, the behavior of such hydrogel composites and induced composite patterns can be determined by consideration of ideas from multiscale homogenization techniques; see Section 1.5.

1.4 Instabilities in soft-active materials and their applications

Soft-active materials undergo various types of instabilities, such as buckling, localization, snapping, wrinkling, creasing, pull-in, and cavitation, among others. The type of instability in a system depends on its material characteristics, geometrical forms, and loading conditions. Since the overall response of a system at an instability point can change unexpectedly, it could render the system expendable. Therefore, the prediction of instability points and the behavior of a considered system after this point are among the important tasks.

An instability point was usually considered a failure point and avoided in the course of the designing process or by deploying systems below the critical loading points. In

recent decades, instabilities are not only seen as unfavorable anymore, but they are rather exploited for the development of soft devices (such as sensors, actuators, absorbers) [192, 76, 108]. These devices can function near, and beyond an instability point [105, 108].

Instabilities can be of structural and material types. Buckling, snapping, and wrinkling are structural instabilities that can depend on the geometrical form of the structure. Slender structures, such as beams, plates, and shells, are known to be prone to buckling- or snapping-type instabilities. Along those lines, shear and kink bands, creasing, pull-in, cavitation, and phase transformation are usually associated with material instabilities. The material and structural instabilities can be related; for example, the buckling at a microscale of a composite has been shown to be related to localization-type material instabilities at the macroscale [1].

Both structural and material instabilities have found a wide range of applications [156, 135, 252, 192, 76, 108]. According to the review paper [76], instabilities are mainly applied in energy-based (such as energy production and dissipation) and motion-based application areas. Examples of energy-based applications can be energy harvesters, sensors, absorbers, and dampers, among others [135, 249, 115, 105, 132, 34, 51]. Examples of the motion-based applications can be actuators [118, 76]. Both applications usually take advantage of buckling or snapping in structures not only under mechanical loading but also under coupled electro-, magneto- and chemo-mechanical interactions. Other structural instabilities such as wrinkling have also found application in the control of stem cell morphology [65]; see also the review paper [36] for further examples.

In addition to the wide range of applications associated with structural instabilities, material instabilities associated with pull-in instabilities, or materials with negative stiffness components have also been exploited in micro-electro-mechanical systems as well as for seismic protection [173, 252]; see also [56, 107, 26]. Furthermore, instabilities are exploited in composites and metamaterials to obtain negative Poisson's ratio [6] and to tune acoustic and optical properties [242, 13, 59, 84, 255]. We refer to [108] for an extensive review of microscopic instabilities.

As discussed above, instabilities play an essential role in various engineering applications. They can be exploited for the development of soft devices. Nevertheless, in specific applications, they can render a system unusable. Furthermore, instabilities in periodic systems can also have mathematical implications. It is known that a microscopic instability influences the size of representative volume elements (RVEs) in periodic systems [163, 61]. Moreover, the development of localization-type macroscopic instabilities can yield mesh sensitivities [164]. Therefore, the prediction of instability points and the behavior of systems beyond this point are of utmost importance. In the present work, instabilities in composites under electro-, magneto- and chemo-mechanical interactions are of interest. In particular, we investigate microscopic structural and macroscopic material instabilities.

1.5 Multiscale modeling and instability analysis

In the above sections, we have discussed three types of coupling phenomena in electro- and magneto-active polymers as well as polymeric hydrogels. These are, namely, electro-mechanical, magneto-mechanical, and chemo-mechanical coupling responses. Above, we have discussed how a material's composition and microstructure can significantly affect

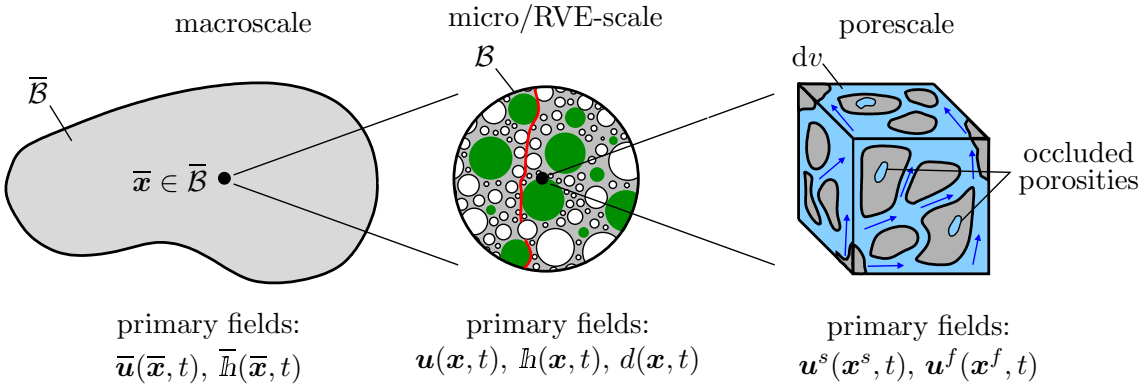

Figure 1.8: *Multi-scale homogenization of heterogeneous porous media.* Response of the material at a macroscale is determined through a highly heterogeneous representative volume element (RVE), which consists of various types of inclusions and micro-cracks. On the other hand, the response of the RVE at each material point may also be determined by means of homogenization over a smaller scale, which could contain, for example, a porous matrix and fluid filling the pores, as in the figure. Since a specific physical phenomenon could be associated with a specific length-scale, the response at a length-scale could be determined by a different set of primary variables than the parameters. Therefore, we need appropriate scale-bridging techniques to exchange kinematic and constitutive fields through the scales.

the coupling behavior. We now focus on the computational prediction of this coupling behavior. An essential approach studying the response of the materials based on their microstructure exploits homogenization techniques [69, 246, 163, 217, 53, 60]. By means of these methods, a heterogenous problem is replaced by an equivalent homogeneous problem, where the heterogeneities due to various effects can be solved at a different length scale assuming scale separation; see Fig. 1.8. An important step is then to bridge different scales, i.e., to downscale driving fields and to upscale the constitutive response. In the computational homogenization framework, these length scales are bridged via the Hill-Mandel macro-homogeneity condition [69, 70, 72].

In the present work, we focus on two scales, which we refer to as macro- and micro-scales, no matter what units of measure for length scales are. We exploit here the computational homogenization approach. In this approach, the macroscopic response is determined by averaging the microscopic response over a selected RVE under consideration of the Hill-Mandel condition [112]. This condition is fulfilled for a set of boundary conditions for the RVE problem, namely *(i)* linear Dirichlet, *(ii)* constant Neumann, and *(iii)* periodic fluctuations boundary conditions [152, 149]. For the pure mechanical case, the results obtained by the periodic boundary conditions are bounded from above by the linear displacement and from below by the constant traction boundary conditions [149]. In [122], a weak format of the periodic boundary conditions has been presented, which relaxes the requirement for a periodic discretization of an RVE. For a detailed discussion of various aspects of computational homogenization as well as boundary conditions, we refer to the review paper [202]. The computational homogenization framework has been successfully applied to determine the behavior of electro-, magneto-, thermo- and chemo-mechanically coupled problems in [205, 154, 100, 101, 40, 170, 227, 123, 165, 88, 180], among others.

Analytical and computational homogenization of electro-active materials with elastic and inelastic properties have been considered in [204, 205, 228, 251, 128, 220] at small

strains and in [187, 117, 103, 133, 155, 129, 130] at finite strains. Furthermore, an investigation of the influence of the microstructure on the effective response in laminated composites has been conducted in [228, 33, 201, 43, 239]. Similarly, homogenization techniques have been successfully applied for magneto-active composites. In [186], an analytical homogenization method has been proposed for magneto-elastic composites. This method has been exploited in [57] to estimate the effective response of composites with spherical and elliptic particles and in [58] for the development of a finite-strain constitutive model for magneto-elastic composites. Homogenization methods have also been used to develop constitutive functions that approximate the effective response. Such an approach has been considered in [126, 127], where constitutive functions for magneto-active composites with non-Gaussian polymer matrix and embedded iron and ferrofluid particles have been constructed; see also [160, 162] in a similar context. Next to analytical methods, computational homogenization methods have been deployed to determine the effective response of magneto-active composites [146, 92, 85, 100, 101, 40].

In the context of thermo-mechanics, computational homogenization techniques have been considered in [170, 227, 226, 35], among others. In these references, Similar to the purely mechanical and the coupled electro- and magneto-mechanical problems, a steady-state heat conduction problem at the microscale is solved. When considering the stationary microscopic problem, the effective response does not depend on the size of a selected RVE. The extension that considers the transient nature is developed in [123]. As a result of a transient microscopic problem, the size-effect is naturally introduced into the equations. The authors in [123] have also discussed that the size-effect becomes less pronounced when the RVE size becomes small. The framework of [123] has been further extended in [165, 89, 88] to model the diffusion-deformation processes. While these works exploit a saddle-point formulation, a minimization-type homogenization framework has also been proposed in [182] following [151, 23]. In [182] (Paper **C**), the impact of the material parameters and the RVE morphology on the effective response are discussed.

Homogenization techniques have also been used to predict material and structural instabilities in composites. Localization-type instabilities in porous elastic materials were first shown in [1]. There it was found that the effective energy function of a composite can lose strong ellipticity (rank-one convexity) while the microscopic energy function is polyconvex, which can manifest itself as a result of microscopic buckling [230, 61]. Material and structural instabilities have been investigated in many references for various types of composites [231, 134, 14, 148, 199, 216, 131]. The microscopic pattern transforming instabilities have found applications to manipulate wave propagation, optical properties and to obtain controllable enhanced performances [15, 84, 242, 108]. In the context of the coupled problems, microscopic instabilities can result in further possibilities as the deformation state of a composite can be controlled utilizing electric and magnetic fields as well as the diffusion of a solvent into the material. Investigations of localization-type macroscopic and buckling-type microscopic instabilities in electro- and magneto-active composites have been conducted in [47, 16, 44, 200, 58, 154, 63], among others. Here, microscopic instabilities have been investigated in laminated composites. Microscopic instabilities in particulate composites have been conducted in [185, 182, 83, 183]. In these references, the Bloch-Floquet analysis has been implemented to investigate the pattern-transforming instabilities in periodic composites; see also discussions in Paper **A** and Paper **B**.

In polymeric hydrogels, wrinkling- and creasing-type surface instabilities have been documented in [224, 234, 66, 65], among others. Associated analytical and numerical studies have been considered in [95, 94, 248, 49, 77, 221, 78]. Furthermore, in-plane pattern-transforming instabilities in periodic systems have been studied in [253, 255] and similar out-of-plane instabilities have been studied in [247, 244, 136]. All these studies have revealed a rich set of controllable patterns. Numerical investigations of such pattern transformations have been conducted in [169, 168] in two dimensions and in [157, 106] in three dimensions, among others. Although the studies in these references revealed vital insights into the underlying complex pattern formations, they did not account for the transient effect of the diffusion process; see [184] or Paper **D** for a detailed discussion.

1.6 Scope of the work and outline of the thesis

Considering the above discussion, the present work deals with computational homogenization and stability analysis of soft active composites. In particular, electro- and magneto-active polymers as well as polymeric hydrogels are under consideration. The present thesis is based on **four scientific publications** [185, 183, 182, 184], which are included in the thesis and denoted as **A**, **B**, **C**, **D**. The effective response of the respective composites is determined by exploiting computational homogenization. The computational homogenization for electro- and magneto-active polymers is based on the minimization formulation presented in [154]. For polymeric hydrogels, we have proposed a minimization-based variational homogenization following the ideas of [123], where a homogenization framework with a saddle-point structure has been presented. The reason for the consideration of minimization principles is due to their convenience in investigating instabilities. Nevertheless, instabilities can also be investigated via formulations with a saddle-point principle [154, 206, 49].

Macroscopic localization-type material instabilities and microscopic buckling-type structural instabilities are investigated for non-dissipative electro- and magneto-active composites (**A** and **B**) and dissipative hydrogel composites (**C** and **D**). The macroscopic instabilities are disclosed by checking the loss of strong ellipticity of coupled incremental moduli tensors. Microscopic instabilities are investigated considering the Bloch-Floquet analysis. For the polymeric hydrogels, the effective response is usually significantly influenced by the size of a considered RVE whenever a transient microscopic problem for hydrogel microstructures is considered. Here, we construct the boundary conditions for periodic microstructures with care based on experimental setups such that the results can be reduced to computations based on a unit-cell RVE.

The thesis is organized as follows. In Chapter 2, we review the basics of the finite-strain continuum mechanics. The chapter comprises four main sections. In Chapter 2.1, we give a geometrical description of a deforming body in a concise manner and introduce equations for the description of thermodynamic processes. Then, in Chapter 2.2 and 2.3, we discuss fundamentals of electro- and magneto-elasticity under quasi-static conditions. Finally, the governing equations of nonlinear magneto-electro-elasticity are given in Chapter 2.4. Coupling of electric and magnetic fields is possible through the deformation field in these equations, see [191, 190]; electrodynamic coupling is however not considered. The modeling of fluid transport is not discussed in this chapter, but carefully introduced in the papers **C** and **D**. We also refer to [39, 141, 22] for a detailed derivation of equations.

The second part of the thesis contains the papers that constitute the core of the thesis and present the obtained results. In the following section of this chapter, we list the associated papers and briefly summarize them.

1.7 List and short summaries of associated publications

1.7.1 Paper A: Computational stability analysis of periodic electroactive polymer composites across scales

Computer Methods in Applied Mechanics and Engineering, volume 337, pages 165–197, accepted: January 16, 2018

DOI: doi.org/10.1016/j.cma.2018.01.020

This publication investigates macroscopic and microscopic instabilities in elastic electroactive particulate composites within a computational homogenization framework. Here we employ a four-field variational formulation to avoid volumetric locking for quasi-incompressible RVEs. In this formulation, we consider linear interpolations for the displacement and vector potential fields and element-wise constant interpolations for the dilatation and pressure fields. The formulation is solved using a finite-element formulation. Discontinuous interpolation of the dilatation and pressure fields allows their condensation from the equations. Hence, we obtain a minimization-type setting. Within the presented formulation, we investigate instabilities. First, we analyze the onset of localization-type material instabilities by checking the loss of strong ellipticity of the effective energy. Then, we detect microscopic instabilities using the Bloch-Floquet analysis. Our numerical examples examine instabilities for a rich set of RVE microstructures with spherical and elliptic inclusions. The influence of the inclusions' volume fraction and aspect ratio have been investigated. Observations show that the larger volume fractions of inclusions reduce the values of critical loadings due to the increased particle-particle interactions. Furthermore, we observe that macroscopic or microscopic instabilities can be primary depending on the loading condition and the geometry. In addition, the alignment of elliptic particles from the applied electric displacement significantly affects the onset and type of instabilities. Moreover, we illustrate various patterns under different values of the macroscopic deformation gradient and electric displacement vector. We have also considered a post-buckling analysis of a microstructure, which shows the evolution of the local deformation and electric field after a microscopic instability point. To conclude, the results of the publication can be considered to determine the RVE size and hence the effective response after a microscopic instability point. Furthermore, the results could help design microstructures to tune the response of a composite and to obtain controllable patterns.

It is noted that this publication builds up on [181] and extends the framework to a Hu-Washizu-type variational formulation. In the developed framework, the macroscopic and microscopic instability analysis are considered. Accordingly, the numerical examples are extended.

1.7.2 Paper B: Multiscale stability analysis of periodic magnetorheological elastomers

Mechanics of Materials, volume 159, pages 103699:1–19, accepted: November 28, 2020

DOI: doi.org/10.1016/j.mechmat.2020.103699

The present publication deals with the material and structural instabilities of magneto-active particulate composites. In particular, we consider microstructures with elastic polymer matrix and embedded magnetically soft and mechanically stiff particles. Hence, the effective response of composite can be determined within a non-dissipative homogenization framework. To solve the microscopic problem, we utilize Q_2P_1-type finite-element formulation utilizing a four-field (displacement, vector potential, dilatation, and pressure) variational principle. The linear, discontinuous dilatation and pressure fields can be condensed out of the equations, yielding a minimization principle. Hence, we obtain a favorable setting for the stability analysis. We further exploit a Langevin-type energy function for the particles to describe the saturation of magnetization. In this setting, we determine localization-type material instabilities by checking the positive definiteness of the generalized acoustic tensor, which we derive in the two-point continuum setting. Following, we analyze the microscopic pattern-transforming instabilities of an equilibrium state by superimposing Bloch-Floquet-type boundary conditions. Finally, we consider a set of numerical examples containing microstructures with spherical and elliptic particles. The parameters of particles are chosen to correspond to carbonyl-iron. The macroscopic deformation gradient and the magnetic induction vector derive the microstructure. Because of the saturation of magnetization, the stability curves for magneto-active composites are substantially different from their electo-active analogous. Above all, we observe that the stability curves saturate in the case of magneto-active composites. The studies include not only the influence of the morphology of particles on the instabilities but also the influence of the saturation magnetization and the magnetic susceptibility parameters. In addition to two-phase microstructures, we have also considered a three-phase microstructure. The obtained results for these composites are in agreement with experimental observations. As a concluding remark, the results help to determine the microscopic patterns in periodic magneto-active composites and their responses after an instability point. Furthermore, determining the loss of strong ellipticity of the effective response is also important concerning the convergence of the macroscopic problem since it implies the loss of quasiconvexity. As a result, the macroscopic problem can suffer from not having regular minimizers when a first-gradient theory is considered. In addition, we note that the patterns could be exploited to design microstructures showing negative Poisson's ratio or to tune the acoustic response of the composites, among others, as exploited in references.

1.7.3 Paper C: Computational homogenization of transient chemo-mechanical processes based on a variational minimization principle

Advanced Modeling and Simulation in Engineering Sciences, volume 7:35, pages 1–26, accepted: May 6, 2020

DOI: doi.org/10.1016/j.jmps.2023.105250

The publication deals with the first-order computational homogenization of diffusion-

deformation processes. In contrast to the common first-order homogenization theories, we consider the RVE problem to be transient in the present work. A transient microscopic problem introduces microscopic size-effect into the equations, which does not appear in the steady-state RVE problems. Such theories have been successfully applied to various problems in the literature within a saddle-point formulation. However, such formulations are known to be limited by inf-sup stability conditions. Here, we propose a minimization-based homogenization theory for chemo-mechanics. This formulation and its implementation into a conforming Raviart-Thomas-type finite-element formulation have been discussed in detail. Finally, we present a wide range of numerical examples to showcase the size-effect due to changes in the RVE size and RVE morphologies. We show how the effective response can go beyond the classical bounds for large enough RVE sizes. Nevertheless, when an RVE size becomes sufficiently small, the results can coincide with the steady-state solutions. We have also included studies that illustrate how the results converge to the stationary solution over time depending on the material parameters of RVE constituents. The formulation can be used to predict the response of highly heterogeneous problems by taking the transient effects into account.

1.7.4 Paper D: Swelling-induced pattern transformations of periodic hydrogels – from the wrinkling of internal surfaces to the buckling of thin films

Journal of the Mechanics and Physics of Solids, volume 175, pages 105250:1–25, accepted February 18, 2023

DOI: doi.org/10.1016/j.jmps.2023.105250

The publication deals with pattern transformations in periodic hydrogel microstructures within a transient framework. Here we employ a minimization-based formulation to model the swelling of hydrogels due to the diffusion of a solvent. Next, we employ the Bloch-Floquet analysis for short- and long-wavelength pattern transformations. Since the long-wavelength instabilities are associated with the loss of strong ellipticity of effective response, we also check these instabilities. To determine the effective mechanical response of the composite, we employ ideas from the computational homogenization of transient microstructures. To avoid any size-effect in the system and reduce computations to a unit-cell RVE, we establish boundary conditions on the microstructures based on experimental setups. Our numerical examples consider two-dimensional periodic structures and three-dimensional in-plane periodic films. Investigations of pattern transformations in 2D single-phase perforated structures yield experimentally observed diamond-plate patterns. However, in perforated structures with coatings, we also observe novel patterns combing the pattern transformation with wrinkling at the internal surfaces. The 3D studies also reveal compelling patterns that highly depend on the morphology of the microstructure. Here not only wrinkling of reinforced films are observed, but also saddle-like shapes are encountered. The observed patterns could be exploited for the development of soft devices.

Chapter 2

Continuum Mechanics of Magneto-Electro-Elasticity

The chapter introduces the continuum thermodynamics of magneto-electro-elasticity. It is organized into three main sections, where the first section introduces thermodynamics in a convected curvilinear and a rectilinear coordinate system. Following, essential concepts, transformation rules and physical quantities that describe the deforming continuum body are discussed; mass, momentum, energy, and entropy balance laws are derived. The second and third sections are dedicated to magneto-electro-elasticity. Here, the coupling of electric and magnetic fields is only possible through the deformation of a continuum body; the electrodynamic coupling of the fields is not considered. After introducing the governing equations of electrostatics and magnetostatics, the balance laws of elasticity are extended to magneto-electro-elasticity under isothermal conditions.

2.1 Fundamentals of Continuum Mechanics

In this section, a geometrical description of the continuum mechanics of a deformable body is reviewed. The fundamental kinematic quantities and equations, as well as the governing partial differential equations are derived. In order to provide descriptive insight into specific concepts of continuum mechanics, such as push-forward and pull-back operations and Lie derivatives, among many others, we consider the description of the body in curvilinear coordinate systems. Nevertheless, all the concepts are related to the Cartesian coordinates, too. A detailed description of the concepts introduced in this section can be found, for example, in [37, 139, 167, 75, 233, 222, 153, 104, 225].

2.1.1 Placement of physical body in Euclidean space

A continuum body being a physical object $\mathfrak{B}$ is characterized by certain physical properties and texture. It can be considered as a set of physical points $\mathfrak{P}$ (e.g., set of molecules) which are embedded into the Euclidean space $\mathcal{R}^3$ via one-to-one point transformations $\boldsymbol{\chi}_t(\mathfrak{P})$ [222, 153, 104]. At a particular time instance t, $\boldsymbol{\chi}_t(\mathfrak{B})$ defines the placement of the deforming physical body in the Euclidean space, which is referred to as a configuration. The set of configurations at various times determines the motion of the continuum body. Here, we distinguish two configurations: the reference or Lagrangian configuration $\mathcal{B}_0 = \boldsymbol{\chi}_0(\mathfrak{B})$ and the current or Eulerian configuration $\mathcal{B}_t = \boldsymbol{\chi}_t(\mathfrak{B})$. The reference configuration, also referred to as the material configuration, is usually associated with an assumed stress-free, undeformed state of the deforming physical body. Therefore, the relative deformation and stresses are defined from this configuration. Consequently, we

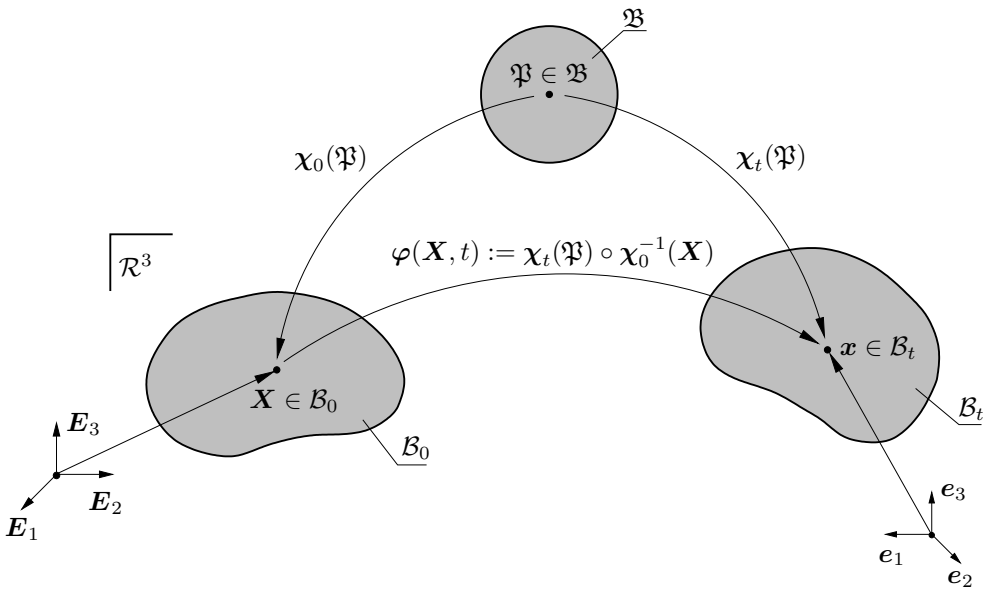

Figure 2.1: *Embedding a physical body into Euclidean space* $\mathcal{R}^3$. A deforming physical body is embedded into the Euclidean space $\mathcal{R}^3$ via a placement mapping $\boldsymbol{\chi}_t(\mathfrak{P})$. A particular placement of the physical body in the Euclidean space is referred to as a configuration. The reference or Lagrangian configuration $\mathcal{B}_0 = \boldsymbol{\chi}_0(\mathfrak{B})$ corresponds to the stress-free undeformed state of the body. The current or Eulerian configuration $\mathcal{B}_t = \boldsymbol{\chi}_t(\mathfrak{B})$ corresponds to the current deformed state of the body. Both configurations are connected via a one-to-one point transformation $\boldsymbol{x} = \boldsymbol{\varphi}(\boldsymbol{X},t)$.

introduce the so-called deformation map as the composition of the current and reference placement maps, i.e., $\boldsymbol{\varphi}(\boldsymbol{X},t) := \boldsymbol{\chi}_t(\mathfrak{P}) \circ \boldsymbol{\chi}_0^{-1}(\boldsymbol{X})$, which links the reference and current configurations, to describe the motion of the body rather than describing it via the placement mapping $\boldsymbol{\chi}_t(\mathfrak{P})$ directly; see also Fig. 2.1 and [37, 139, 153],

$$\boldsymbol{\varphi}(\boldsymbol{X},t) = \boldsymbol{\chi}_t(\mathfrak{P}) \circ \boldsymbol{\chi}_0^{-1}(\boldsymbol{X}) : \begin{cases} \mathcal{B}_0 \times \mathcal{T} \to \mathcal{B}_t \in \mathcal{R}^3 \\ (\boldsymbol{X},t) \mapsto \boldsymbol{x} = \boldsymbol{\varphi}(\boldsymbol{X},t) \end{cases}, \tag{2.1}$$

where $\boldsymbol{x}$ denotes the position of a physical point $\mathfrak{P}$ in the current (or spatial) configuration $\mathcal{B}_t$. The velocity and acceleration of a material point in the current configuration can thus be defined, respectively, as

$$\begin{aligned} \boldsymbol{v}(\boldsymbol{x},t) &= \big\{\frac{\partial}{\partial t}\boldsymbol{\varphi}(\boldsymbol{X},t)\big\} \circ \boldsymbol{\varphi}^{-1}(\boldsymbol{x},t) = \boldsymbol{V}(\boldsymbol{X},t) \circ \boldsymbol{\varphi}^{-1}(\boldsymbol{x},t) \quad \text{and} \\ \boldsymbol{a}(\boldsymbol{x},t) &= \big\{\frac{\partial^2}{\partial t^2}\boldsymbol{\varphi}(\boldsymbol{X},t)\big\} \circ \boldsymbol{\varphi}^{-1}(\boldsymbol{x},t) = \boldsymbol{A}(\boldsymbol{X},t) \circ \boldsymbol{\varphi}^{-1}(\boldsymbol{x},t)\,, \end{aligned} \tag{2.2}$$

where $\boldsymbol{V}(\boldsymbol{X},t)$ and $\boldsymbol{A}(\boldsymbol{X},t)$ are the material velocity and acceleration vectors parameterized with the material position vectors; however belong to the current configuration. The acceleration $\boldsymbol{a}(\boldsymbol{x},t)$ in the current configuration can also be computed from the spatial velocity $\boldsymbol{v}(\boldsymbol{x},t)$

$$\boldsymbol{a}(\boldsymbol{x},t) = \frac{d}{\mathrm{d}t}\boldsymbol{v}(\boldsymbol{x},t) = \frac{\partial}{\partial t}\boldsymbol{v}(\boldsymbol{x},t) + \operatorname{grad}\boldsymbol{v}(\boldsymbol{x},t) \cdot \boldsymbol{v}(\boldsymbol{x},t)\,, \tag{2.3}$$

where $\operatorname{grad}\boldsymbol{v} := \boldsymbol{l}$ is the spatial velocity gradient.

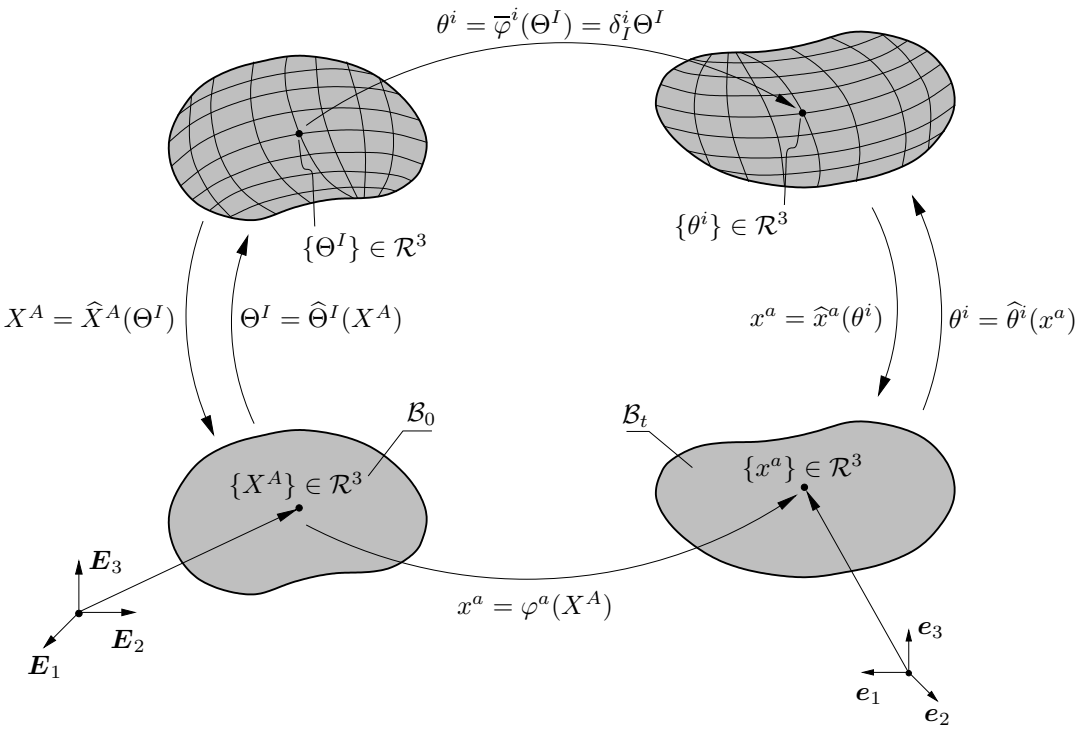

Figure 2.2: *Parameterization of the continuum body using Cartesian and curvilinear coordinates.* The physical body embedded into the Euclidean space can be parameterized via Cartesian coordinates as well as curvilinear coordinates. In this work we consider convected curvilinear coordinates. This means that the coordinates of the points in the reference and current configurations are the same when curvilinear coordinates are useed, i.e., $\theta^i = \delta^i_I \Theta^I$.

2.1.2 Parameterization of continuum body: rectilinear and curvilinear coordinates

The physical body embedded into the Euclidean space can be parameterized with either rectilinear coordinates (e.g., Cartesian coordinates) or curvilinear coordinates, see Fig. 2.2. In this section, we describe the parameterization with respect to both coordinates and, therefore, we will also represent the same quantities with respect to both coordinates [222, 104]. For the rectilinear coordinates, we assume that each physical point $\mathfrak{P}$ is described by the material $X^A \in \mathcal{R}^3$ and spatial $x^a \in \mathcal{R}^3$ rectilinear coordinates in the Euclidean space. As in [222], the indices A, B, C, D and a, b, c, d are reserved for rectilinear coordinates in the reference and current configurations, respectively. Similarly, we consider $\Theta^I \in \mathcal{R}^3$ and $\theta^i \in \mathcal{R}^3$ for the curvilinear coordinates of the physical body in the material and spatial configurations, respectively. In this case, the indices I, J, K, L and i, j, k, l are reserved for curvilinear coordinates correspondingly in the reference and current configurations. The rectilinear and curvilinear coordinates can be related via one-to-one coordinate transformations as described in Fig. 2.2 (see also [222])

$$X^A = \widehat{X}^A(\Theta^I) \quad \text{or} \quad \Theta^I = \widehat{\Theta}^I(X^A) \quad \text{and} \quad x^a = \widehat{x}^a(\theta^i) \quad \text{or} \quad \theta^i = \widehat{\theta}^i(x^a)\,. \tag{2.4}$$

In addition, we focus on convected curvilinear coordinates, which means that the position of a material point in the reference and current configurations can be described by the same set of parameters. In other words, the relation $\theta^i = \delta^i_I \Theta^I = \Theta^i \in \mathcal{R}^3$ between the curvilinear coordinates of the reference and current configurations holds. Here, $\delta^i_I = 1$ for $i = I$ and $\delta^i_I = 0$ for $i \neq I$ is the Kronecker delta.

The position vectors $\boldsymbol{X}$ and $\boldsymbol{x}$ in the current and reference configurations, respectively, are given as follows

$$\boldsymbol{X} = X^A \boldsymbol{E}_A = \widehat{X}^A(\Theta^I)\boldsymbol{E}_A = \widehat{\boldsymbol{X}}(\Theta^I) \quad \text{and} \quad \boldsymbol{x} = x^a \boldsymbol{e}_a = \widehat{x}^a(\theta^i)\boldsymbol{e}_a = \widehat{\boldsymbol{x}}(\theta^i)\,, \tag{2.5}$$

where $\boldsymbol{E}_A \in \mathcal{R}^3$ and $\boldsymbol{e}_a \in \mathcal{R}^3$ denote the orthonormal bases of the Cartesian coordinate system correspondingly in the reference and current configurations[1].These bases are constant and do not change with the material point. Therefore, the corresponding infinitesimal line elements can be determined as

$$\begin{aligned} \mathrm{d}\boldsymbol{X} &= \mathrm{d}X^A \boldsymbol{E}_A = \frac{\partial \widehat{X}^A}{\partial \Theta^I}\mathrm{d}\Theta^I \boldsymbol{E}_A = \mathrm{d}\Theta^I \widehat{X}^A_{,I}\boldsymbol{E}_A = \mathrm{d}\Theta^I \boldsymbol{G}_I \quad \text{and} \\ \mathrm{d}\boldsymbol{x} &= \mathrm{d}x^a \boldsymbol{e}_a = \frac{\partial \widehat{x}^a}{\partial \theta^i}\mathrm{d}\theta^i \boldsymbol{e}_a = \mathrm{d}\theta^i \widehat{x}^a_{,i}\boldsymbol{e}_a = \mathrm{d}\theta^i \boldsymbol{g}_i\,, \end{aligned} \tag{2.6}$$

where $\boldsymbol{G}_I = \partial\widehat{\boldsymbol{X}}/\partial\Theta^I = \widehat{X}^A_{,I}\boldsymbol{E}_A$ is the material tangent vector to the material curvilinear coordinate line Θ^I (where $\Theta^J = const.$ and $\Theta^K = const.$ with $I \neq J \neq K$) and $\boldsymbol{g}_i = \partial\widehat{\boldsymbol{x}}/\partial\theta^i = \widehat{x}^a_{,i}\boldsymbol{e}_a$ is the spatial tangent vector to the spatial curvilinear coordinate line θ^i (where $\theta^j = const.$ and $\theta^k = const.$ with $i \neq j \neq k$); see, e.g., [222, 153, 104]. We refer to these vectors as covariant base vectors. They form the material and spatial tangent spaces denoted as $T_{\boldsymbol{X}}\mathcal{B}_0$ and $T_{\boldsymbol{x}}\mathcal{B}_t$, respectively. The dual contravariant bases of $\boldsymbol{G}_I$ and $\boldsymbol{g}_i$ are defined from the following relation

$$\boldsymbol{G}_I \cdot \boldsymbol{G}^J = \delta^J_I \quad \text{and} \quad \boldsymbol{g}_i \cdot \boldsymbol{g}^j = \delta^j_i\,, \tag{2.7}$$

where δ^J_I and δ^j_i are Kronecker deltas. The above relations hold for the following definitions of $\boldsymbol{G}^I$ and $\boldsymbol{g}^i$ from the corresponding curvilinear coordinates as

$$\begin{aligned} \boldsymbol{G}^I &= \mathrm{Grad}\,\widehat{\Theta}^I = \frac{\partial\widehat{\Theta}^I}{\partial\boldsymbol{X}} = \frac{\partial\widehat{\Theta}^I}{\partial X^A}\boldsymbol{E}^A = \widehat{\Theta}^I_{,A}\boldsymbol{E}^A \quad \text{and} \\ \boldsymbol{g}^i &= \mathrm{grad}\,\widehat{\theta}^i = \frac{\partial\widehat{\theta}^i}{\partial\boldsymbol{x}} = \frac{\partial\widehat{\theta}^i}{\partial x^a}\boldsymbol{e}^a = \widehat{\theta}^i_{,a}\boldsymbol{e}^a, \end{aligned} \tag{2.8}$$

which are normal to the material ($\Theta^I = const.$) and spatial ($\theta^i = const.$) hypersurfaces, respectively. These normals form the bases for the material and spatial normal or cotangent spaces denoted by $T^\star_{\boldsymbol{X}}\mathcal{B}_0$ and $T^\star_{\boldsymbol{x}}\mathcal{B}_t$, respectively.

2.1.3 Metric tensors: covariant and contravariant identity tensors

In order to be able to measure the distances between points, the lengths of vectors, and the angles between vectors, we introduce the covariant material and spatial metrics, respectively, ([222, 153, 104])

$$\begin{aligned} G_{IJ} &= \boldsymbol{G}_I \cdot \boldsymbol{G}_J = \widehat{X}^A_{,I}\widehat{X}^B_{,J}\boldsymbol{E}_A \cdot \boldsymbol{E}_B = \widehat{X}^A_{,I}\widehat{X}^B_{,J}\delta_{AB} \quad \text{and} \\ g_{ij} &= \boldsymbol{g}_i \cdot \boldsymbol{g}_j = \widehat{x}^a_{,i}\widehat{x}^b_{,j}\boldsymbol{e}_a \cdot \boldsymbol{e}_b = \widehat{x}^a_{,i}\widehat{x}^b_{,j}\delta_{ab} \end{aligned} \tag{2.9}$$

[1]Einstein's summation convention over the repeated indices of the same type are considered if one of them is upper and the other is a lower index.

as well as the contravariant material and spatial metrics, respectively,

$$\begin{aligned} G^{IJ} &= \boldsymbol{G}^I \cdot \boldsymbol{G}^J = \frac{\partial \widehat{\Theta}^I}{\partial \boldsymbol{X}} \cdot \frac{\partial \widehat{\Theta}^J}{\partial \boldsymbol{X}} = \widehat{\Theta}^I_{,A} \boldsymbol{E}^A \cdot \widehat{\Theta}^J_{,B} \boldsymbol{E}^B = \widehat{\Theta}^I_{,A} \widehat{\Theta}^J_{,B} \delta^{AB} \quad \text{and} \\ g^{ij} &= \boldsymbol{g}^i \cdot \boldsymbol{g}^j = \frac{\partial \widehat{\theta}^i}{\partial \boldsymbol{x}} \cdot \frac{\partial \widehat{\theta}^j}{\partial \boldsymbol{x}} = \widehat{\theta}^i_{,a} \boldsymbol{e}^a \cdot \widehat{\theta}^j_{,b} \boldsymbol{e}^b = \widehat{\theta}^i_{,a} \widehat{\theta}^j_{,b} \delta^{ab} \,. \end{aligned} \tag{2.10}$$

With these metrics at hand, we can derive the subsequent relations

$$G^{IJ} G_{JK} = \delta^I_K \quad \text{and} \quad g^{ij} g_{jk} = \delta^i_k \tag{2.11}$$

and the metrics have the properties to lower or raise the indices

$$\boldsymbol{G}_I = G_{IJ} \boldsymbol{G}^J, \quad \boldsymbol{G}^I = G^{IJ} \boldsymbol{G}_J \quad \text{and} \quad \boldsymbol{g}_i = g_{ij} \boldsymbol{g}^j, \quad \boldsymbol{g}^i = g^{ij} \boldsymbol{g}_j \,. \tag{2.12}$$

Based on the above introduced covariant and contravariant metrics, we present the material and spatial covariant identity tensors $\boldsymbol{G}$ and $\boldsymbol{g}$ (without indices), respectively. We start from their representation in the rectilinear coordinates and give the alternative representation in the curvilinear coordinates

$$\begin{aligned} \boldsymbol{G} :=& \delta_{AB} \boldsymbol{E}^A \otimes \boldsymbol{E}^B = \widehat{X}^C_{,A} \widehat{X}^D_{,B} \delta_{CD} \boldsymbol{E}^A \otimes \boldsymbol{E}^B = \frac{\partial \widehat{X}^C}{\partial \Theta^I} \frac{\partial \widehat{\Theta}^I}{\partial X^A} \frac{\partial \widehat{X}^D}{\partial \Theta^J} \frac{\partial \widehat{\Theta}^J}{\partial X^B} \delta_{CD} \boldsymbol{E}^A \otimes \boldsymbol{E}^B \\ &= \frac{\partial \widehat{X}^C}{\partial \Theta^I} \frac{\partial \widehat{X}^D}{\partial \Theta^J} \delta_{CD} \big(\frac{\partial \widehat{\Theta}^I}{\partial X^A} \boldsymbol{E}^A \big) \otimes \big(\frac{\partial \widehat{\Theta}^J}{\partial X^B} \boldsymbol{E}^B \big) = G_{IJ} \boldsymbol{G}^I \otimes \boldsymbol{G}^J \quad \text{and} \\ \boldsymbol{g} :=& \delta_{ab} \boldsymbol{e}^a \otimes \boldsymbol{e}^b = g_{ij} \boldsymbol{g}^i \otimes \boldsymbol{g}^j \,. \end{aligned} \tag{2.13}$$

Analogously, the covariant identity tensors in the material and spatial configurations denoted by $\boldsymbol{G}^{-1}$ and $\boldsymbol{g}^{-1}$, respectively, read

$$\boldsymbol{G}^{-1} := \delta^{AB} \boldsymbol{E}_A \otimes \boldsymbol{E}_B = G^{IJ} \boldsymbol{G}_I \otimes \boldsymbol{G}_J \quad \text{and} \quad \boldsymbol{g}^{-1} := \delta^{ab} \boldsymbol{e}_a \otimes \boldsymbol{e}_b = g^{ij} \boldsymbol{g}_i \otimes \boldsymbol{g}_j \,. \tag{2.14}$$

Please note that although $\boldsymbol{G} \equiv \boldsymbol{G}^{-1}$ and $\boldsymbol{g} \equiv \boldsymbol{g}^{-1}$, we use different tensorial notations in order to distinguish the contravariant and covariant representations of the same object in the index notation[2]. In addition, the following tensorial notations are sometimes used to differentiate the covariant and contravariant representation of the same vector in the index notation, i.e., we have in the material configuration

$$\boldsymbol{M}^\sharp := M^A \boldsymbol{E}_A = \mathsf{M}^I \boldsymbol{G}_I \quad \text{and} \quad \boldsymbol{M}^\flat := M_A \boldsymbol{E}^A = \mathsf{M}_I \boldsymbol{G}^I, \tag{2.15}$$

and in the spatial configuration

$$\boldsymbol{m}^\sharp := m^a \boldsymbol{e}_a = \mathsf{m}^i \boldsymbol{g}_i \quad \text{and} \quad \boldsymbol{m}^\flat := m_a \boldsymbol{e}^a = \mathsf{m}_i \boldsymbol{g}^i, \tag{2.16}$$

where $\boldsymbol{M}^\sharp \equiv \boldsymbol{M}^\flat$ and $\boldsymbol{m}^\sharp \equiv \boldsymbol{m}^\flat$ denote the same vectors but in different representations[3]. Thus, regardless of whether the covariant or contravariant representation is used, the vectors stay invariant.

[2]Here a covariant (contravariant) representation of a vector means that the vector's coefficients are given in the covariant form (contravariant form) and its bases in the contravariant form (covariant form).

[3]Note that here $\boldsymbol{M}^\sharp$ and $\boldsymbol{m}^\sharp$ or $\boldsymbol{M}^\flat$ and $\boldsymbol{m}^\flat$ are not related to each other via any mapping.

For the tensor operations in the index notation, it is convenient not to consider the bases explicitly. Therefore, we accept the following relations

$$\boldsymbol{M}^\flat = \boldsymbol{G}\boldsymbol{M}^\sharp \quad \text{or} \quad \boldsymbol{M}^\sharp = \boldsymbol{G}^{-1}\boldsymbol{M}^\flat \quad \text{and} \quad \boldsymbol{m}^\flat = \boldsymbol{g}\boldsymbol{m}^\sharp \quad \text{or} \quad \boldsymbol{m}^\sharp = \boldsymbol{g}^{-1}\boldsymbol{m}^\flat\,, \tag{2.17}$$

which can be given in the index notations w.r.t. the curvilinear coordinates as follows

$$\mathsf{M}_I = G_{IJ}\mathsf{M}^J \quad \text{or} \quad \mathsf{M}^I = G^{IJ}\mathsf{M}_J \quad \text{and} \quad \mathsf{m}_i = G_{ij}\mathsf{M}^j \quad \text{or} \quad \mathsf{M}^i = G^{ij}\mathsf{M}_j\,. \tag{2.18}$$

In the following, we will drop the superscripts and consider them explicitly only when necessary. Furthermore, we accept $\boldsymbol{M} := \boldsymbol{M}^\sharp$ and $\boldsymbol{m} := \boldsymbol{m}^\sharp$.

Having introduced the metrics as well as the metric tensors, the inner product takes the following form in the reference configuration

$$\boldsymbol{M}\cdot\boldsymbol{M} = \boldsymbol{M}\cdot\boldsymbol{M}^\flat = \boldsymbol{M}\cdot\boldsymbol{G}\boldsymbol{M} = \underbrace{M^A M^B \delta_{AB} = M^A M_A}_{\substack{\text{Cartesian}\\ \text{coordinates}}} = \underbrace{\mathsf{M}^I\mathsf{M}^J G_{IJ} = \mathsf{M}^I\mathsf{M}_I}_{\substack{\text{curvilinear}\\ \text{coordinates}}}, \tag{2.19}$$

and in the current configuration

$$\boldsymbol{m}\cdot\boldsymbol{m} = \boldsymbol{m}\cdot\boldsymbol{m}^\flat = \boldsymbol{m}\cdot\boldsymbol{g}\boldsymbol{m} = \underbrace{m^a m^b \delta_{ab} = m^a m_a}_{\substack{\text{Cartesian}\\ \text{coordinates}}} = \underbrace{\mathsf{m}^i\mathsf{m}^j g_{ij} = \mathsf{m}^i\mathsf{m}_i}_{\substack{\text{curvilinear}\\ \text{coordinates}}}. \tag{2.20}$$

2.1.4 Fundamental mappings of continuum mechanics

Deformation gradient: tangent and normal maps. Considering the convected coordinates, i.e., $\theta^i = \delta^i_I \Theta^I$ and the definition of the spatial tangent vector, we can write

$$\begin{aligned}\boldsymbol{g}_i = \widehat{x}^a_{,i}\boldsymbol{e}_a &= \frac{\partial\varphi^a}{\partial X^A}\frac{\partial\widehat{X}^A}{\partial\Theta^I}\delta^I_i\boldsymbol{e}_a = \frac{\partial\varphi^a}{\partial X^A}\frac{\partial\widehat{X}^B}{\partial\Theta^I}\delta^A_B\delta^I_i\boldsymbol{e}_a \\ &= \frac{\partial\varphi^a}{\partial X^A}\frac{\partial\widehat{X}^B}{\partial\Theta^I}\boldsymbol{E}^A\cdot\boldsymbol{E}_B\delta^I_i\boldsymbol{e}_a = \underbrace{\left[\frac{\partial\varphi^a}{\partial X^A}(\boldsymbol{e}_a\otimes\boldsymbol{E}^A)\right]}_{\boldsymbol{F}}\underbrace{\left[\frac{\partial\widehat{X}^B}{\partial\Theta^I}\delta^I_i\boldsymbol{E}_B\right]}_{\boldsymbol{G}_I\delta^I_i = \boldsymbol{G}_i} = \boldsymbol{F}\boldsymbol{G}_i\,,\end{aligned} \tag{2.21}$$

where $\boldsymbol{g}_i \equiv \boldsymbol{g}_I$ or $\boldsymbol{G}_i \equiv \boldsymbol{G}_I$ can be considered, since $\theta^i \equiv \Theta^i$ or $\theta^I \equiv \Theta^I$ holds in the case of convected coordinates. In the above equation, we identify $\boldsymbol{F}$ as the *tangent map* which is defined as Fréchet derivative of deformation map $\boldsymbol{\varphi}(\boldsymbol{X}, t)$

$$\boxed{\boldsymbol{F}(\boldsymbol{X},t) = D\boldsymbol{\varphi}(\boldsymbol{X},t) = \underbrace{F^a{}_A\,\boldsymbol{e}_a\otimes\boldsymbol{E}^A}_{\substack{\text{Cartesian}\\ \text{coordinates}}} = \underbrace{\delta^i_I\boldsymbol{g}_i\otimes\boldsymbol{G}^I}_{\substack{\text{curvilinear}\\ \text{coordinates}}}\,,} \tag{2.22}$$

where $F^a{}_A = \partial\varphi^a/\partial X^A = \varphi^a_{,A}$ are the coefficients of the deformation gradient in the Cartesian coordinates. Analogously, if we start from the definition of the material tangent

vector, we obtain

$$\begin{aligned}\boldsymbol{G}_I = \widehat{X}^A_{,I}\boldsymbol{E}_A = \frac{\partial X^A}{\partial x^a}\frac{\partial \widehat{x}^a}{\partial \theta^i}\delta^i_I\boldsymbol{E}_A = \frac{\partial X^A}{\partial x^a}\frac{\partial \widehat{x}^b}{\partial \theta^i}\delta^a_b\delta^i_I\boldsymbol{E}_A \\ = \frac{\partial X^A}{\partial x^a}\frac{\partial \widehat{x}^b}{\partial \theta^i}\boldsymbol{e}^a\cdot\boldsymbol{e}_b\delta^i_I\boldsymbol{E}_A = \underbrace{\left[\frac{\partial X^A}{\partial x^a}(\boldsymbol{E}_A\otimes\boldsymbol{e}^a)\right]}_{\boldsymbol{F}^{-1}}\underbrace{\left[\frac{\partial \widehat{x}^b}{\partial \theta^i}\delta^i_I\boldsymbol{e}_b\right]}_{\boldsymbol{g}_i\delta^i_I=\boldsymbol{g}_I} = \boldsymbol{F}^{-1}\boldsymbol{g}_I\,,\end{aligned} \tag{2.23}$$

where the inverse of the deformation gradient $\boldsymbol{F}^{-1}$ reads

$$\boxed{\boldsymbol{F}^{-1} = \underbrace{(F^{-1})^A{}_a\boldsymbol{E}_A\otimes\boldsymbol{e}^a}_{\substack{\text{Cartesian}\\ \text{coordinates}}} = \underbrace{\delta^I_i\boldsymbol{G}_I\otimes\boldsymbol{g}^i}_{\substack{\text{curvilinear}\\ \text{coordinates}}}\,.} \tag{2.24}$$

Consequently, the deformation gradient $\boldsymbol{F}: T_{\boldsymbol{X}}\mathcal{B}_0 \to T_{\boldsymbol{x}}\mathcal{B}_t$ maps a tangent vector in the reference configuration to a tangent vector in the current configuration. Likewise, the inverse deformation gradient $\boldsymbol{F}^{-1}: T_{\boldsymbol{x}}\mathcal{B}_t \to T_{\boldsymbol{X}}\mathcal{B}_0$ is a tangent map from the current to the reference configuration. Thus, the following results hold

$$\mathrm{d}\boldsymbol{x} = \boldsymbol{F}\mathrm{d}\boldsymbol{X} = F^a{}_A\,\mathrm{d}X^A\boldsymbol{e}_a = \delta^i_I\mathrm{d}\mathsf{X}^I\boldsymbol{g}_i = \mathrm{d}\mathsf{x}^i\boldsymbol{g}_i\,, \tag{2.25}$$

and

$$\mathrm{d}\boldsymbol{X} = \boldsymbol{F}^{-1}\mathrm{d}\boldsymbol{x} = (F^{-1})^A{}_a\mathrm{d}x^a\boldsymbol{E}_A = \delta^I_i\mathrm{d}\mathsf{x}^i\boldsymbol{G}_I\,. \tag{2.26}$$

Analogously, we can derive the following relation for the material and spatial normals

$$\boldsymbol{g}^i = \boldsymbol{F}^{-T}\boldsymbol{G}^i \quad\text{and}\quad \boldsymbol{G}^I = \boldsymbol{F}^T\boldsymbol{g}^I\,, \tag{2.27}$$

where $\boldsymbol{F}^{-T}$ is identified as the *normal map*. $\boldsymbol{F}^{-T}: T^\star_{\boldsymbol{X}}\mathcal{B}_0 \to T^\star_{\boldsymbol{x}}\mathcal{B}_t$ maps a normal vector in the reference configuration to a normal vector in the current configuration. Likewise, $\boldsymbol{F}^T: T^\star_{\boldsymbol{x}}\mathcal{B}_t \to T^\star_{\boldsymbol{X}}\mathcal{B}_0$ is a normal map from the current configuration to the reference configuration.

Area map. In order to arrive at a mapping between the area elements of the reference and current configurations, we first introduce an infinitesimal referential and a current area element using the definition of the cross-product from two infinitesimal line elements in the reference and current configurations, respectively, i.e., $\mathrm{d}\boldsymbol{A} = \mathrm{d}\boldsymbol{X}_1\times\mathrm{d}\boldsymbol{X}_2 \in T^\star_{\boldsymbol{X}}\mathcal{B}_0$ and $\mathrm{d}\boldsymbol{a} = \mathrm{d}\boldsymbol{x}_1\times\mathrm{d}\boldsymbol{x}_2 = \boldsymbol{F}\mathrm{d}\boldsymbol{X}_1\times\boldsymbol{F}\mathrm{d}\boldsymbol{X}_2 = \operatorname{cof}\boldsymbol{F}[\mathrm{d}\boldsymbol{X}_1\times\mathrm{d}\boldsymbol{X}_2] \in T^\star_{\boldsymbol{X}}\mathcal{B}_t$. This reveals that the cofactor of the deformation gradient $\operatorname{cof}\boldsymbol{F}: T^\star_{\boldsymbol{X}}\mathcal{B}_0 \to T^\star_{\boldsymbol{x}}\mathcal{B}_t$ is the area map between the reference and current configurations

$$\mathrm{d}\boldsymbol{a} = J\boldsymbol{F}^{-T}\mathrm{d}\boldsymbol{A} = J(F^{-1})^A{}_a\mathrm{d}A_A\boldsymbol{e}^a = J\delta^I_i\mathrm{d}\mathsf{A}_I\boldsymbol{g}^i\,. \tag{2.28}$$

If we compare the last equation with the normal map given in (2.27), we can notice a similarity. This is also due to the association of the area elements with the normal vectors.

Volume map. Similar to the area map, we also establish a mapping relationship between the current infinitesimal volume element $\mathrm{d}v$ and the referential infinitesimal volume element $\mathrm{d}V$ exploiting the triple-product among three infinitesimal line elements,

i.e., $\mathrm{d}v = \boldsymbol{F}\mathrm{d}\boldsymbol{X}_1 \cdot (\boldsymbol{F}\mathrm{d}\boldsymbol{X}_2 \times \boldsymbol{F}\mathrm{d}\boldsymbol{X}_3) = \det \boldsymbol{F}[\mathrm{d}\boldsymbol{X}_1 \cdot (\mathrm{d}\boldsymbol{X}_2 \times \mathrm{d}\boldsymbol{X}_3)] = J\mathrm{d}V$. As a result, the deformation gradient's determinant (also referred to as Jacobian) $J = \det \boldsymbol{F} : \mathcal{R}^{3\times 3} \to \mathcal{R}_+$ is obtained to be the volume map

$$\mathrm{d}v = \det \boldsymbol{F}\mathrm{d}V = \det[F^a{}_A]\mathrm{d}V = \frac{\sqrt{\det[g_{ij}]}}{\sqrt{\det[G_{IJ}]}}\mathrm{d}V\,, \tag{2.29}$$

where it is clear that $J = \det \boldsymbol{F} > 0$ should hold since vanishing or negative volume is not physical. The last term in the above equations can be derived considering the relations $F^a{}_A = \varphi^a_{,A} = \widehat{x}^a_{,i}\delta^i_I\widehat{\Theta}^I_{,A}$, $\det[\widehat{x}^a_{,i}] = \sqrt{\det[g_{ij}]}$ and $\det[\widehat{X}^A_{,I}] = \sqrt{\det[G_{IJ}]}$.

2.1.5 Push-forward and pull-back operations

Based on the tangent and normal maps given above, we introduce two kinds of *push-forward* operations of a referential vector to the current configuration

$$\begin{aligned} \boldsymbol{m} &= \boldsymbol{\varphi}_t^\star(\boldsymbol{M}) = \boldsymbol{F}\boldsymbol{M} = \boldsymbol{F}(\mathsf{M}^I\boldsymbol{G}_I) = \mathsf{M}^I\boldsymbol{g}_I \quad \text{and} \\ \overline{\boldsymbol{m}}^\flat &= \boldsymbol{\varphi}_t^\star(\boldsymbol{M}^\flat) = \boldsymbol{F}^{-T}\boldsymbol{M}^\flat = \boldsymbol{F}^{-T}(\mathsf{M}_I\boldsymbol{G}^I) = \mathsf{M}_I\boldsymbol{g}^I. \end{aligned} \tag{2.30}$$

The particular push-forward operation is established in relation to the transformation property of the vector, e.g., the tangent and normal vectors undergo different transformations under a deformation, as discussed above.

From (2.30), we observe that the coefficients of the vectors in the reference and current configurations do not change after the push-forward operations in the convected curvilinear coordinates. Although we can choose the vector in the reference configuration in a way that $\mathsf{M}^I = G^{IJ}\mathsf{M}_J$ holds, $\mathsf{M}^I \neq g^{IJ}\mathsf{M}_J$ since $\boldsymbol{m} \neq \overline{\boldsymbol{m}}^\flat$ are not the same objects after the push-forward operations.

After the push-forward operation using the tangent map, the tangential components of the vector in the reference configuration stay tangential to the convected coordinate lines in the current configuration. Likewise, after the push-forward operation using the normal map, the normal components of the vector in the reference configuration stay normal to the convected coordinate lines in the current configuration; see Fig. 2.3 for a geometrical interpretation in a simplified two-dimensional body.

Similarly, we also introduce two kinds of *pull-back* operations of spatial vectors to the reference configuration

$$\begin{aligned} \boldsymbol{M} &= \boldsymbol{\varphi}_{t\star}(\boldsymbol{m}) = \boldsymbol{F}^{-1}\boldsymbol{m} = \boldsymbol{F}^{-1}(\mathsf{m}^i\boldsymbol{g}_i) = \mathsf{m}^i\boldsymbol{G}_i \quad \text{and} \\ \overline{\boldsymbol{M}}^\flat &= \boldsymbol{\varphi}_{t\star}(\boldsymbol{m}^\flat) = \boldsymbol{F}^T\boldsymbol{m}^\flat = \boldsymbol{F}^T(\mathsf{m}_i\boldsymbol{g}^i) = \mathsf{m}_i\boldsymbol{G}^i. \end{aligned} \tag{2.31}$$

Likewise, the coefficients of the vectors do not change after the pull-back operation in the convected curvilinear coordinates. Again, although $\mathsf{m}^i = g^{ij}\mathsf{m}_j$ holds, but $\mathsf{m}^i \neq G^{ij}\mathsf{m}_j$, since $\boldsymbol{M} \neq \overline{\boldsymbol{M}}^\flat$ after pull-back operation.

2.1.6 Measures of deformation: strain tensors

Having introduced the fundamental mappings with respect to the reference and current configurations, we can also determine the length of a vector in the current configuration

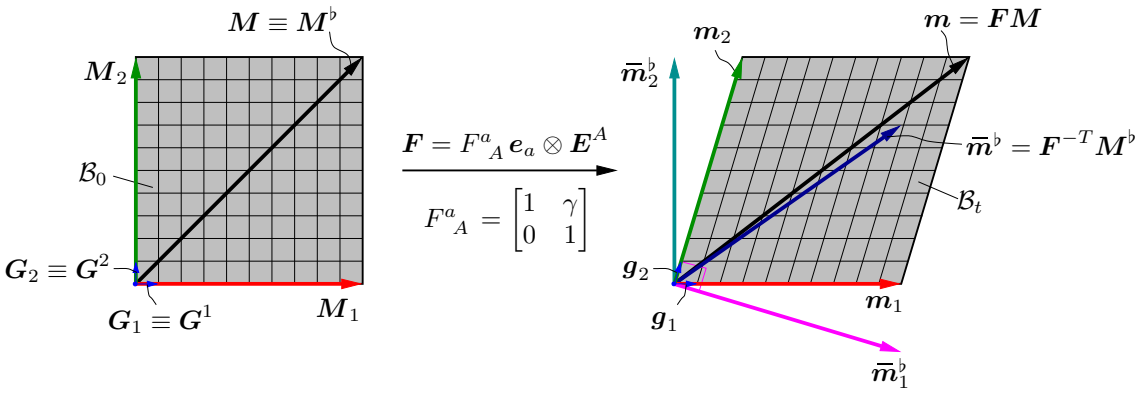

Figure 2.3: *Push-forward of a vector $\boldsymbol{M}$ using the tangent and normal maps in two dimensions.* In the figure, the push-forward operation is described for a two-dimensional body which undergoes a pure shear deformation. When the vector $\boldsymbol{M}$ is pushed forward to the current configuration using the tangent map $\boldsymbol{F}$, the components $\boldsymbol{m}_1 = \boldsymbol{F}\boldsymbol{M}_1$ and $\boldsymbol{m}_2 = \boldsymbol{F}\boldsymbol{M}_2$ of the vector stay tangent to the convected coordinate lines. Likewise, when the vector $\boldsymbol{M}$ is pushed forward to the current configuration using the normal map $\boldsymbol{F}^{-T}$, the components which are also normal to the coordinate lines in the references configurations stay normal in the current configuration. In the latter case, $\overline{\boldsymbol{m}}^\flat_1 = \boldsymbol{F}^{-T}\boldsymbol{M}_1$ and $\overline{\boldsymbol{m}}^\flat_2 = \boldsymbol{F}^{-T}\boldsymbol{M}_2$ are considered. Here, $\boldsymbol{m} = \boldsymbol{c}\overline{\boldsymbol{m}}^\flat$, with $\boldsymbol{c}$ being the Finger tensor, holds, see (2.34)$_2$.

from its referential counterpart as ([37, 139, 222, 153, 104])

$$\|\mathrm{d}\boldsymbol{x}\|^2_{\boldsymbol{g}} = \mathrm{d}\boldsymbol{x}\cdot\mathrm{d}\boldsymbol{x} = \mathrm{d}\boldsymbol{x}\cdot\boldsymbol{g}\mathrm{d}\boldsymbol{x} = \mathrm{d}\boldsymbol{X}\cdot(\boldsymbol{F}^T\boldsymbol{g}\boldsymbol{F})\mathrm{d}\boldsymbol{X} = \mathrm{d}\boldsymbol{X}\cdot\boldsymbol{C}\mathrm{d}\boldsymbol{X} = \|\mathrm{d}\boldsymbol{X}\|^2_{\boldsymbol{C}}\,, \tag{2.32}$$

and the length of a vector in the reference configuration from its spatial counterpart as

$$\|\mathrm{d}\boldsymbol{X}\|^2_{\boldsymbol{G}} = \mathrm{d}\boldsymbol{X}\cdot\mathrm{d}\boldsymbol{X} = \mathrm{d}\boldsymbol{X}\cdot\boldsymbol{G}\mathrm{d}\boldsymbol{X} = \mathrm{d}\boldsymbol{x}\cdot(\boldsymbol{F}^{-T}\boldsymbol{G}\boldsymbol{F}^{-1})\mathrm{d}\boldsymbol{x} = \mathrm{d}\boldsymbol{x}\cdot\boldsymbol{c}\mathrm{d}\boldsymbol{x} = \|\mathrm{d}\boldsymbol{x}\|^2_{\boldsymbol{c}}\,, \tag{2.33}$$

where we have employed the right Cauchy-Green deformation tensors $\boldsymbol{C}$ and the Finger tensor $\boldsymbol{c}$ as the pull-back of the spatial metric tensor $\boldsymbol{g}$ and push-forward of the material metric tensor $\boldsymbol{G}$, respectively, i.e.,

$$\begin{aligned}
\boldsymbol{C} &:= \boldsymbol{\varphi}_t^\star(\boldsymbol{g}) = \boldsymbol{F}^T\boldsymbol{g}\boldsymbol{F} = \boldsymbol{F}^T\boldsymbol{F} \\
&= F^a{}_A\, F^b{}_B\, \delta_{ab}\boldsymbol{E}^A\otimes\boldsymbol{E}^B = C_{AB}\boldsymbol{E}^A\otimes\boldsymbol{E}^B = g_{IJ}\boldsymbol{G}^I\otimes\boldsymbol{G}^J \quad \text{and} \\
\boldsymbol{c} &:= \boldsymbol{\varphi}_{t\star}(\boldsymbol{G}) = \boldsymbol{F}^{-T}\boldsymbol{G}\boldsymbol{F}^{-1} = \boldsymbol{F}^{-T}\boldsymbol{F}^{-1} \\
&= (F^{-1})^A{}_a (F^{-1})^B{}_b \delta_{AB}\boldsymbol{e}^a\otimes\boldsymbol{e}^b = c_{ab}\boldsymbol{e}^a\otimes\boldsymbol{e}^b = G_{ij}\boldsymbol{g}^i\otimes\boldsymbol{g}^j\,.
\end{aligned} \tag{2.34}$$

where $g_{ij} \equiv g_{IJ}$ and $G_{ij} \equiv G_{IJ}$ hold due to the considered convected coordinates. Here we also observe that when considering the convected curvilinear coordinates, the coefficients of the tensors $\boldsymbol{C}$ and $\boldsymbol{g}$ and $\boldsymbol{G}$ and $\boldsymbol{c}$ in the reference and current configurations are the same. This directly allows interpreting $\boldsymbol{C}$ as the spatial metric tensor in the reference configuration and $\boldsymbol{c}$ as the material metric tensor in the current configuration. $\boldsymbol{C}$ and $\boldsymbol{c}$, being metric tensors in the Euclidean space, are also symmetric and positive-definite. Thus, the Finger tensor $\boldsymbol{c}$ acts on an Eulerian vector and allows measuring the length of this vector in the reference configuration, and the right Cauchy-Green deformation tensor $\boldsymbol{C}$ acts on a Lagrangian vector and allows measuring the length of this vector in the current configuration; see (2.32) and (2.33). For the geometrical description of the mapping of these tensors between the tangent and cotangent spaces, see Fig. 2.4.

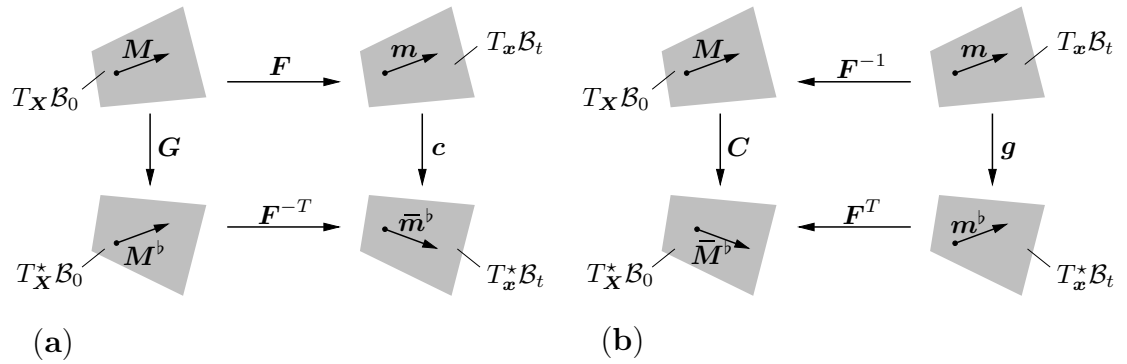

Figure 2.4: *Mapping properties of metric tensors.* (**a**) The metric tensors $\boldsymbol{G}$ and $\boldsymbol{c}$ allow to determine the length of a vector in the reference configuration from the reference and current representations of a vector, respectively, i.e., $\|\boldsymbol{M}\|^2_{\boldsymbol{G}} = \|\boldsymbol{m}\|^2_{\boldsymbol{c}}$; (**b**) The metric tensors $\boldsymbol{C}$ and $\boldsymbol{g}$ allow to determine the length of a vector in the current configuration from the reference and current representations of a vector, respectively, i.e., $\|\boldsymbol{M}\|^2_{\boldsymbol{C}} = \|\boldsymbol{m}\|^2_{\boldsymbol{g}}$.

Based on the metric tensors and their material and spatial representations, the local *strain tensors* are introduced. Two of the most commonly used strain tensors are the Green-Lagrange and the Euler-Almansi tensor [153]. These tensors are defined below as the difference between the spatial and material metric tensors

$$\boldsymbol{E} = \frac{1}{2}(\boldsymbol{C} - \boldsymbol{G}) \quad \text{and} \quad \boldsymbol{e} = \frac{1}{2}(\boldsymbol{g} - \boldsymbol{c})\,. \tag{2.35}$$

They are given in the Cartesian coordinates as

$$E_{AB} = \frac{1}{2}(C_{AB} - G_{AB}) \quad \text{and} \quad e_{ab} = \frac{1}{2}(g_{ab} - c_{ab})\,. \tag{2.36}$$

For the more generalized forms of these strain tensors, i.e., the so-called Seth-Hill family of strain tensors, see [211, 71, 150].

2.1.7 Rate of spatial variables and Lie derivative

We start with the time derivative of the covariant bases in the spatial configuration, i.e.,

$$\boldsymbol{g}_i = \boldsymbol{F}\boldsymbol{G}_i \quad \Rightarrow \quad \dot{\boldsymbol{g}}_i = \overline{\boldsymbol{F}\boldsymbol{G}_i}^{\cdot} = \dot{\boldsymbol{F}}\boldsymbol{F}^{-1}\boldsymbol{F}\boldsymbol{G}_i = \boldsymbol{l}\boldsymbol{g}_i\,, \tag{2.37}$$

where $\boldsymbol{l} := \dot{\boldsymbol{F}}\boldsymbol{F}^{-1} = \operatorname{grad}\boldsymbol{v}$ is the spatial velocity gradient. It is a second-order mixed-variant tensor, i.e., $\boldsymbol{l} = l^a{}_b \boldsymbol{e}_a \otimes \boldsymbol{e}^b$ in the Cartesian coordinates. Thus, the time derivative of Eulerian tangent vectors can be determined using a mapping with the spatial velocity gradient. Likewise, the time derivative of an infinitesimal line element in the spatial configuration is determined as $\overline{\mathrm{d}\boldsymbol{x}}^{\cdot} = \boldsymbol{l}\mathrm{d}\boldsymbol{x}$.

Analogously, the time derivative of the contravariant bases in the spatial configuration can also be defined using the spatial velocity gradient $\boldsymbol{l}$ as

$$\boldsymbol{G}^i = \boldsymbol{F}^T\boldsymbol{g}^i \quad \Rightarrow \quad \boldsymbol{0} = \overline{\boldsymbol{F}^T}^{\cdot}\boldsymbol{g}^i + \boldsymbol{F}^T\dot{\boldsymbol{g}}^i \quad \Rightarrow \quad \dot{\boldsymbol{g}}^i = -\boldsymbol{l}^T\boldsymbol{g}^i\,. \tag{2.38}$$

Having the above results at hand, we take the rate of the squared length of an infinitesimal line element in the spatial configuration as

$$\overline{\|\mathrm{d}\boldsymbol{x}\|^2_{\boldsymbol{g}}}^{\cdot} = \overline{\mathrm{d}\boldsymbol{x}\cdot\boldsymbol{g}\mathrm{d}\boldsymbol{x}}^{\cdot} = \overline{\mathrm{d}\boldsymbol{x}}^{\cdot}\cdot\boldsymbol{g}\mathrm{d}\boldsymbol{x} + \boldsymbol{g}\mathrm{d}\boldsymbol{x}\cdot\overline{\mathrm{d}\boldsymbol{x}}^{\cdot} = 2\mathrm{d}\boldsymbol{x}\cdot\frac{1}{2}[(\boldsymbol{g}\boldsymbol{l})^T + \boldsymbol{g}\boldsymbol{l}]\mathrm{d}\boldsymbol{x} = 2\mathrm{d}\boldsymbol{x}\cdot\boldsymbol{d}\mathrm{d}\boldsymbol{x}\,, \tag{2.39}$$

where we have used $\dot{\boldsymbol{g}} = \boldsymbol{0}$. The latter immediately follows from the representation of the covariant identity tensor $\boldsymbol{g}$ in the Cartesian coordinates; see $(2.13)_2$. In the above equation, $\boldsymbol{d} := \mathrm{sym}(\boldsymbol{gl})$ is called the covariant rate of deformation tensor, which characterizes the rate of change in the length of a vector. Although we do not show here, $\boldsymbol{d}$ can also be used to characterize the rate of change of an angle between two infinitesimal line elements due to shear deformation, see [167]. Thus, it follows from (2.39) that in the following relation

$$\overline{\mathrm{d}\dot{\boldsymbol{x}}} = \boldsymbol{l}\mathrm{d}\boldsymbol{x} = \boldsymbol{g}^{-1}(\boldsymbol{d} + \boldsymbol{w})\mathrm{d}\boldsymbol{x} \tag{2.40}$$

the skew-symmetric spin tensor $\boldsymbol{w} = \mathrm{skew}(\boldsymbol{gl})$ characterizes the rate of change in a vector due to a rigid rotation. This interpretation becomes clear, if we consider the rate of an Eulerian unit vector $\widetilde{\boldsymbol{m}}$

$$\dot{\widetilde{\boldsymbol{m}}} = \overline{\Big(\frac{\mathrm{d}\dot{\boldsymbol{x}}}{\|\mathrm{d}\boldsymbol{x}\|}\Big)} = \boldsymbol{l}\widetilde{\boldsymbol{m}} - (\widetilde{\boldsymbol{m}} \cdot \boldsymbol{d}\widetilde{\boldsymbol{m}})\widetilde{\boldsymbol{m}}\,. \tag{2.41}$$

Contracting the last equation with $\widetilde{\boldsymbol{m}}^\flat = \boldsymbol{g}\widetilde{\boldsymbol{m}}$ and considering $\widetilde{\boldsymbol{m}} \cdot \widetilde{\boldsymbol{m}}^\flat = 1$, we can write the following expression

$$\dot{\widetilde{\boldsymbol{m}}} \cdot \boldsymbol{g}\widetilde{\boldsymbol{m}} = \widetilde{\boldsymbol{m}} \cdot \boldsymbol{gl}\widetilde{\boldsymbol{m}} - \widetilde{\boldsymbol{m}} \cdot \boldsymbol{d}\widetilde{\boldsymbol{m}} = \widetilde{\boldsymbol{m}} \cdot \boldsymbol{w}\widetilde{\boldsymbol{m}} = \boldsymbol{0} \quad \Rightarrow \quad \dot{\widetilde{\boldsymbol{m}}} = \boldsymbol{g}^{-1}\boldsymbol{w}\widetilde{\boldsymbol{m}}\,, \tag{2.42}$$

where we have exploited the skew-symmetry of the spin tensor $\boldsymbol{w}$. Thus, we can interpret the spin tensor as the rate of change of an Eulerian unit tangent vector due to a rigid rotation.

The rate of deformation tensor can also be defined as the *Lie derivative* of the covariant metric tensor $\boldsymbol{g}$ as

$$\boldsymbol{d} = \frac{1}{2}\pounds_{\boldsymbol{v}}\boldsymbol{g} \quad \text{with} \quad \pounds_{\boldsymbol{v}}\boldsymbol{g} = \boldsymbol{gl} + (\boldsymbol{gl})^T = \boldsymbol{\varphi}_t^\star(\dot{\boldsymbol{C}})\,. \tag{2.43}$$

The Lie derivative of a spatial object is invariant under a rigid rotation of a continuum body and is, therefore, often considered to describe the incremental or rate-type constitutive equations of the material in the Eulerian configuration. It is defined as follows ([222, 153, 104])

$$\pounds_{\boldsymbol{v}}(\cdot) := \boldsymbol{\varphi}_t^\star\Big(\frac{\mathrm{d}}{\mathrm{d}t}\{\boldsymbol{\varphi}_{t\star}(\cdot)\}\Big) \quad \text{or} \quad \pounds_{\boldsymbol{v}}(\cdot) := \text{push-forward}\Big(\frac{\mathrm{d}}{\mathrm{d}t}\{\text{pull-back}(\cdot)\}\Big)\,. \tag{2.44}$$

In order to have some insight into this derivative, we consider an Eulerian tangent vector $\boldsymbol{m}$ and take the Lie derivative as given below

$$\pounds_{\boldsymbol{v}}\boldsymbol{m} = \boldsymbol{\varphi}_t^\star\Big(\frac{\mathrm{d}}{\mathrm{d}t}\{\boldsymbol{\varphi}_{t\star}(\boldsymbol{m})\}\Big) = \boldsymbol{F}\overline{\dot{\boldsymbol{F}^{-1}\boldsymbol{m}}} = \dot{\boldsymbol{m}} - \boldsymbol{l}\boldsymbol{m} = \overline{\dot{\mathsf{m}}^i}\boldsymbol{g}_i\,, \tag{2.45}$$

where we have used the relation (2.37). This equation allows interpreting the Lie derivative as the temporal change of an object relative to a deforming observer with the continuum body.

For completeness, we also give the Lie derivative of an Eulerian normal vector $\boldsymbol{n}$

$$\pounds_{\boldsymbol{v}}\boldsymbol{n} = \boldsymbol{\varphi}_t^\star\Big(\frac{\mathrm{d}}{\mathrm{d}t}\{\boldsymbol{\varphi}_{t\star}(\boldsymbol{n})\}\Big) = \boldsymbol{F}^{-T}\overline{\dot{\boldsymbol{F}^T\boldsymbol{n}}} = \dot{\boldsymbol{n}} + \boldsymbol{l}^T\boldsymbol{n} = \overline{\dot{\mathsf{n}}_i}\boldsymbol{g}^i\,, \tag{2.46}$$

where we have used the relation (2.38). Likewise, we observe that the Lie derivative is only associated with the rate of change of the curvilinear coefficient with fixed bases.

Furthermore, we introduce the contravariant rate of deformation tensor $\boldsymbol{d}^\sharp$ as

$$\boldsymbol{d}^\sharp = -\frac{1}{2}\pounds_{\boldsymbol{v}}\boldsymbol{g}^{-1} \quad \text{with} \quad \pounds_{\boldsymbol{v}}\boldsymbol{g}^{-1} = -\boldsymbol{l}\boldsymbol{g}^{-1} - (\boldsymbol{l}\boldsymbol{g}^{-1})^T = \boldsymbol{\varphi}_t^\star(\overline{\dot{\boldsymbol{C}^{-1}}})\,, \tag{2.47}$$

where $\overline{\dot{\boldsymbol{g}^{-1}}} = \boldsymbol{0}$ has been considered. $\boldsymbol{d}^\sharp$ can analogously be exploited to measure the rate of change in the squared length of spatial normal vectors.

Finally, we give the material rate of the infinitesimal spatial area and volume elements, which can be obtained from (2.28) and (2.29) as

$$\frac{\mathrm{d}}{\mathrm{d}t}(\mathrm{d}\boldsymbol{a}) = \overline{\dot{\mathrm{d}\boldsymbol{a}}} = -\boldsymbol{l}^T\mathrm{d}\boldsymbol{a} + \mathrm{d}\boldsymbol{a}\,\mathrm{div}\,\boldsymbol{v} \quad \text{and} \quad \frac{\mathrm{d}}{\mathrm{d}t}(\mathrm{d}v) = \overline{\dot{\mathrm{d}v}} = \mathrm{d}v\,\mathrm{div}\,\boldsymbol{v}\,. \tag{2.48}$$

2.1.8 Integral theorems and rate of volume integrals

As a basis for the derivations of the following sections, we introduce integral identities and rate of volume integrals in this section. In particular, we focus on two integral theorems, namely Gauss' theorem and Stokes' theorem. The theorems are used to transfer, for example, a volume integral to a surface integral or vice versa. Such transformations are essential to derive local balance equations from their global forms. In addition to the integral theorems, we also discuss in detail the rate of volume integrals in the Lagrangian and Eulerian configurations.

Gauss' theorem. This theorem is also referred to as the *divergence theorem*. The theorem can be applied to transfer a surface integral of a continuous variable to a volume integral. Let us consider a subdomain $\mathcal{P}_0 \subseteq \mathcal{B}_0$ in the Lagrangian configuration, which deforms to an Eulerian subdomain $\mathcal{P}_t \subseteq \mathcal{B}_t$. Surfaces of the subdomains are denoted as $\partial\mathcal{P}_0$ and $\partial\mathcal{P}_t$, respectively. The divergence theorem then reads in the reference and current configurations as

$$\begin{aligned}\int_{\partial\mathcal{P}_0} \boldsymbol{\mathfrak{Q}}(\boldsymbol{X},t)\cdot\mathrm{d}\boldsymbol{A} = \int_{\partial\mathcal{P}_0} \boldsymbol{\mathfrak{Q}}(\boldsymbol{X},t)\cdot\boldsymbol{N}\,\mathrm{d}A = \int_{\mathcal{P}_0} \mathrm{Div}[\boldsymbol{\mathfrak{Q}}(\boldsymbol{X},t)]\mathrm{d}V \quad \text{and}\\ \int_{\partial\mathcal{P}_t} \mathfrak{q}(\boldsymbol{x},t)\cdot\mathrm{d}\boldsymbol{a} = \int_{\partial\mathcal{P}_t} \mathfrak{q}(\boldsymbol{x},t)\cdot\boldsymbol{n}\,\mathrm{d}a = \int_{\mathcal{P}_t} \mathrm{div}[\mathfrak{q}(\boldsymbol{x},t)]\mathrm{d}v\,,\end{aligned} \tag{2.49}$$

respectively. Here $\boldsymbol{N}$ and $\boldsymbol{n}$ are the Lagrangian and Eulerian outward normals of the surfaces $\partial\mathcal{P}_0$ and $\partial\mathcal{P}_t$, respectively. The notations Div and div denote the divergence operations with respect to $\boldsymbol{X}$ and $\boldsymbol{x}$, correspondingly. $\boldsymbol{\mathfrak{Q}}$ and $\mathfrak{q}$ are arbitrary Lagrangian and Eulerian quantities. In case the following relation between these quantities holds

$$\int_{\partial\mathcal{P}_t} \mathfrak{q}(\boldsymbol{x},t)\cdot\mathrm{d}\boldsymbol{a} = \int_{\partial\mathcal{P}_0} \boldsymbol{\mathfrak{Q}}(\boldsymbol{X},t)\cdot\mathrm{d}\boldsymbol{A}\,, \tag{2.50}$$

we deduce push-forward and pull-back relations between $\boldsymbol{\mathfrak{Q}}$ and $\mathfrak{q}$ as well as their divergences

$$\boxed{J\boldsymbol{F}^{-1}\mathfrak{q} = \boldsymbol{\mathfrak{Q}} \quad \text{or} \quad \mathfrak{q} = J^{-1}\boldsymbol{F}\boldsymbol{\mathfrak{Q}} \quad \text{and} \quad \mathrm{div}\,\mathfrak{q} = J^{-1}\,\mathrm{Div}\,\boldsymbol{\mathfrak{Q}}\,,} \tag{2.51}$$

where $J = \det[\boldsymbol{F}]$ is the Jacobian.

Now, let us consider the material time derivative of the integral expression in (2.50) as

$$\frac{\mathrm{d}}{\mathrm{d}t}\int_{\partial\mathcal{P}_t} \mathfrak{q}(\boldsymbol{x},t)\cdot\mathrm{d}\boldsymbol{a} = \frac{\mathrm{d}}{\mathrm{d}t}\int_{\partial\mathcal{P}_0} \mathfrak{Q}(\boldsymbol{X},t)\cdot\mathrm{d}\boldsymbol{A}\,. \tag{2.52}$$

After carrying out the material time differentiation in the latter expression

$$\int_{\partial\mathcal{P}_t} \boldsymbol{\pounds}_{\boldsymbol{v}}\mathfrak{q}\cdot\mathrm{d}\boldsymbol{a} = \int_{\partial\mathcal{P}_t} (\dot{\mathfrak{q}} - \boldsymbol{l}\mathfrak{q} + \mathfrak{q}\,\mathrm{div}\,\boldsymbol{v})\cdot\mathrm{d}\boldsymbol{a} = \int_{\partial\mathcal{P}_0} \dot{\mathfrak{Q}}\cdot\mathrm{d}\boldsymbol{A} \tag{2.53}$$

and applying Gauss' theorem and localizing the integral, we obtain

$$\mathrm{div}[\boldsymbol{\pounds}_{\boldsymbol{v}}\mathfrak{q}] = \mathrm{div}[\dot{\mathfrak{q}} - \boldsymbol{l}\mathfrak{q} + \mathfrak{q}\,\mathrm{div}\,\boldsymbol{v}] = J^{-1}\,\mathrm{Div}\,\dot{\mathfrak{Q}}\,. \tag{2.54}$$

Conversely, if we first apply Gauss' theorem in (2.52) and then carry out the material time derivative, we arrive at

$$\boldsymbol{\pounds}_{\boldsymbol{v}}[\mathrm{div}\,\mathfrak{q}] = \dot{\overline{\mathrm{div}\,\mathfrak{q}}} + \mathrm{div}\,\mathfrak{q}\,\mathrm{div}\,\boldsymbol{v} = J^{-1}\,\mathrm{Div}\,\dot{\mathfrak{Q}}\,, \tag{2.55}$$

where we have considered the commutativity of the material divergence and the material time derivative. Furthermore, we observe that the spatial divergence and the Lie derivative commute, i.e.,

$$\boldsymbol{\pounds}_{\boldsymbol{v}}[\mathrm{div}\,\mathfrak{q}] = \mathrm{div}[\boldsymbol{\pounds}_{\boldsymbol{v}}\mathfrak{q}]\,. \tag{2.56}$$

However, the spatial divergence and the material time derivative do not commute. Considering (2.54) and (2.55), we can derive the following expression for the material time derivative of $\mathrm{div}\,\mathfrak{q}$

$$\dot{\overline{\mathrm{div}\,\mathfrak{q}}} = \mathrm{div}\,\dot{\mathfrak{q}} - \boldsymbol{l}^T : \mathrm{grad}\,\mathfrak{q}\,. \tag{2.57}$$

It is worth emphasizing that the above derivations are results of the requirement (2.50).

Stokes' theorem. Like Gauss's theorem, Stokes' theorem can be applied to transfer a closed line integral of a continuous variable to a surface integral. Let us denote a Lagrangian surface by $\mathcal{S}_0$ and its boundary by $\partial\mathcal{S}_0$, which deforms to an Eulerian surface $\mathcal{S}_t$ with the boundary $\partial\mathcal{S}_t$. The theorem then can be utilized in the reference and current configurations as

$$\begin{aligned} \oint_{\partial\mathcal{S}_0} \mathfrak{S}(\boldsymbol{X},t)\cdot\mathrm{d}\boldsymbol{X} &= \int_{\mathcal{S}_0} \mathrm{Curl}[\mathfrak{S}(\boldsymbol{X},t)]\cdot\mathrm{d}\boldsymbol{A} \quad \text{and} \\ \oint_{\partial\mathcal{S}_t} \mathfrak{s}(\boldsymbol{x},t)\cdot\mathrm{d}\boldsymbol{x} &= \int_{\mathcal{S}_t} \mathrm{curl}[\mathfrak{s}(\boldsymbol{x},t)]\cdot\mathrm{d}\boldsymbol{a}\,, \end{aligned} \tag{2.58}$$

respectively. Here, Curl and curl are operations with reference to the positions $\boldsymbol{X}$ and $\boldsymbol{x}$ correspondingly. In this case, if the following relation holds

$$\oint_{\partial\mathcal{S}_t} \mathfrak{s}(\boldsymbol{x},t)\cdot\mathrm{d}\boldsymbol{x} = \oint_{\partial\mathcal{S}_0} \mathfrak{S}(\boldsymbol{X},t)\cdot\mathrm{d}\boldsymbol{X}\,, \tag{2.59}$$

we now arrive at different push-forward and pull-back relations between the quantities $\mathfrak{S}$ and $\mathfrak{s}$ as well as their curls

$$\boxed{\boldsymbol{F}^T\mathfrak{s} = \mathfrak{S} \quad \text{or} \quad \mathfrak{s} = \boldsymbol{F}^{-T}\mathfrak{S} \quad \text{and} \quad \operatorname{curl}\mathfrak{s} = J^{-1}\boldsymbol{F}\operatorname{Curl}\mathfrak{S}\,.} \tag{2.60}$$

Now let us consider again the material time derivative of the integral expression in (2.59) as

$$\frac{\mathrm{d}}{\mathrm{d}t}\oint_{\partial\mathcal{S}_t}\mathfrak{s}(\boldsymbol{x},t)\cdot\mathrm{d}\boldsymbol{x} = \frac{\mathrm{d}}{\mathrm{d}t}\oint_{\partial\mathcal{S}_0}\mathfrak{S}(\boldsymbol{X},t)\cdot\mathrm{d}\boldsymbol{X}\,. \tag{2.61}$$

After carrying out the material time differentiation in the latter expression

$$\oint_{\partial\mathcal{S}_t}\pounds_{\boldsymbol{v}}\mathfrak{s}\cdot\mathrm{d}\boldsymbol{x} = \oint_{\partial\mathcal{S}_t}(\dot{\mathfrak{s}}+\boldsymbol{l}^T\mathfrak{s})\cdot\mathrm{d}\boldsymbol{x} = \oint_{\partial\mathcal{S}_0}\dot{\mathfrak{S}}(\boldsymbol{X},t)\cdot\mathrm{d}\boldsymbol{X} \tag{2.62}$$

and applying Stokes' theorem and localizing the integral, we obtain

$$\operatorname{curl}\pounds_{\boldsymbol{v}}\mathfrak{s} = \operatorname{curl}[\dot{\mathfrak{s}}+\boldsymbol{l}^T\mathfrak{s}] = J^{-1}\boldsymbol{F}\operatorname{Curl}\dot{\mathfrak{S}}\,. \tag{2.63}$$

Conversely, if we first apply Stokes' theorem in (2.61) and then carry out the material time derivative, we arrive at

$$\pounds_{\boldsymbol{v}}[\operatorname{curl}\mathfrak{s}] = \dot{\overline{\operatorname{curl}\mathfrak{s}}} - \boldsymbol{l}\operatorname{curl}\mathfrak{s} + \operatorname{curl}\mathfrak{s}\operatorname{div}\boldsymbol{v} = J^{-1}\boldsymbol{F}\operatorname{Curl}\dot{\mathfrak{S}}\,, \tag{2.64}$$

where we have considered the commutativity of the material Curl operator and the material time derivative. Furthermore, we observe that the spatial curl operator and the Lie derivative commute, i.e.,

$$\pounds_{\boldsymbol{v}}[\operatorname{curl}\mathfrak{s}] = \operatorname{curl}[\pounds_{\boldsymbol{v}}\mathfrak{s}]\,. \tag{2.65}$$

However, the spatial curl operator and the material time derivative do not commute. Considering (2.63) and (2.64), we can derive the following expression for the material time derivative of $\operatorname{curl}\mathfrak{s}$

$$\dot{\overline{\operatorname{curl}\mathfrak{s}}} = \operatorname{curl}\dot{\mathfrak{s}} + \operatorname{curl}[\boldsymbol{l}^T\mathfrak{s}] + \boldsymbol{l}\operatorname{curl}\mathfrak{s} - \operatorname{curl}\mathfrak{s}\operatorname{div}\boldsymbol{v} = \operatorname{curl}\dot{\mathfrak{s}} - \boldsymbol{\epsilon}:(\boldsymbol{l}^T\operatorname{grad}^T\mathfrak{s})\,. \tag{2.66}$$

where $\operatorname{grad}^T\mathfrak{s} = (\operatorname{grad}\mathfrak{s})^T$ and $\boldsymbol{\epsilon}$ is the third-order permutation tensor.[4] It is worth emphasizing that the above derivations are results of the requirement (2.59).

Rate of volume integrals. Let $\mathcal{F}$ denote a global quantity defined over an arbitrary subdomain, either Lagrangian $\mathcal{P}_0 \subseteq \mathcal{B}_0$ or Eulerian $\mathcal{P}_t \subseteq \mathcal{B}_t$ as follows

$$\mathcal{F} = \int_{\mathcal{P}_0} F(\boldsymbol{X},t)\,\mathrm{d}V = \int_{\mathcal{P}_t} f(\boldsymbol{x},t)\,\mathrm{d}v\,, \tag{2.67}$$

[4] Here, we have used the following identity to simplify this equation

$$(\operatorname{div}\boldsymbol{v}\boldsymbol{1}-\boldsymbol{l})\operatorname{curl}\mathfrak{s} = \boldsymbol{\epsilon}:(\boldsymbol{l}^T\operatorname{grad}^T\mathfrak{s}) - \boldsymbol{\epsilon}:(\boldsymbol{l}^T\operatorname{grad}\mathfrak{s}) \quad \text{and} \quad \operatorname{curl}(\boldsymbol{l}^T\mathfrak{s}) = -\boldsymbol{\epsilon}:(\boldsymbol{l}^T\operatorname{grad}\mathfrak{s})\,,$$

where the first equation can also be obtained from the following expression (see also [50], Section 2.8)

$$(\operatorname{div}\boldsymbol{v}\boldsymbol{1}-\boldsymbol{l})\boldsymbol{m}\times\boldsymbol{n} = (\boldsymbol{l}^T\boldsymbol{m})\times\boldsymbol{n} - (\boldsymbol{l}^T\boldsymbol{n})\times\boldsymbol{m} = \boldsymbol{\epsilon}:(\boldsymbol{l}^T\boldsymbol{m}\otimes\boldsymbol{n}) - \boldsymbol{\epsilon}:(\boldsymbol{l}^T\boldsymbol{n}\otimes\boldsymbol{m})\,.$$

with $\boldsymbol{m}$ and $\boldsymbol{n}$ being arbitrary vectors.

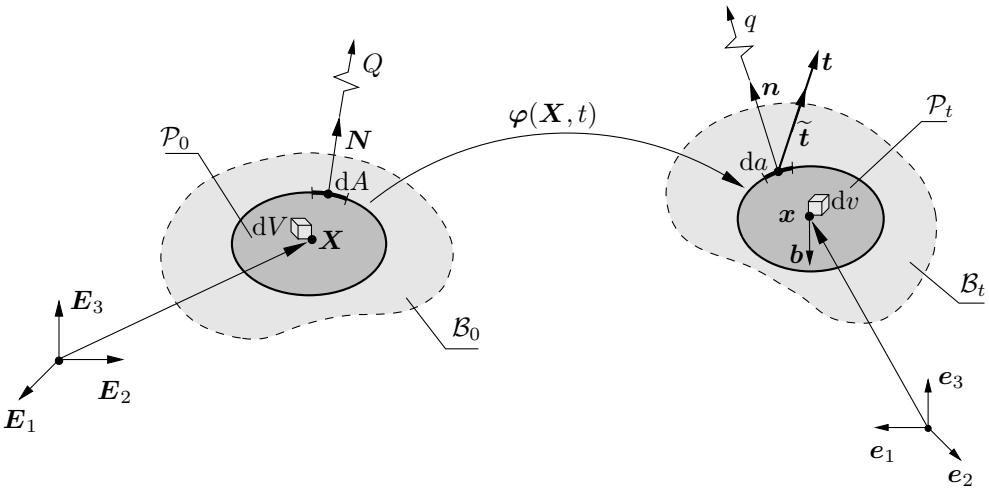

Figure 2.5: *Thermomechanical forces acting on a subdomain $\mathcal{P}_t \subseteq \mathcal{B}_t$.* An arbitary subdomain $\mathcal{P}_t$ cut out of the body $\mathcal{B}_t$ via *Euler's cut principle* is described. The subdomain undergoes action of body forces $\boldsymbol{b}$ in the volume and a thermomechanical interactions on the surface. The thermomechanical interactions are induced by the remaining domain $\mathcal{P}_t \backslash \mathcal{B}_t$ and described by a Cauchy surface traction $\boldsymbol{t}$ or $\widetilde{\boldsymbol{t}}$ and surface heat flux q in the current configurations.

where $F(\boldsymbol{X},t)$ and $f(\boldsymbol{x},t) = J^{-1}F(\boldsymbol{X},t)$ are continous Lagrangian and Eulerian volume densities of $\mathcal{F}$ defined per unit volume of $\mathcal{P}_0$ and $\mathcal{P}_t$, respectively. Then, the rate of the global quantity $\mathcal{F}$ can be determined by

$$\dot{\mathcal{F}} = \frac{\mathrm{d}}{\mathrm{d}t}\mathcal{F} = \frac{\mathrm{d}}{\mathrm{d}t}\int_{\mathcal{P}_0} F(\boldsymbol{X},t)\,\mathrm{d}V = \int_{\mathcal{P}_0} \frac{\partial F}{\partial t}\,\mathrm{d}V \tag{2.68}$$

in the Lagrangian configuration and

$$\dot{\mathcal{F}} = \frac{\mathrm{d}}{\mathrm{d}t}\int_{\mathcal{P}_t} f(\boldsymbol{x},t)\,\mathrm{d}v = \int_{\mathcal{P}_t} \frac{\mathrm{d}}{\mathrm{d}t}\big(f\,\mathrm{d}v\big) = \int_{\mathcal{P}_t} \big(\frac{\mathrm{d}f}{\mathrm{d}t} + f\,\mathrm{div}[\boldsymbol{v}]\big)\,\mathrm{d}v \tag{2.69}$$

in the Eulerian configuration. If we consider the total (or material) time derivative of the Eulerian density $f(\boldsymbol{x},t)$ in the above equation, we obtain the *Reynolds transport theorem*

$$\dot{\mathcal{F}} = \int_{\mathcal{P}_t} \big(\frac{\partial f}{\partial t} + \mathrm{div}[f\boldsymbol{v}]\big)\,\mathrm{d}v = \int_{\mathcal{P}_t} \frac{\partial f}{\partial t}\,\mathrm{d}v + \int_{\partial\mathcal{P}_t} f\boldsymbol{v}\cdot\,\mathrm{d}\boldsymbol{a}\,, \tag{2.70}$$

where we have used Gauss' theorem. Consequently, the change of a global quantity defined over $\mathcal{P}_t$ is due to the temporal change of the quantity in the volume of the subdomain $\mathcal{P}_t$ and its flux on the boundary $\partial\mathcal{P}_t$. Nevertheless, when we consider the Lagrangian configuration to describe the rate of a global quantity, we do not have a flux term.

2.1.9 Cauchy's theorem: stress tensor and heat flux vector

Mechanical stress tensor. Let $\mathcal{P}_t \subseteq \mathcal{B}_t$ denote an arbitrary cut-out subdomain of $\mathcal{B}_t$ in the current configuration. Likewise, let $\mathcal{P}_0 \subseteq \mathcal{B}_0$ denote the Lagrangian counterpart of $\mathcal{P}_t$, see Fig. 2.5. If we denote the resultant force as $\mathcal{F}^S_{\mathcal{P}_t}$ due to mechanical interaction between the subdomain $\mathcal{P}_t$ and the rest of the body $\mathcal{B}_t \backslash \mathcal{P}_t$ on the contact surface $\partial\mathcal{P}_t$, we

can write

$$\mathfrak{F}^S_{\mathcal{P}_t} = \int_{\partial\mathcal{P}_t} \boldsymbol{t}(\boldsymbol{x}, t; \boldsymbol{n})\, \mathrm{d}a = \int_{\partial\mathcal{P}_0} \widetilde{\boldsymbol{t}}(\boldsymbol{x}, t; \boldsymbol{N})\, \mathrm{d}A\,, \tag{2.71}$$

where $\boldsymbol{t}$ and $\widetilde{\boldsymbol{t}}$ denote traction vectors, which describe the surface density of the resultant contact force per unit area of $\partial\mathcal{P}_t$ and $\partial\mathcal{P}_0$, respectively. The unit of surface tractions is newtons per meter squared ($\mathrm{N/m^2}$). $\boldsymbol{n}$ and $\boldsymbol{N}$ denote the outward surface normals of the current and reference areas correspondingly.

Cauchy's theorem postulates that the current traction vector can be expressed employing *the Cauchy stress tensor* $\boldsymbol{\sigma}$ and outward normal $\boldsymbol{n}$ of the current area as follows [139, 167, 153]

$$\boldsymbol{t}(\boldsymbol{x}, t; \boldsymbol{n}) := \boldsymbol{\sigma}(\boldsymbol{x}, t)\boldsymbol{n} \quad \text{or} \quad t^a := \sigma^{ab} n_b\,. \tag{2.72}$$

Furthermore, considering a similar relation for $\widetilde{\boldsymbol{t}}(\boldsymbol{x}, t; \boldsymbol{N})$ utilizing *the first Piola-Kirchhoff stress tensor* and outward normal $\boldsymbol{N}$ of the referential area [139, 167, 153], we can write

$$\widetilde{\boldsymbol{t}}(\boldsymbol{x}, t; \boldsymbol{N}) := \widetilde{\boldsymbol{P}}(\boldsymbol{X}, t)\boldsymbol{N} \quad \text{or} \quad \widetilde{t}^a := \widetilde{P}^{aB} N_B\,, \tag{2.73}$$

where $\widetilde{\boldsymbol{P}}$ is a second-order two-point tensor; one of its bases is defined in the current configuration and the another in the reference configuration. In addition to the given representation, we further introduce another representation of the first Piola-Kirchhoff stress tensor, i.e., $\boldsymbol{P} = \boldsymbol{g}\widetilde{\boldsymbol{P}} = P_a{}^A \boldsymbol{e}^a \otimes \boldsymbol{E}_A$.

Considering Cauchy's and the divergence theorem in (2.71), we obtain the following relations between the Cauchy and the first Piola-Kirchhoff stress tensor as well as their divergence

$$J\boldsymbol{\sigma}\boldsymbol{F}^{-T} = \widetilde{\boldsymbol{P}} \quad \text{and} \quad J \operatorname{div} \boldsymbol{\sigma} = \operatorname{Div} \widetilde{\boldsymbol{P}}\,. \tag{2.74}$$

Finally, we introduce the symmetric *Kirchhoff* and *the second Piola-Kirchhoff stress tensor* as $\boldsymbol{\tau} := J\boldsymbol{\sigma}$ and $\boldsymbol{S} := \boldsymbol{F}^{-1}\widetilde{\boldsymbol{P}} = \boldsymbol{F}^{-1}\boldsymbol{\tau}\boldsymbol{F}^{-T}$ correspondingly. Although $\boldsymbol{\tau}$ and $\boldsymbol{S}$ are defined in different configurations, both stress tensors with their dual strains yield a stress power per unit volume of the reference configuration. The last two stress tensors can be obtained from the equivalence of the stress power in different configurations.

Heat flux vector. Similar to the mechanical interactions, the thermal interactions on the contact surface between the subdomain $\mathcal{P}_t$ and the rest of the body $\mathcal{B}_t \backslash \mathcal{P}_t$ can be characterized by the amount of heat exchange $\mathcal{Q}^S_{\mathcal{P}_t}$ through the boundary of $\mathcal{P}_t$

$$\mathcal{Q}^S_{\mathcal{P}_t} = \int_{\partial\mathcal{P}_t} q(\boldsymbol{x}, t; \boldsymbol{n})\, \mathrm{d}a = \int_{\partial\mathcal{P}_0} Q(\boldsymbol{x}, t; \boldsymbol{N})\, \mathrm{d}A\,, \tag{2.75}$$

where q and Q are outward scalar heat fluxes defined per unit areas of $\mathcal{P}_t$ and $\mathcal{P}_0$, respectively. The unit of the heat fluxes is joules per second per meter squared ($\mathrm{J/(sec \cdot m^2)}$). In this case, Cauchy's theorem postulates that the heat fluxes can be given in terms of a heat flux vector and the outward normal of the area. In the current configuration, the theorem can be written as

$$q(\boldsymbol{x}, t; \boldsymbol{n}) := \boldsymbol{q}(\boldsymbol{x}, t) \cdot \boldsymbol{n} \quad \text{or} \quad q := q^a n_a\,, \tag{2.76}$$

where $\boldsymbol{q}$ is referred to as the *Cauchy heat flux vector*. A similar relation can also be constructed for the referential heat flux Q as [139, 153]

$$Q(\boldsymbol{X}, t; \boldsymbol{N}) := \boldsymbol{Q}(\boldsymbol{X}, t) \cdot \boldsymbol{N} \quad \text{or} \quad Q := Q^A N_A \,, \tag{2.77}$$

where $\boldsymbol{Q}$ is referred to as the *Piola-Kirchoff heat flux vector*. The following relationships between the heat flux vectors and their divergences can be derived from (2.75) as [139, 153]

$$J\boldsymbol{q}\boldsymbol{F}^{-T} = \boldsymbol{Q} \quad \text{and} \quad J \operatorname{div} \boldsymbol{q} = \operatorname{Div} \boldsymbol{Q} \,. \tag{2.78}$$

2.1.10 Conjugate stress and strain tensors in stress power

The stress power is associated with the power of external mechanical volume and surface forces acting on a subdomain $\mathcal{P}_t \subseteq \mathcal{B}_t$. It is expressed by the contraction of a stress tensor with its *conjugate* (or *dual*) deformation tensor. Based on the above definition of the stress tensors, we can define the stress power as follows

$$\mathcal{P}_{\mathcal{P}_t} = \int_{\mathcal{P}_t} \boldsymbol{\sigma} : \boldsymbol{d} \, \mathrm{d}v = \int_{\mathcal{P}_0} \boldsymbol{\tau} : \boldsymbol{d} \, \mathrm{d}V = \int_{\mathcal{P}_0} \boldsymbol{P} : \dot{\boldsymbol{F}} \, \mathrm{d}V = \int_{\mathcal{P}_0} \boldsymbol{S} : \frac{1}{2}\dot{\boldsymbol{C}} \, \mathrm{d}V \,, \tag{2.79}$$

where the Kirchhoff stress with its dual strain rate yields a stress power density per unit volume of the reference configuration. Recall that the following relation holds between the rate of the deformation tensor and the rate of the right Cauchy-Green tensor

$$\boldsymbol{d} = \frac{1}{2}\boldsymbol{\varphi}_{t\star}(\dot{\boldsymbol{C}}) = \frac{1}{2}\pounds_{\boldsymbol{v}}\boldsymbol{g} = \frac{1}{2}\boldsymbol{F}^{-T}\dot{\boldsymbol{C}}\boldsymbol{F}^{-1}. \tag{2.80}$$

2.1.11 Governing equations of thermomechanics

This subsection introduces some fundamental physical properties of a deformable body – mass, linear momentum, angular momentum, energy, and entropy – associated with an arbitrary subdomain $\mathcal{P}_t \subseteq \mathcal{B}_t$ of a body $\mathcal{B}_t$ in the current configuration. The subdomain is usually assumed to be cut out of the body via Euler's cut principle. These physical quantities change due to thermomechanical interactions between the part $\mathcal{P}_t$ and the rest of the body $\mathcal{B}_t \backslash \mathcal{P}_t$ as well as due to the supply and production of a quantity in the volume of $\mathcal{P}_t$. The interaction can be due to mechanical tractions and heat flux on the surface $\partial\mathcal{P}_t$ of the part in the case of thermomechanical loading. In the case of electro- or magneto-mechanics, we need to account for further interactions, which we deal with in the following sections.

The objective of this section is to derive governing differential equations (also referred to as *balance equations*) of the fundamental physical quantities associated with a continuum body undergoing thermomechanical loading. At first, we formulate these equations for an arbitrary part $\mathcal{P}_t$, which are defined in integral form and referred to as *global forms*. Next, considering that the equations must hold for an arbitrary cut-out part, we deduce the so-called *local forms*, which hold at each continuum point. These equations are formulated independent of the material response. Instead, the response of a specific material is accounted for by an additional set of material equations building relations between dual quantities in the governing equations. The material equations are also necessary for the closure of the balance equations. For more detailed treatements, we refer to [139, 167, 75, 233, 39, 153, 141, 22, 225], among others.

Balance of mass. Assuming that there is no source or sink of mass in the volume as well as no mass flux on the surface of an arbitrary subdomain $\mathcal{P}_t$, this balance law requires the mass of a part $\mathcal{P}_t$ to stay unchanged in the course of a deformation

$$\frac{\mathrm{d}}{\mathrm{d}t}\mathcal{M}_{\mathcal{P}_t} := \frac{\mathrm{d}}{\mathrm{d}t}\int_{\mathcal{P}_t}\rho(\boldsymbol{x},t)\,\mathrm{d}v = \frac{\mathrm{d}}{\mathrm{d}t}\int_{\mathcal{P}_0}\rho_0(\boldsymbol{X})\,\mathrm{d}V = 0\,. \tag{2.81}$$

Taking the rate of integrals above and considering $\mathcal{P}_t$ is an arbitrary subdomain, we arrive at the local mass balance laws in the current and reference configurations

$$\dot{\rho} + \rho\,\mathrm{div}\,\boldsymbol{v} = 0 \quad \text{and} \quad \rho_0(\boldsymbol{X}) = J\rho(\boldsymbol{x},t)\,, \tag{2.82}$$

respectively. $\rho(\boldsymbol{x},t)$ and $\rho_0(\boldsymbol{X})$ are the current and reference mass densities of the body.

Balance of linear momentum. The balance law governs the change in the linear momentum $\mathfrak{J}_{\mathcal{P}_t}$ of a subdomain $\mathcal{P}_t$, resulting from the mechanical surface and body forces. It can be stated as follows

$$\frac{\mathrm{d}}{\mathrm{d}t}\mathfrak{J}_{\mathcal{P}_t} = \mathfrak{F}_{\mathcal{P}_t} \quad \text{or} \quad \frac{\mathrm{d}}{\mathrm{d}t}\int_{\mathcal{P}_t}\rho\boldsymbol{v}\,\mathrm{d}v = \int_{\mathcal{P}_t}\rho\boldsymbol{b}\,\mathrm{d}v + \int_{\partial\mathcal{P}_t}\boldsymbol{t}\,\mathrm{d}a\,, \tag{2.83}$$

where $\boldsymbol{b}$ denotes a mass-specific body force; it is measured by newtons per kilogram (N/kg). Again, taking the rate of the integral in the above equation and using Cauchy's and Gauss' theorems, we obtain the local form of the balance of linear momentum in the current configuration as

$$\rho\dot{\boldsymbol{v}} = \mathrm{div}\,\boldsymbol{\sigma} + \rho\boldsymbol{b} \quad \text{or} \quad \rho\dot{v}^a = \sigma^{ab}{}_{,b} + \rho b^a\,. \tag{2.84}$$

Analogously, we can also express $(2.83)_1$ in the reference configuration

$$\frac{\mathrm{d}}{\mathrm{d}t}\int_{\mathcal{P}_0}\rho_0\boldsymbol{V}\,\mathrm{d}V = \int_{\mathcal{P}_0}\rho_0\boldsymbol{b}\,\mathrm{d}V + \int_{\partial\mathcal{P}_0}\widetilde{\boldsymbol{t}}\,\mathrm{d}A\,, \tag{2.85}$$

and then apply Cauchy's and Gauss' theorems to obtain the local form as

$$\rho_0\dot{\boldsymbol{V}} = \mathrm{div}\,\widetilde{\boldsymbol{P}} + \rho_0\boldsymbol{b} \quad \text{or} \quad \rho_0\dot{V}^a = \widetilde{P}^{aB}{}_{,B} + \rho_0 b^a\,. \tag{2.86}$$

Balance of angular momentum. This balance law links the change in the angular momentum $\mathfrak{D}_{\mathcal{P}_t}$ of a subdomain $\mathcal{P}_t$ to the momentum $\mathfrak{M}_{\mathcal{P}_t}$ of forces acting on this subdomain. Thus, the angular momentum's change with reference to a point $\mathcal{O}$ can be expressed as

$$\frac{\mathrm{d}}{\mathrm{d}t}\mathfrak{D}^{\mathcal{O}}_{\mathcal{P}_t} = \mathfrak{M}^{\mathcal{O}}_{\mathcal{P}_t} \quad \text{or} \quad \frac{\mathrm{d}}{\mathrm{d}t}\int_{\mathcal{P}_t}\boldsymbol{x}\times\rho\boldsymbol{v}\,\mathrm{d}v = \int_{\mathcal{P}_t}\boldsymbol{x}\times\rho\boldsymbol{b}\,\mathrm{d}v + \int_{\partial\mathcal{P}_t}\boldsymbol{x}\times\boldsymbol{t}\,\mathrm{d}a\,. \tag{2.87}$$

Similarly, taking the rate of the integral on the left-hand side and applying Cauchy's and Gauss' theorems, we obtain the local balance equations in the current configuration and in the two-point setting, respectively, as

$$\boldsymbol{\sigma} = \boldsymbol{\sigma}^T \quad \text{and} \quad \boldsymbol{F}\widetilde{\boldsymbol{P}}^T = \widetilde{\boldsymbol{P}}\boldsymbol{F}^T. \tag{2.88}$$

Balance of energy. The balance of energy is also known as *the first law of thermodynamics*. It governs the change of the total energy of the subdomain $\mathcal{P}_t$ depending on the

applied mechanical $\mathcal{P}_{\mathcal{P}_t}$ and thermal $\mathcal{Q}_{\mathcal{P}_t}$ powers. The total energy is defined as the sum of the kinetic energy $\mathcal{K}_{\mathcal{P}_t}$ and the internal energy $\mathcal{E}_{\mathcal{P}_t}$ of $\mathcal{P}_t$ with the following definitions

$$\mathcal{K}_{\mathcal{P}_t} = \frac{1}{2}\int_{\mathcal{P}_t} \rho \boldsymbol{v}\cdot\boldsymbol{v}\,\mathrm{d}v = \frac{1}{2}\int_{\mathcal{P}_0} \rho_0 \boldsymbol{V}\cdot\boldsymbol{V}\,\mathrm{d}V \quad \text{and} \quad \mathcal{E}_{\mathcal{P}_t} = \int_{\mathcal{P}_t} \rho e\,\mathrm{d}v = \int_{\mathcal{P}_0} \rho_0 e\,\mathrm{d}V\,, \tag{2.89}$$

where e is a mass-specific internal energy density; it is measured by joules per kilogram (J/kg = (N·m)/kg). The first law of thermodynamics in the global form can be expressed as

$$\frac{\mathrm{d}}{\mathrm{d}t}\big(\mathcal{K}_{\mathcal{P}_t} + \mathcal{E}_{\mathcal{P}_t}\big) = \mathcal{P}_{\mathcal{P}_t} + \mathcal{Q}_{\mathcal{P}_t}\,, \tag{2.90}$$

which states that the total energy of the subdomain $\mathcal{P}_t$ is conserved if the subdomain does not undergo any external action. Here, $\mathcal{P}_{\mathcal{P}_t}$ is the power of a mass-specific body force $\boldsymbol{b}$ in $\mathcal{P}_t$ and a surface traction $\boldsymbol{t}(\boldsymbol{x},t;\boldsymbol{n})$ on $\mathcal{P}_t$ (see also (2.79))

$$\mathcal{P}_{\mathcal{P}_t} = \int_{\mathcal{P}_t} \rho\boldsymbol{b}\cdot\boldsymbol{v}\,\mathrm{d}v + \int_{\partial\mathcal{P}_t} \boldsymbol{t}\cdot\boldsymbol{v}\,\mathrm{d}a \overset{(2.84)}{=} \int_{\mathcal{P}_t} \boldsymbol{\sigma}:\boldsymbol{d}\,\mathrm{d}v \overset{(2.79)}{=} \int_{\mathcal{P}_0} \boldsymbol{P}:\dot{\boldsymbol{F}}\,\mathrm{d}V\,, \tag{2.91}$$

and $\mathcal{Q}_{\mathcal{P}_t}$ is the thermal power associated with a mass-specific heat source $r(\boldsymbol{x},t)$ in $\mathcal{P}_t$ and an outward surface heat flux $q(\boldsymbol{x},t;\boldsymbol{n})$ on $\partial\mathcal{P}_t$

$$\mathcal{Q}_{\mathcal{P}_t} = \int_{\mathcal{P}_t} \rho r\mathrm{d}v - \int_{\partial\mathcal{P}_t} q\,\mathrm{d}a\,, \tag{2.92}$$

where $q = \boldsymbol{q}\cdot\boldsymbol{n}$ is considered positive if the heat flows out of the subdomain $\mathcal{P}_t$. Considering the local forms of the balance of linear momentum, the balance of mass, and Cauchy's and Gauss' theorems, the local form of the balance of energy in the current and reference configurations are obtained as follows

$$\rho\dot{e} = \boldsymbol{\sigma}:\boldsymbol{d} + \rho r - \operatorname{div}\boldsymbol{q} \quad \text{and} \quad \rho_0\dot{e} = \boldsymbol{P}:\dot{\boldsymbol{F}} + \rho_0 r - \operatorname{Div}\boldsymbol{Q}\,. \tag{2.93}$$

Balance of entropy. The entropy of a subdomain $\mathcal{P}_t$ in continuum mechanics, in particular, a change in entropy of $\mathcal{P}_t$ characterizes that an external power put on this subdomain $\mathcal{P}_t$ is not completely stored in the material to do useful work. However, some part of this energy is dissipated as heat due to either inelastic material response or heat transfer.

The balance of entropy governs the evolution of entropy $\mathcal{H}_{\mathcal{P}_t}$ depending on the entropy power $\mathcal{S}_{\mathcal{P}_t}$ and entropy production $\mathcal{G}_{\mathcal{P}_t}$

$$\frac{\mathrm{d}}{\mathrm{d}t}\mathcal{H}_{\mathcal{P}_t} = \mathcal{S}_{\mathcal{P}_t} + \mathcal{G}_{\mathcal{P}_t}\,, \tag{2.94}$$

where the global variables associated with the subdomain $\mathcal{P}_t$ can be expressed in terms of the density fields as follows

$$\mathcal{H}_{\mathcal{P}_t} = \int_{\mathcal{P}_t} \rho\eta\,\mathrm{d}v\,, \quad \mathcal{S}_{\mathcal{P}_t} = \int_{\mathcal{P}_t} \rho\gamma\,\mathrm{d}v \quad \text{and} \quad \mathcal{G}_{\mathcal{P}_t} = \int_{\mathcal{P}_t} \frac{\rho r}{\vartheta}\mathrm{d}v - \int_{\partial\mathcal{P}_t} \frac{q}{\vartheta}\,\mathrm{d}a\,, \tag{2.95}$$

where η and γ are mass-specific entropy and entropy production densities correspondingly; they are measured by joules per kilogram per kelvin (J/(kg · K)) and joules per

kilogram per second per kelvin (J/(kg·sec·K)) correspondingly. Furthermore, we observe that the entropy power or supply expression is similar to the thermal power expression (2.92), namely the heat source ρr as well as the heat flux q is divided by the absolute temperature $\vartheta(\boldsymbol{x}, t)$ (unit of measure for the absolute temperature is kelvin (K). This form is because, at high temperatures, the same amount of thermal power can be transferred to mechanical energy more efficiently than at lower temperatures; see, for example, Coussy [39]. Therefore, at higher temperatures, the same amount of heat source and heat flux induces a lower increase in entropy than at lower temperatures.

The Eulerian and Lagrangian forms of the balance of entropy can be obtained as

$$\begin{aligned} \rho\dot{\eta} &= \rho\gamma + \frac{1}{\vartheta}(\rho r - \operatorname{div}\boldsymbol{q}) + \frac{1}{\vartheta^2}\boldsymbol{q}\cdot\operatorname{grad}\vartheta \quad \text{and} \\ \rho_0\dot{\eta} &= \rho_0\gamma + \frac{1}{\vartheta}(\rho_0 r - \operatorname{Div}\boldsymbol{Q}) + \frac{1}{\vartheta^2}\boldsymbol{Q}\cdot\operatorname{Grad}\vartheta\,, \end{aligned} \tag{2.96}$$

respectively. Here $\rho_0\gamma$ is the Lagrangian entropy production density. Considering the balance of energy $(2.93)_2$ in $(2.96)_2$, we can obtain the final form of the Lagrangian balance law for entropy

$$\rho_0\dot{\eta} = \rho_0\gamma + \frac{1}{\vartheta}(\rho_0\dot{e} - \boldsymbol{P} : \dot{\boldsymbol{F}}) + \frac{1}{\vartheta^2}\boldsymbol{Q}\cdot\operatorname{Grad}\vartheta\,, \tag{2.97}$$

where we identify the dissipation density as the product of the entropy production and absolute temperature $\rho\mathcal{D} := \rho\vartheta\gamma$, which is the power density dissipated from the considered system in the form of heat.

The second law of thermodynamics. This law describes the irreversibility of thermodynamic processes. It requires the non-negativity of the entropy production, such that the entropy of a thermally closed system cannot reduce. Hence, we can write this law in terms of the dissipation in the Lagrangian configuration as

$$\rho_0\mathcal{D} = \rho_0\vartheta\gamma = \boldsymbol{P} : \dot{\boldsymbol{F}} + \rho_0\vartheta\dot{\eta} - \rho_0\dot{e} - \frac{1}{\vartheta}\boldsymbol{Q}\cdot\operatorname{Grad}\vartheta \geq 0\,. \tag{2.98}$$

The above inequality is also referred to as the *Clausius-Duhem Inequality* (CDI). From the CDI, we observe that the rate of the internal energy density is associated with the rates of the deformation gradient and entropy, thus $e_0 = \widehat{e}_0(\boldsymbol{F}, \eta, \boldsymbol{\alpha})$ with $\boldsymbol{\alpha}$ characterizing the inelastic response. Although this form can be considered, it is rather convenient to have an energy function in terms of temperature since it can be easily prescribed and measured during an experiment. By doing so, we introduce the Helmholtz energy density via a partial Legendre-Fenchel transformation as

$$\widehat{\psi}(\boldsymbol{F}, \vartheta, \boldsymbol{\alpha}) := \inf_{\eta}\left(\widehat{e}(\boldsymbol{F}, \eta, \boldsymbol{\alpha}) - \vartheta\eta\right). \tag{2.99}$$

Thus, the CDI can be given in relation to the Helmholtz energy density as follows

$$\rho_0\mathcal{D} = \rho_0\vartheta\gamma = \boldsymbol{P} : \dot{\boldsymbol{F}} - \rho_0\dot{\vartheta}\eta - \rho_0\dot{\psi} - \frac{1}{\vartheta}\boldsymbol{Q}\cdot\operatorname{Grad}\vartheta \geq 0\,. \tag{2.100}$$

The CDI is usually split into a local and a heat conduction part, which are required to be fulfilled separately according to *Coleman's exploitation method*, [38]. Thus, we obtain the *Clausius-Planck Inequality* (CPI) in the Lagrangian configuration as the local part

$$\rho_0\mathcal{D}_{loc} := \boldsymbol{P} : \dot{\boldsymbol{F}} - \rho_0\dot{\vartheta}\eta - \rho_0\dot{\psi} \geq 0 \tag{2.101}$$

and *Fourier's Inequality* in the referential configuration as the heat conduction part

$$\rho_0 \mathcal{D}_{con} := -\frac{1}{\vartheta} \boldsymbol{Q} \cdot \operatorname{Grad} \vartheta \geq 0 \,. \tag{2.102}$$

The local part of the dissipation is associated with inelastic material response. In the case of elasticity, we do not have any local dissipation. Hence, (2.101) turns into an equality that needs to be satisfied for arbitrary deformation gradient and temperature rates. As a result, we obtain the following constitutive functions that define the first Piola-Kirchhoff stresses and the entropy in terms of the deformation gradient and the temperature

$$\boldsymbol{P} = \rho_0 \partial_{\boldsymbol{F}} \widehat{\psi}(\boldsymbol{F}, \vartheta) \quad \text{and} \quad \eta = -\partial_{\vartheta} \widehat{\psi}(\boldsymbol{F}, \vartheta) \,. \tag{2.103}$$

These are the constitutive equations in the so-called two-point setting. We can also derive the constitutive equations for the second Piola-Kirchhoff stress tensor $\boldsymbol{S}$, Kirchoff stress tensor $\boldsymbol{\tau}$ or Cauchy stress tensor $\boldsymbol{\sigma}$ based on the relation provided in Section 2.1.10. The latter will be demonstrated in Section 2.4.

In order to fulfill Fourier's inequality, we introduce a heat-flux potential function $\widehat{\phi}(\operatorname{Grad} \vartheta; \boldsymbol{F})$, which governs the heat flux vector in terms of the gradient of the temperature field at a given deformation state, i.e.,

$$\boldsymbol{Q} = -\partial_{\operatorname{Grad} \vartheta} \widehat{\phi}(\operatorname{Grad} \vartheta; \boldsymbol{F}) \,. \tag{2.104}$$

The potential function ϕ is chosen as a convex function of the temperature gradient and satisfies

$$\widehat{\phi}(\operatorname{Grad} \vartheta = \boldsymbol{0}; \boldsymbol{F}) = 0 \quad \text{and} \quad \partial_{\operatorname{Grad} \vartheta} \widehat{\phi}(\operatorname{Grad} \vartheta = \boldsymbol{0}; \boldsymbol{F}) = \boldsymbol{0} \,, \tag{2.105}$$

such that it fulfills Fourier's inequality a priori.

Principle of Objectivity. This principle requires that the constitutive functions are objective under rigid body transformations superimposed onto the deformed configuration. The rigid body transformation $\boldsymbol{\varphi}^+$ can be expressed as

$$\boldsymbol{\varphi}^+ = \boldsymbol{c}(t) + \boldsymbol{Q}(t) \boldsymbol{x} \tag{2.106}$$

in terms of a rigid translation $\boldsymbol{c}(t)$ and a rigid rotation $\boldsymbol{Q}(t)$. Thus, the principle of objectivity can be stated as

$$\widehat{\psi}(\boldsymbol{F}, \theta) = \widehat{\psi}(\boldsymbol{Q}\boldsymbol{F}, \theta) \quad \text{and} \quad \widehat{\phi}(\operatorname{Grad} \vartheta; \boldsymbol{F}) = \widehat{\phi}(\operatorname{Grad} \vartheta; \boldsymbol{Q}\boldsymbol{F}) \quad \forall \boldsymbol{Q} \in \mathcal{SO}(3) \,, \tag{2.107}$$

where $\mathcal{SO}(3)$ denotes the proper orthogonal group, and it is defined as

$$\mathcal{SO}(3) := \{ \boldsymbol{Q} \,|\, \boldsymbol{Q}^T \boldsymbol{Q} = \boldsymbol{g} \quad \text{and} \quad \det \boldsymbol{Q} = 1 \} \,. \tag{2.108}$$

The principle of objectivity is a priori fulfilled when the free-energy function and the heat-flux potential are formulated employing the right Cauchy-Green deformation tensor or its invariants, i.e.,

$$\widehat{\psi}(\boldsymbol{F}, \vartheta) = \widetilde{\psi}(\boldsymbol{C}, \vartheta) = \overline{\psi}(I_1, I_2, I_3) \quad \text{and} \quad \widehat{\phi}(\operatorname{Grad} \vartheta; \boldsymbol{F}) = \widetilde{\phi}(\operatorname{Grad} \vartheta; \boldsymbol{C}) \,, \tag{2.109}$$

where $I_1 := \operatorname{tr} \boldsymbol{C} = \operatorname{tr}(\boldsymbol{F}^T \boldsymbol{F})$, $I_2 := \operatorname{tr}(\operatorname{cof} \boldsymbol{C}) = \operatorname{tr}(\operatorname{cof}[\boldsymbol{F}^T] \operatorname{cof}[\boldsymbol{F}])$ and $I_3 := \det \boldsymbol{C} = (\det \boldsymbol{F})^2$ are the principle invariants of $\boldsymbol{C}$. The energy function of isotropic elastic materials can be characterized by these three invariants.

2.2 Fundamentals of Electrostatics

In the present section, we deal with the basic notions of electrostatics. Hence, electrodynamic coupling of the electric field to magnetism is not considered. This means that we do not take into account any currents or a changing magnetic field. Starting with the interactions of discrete electric charges in a vacuum and using the principle of linear superposition, we define the electric field and derive Faraday's law and Gauss' flux theorem in a continuous setting. Next, electrostatic fields and equations are extended to deformable dielectric bodies under isothermal conditions. The brief discussion is based on the works of [229, 121, 171, 79, 81, 64, 48, 98], among many others.

2.2.1 Coulomb force and definition of electric field

The most fundamental quantity in electrostatics is the electric charge of a particle. Similar to masses of objects characterizing their gravitational interactions, electric charges characterize electromagnetic interactions of particles; see [79, 64]. Electric charges have negative and positive forms. Two particles with the same type of charges repel each other while the different charges attract. The charge of a particle is quantized. It is integer multiples of a quantity $e \approx 1.602 \cdot 10^{-19}\,\mathrm{C}$ with units measured in coulombs (C). The magnitude of e corresponds to the charge of an electron $(-e)$ or a proton $(+e)$.

The interaction between discrete charges has been quantified experimentally by Coulomb. Assuming two stationary point charges in a vacuum, the interaction force between them, according to Coulomb, is defined as

$$\boldsymbol{f}^e_{12}(\boldsymbol{x}_1) = -\boldsymbol{f}^e_{21}(\boldsymbol{x}_2) = kq_1q_2\frac{\boldsymbol{x}_1 - \boldsymbol{x}_2}{\|\boldsymbol{x}_1 - \boldsymbol{x}_2\|^3}\,, \tag{2.110}$$

where k is a constant of proportionality. In the SI unit system $k = 1/(4\pi\epsilon_0)$ with $\epsilon_0 \approx 8.854 \cdot 10^{-12}\,\mathrm{C}^2/(\mathrm{Nm}^2)$ the permittivity of free space. $\boldsymbol{f}^e_{ij}$ is the force acting from the particle j on the particle i; see Fig. 2.6.

In the case of N point charges at rest distributed in free space, the force acting on a test particle placed at a position $\boldsymbol{x}$ is determined using the principle of linear superposition

$$\boldsymbol{f}^e(\boldsymbol{x}) = \frac{q}{4\pi\epsilon_0}\sum_{i=1}^{N} q_i\frac{\boldsymbol{x} - \boldsymbol{x}_i}{\|\boldsymbol{x} - \boldsymbol{x}_i\|^3}\,. \tag{2.111}$$

Since at every point in free space, we can assume a test charge and define the force acting on this charge due to the distributed point charges, we obtain a force field as a result of the electrostatic interaction. Hence, we introduce the electric field to characterize the intensity of this force field as follows

$$e(\boldsymbol{x}) = \lim_{q\to 0}\frac{\boldsymbol{f}^e(\boldsymbol{x})}{q}\,. \tag{2.112}$$

The electric field is measured by newtons per coulomb (N/C) or volts per meter (V/m). Based on the latter equation and the Coulomb force (2.111), we determine the electric field of the stationary N point charges as given below

$$e(\boldsymbol{x}) = \frac{1}{4\pi\epsilon_0}\sum_{i=1}^{N} q_i\frac{\boldsymbol{x} - \boldsymbol{x}_i}{\|\boldsymbol{x} - \boldsymbol{x}_i\|^3}\,. \tag{2.113}$$

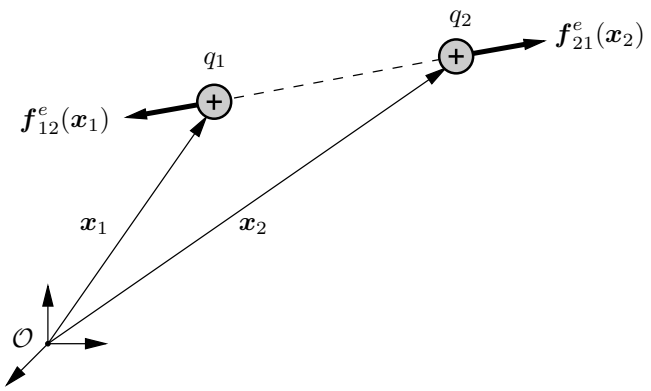

Figure 2.6: *Coulomb force between two stationary charges.* The induced force on the charged particles is aligned along the line connecting the particles.

Assuming the charges distributed continuously over a volume $\mathcal{V}_t$ with a charge density ρ^e, i.e., $\sum_i^N q_i = \int_{\mathcal{V}_t} \rho^e(\boldsymbol{x}')\mathrm{d}v(\boldsymbol{x}')$, we obtain an integral expression for the electric field[5]

$$e(\boldsymbol{x}) = \frac{1}{4\pi\epsilon_0}\int_{\mathcal{V}_t} \rho^e(\boldsymbol{x}')\frac{\boldsymbol{x}-\boldsymbol{x}'}{\|\boldsymbol{x}-\boldsymbol{x}'\|^3}\,\mathrm{d}v(\boldsymbol{x}') = -\operatorname{grad}\left[\frac{1}{4\pi\epsilon_0}\int_{\mathcal{V}_t}\frac{\rho^e(\boldsymbol{x}')}{\|\boldsymbol{x}-\boldsymbol{x}'\|}\,\mathrm{d}v(\boldsymbol{x}')\right], \quad (2.114)$$

where $\boldsymbol{x}'$ is a radius vector pointing to the charged volume elements $\mathrm{d}v$ and $\boldsymbol{x}$ is a radius vector where we calculate the electric field. In the above equations, the gradient operator is with respect to $\boldsymbol{x}$ coordinates, and the integral is with respect to $\boldsymbol{x}'$ coordinates. The gradient operator has therefore been taken out of the integral. The term within the gradient operator is referred to as the electric potential, which allows having a compact representation of the electric field

$$e(\boldsymbol{x}) = -\operatorname{grad}[\phi(\boldsymbol{x})] \quad \text{with} \quad \phi(\boldsymbol{x}) := \frac{1}{4\pi\epsilon_0}\int_{\mathcal{V}_t}\frac{\rho^e(\boldsymbol{x})}{\|\boldsymbol{x}-\boldsymbol{x}'\|}\,\mathrm{d}v(\boldsymbol{x}')\,. \quad (2.115)$$

The electric potential is measured by volts (V).

2.2.2 Faraday's law and Gauss' flux theorem

Based on the definition of the electric field in (2.115), we deduce that the gradient of the electric field is symmetric $\operatorname{grad}[e] = (\operatorname{grad}[e])^T$. This implies that the curl of the electric field vanishes. As a result, we obtain *Faraday's law of electrostatics* in a compact form

$$\operatorname{curl} e = \boldsymbol{0}\,. \quad (2.116)$$

An important outcome of the above equation is that the electric field is a conservative field, and its integral over any closed path in space does not depend on the path itself. This can be shown as follows using Stokes' theorem

$$\oint_{\mathcal{C}_t} e\cdot\mathrm{d}\boldsymbol{x} = \int_{\mathcal{S}_t}\operatorname{curl} e\cdot\mathrm{d}\boldsymbol{a} = 0\,, \quad (2.117)$$

[5]In the following, the subscript t in a volume $\mathcal{V}_t$, a surface $\mathcal{S}_t$ and a curve $\mathcal{C}_t$ domain of integration is introduced to show that corresponding entities refer to the current (observed) configuration. Note that these domains are not associated with any material volume; hence, the domains can differ in different expressions.

where $\mathcal{C}_t$ is any closed curve and $\mathcal{S}_t$ is the area bounded by this curve. The left-hand side of this equation corresponds to the electric-potential difference. This can be seen from $(2.115)_1$. Thus, the electric potential is path independent, and it can alternatively be determined at a position $\boldsymbol{x}$ for the known electric field by the following expression

$$\phi(\boldsymbol{x}) = -\int_{\boldsymbol{x}_0}^{\boldsymbol{x}} \mathbb{e} \cdot \mathrm{d}\boldsymbol{x}\,, \tag{2.118}$$

where $\boldsymbol{x}_0$ is a chosen reference point; at this point, the electric potential is assumed to be known in order to determine the integration constant. The reference point is often assumed to be at an infinite distance from the origin of the electric field; hence $\phi(\boldsymbol{x}_0) = 0$ can be considered. Since the electric field can be interpreted as force per a test charge (2.112), the electric potential (or $q\phi(\boldsymbol{x})$) can be physically interpreted as the work required to bring a charge (e.g., q) from a reference position $\boldsymbol{x}_0$ to its actual position $\boldsymbol{x}$ against the electric field.

Gauss's theorem of electricity relates the flux of electric field $\mathbb{e} \cdot \mathrm{d}\boldsymbol{a}$ across a closed surface $\mathcal{S}_t$ to the total electric charge $Q^{enc} = \int_{\mathcal{V}_t'} \rho^e(\boldsymbol{x}')\, \mathrm{d}v(\boldsymbol{x}')$ that is enclosed by this surface. Thus, if $\mathcal{V}_t$ is the volume bounded by the surface $\mathcal{S}_t$, then $\mathcal{V}_t' \subseteq \mathcal{V}_t$ is the part of the charged volume that lies within $\mathcal{V}_t$. We assume a spherical closed surface $\mathcal{S}_t$ concentric with the enclosed charge for simplicity. Then, the theorem can be stated as follows

$$\oint_{\mathcal{S}_t} \mathbb{e}(\boldsymbol{x}) \cdot \mathrm{d}\boldsymbol{a}(\boldsymbol{x}) = \frac{Q^{enc}}{4\pi\epsilon_0} \oint_{\mathcal{S}_t} \frac{\boldsymbol{x} - \boldsymbol{x}'}{\|\boldsymbol{x} - \boldsymbol{x}'\|^3} \cdot \mathrm{d}\boldsymbol{a}(\boldsymbol{x}) = \frac{Q^{enc}}{\epsilon_0} = \frac{1}{\epsilon_0} \int_{\mathcal{V}_t} \rho^e(\boldsymbol{x}')\, \mathrm{d}v(\boldsymbol{x}')\,, \tag{2.119}$$

where it has been considered that the integral in $(2.119)_2$ yields the solid angle 4π and $\rho^e(\boldsymbol{x}') = 0$ for $\boldsymbol{x}' \in \mathcal{V}_t \backslash \mathcal{V}_t'$ in $(2.119)_3$. Considering the divergence theorem in $(2.119)_1$, we obtain the differential form of Gauss' law

$$\operatorname{div} \mathbb{e} = \frac{1}{\epsilon_0}\rho^e \qquad \text{or} \qquad \operatorname{div} \mathbb{d} = \rho^e\,, \tag{2.120}$$

where we have introduced the electric displacement vector $\mathbb{d} = \epsilon_0 \mathbb{e}$ in free space. Its unit of measure is coulomb per meter squared ($\mathrm{C/m^2}$). Considering the definition of the electric field (2.115), we obtain the following second-order partial differential equation to determine the electric potential in free space for given ρ^e

$$-\operatorname{div}[\operatorname{grad}\phi] = \frac{1}{\epsilon_0}\rho^e\,, \tag{2.121}$$

where the $\operatorname{div}[\operatorname{grad}\{\cdot\}]$ is referred to as the Laplacian operator. Hence, the continuous formulation of the electric field based on the definition $(2.115)_1$ allows determining the electric potential as well as the electric field at any point in space without having to deal with singularities contrary to (2.113).

2.2.3 Polarization of a body in an electric field

Up to this section, we have considered the electric field of discrete or continuously distributed charges in free space. However, the electric field inside a body can be substantially different from that in free space. Since bodies contain atoms, ions, or molecules, they usually respond in different ways when brought to an external electric field. In particular,

we distinguish two kinds of bodies: conductors and insulators. The former are capable of conducting electric currents due to the existence of free charges (electrons) in its volume. Under external electric fields, the free electrons travel through the conductor, inducing current. On the contrary, the latter do not generally conduct an electric current. Such types of materials are also referred to as dielectrics. However, dielectrics can undergo polarization and alter the electric field within the body when exposed to an external electric field. A simple example of a setup can be envisioned as a dielectric sandwiched between two electrodes.

The dielectrics themselves can be polar and non-polar. Polar dielectrics contain randomly oriented permanent dipole moments, for example, water molecules. In such molecules, the centers of the positive and negative charges mismatch, inducing a dipole moment. Since they are usually randomly oriented at the initial state, the overall dipole moment (polarization) vanishes without an external field or deformation. Under an external electric field or mechanical deformation, the molecules can re-orient themselves (polarize) and induce an additional electric field. In non-polar dielectrics, there are no permanent dipole moments. However, due to an external electric field or mechanical deformation again, the molecules or atoms of this type of material can deform. As a result, the centers of positive and negative charges will not coincide anymore. This process is referred to as polarization.

In order to describe the polarization phenomenon, we take a look at a simplified dipole, which contains a positive $q_b(\boldsymbol{x}')$ and a negative $q_b(\boldsymbol{x}'+\boldsymbol{\delta}) = -q_b(\boldsymbol{x}')$ charge. The electric potential due to such a dipole moment can be determined as

$$\widetilde{\phi}(\boldsymbol{x}) = \frac{1}{4\pi\epsilon_0}\frac{q_b(\boldsymbol{x}')}{\|\boldsymbol{x}-\boldsymbol{x}'\|} + \frac{1}{4\pi\epsilon_0}\frac{q_b(\boldsymbol{x}'+\boldsymbol{\delta})}{\|\boldsymbol{x}-\boldsymbol{x}'-\boldsymbol{\delta}\|} \approx \frac{1}{4\pi\epsilon_0}\frac{\widetilde{\mathbb{p}}\cdot(\boldsymbol{x}-\boldsymbol{x}')}{\|\boldsymbol{x}-\boldsymbol{x}'\|^3}\,, \tag{2.122}$$

where we have considered $q_b(\boldsymbol{x}') = -q_b(\boldsymbol{x}'+\boldsymbol{\delta})$ and introduced the so-called dipole moment $\widetilde{\mathbb{p}}(\boldsymbol{x}') = q_b(\boldsymbol{x}')\boldsymbol{\delta}$ with $\|\boldsymbol{\delta}\| \ll 1$. Considering that a volume element $\mathrm{d}v(\boldsymbol{x}')$ contains N dipoles, we can introduce the dipole moment density as $\mathbb{p}(\boldsymbol{x}') = \lim_{\mathrm{d}v\to 0}\sum_i^N \widetilde{\mathbb{p}}^i(\boldsymbol{x}')/\mathrm{d}v(\boldsymbol{x}')$ in a continuous setting. Based on the above equation (2.122), the total electric potential at a point $\boldsymbol{x}$ due to the polarization of a material sub-body $\mathcal{P}_t$ can thus be determined as follows

$$\phi(\boldsymbol{x}) = \frac{1}{4\pi\epsilon_0}\int_{\mathcal{P}_t}\frac{\mathbb{p}(\boldsymbol{x}')\cdot(\boldsymbol{x}-\boldsymbol{x}')}{\|\boldsymbol{x}-\boldsymbol{x}'\|^3}\,\mathrm{d}v(\boldsymbol{x}')\,. \tag{2.123}$$

This expression can further be simplified using the divergence theorem and $\operatorname{grad}[\frac{1}{\|\boldsymbol{x}-\boldsymbol{x}'\|}] = -\operatorname{grad}'[\frac{1}{\|\boldsymbol{x}-\boldsymbol{x}'\|}]$

$$\phi(\boldsymbol{x}) = \frac{1}{4\pi\epsilon_0}\int_{\mathcal{P}_t}\frac{\rho_b^e(\boldsymbol{x}')}{\|\boldsymbol{x}-\boldsymbol{x}'\|}\,\mathrm{d}v(\boldsymbol{x}') + \frac{1}{4\pi\epsilon_0}\int_{\partial\mathcal{P}_t}\frac{\sigma_b^e(\boldsymbol{x}')}{\|\boldsymbol{x}-\boldsymbol{x}'\|}\,\mathrm{d}a(\boldsymbol{x}')\,, \tag{2.124}$$

where $\rho_b^e = -\operatorname{div}\mathbb{p}$ is the volume bound charge density and $\sigma_b^e = \mathbb{p}\cdot\boldsymbol{n}$ is the surface bound charge density. Thus, the total charge within the volume of a body is contained from free charges and bound charges, i.e., $\rho^e = \rho_f^e + \rho_b^e$. If we define the electric displacement to be $\mathbb{d} := \epsilon_0\mathbb{e} + \mathbb{p}$, then Gauss' law of electricity in a matter yields

$$\operatorname{div}\mathbb{d} = \epsilon_0\operatorname{div}\mathbb{e} + \operatorname{div}\mathbb{p} = \rho_f^e\,. \tag{2.125}$$

Linear dielectrics. The observed polarization of a linear isotropic dielectric under an external electric field is determined by $\mathbb{p} = \epsilon_0 \chi^e \mathbb{e}$. Here χ^e denotes the electric susceptibility of the material. It is a dimensionless quantity and relates the electric displacement to the electric field as

$$\mathbb{d} = \epsilon_0 \mathbb{e} + \mathbb{p} = \epsilon_0 (1 + \chi^e) \mathbb{e} = \epsilon_0 \epsilon_r \mathbb{e} = \epsilon \mathbb{e} \,, \tag{2.126}$$

where $\epsilon_r = (1+\chi^e) \geq 1$ is referred to as the relative permittivity (a dimensionless quantity) and ϵ is the dielectric constant of the material.

2.2.4 Geometrical transformations of fields in electrostatics

Heretofore, we have considered fundamental equations of electrostatics in terms of spatial (Eulerian) fields. However, to describe the deformation of a solid material in an electric field within a continuum setting, it is convenient to have the fundamental equations of electrostatics also in the reference (Lagrangian) configuration. Therefore, in this section, we will introduce the referential (Lagrangian) forms of fundamental quantities of electrostatics and show the relationship to the spatial configurations.

We introduce the Lagrangian electric field based on the invariance of the scalar electric potential ϕ based on (2.118) as

$$\phi(\boldsymbol{x}) = -\int_{\boldsymbol{x}_0}^{\boldsymbol{x}} \mathbb{e} \cdot \mathrm{d}\boldsymbol{x} = -\int_{\boldsymbol{X}_0}^{\boldsymbol{X}} \mathbb{E} \cdot \mathrm{d}\boldsymbol{X} \,, \tag{2.127}$$

where $\mathbb{E}$ is the Lagrangian electric field. It is related to the spatial electric field via the following push-forward and pull-back relations

$$\mathbb{e} = \boldsymbol{F}^{-T} \mathbb{E} \quad \text{or} \quad \mathbb{E} = \boldsymbol{F}^T \mathbb{e} \,. \tag{2.128}$$

Considering (2.127) over a closed curve and applying Stokes' theorem, we also obtain push-forward and pull-back relations for curls of the referential and spatial electric fields

$$\operatorname{curl} \mathbb{e} = J \boldsymbol{F}^{-1} \operatorname{Curl} \mathbb{E} = \boldsymbol{0} \,. \tag{2.129}$$

If we consider the material time derivative of the integrals in (2.127) for a closed curve, we further obtain the following relations

$$\boldsymbol{\pounds}_{\boldsymbol{v}} \mathbb{e} = \boldsymbol{F}^{-T} \dot{\mathbb{E}} \quad \text{and} \quad \operatorname{curl}[\boldsymbol{\pounds}_{\boldsymbol{v}} \mathbb{e}] = J \boldsymbol{F}^{-1} \operatorname{Curl} \dot{\mathbb{E}} = \boldsymbol{0} \,, \tag{2.130}$$

where $\boldsymbol{\pounds}_{\boldsymbol{v}} \mathbb{e} = \dot{\mathbb{e}} + \boldsymbol{l}^T \mathbb{e}$, see Section 2.1.8. Equation $(2.130)_2$ is the incremental form of Faraday's law with respect to the deformed configuration.

Analogously, we define the Lagrangian electric displacement from the following invariance relation

$$\int_{\mathcal{P}_t} \rho_f^e \, \mathrm{d}v = \int_{\partial \mathcal{P}_t} \mathbb{d} \cdot \mathrm{d}\boldsymbol{a} = \int_{\partial \mathcal{P}_0} \mathbb{D} \cdot \mathrm{d}\boldsymbol{A} \,, \tag{2.131}$$

where $\mathbb{D}$ is the Lagrangian electric displacement and related to the spatial electric displacement via the following relations

$$\mathbb{d} = J^{-1} \boldsymbol{F} \mathbb{D} \quad \text{or} \quad \mathbb{D} = J \boldsymbol{F}^{-1} \mathbb{d} \,. \tag{2.132}$$

Applying Gauss' theorem in (2.131), we obtain Gauss' law of electricity in terms of the referential and spatial electric displacements

$$\rho_f^e = \operatorname{div} \mathit{d} = J^{-1} \operatorname{Div} \mathbb{D} \,. \tag{2.133}$$

Furthermore, if we consider the material time derivative of the integrals in (2.127), we further arrive at

$$\boldsymbol{\pounds}_{\boldsymbol{v}} \mathit{d} = J^{-1} \boldsymbol{F} \dot{\mathbb{D}} \quad \text{and} \quad \frac{1}{J} \frac{\mathrm{d}}{\mathrm{d}t} (J \rho_f^e) = \operatorname{div}[\boldsymbol{\pounds}_{\boldsymbol{v}} \mathit{d}] = J^{-1} \operatorname{Div} \dot{\mathbb{D}} \,, \tag{2.134}$$

where, $\boldsymbol{\pounds}_{\boldsymbol{v}} \mathit{d} = \dot{\mathit{d}} - \boldsymbol{l} \mathit{d} + \mathit{d} \operatorname{div} \boldsymbol{v}$, see Section 2.1.8. $(2.134)_2$ is the incremental form of Gauss' law of electricity.

Finally, in order to determine the referential polarization vector, we start from the definition of the electric displacement d depending on the electric field and the polarization vector

$$\mathit{d} = \epsilon_0 \mathit{e} + \mathit{p} \quad \Rightarrow \quad J^{-1} \boldsymbol{F} \mathbb{D} = \epsilon_0 \boldsymbol{F}^{-T} \mathbb{E} + \mathbb{p} \,. \tag{2.135}$$

Simplifying the latter equation, we obtain

$$\mathbb{D} = \epsilon_0 J \boldsymbol{F}^{-1} \boldsymbol{F}^{-T} \mathbb{E} + J \boldsymbol{F}^{-1} \mathbb{p} = \epsilon_0 J \boldsymbol{C}^{-1} \mathbb{E} + \mathbb{P} \,, \tag{2.136}$$

where $\mathbb{P} = J \boldsymbol{F}^{-1} \mathbb{p}$ is the Lagrangian polarization vector and $\boldsymbol{C}$ is the right Cauchy-Green deformation tensor. We note that the mapping relation between the Lagrangian and Eulerian polarization fields can also be deduced from the relationships $\sigma_b = \mathit{p} \cdot \boldsymbol{n}$ and $\rho_b = -\operatorname{div} \mathit{p}$ considering the invariance of the bound charges, similar to (2.131).

From (2.135) and (2.136), we observe that the vector $\epsilon_0 \mathit{e}$ does not transform as the electric field e itself, but as the electric displacement, i.e., the Lagrangian form of this vector reads $J \boldsymbol{F}^{-1} (\epsilon_0 \mathit{e})$. This is because the scalar electric permittivity is associated with the *Hodge operator* as discussed in [189]; see also [25, 55]. Nevertheless, special care must be given when dealing with tensorial objects multiplied or divided with the permittivity tensor.

2.2.5 Electric force, momentum, and energy supply in matter

In this section, we determine electric forces, momentum, and energy supply in a deformable medium due to an applied electric field and polarization phenomenon. We focus on the behavior of dielectrics and therefore do not consider free volume charges. The derived equations are in line with the literature; see [171] and dissertations [197, 250, 235] as well as [64, 48].

The electric force due to the bound charges can be computed based on Coulomb's law, which yields the so-called electric body force $\boldsymbol{\gamma}_b^e$ as given below

$$\boldsymbol{\mathcal{F}}_b^e = \int_{\mathcal{P}_t} \rho_b^e \mathit{e} \, \mathrm{d}v + \int_{\partial \mathcal{P}_t} \sigma_b^e \mathit{e} \, \mathrm{d}a = \int_{\mathcal{P}_t} (\operatorname{grad} \mathit{e}) \mathit{p} \, \mathrm{d}v =: \int_{\mathcal{P}_t} \boldsymbol{\gamma}^e \, \mathrm{d}v \,, \tag{2.137}$$

where we have considered $\rho_b^e = -\operatorname{div} \mathit{p}$ and $\sigma_b^e = \mathit{p} \cdot \boldsymbol{n}$ together with the divergence theorem.

The momentum due to the bound charges is determined in a similar way

$$\begin{aligned}\mathfrak{M}_b^e &= \int_{\mathcal{P}_t} \boldsymbol{x} \times \rho_b^e \mathbb{e}\, \mathrm{d}v + \int_{\partial\mathcal{P}_t} \boldsymbol{x} \times \sigma_b^e \mathbb{e}\, \mathrm{d}a \\ &= \int_{\mathcal{P}_t} (\mathbb{p} \times \mathbb{e} + \boldsymbol{x} \times [(\operatorname{grad} \mathbb{e})\mathbb{p}])\, \mathrm{d}v = \int_{\mathcal{P}_t} (\boldsymbol{\omega}_b^e + \boldsymbol{x} \times \boldsymbol{\gamma}_b^e)\, \mathrm{d}v\,,\end{aligned} \tag{2.138}$$

where $\boldsymbol{\omega}_b^e := \mathbb{p} \times \mathbb{e}$ is the so-called electric couple vector characterizing the infinitesimal rotation of the dipoles with an infinitesimal volume element $\mathrm{d}v$ at a position $\boldsymbol{x}$. The second-order skew-symmetric couple tensor is defined as $\widehat{\boldsymbol{\omega}}_b^e = -\frac{1}{2}\boldsymbol{\epsilon} \cdot \boldsymbol{\omega}_b^e = \operatorname{skew}[\mathbb{e} \otimes \mathbb{p}]$. Hence, the electric couple vector $\boldsymbol{\omega}_b^e = -\boldsymbol{\epsilon} : \widehat{\boldsymbol{\omega}}_b^e$ of the bound charges is the axial vector of $\widehat{\boldsymbol{\omega}}_b^e$.

The electric energy supply due to the bound charges are assumed to have two contributions in electrostatics. The first contribution is associated with the power of Coulomb's force of the charges due to the deformation at a position $\boldsymbol{x}$. The second contribution is associated with a change in the bound charges due to a change in dipoles. This can be expressed as follows

$$\begin{aligned}\mathcal{P}_b^e &= \int_{\mathcal{P}_t} \rho_b^e(\boldsymbol{x}) \mathbb{e} \cdot \boldsymbol{v}\, \mathrm{d}v + \int_{\partial\mathcal{P}_t} \sigma_b^e \mathbb{e} \cdot \boldsymbol{v}\, \mathrm{d}a + \int_{\mathcal{P}_t} \phi \frac{\mathrm{d}}{\mathrm{d}t}(\rho_b \mathrm{d}v) + \int_{\partial\mathcal{P}_t} \phi \frac{\mathrm{d}}{\mathrm{d}t}(\sigma_b \mathrm{d}a) \\ &= \int_{\mathcal{P}_t} (\boldsymbol{\gamma}_b^e \cdot \boldsymbol{v} + (\mathbb{e} \otimes \mathbb{p}) : \boldsymbol{g}\boldsymbol{l} + \mathbb{e} \cdot \boldsymbol{\pounds}_{\boldsymbol{v}} \mathbb{p})\, \mathrm{d}v\,,\end{aligned} \tag{2.139}$$

where we have considered the material time derivative of bound charges $\frac{1}{J}\frac{\mathrm{d}}{\mathrm{d}t}(J\rho_b) = -\operatorname{div}[\boldsymbol{\pounds}_{\boldsymbol{v}}\mathbb{p}]$ and $\frac{\mathrm{d}}{\mathrm{d}t}(\sigma_b\, \mathrm{d}a) = -\boldsymbol{\pounds}_{\boldsymbol{v}}\mathbb{p} \cdot \boldsymbol{n}\, \mathrm{d}a$[6].The objective Lie derivative of polarization $\boldsymbol{\pounds}_{\boldsymbol{v}}\mathbb{p} = \dot{\mathbb{p}} - \boldsymbol{l}\mathbb{p} + \mathbb{p} \operatorname{div} \boldsymbol{v}$ is considered above. Note that the obtained energy supply term is in line with the derivations of [171] for further details, we confer to [143, 197, 250].

[6]The identities are obtained from the following definition of the volume and surface bound charges

$$\frac{\mathrm{d}}{\mathrm{d}t}\int_{\mathcal{P}_t} \rho_b\, \mathrm{d}v = -\frac{\mathrm{d}}{\mathrm{d}t}\int_{\mathcal{P}_t} \operatorname{div} \mathbb{p}\, \mathrm{d}v \quad \text{and} \quad \frac{\mathrm{d}}{\mathrm{d}t}\int_{\partial\mathcal{P}_t} \sigma_b\, \mathrm{d}a = -\frac{\mathrm{d}}{\mathrm{d}t}\int_{\partial\mathcal{P}_t} \mathbb{p} \cdot \boldsymbol{n}\, \mathrm{d}a\,. \tag{2.140}$$

We can recast $(2.140)_1$ into the following form

$$\frac{\mathrm{d}}{\mathrm{d}t}\int_{\mathcal{P}_t} \rho_b\, \mathrm{d}v = \int_{\mathcal{P}_t} \frac{1}{J}\frac{\mathrm{d}}{\mathrm{d}t}(J\rho_b)\, \mathrm{d}v = -\int_{\mathcal{P}_t} (\dot{\overline{\operatorname{div} \mathbb{p}}} + \operatorname{div} \mathbb{p} \operatorname{div} \boldsymbol{v})\, \mathrm{d}v = -\int_{\mathcal{P}_t} \operatorname{div}[\boldsymbol{\pounds}_{\boldsymbol{v}}\mathbb{p}]\,. \tag{2.141}$$

Similarly, we carry out the material time derivatives in $(2.140)_2$ as

$$\frac{\mathrm{d}}{\mathrm{d}t}\int_{\partial\mathcal{P}_t} \sigma_b\, \mathrm{d}a = \frac{\mathrm{d}}{\mathrm{d}t}\int_{\partial\mathcal{P}_t} \mathbb{p} \cdot \boldsymbol{n}\, \mathrm{d}a = -\int_{\partial\mathcal{P}_t} (\frac{\mathrm{d}}{\mathrm{d}t}\mathbb{p} + \mathbb{p} \operatorname{div} \boldsymbol{v} - \boldsymbol{l}\mathbb{p}) \cdot \boldsymbol{n}\, \mathrm{d}a\,, \tag{2.142}$$

where the term under the integral sign on the right-hand side can be identified as the Lie derivative of the polarization. By localizing the integral equations, we obtained the sought-after expressions. $(2.141)_2$ is also referred to as the spatial nominal time derivative; see Pelteret and Steinmann [176], eq. (5.19a) and (5.19b)

2.3 Fundamentals of Magnetostatics

In the previous section, we have considered the electric field of stationary charges. This assumption was made to exclude any other effects since experiments show that a moving charge generates a magnetic field. Here we relax this assumption. However, we consider only steady currents. The magnetic field induced by steady currents does not change in time; thus, we can neglect the electrodynamic coupling with an electric field. Nevertheless, magnetostatics has proven useful for applications considered in this thesis; see also [64], Chapter 5.2.1.

Similar to the interactions between two charges in electrostatics, observations show that two parallel wires attract each other when an electric current flows through the wires in the same direction and repels otherwise ([64], Chapter 5.1). The electric current of amount I in a straight wire generates an azimuthal magnetic field of strength $\mu_0 I/(2\pi r)$ at a distance r from the wire with the magnetic permeability of vacuum $\mu_0 = 4\pi{\cdot}10^{-7}\,\mathrm{N/A}$ (e.g., [48], Chapter 2.2.1). The direction of the magnetic field can be identified by the right-hand rule; given that the thumb of the right hand is directed along the current flow, the curling of fingers will be along the magnetic field. Then, the induced force is perpendicular to the direction of the electric current and the magnetic field at any point in space. This has been described in Fig. 2.7.

The primary source of the magnetic field – the magnetic dipole – is considered to be a small current-carrying circuit similar to electric charges in electrostatics. This is known as the Ampère model, and it is sometimes considered to correspond to electron spin at the atomic scale. It is worth noting that there is also the Gilbert model, which assumes that a dipole is contained of two poles (similar to the north and south poles of a bar magnet) separated by a small distance similar to the dipole in electrostatics ([64], Chapter 6.1.2). A similar model to the latter has been exploited in [171] to derive the governing equations of electrodynamics in deformable solids. Despite the usefulness of the Gilbert model, it is not considered physically well-motivated because of the non-existence of magnetic monopoles or magnetic charges. It is worth mentioning that the former type of the dipole model forms the bases for the Ampère formulation of electromagnetism and the latter for the Chu formulation [171].

In this section, we concentrate on quasi-static processes and consider the magnetic field of steady electric currents based on the Ampère model. We start with the conservation of charge and concisely introduce the fundamental equations of magnetostatics in a continuous setting. The brief introduction is based on [113, 96, 64, 48], among others.

2.3.1 Conservation of electric charge

This conservation law governs the temporal change of electric charge $\rho^e(\boldsymbol{x}, t)$ in an arbitrary volume $\mathcal{V}_t$ depending on the flux $\boldsymbol{j}(\boldsymbol{x}, t)$ of the electric charge through the surface of this volume $\partial\mathcal{V}_t$. In a continuous setting, where the charges and fluxes are smeared out over a considered volume, the conservation law can be stated as follows

$$\frac{\mathrm{d}}{\mathrm{d}t}\int_{\mathcal{V}_t} \rho^e \,\mathrm{d}v = -\int_{\partial\mathcal{V}_t} \boldsymbol{j}\cdot\mathrm{d}\boldsymbol{a}\,, \tag{2.143}$$

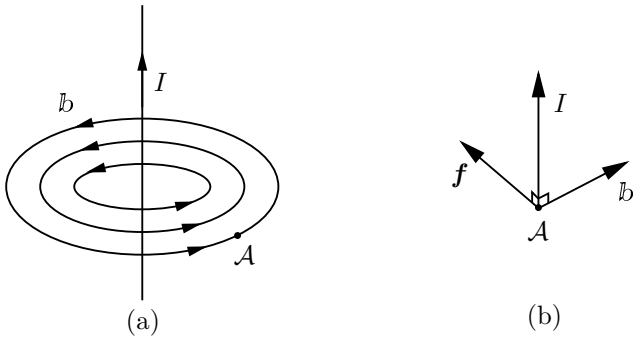

Figure 2.7: *Magnetic field of electric current in a wire.* (**a**) An electric current of magnitude I in a straight wire induces a radial magnetic induction $\|\mathbb{b}\| = \mu_0 I/(2\pi r)$ at a radial distance r from the wire. (**b**) The induced force due to the magnetic induction is perpendicular to the direction of the electric current and the magnetic induction.

where $\boldsymbol{j}$ is referred to as electric current density. It defines the charge per unit time per unit area and measured by ampère per meter squared ($\mathrm{A/m^2} = \mathrm{C/(m^2 \cdot sec)}$).

Applying Gauss' integral theorem to transform the surface integral in (2.143) to a volume integral and considering that $\mathcal{V}_t$ can be arbitrary, we obtain the following differential form for the balance of electric charge

$$\dot{\rho}^e = -\operatorname{div} \boldsymbol{j} \,. \tag{2.144}$$

Since we are concentrating on magnetostatics, we furthermore consider steady currents and do not consider any time dependence. This means that if steady current flows in a wire, then at any time instance, the amount of the charge within any infinitesimal volume of this wire is conserved. This can be expressed as follows

$$\dot{\rho}^e = 0 \quad \text{and} \quad \operatorname{div} \boldsymbol{j} = 0 \,. \tag{2.145}$$

The steady electric current is a divergence-free vector; hence, it can be expressed as $\boldsymbol{j} = \operatorname{curl} \mathbb{h}$ to fulfill $(2.145)_2$ apriori. Here, $\mathbb{h}$ is referred to as the magnetic field, which will be discussed in the following sections.

2.3.2 The Biot-Savart law

As we have briefly discussed above, a steady current flowing in a wire induces a magnetic field. Let us assume that a wire with an infinitesimal cross section $\mathrm{d}\boldsymbol{a}'$ is given and a steady current of magnitude $I \approx \boldsymbol{j} \cdot \mathrm{d}\boldsymbol{a}'$ flows in this wire. Then, according to the experimental observations of Biot and Savart as well as Ampère, the magnetic induction at a point $\boldsymbol{x}$ in space induced by an infinitesimal length $\mathrm{d}\boldsymbol{x}$ of this wire is determined by

$$\mathrm{d}\mathbb{b}(\boldsymbol{x}) = \frac{\mu_0 I}{4\pi} \frac{\mathrm{d}\boldsymbol{x}' \times (\boldsymbol{x} - \boldsymbol{x}')}{\|\boldsymbol{x} - \boldsymbol{x}'\|^3} \,, \tag{2.146}$$

where $\mu_0 = 4\pi \cdot 10^{-7}\,\mathrm{N/A^2}$ denotes the permeability of free space. The total magnetic field of the whole length $\mathcal{C}_t$ of the wire is then determined by the following integral

$$\mathbb{b}(\boldsymbol{x}) = \frac{\mu_0 I}{4\pi} \int_{\mathcal{C}_t} \frac{\mathrm{d}\boldsymbol{x}' \times (\boldsymbol{x} - \boldsymbol{x}')}{\|\boldsymbol{x} - \boldsymbol{x}'\|^3} = \frac{\mu_0}{4\pi} \int_{\mathcal{V}_t} \frac{\boldsymbol{j}(\boldsymbol{x}') \times (\boldsymbol{x} - \boldsymbol{x}')}{\|\boldsymbol{x} - \boldsymbol{x}'\|^3} \mathrm{d}v' \,, \tag{2.147}$$

where $I\mathrm{d}\boldsymbol{x}' = \boldsymbol{j}(\boldsymbol{x}')\mathrm{d}v'$ is considered and $\mathcal{V}_t$ denotes the volume of the wire. This equation is the *Biot-Savart law*. In the subsequent sections, we refer to $\mathbb{b}$ as the magnetic induction. The unit of magnetic induction is given in teslas (T), which is determined as newtons per ampère per meter $\mathrm{T} = \mathrm{N}/(\mathrm{A}\cdot\mathrm{m})$. We can further simplify this equation as follows (compare with (2.114) and (2.115))

$$\mathbb{b}(\boldsymbol{x}) = \frac{\mu_0}{4\pi}\,\mathrm{curl}\left[\int_{\mathcal{V}_t}\frac{\boldsymbol{j}(\boldsymbol{x}')}{\|\boldsymbol{x}-\boldsymbol{x}'\|}\mathrm{d}v'\right], \tag{2.148}$$

where the curl operator is w.r.t. the radius vector $\boldsymbol{x}$. Hence, we can introduce a vector potential $\boldsymbol{a}^m(\boldsymbol{x})$ as

$$\boldsymbol{a}^m(\boldsymbol{x}) = \frac{\mu_0}{4\pi}\int_{\mathcal{V}_t}\frac{\boldsymbol{j}(\boldsymbol{x}')}{\|\boldsymbol{x}-\boldsymbol{x}'\|}\mathrm{d}v'\,. \tag{2.149}$$

Then, the Biot-Savart law takes the following compact form

$$\mathbb{b} = \mathrm{curl}\,\boldsymbol{a}^m\,. \tag{2.150}$$

Since the divergence of the curl is zero, we arrive at one of the fundamental equations of magnetostatics

$$\mathrm{div}\,\mathbb{b} = 0\,. \tag{2.151}$$

This equation is similar to Gauss' law of electricity, which is also referred to as *Gauss' law of magnetism*. It implies that the flux of magnetic induction through a closed surface is always zero. The equation is also valid for the most general case of electrodynamics and implies the non-existence of magnetic monopoles or charges.

It is essential to notice in (2.150), the magnetic vector potential does not define the magnetic induction uniquely since any gradient term added to magnetic vector potential will vanish, i.e., $\mathrm{curl}\,\boldsymbol{a}^m = \mathrm{curl}(\boldsymbol{a}^m + \mathrm{grad}\,\omega)$ for any sufficiently smooth $\omega \in \mathcal{R}$. In order to have a unique vector potential, a *Coulomb gauge transformation* is considered in magnetostatics which reads as

$$\mathrm{div}\,\boldsymbol{a}^m = 0\,. \tag{2.152}$$

2.3.3 Ampère's circuital law

In analogy to Faraday's law of electrostatics, we now take a look at the curl of the magnetic induction

$$\mathrm{curl}\,\mathbb{b} = \mathrm{curl}\,\mathrm{curl}\,\boldsymbol{a}^m = \mathrm{grad}\,\mathrm{div}\,\boldsymbol{a}^m - \mathrm{div}\,\mathrm{grad}\,\boldsymbol{a}^m = -\,\mathrm{div}\,\mathrm{grad}\,\boldsymbol{a}^m\,, \tag{2.153}$$

where (2.152) is considered. Furthermore, taking the definition of the vector potential (2.149) in (2.153) into account and after some manipulations, we obtain

$$\mathrm{curl}\,\mathbb{b} = -\,\mathrm{div}\,\mathrm{grad}\,\boldsymbol{a}^m = \mu_0\boldsymbol{j}\,, \tag{2.154}$$

where the following relations are considered

$$\mathrm{div}\left[\frac{\boldsymbol{x}-\boldsymbol{x}'}{\|\boldsymbol{x}-\boldsymbol{x}'\|^3}\right] = 4\pi\delta(\boldsymbol{x}-\boldsymbol{x}') \quad \text{and} \quad \int_{\mathcal{V}_t}\boldsymbol{j}(\boldsymbol{x}')4\pi\delta(\boldsymbol{x}-\boldsymbol{x}')\,\mathrm{d}v' = 4\pi\boldsymbol{j}(\boldsymbol{x})\,, \tag{2.155}$$

where $\delta(\boldsymbol{x}-\boldsymbol{x}')$ is the Dirac delta function; see Griffiths [64], Chapters 1.5.1–1.5.3 and 5.3.2 for a detailed derivation. (2.154) is a local statement of *Ampère's law of magnetostatics*. It defines Laplace's equation for the magnetic vector potential (compare with (2.121)) and, together with suitable boundary conditions, determines $\boldsymbol{a}^m$ uniquely for a given electric current density $\boldsymbol{j}$.

Ampère's law of magnetostatics can also be given in terms of the magnetic field $\mathbb{h}$

$$\operatorname{curl} \mathbb{h} = \boldsymbol{j}\,, \tag{2.156}$$

where $\mathbb{b} = \mu_0 \mathbb{h}$ is considered in free space. This equation was also derived in Section 2.3.1 from the conservation of electric charge. The magnetic field in magnetostatics resembles the electric field $\mathbb{e}$ in electrostatics in terms of the mapping properties and boundary conditions. Likewise, the magnetic induction $\mathbb{b}$ resembles the electric displacement $\mathbb{d}$. This will be clear when we derive the geometric transformations for the magnetostatic fields below.

2.3.4 Magnetization of a body in a magnetic field

As we have already briefly discussed, the magnetic field is generated by charges in motion. In the atomic scale of magnetic materials, electrons revolve around nuclei and spin about their axis, which can be considered to generate infinitesimal current loops or magnetic dipoles; see Fig. 2.8. Without external action, these magnetic dipoles are usually randomly oriented and, therefore, do not induce a magnetic field. However, in an external magnetic field the dipoles can align themselves. Hence, the material becomes magnetized. Depending on the alignment of the magnetization, we can distinguish paramagnetic, diamagnetic, ferromagnetic, and even ferrimagnetic materials. Depending on the type of magnetic material, the induced magnetic field in the material can be in the opposite direction (e.g., in diamagnetic materials) or in the same direction (e.g., in paramagnetic or ferromagnetic materials) as the applied magnetic field. As a result, the materials can show different effects. Such as, diamagnets are repelled away by a non-uniform magnetic field and paramagnets are attracted; see [64], Chapter 6.

In order to describe the magnetization, we take a look at the magnetic vector potential at position $\boldsymbol{x}$ due to a simplified infinitesimal current loop centered at position $\boldsymbol{x}'$

$$\begin{aligned}
\widetilde{\boldsymbol{a}}^m(\boldsymbol{x}) &= \frac{\mu_0}{4\pi}\int_{\mathcal{V}_t} \frac{\boldsymbol{j}(\boldsymbol{\delta})}{\|\boldsymbol{x}-\boldsymbol{x}'-\boldsymbol{\delta}\|}\mathrm{d}v(\boldsymbol{\delta}) = \frac{\mu_0 I}{4\pi}\int_{\mathcal{C}_t} \frac{\mathrm{d}\boldsymbol{\delta}}{\|\boldsymbol{x}-\boldsymbol{x}'-\boldsymbol{\delta}\|} \\
&\approx \frac{\mu_0 I}{4\pi}\int_{\mathcal{C}_t}\left[\frac{1}{\|\boldsymbol{x}-\boldsymbol{x}'\|} - \boldsymbol{\delta}\cdot\operatorname{grad}\Big(\frac{1}{\|\boldsymbol{x}-\boldsymbol{x}'\|}\Big)\right]\mathrm{d}\boldsymbol{\delta} \\
&= \frac{\mu_0 I}{4\pi}\int_{\mathcal{C}_t}(\mathrm{d}\boldsymbol{\delta}\otimes\boldsymbol{\delta})\frac{(\boldsymbol{x}-\boldsymbol{x}')}{\|\boldsymbol{x}-\boldsymbol{x}'\|^3} = \frac{\mu_0}{4\pi}\frac{\widetilde{\boldsymbol{\mathcal{M}}}(\boldsymbol{x}-\boldsymbol{x}')}{\|\boldsymbol{x}-\boldsymbol{x}'\|^3} = \frac{\mu_0}{4\pi}\frac{\widetilde{m}\times(\boldsymbol{x}-\boldsymbol{x}')}{\|\boldsymbol{x}-\boldsymbol{x}'\|^3}\,,
\end{aligned} \tag{2.157}$$

where $\|\boldsymbol{\delta}\| \ll 1$ is the radius vector pointing from $\boldsymbol{x}'$ to an infinitesimal part of the current loop $\mathrm{d}\boldsymbol{\delta}$. $\widetilde{\boldsymbol{\mathcal{M}}}$ is the second-order skew-symmetric magnetization tensor of a single dipole, and $\widetilde{\boldsymbol{m}}$ is its axial (magnetization) vector, which are defined as

$$\widetilde{\boldsymbol{\mathcal{M}}} = I\int_{\mathcal{C}_t}\mathrm{d}\boldsymbol{\delta}\otimes\boldsymbol{\delta} \quad\text{and}\quad \widetilde{m} = -\frac{1}{2}\boldsymbol{\epsilon} : \operatorname{skew}\widetilde{\boldsymbol{M}} = I\int_{\mathcal{S}_t}\mathrm{d}\boldsymbol{a}(\boldsymbol{\delta})\,, \tag{2.158}$$

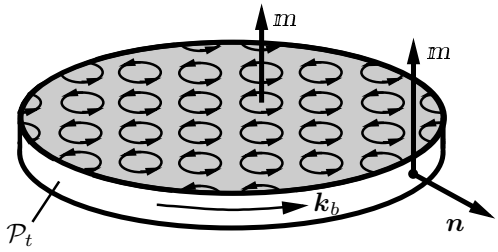

Figure 2.8: *Bound electric currents of magnetic dipoles.* The magnetic dipole moment induced in sub-body $\mathcal{P}_t$ as a result of an external magnetic field is described via infinitesimal current loops, which are distributed throughout the volume of the body. In a uniform magnetic field, the volume bound current cancels since the currents flow in opposite directions in the neighboring dipoles. However, we still have the bound currents on the surface. In a non-uniform magnetic field, the volume bound current does not cancel. In this case, we have both volume and surface bound currents. The volume bound current is determined by the curl of the magnetization vector, $\boldsymbol{j}_b = \operatorname{curl} \mathbb{m}$, and the bound surface current is determined at the surface by $\boldsymbol{k}_b = \mathbb{m} \times \boldsymbol{n}$.

where $\mathrm{d}\boldsymbol{a}(\boldsymbol{\delta})$ denotes the area enclosed by the current loop.

Considering that a volume element $\mathrm{d}v(\boldsymbol{x}')$ contains N infinitesimal dipoles (current loops), we can introduce the dipole moment density as $\mathbb{m}(\boldsymbol{x}') = \lim_{\mathrm{d}v \to 0} \sum_i^N \widetilde{\mathbb{m}}^i(\boldsymbol{x}')/\mathrm{d}v(\boldsymbol{x}')$ in a continuous setting. Based on the above (2.157), the magnetic vector potential at a point $\boldsymbol{x}$ due to the magnetization of a material sub-body $\mathcal{P}_t$ can thus be determined by integrating (2.157) over the volume of the sub-body as follows (Griffiths [64], Chapter 6.2.1)

$$\boldsymbol{a}^m(\boldsymbol{x}) = \frac{\mu_0}{4\pi} \int_{\mathcal{P}_t} \frac{\boldsymbol{j}_b(\boldsymbol{x}')}{\|\boldsymbol{x} - \boldsymbol{x}'\|} \,\mathrm{d}v' + \frac{\mu_0}{4\pi} \int_{\partial\mathcal{P}_t} \frac{\boldsymbol{k}_b(\boldsymbol{x}')}{\|\boldsymbol{x} - \boldsymbol{x}'\|} \,\mathrm{d}a' \,, \tag{2.159}$$

where $\boldsymbol{j}_b = \operatorname{curl} \mathbb{m}$ denotes the volume bound current density and $\boldsymbol{k}_b = \mathbb{m} \times \boldsymbol{n}$ denotes the surface bound current density. Thus, the total electric current density can be considered to be contained from free current density $\boldsymbol{j}_f$ and bound current density $\boldsymbol{j}_b$, i.e., $\boldsymbol{j} = \boldsymbol{j}_f + \boldsymbol{j}_b$.

Because of the magnetization, the magnetic field in the material is altered, which is considered to take the following form

$$\mathbb{b} = \mu_0(\mathbb{h} + \mathbb{m}) \,. \tag{2.160}$$

Therefore, Ampère's law of magnetostatics needs to be changed in the material body to

$$\operatorname{curl} \mathbb{h} = \boldsymbol{j}_f \,. \tag{2.161}$$

Linear and nonlinear media. For linear isotropic magnetic materials, the induced magnetization in terms of the external magnetic field can be given as $\mathbb{m} = \chi_h^m \mathbb{h}$ with χ_h^m being the magnetic susceptibility. The latter is a dimensionless quantity and relates the magnetic induction to the magnetic field as

$$\mathbb{b} = \mu_0(\mathbb{h} + \mathbb{m}) = \mu_0(1 + \chi_h^m)\mathbb{h} = \mu \mathbb{h} \,, \tag{2.162}$$

where μ is called the permeability of the material. Examples of linear materials can be paramagnetic ($\chi_h^m > 0$) and diamagnetic ($\chi_h^m < 0$) materials.

From the above equation, we can also express the magnetization in terms of the magnetic induction as

$$\mu_0 \mathbb{m} = \frac{\chi_h^m}{1+\chi_h^m}\mathbb{b} = \chi^m \mathbb{b} \quad \rightarrow \quad \chi^m = \frac{\chi_h^m}{1+\chi_h^m} \quad \text{or} \quad \chi_h^m = \frac{\chi^m}{1-\chi^m}\,, \tag{2.163}$$

where χ^m is also referred to as the magnetic susceptibility; see [113], Chapter 11.43.

In general, paramagnetism and diamagnetism are much weaker than ferromagnetism, and induced magnetization vanishes once the external field is removed. In contrast to paramagnetic and diamagnetic materials, ferromagnetic materials show a nonlinear, hysteretic behavior. Induced magnetization in a magnetic field shows characteristic saturation and irreversible behavior. Examples of these materials can be iron, nickel, cobalt, and Nd-Fe-B alloys. These materials can be embbeded into elastomers. As a result, the obtained composites – magnetorheological elastomers (MREs) – show characteristics of both phases. Depending on the hysteresis observed in the $\mathbb{b} - \mathbb{h}$ (or $\mathbb{m} - \mathbb{h}$) diagram upon loading and unloading of magnetic materials, soft and hard magnetic materials are distinguished. The soft magnetic materials magnetize and demagnetize relatively fast; as a result, the hysteresis is not pronounced and can often be neglected. In that case, a Langevin or a hyperbolic function is considered to describe the saturation of the magnetization; see, e.g., [186, 40, 91] and Paper **B**. For the Langevin model of soft MREs, the magnetization reads

$$\mathbb{m} = \frac{m_s}{\|\mathbb{b}\|}\left[\coth\left(\frac{3\chi^m\|\mathbb{b}\|}{\mu_0 m_s}\right) - \frac{\mu_0 m_s}{3\chi^m\|\mathbb{b}\|}\right], \tag{2.164}$$

where m_s is a parameter characterizing the saturation magnetization and $\|\mathbb{b}\| = \sqrt{\mathbb{b}\cdot\mathbb{b}}$ denotes magnitude of the magnetic induction.

Hard magnetic materials show pronounced hysteresis, and therefore, their response depends on the history; see recent works [102, 161] in the context of MREs and references therein for more information. In this thesis, soft magnetic materials will be under consideration.

2.3.5 Geometrical transformations of fields in magnetostatics

In analogy to Section 2.2.4, we introduce here Lagrangian analogues of spatial magnetostatic fields and their geometrical transformations.

The Lagrangian magnetic induction $\mathbb{B}$ is introduced based on Gauss' law of magnetism as follows

$$\int_{\partial\mathcal{P}_t} \mathbb{b}\cdot \mathrm{d}\boldsymbol{a} = \int_{\partial\mathcal{P}_0} \mathbb{B}\cdot \mathrm{d}\boldsymbol{A} = 0\,, \tag{2.165}$$

which yields the push-forward and pull-back relations for the magnetic induction as well as the Lagrangian form of Gauss' law of magnetism

$$\mathbb{b} = J^{-1}\boldsymbol{F}\mathbb{B} \quad \text{and} \quad \operatorname{div}\mathbb{b} = J^{-1}\operatorname{Div}\mathbb{B} = 0\,. \tag{2.166}$$

Taking the material time derivative of (2.165) and simplifying the results, we obtain the incremental relations

$$\boldsymbol{\pounds}_{\boldsymbol{v}}\mathbb{b} = J^{-1}\boldsymbol{F}\dot{\mathbb{B}} \quad \text{and} \quad \operatorname{div}[\boldsymbol{\pounds}_{\boldsymbol{v}}\mathbb{b}] = J^{-1}\operatorname{Div}\dot{\mathbb{B}} = 0\,, \tag{2.167}$$

where $\boldsymbol{\pounds}_{\boldsymbol{v}}\, \mathbb{b} = \dot{\mathbb{b}} - \boldsymbol{l}\mathbb{b} + \mathbb{b}\,\mathrm{div}\,\boldsymbol{v}$.

In a similar manner, the Lagrangian magnetic field $\mathbb{H}$ and electric free current $\boldsymbol{J}_f$ are obtained from Ampère's law (2.161) as follows

$$\begin{aligned} \int_{\mathcal{C}_t} \mathbb{h} \cdot \mathrm{d}\boldsymbol{x} &= \int_{\mathcal{S}_t} \boldsymbol{j}_f \cdot \mathrm{d}\boldsymbol{a} = \\ \int_{\mathcal{C}_0} \mathbb{H} \cdot \mathrm{d}\boldsymbol{X} &= \int_{\mathcal{S}_0} \boldsymbol{J}_f \cdot \mathrm{d}\boldsymbol{A}\,, \end{aligned} \tag{2.168}$$

which yields the push-forward and pull-back relations for the magnetic field and the electric current as follows

$$\mathbb{h} = \boldsymbol{F}^{-T}\mathbb{H} \quad \text{and} \quad \boldsymbol{j}_f = J^{-1}\boldsymbol{F}\boldsymbol{J}_f\,. \tag{2.169}$$

As a result, we obtain Ampère's law in the Lagrangian configuration as follows

$$\mathrm{Curl}\,\mathbb{H} = \boldsymbol{J}_f\,. \tag{2.170}$$

The incremental forms of the geometrical relations can be easily derived as

$$\boldsymbol{\pounds}_{\boldsymbol{v}}\mathbb{h} = \boldsymbol{F}^{-T}\dot{\mathbb{H}} \quad \text{and} \quad \boldsymbol{\pounds}_{\boldsymbol{v}}\boldsymbol{j}_f = J^{-1}\boldsymbol{F}\dot{\boldsymbol{J}}_f\,, \tag{2.171}$$

where $\boldsymbol{\pounds}_{\boldsymbol{v}}\mathbb{h} = \dot{\mathbb{h}} + \boldsymbol{l}^T\mathbb{h}$ and $\boldsymbol{\pounds}_{\boldsymbol{v}}\boldsymbol{j}_f = \dot{\boldsymbol{j}}_f - \boldsymbol{l}\boldsymbol{j}_f + \boldsymbol{j}_f\,\mathrm{div}\,\boldsymbol{v}$.

The incremental versions of Ampère's law in the Eulerian and the Lagrangian configurations take the form

$$\mathrm{curl}[\boldsymbol{\pounds}_{\boldsymbol{v}}\mathbb{h}] = \boldsymbol{\pounds}_{\boldsymbol{v}}\boldsymbol{j}_f \quad \text{and} \quad \mathrm{Curl}\,\dot{\mathbb{H}} = \dot{\boldsymbol{J}}_f\,. \tag{2.172}$$

Similar to the polarization vector, we can also introduce a Lagrangian magnetization vector. We start with the following relation

$$\mathbb{b} = \mu_0(\mathbb{h} + \mathbb{m}) \quad \Rightarrow \quad \mathbb{B} = \mu_0 J\boldsymbol{F}^{-1}\boldsymbol{F}^{-T}(\mathbb{H} + \mathbb{M}) = \mu_0 J\boldsymbol{C}^{-1}(\mathbb{H} + \mathbb{M})\,, \tag{2.173}$$

where $\mathbb{m} = \boldsymbol{F}^{-T}\mathbb{M}$ is obtained. In contrast to the polarization vector, we observe that the magnetization vector transforms differently. Nevertheless, the transformation rule is consistent with the definition of magnetization in terms of the bound currents, i.e., $\boldsymbol{j}_b = \mathrm{curl}\,\mathbb{m}$ and $\boldsymbol{k}_b = \mathbb{m} \times \boldsymbol{n}$.

The geometrical transformations of the magnetic vector potential $\boldsymbol{a}^m$ can be derived from (2.166) as

$$\mathbb{b} = J^{-1}\boldsymbol{F}\mathbb{B} \quad \Rightarrow \quad \mathrm{curl}\,\boldsymbol{a}^m = J^{-1}\boldsymbol{F}\,\mathrm{Curl}\,\boldsymbol{A}^m \quad \Rightarrow \quad \boldsymbol{a}^m = \boldsymbol{F}^{-T}\boldsymbol{A}^m\,. \tag{2.174}$$

The Lie derivative of the magnetic vector potential can easily be shown to be $\boldsymbol{\pounds}_{\boldsymbol{v}}\boldsymbol{a}^m = \boldsymbol{F}^{-T}\dot{\boldsymbol{A}}^m = \dot{\boldsymbol{a}} + \boldsymbol{l}^T\boldsymbol{a}^m$. Furthermore, the Coulomb gauge condition in the reference configuration consistent with (2.152) can be derived as

$$\mathrm{div}\,\boldsymbol{a}^m = J^{-1}\,\mathrm{Div}[J\boldsymbol{F}^{-1}\boldsymbol{a}^m] = J^{-1}\,\mathrm{Div}[J\boldsymbol{C}^{-1}\boldsymbol{A}^m] = 0\,, \tag{2.175}$$

where $J = \det\boldsymbol{F}$ is the Jacobian of the deformation gradient. We note that the standard version of the gauge condition, i.e., $\mathrm{Div}\,\boldsymbol{A}^m = 0$, is mainly considered in references such as [20, 209, 210] and [176], Chapter 5.3.5, since the underlying idea is to obtain a unique magnetic vector potential field.

2.3.6 Magnetic force, momentum, and energy supply in matter

In this section, we determine magnetic forces, momentum, and energy supply in a deformable medium due to an applied magnetic field and magnetization phenomenon. Magneto-elastic response is assumed, and no free electric currents are considered. For further information, we refer to [29, 113, 64, 140, 166, 48].

The force acting on a magnetic dipole due to the bound electric currents can be computed based on Lorentz's force, which yields a so-called magnetic body force $\boldsymbol{\gamma}_b^m$ similar to the electric body force

$$\boldsymbol{\mathcal{F}}_b^m = \int_{\mathcal{P}_t} \boldsymbol{j}_b \times \mathbb{b}\, \mathrm{d}v + \int_{\partial\mathcal{P}_t} \boldsymbol{k}_b \times \mathbb{b}\, \mathrm{d}a = \int_{\mathcal{P}_t} (\operatorname{grad} \mathbb{b})^T \mathbb{m}\, \mathrm{d}v = \int_{\mathcal{P}_t} \boldsymbol{\gamma}_b^m\, \mathrm{d}v\,, \quad (2.176)$$

where we have considered $\boldsymbol{j}_b = \operatorname{curl} \mathbb{m}$ and $\boldsymbol{k}_b = \boldsymbol{m} \times \boldsymbol{n}$ together with the divergence theorem.

The momentum due to the bound currents is determined as

$$\begin{aligned} \boldsymbol{\mathfrak{M}}_b^m &= \int_{\mathcal{P}_t} \boldsymbol{x} \times (\boldsymbol{j}_b \times \mathbb{b})\, \mathrm{d}v + \int_{\partial\mathcal{P}_t} \boldsymbol{x} \times (\boldsymbol{k}_b \times \mathbb{b})\, \mathrm{d}a \\ &= \int_{\mathcal{P}_t} (\mathbb{m} \times \mathbb{b} + \boldsymbol{x} \times [(\operatorname{grad} \mathbb{b})^T \mathbb{m}])\, \mathrm{d}v = \int_{\mathcal{P}_t} (\boldsymbol{\omega}_b^m + \boldsymbol{x} \times \boldsymbol{\gamma}_b^m)\, \mathrm{d}v\,, \end{aligned} \quad (2.177)$$

where $\boldsymbol{\omega}_b^m := \mathbb{m} \times \mathbb{b}$ is the so-called magnetic couple vector. We can also introduce the second-order skew-symmetric couple tensor as $\widehat{\boldsymbol{\omega}}_b^m = -\frac{1}{2}\boldsymbol{\epsilon} \cdot \boldsymbol{\omega}_b^m = \operatorname{skew}[\mathbb{b} \otimes \mathbb{m}]$. For the given couple tensor, the magnetic couple vector is determined as $\boldsymbol{\omega}_b^m = -\boldsymbol{\epsilon} : \widehat{\boldsymbol{\omega}}_b^m$.

The magnetic energy supply due to the bound currents is assumed to have two contributions in magnetostatics. The first contribution is associated with the power of the Lorentz force of the bound currents due to the deformation at a position $\boldsymbol{x}$. The second contribution is associated with an objective change in the bound currents due to a change in dipoles. This can be expressed as follows

$$\begin{aligned} \mathcal{P}_b^e &= \int_{\mathcal{P}_t} (\boldsymbol{j}_b \times \mathbb{b}) \cdot \boldsymbol{v}\, \mathrm{d}v + \int_{\partial\mathcal{P}_t} (\boldsymbol{k}_b \times \mathbb{b}) \cdot \boldsymbol{v}\, \mathrm{d}a + \int_{\mathcal{P}_t} \boldsymbol{a}^m \cdot \boldsymbol{\pounds}_{\boldsymbol{v}} \boldsymbol{j}_b\, \mathrm{d}v + \int_{\partial\mathcal{P}_t} \boldsymbol{a}^m \cdot (\boldsymbol{\pounds}_{\boldsymbol{v}} \boldsymbol{m} \times \boldsymbol{n})\, \mathrm{d}a \\ &= \int_{\mathcal{P}_t} (\boldsymbol{\gamma}_b^m \cdot \boldsymbol{v} - (\mathbb{m} \otimes \mathbb{b}) : \boldsymbol{g}\boldsymbol{l} + \boldsymbol{m} \cdot \mathbb{b} \operatorname{div} \boldsymbol{v} + \mathbb{b} \cdot \boldsymbol{\pounds}_{\boldsymbol{v}} \mathbb{m})\, \mathrm{d}v\,. \end{aligned} \quad (2.178)$$

2.4 Governing Equations of Nonlinear Magneto-Electro-Elasticity

This section provides the equations of the coupled magneto-electro-elasticity in the Eulerian configuration. Considering the electric and magnetic forces and momenta in the balance equations results in a non-symmetric mechanical stress tensor. In order to derive a convenient setting in terms of a symmetric stress tensor, we introduce the so-called electric and magnetic "Maxwell" stress tensors. Following this, the balance laws are reformulated, and the constitutive relations are derived. The equations are supplemented with boundary conditions required to solve the partial differential equations. For further details, see, for example, [171, 113, 96, 64, 48].

2.4.1 Balance laws and constitutive relations

Having introduced the electric and magnetic forces, momenta, and energies as a result of polarization and magnetization in a deformable medium, we can now introduce the balance laws of coupled magneto-electro-elasticity. For simplicity, we do not consider a direct coupling between magnetic and electric fields and concentrate on an isothermal case. Then, the local balance laws can be derived as follows

$$
\begin{aligned}
&1.\ \text{mass} && \dot{\rho} + \rho \operatorname{div} \boldsymbol{v} = 0 \,, \\
&2.\ \text{linear momentum} && \rho \dot{\boldsymbol{v}} = \operatorname{div}[\boldsymbol{\sigma}^{mec}] + \rho \boldsymbol{b} + \boldsymbol{\gamma}_b^e + \boldsymbol{\gamma}_b^m \,, \\
&3.\ \text{angular momentum} && \operatorname{skew}[\boldsymbol{\sigma}^{mec}] = \widehat{\boldsymbol{\omega}}_b^e + \widehat{\boldsymbol{\omega}}_b^m \,, \\
&4.\ \text{internal energy} && \rho \dot{e} = (\boldsymbol{\sigma}^{mec} + e^\sharp \otimes \mathbb{p} - m^\sharp \otimes \mathbb{b}) : (\boldsymbol{g}\boldsymbol{l}) + (m \cdot \mathbb{b}) \operatorname{div} \boldsymbol{v} \\
& && \quad + e \cdot \boldsymbol{\pounds}_{\boldsymbol{v}} \mathbb{p} + \mathbb{b} \cdot \boldsymbol{\pounds}_{\boldsymbol{v}} m \,,
\end{aligned}
\tag{2.179}
$$

where $e = \widehat{e}(\boldsymbol{F}, \mathbb{p}, m)$ characterizes the internal energy in terms of deformation, polarization and magnetization. The energy can also be written in terms of the electric field and the magnetic induction considering a Legendre-Fenchel transformation

$$
\rho \widetilde{\psi}(\boldsymbol{F}, e, \mathbb{b}) := \sup_{e} \inf_{\mathbb{b}} \left\{ \rho \widehat{e}(\boldsymbol{F}, \mathbb{p}, m) - e \cdot \mathbb{p} - \mathbb{b} \cdot m \right\} , \tag{2.180}
$$

which yields an alternative representation of the balance of energy

$$
\rho \dot{\widetilde{\psi}} = (\boldsymbol{\sigma}^{mec} + e^\sharp \otimes \mathbb{p} - m^\sharp \otimes \mathbb{b}) : (\boldsymbol{g}\boldsymbol{l}) + (m \cdot \mathbb{b}) \operatorname{div} \boldsymbol{v} - \mathbb{p} \cdot \boldsymbol{\pounds}_{\boldsymbol{v}} e - m \cdot \boldsymbol{\pounds}_{\boldsymbol{v}} \mathbb{b} \,. \tag{2.181}
$$

Electric and magnetic stress tensor. As we observe from the balance of angular momentum, the mechanical stress tensor is not symmetric. In order to arrive at a more convenient setting based on a symmetric stress tensor, we introduce the so-called electric and magnetic Maxwell stress tensors ([171, 197] and [96], Table 1)

$$
\begin{aligned}
\boldsymbol{\sigma}^e &= e^\sharp \otimes d - \frac{1}{2} \epsilon_0 (e \cdot e) \boldsymbol{g}^{-1} \quad \text{and} \\
\boldsymbol{\sigma}^m &= \mathbb{h}^\sharp \otimes \mathbb{b} - \frac{1}{2\mu_0} (\mathbb{b} \cdot \mathbb{b}) \boldsymbol{g}^{-1} + (\mathbb{b} \cdot m) \boldsymbol{g}^{-1} \,,
\end{aligned}
\tag{2.182}
$$

such that the electric and magnetic body forces and momenta can be determined as

$$
\operatorname{div}[\boldsymbol{\sigma}^e + \boldsymbol{\sigma}^m] = \boldsymbol{\gamma}_b^e + \boldsymbol{\gamma}_b^m \quad \text{and} \quad \operatorname{skew}[\boldsymbol{\sigma}^e + \boldsymbol{\sigma}^m] = \boldsymbol{\omega}_b^e + \boldsymbol{\omega}_b^m \,. \tag{2.183}
$$

Furthermore, the power of the electric and magnetic stress tensors in a deformable medium can be derived as follows

$$\begin{aligned} \boldsymbol{\sigma}^e : (\boldsymbol{gl}) &= -\rho \dot{u}^e + \epsilon_0 e \cdot \boldsymbol{\pounds}_{\boldsymbol{v}} e + (e^\sharp \otimes \mathbb{p}) : (\boldsymbol{gl}) \quad \text{and} \\ \boldsymbol{\sigma}^m : (\boldsymbol{gl}) &= \rho \dot{u}^m - \frac{1}{\mu_0} b \cdot \boldsymbol{\pounds}_{\boldsymbol{v}} b - (m^\sharp \otimes b) : (\boldsymbol{gl}) + (b \cdot m) \operatorname{div} \boldsymbol{v} \,, \end{aligned} \tag{2.184}$$

where we have introduced the energy of the electric and magnetic fields

$$\int_{\mathcal{P}_t} \rho u^e \, \mathrm{d}v = \int_{\mathcal{P}_t} \frac{\epsilon_0}{2} e \cdot e \, \mathrm{d}v \quad \text{and} \quad \int_{\mathcal{P}_t} \rho u^m \, \mathrm{d}v = \int_{\mathcal{P}_t} \frac{1}{2\mu_0} b \cdot b \, \mathrm{d}v \,. \tag{2.185}$$

Considering the above equations, associated with the electric and magnetic stress tensors, in the balance laws with further manipulations (see [171, 197]), we obtain the final form of the balance laws in the current configuration

1.	mass	$\dot{\rho} + \rho \operatorname{div} \boldsymbol{v} = 0 \,,$
2.	linear momentum	$\rho \dot{\boldsymbol{v}} = \operatorname{div} \boldsymbol{\sigma} + \rho \boldsymbol{b} \,,$
3.	angular momentum	$\operatorname{skew}[\boldsymbol{\sigma}] = \boldsymbol{0} \,,$
4.	internal energy	$\rho \dot{\psi} = \boldsymbol{\sigma} : \boldsymbol{d} + e \cdot \boldsymbol{\pounds}_{\boldsymbol{v}} d + h \cdot \boldsymbol{\pounds}_{\boldsymbol{v}} b \,,$

(2.186)

where we have introduced the total stress $\boldsymbol{\sigma} = \boldsymbol{\sigma}^{mec} + \boldsymbol{\sigma}^e + \boldsymbol{\sigma}^m$ and considered the following partial Legendre-Fenchel transformation

$$\rho \psi(\boldsymbol{F}, d, h) := \sup_{e} \left\{ \rho \widetilde{\psi}(\boldsymbol{F}, e, b) + \rho \widehat{u}^e(\boldsymbol{F}, e) + \rho \widehat{u}^m(\boldsymbol{F}, b) + e \cdot d \right\} . \tag{2.187}$$

Finally, the mathematical statement of the second law of thermodynamics expressed by the Clausius-Planck inequality can also be derived as

$$\rho \mathcal{D} = \boldsymbol{\sigma} : \boldsymbol{d} + e \cdot \boldsymbol{\pounds}_{\boldsymbol{v}} d + h \cdot \boldsymbol{\pounds}_{\boldsymbol{v}} b - \rho \dot{\psi} \geq 0 \,, \tag{2.188}$$

which together with $\boldsymbol{d} = 1/2 \boldsymbol{\pounds}_{\boldsymbol{v}} \boldsymbol{g}$ and under the assumption of elastic response, yields the following constitutive relations

$$\boldsymbol{\sigma} = 2\rho \partial_{\boldsymbol{g}} \psi \,, \quad e = \rho \partial_d \psi \quad \text{and} \quad h = \rho \partial_b \psi \,. \tag{2.189}$$

$(2.189)_1$ is also referred to as the Doyle-Ericksen formula; see [139], Chapter 3.2.

The above equations are coupled with the Maxwell equations for a quasi-static case in the current configuration

1.	Gauss law	$\operatorname{div} e = 0 \,,$
2.	Faraday law	$\operatorname{curl} e = \boldsymbol{0} \,,$
3.	Gauss-Ampère law	$\operatorname{div} b = 0 \,,$
4.	Ampère law	$\operatorname{curl} h = \boldsymbol{0} \,,$

(2.190)

where we have neglected any free electric charges and free electric currents.

We note that all the above equations can also be given in the Lagrangian configuration. The required transformations have already been introduced in the previous sections and will not be repeated again. For the formulations in the Lagrangian configuration, we further refer to the variational formulations provided in Papers **A** and **B**.

2.4.2 Boundary conditions at interfaces

Boundary conditions for the electrostatic and magnetostatic fields are derived by applying the Maxwell equations at the interface of two materials (e.g., deformable body and embedding air); see [64, 48, 176], among others. From the Gauss law of electro- and magnetostatics, we determine the following boundary conditions for the electric displacement and the magnetic induction field

$$[\![d]\!] \cdot \boldsymbol{n} = -\sigma_f \quad \text{and} \quad [\![b]\!] \cdot \boldsymbol{n} = 0 \,, \tag{2.191}$$

where σ_f denotes the free surface electric charges.

Similarly, we identify the boundary conditions for the electric and magnetic fields from the Faraday and the Ampère law as follows

$$[\![e]\!] \times \boldsymbol{n} = \boldsymbol{0} \quad \text{and} \quad [\![h]\!] \times \boldsymbol{n} = \boldsymbol{0} \,. \tag{2.192}$$

On the mechanical side, from the balance of linear momentum and compatibilty of deformation (i.e., $\operatorname{Curl} \boldsymbol{F} = \boldsymbol{0}$ or $\operatorname{curl} \boldsymbol{g} = \boldsymbol{0}$)[7], we obtain the following jump boundary conditions

$$[\![\boldsymbol{\sigma}]\!] \cdot \boldsymbol{n} = \boldsymbol{t}^{mec} \quad \text{and} \quad [\![\boldsymbol{g}]\!] \times \boldsymbol{n} = \boldsymbol{0} \,, \tag{2.195}$$

where $\boldsymbol{t}^{mec}$ is the mechanical traction vector. Furthermore, for the deformation map (or displacement field), fixed boundary conditions without a jump on the Dirichlet boundary can be prescribed depending on boundary value problems.

[7] The compatbility conditions $\operatorname{Curl} \boldsymbol{F} = \boldsymbol{0}$ and $\operatorname{curl} \boldsymbol{g} = \boldsymbol{0}$ can be derived, integrating an infinitesimal line element $\mathrm{d}\boldsymbol{x}$ over a closed curve

$$\int_{\mathcal{C}_t} \mathrm{d}\boldsymbol{x} = \int_{\mathcal{C}_t} \boldsymbol{g} \mathrm{d}\boldsymbol{x} = \int_{\mathcal{C}_0} \boldsymbol{F} \mathrm{d}\boldsymbol{X} = \boldsymbol{0} \,. \tag{2.193}$$

We obtain teh sought-after expressions by appling Stokes' theorems in the current and reference configurations and assuming that there is no discontinuity in the associated continuum. Moreover, we can derive another set of compatbility conditions, starting the same procedure from the reference configuration

$$\int_{\mathcal{C}_0} \mathrm{d}\boldsymbol{X} = \int_{\mathcal{C}_0} \boldsymbol{G} \mathrm{d}\boldsymbol{X} = \int_{\mathcal{C}_t} \boldsymbol{F}^{-1} \mathrm{d}\boldsymbol{x} = \boldsymbol{0} \,, \tag{2.194}$$

which yields $\operatorname{Curl} \boldsymbol{G} = \boldsymbol{0}$ or $\operatorname{curl}[\boldsymbol{F}^{-1}] = \boldsymbol{0}$; see [222], Chapter 7.2.1.

2.4.3 Summary of equations in the Lagrangian configuration

We finally summarize the governing and constitutive equations in the reference configuration. The balance equations take the following form

$$\boxed{\begin{aligned} &1.\ \text{mass} && \rho \det \boldsymbol{F} = \rho_0 \,, \\ &2.\ \text{linear momentum} && \rho \dot{\boldsymbol{V}} = \operatorname{Div} \widetilde{\boldsymbol{P}} + \rho_0 \boldsymbol{b} \,, \\ &3.\ \text{angular momentum} && \widetilde{\boldsymbol{P}} \boldsymbol{F}^T = \boldsymbol{F} \widetilde{\boldsymbol{P}}^T \,, \\ &4.\ \text{internal energy} && \rho \dot{\psi} = \boldsymbol{P} : \dot{\boldsymbol{F}} + \mathbb{E} \cdot \dot{\mathbb{D}} + \mathbb{H} \cdot \dot{\mathbb{B}} \,. \end{aligned}} \tag{2.196}$$

The Maxwell equations in the Lagrangian configuration can be written as

$$\boxed{\begin{aligned} &1.\ \text{Gauss law} && \operatorname{Div} \mathbb{E} = 0 \,, \\ &2.\ \text{Faraday law} && \operatorname{Curl} \mathbb{E} = \boldsymbol{0} \,, \\ &3.\ \text{Gauss-Ampère law} && \operatorname{Div} \mathbb{B} = 0 \,, \\ &4.\ \text{Ampère law} && \operatorname{Curl} \mathbb{H} = \boldsymbol{0} \,. \end{aligned}} \tag{2.197}$$

Finally, we give the constitutive equations in the Lagrangian configuration as

$$\boldsymbol{P} = \rho_0 \partial_{\boldsymbol{F}} \psi \,, \quad \mathbb{E} = \rho_0 \partial_{\mathbb{D}} \psi \quad \text{and} \quad \mathbb{H} = \rho_0 \partial_{\mathbb{B}} \psi \,. \tag{2.198}$$

In order to fulfill the principle of material objectivity, the energy-storage function needs to depend on the deformation gradient through the right Cauchy-Green deformation tensor, i.e.,

$$\psi = \widehat{\psi}(\boldsymbol{C}, \mathbb{D}, \mathbb{B}) \,. \tag{2.199}$$

Furthermore, the energy-storage function is chosen as a polyconvex function at finite strains. We refer to [45, 27, 46, 96] for the construction of objective energy functions and to [80, 214, 215] for the polyconvexity requirement.

Bibliography: Chapter 1 & 2

[1] Abeyaratne, R., Triantafyllidis, N., [1984]. *An investigation of localization in a porous elastic material using homogenization theory*. ASME Journal of Applied Mechanics 51(3), 481–486. (doi:doi:10.1115/1.3167661)

[2] Ahamed, R., Choi, S.-B., Ferdaus, M. M., [2018]. *A state of art on magneto-rheological materials and their potential applications*. Journal of Intelligent Material Systems and Structures 29 (10), 2051–2095.

[3] Ahmad Khairi, M. H., Mazlan, S. A., Choi, S.-B., Abdul Aziz, S. A., Mohamad, N., Hapipi, N. M., Nordin, N., [2019]. *Role of additives in enhancing the rheological properties of magnetorheological solids: A review*. Advanced Engineering Materials 21 (3), 1800696.

[4] Ahmed, E. M., [2015]. *Hydrogel: Preparation, characterization, and applications: A review*. Journal of advanced research 6 (2), 105–121.

[5] Anton, S. R., Sodano, H. A., [2007]. *A review of power harvesting using piezoelectric materials (2003–2006)*. Smart materials and Structures 16 (3), R1.

[6] Babaee, S., Shim, J., Weaver, J. C., Chen, E. R., Patel, N., Bertoldi, K., [2013]. *3D soft metamaterials with negative poisson's ratio*. Advanced Materials 25 (36), 5044–5049.

[7] Bar-Cohen, Y., [2002]. *Electro-active polymers: Current capabilities and challenges*. Proceedings of the SPIE Smart Structures and Materials Symposium 4695-02, 1–6.

[8] Bar-Cohen, Y., Zhang, Q., [2008]. *Electro-active polymer actuators and sensors*. MRS Bulletin 33, 173–181.

[9] Bastola, A., Hoang, V., Li, L., [2017]. *A novel hybrid magnetorheological elastomer developed by 3d printing*. Materials & Design 114, 391–397.

[10] Bastola, A., Paudel, M., Li, L., [2018]. *Development of hybrid magnetorheological elastomers by 3D printing*. Polymer 149, 213–228.

[11] Bastola, A. K., Hossain, M., [2020]. *A review on magneto-mechanical characterizations of magnetorheological elastomers*. Composites Part B: Engineering 200, 108348.

[12] Bastola, A. K., Paudel, M., Li, L., Li, W., [2020]. *Recent progress of magnetorheological elastomers: a review*. Smart Materials and Structures 29 (12), 123002.

[13] Bertoldi, K., [2017]. *Harnessing instabilities to design tunable architected cellular materials*. Annu. Rev. Mater. Res 47 (1), 51–61.

[14] Bertoldi, K., Boyce, M., Deschanel, S., Prange, S., Mullin, T., [2008]. *Mechanics of deformation-triggered pattern transformations and superelastic behavior in periodic elastomeric structures*. Journal of the Mechanics and Physics of Solids 56, 2642–2668. (doi:doi:10.1016/j.jmps.2008.03.006)

[15] Bertoldi, K., Boyce, M. C., [2008]. *Wave propagation and instabilities in monolithic and periodically structured elastomeric materials undergoing large deformations*. Physical Review B 78 (18), 184107. (doi:10.1103/PhysRevB.78.184107)

[16] Bertoldi, K., Gei, M., [2011]. *Instabilities in multilayered soft dielectrics*. Journal of the Mechanics and Physics of Solids 59, 18–42. (http://www.sciencedirect.com/science/article/pii/S0022509610002036)

[17] Bichara, D. A., O'Sullivan, N.-A., Pomerantseva, I., Zhao, X., Sundback, C. A., Vacanti, J. P., Randolph, M. A., [2012]. *The tissue-engineered auricle: past, present, and future*. Tissue Engineering Part B: Reviews 18 (1), 51–61.

[18] Bichara, D. A., Zhao, X., Hwang, N. S., Bodugoz-Senturk, H., Yaremchuk, M. J., Randolph, M. A., Muratoglu, O. K., [2010]. *Porous poly (vinyl alcohol)-alginate gel hybrid construct for neocartilage formation using human nasoseptal cells*. Journal of Surgical Research 163 (2), 331–336.

[19] Biggins, J., Warner, M., Bhattacharya, K., [2012]. *Elasticity of polydomain liquid crystal elastomers*. Journal of the Mechanics and Physics of Solids 60 (4), 573–590.

[20] Biro, O., Preis, K., [1989]. *On the use of the magnetic vector potential in the finite element analysis of three-dimensional eddy currents*. IEEE Transactions on Magnetics 25 (4), 3145–3159.

[21] Bodelot, L., Voropaieff, J.-P., Pössinger, T., [2018]. *Experimental investigation of the coupled magneto-mechanical response in magnetorheological elastomers*. Experimental Mechanics 58 (2), 207–221.

[22] Böger, L., [2020]. *Saddle-point and minimization principles for diffusion in solids: phase separation, swelling and fracture*. Ph.D. thesis, Stuttgart: Institute of Applied Mechanics.

[23] Böger, L., Nateghi, A., Miehe, C., [2017]. *A minimization principle for deformation-diffusion processes in polymeric hydrogels: constitutive modeling and fe implementation*. International Journal of Solids and Structures 121, 257–274.

[24] Borges, F. T., Papavasiliou, G., Teymour, F., [2020]. *Characterizing the molecular architecture of hydrogels and crosslinked polymer networks beyond Flory–Rehner-I. Theory*. Biomacromolecules 21 (12), 5104–5118.

[25] Bossavit, A., [2010]. *Discrete magneto-elasticity: a geometrical approach*. IEEE transactions on magnetics 46 (8), 3485–3491.

[26] Bradford, S. C., Hofmann, D. C., Roberts, S. N., Steeves, J. B., Wojnar, C. S., Kochmann, D. M., [2016]. *Energy-efficient active reflectors with improved mechanical stability and improved thermal performance*. In: *3rd AIAA Spacecraft structures conference*. p. 0702.

[27] Brigadnov, I., Dorfmann, A., [2003]. *Mathematical modeling of magneto-sensitive elastomers*. International Journal of Solids and Structures 40 (18), 4659–4674.

[28] Brochu, P., Pei, Q., [2012]. *Dielectric elastomers for actuators and artificial muscles*. In: *Electroactivity in polymeric materials*. Springer, pp. 1–56.

[29] Brown, W. F., [1966]. *Magnetoelastic interactions*. Vol. 9. Springer.

[30] Brusa da Costa Linn, L., Danas, K., Bodelot, L., [2022]. *Towards 4D printing of very soft heterogeneous magnetoactive layers for morphing surface applications via liquid additive manufacturing*. Polymers 14 (9), 1684.

[31] Buwalda, S. J., Boere, K. W., Dijkstra, P. J., Feijen, J., Vermonden, T., Hennink, W. E., [2014]. *Hydrogels in a historical perspective: From simple networks to smart materials*. Journal of controlled release 190, 254–273.

[32] Caló, E., Khutoryanskiy, V. V., [2015]. *Biomedical applications of hydrogels: A review of patents and commercial products*. European polymer journal 65, 252–267.

[33] Cao, C., Zhao, X., [2013]. *Tunable stiffness of electrorheological elastomers by designing mesostructures*. Applied Physics Letters 103 (4), 041901.

[34] Cellini, F., Cha, Y., Porfiri, M., [2014]. *Energy harvesting from fluid-induced buckling of ionic polymer metal composites*. Journal of intelligent material systems and structures 25 (12), 1496–1510.

[35] Chatzigeorgiou, G., Charalambakis, N., Chemisky, Y., Meraghni, F., [2016]. *Periodic homogenization for fully coupled thermomechanical modeling of dissipative generalized standard materials*. International Journal of Plasticity 81, 18–39.

[36] Chen, C.-M., Yang, S., [2012]. *Wrinkling instabilities in polymer films and their applications*. Polymer International 61 (7), 1041–1047.

[37] Ciarlet, P. G., [1988]. *Three-dimensional elasticity*. Elsevier.

[38] Coleman, B. D., Gurtin, M. E., [1967]. *Thermodynamics with internal state variables*. The journal of chemical physics 47 (2), 597–613.

[39] Coussy, O., [2004]. *Poromechanics*. John Wiley & Sons.

[40] Danas, K., [2017]. *Effective response of classical, auxetic and chiral magnetoelastic materials by use of a new variational principle*. Journal of the Mechanics and Physics of Solids 105, 25–53.

[41] Danas, K., Kankanala, S., Triantafyllidis, N., [2012]. *Experiments and modeling of iron-particle-filled magnetorheological elastomers*. Journal of the Mechanics and Physics of Solids 60 (1), 120 – 138. (doi:http://dx.doi.org/10.1016/j.jmps.2011.09.006)

[42] De Jeu, W. H., [2012]. *Liquid crystal elastomers: materials and applications*. Vol. 250. Springer.

[43] deBotton, G., Tevet-Deree, L., Socolsky, E. A., [2007]. *Electroactive heterogeneous polymers: analysis and applications to laminated composites*. Mechanics of Advanced Materials and Structures 14 (1), 13–22.

[44] Destrade, M., Ogden, R. W., [2011]. *On magneto-acoustic waves in finitely deformed elastic solids*. Mathematics and Mechanics of Solids 16 (6), 594–604.

[45] Dorfmann, A., Ogden, R., [2003]. *Magnetoelastic modelling of elastomers*. European Journal of Mechanics-A/Solids 22 (4), 497–507.

[46] Dorfmann, A., Ogden, R., [2004]. *Nonlinear magnetoelastic deformations of elastomers*. Acta Mechanica 167 (1), 13–28.

[47] Dorfmann, A., Ogden, R. W., [2010]. *Nonlinear electroelastostatics: Incremental equations and stability*. International Journal of Engineering Science 48, 1–14. (http://www.sciencedirect.com/science/article/pii/S0020722508001043)

[48] Dorfmann, L., Ogden, R. W., [2014]. *Nonlinear theory of electroelastic and magnetoelastic interactions*. Vol. 1. Springer.

[49] Dortdivanlioglu, B., Linder, C., [2019]. *Diffusion-driven swelling-induced instabilities of hydrogels*. Journal of the Mechanics and Physics of Solids 125, 38–52.

[50] Ehlers, W., [2018]. *Vector and Tensor Calculus: An Intorduction*. Lecture Notes at the University of Stuttgart.

[51] Fargette, A., Neukirch, S., Antkowiak, A., [2014]. *Elastocapillary snapping: Capillarity induces snap-through instabilities in small elastic beams*. Physical review letters 112 (13), 137802.

[52] Farshad, M., Benine, A., [2004]. *Magnetoactive elastomer composites*. Polymer testing 23 (3), 347–353.

[53] Feyel, F., Chaboche, J.-L., [2000]. *FE^2 multiscale approach for modelling the elasto-viscoplastic behaviour of long fibre SiC/Ti composite materials*. Computer methods in applied mechanics and engineering 183, 309–330.

[54] Filipcsei, G., Csetneki, I., Szilágyi, A., Zrínyi, M., [2007]. *Magnetic field-responsive smart polymer composites*. Oligomers-polymer composites-molecular imprinting, 137–189.

[55] Frankel, T., [2011]. *The geometry of physics: an introduction*. Cambridge university press.

[56] Fritzen, F., Kochmann, D. M., [2014]. *Material instability-induced extreme damping in composites: A computational study*. International Journal of Solids and Structures 51 (23-24), 4101–4112.

[57] Galipeau, E., Ponte Castañeda, P., [2012]. *The effect of particle shape and distribution on the macroscopic behavior of magnetoelastic composites*. International Journal of Solids and Structures 49 (1), 1–17.

[58] Galipeau, E., Ponte Castañeda, P., [2013]. *A finite-strain constitutive model for magnetorheological elastomers: magnetic torques and fiber rotations*. Journal of the Mechanics and Physics of Solids 61 (4), 1065–1090.

[59] Gao, C., Slesarenko, V., Boyce, M. C., Rudykh, S., Li, Y., [2018]. *Instability-induced pattern transformation in soft metamaterial with hexagonal networks for tunable wave propagation*. Scientific Reports 8 (1), 1–9.

[60] Geers, M. G., Kouznetsova, V. G., Brekelmans, W., [2010]. *Multi-scale computational homogenization: Trends and challenges*. Journal of computational and applied mathematics 234 (7), 2175–2182.

[61] Geymonat, G., Müller, S., Triantafyllidis, N., [1993]. *Homogenization of nonlinearly elastic materials, microscopic bifurcation and macroscopic loss of rank-one convexity*. Archive for Rational Mechanics and Analysis 122, 231–290. (doi:DOI: 10.1007/BF00380256)

[62] Ginder, J. M., Nichols, M. E., Elie, L. D., Tardiff, J. L., [1999]. *Magnetorheological elastomers: properties and applications*. In: *Proc. SPIE*. Vol. 3675. pp. 131–138.

[63] Goshkoderia, A., Rudykh, S., [2017]. *Stability of magnetoactive composites with periodic microstructures undergoing finite strains in the presence of a magnetic field*. Composites Part B: Engineering 128 (Supplement C), 19 – 29. (doi:https://doi.org/10.1016/j.compositesb.2017.06.014)

[64] Griffiths, D. J., [2005]. *Introduction to electrodynamics*. American Association of Physics Teachers.

[65] Guvendiren, M., Burdick, J. A., [2010]. *The control of stem cell morphology and differentiation by hydrogel surface wrinkles*. Biomaterials 31 (25), 6511–6518.

[66] Guvendiren, M., Burdick, J. A., Yang, S., [2010]. *Solvent induced transition from wrinkles to creases in thin film gels with depth-wise crosslinking gradients*. Soft Matter 6 (22), 5795–5801.

[67] Haertling, G. H., [1999]. *Ferroelectric ceramics: history and technology*. Journal of the American Ceramic Society 82 (4), 797–818.

[68] Haldon, R., Lee, B., [1972]. *Structure and permeability of porous films of poly (hydroxy ethyl methacrylate)*. British Polymer Journal 4 (6), 491–501.

[69] Hill, R., [1963]. *Elastic properties of reinforced solids: Some theoretical principles*. Journal of the Mechanics and Physics of Solids 11, 357–372.

[70] Hill, R., [1965]. *A self-consistent mechanics of composite materials*. Journal of the Mechanics and Physics of Solids 13, 213–222.

[71] Hill, R., [1968]. *On constitutive inequalities for simple materials-I*. Journal of the Mechanics and Physics of Solids 16 (4), 229–242.

[72] Hill, R., [1972]. *On constitutive macro-variables for heterogeneous solids at finite strain*. Proceedings of the Royal Society of London (Series A) 326, 131–147.

[73] Hoffman, A. S., [1995]. *"intelligent" polymers in medicine and biotechnology*. Artificial organs 19 (5), 458–467.

[74] Hoffman, A. S., [2012]. *Hydrogels for biomedical applications*. Advanced drug delivery reviews 64, 18–23.

[75] Holzapfel, G. A., [2002]. *Nonlinear solid mechanics: a continuum approach for engineering science*. Vol. 37. Kluwer Academic Publishers.

[76] Hu, N., Burgueño, R., [2015]. *Buckling-induced smart applications: recent advances and trends*. Smart Materials and Structures 24 (6), 063001.

[77] Ilseng, A., Prot, V., Skallerud, B. H., Stokke, n. B. T., [2019]. *Buckling initiation in layered hydrogels during transient swelling*. Journal of the Mechanics and Physics of Solids 128, 219–238.

[78] Ilseng, A., Skallerud, B. H., Stokke, B. T., Prot, V., [2021]. *A perturbation analysis approach for studying the effect of swelling kinetics on instabilities in hydrogel plates*. Journal of Applied Mechanics 88 (5).

[79] Irodov, I. E., [1986]. *Basic laws of electromagnetism*. Imported Publication.

[80] Itskov, M., Khiêm, V. N., [2016]. *A polyconvex anisotropic free energy function for electro- and magneto-rheological elastomers*. Mathematics and Mechanics of Solids 21 (9), 1126–1137. (doi:10.1177/1081286514555140)

[81] Jackson, J. D., [1999]. *Classical Electrodynamics*, 3rd Edition. John Wiley & Sons.

[82] Jaffe, H., [1958]. *Piezoelectric ceramics*. Journal of the American Ceramic Society 41 (11), 494–498.

[83] Jandron, M., Henann, D. L., [2020]. *Electromechanical instabilities in periodic dielectric elastomer composites*. International Journal of Solids and Structures 191, 220–242.

[84] Jang, J.-H., Koh, C. Y., Bertoldi, K., Boyce, M. C., Thomas, E. L., [2009]. *Combining pattern instability and shape-memory hysteresis for phononic switching*. Nano letters 9 (5), 2113–2119.

[85] Javili, A., Chatzigeorgiou, G., Steinmann, P., [2013]. *Computational homogenization in magneto-mechanics*. International Journal of Solids and Structures 50 (25), 4197–4216.

[86] Jolly, M. R., Carlson, J. D., Munoz, B. C., [1996]. *A model of the behaviour of magnetorheological materials*. Smart Materials and Structures 5 (5), 607.

[87] Jordi, C., Michel, S., Fink, E., [2010]. *Fish-like propulsion of an airship with planar membrane dielectric elastomer actuators*. Bioinspiration & biomimetics 5 (2), 026007.

[88] Kaessmair, S., Runesson, K., Steinmann, P., Jänicke, R., Larsson, F., [2021]. *Variationally consistent computational homogenization of chemomechanical problems with stabilized weakly periodic boundary conditions*. International Journal for Numerical Methods in Engineering 122 (22), 6429–6454.

[89] Kaessmair, S., Steinmann, P., [2018]. *Computational first-order homogenization in chemo-mechanics*. Archive of Applied Mechanics 88 (1-2), 271–286.

[90] Kalina, K. A., Brummund, J., Metsch, P., Kästner, M., Borin, D. Y., Linke, J., Odenbach, S., [2017]. *Modeling of magnetic hystereses in soft mres filled with ndfeb particles*. Smart Materials and Structures 26 (10), 105019.

[91] Kalina, K. A., Metsch, P., Brummund, J., Kästner, M., [2020]. *A macroscopic model for magnetorheological elastomers based on microscopic simulations*. International Journal of Solids and Structures 193, 200–212.

[92] Kalina, K. A., Metsch, P., Kästner, M., [2016]. *Microscale modeling and simulation of magnetorheological elastomers at finite strains: A study on the influence of mechanical preloads*. International Journal of Solids and Structures 102, 286–296.

[93] Kaneko, D., Gong, J. P., Osada, Y., [2002]. *Polymer gels as soft and wet chemomechanical systems–an approach to artificial muscles*. Journal of Materials Chemistry 12 (8), 2169–2177.

[94] Kang, M. K., Huang, R., [2010]. *Effect of surface tension on swell-induced surface instability of substrate-confined hydrogel layers*. Soft Matter 6 (22), 5736–5742.

[95] Kang, M. K., Huang, R., [2010]. *Swell-induced surface instability of confined hydrogel layers on substrates*. Journal of the Mechanics and Physics of Solids 58 (10), 1582–1598.

[96] Kankanala, S., Triantafyllidis, N., [2004]. *On finitely strained magnetorheological elastomers*. Journal of the Mechanics and Physics of Solids 52 (12), 2869–2908.

[97] Kawai, H., [1969]. *The piezoelectricity of poly (vinylidene fluoride)*. Japanese journal of applied physics 8 (7), 975.

[98] Keip, M.-A., [2022]. *Micromechanics of Smart and Mulifunctional Materials*. Lecture Notes at the University of Stuttgart.

[99] Keip, M.-A., Nadgir, O., [2017]. *An electro-elastic phase-field model for nematic liquid crystal elastomers based on Landau-de-Gennes theory*. GAMM-Mitteilungen 40 (2), 102–124.

[100] Keip, M.-A., Rambausek, M., [2016]. *A multiscale approach to the computational characterization of magnetorheological elastomers*. International Journal for Numerical Methods in Engineering 107, 338–360.

[101] Keip, M.-A., Rambausek, M., [2017]. *Computational and analytical investigations of shape effects in the experimental characterization of magnetorheological elastomers*. International Journal of Solids and Structures 121, 1–20.

[102] Keip, M.-A., Sridhar, A., [2019]. *A variationally consistent phase-field approach for micro-magnetic domain evolution at finite deformations*. Journal of the Mechanics and Physics of Solids 125, 805–824.

[103] Keip, M.-A., Steinmann, P., Schröder, J., [2014]. *Two-scale computational homogenization of electro-elasticity at finite strains*. Computer Methods in Applied Mechanics and Engineering 278, 62–79.

[104] Kelly, P., [2018]. *Solid Mechanics Lecture Notes Part III*. The University of Auckland.

[105] Keplinger, C., Li, T., Baumgartner, R., Suo, Z., Bauer, S., [2012]. *Harnessing snap-through instability in soft dielectrics to achieve giant voltage-triggered deformation*. Soft Matter 8 (2), 285–288.

[106] Kikuchi, S., Matsubara, S., Nagashima, S., Okumura, D., [2022]. *Diversity of the bifurcations and deformations on films bonded to soft substrates: Robustness of the herringbone pattern and its cognate patterns*. Journal of the Mechanics and Physics of Solids 159, 104757.

[107] Kochmann, D. M., [2014]. *Stable extreme damping in viscoelastic two-phase composites with non-positive-definite phases close to the loss of stability*. Mechanics Research Communications 58, 36–45.

[108] Kochmann, D. M., Bertoldi, K., [2017]. *Exploiting microstructural instabilities in solids and structures: From metamaterials to structural transitions*. Applied mechanics reviews 69 (5), 050801.

[109] Kofod, G., Sommer-Larsen, P., Kornbluh, R., Pelrine, R., [2003]. *Actuation response of polyacrylate dielectric elastomers*. Journal of intelligent material systems and structures 14 (12), 787–793.

[110] Kornbluh, R., Pelrine, R., Joseph, J., [1995]. *Elastomeric dielectric artificial muscle actuators for small robots*. Proceedings of the Materials Research Society.

[111] Kornbluh, R., Pelrine, R., Joseph, J., Heydt, R., Pei, Q., Chiba, S., [1999]. *High-field electrostriction of elastomeric polymer dielectrics for actuation*. Proceedings of the SPIE: Smart Structures and Materials 3669, 149–161. (doi:10.1117/12.349672)

[112] Kouznetsova, V. G., Geers, M. G. D., Brekelmans, W. A. M., [2004]. *Multi-scale second-order computational homogenization of multi-phase materials: a nested finite element solution strategy*. Computer Methods in Applied Mechanics and Engineering 193, 5525–5550.

[113] Kovetz, A., [2000]. *Electromagnetic theory*. Vol. 975. Oxford University Press Oxford.

[114] Kramarenko, E. Y., Chertovich, A., Stepanov, G., Semisalova, A., Makarova, L., Perov, N., Khokhlov, A., [2015]. *Magnetic and viscoelastic response of elastomers with hard magnetic filler*. Smart materials and structures 24 (3), 035002.

[115] Krylov, S., Ilic, B. R., Lulinsky, S., [2011]. *Bistability of curved microbeams actuated by fringing electrostatic fields*. Nonlinear Dynamics 66 (3), 403–426.

[116] Kularatne, R. S., Kim, H., Boothby, J. M., Ware, T. H., [2017]. *Liquid crystal elastomer actuators: Synthesis, alignment, and applications*. Journal of Polymer Science Part B: Polymer Physics 55 (5), 395–411.

[117] Kuznetsov, S., Fish, J., [2012]. *Mathematical homogenization theory for electroactive continuum*. International Journal for Numerical Methods in Engineering 91 (11), 1199–1226.

[118] Lachenal, X., Daynes, S., Weaver, P. M., [2013]. *Review of morphing concepts and materials for wind turbine blade applications*. Wind energy 16 (2), 283–307.

[119] Laftah, W. A., Hashim, S., Ibrahim, A. N., [2011]. *Polymer hydrogels: A review*. Polymer-Plastics Technology and Engineering 50 (14), 1475–1486.

[120] Landa, R. A., Soledad Antonel, P., Ruiz, M. M., Perez, O. E., Butera, A., Jorge, G., Oliveira, C. L., Negri, R. M., [2013]. *Magnetic and elastic anisotropy in magnetorheological elastomers using nickel-based nanoparticles and nanochains*. Journal of Applied Physics 114 (21), 213912.

[121] Landau, L. D., Lifshitz, E. M., [1960]. *Electrodynamics of Continuous Media*. Pergamon Press.

[122] Larsson, F., Runesson, K., Saroukhani, S., Vafadari, R., [2011]. *Computational homogenization based on a weak format of micro-periodicity for RVE-problems*. Computer Methods in Applied Mechanics and Engineering 200 (1-4), 11–26.

[123] Larsson, F., Runesson, K., Su, F., [2010]. *Variationally consistent computational homogenization of transient heat flow*. International Journal for Numerical Methods in Engineering 81 (13), 1659–1686.

[124] Lee, C. J., Kwon, S. H., Choi, H. J., Chung, K. H., Jung, J. H., [2018]. *Enhanced magnetorheological performance of carbonyl iron/natural rubber composite elastomer with gamma-ferrite additive*. Colloid and Polymer Science 296 (9), 1609–1613.

[125] Lee, J.-W., Yoo, Y.-T., Lee, J. Y., [2014]. *Ionic polymer–metal composite actuators based on triple-layered polyelectrolytes composed of individually functionalized layers*. ACS applied materials & interfaces 6 (2), 1266–1271.

[126] Lefèvre, V., Danas, K., Lopez-Pamies, O., [2017]. *A general result for the magnetoelastic response of isotropic suspensions of iron and ferrofluid particles in rubber, with applications to spherical and cylindrical specimens*. Journal of the Mechanics and Physics of Solids 107, 343–364.

[127] Lefèvre, V., Danas, K., Lopez-Pamies, O., [2020]. *Two families of explicit models constructed from a homogenization solution for the magnetoelastic response of mres containing iron and ferrofluid particles*. International Journal of Non-Linear Mechanics 119, 103362.

[128] Lefèvre, V., Lopez-Pamies, O., [2014]. *The overall elastic dielectric properties of a suspension of spherical particles in rubber: An exact explicit solution in the small-deformation limit*. Journal of Applied Physics 116 (13), 134106. (doi:10.1063/1.4897199)

[129] Lefèvre, V., Lopez-Pamies, O., [2017]. *Nonlinear electroelastic deformations of dielectric elastomer composites: I – Ideal elastic dielectrics*. Journal of the Mechanics and Physics of Solids 99, 409–437.

[130] Lefèvre, V., Lopez-Pamies, O., [2017]. *Nonlinear electroelastic deformations of dielectric elastomer composites: II – Non-Gaussian elastic dielectrics*. Journal of the Mechanics and Physics of Solids 99, 438 – 470. (doi:https://doi.org/10.1016/j.jmps.2016.07.005)

[131] Li, C. Y., Hao, X. P., Wu, Z. L., Zheng, Q., [2019]. *Photolithographically patterned hydrogels with programmed deformations*. Chemistry–An Asian Journal 14 (1), 94–104.

[132] Li, T., Qu, S., Yang, W., [2012]. *Energy harvesting of dielectric elastomer generators concerning inhomogeneous fields and viscoelastic deformation*. Journal of Applied Physics 112 (3), 034119.

[133] Lopez-Pamies, O., [2014]. *Elastic dielectric composites: Theory and application to particle-filled ideal dielectrics*. Journal of the Mechanics and Physics of Solids 64, 61–82. (doi:http://dx.doi.org/10.1016/j.jmps.2013.10.016)

[134] Lopez-Pamies, O., Castañeda, P. P., [2006]. *On the overall behavior, microstructure evolution, and macroscopic stability in reinforced rubbers at large deformations: II–application to cylindrical fibers*. Journal of the Mechanics and Physics of Solids 54 (4), 831–863.

[135] Lynch, J. P., Loh, K. J., [2006]. *A summary review of wireless sensors and sensor networks for structural health monitoring*. Shock and Vibration Digest 38 (2), 91–130.

[136] Ma, P., Niu, B., Lin, J., Kang, T., Qian, J., Wu, Z. L., Zheng, Q., [2019]. *Sequentially controlled deformations of patterned hydrogels into 3d configurations with multilevel structures*. Macromolecular Rapid Communications 40 (3), 1800681.

[137] Ma, S., Yu, B., Pei, X., Zhou, F., [2016]. *Structural hydrogels*. Polymer 98, 516–535.

[138] Mahinroosta, M., Farsangi, Z. J., Allahverdi, A., Shakoori, Z., [2018]. *Hydrogels as intelligent materials: A brief review of synthesis, properties and applications*. Materials Today Chemistry 8, 42–55.

[139] Marsden, J. E., Hughes, T. J., [1994]. *Mathematical foundations of elasticity*. Courier Corporation.

[140] Maugin, G. A., [2009]. *On modelling electromagnetomechanical interactions in deformable solids*. International Journal of Advances in Engineering Sciences and Applied Mathematics 1 (1), 25–32.

[141] Mauthe, S. A., [2017]. *Variational multiphysics modeling of diffusion in elastic solids and hydraulic fracturing in porous media*. Ph.D. thesis, Stuttgart: Institute of Applied Mechanics.

[142] Mazzoldi, A., Santa, A. D., Rossi, D. D., [2000]. *Conducting polymer actuators: Properties and modeling*. In: *Polymer sensors and actuators*. Springer, pp. 207–244.

[143] McMeeking, R. M., Landis, C. M., [2005]. *Electrostatic forces and stored energy for deformable dielectric materials*.

[144] Mehnert, M., Hossain, M., Steinmann, P., [2021]. *A complete thermo–electro–viscoelastic characterization of dielectric elastomers, part I: Experimental investigations*. Journal of the Mechanics and Physics of Solids 157, 104603.

[145] Mehnert, M., Hossain, M., Steinmann, P., [2021]. *A complete thermo-electro-viscoelastic characterization of dielectric elastomers, part II: Continuum modeling approach*. Journal of the Mechanics and Physics of Solids 157, 104625.

[146] Metsch, P., Kalina, K. A., Spieler, C., Kästner, M., [2016]. *A numerical study on magnetostrictive phenomena in magnetorheological elastomers*. Computational Materials Science 124, 364–374.

[147] Michel, B., Bernard, A., Bietsch, A., Delamarche, E., Geissler, M., Juncker, D., Kind, H., Renault, J.-P., Rothuizen, H., Schmid, H., et al., [2001]. *Printing meets lithography: Soft approaches to high-resolution patterning*. IBM Journal of Research and Development 45 (5), 697–719.

[148] Michel, J., Lopez-Pamies, O., Ponte Castañeda, P., Triantafyllidis, N., [2010]. *Microscopic and macroscopic instabilities in finitely strained fiber-reinforced elastomers*. Journal of the Mechanics and Physics of Solids 58, 1776–1803. (doi:doi:10.1016/j.jmps.2010.08.006)

[149] Miehe, C., Koch, A., [2002]. *Computational micro-to-macro transitions of discretized microstructures undergoing small strains*. Archive of Applied Mechanics 72 (4), 300–317.

[150] Miehe, C., Lambrecht, M., [2001]. *Algorithms for computation of stresses and elasticity moduli in terms of Seth–Hill's family of generalized strain tensors*. Communications in numerical methods in engineering 17 (5), 337–353.

[151] Miehe, C., Mauthe, S., Teichtmeister, S., [2015]. *Minimization principles for the coupled problem of darcy–biot-type fluid transport in porous media linked to phase field modeling of fracture*. Journal of the Mechanics and Physics of Solids 82, 186–217.

[152] Miehe, C., Schotte, J., Schröder, J., [1999]. *Computational micro-macro transitions and overall moduli in the analysis of polycrystals at large strains*. Computational Materials Science 16, 372–382.

[153] Miehe, C., Teichtmeister, S., [2016]. *Geometrical Methods of Non-linear Continuum Mechanics and Continuum Thermodynamics*. Lecture Notes at the University of Stuttgart.

[154] Miehe, C., Vallicotti, D., Teichtmeister, S., [2016]. *Homogenization and multiscale stability analysis in finite magneto-electro-elasticity. application to soft matter EE, ME and MEE composites*. Computer Methods in Applied Mechanics and Engineering 300, 294–346.

[155] Miehe, C., Vallicotti, D., Teichtmeister, S., [2016]. *Homogenization and multiscale stability analysis in finite magneto-electro-elasticity. application to soft matter EE, ME and MEE composites*. Computer Methods in Applied Mechanics and Engineering 300, 294–346. (doi:http://dx.doi.org/10.1016/j.cma.2015.10.013)

[156] Mita, A., Takhira, S., [2003]. *A smart sensor using a mechanical memory for structural health monitoring of a damage-controlled building*. Smart Materials and Structures 12 (2), 204.

[157] Miyoshi, H., Matsubara, S., Okumura, D., [2021]. *Bifurcation and deformation during the evolution of periodic patterns on a gel film bonded to a soft substrate*. Journal of the Mechanics and Physics of Solids 148, 104272.

[158] Moreno-Mateos, M., Lopez-Donaire, M., Hossain, M., Garcia-Gonzalez, D., [2022]. *Effects of soft and hard magnetic particles on the mechanical performance of ultrasoft magnetorheological elastomers*. Smart Materials and Structures 31 (6), 065018.

[159] Moulson, A. J., Herbert, J. M., [2003]. *Electroceramics: materials, properties, applications*. John Wiley & Sons.

[160] Mukherjee, D., Bodelot, L., Danas, K., [2020]. *Microstructurally-guided explicit continuum models for isotropic magnetorheological elastomers with iron particles*. International Journal of Non-Linear Mechanics 120, 103380.

[161] Mukherjee, D., Danas, K., [2019]. *An evolving switching surface model for ferromagnetic hysteresis*. Journal of Applied Physics 125 (3), 033902.

[162] Mukherjee, D., Rambausek, M., Danas, K., [2021]. *An explicit dissipative model for isotropic hard magnetorheological elastomers*. Journal of the Mechanics and Physics of Solids 151, 104361.

[163] Müller, S., [1987]. *Homogenization of nonconvex integral functionals and cellular elastic materials*. Archive of Rational Mechanics and Analysis 99, 189–212.

[164] Needleman, A., [1988]. *Material rate dependence and mesh sensitivity in localization problems*. Computer methods in applied mechanics and engineering 67 (1), 69–85.

[165] Nilenius, F., Larsson, F., Lundgren, K., Runesson, K., [2014]. *Computational homogenization of diffusion in three-phase mesoscale concrete*. Computational Mechanics 54 (2), 461–472.

[166] Ogden, R., Steigmann, D., [2011]. *Mechanics and electrodynamics of magneto-and electro-elastic materials*. Vol. 527. Springer Science & Business Media.

[167] Ogden, R. W., [1997]. *Non-linear elastic deformations*. Courier Corporation.

[168] Okumura, D., Inagaki, T., Ohno, N., [2015]. *Effect of prestrains on swelling-induced buckling patterns in gel films with a square lattice of holes*. International Journal of Solids and Structures 58, 288–300. (doi:https://doi.org/10.1016/j.ijsolstr.2015.01.015)

[169] Okumura, D., Kuwayama, T., Ohno, N., [2014]. *Effect of geometrical imperfections on swelling-induced buckling patterns in gel films with a square lattice of holes*. International Journal of Solids and Structures 51 (1), 154–163. (doi:https://doi.org/10.1016/j.ijsolstr.2013.09.018)

[170] Özdemir, I., Brekelmans, W., Geers, M., [2008]. *Computational homogenization for heat conduction in heterogeneous solids*. International journal for numerical methods in engineering 73 (2), 185–204.

[171] Pao, Y.-H., Hutter, K., [1975]. *Electrodynamics for moving elastic solids and viscous fluids*. Proceedings of the IEEE 63 (7), 1011–1021.

[172] Park, J. H., Kwon, M. H., Park, O. O., [2001]. *Rheological properties and stability of magnetorheological fluids using viscoelastic medium and nanoadditives*. Korean Journal of Chemical Engineering 18 (5), 580–585.

[173] Pasala, D., Sarlis, A., Nagarajaiah, S., Reinhorn, A., Constantinou, M., Taylor, D., [2013]. *Adaptive negative stiffness: new structural modification approach for seismic protection*. Journal of structural Engineering 139 (7), 1112–1123.

[174] Pelrine, R., Kornbluh, R., Joseph, J., Heydt, R., Pei, Q., Chiba, S., [2000]. *High-field deformation of elastomeric dielectrics for actuators*. Materials Science and Engineering: C 11 (2), 89–100. (doi:10.1016/S0928-4931(00)00128-4)

[175] Pelrine, R., Kornbluh, R. D., Joseph, J., [1998]. *Electrostriction of polymer dielectrics with compliant electrodes as a means of actuation*. Sensors and Actuators A: Physical 64, 77–85.

[176] Pelteret, J.-P., Steinmann, P., [2019]. *Magneto-Active Polymers: Fabrication, characterisation, modelling and simulation at the micro-and macro-scale*. Walter de Gruyter GmbH & Co KG.

[177] Peppas, N. A., Hilt, J. Z., Khademhosseini, A., Langer, R., [2006]. *Hydrogels in biology and medicine: from molecular principles to bionanotechnology*. Advanced materials 18 (11), 1345–1360.

[178] Peppas, N. A., Khare, A. R., [1993]. *Preparation, structure and diffusional behavior of hydrogels in controlled release*. Advanced drug delivery reviews 11 (1-2), 1–35.

[179] Plante, J.-S., Dubowsky, S., [2006]. *Large-scale failure modes of dielectric elastomer actuators*. International journal of solids and structures 43 (25-26), 7727–7751.

[180] Pollmann, N., Larsson, F., Runesson, K., Lundgren, K., Zandi, K., Jänicke, R., [2021]. *Modeling and computational homogenization of chloride diffusion in three-phase meso-scale concrete*. Construction and Building Materials 271, 121558.

[181] Polukhov, E., [2016]. *Computational Multi-scale Instability Analysis of Periodic EAP Composites in Finite Strains*. Master's thesis, Stuttgart: Institute of Applied Mechanics.

[182] Polukhov, E., Keip, M.-A., [2020]. *Computational homogenization of transient chemo-mechanical processes based on a variational minimization principle*. Advanced Modeling and Simulation in Engineering Sciences 7 (1), 1–26.

[183] Polukhov, E., Keip, M.-A., [2021]. *Multiscale stability analysis of periodic magnetorheological elastomers*. Mechanics of Materials 159, 103699.

[184] Polukhov, E., Pytel, L., Keip, M.-A., [2023]. *Swelling-induced pattern transformations of periodic hydrogels–from the wrinkling of internal surfaces to the buckling of thin films*. Journal of the Mechanics and Physics of Solids.

[185] Polukhov, E., Vallicotti, D., Keip, M.-A., [2018]. *Computational stability analysis of periodic electroactive polymer composites across scales*. Computer Methods in Applied Mechanics and Engineering 337, 165–197.

[186] Ponte Castañeda, P., Galipeau, E., [2011]. *Homogenization-based constitutive models for magnetorheological elastomers at finite strain*. Journal of the Mechanics and Physics of Solids 59, 194–215.

[187] Ponte Castañeda, P., Siboni, M. H., [2012]. *A finite-strain constitutive theory for electro-active polymer composites via homogenization*. International Journal of Non-Linear Mechanics 47, 293–306.

[188] Qi, S., Guo, H., Fu, J., Xie, Y., Zhu, M., Yu, M., [2020]. *3D printed shape-programmable magneto-active soft matter for biomimetic applications*. Composites Science and Technology 188, 107973.

[189] Rambausek, M., [2020]. *Magneto-electro-elasticity of soft bodies across scales*. Ph.D. thesis, Stuttgart: Institute of Applied Mechanics.

[190] Rambausek, M., Göküzüm, F. S., Nguyen, L. T. K., Keip, M.-A., [2019]. *A two-scale FE-FFT approach to nonlinear magneto-elasticity*. International Journal for Numerical Methods in Engineering 117 (11), 1117–1142.

[191] Rambausek, M., Keip, M.-A., [2018]. *Analytical estimation of non-local deformation-mediated magneto-electric coupling in soft composites*. Proceedings of the Royal Society A: Mathematical, Physical and Engineering Sciences 474 (2216), 20170803.

[192] Reis, P. M., [2015]. *A perspective on the revival of structural (in) stability with novel opportunities for function: from buckliphobia to buckliphilia*. Journal of Applied Mechanics 82 (11), 111001.

[193] Romasanta, L. J., Hernández, M., López-Manchado, M. A., Verdejo, R., [2011]. *Functionalised graphene sheets as effective high dielectric constant fillers*. Nanoscale research letters 6 (1), 1–6.

[194] Romasanta, L. J., Leret, P., Casaban, L., Hernández, M., Miguel, A., Fernández, J. F., Kenny, J. M., Lopez-Manchado, M. A., Verdejo, R., [2012]. *Towards materials with enhanced electro-mechanical response: $CaCu_3Ti_4O_{12}$–polydimethylsiloxane composites*. Journal of Materials Chemistry 22 (47), 24705–24712.

[195] Romasanta, L. J., López-Manchado, M. A., Verdejo, R., [2015]. *Increasing the performance of dielectric elastomer actuators: A review from the materials perspective*. Progress in Polymer Science 51, 188–211.

[196] Roorda, W., Bodde, H., De Boer, A., Junginger, H., [1986]. *Synthetic hydrogels as drug delivery systems*. Pharmaceutisch Weekblad 8 (3), 165–189.

[197] Rosato, D., [2010]. *On the formulation and numerical implementation of dissipative electro-mechanics at large strains*. Ph.D. thesis, Institute of Applied Mechanics (CE), Chair of Material Theory, University of Stuttgart.

[198] Rosiak, J. M., Yoshii, F., [1999]. *Hydrogels and their medical applications*. Nuclear Instruments and Methods in Physics Research Section B: Beam Interactions with Materials and Atoms 151 (1-4), 56–64.

[199] Rudykh, S., deBotton, G., [2012]. *Instabilities of hyperelastic fiber composites: Micromechanical versus numerical analyses*. Journal of Elasticity 106, 123–147. (doi:DOI 10.1007/s10659-011-9313-x)

[200] Rudykh, S., deBotton, G., [2012]. *Stability of anisotropic electroactive polymers with application to layered media*. Zeitschrift für angewandte Mathematik und Physik 62, 1131–1142. (doi:DOI 10.1007/s10659-011-9313-x)

[201] Rudykh, S., Lewinstein, A., Uner, G., Debotton, G., [2013]. *Analysis of microstructural induced enhancement of electromechanical coupling in soft dielectrics*. Applied physics letters 102 (15), 151905.

[202] Saeb, S., Steinmann, P., Javili, A., [2016]. *Aspects of computational homogenization at finite deformations: a unifying review from Reuss' to Voigt's bound*. Applied Mechanics Reviews 68 (5).

[203] Sapouna, K., Xiong, Y., Shenoi, R., [2017]. *Dynamic mechanical properties of isotropic/anisotropic silicon magnetorheological elastomer composites*. Smart Materials and Structures 26 (11), 115010.

[204] Schröder, J., [2009]. *Derivation of the localization and homogenization conditions for electro-mechanically coupled problems*. Computational Materials Science 46, 595–599.

[205] Schröder, J., Keip, M.-A., [2012]. *Two-scale homogenization of electromechanically coupled boundary value problems*. Computational Mechanics 50 (2), 229–244.

[206] Schröder, J., Viebahn, N., Wriggers, P., Auricchio, F., Steeger, K., [2017]. *On the stability analysis of hyperelastic boundary value problems using three-and two-field mixed finite element formulations*. Computational Mechanics 60 (3), 479–492.

[207] Schuhladen, S., Preller, F., Rix, R., Petsch, S., Zentel, R., Zappe, H., [2014]. *Iris-like tunable aperture employing liquid-crystal elastomers*. Advanced materials 26 (42), 7247–7251.

[208] Schümann, M., Borin, D. Y., Huang, S., Auernhammer, G. K., Müller, R., Odenbach, S., [2017]. *A characterisation of the magnetically induced movement of ndfeb-particles in magnetorheological elastomers*. Smart Materials and Structures 26 (9), 095018.

[209] Semenov, A. S., Kessler, H., Liskowsky, A., Balke, H., [2006]. *On a vector potential formulation for 3D electromechanical finite element analysis*. Communication in Numerical Methods in Engineering 22, 357–375.

[210] Semenov, A. S., Liskowsky, A., Balke, H., [2007]. *Vector potential formulation for the three-dimensional finite element analysis of nonlinear electromechanical problems*. In: Dapino, M. J. (Ed.), *Behavior and Mechanics of Multifunctional and Composite Materials 2007*. Proceeding of SPIE Vol. 6526.

[211] Seth, B., [1964]. *Generalized strain measure with applications to physical problems*. In.: Second-Order Effects in Elasticity, Plasticity and Fluid Dynamics,Reiner M, Abir D (eds). Pergamon Press, Oxford.

[212] Shamonin, M., Kramarenko, E. Y., [2018]. *Highly responsive magnetoactive elastomers*. In: *Novel Magnetic Nanostructures*. Elsevier, pp. 221–245.

[213] Shintake, J., Schubert, B., Rosset, S., Shea, H., Floreano, D., [2015]. *Variable stiffness actuator for soft robotics using dielectric elastomer and low-melting-point alloy*. In: *2015 IEEE/RSJ International Conference on Intelligent Robots and Systems (IROS)*. IEEE, pp. 1097–1102.

[214] Šilhavỳ, M., [2017]. *Isotropic polyconvex electromagnetoelastic bodies*. Mathematics and Mechanics of Solids, 1081286518754567.

[215] Šilhavỳ, M., [2018]. *A variational approach to nonlinear electro-magneto-elasticity: convexity conditions and existence theorems*. Mathematics and Mechanics of Solids 23 (6), 907–928.

[216] Slesarenko, V., Rudykh, S., [2017]. *Microscopic and macroscopic instabilities in hyperelastic fiber composites*. Journal of the Mechanics and Physics of Solids 99, 471–482.

[217] Smit, R., Brekelmans, W., Meijer, H., [1998]. *Prediction of the mechanical behavior of nonlinear heterogeneous systems by multi-level finite element modeling*. Computer Methods in Applied Mechanics and Engineering 155, 181–192.

[218] Sorokin, V. V., Stepanov, G. V., Shamonin, M., Monkman, G. J., Kramarenko, E. Y., [2017]. *Magnetorheological behavior of magnetoactive elastomers filled with bimodal iron and magnetite particles*. Smart materials and structures 26 (3), 035019.

[219] Spaldin, N. A., [2010]. *Magnetic materials: fundamentals and applications*. Cambridge university press.

[220] Spinelli, S. A., Lefèvre, V., Lopez-Pamies, O., [2015]. *Dielectric elastomer composites: A general closed-form solution in the small-deformation limit*. Journal of the Mechanics and Physics of Solids 83, 263 – 284. (doi:https://doi.org/10.1016/j.jmps.2015.06.009)

[221] Sriram, S., Polukhov, E., Keip, M.-A., [2021]. *Transient stability analysis of composite hydrogel structures based on a minimization-type variational formulation*. International Journal of Solids and Structures 230-231, 111080. (doi:https://doi.org/10.1016/j.ijsolstr.2021.111080)

[222] Steinmann, P., [2015]. *Geometrical foundations of continuum mechanics*. Vol. 2. Springer.

[223] Sutrisno, J., Purwanto, A., Mazlan, S. A., [2015]. *Recent progress on magnetorheological solids: materials, fabrication, testing, and applications*. Advanced Engineering Materials 17 (5), 563–597.

[224] Tanaka, T., Sun, S.-T., Hirokawa, Y., Katayama, S., Kucera, J., Hirose, Y., Amiya, T., [1987]. *Mechanical instability of gels at the phase transition*. Nature 325 (6107), 796–798.

[225] Teichtmeister, S., [2021]. *Variational methods for dissipative multifield problems in solid mechanics*. Ph.D. thesis, Stuttgart: Institute of Applied Mechanics.

[226] Temizer, I., [2012]. *On the asymptotic expansion treatment of two-scale finite thermoelasticity*. International Journal of Engineering Science 53, 74–84.

[227] Temizer, I., Wriggers, P., [2011]. *Homogenization in finite thermoelasticity*. Journal of the Mechanics and Physics of Solids 59 (2), 344–372.

[228] Tian, L., Tevet-Deree, L., deBotton, G., Bhattacharya, K., [2012]. *Dielectric elastomer composites*. Journal of the Mechanics and Physics of Solids 60 (1), 181–198. (doi:10.1016/j.jmps.2011.08.005)

[229] Toupin, R. A., [1956]. *The elastic dielectric*. Archive for Rational Mechanics and Analysis 5, 849–915.

[230] Triantafyllidis, N., Maker, B. N., [1985]. *On the comparison between microscopic and macroscopic instability mechanisms in a class of fiber-reinforced composites*. ASME Journal of Applied Mechanics 52, 794–800. (doi:doi:10.1115/1.3169148)

[231] Triantafyllidis, N., Nestorović, M. D., Schraad, M. W., [2006]. *Failure surfaces for finitely strained two-phase periodic solids under general in-plane loading*. ASME Journal of Applied Mechanics 73(3), 505–515. (doi:doi:10.1115/1.2126695)

[232] Tröls, A., Kogler, A., Baumgartner, R., Kaltseis, R., Keplinger, C., Schwödiauer, R., Graz, I., Bauer, S., [2013]. *Stretch dependence of the electrical breakdown strength and dielectric constant of dielectric elastomers*. Smart Materials and Structures 22 (10), 104012.

[233] Truesdell, C., Noll, W., [2004]. *The non-linear field theories of mechanics*. Springer.

[234] Trujillo, V., Kim, J., Hayward, R. C., [2008]. *Creasing instability of surface-attached hydrogels*. Soft Matter 4 (3), 564–569.

[235] Vallicotti, D., [2019]. *Magneto-electro-mechanical coupling phenomena across multiple length scales: variational framework and stability analysis*. Ph.D. thesis, Stuttgart: Institute of Applied Mechanics.

[236] Varaprasad, K., Raghavendra, G. M., Jayaramudu, T., Yallapu, M. M., Sadiku, R., [2017]. *A mini review on hydrogels classification and recent developments in miscellaneous applications*. Materials Science and Engineering: C 79, 958–971.

[237] Varga, Z., Filipcsei, G., Zrínyi, M., [2005]. *Smart composites with controlled anisotropy*. Polymer 46 (18), 7779 – 7787, stimuli Responsive Polymers. (doi:http://dx.doi.org/10.1016/j.polymer.2005.03.102)

[238] Varga, Z., Filipcsei, G., Zrínyi, M., [2006]. *Magnetic field sensitive functional elastomers with tuneable elastic modulus*. Polymer 47 (1), 227 – 233. (doi:http://dx.doi.org/10.1016/j.polymer.2005.10.139)

[239] Volpini, V., Bardella, L., Gei, M., [2019]. *A note on the solution of the electro-elastic boundary-value problem for rank-two laminates at finite strains*. Meccanica 54 (13), 1971–1982.

[240] Walter, B. L., Pelteret, J.-P., Kaschta, J., Schubert, D. W., Steinmann, P., [2017]. *Preparation of magnetorheological elastomers and their slip-free characterization by means of parallel-plate rotational rheometry*. Smart Materials and Structures 26 (8), 085004.

[241] Wang, H., Wang, C., Yuan, T., [2012]. *On the energy conversion and efficiency of a dielectric electroactive polymer generator*. Applied Physics Letters 101 (3), 033904.

[242] Wang, P., Casadei, F., Shan, S., Weaver, J. C., Bertoldi, K., [2014]. *Harnessing buckling to design tunable locally resonant acoustic metamaterials*. Physical review letters 113 (1), 014301.

[243] Wang, Z. J., Zhu, C. N., Hong, W., Wu, Z. L., Zheng, Q., [2016]. *Programmed planar-to-helical shape transformations of composite hydrogels with bioinspired layered fibrous structures*. Journal of Materials Chemistry B 4 (44), 7075–7079.

[244] Wang, Z. J., Zhu, C. N., Hong, W., Wu, Z. L., Zheng, Q., [2017]. *Cooperative deformations of periodically patterned hydrogels*. Science Advances 3 (9), e1700348.

[245] Wichterle, O., Lim, D., [1960]. *Hydrophilic gels for biological use*. Nature 185 (4706), 117–118.

[246] Willis, J. R., [1981]. *Variational and related methods for the overall properties of composites*. Advances in Applied Mechanics 21, 1–78.

[247] Wu, G., Xia, Y., Yang, S., [2014]. *Buckling, symmetry breaking, and cavitation in periodically micro-structured hydrogel membranes*. Soft Matter 10 (9), 1392–1399.

[248] Wu, Z., Bouklas, N., Huang, R., [2013]. *Swell-induced surface instability of hydrogel layers with material properties varying in thickness direction*. International Journal of Solids and Structures 50 (3-4), 578–587.

[249] Xia, C., Lee, H., Fang, N., [2010]. *Solvent-driven polymeric micro beam device*. Journal of Micromechanics and Microengineering 20 (8), 085030.

[250] Zäh, D., [2014]. *Variational homogenization in electro-mechanics: from micro-electro-elasticity to electroactive polymers*. Ph.D. thesis, Institute of Applied Mechanics (CE), Chair of Material Theory, University of Stuttgart.

[251] Zäh, D., Miehe, C., [2013]. *Computational homogenization in dissipative electro-mechanics of functional materials*. Computer Methods in Applied Mechanics and Engineering 267, 487–510.

[252] Zhang, W.-M., Yan, H., Peng, Z.-K., Meng, G., [2014]. *Electrostatic pull-in instability in MEMS/NEMS: A review*. Sensors and Actuators A: Physical 214, 187–218.

[253] Zhang, Y., Matsumoto, E. A., Peter, A., Lin, P.-C., Kamien, R. D., Yang, S., [2008]. *One-step nanoscale assembly of complex structures via harnessing of an elastic instability*. Nano letters 8 (4), 1192–1196.

[254] Zhou, H., Bhattacharya, K., [2021]. *Accelerated computational micromechanics and its application to polydomain liquid crystal elastomers*. Journal of the Mechanics and Physics of Solids 153, 104470.

[255] Zhu, X., Wu, G., Dong, R., Chen, C.-M., Yang, S., [2012]. *Capillarity induced instability in responsive hydrogel membranes with periodic hole array*. Soft Matter 8 (31), 8088–8093.

Associated Publications

Chapter 3: Paper A

Computational Stability Analysis of Periodic Electroactive Polymer Composites across Scales

Computational Stability Analysis of Periodic Electroactive Polymer Composites across Scales

Original publication:

Polukhov, E., Vallicotti, D., & Keip, M.-A. [2018]. *Computational Stability Analysis of Perodic Electroactive Polymer Composites across Scales.* Computer Methods in Applied Mechanics and Engineering 337, 165–197.

Remark:

The work presented in this publication has been initially developed in [181], page 57 (see also the last paragraph in Section 1.7.1). Here, the framework is further extended to a Hu-Washizu-type variational formulation. Hence, the macroscopic and microscopic stability analysis considered within this setting and numerical examples are extended accordingly.

Abstract

This paper is devoted to the multi-scale stability analysis of periodic electroactive polymer composites at finite deformations. A particular focus is on the investigation of macroscopic loss of strong ellipticity and microscopic bifurcation-type instabilities. Macroscopic homogenized quantities are determined by use of computational homogenization over selected representative volume elements (RVE). The quasi-incompressible nature of the electroactive polymers is taken into account by considering a four-field variational formulation at micro-level. This formulation includes continuous interpolations of displacement fields and electric vector potentials as well as discontinuous interpolations of pressure and dilatation terms, yielding a saddle-point principle for coupled problems. Static condensation of the terms related to the element-wise constant pressure and dilatation results in a positive definite global microscopic stiffness matrix until a microscopic instability occurs. The microstructure is embedded into a macroscopic driving procedure that imposes periodic mechanical and electrical boundary conditions on the surface of the RVEs. It is known that at certain finite deformations the initial periodicity of microstructures might be altered due to microscopic bifurcation-type instabilities. To incorporate microscopic instabilities and to determine the critical periodicity of microstructures, Bloch-Floquet wave analysis in the context of a finite element discretization is implemented. The macroscopic instabilities, which are related to the long-wavelength microscopic instabilities, are determined by checking the loss of strong ellipticity at macro-scale. The proposed setting is used to study the multi-scale stability analysis of electroactive polymer composites with embedded fibers. The influence of fiber volume fraction and aspect ratio of fiber cross sections on instabilities are investigated in detail. Critical periodicities and bifurcation modes are demonstrated for selected boundary value problems.

Keywords: Homogenization; Electro-mechanics; Multi-scale stability; Rank-one convexity; Buckling; Electroactive polymer composites

3.1 Introduction

Dielectric electro-active polymers (dielectric EAPs) exhibit electrostrictive response to externally applied electrostatic loading, see for example Bar-Cohen and Zhang [6]. Such phenomenon can be observed placing an elastomer between deformable electrodes. Upon application of an electric stimulus, thinning of the EAP structure in field direction and extension in transverse directions are observed. Associated materials have been experimentally explored in e.g. Kornbluh et al. [33, 34] and Pelrine et al. [58, 57].

Moreover, dielectric EAPs have advantageous properties such as light weight, fast coupled response, tractable deformation state and easiness of fabrication, see Bar-Cohen [5], Bar-Cohen and Zhang [6], Carpi [13] and references therein. These properties allow EAPs to be applied in biologically inspired engineering designs (e.g., to mimic the movement of animals and insects), as artificial muscles, and in robotics as sensors or actuators. However, due to low dielectric constants high activation fields are needed to induce large mechanical deformation. Investigations show that electro-mechanical coupling can be enhanced by tuning dielectric elastomers with fibers or inclusions of various geometrical and physical properties, see Zhang et al. [98], Huang et al. [28], Tian et al. [84], Ponte Castañeda and Siboni [61], Siboni and Ponte Castañeda [75], Lopez-Pamies [41], Lefèvre and Lopez-Pamies [38]. In any case, tailoring dielectric EAPs through the design of composites requires to study the influence of the geometrical properties of microstructures on the response of these materials and to determine stable mechanical and electrical loading ranges. The subsequent sub-sections review aspects of associated modeling approaches and related stability issues at finite strains.

3.1.1 Multiscale modeling of dielectric EAP composites

Fundamentals of continuum modeling of electro-mechanical response of EAPs were developed byToupin [86], Tiersten [85], Maugin [44], Dorfmann and Ogden [16], McMeeking and Landis [45], Vu et al. [93], Suo et al. [82], Bustamante et al. [12], Dorfmann and Ogden [18], Vogel et al. [91], Vu and Steinmann [92], among others. Recently, computational homogenization is getting widely used to investigate the response of EAP composites in terms of inhomogeneous representative volume elements (RVEs). Fundamental ideas of homogenization can be found in the works of Hill [26, 27] and Willis [94]. For the development of computational methods of homogenization, see Smit et al. [79], Miehe et al. [49], Feyel and Chaboche [19], Terada and Kikuchi [83] and Kouznetsova et al. [35]. The computational homogenization of electro-active materials for non-dissipative and dissipative responses are treated in Schröder [67], Schröder and Keip [68], Zäh and Miehe [97] at small strains, and in Ponte Castañeda and Galipeau [60], Ponte Castañeda and Siboni [61], Keip et al. [31] at large strains. Furthermore, Lefèvre and Lopez-Pamies [38, 39] have derived the analytical closed-form solutions to determine the effective response of ideal as well as non-Gaussian elastic dielectrics, having microstructures with monodispersed and polydispersed spherical particles under large deformation scenarios, see also Lefèvre and Lopez-Pamies [37], Spinelli et al. [80] for solutions at small strains. In Miehe et al. [51] minimization- and saddle-point-based homogenization framework have been discussed in detail. There it could be shown that saddle-point-based homogenization under Neumann boundary conditions becomes equivalent to the minimization-based formulation under Dirichlet boundary conditions. For microscopic stability analysis, the minimization-based formulation under Dirichlet boundary condition is the natural choice, as the minimization principle yields a positive definite stiffness matrix in finite element discretization until the instability occurs. Recall that Dirichlet boundary conditions also allow to follow the whole equilibrium response without getting limited by pull-in instabilities which might be the case under electric field loading, as discusse, e.g., in Miehe et al. [51].

3.1.2 Multiscale stability analysis in coupled electro-mechanics

In this work, we investigate stability analysis of electroactive polymers. We are interested in macroscopic and microscopic instabilities in the context of computational multiscale stability analysis. Such stability analysis has been investigated in periodic structures under finite mechanical loading conditions in-depth in, for example, Geymonat et al. [21], Miehe et al. [50], Triantafyllidis et al. [89], Michel et al. [46], Bertoldi et al. [7], Bertoldi and Boyce [8] and Michel et al. [47].

Macroscopic instabilities associated with the loss of rank-one convexity of homogenized incremental moduli at finite deformation have been observed in Abeyaratne and Triantafyllidis [1]. They have shown that a polyconvex microscopic energy in the sense of Ball [4] does not always produce a rank-one convex homogenized macroscopic energy. This criterion has been used to detect the onset of localization-type material instabilities at macroscale. On the other hand at certain macroscopic deformation thresholds, the solution of periodic microstructures might not be unique yielding bifurcation-type instabilities which can alter the size of periodicity of the microstructure. For incompressible layered composites Triantafyllidis and Maker [88] have shown the relation between the loss of rank-one convexity of homogenized moduli at macroscale and the periodic bifurcation at microscale. When the microscopic instability occurs unit cell representative volume elements are no longer suitable due to the changed periodicity of the microstructure. Consequently, homogenization principles should not be applied over a single unit cell for large deformations, see Triantafyllidis and Maker [88] and Geymonat et al. [21].

Marcellini [43] has shown that homogenization over a unit cell yields always a unique solution provided that the microscopic energy is convex. However, for large elastic deformations convexity is a strong condition which restricts materials from describing physical phenomena such as buckling and furthermore violate the objectivity and the growth condition, see Hill [24], Coleman and Noll [14] and Ball [4]. More suitable formulations are based on polyconvex constitutive equations in the sense of Ball [4]. Furthermore, for the construction of polyconvex materials in case of the transversely isotropic and anisotropic materials at large strains refer to, e.g., Schröder and Neff [69], Schröder et al. [70].

As discussed above, homogenization over an RVE containing a single unit cell might not be reasonable for certain deformations, because the macroscopic energy of an RVE containing several unit cells might be lower due to possible existence of buckling modes, see Geymonat et al. [21]. They have shown that microscopic stability analysis still can be performed on a unit cell considering Bloch (or Bloch-Floquet) wave analysis, which can be understood as checking the stability of a unit cell under small amplitude perturbations of various wavelengths. The critical wavelength at microscopic instability points determines the size of RVE, see Bertoldi and Boyce [8], Bertoldi et al. [7], Michel et al. [47], Triantafyllidis et al. [89]. Based on these observations Michel et al. [46, 47], Nestorović and Triantafyllidis [55], Triantafyllidis and Bardenhagen [87], Triantafyllidis and Schraad [90], Triantafyllidis et al. [89], among others, studied the failure mechanism of periodic structures in various applications and under different loading conditions. Furthermore, Bertoldi et al. [7] and Bertoldi and Boyce [8] investigated deformation-triggered pattern transformations and wave propagations in periodic structures under the influence of microscopic and macroscopic instabilities.

On the electromechanical side, Dorfmann and Ogden [17] considered the electro-elastic

wave propagation in finitely deformed electroactive materials and gave the criterion for the loss of strong ellipticity for compressible as well as incompressible materials. Futhermore, Bertoldi and Gei [9] have analytically investigated the microscopic and macroscopic instabilities in incompressible soft layered dielectrics. Rudykh and Bertoldi [63], Rudykh and deBotton [65, 64] and Rudykh et al. [66] have also studied the instability phenomenon in coupled loading scenarios for composites with different lamination angles and volume fractions of layers. See also the recent works Slesarenko and Rudykh [78] and Goshkoderia and Rudykh [22] for the investigation of the multiscale instabilities of fiber composites and soft dielectric elastomeric composites at finite strains, respectively. Moreover, Siboni et al. [74], Siboni and Ponte Castañeda [75] investigated electro-mechanical instabilities of circular and elliptical shaped fiber-reinforced composites. They explored especially the loss of strong ellipticity and positive definiteness of analytically estimated homogenized coupled moduli of composites with randomly distributed fibers in transversal direction. For analytical investigations of the loss of strong ellipticity of compressible and incompressible dielectric elastomer composites involving a generalized approach for the determination of macroscopic instabilities of composites under generalized loading conditions please refer to Spinelli and Lopez-Pamies [81]. In Miehe et al. [52, 51] the stability analysis of electro-elastic, magneto-elastic and magneto-electro-elastic composites has been considered in saddle-point- and minimization-based variational formulations.

Our aim in this work is to study the multiscale instabilities of quasi-incompressible periodic EAP composites at finite strains in the context of computational homogenization. Of particular interest are the microscopic and the macroscopic stability analysis as well as the determination of stable loading ranges. To the best knowledge of the authors, the analysis of bifurcation-type microscopic instabilities under electro-mechanical loading has been mostly limited to analytical investigations of layered composites so far. We therefore discuss basic theoretical aspects as well as associated ingredients of numerical implementations for the computational detection of (i) the loss of strong ellipticity of homogenized moduli, (ii) microscopic bifurcation-type instabilities and (iii) microscopic buckling modes, each for various microstructures and loading conditions. The multiscale method is embedded into a variational approach to computational homogenization and motivated by the works of Bertoldi and Boyce [8], Bertoldi et al. [7], Geymonat et al. [21] and Triantafyllidis et al. [89]. Based on the present computational approach, we are able to investigate the stability of multi-phase EAP composites with various microstructures without any restriction on the geometry of the microstructure. Particularly, in the present work, microstructures with circular and elliptical fibers of different volume fractions and aspect ratios will be analyzed.

The quasi-incompressible nature of electroactive polymers can be described by imposing the incompressibility constraint on the RVE. Following this, we implement a four-field mixed formulation for the microstructures based on the Hu-Washizu variational formulation of Simo et al. [76], see also Nagtegaal et al. [54], Miehe [48] and Yamamoto and Hisada [95] as well as Auricchio et al. [3] and Schröder et al. [71] for instability anlysis using mixed finite element formulation.

The outline of the paper is as follows. In Section 3.2, we introduce the variational formulation of quasi-incompressible homogenization. In Section 3.3, the macroscopic stability analysis based on the loss of strong ellipticity and microscopic stability analysis based on the Bloch-Floquet wave analysis are considered. The numerical implementation

of Bloch-Floquet wave analysis in the context of a finite element discretization is accounted for in detail. Representative numerical examples in two-dimensional plane-strain condition are given in Section 3.4. The boundary value problems cover microstructures with fibers of different volume fraction and shape. The work is summarized in Section 3.5.

Notation. In order to ease readability of the following sections, we introduce already at this point some basic symbolic notations of frequently used operators and variables. The divergence of a field $(\cdot)$ is denoted as $\mathrm{Div}(\cdot) := (\cdot)^{A}{}_{,A}$, its gradient as $\mathrm{Grad}(\cdot) := (\cdot)^{A}{}_{,B}$ and its rotation as $\mathrm{Curl}(\cdot) := \varepsilon^{ABC}(\cdot)_{C,B}$, where ε is the Levi-Civita symbol (uppercase letters refer to the reference configuration). Likewise, $\mathrm{div}(\cdot) := (\cdot)^{a}{}_{,a}$, $\mathrm{grad}(\cdot) := (\cdot)^{a}{}_{,b}$ and $\mathrm{curl}(\cdot) := \varepsilon^{abc}(\cdot)_{c,b}$ denote analogous operations with respect to the deformed configuration. Moreover, the notation $\overline{(\cdot)}$ for macroscopic analogues of microscopic fields $(\cdot)$ is considered in the following.

3.2 Variational homogenization of quasi-incompressible electro-elasticity at finite strains

In the context of computational homogenization, we assume that the material response of a macrostructure $\overline{\mathcal{B}} \subset \mathcal{R}^3$ is not explicitly based on known constitutive functions, but to be defined at each material point $\overline{\boldsymbol{X}} \in \overline{\mathcal{B}}$ by averaging microscopic counterparts over attached representative volume elements (RVE) $\mathcal{B} \subset \mathcal{R}^3$. We assume separation of the length scales of macro- and micro-scales, such that the macroscopic fields are uniform over the RVE. The microscopic boundary value problem (BVP) is nested within a macroscopic BVP and the total response of the macrostructure is determined, see Fig. 3.1. However, please note that we limit the framework of this paper to analyze the behavior of microstructures at a single material point of macrostructures (i.e., no BVP at macroscale is solved). The intrinsic notation $\overline{(\cdot)}$ for macroscopic analogues of microscopic variables $(\cdot)$ is considered in the following. In what follows, we restrict ourselves to electro-elasto-static processes. That means that thermal, magnetic, dynamic and relativistic effects are not considered.

3.2.1 Description of microscopic kinematic fields

Let $\mathcal{B}$ denote an RVE of a periodic microstructure in the reference configuration. We consider the microscopic boundary value problem to be governed by the primary variables

$$\boldsymbol{\varphi} : \begin{cases} \mathcal{B} \times \mathcal{T} \to \mathcal{R}^3 \\ (\boldsymbol{X}, t) \mapsto \boldsymbol{\varphi}(\boldsymbol{X}, t) \end{cases} \quad \text{and} \quad \boldsymbol{a} : \begin{cases} \mathcal{B} \times \mathcal{T} \to \mathcal{R}^3 \\ (\boldsymbol{X}, t) \mapsto \boldsymbol{a}(\boldsymbol{X}, t)\,, \end{cases} \tag{3.1}$$

where $\boldsymbol{\varphi}$ is a bijective deformation map that maps the material point $\boldsymbol{X} \in \mathcal{B}$ onto $\boldsymbol{x} = \boldsymbol{\varphi}_t(\boldsymbol{X}) \in \mathcal{S}$ in the current configuration $\mathcal{S} = \boldsymbol{\varphi}_t(\mathcal{B})$. The consideration of the electric vector potential $\boldsymbol{a}(\boldsymbol{X}, t)$ as primary variable is associated with a thermodynamic potential in terms of the electric displacement as independent field. Such thermodynamic potential is associated with a *minimization structure* of coupled electroelasticity, which is favorable for stability analysis[8] [51]. Note that in three dimensions, non-unique solutions of electric

[8] We note that due to the vectorial nature of $\boldsymbol{a}$, such formulation is in three spatial dimensions computationally more demanding than classical formulations based on the (scalar-valued) electric potential

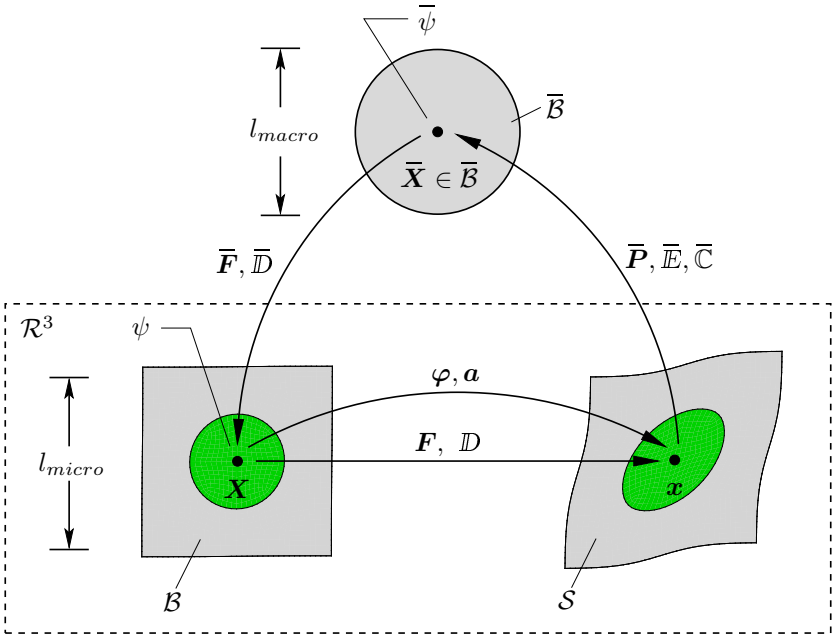

Figure 3.1: *Description of computational homogenization.* The figure describes the computational homogenization at an integration point $\overline{\boldsymbol{X}}$ of the macrostructure. The *macro-to-micro* transition is carried out by imposing boundary conditions associated with the macroscopic deformation gradient $\overline{\boldsymbol{F}}$ and electric displacement $\overline{\mathbb{D}}$ on the RVE under the assumption $l_{micro} << l_{macro}$. After obtaining the solution of the microscopic boundary value problem, *micro-to-macro* transition is considered, i.e., the averaged macroscopic dual fields $\overline{\boldsymbol{P}}, \overline{\mathbb{E}}$ and coupled moduli $\overline{\mathbb{C}}$ are obtained.

vector potentials can be circumvented, e.g., by imposing Coulomb-gauge conditions. Such condition requires $\operatorname{Div} \boldsymbol{a} = 0$ to hold in $\mathcal{B}$ to eliminate the ill-conditioning of the problem. However in two dimensions, this condition is satisfied automatically due to the vanishing plane components of the electric vector potential, see Semenov et al. [73].

The associated deformation gradient and electric displacement vector are given by

$$\boldsymbol{F} = \operatorname{Grad} \boldsymbol{\varphi}(\boldsymbol{X}, t) \quad \text{and} \quad \mathbb{D} = \operatorname{Curl} \boldsymbol{a}(\boldsymbol{X}, t)\,, \tag{3.2}$$

where the deformation gradient must satisfy $\det[\boldsymbol{F}] > 0$ and the Gauss law $\operatorname{Div} \mathbb{D} = 0$ holds a priori [9]. It is assumed that the microstructure is driven by the macroscopic deformation gradient and electric displacement vector. The microscopic kinematic fields

as primary field (in two spatial dimensions the number of degrees of freedom for both formulations is identical). This drawback could slightly be compensated by generally better convergence rates due to the positive definiteness of the system matrices in stable loading paths [73]. Furthermore, formulations based on the electric vector potential (as advocated in the present contribution) allow to track the response of (micro-)structures throughout the full range of loading paths, see also [40, 51].

[9] Note that in three spatial dimensions the electric vector-potential formulation becomes non-unique. This is because the Curl operation in $(3.2)_2$ is invariant w.r.t. an addition of any gradient field to $\boldsymbol{a}(\boldsymbol{X}, t)$, i.e., $\operatorname{Curl}(\boldsymbol{a} + \operatorname{Grad} \omega) = \operatorname{Curl}(\boldsymbol{a})\ \forall\ \omega \in \mathcal{R}$. The issue of non-uniqueness is usually treated by the imposition of Coulomb gauges. Such additional condition requires $\operatorname{Div} \boldsymbol{a} = 0$ to be fulfilled thoughout the whole body $\mathcal{B}$ and can be implemented, for example, by using Lagrange or penalty formulations, see Biro and Preis [10], Kovetz [36], Semenov et al. [72, 73] amongst others. Please note that in two spatial dimensions, the vector potential is unique since it has only one out-of-plane component and $a_{3,3} = 0$ is fulfilled automatically.

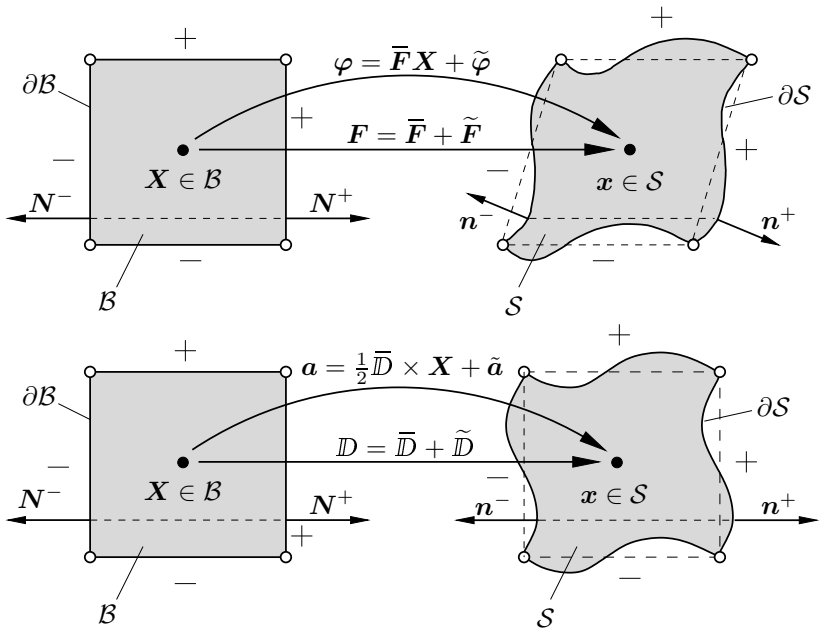

Figure 3.2: *RVE boundary conditions.* The RVE is driven by the macroscopic deformation gradient $\overline{\boldsymbol{F}}$ and electric displacement $\overline{\mathbb{D}}$ under the assumption of periodic boundary conditions for fluctuations. In the figure, '+' and '−' denote the boundaries $\partial\mathcal{B}^+$ and $\partial\mathcal{B}^-$, respectively.

can be expressed as

$$\boldsymbol{\varphi}(\boldsymbol{X},t) = \overline{\boldsymbol{F}}(t)\boldsymbol{X} + \widetilde{\boldsymbol{\varphi}}(\boldsymbol{X},t) \quad \text{and} \quad \boldsymbol{a}(\boldsymbol{X},t) = \frac{1}{2}\overline{\mathbb{D}}(t) \times \boldsymbol{X} + \widetilde{\boldsymbol{a}}(\boldsymbol{X},t)\,, \tag{3.3}$$

where $\widetilde{\boldsymbol{\varphi}}^+(\boldsymbol{X}^+,t) = \widetilde{\boldsymbol{\varphi}}^-(\boldsymbol{X}^-,t)$ and $\widetilde{\boldsymbol{a}}^+(\boldsymbol{X}^+,t) = \widetilde{\boldsymbol{a}}^-(\boldsymbol{X}^-,t)$ are periodic fluctuations on the boundary $\partial\mathcal{B} = \partial\mathcal{B}^+ \cup \partial\mathcal{B}^-$ of the RVE such that $\boldsymbol{X}^+ \in \partial\mathcal{B}^+$ and $\boldsymbol{X}^- \in \partial\mathcal{B}^-$, see Fig. 3.2. Therefore, we seek the solution of the microscopic boundary value problem under periodic boundary conditions which satisfy the Hill-Mandel homogeneity assumption, see [25, 42, 68, 51, 29, 30] and references cited therein for more details.

Considering above definitions of the deformation map and electric vector potential, the microscopic deformation gradient and displacement vector read

$$\boldsymbol{F} = \overline{\boldsymbol{F}} + \operatorname{Grad}\widetilde{\boldsymbol{\varphi}} \quad \text{and} \quad \mathbb{D} = \overline{\mathbb{D}} + \operatorname{Curl}\widetilde{\boldsymbol{a}}\,, \tag{3.4}$$

where $\overline{\boldsymbol{F}}$ and $\overline{\mathbb{D}}$ are the prescribed homogeneous macroscopic deformation gradient and electric displacement vector. The following expressions for macroscopic kinematic fields are assumed, c.f. Hill [27], Miehe et al. [51]

$$\begin{aligned} \overline{\boldsymbol{F}} &:= \frac{1}{|\mathcal{B}|}\int_{\partial\mathcal{B}} \boldsymbol{\varphi} \otimes \boldsymbol{N}\,\mathrm{d}A = \frac{1}{|\mathcal{B}|}\int_{\mathcal{B}} \boldsymbol{F}\,\mathrm{d}V \quad \text{and} \\ \overline{\mathbb{D}} &:= \frac{1}{|\mathcal{B}|}\int_{\partial\mathcal{B}} \boldsymbol{N} \times \boldsymbol{a}\,\mathrm{d}A = \frac{1}{|\mathcal{B}|}\int_{\mathcal{B}} \mathbb{D}\,\mathrm{d}V\,. \end{aligned} \tag{3.5}$$

3.2.2 Stored energy density function of microstructure

The constitutive response of the microstructure is assumed to be governed by an additive free-energy function, see [51]

$$\psi(\boldsymbol{F}, \mathbb{D}) = \psi^m(\boldsymbol{F}) + \psi^e(\boldsymbol{F}, \mathbb{D})\,, \tag{3.6}$$

where, $\boldsymbol{F}$ and $\mathbb{D}$ are defined by (3.4). The first term describes a polyconvex energy of the material in terms of the mechanical deformation. The second term describes a dielectric energy of the material, which is modeled as a convex function in $\mathbb{D}$. Moreover, the objectivity of ψ with respect to rigid-body motions $\boldsymbol{\varphi}^+ = \boldsymbol{Q}\boldsymbol{\varphi} + \boldsymbol{c}$ superimposed onto the current configuration is a priori satisfied for all translations $\boldsymbol{c}(t)$ and rotations $\boldsymbol{Q}(t) \in \mathcal{SO}(3)$ considering the reduced form

$$\psi(\boldsymbol{F}, \mathbb{D}) = \psi_{red}(\boldsymbol{C}, \mathbb{D})\,, \tag{3.7}$$

where, $\boldsymbol{C} = \boldsymbol{F}^T\boldsymbol{g}\boldsymbol{F}$ is the right Cauchy-Green deformation tensor and $\boldsymbol{g} \in Sym_+(3)$ is the spatial metric tensor defined in the current configuration.

For incompressible materials, we consider a split of the mechanical energy into *volumetric* and *isochoric* parts, see also [59]

$$\boxed{\psi(\boldsymbol{F}, J, \mathbb{D}) = U^m(J) + \psi^{m,iso}(\boldsymbol{F}^{iso}) + \psi^e(\boldsymbol{F}, \mathbb{D})\,.} \tag{3.8}$$

Here, $U^m(J)$ describes the volumetric part of the mechanical free-energy function depending on $J = \det[\boldsymbol{F}]$ and $\psi^{m,iso}$ is the isochoric part of the mechanical free-energy function which depends on the isochoric deformation gradient $\boldsymbol{F}^{iso} = J^{-1/3}\boldsymbol{F}$.

3.2.3 Variational formulation of quasi-incompressible homogenization

To describe the quasi-incompressible nature of electroactive polymers in the context of homogenization we implement a four-field formulation for microstructures based on [54, 76, 77, 48]. At the same time such approach overcomes the weak performance of the displacement formulation, specifically with regard to volumetric locking. A similar homogenization method for quasi-incompressible materials in the purely mechanical case has been considered in [95].

In the present approach, the incompressibility condition $J = \det[\boldsymbol{F}] = 1$ is satisfied in approximate sense by penalizing the Jacobian J element-wise. Therefore, an element-wise scalar dilatation θ is introduced in the microscopic energy functional and constant microscopic pressure p forces the constraint $J = \theta$ in each finite element. Thus, the homogenized macroscopic energy function at a macroscopic material point $\overline{\boldsymbol{X}}$ can be expressed by

$$\overline{\psi}(\overline{\boldsymbol{F}}, \overline{\mathbb{D}}; \overline{\boldsymbol{X}}) = \inf_{\widetilde{\boldsymbol{\varphi}} \in \mathcal{W}_{\widetilde{\boldsymbol{\varphi}}}} \inf_{\widetilde{\boldsymbol{a}} \in \mathcal{W}_{\widetilde{\boldsymbol{a}}}} \inf_{\theta \in \mathcal{W}_\theta} \sup_{p \in \mathcal{W}_p} \left\{\hat{\Pi}(\overline{\boldsymbol{F}} + \operatorname{Grad}\widetilde{\boldsymbol{\varphi}}, \overline{\mathbb{D}} + \operatorname{Curl}\widetilde{\boldsymbol{a}}, \theta, p)\right\}, \tag{3.9}$$

where the macroscopic potential density $\hat{\Pi}$ is obtained through homogenization over a microscopic RVE

$$\hat{\Pi} = \frac{1}{|\mathcal{B}|}\int_{\mathcal{B}} \hat{\pi}^{micro}\,\mathrm{d}V\,. \tag{3.10}$$

Here $\hat{\pi}^{micro}$ is the *microscopic potential density* per unit volume of the reference configuration $\mathcal{B}$ given by

$$\begin{aligned}\hat{\pi}^{micro} &= U^m(\theta) + p(J-\theta) + \psi^{m,iso}(J^{-1/3}(\overline{\boldsymbol{F}} + \operatorname{Grad}\widetilde{\boldsymbol{\varphi}})) \\ &\quad + \psi^e(\overline{\boldsymbol{F}} + \operatorname{Grad}\widetilde{\boldsymbol{\varphi}}, \overline{\mathbb{D}} + \operatorname{Curl}\widetilde{\boldsymbol{a}})\,.\end{aligned} \tag{3.11}$$

Thus, the macroscopic energy is defined as the stationary point of the volume averaged microscopic free-energy in the admissible spaces

$$\begin{aligned}
\widetilde{\boldsymbol{\varphi}} &\in \mathcal{W}_{\widetilde{\varphi}} &&:= \big\{\widetilde{\boldsymbol{\varphi}} \in H^1(\mathcal{B}) &&\mid \widetilde{\boldsymbol{\varphi}}^+ = \widetilde{\boldsymbol{\varphi}}^- \quad \text{on } \partial\mathcal{B} = \partial\mathcal{B}^+ \cup \partial\mathcal{B}^-\big\} \\
\widetilde{\boldsymbol{a}} &\in \mathcal{W}_{\widetilde{\boldsymbol{a}}} &&:= \big\{\widetilde{\boldsymbol{a}} \in H(\operatorname{Curl},\mathcal{B}) &&\mid \widetilde{\boldsymbol{a}}^+ = \widetilde{\boldsymbol{a}}^- \quad \text{on } \partial\mathcal{B} = \partial\mathcal{B}^+ \cup \partial\mathcal{B}^-\big\} \\
\theta &\in \mathcal{W}_{\theta} &&:= \big\{\theta \in L^2(\mathcal{B}) \text{ in } \mathcal{B} &&\big\} \\
p &\in \mathcal{W}_{p} &&:= \big\{p \in L^2(\mathcal{B}) \text{ in } \mathcal{B} &&\big\}\,.
\end{aligned} \tag{3.12}$$

Note that $\overline{\psi}$, in general, describes the macroscopic energy at a microscopic solution state which might still not represent the minimum macroscopic energy for a given macroscopic deformation state. We define the minimum macroscopic homogenized energy state under macroscopic stress-free state assumptions within a macroscopic driving procedure for the microstructure which will be described later (see also Miehe et al. [51]).

The macroscopic stresses and coupled moduli can be obtained from the homogenized energy (3.9) by the following equations

$$\overline{\mathbf{P}} := \partial_{\overline{\mathbf{F}}}\overline{\psi}(\overline{\boldsymbol{F}}, \overline{\mathbb{D}}; \overline{\boldsymbol{X}}) \quad \text{and} \quad \overline{\mathbb{C}} := \partial^2_{\overline{\mathbf{F}}\,\overline{\mathbf{F}}}\overline{\psi}(\overline{\boldsymbol{F}}, \overline{\mathbb{D}}; \overline{\boldsymbol{X}})\,, \tag{3.13}$$

where $\overline{\mathbf{F}} := [\overline{\boldsymbol{F}}, \overline{\mathbb{D}}]^T$ and $\overline{\mathbf{P}} := [\overline{\boldsymbol{P}}, \overline{\mathbb{E}}]^T$ are the generalized arrays of the gradient fields and the constitutive fields of electro-elasticity at macroscale, respectively, while $\overline{\mathbb{C}}$ is the coupled macroscopic moduli tensor.

3.2.4 Euler-Lagrange equations and linearization of variational formulation

Taking the necessary condition for the optimization problem (3.9) into account yields

$$\delta\hat{\Pi} = \frac{1}{|\mathcal{B}|}\int_{\mathcal{B}} \begin{bmatrix} \operatorname{Grad}\delta\widetilde{\boldsymbol{\varphi}} \\ \operatorname{Curl}\delta\widetilde{\boldsymbol{a}} \\ \delta\theta \\ \delta p \end{bmatrix} \cdot \begin{bmatrix} \partial_{\boldsymbol{F}}(\psi^{m,iso} + \psi^e) + pJ\boldsymbol{F}^{-T} \\ \partial_{\mathbb{D}}\psi^e \\ \partial_\theta U^m(\theta) - p \\ J - \theta \end{bmatrix} \mathrm{d}V = 0\,, \tag{3.14}$$

where $\delta\widetilde{\boldsymbol{\varphi}} \in \mathcal{W}_{\widetilde{\varphi}}$, $\delta\widetilde{\boldsymbol{a}} \in \mathcal{W}_{\widetilde{\boldsymbol{a}}}$, $\delta\theta \in \mathcal{W}_\theta$ and $\delta p \in \mathcal{W}_p$ are the admissible variations. Applying integral theorems the Euler-Lagrange equations can be obtained as follows

$$\boxed{\begin{aligned}
\operatorname{Div}[\partial_{\boldsymbol{F}}(\psi^{m,iso} + \psi^e) + pJ\boldsymbol{F}^{-T}] &= \boldsymbol{0} \quad \text{in} \quad \mathcal{B} \\
\operatorname{Curl}[\partial_{\mathbb{D}}\psi^e] &= \boldsymbol{0} \quad \text{in} \quad \mathcal{B} \\
\big[\!\big[\partial_{\boldsymbol{F}}(\psi^{m,iso} + \psi^e) + pJ\boldsymbol{F}^{-T}\big]\!\big] \cdot \boldsymbol{N} &= \boldsymbol{0} \quad \text{on} \quad \partial\mathcal{B} \\
\big[\!\big[\partial_{\mathbb{D}}\psi^e\big]\!\big] \times \boldsymbol{N} &= \boldsymbol{0} \quad \text{on} \quad \partial\mathcal{B} \\
\partial_\theta U^m(\theta) - p &= 0 \quad \text{in} \quad \mathcal{B} \\
J - \theta &= 0 \quad \text{in} \quad \mathcal{B}
\end{aligned}} \tag{3.15}$$

where $[\![(\cdot)]\!] = (\cdot)^+ - (\cdot)^-$ denotes the jump of $(\cdot)$ across the surfaces $\partial\mathcal{B}^+$ and $\partial\mathcal{B}^-$ of the RVE. The normals $\boldsymbol{N}^+$ at $\boldsymbol{X}^+ \in \partial\mathcal{B}^+$ and $\boldsymbol{N}^-$ at $\boldsymbol{X}^- \in \partial\mathcal{B}^-$ are defined such that $\boldsymbol{N}^+ = -\boldsymbol{N}^-$, see Fig. 3.2 for a schematic visualization. The first and the second Euler-Lagrange equations represent the balance of linear momentum and Faraday's law with the first Piola-Kirchhoff stress tensor $\boldsymbol{P} = \partial_{\boldsymbol{F}}(\psi^{m,iso} + \psi^e) + pJ\boldsymbol{F}^{-T}$ and the electric field $\mathbb{E} = \partial_{\mathbb{D}}\psi^e$.[10] The linearization of (3.14) yields the following expression in compact form

$$\Delta\delta\hat{\Pi} = \frac{1}{|\mathcal{B}|}\int_{\mathcal{B}} \begin{bmatrix} \delta\widetilde{\boldsymbol{F}} \\ \delta\widetilde{\mathbb{D}} \\ \delta\theta \\ \delta p \end{bmatrix} \cdot \begin{bmatrix} \mathbb{A} & \mathbb{H} & \boldsymbol{0} & J\boldsymbol{F}^{-T} \\ \mathbb{H}^T & \mathbb{K} & \boldsymbol{0} & \boldsymbol{0} \\ \boldsymbol{0} & \boldsymbol{0} & \partial^2_{\theta\theta}U^m(\theta) & -1 \\ J\boldsymbol{F}^{-T} & \boldsymbol{0} & -1 & 0 \end{bmatrix} \cdot \begin{bmatrix} \Delta\widetilde{\boldsymbol{F}} \\ \Delta\widetilde{\mathbb{D}} \\ \Delta\theta \\ \Delta p \end{bmatrix} \mathrm{d}V\,, \tag{3.17}$$

where $\Delta\widetilde{\boldsymbol{F}} = \mathrm{Grad}\,\Delta\widetilde{\boldsymbol{\varphi}}$ and $\Delta\widetilde{\mathbb{D}} = \mathrm{Curl}\,\Delta\widetilde{\boldsymbol{a}}$ are considered. $\mathbb{A} = \partial^2_{\boldsymbol{F}\boldsymbol{F}}(\psi^{m,iso} + \psi^e) + pJ\boldsymbol{F}^{-T}\otimes\boldsymbol{F}^{-T} + pJ\frac{\partial\boldsymbol{F}^{-T}}{\partial\boldsymbol{F}}$ is the mechanical moduli tensor, $\mathbb{H} = \partial^2_{\boldsymbol{F}\mathbb{D}}\psi^e$ is the coupling term and $\mathbb{K} = \partial^2_{\mathbb{D}\mathbb{D}}\psi^e$ is the electric moduli tensor of the microstructure.

Due to the discontinuous element-wise constant interpolations of the dilatation θ and pressure p, we can solve these terms on element level and condense them out of the global algebraic system of equations

$$\int_{\mathcal{B}^e}\delta p(J-\theta^e)\,\mathrm{d}V = 0 \quad \text{and} \quad \int_{\mathcal{B}^e}\delta\theta\big(\partial_\theta U^m(\theta^e) - p^e\big)\,\mathrm{d}V = 0 \tag{3.18}$$

yields expressions for dilatation and pressure in a finite element $\mathcal{B}^e$

$$\theta^e = \frac{1}{|\mathcal{B}^e|}\int_{\mathcal{B}^e} J\;\mathrm{d}V = \frac{|\mathcal{S}^e|}{|\mathcal{B}^e|} \quad \text{and} \quad p^e = \partial_\theta U^m(\theta^e)\,, \tag{3.19}$$

where $|\mathcal{B}^e| = \int_{\mathcal{B}^e}\mathrm{d}V$ is the volume of a finite element $\mathcal{B}^e$ in the reference configuration and $|\mathcal{S}^e| = \int_{\mathcal{B}^e} J\,\mathrm{d}V$ is the volume of a deformed finite element $\mathcal{S}^e$ in the current configuration. Similarly, the increments $\Delta\theta$ and Δp can be expressed as

$$\Delta\theta^e = \frac{1}{|\mathcal{B}^e|}\int_{\mathcal{B}^e} J\boldsymbol{F}^{-T} : \Delta\widetilde{\boldsymbol{F}}\,\mathrm{d}V \quad \text{and} \quad \Delta p^e = \frac{\partial^2_{\theta\theta}U^m(\theta^e)}{|\mathcal{B}^e|}\int_{\mathcal{B}^e} J\boldsymbol{F}^{-T} : \Delta\widetilde{\boldsymbol{F}}\,\mathrm{d}V\,. \tag{3.20}$$

Inserting equations (3.19) and (3.20) into (3.14) and (3.17) yields the reduced variation of the microscopic potential and its linearization depending on only the displacement and electric vector potential as primary variables

$$\delta\widetilde{\Pi}_{red} = \frac{1}{|\mathcal{B}|}\int_{\mathcal{B}^e}\big\{\delta\widetilde{\boldsymbol{F}} : \boldsymbol{P} + \delta\widetilde{\mathbb{D}}\cdot\mathbb{E}\big\}\,\mathrm{d}V \tag{3.21}$$

[10] Note that that the present approach is based on a referential description of the Maxwell equations, see, e.g., Dorfmann and Ogden [16] for more details. In the current configuration the corresponding Maxwell equations read

$$\mathrm{div}\,\mathrm{d} = 0 \quad \text{and} \quad \mathrm{curl}\,\mathrm{e} = \boldsymbol{0} \tag{3.16}$$

where $\mathrm{d} = \boldsymbol{\varphi}_{t*}(\mathbb{D}) = J^{-1}\boldsymbol{F}\mathbb{D}$ and $\mathrm{e} = \boldsymbol{\varphi}_{t*}(\mathbb{E}) = \boldsymbol{F}^{-T}\mathbb{E}$ are the push-forwards of the referential electric displacement $\mathbb{D}$ and electric field $\mathbb{E}$, respectively.

and

$$\Delta\delta\widetilde{\Pi}_{red} = \frac{1}{|\mathcal{B}|}\int_{\mathcal{B}^e}\left\{\delta\widetilde{\boldsymbol{F}} : \mathbb{A} : \Delta\widetilde{\boldsymbol{F}} + \delta\widetilde{\boldsymbol{F}} : \mathbb{H}\cdot\Delta\widetilde{\mathbb{D}} + \delta\widetilde{\mathbb{D}}\cdot\mathbb{H}^T : \Delta\widetilde{\boldsymbol{F}} + \delta\widetilde{\mathbb{D}}\cdot\mathbb{K}\cdot\Delta\widetilde{\mathbb{D}}\right\}\mathrm{d}V + \frac{1}{|\mathcal{B}|}\left[\int_{\mathcal{B}^e}\delta\widetilde{\boldsymbol{F}} : J\boldsymbol{F}^{-T}\,\mathrm{d}V\right]\frac{\partial^2_{\theta\theta}U^m(\theta^e)}{|\mathcal{B}^e|}\left[\int_{\mathcal{B}^e}J\boldsymbol{F}^{-T} : \Delta\widetilde{\boldsymbol{F}}\,\mathrm{d}V\right]. \tag{3.22}$$

3.2.5 Finite element implementation of the homogenization procedure

The solution of the microscopic boundary value problem (3.21) is carried out by the isoparametric finite element method. The nodal degrees of freedom are the fluctuations of the deformation map and electric vector potential. We consider the same ansatz space for the primary fields $\mathbf{d}^e := [\boldsymbol{d}^e_{\widetilde{\boldsymbol{\varphi}}}, \boldsymbol{d}^e_{\widetilde{\boldsymbol{a}}}]^T$, their increments $\Delta\mathbf{d}^e := [\Delta\boldsymbol{d}^e_{\widetilde{\boldsymbol{\varphi}}}, \Delta\boldsymbol{d}^e_{\widetilde{\boldsymbol{a}}}]^T$ and their variations $\delta\mathbf{d}^e := [\delta\boldsymbol{d}^e_{\widetilde{\boldsymbol{\varphi}}}, \delta\boldsymbol{d}^e_{\widetilde{\boldsymbol{a}}}]^T$. Then, the fluctuations of the deformation map and electric vector potential are discretized as

$$\widetilde{\boldsymbol{\varphi}} \approx \widetilde{\boldsymbol{\varphi}}^h = \sum_{I=1}^{n_{node}} N^I\boldsymbol{d}^I_{\widetilde{\boldsymbol{\varphi}}} =: \boldsymbol{N}^{\widetilde{\boldsymbol{\varphi}}}\boldsymbol{d}^e_{\widetilde{\boldsymbol{\varphi}}} \quad \text{and} \quad \widetilde{\boldsymbol{a}} \approx \widetilde{\boldsymbol{a}}^h = \sum_{I=1}^{n_{node}} N^I\boldsymbol{d}^I_{\widetilde{\boldsymbol{a}}} =: \boldsymbol{N}^{\widetilde{\boldsymbol{a}}}\boldsymbol{d}^e_{\widetilde{\boldsymbol{a}}}\,, \tag{3.23}$$

where N^I is the shape function of the node I of a corresponding finite element $\mathcal{B}^e$.

The gradient and the curl of the fluctuation fields are approximated as

$$\begin{aligned}\widetilde{\boldsymbol{F}} \approx \widetilde{\boldsymbol{F}}^h = \mathrm{Grad}\,\widetilde{\boldsymbol{\varphi}}^h &= \sum_{I=1}^{n_{node}} \boldsymbol{d}^I_{\widetilde{\boldsymbol{\varphi}}}\otimes\mathrm{Grad}_{\boldsymbol{X}}N^I := \boldsymbol{N}^{\widetilde{\boldsymbol{\varphi}}}_{,\boldsymbol{X}}\boldsymbol{d}^e_{\widetilde{\boldsymbol{\varphi}}}\\ \widetilde{\mathbb{D}} \approx \widetilde{\mathbb{D}}^h = \mathrm{Curl}\,\widetilde{\boldsymbol{a}}^h &= \sum_{I=1}^{n_{node}} \mathrm{Grad}_{\boldsymbol{X}}N^I\times\boldsymbol{d}^I_{\widetilde{\boldsymbol{a}}} := \boldsymbol{N}^{\widetilde{\boldsymbol{a}}}_{,\boldsymbol{X}}\boldsymbol{d}^e_{\widetilde{\boldsymbol{a}}}\,,\end{aligned} \tag{3.24}$$

where, $\boldsymbol{N}^{\widetilde{\boldsymbol{\varphi}}}_{,\boldsymbol{X}}$ and $\boldsymbol{N}^{\widetilde{\boldsymbol{a}}}_{,\boldsymbol{X}}$ are interpolation matrices comprising the gradients of the shape functions with respect to the reference configuration.[11] The tensorial gradient of mechanical fluctuations is implemented in a vectorial form, i.e., $\widetilde{\boldsymbol{F}}^h = [\widetilde{F}_{11},\ \widetilde{F}_{22},\ \widetilde{F}_{12},\ \widetilde{F}_{21}]^T$ in two dimensions, which is considered in the last term of $(3.24)_1$.

For later use, we consider the following expression

$$\begin{aligned}&\int_{\mathcal{B}^e} J\boldsymbol{F}^{-T} : \Delta\widetilde{\boldsymbol{F}}^h\,\mathrm{d}V = \int_{\mathcal{B}^e} J\boldsymbol{F}^{-T} : \Big(\sum_{I=1}^{n_{node}}\Delta\boldsymbol{d}^I_{\widetilde{\boldsymbol{\varphi}}}\otimes\mathrm{Grad}_{\boldsymbol{X}}N^I\Big)\,\mathrm{d}V\\ &= \int_{\mathcal{B}^e}\sum_{I=1}^{n_{node}} J\Delta\boldsymbol{d}^I_{\widetilde{\boldsymbol{\varphi}}}\cdot\big(\mathrm{Grad}_{\boldsymbol{X}}N^I\boldsymbol{F}^{-1}\big)\,\mathrm{d}V = \int_{\mathcal{B}^e}\sum_{I=1}^{n_{node}} J\Delta\boldsymbol{d}^I_{\widetilde{\boldsymbol{\varphi}}}\cdot\mathrm{grad}_{\boldsymbol{x}}N^I\,\mathrm{d}V\\ &:= \Big\{\int_{\mathcal{S}^e}\boldsymbol{N}^{\widetilde{\boldsymbol{\varphi}}}_{,\boldsymbol{x}}\,\mathrm{d}v\Big\}\Delta\boldsymbol{d}^e_{\widetilde{\boldsymbol{\varphi}}} = \bar{\boldsymbol{N}}^{\widetilde{\boldsymbol{\varphi}}}_{,\boldsymbol{x}}\Delta\boldsymbol{d}^e_{\widetilde{\boldsymbol{\varphi}}}\,.\end{aligned} \tag{3.26}$$

[11] For two-dimensional problems, $\boldsymbol{N}^{\widetilde{\boldsymbol{\varphi}}}_{,\boldsymbol{X}}$ and $\boldsymbol{N}^{\widetilde{\boldsymbol{a}}}_{,\boldsymbol{X}}$ at node I are assembled as

$$\big[\boldsymbol{N}^{\widetilde{\boldsymbol{\varphi}}}_{,\boldsymbol{X}}\big]_I = \begin{bmatrix}N^I_{,X_1} & & N^I_{,X_2} & \\ & N^I_{,X_2} & & N^I_{,X_1}\end{bmatrix}^T \quad \text{and} \quad \big[\boldsymbol{N}^{\widetilde{\boldsymbol{a}}}_{,\boldsymbol{X}}\big]_I = \begin{bmatrix}N^I_{,X_2} & -N^I_{,X_1}\end{bmatrix}^T. \tag{3.25}$$

Similarly, we can write

$$\int_{\mathcal{B}^e} \delta\widetilde{\boldsymbol{F}}^h : J\boldsymbol{F}^{-T}\,\mathrm{d}V := \overline{\boldsymbol{N}}^{\widetilde{\boldsymbol{\varphi}}}_{,\boldsymbol{x}}\delta\boldsymbol{d}^e_{\widetilde{\boldsymbol{\varphi}}}\,. \tag{3.27}$$

Above the row vectors $\boldsymbol{N}^{\widetilde{\boldsymbol{\varphi}}}_{,\boldsymbol{x}}$ and $\overline{\boldsymbol{N}}^{\widetilde{\boldsymbol{\varphi}}}_{,\boldsymbol{x}}$ contain the spatial derivative of the shape functions with respect to the current configuration and their integration over the deformed finite element $\mathcal{S}^e$, respectively. [12]

The total degrees of freedom become

$$\mathbf{d} := \mathop{\mathsf{A}}_{e=1}^{n_{elem}} \begin{bmatrix} \boldsymbol{d}^e_{\widetilde{\boldsymbol{\varphi}}} \\ \boldsymbol{d}^e_{\widetilde{\boldsymbol{a}}} \end{bmatrix} \in \mathcal{R}^m\,, \tag{3.29}$$

where $\mathsf{A}_{e=1}^{n_{elem}}$ denotes the assembly operator over all finite elements $\mathcal{B}^e \subset \mathcal{B}^h$. Considering the above discretization in (3.9) together with (3.19), (3.20) and (3.21) yields

$$\overline{\psi}^h(\overline{\mathbf{F}}, \mathbf{d}; \overline{\boldsymbol{X}}) = \frac{1}{|\mathcal{B}|} \mathop{\mathsf{A}}_{e=1}^{n_{elem}} \widetilde{\Pi}^h_{red}\big(\overline{\boldsymbol{F}} + \boldsymbol{N}^{\widetilde{\boldsymbol{\varphi}}}_{,\boldsymbol{X}}\boldsymbol{d}^e_{\widetilde{\boldsymbol{\varphi}}}, \overline{\mathbb{D}} + \boldsymbol{N}^{\widetilde{\boldsymbol{\varphi}}}_{,\boldsymbol{X}}\boldsymbol{d}^e_{\widetilde{\boldsymbol{a}}}, \theta^e(\boldsymbol{d}^e_{\widetilde{\boldsymbol{\varphi}}}), p^e(\boldsymbol{d}^e_{\widetilde{\boldsymbol{\varphi}}})\big)\,\mathrm{d}V \tag{3.30}$$

with

$$\boxed{\overline{\psi}(\overline{\mathbf{F}}; \overline{\boldsymbol{X}}) = \inf_{\mathbf{d}\in\mathcal{R}^m} \overline{\psi}^h(\overline{\mathbf{F}}, \mathbf{d}; \overline{\boldsymbol{X}})\,.} \tag{3.31}$$

The necessary condition $(3.21)_1$ of the minimization problem defines the nonlinear algebraic system of equations

$$\mathbf{R} := \overline{\psi}^h_{,\mathbf{d}} = \frac{1}{|\mathcal{B}|} \mathop{\mathsf{A}}_{e=1}^{n_{elem}} \int_{\mathcal{B}^e} \begin{bmatrix} \boldsymbol{N}^{\widetilde{\boldsymbol{\varphi}}T}_{,\boldsymbol{X}} \\ \boldsymbol{N}^{\widetilde{\boldsymbol{a}}T}_{,\boldsymbol{X}} \end{bmatrix} \cdot \begin{bmatrix} \boldsymbol{P} \\ \mathbb{E} \end{bmatrix} \mathrm{d}V = \boldsymbol{0}\,, \tag{3.32}$$

where the first Piola-Kirchhoff stress tensor $\boldsymbol{P}$ is implemented as a vectorial object, i.e., $\boldsymbol{P} = [P_{11},\ P_{22},\ P_{12},\ P_{21}]^T$ in two dimensions.

The microscopic converged energy state is obtained by applying the Newton-Raphson iteration scheme

$$\mathbf{d} \Leftarrow \mathbf{d} - \mathbf{K}^{-1}\mathbf{R} \quad \text{until} \quad ||\mathbf{R}|| \leq tol_{micro}\,, \tag{3.33}$$

where $\mathbf{K}$ is the stiffness matrix of the microstructure. It is defined from (3.22) and given by

$$\begin{aligned} \mathbf{K} := \overline{\psi}^h_{,\mathbf{dd}} = \frac{1}{|\mathcal{B}|} \mathop{\mathsf{A}}_{e=1}^{n_{elem}} \Bigg\{ & \int_{\mathcal{B}^e} \begin{bmatrix} \boldsymbol{N}^{\widetilde{\boldsymbol{\varphi}}T}_{,\boldsymbol{X}} \\ \boldsymbol{N}^{\widetilde{\boldsymbol{a}}T}_{,\boldsymbol{X}} \end{bmatrix} \cdot \begin{bmatrix} \mathbb{A} & \mathbb{H} \\ \mathbb{H}^T & \mathbb{K} \end{bmatrix} \cdot \begin{bmatrix} \boldsymbol{N}^{\widetilde{\boldsymbol{\varphi}}}_{,\boldsymbol{X}} \\ \boldsymbol{N}^{\widetilde{\boldsymbol{a}}}_{,\boldsymbol{X}} \end{bmatrix} \mathrm{d}V \\ & + \begin{bmatrix} \overline{\boldsymbol{N}}^{\widetilde{\boldsymbol{\varphi}}T}_{,\boldsymbol{x}} \frac{\partial^2_{\theta\theta} U^m(\theta^e)}{|\mathcal{B}^e|} \overline{\boldsymbol{N}}^{\widetilde{\boldsymbol{\varphi}}}_{,\boldsymbol{x}} & \boldsymbol{0} \\ \boldsymbol{0} & \boldsymbol{0} \end{bmatrix} \Bigg\}, \end{aligned} \tag{3.34}$$

[12] For two-dimensional problems, $\boldsymbol{N}^{\widetilde{\boldsymbol{\varphi}}}_{,\boldsymbol{x}}$ at node I reads

$$\big[\boldsymbol{N}^{\widetilde{\boldsymbol{\varphi}}}_{,\boldsymbol{x}}\big]_I = \begin{bmatrix} N^I_{,x_1} & N^I_{,x_2} \end{bmatrix} \tag{3.28}$$

where θ^e is constant on each finite element and defined by $(3.19)_1$. For compactness, we define with

$$\mathbb{C} := \begin{bmatrix} \mathbb{A} & \mathbb{H} \\ \mathbb{H}^T & \mathbb{K} \end{bmatrix} \tag{3.35}$$

the coupled electro-mechanical moduli of the microstructure. Here, $\mathbb{C}$ is not the direct derivative of the reduced microscopic potential $\widetilde{\Pi}_{red}$ with respect to the array of gradient fields $\mathbf{F} := [\boldsymbol{F}, \mathbb{D}]^T$. This is due to the fact that the pressure p is not an independent variable but depends on the microscopic deformation gradient $\boldsymbol{F}$. Furthermore, as the dilatation θ and pressure p are condensed out of the stiffness matrix, $\mathbf{K}$ is positive definite until a microscopic structural instability occurs. This effect has advantages for stability analysis.

3.2.6 Homogenized stresses and elasticity moduli

In the finite element context, the first Piola-Kirchhoff stress and the electric field in the compact form $\overline{\mathbf{P}} := [\overline{\boldsymbol{P}}, \overline{\mathbb{E}}]^T$ are defined by expressions given in $(3.13)_1$ based on the discrete minimization problem (3.31)

$$\overline{\mathbf{P}} = \partial_{\overline{\mathbf{F}}} \overline{\psi} = \overline{\psi}^h_{,\overline{\mathbf{F}}} + [\overline{\psi}^h_{,\mathbf{d}}][\mathbf{d}_{,\overline{\mathbf{F}}}] \tag{3.36}$$

which simplifies further at the converged state due to the necessary condition (3.32). In detail we have

$$\overline{\boldsymbol{P}} = \overline{\psi}^h_{,\overline{\boldsymbol{F}}} \quad \text{and} \quad \overline{\mathbb{E}} = \overline{\psi}^h_{,\overline{\mathbb{D}}}\,, \tag{3.37}$$

where

$$\overline{\psi}^h_{,\overline{\boldsymbol{F}}} = \frac{1}{|\mathcal{B}|} \mathop{\mathsf{A}}_{e=1}^{n_{elem}} \int_{\mathcal{B}^e} \boldsymbol{P}\, \mathrm{d}V \quad \text{and} \quad \overline{\psi}^h_{,\overline{\mathbb{D}}} = \frac{1}{|\mathcal{B}|} \mathop{\mathsf{A}}_{e=1}^{n_{elem}} \int_{\mathcal{B}^e} \mathbb{E}\, \mathrm{d}V\,. \tag{3.38}$$

Likewise, the macroscopic coupled moduli tensor is determined by expression $(3.13)_2$

$$\overline{\mathbb{C}} = \partial^2_{\overline{\mathbf{F}}\,\overline{\mathbf{F}}} \overline{\psi} = \overline{\psi}^h_{,\overline{\mathbf{F}}\,\overline{\mathbf{F}}} + \overline{\psi}^h_{,\overline{\mathbf{F}}\mathbf{d}} \mathbf{d}_{,\overline{\mathbf{F}}}\,, \tag{3.39}$$

where $\overline{\mathbf{F}} = [\overline{\boldsymbol{F}}, \overline{\mathbb{D}}]^T$ is considered for the concise representation. The first term on the right-hand side in (3.39) is defined as

$$\overline{\psi}^h_{,\overline{\mathbf{F}}\,\overline{\mathbf{F}}} := \begin{bmatrix} \overline{\psi}^h_{,\overline{\boldsymbol{F}}\,\overline{\boldsymbol{F}}} & \overline{\psi}^h_{,\overline{\boldsymbol{F}}\,\overline{\mathbb{D}}} \\ \overline{\psi}^h_{,\overline{\mathbb{D}}\,\overline{\boldsymbol{F}}} & \overline{\psi}^h_{,\overline{\mathbb{D}}\,\overline{\mathbb{D}}} \end{bmatrix} \tag{3.40}$$

along with the following definitions

$$\begin{aligned}
\overline{\psi}^h_{,\overline{\boldsymbol{F}}\,\overline{\boldsymbol{F}}} &= \frac{1}{|\mathcal{B}|} \mathop{\mathsf{A}}_{e=1}^{n_{elem}} \left\{ \int_{\mathcal{B}^e} \left[\mathbb{A} + J\boldsymbol{F}^{-T} \otimes \frac{\partial^2_{\theta\theta} U^m(\theta^e)}{|\mathcal{B}^e|} \int_{\mathcal{B}^e} J\boldsymbol{F}^{-T}\, \mathrm{d}V \right] \mathrm{d}V \right\} \\
\overline{\psi}^h_{,\overline{\boldsymbol{F}}\,\overline{\mathbb{D}}} &= \frac{1}{|\mathcal{B}|} \mathop{\mathsf{A}}_{e=1}^{n_{elem}} \left\{ \int_{\mathcal{B}^e} \partial^2_{\boldsymbol{F}\mathbb{D}} \psi^e\, \mathrm{d}V \right\} \\
\overline{\psi}^h_{,\overline{\mathbb{D}}\,\overline{\boldsymbol{F}}} &= \frac{1}{|\mathcal{B}|} \mathop{\mathsf{A}}_{e=1}^{n_{elem}} \left\{ \int_{\mathcal{B}^e} \partial^2_{\mathbb{D}\boldsymbol{F}} \psi^e\, \mathrm{d}V \right\} \\
\overline{\psi}^h_{,\overline{\mathbb{D}}\,\overline{\mathbb{D}}} &= \frac{1}{|\mathcal{B}|} \mathop{\mathsf{A}}_{e=1}^{n_{elem}} \left\{ \int_{\mathcal{B}^e} \partial^2_{\mathbb{D}\mathbb{D}} \psi^e\, \mathrm{d}V \right\}.
\end{aligned} \tag{3.41}$$

The second term in (3.39) is given as

$$\begin{aligned}\mathbf{L} := \overline{\psi}^{h}_{,\mathbf{d}\overline{\mathbf{F}}} = \frac{1}{|\mathcal{B}|} \mathop{\mathsf{A}}_{e=1}^{n_{elem}} \Big\{ \int_{\mathcal{B}^e} \begin{bmatrix} \boldsymbol{N}^{\widetilde{\boldsymbol{\varphi}}T}_{,\boldsymbol{X}} \\ \boldsymbol{N}^{\widetilde{\boldsymbol{a}}T}_{,\boldsymbol{X}} \end{bmatrix} \cdot \begin{bmatrix} \mathbb{A} & \mathbb{H} \\ \mathbb{H}^T & \mathbb{K} \end{bmatrix} \mathrm{d}V \\ + \begin{bmatrix} \overline{\boldsymbol{N}}^{\widetilde{\boldsymbol{\varphi}}T}_{,\boldsymbol{x}} \frac{\partial^2_{\theta\theta} U^m(\theta^e)}{|\mathcal{B}^e|} \int_{\mathcal{B}^e} J\boldsymbol{F}^{-T} \mathrm{d}V & \boldsymbol{0} \\ \boldsymbol{0} & \boldsymbol{0} \end{bmatrix} \Big\} .\end{aligned} \tag{3.42}$$

The sensitivity of fluctuations with respect to the macroscopic deformation gradient and electric displacement $\overline{\mathbf{F}} = [\overline{\boldsymbol{F}}, \overline{\mathbb{D}}]^T$ can be determined from (3.32)

$$\mathbf{d}_{,\overline{\mathbf{F}}} = -[\overline{\psi}^{h}_{,\mathbf{dd}}]^{-1} [\overline{\psi}^{h}_{,\mathbf{d}\overline{\mathbf{F}}}] = -\mathbf{K}^{-1}\mathbf{L} . \tag{3.43}$$

Inserting the latter equation in (3.39) yields the for coupled macroscopic electro-mechanical moduli

$$\overline{\mathbb{C}} = \overline{\psi}^{h}_{,\overline{\mathbf{F}}\,\overline{\mathbf{F}}} - \mathbf{L}^T \mathbf{K}^{-1} \mathbf{L} . \tag{3.44}$$

In general, computational homogenization requires to solve the microscopic variational problem on inhomogeneous RVEs at each Gauss-point of the macrostructure. Therefore, the solution at the macro-level is carried out in consideration of nested microscopic boundary value problems at each macroscopic load increment. However, for our framework we constrain our attention to a single macroscopic Gauss-point and study the microscopic and macroscopic stability behavior at this point. In this way, the RVE at the macroscopic Gauss-point is considered to be driven by the macroscopic deformation gradient $\overline{\boldsymbol{F}}$ and electric displacement $\overline{\mathbb{D}}$. We assume that the minimum macroscopic energy state is reached if the macroscopic homogenized stress and electric field components satisfy the macroscopic conservation laws. The converged macroscopic stress and electric field components are then associated with the prescribed deformation gradient and displacement vector components, see Miehe et al. [51], Zäh [96, p.137] for more details. The macroscopic stress and electric field tensors at converged microscopic state are determined by (3.37).

3.3 Stability analysis of periodic electroactive polymers

3.3.1 Localization-type macroscopic stability analysis

At a certain deformation threshold the homogenized incremental moduli might not hold the strong ellipticity condition leading to localization on the macro-level, see Abeyaratne and Triantafyllidis [1]. Therefore, it is of particular interest to determine the macroscopic deformations that lead to the loss of strong ellipticity. We determine these instability points Based on the criterion that has been given by Dorfmann and Ogden [17]. This criterion is described below.

Consider a time-dependent infinitesimal elastic perturbation $\overline{\boldsymbol{v}}(\overline{\boldsymbol{X}}, \overline{t})$ superimposed onto the current configuration. The linearized Euler-Lagrange equations in two-point setting can be written as

$$\begin{aligned} \mathrm{Div}[\overline{\mathbb{A}} : \dot{\overline{\boldsymbol{F}}} + \overline{\mathbb{H}} \cdot \dot{\overline{\mathbb{D}}}] &= \overline{\rho}_0 \overline{\boldsymbol{g}}\, \ddot{\overline{\boldsymbol{v}}}(\overline{\boldsymbol{X}}, \overline{t}) \\ \mathrm{Curl}[\overline{\mathbb{H}}^T : \dot{\overline{\boldsymbol{F}}} + \overline{\mathbb{K}} \cdot \dot{\overline{\mathbb{D}}}] &= \boldsymbol{0} , \end{aligned} \tag{3.45}$$

where, $\dot{\overline{\boldsymbol{F}}} = \operatorname{Grad}\overline{\boldsymbol{v}}(\overline{\boldsymbol{X}},\overline{t})$ and $\dot{\overline{\mathbb{D}}}$ are the increments of the macroscopic deformation gradient and electric displacement, respectively, $\overline{\boldsymbol{g}} \in Sym_+(3)$ is the symmetric spatial metric in the current macroscopic configuration and $\overline{\mathbb{A}} = \partial^2_{\overline{\boldsymbol{F}}\,\overline{\boldsymbol{F}}}\overline{\psi}$, $\overline{\mathbb{H}} = \partial^2_{\overline{\boldsymbol{F}}\,\overline{\mathbb{D}}}\overline{\psi}$ as well as $\overline{\mathbb{K}} = \partial^2_{\overline{\mathbb{D}}\,\overline{\mathbb{D}}}\overline{\psi}$ assemble the coupled macroscopic moduli $\overline{\mathbb{C}}$, which are defined by (3.44).

The incremental Gauss law in terms of the referential electric displacement is given by

$$\operatorname{Div}[\dot{\overline{\mathbb{D}}}] = 0\,. \tag{3.46}$$

For incompressible materials, it is convenient for the subsequent stability analysis to consider incremental Euler-Lagrange equations in the current configuration:

$$\begin{aligned} \operatorname{div}[\overline{\mathbb{a}} : \overline{\boldsymbol{d}} + \overline{\mathbb{h}} \cdot \boldsymbol{\pounds}_{\overline{\boldsymbol{v}}}\overline{d}] &= \overline{\rho}\,\overline{\boldsymbol{g}}\,\ddot{\overline{\boldsymbol{v}}}(\overline{\boldsymbol{X}},\overline{t}) \\ \operatorname{curl}[\overline{\mathbb{h}}^T : \overline{\boldsymbol{d}} + \overline{\mathbb{k}} \cdot \boldsymbol{\pounds}_{\overline{\boldsymbol{v}}}\overline{d}] &= \boldsymbol{0}\,, \end{aligned} \tag{3.47}$$

where $\overline{\mathbb{a}}_a{}^b{}_c{}^d = \overline{J}^{-1}\overline{F}^b{}_A\overline{F}^d{}_B\overline{\mathbb{A}}_a{}^A{}_c{}^B$, $\overline{\mathbb{h}}_a{}^b{}_c = \overline{F}^b{}_A(\overline{F}^{-1})^B{}_c\overline{\mathbb{H}}_a{}^A{}_B$ and $\overline{\mathbb{k}}_{ab} = \overline{J}(\overline{F}^{-1})^A{}_a(\overline{F}^{-1})^B{}_b\overline{\mathbb{K}}_{AB}$ are the current analogues of the mechanical, electro-mechanical and electric terms of coupled moduli $\overline{\mathbb{C}}$. $\overline{\boldsymbol{d}} = \operatorname{sym}[\operatorname{grad}\overline{\boldsymbol{v}}]$ is the symmetric part of the spatial gradient of the perturbation $\overline{\boldsymbol{v}}$, and $\boldsymbol{\pounds}_{\overline{\boldsymbol{v}}}\overline{d} = \boldsymbol{\varphi}_{t*}(\dot{\overline{\mathbb{D}}})$ is the objective Lie derivative of the electric displacement, which is defined as the push-forward of $\dot{\overline{\mathbb{D}}}$.

The incremental Gauss-law in the current configuration becomes

$$\operatorname{div}[\boldsymbol{\pounds}_{\overline{\boldsymbol{v}}}\overline{d}] = 0\,. \tag{3.48}$$

We consider that the homogeneous perturbations have the following form

$$\overline{\boldsymbol{v}} = \overline{\boldsymbol{p}} f(\overline{\boldsymbol{x}} \cdot \overline{\boldsymbol{n}} - \overline{c}\,\overline{t}) \quad \text{and} \quad \boldsymbol{\pounds}_{\overline{\boldsymbol{v}}}\overline{d} = \overline{\boldsymbol{s}} g(\overline{\boldsymbol{x}} \cdot \overline{\boldsymbol{n}} - \overline{c}\,\overline{t})\,, \tag{3.49}$$

where $\overline{\boldsymbol{p}}$ and $\overline{\boldsymbol{s}}$ are the propagation directions and $\overline{\boldsymbol{n}}$ is the amplitude direction of the perturbations with real wave speed $\overline{c}$. We assume that f is a twice continuously differentiable function and g is a continuously differentiable function (see Dorfmann and Ogden [17]).

Plugging $(3.49)_2$ in (3.48) results in $\overline{\boldsymbol{s}} \cdot \overline{\boldsymbol{n}} = 0$. Considering this and (3.49) in (3.47) yields the following condition for the strong ellipticity of the macroscopic moduli

$$\overline{\Lambda} = \inf_{|\overline{\boldsymbol{p}}|=|\overline{\boldsymbol{s}}|=|\overline{\boldsymbol{n}}|=1} \left\{ \overline{\boldsymbol{p}} \cdot \overline{\mathbb{q}}(\overline{\boldsymbol{n}}) \cdot \overline{\boldsymbol{p}} - \frac{[\overline{\boldsymbol{p}} \cdot \overline{\mathbb{r}}(\overline{\boldsymbol{n}}) \cdot \overline{\boldsymbol{s}}][\overline{\boldsymbol{p}} \cdot \overline{\mathbb{r}}(\overline{\boldsymbol{n}}) \cdot \overline{\boldsymbol{s}}]}{\overline{\boldsymbol{s}} \cdot \overline{\mathbb{k}} \cdot \overline{\boldsymbol{s}}} \right\} = \inf_{|\overline{\boldsymbol{p}}|=|\overline{\boldsymbol{s}}|=|\overline{\boldsymbol{n}}|=1} \{\overline{\rho}\,\overline{c}^2\} > 0\,, \tag{3.50}$$

where $\overline{\mathbb{q}}_{ac} = \overline{\mathbb{a}}_a{}^b{}_c{}^d\overline{n}_b\overline{n}_d$ and $\overline{\mathbb{r}}_{ac} = \overline{\mathbb{h}}_a{}^b{}_c\overline{n}_b$ (please refer to [50] for the treatment of purely mechanical problems). We call $\overline{\Lambda}$ the macroscopic coercivity constant. A vanishing $\overline{\Lambda}$ corresponds to the propagation of perturbations with zero wave speed $\overline{c}$, such that localizations can be developed at macroscale. Therefore, these points are of special importance.

For incompressible materials $\operatorname{div}\overline{\boldsymbol{v}} = 0$ yields

$$\overline{\boldsymbol{p}} \cdot \overline{\boldsymbol{n}} = 0\,, \tag{3.51}$$

which can be considered in (3.50).

For two-dimensional incompressible problems the loss of strong ellipticity can be determined by solving the sixth-order polynomial equation as given by Rudykh and deBotton [65]

$$a_0\xi^6 + a_1\xi^5 + a_2\xi^4 + a_3\xi^3 + a_4\xi^2 + a_5\xi + a_6 = 0\,, \tag{3.52}$$

where $\xi = \overline{n}_2/\overline{n}_1$ with $\overline{n}_2$ and $\overline{n}_1$ are the components of $\overline{\boldsymbol{n}}$ in two dimension. The coefficients are defined as

$$\begin{aligned}
a_0 =&(\overline{\mathbb{h}}_1{}^2{}_1)^2 - \overline{\mathbb{a}}_1{}^2{}_1{}^2\overline{\mathbb{k}}_{11}\\
a_1 =&2((\overline{\mathbb{a}}_1{}^2{}_2{}^2 - \overline{\mathbb{a}}_1{}^1{}_1{}^2)\overline{\mathbb{k}}_{11} + \overline{\mathbb{a}}_1{}^2{}_1{}^2\overline{\mathbb{k}}_{12} + \overline{\mathbb{h}}_1{}^2{}_1(\overline{\mathbb{h}}_1{}^1{}_1 - \overline{\mathbb{h}}_1{}^2{}_2 - \overline{\mathbb{h}}_2{}^2{}_1))\\
a_2 =&-(\overline{\mathbb{a}}_1{}^1{}_1{}^1 - 2\overline{\mathbb{a}}_1{}^1{}_2{}^2 - 2\overline{\mathbb{a}}_1{}^2{}_2{}^1 + \overline{\mathbb{a}}_2{}^2{}_2{}^2)\overline{\mathbb{k}}_{11} + 4(\overline{\mathbb{a}}_1{}^1{}_1{}^2 - \overline{\mathbb{a}}_1{}^2{}_2{}^2)\overline{\mathbb{k}}_{12} - \overline{\mathbb{a}}_1{}^2{}_1{}^2\overline{\mathbb{k}}_{22}\\
&+(\overline{\mathbb{h}}_1{}^2{}_2 + \overline{\mathbb{h}}_2{}^2{}_1 - \overline{\mathbb{h}}_1{}^1{}_1)^2 - 2\overline{\mathbb{h}}_1{}^2{}_1(\overline{\mathbb{h}}_1{}^1{}_2 + \overline{\mathbb{h}}_1{}^2{}_1 - \overline{\mathbb{h}}_2{}^2{}_2)\\
a_3 =&2((\overline{\mathbb{a}}_1{}^1{}_2{}^1 - \overline{\mathbb{a}}_2{}^1{}_2{}^2)\overline{\mathbb{k}}_{11} + (\overline{\mathbb{a}}_1{}^1{}_1{}^1 - 2\overline{\mathbb{a}}_1{}^1{}_2{}^2 - 2\overline{\mathbb{a}}_1{}^2{}_2{}^1 + \overline{\mathbb{a}}_2{}^2{}_2{}^2)\overline{\mathbb{k}}_{12}\\
&+(\overline{\mathbb{a}}_1{}^2{}_2{}^2 - \overline{\mathbb{a}}_1{}^1{}_1{}^2)\overline{\mathbb{k}}_{22} + (\overline{\mathbb{h}}_1{}^2{}_1\overline{\mathbb{h}}_1{}^2{}_2 - (\overline{\mathbb{h}}_1{}^1{}_1 - \overline{\mathbb{h}}_1{}^2{}_2 - \overline{\mathbb{h}}_2{}^2{}_1)\\
&\times(\overline{\mathbb{h}}_1{}^1{}_2 + \overline{\mathbb{h}}_1{}^2{}_1 - \overline{\mathbb{h}}_2{}^2{}_2)))\\
a_4 =&-\overline{\mathbb{a}}_2{}^1{}_2{}^1\overline{\mathbb{k}}_{11} - 4(\overline{\mathbb{a}}_1{}^1{}_2{}^1 - \overline{\mathbb{a}}_2{}^1{}_2{}^2)\overline{\mathbb{k}}_{12} - (\overline{\mathbb{a}}_1{}^1{}_1{}^1 - 2\overline{\mathbb{a}}_1{}^1{}_2{}^2\\
&-2\overline{\mathbb{a}}_1{}^2{}_2{}^1 + \overline{\mathbb{a}}_2{}^2{}_2{}^2)\overline{\mathbb{k}}_{22} + 2\overline{\mathbb{h}}_1{}^2{}_2(\overline{\mathbb{h}}_1{}^1{}_1 - \overline{\mathbb{h}}_1{}^2{}_2 - \overline{\mathbb{h}}_2{}^2{}_1)\\
&+(\overline{\mathbb{h}}_1{}^1{}_2 + \overline{\mathbb{h}}_1{}^2{}_1 - \overline{\mathbb{h}}_2{}^2{}_2)^2\\
a_5 =&2(\overline{\mathbb{a}}_2{}^1{}_2{}^1\overline{\mathbb{k}}_{12} + (\overline{\mathbb{a}}_1{}^1{}_2{}^1 - \overline{\mathbb{a}}_2{}^1{}_2{}^2)\overline{\mathbb{k}}_{22} - \overline{\mathbb{h}}_1{}^2{}_2(\overline{\mathbb{h}}_1{}^1{}_2 + \overline{\mathbb{h}}_1{}^2{}_1 - \overline{\mathbb{h}}_2{}^2{}_2))\\
a_6 =&(\overline{\mathbb{h}}_1{}^2{}_2)^2 - \overline{\mathbb{a}}_2{}^1{}_2{}^1\overline{\mathbb{k}}_{22}\,.
\end{aligned} \tag{3.53}$$

The instability point is considered to be detected at a deformation state if there exist a real solution of (3.52).

3.3.2 Bifurcation-type microscopic stability analysis

We treat the microscopic bifurcation-type instabilities of periodic electro-active polymers by considering Bloch-Floquet wave analysis in electro-elasticity motivated from the works of Bertoldi et al. [7] and Triantafyllidis et al. [89] in elasticity. Consider an EAP which is periodic at the microscale, i.e., it can be described by a generic unit cell and possesses the following translational symmetry

$$\mathbb{C}(\boldsymbol{X} + \boldsymbol{m}\boldsymbol{L}) = \mathbb{C}(\boldsymbol{X})\,, \tag{3.54}$$

where, $\boldsymbol{m} = [m_1, m_2, m_3]^T$ are arbitrary integers. $\boldsymbol{L} = [L_1, L_2, L_3]^T \in \mathcal{R}^3$ are the dimensions of the unit cell, $\boldsymbol{X}$ are the coordinates of the unit cell and $\mathbb{C}$ is the coupled moduli tensor of the microstructure given by (3.35).

The consideration of a polyconvex microscopic energy allows the description of buckling phenomena at microscale. However, when such microscopic instabilities occur the periodicity of the microstructure might change. Consequently, the RVE should contain the critical number $\boldsymbol{n} = [n_1, n_2, n_3]^T \in \mathbb{N}^3$ of unit cells (see Fig. 3.3) corresponding to the wavelength of the buckling to describe effective material response at macroscale and the buckling mode. The effective macroscopic energy should be defined by, see Müller [53]

$$\overline{\psi}(\overline{\boldsymbol{F}}, \overline{\mathbb{D}}; \overline{\boldsymbol{X}}) = \inf_{\boldsymbol{n}\in\mathbb{N}^3} \hat{\psi}^{\boldsymbol{n}}(\overline{\boldsymbol{F}}, \overline{\mathbb{D}}; \overline{\boldsymbol{X}}) \tag{3.55}$$

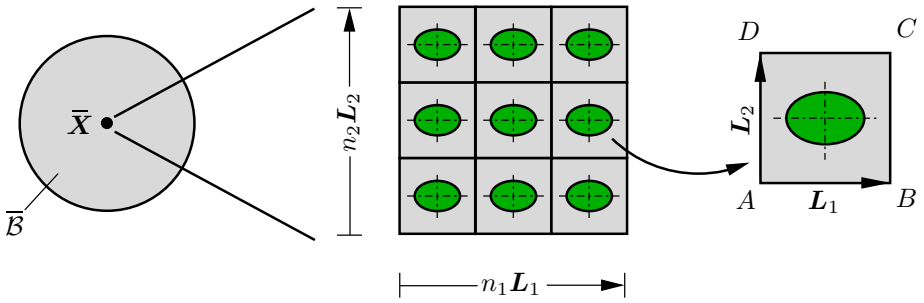

Figure 3.3: *Critical size of RVE in two dimensions.* The microscopic bifurcation-type periodic instabilities can alter the periodicity of the microstructure corresponding to the wavelength of the buckling requiring the enlargement of the RVE to $n_1\boldsymbol{L}_1 \times n_2\boldsymbol{L}_2$ from initial unit-cell size $\boldsymbol{L}_1 \times \boldsymbol{L}_2$. Here, n_1 and n_2 in 2D are the critical number of unit cells in $\boldsymbol{L}_1$ and $\boldsymbol{L}_2$ directions. These instabilities can be detected on the unit cell by taking advantage of Bloch-Floquet wave analysis rather than searching the first critical instability point on all possible enlargments of the RVE.

with

$$\hat{\psi}^{\boldsymbol{n}}(\overline{\boldsymbol{F}}, \overline{\mathbb{D}}; \overline{\boldsymbol{X}}) = \inf_{\widetilde{\boldsymbol{\varphi}} \in \mathcal{W}_{\widetilde{\boldsymbol{\varphi}}\#}} \inf_{\widetilde{\boldsymbol{a}} \in \mathcal{W}_{\widetilde{\boldsymbol{a}}\#}} \frac{1}{|\boldsymbol{n}\mathcal{D}|} \int_{\boldsymbol{n}\mathcal{D}} \psi(\overline{\boldsymbol{F}} + \operatorname{Grad} \widetilde{\boldsymbol{\varphi}}, \overline{\mathbb{D}} + \operatorname{Curl} \widetilde{\boldsymbol{a}}; \boldsymbol{X}) \, \mathrm{d}V \tag{3.56}$$

where $\boldsymbol{n}\mathcal{D}$ describes the enlarged RVE and $\mathcal{D}$ denotes the generic unit cell corresponding to the periodicity of the microstructure at the reference configuration. Admissible spaces for $\boldsymbol{n}\mathcal{D}$ periodic fine scale fluctuations are given by

$$\begin{aligned} \widetilde{\boldsymbol{\varphi}} \in \mathcal{W}_{\widetilde{\boldsymbol{\varphi}}\#} &:= \left\{ \widetilde{\boldsymbol{\varphi}} \in H^1(\mathcal{B}) \quad \middle| \; \widetilde{\boldsymbol{\varphi}}^+ = \widetilde{\boldsymbol{\varphi}}^- \text{ on } \partial\boldsymbol{n}\mathcal{D} \right\}, \\ \widetilde{\boldsymbol{a}} \in \mathcal{W}_{\widetilde{\boldsymbol{a}}\#} &:= \left\{ \widetilde{\boldsymbol{a}} \in H(\operatorname{Curl}, \mathcal{B}) \quad \middle| \; \widetilde{\boldsymbol{a}}^+ = \widetilde{\boldsymbol{a}}^- \text{ on } \partial\boldsymbol{n}\mathcal{D} \right\}. \end{aligned} \tag{3.57}$$

The microscopic instability is described by the following expression

$$\hat{\Lambda}_{\boldsymbol{n}\mathcal{D}} = \inf_{\boldsymbol{n} \in \mathbb{N}^3} \left\{ \inf_{\widetilde{\boldsymbol{\varphi}} \in \mathcal{W}_{\widetilde{\boldsymbol{\varphi}}\#}} \inf_{\widetilde{\boldsymbol{a}} \in \mathcal{W}_{\widetilde{\boldsymbol{a}}\#}} \left\{ \int_{\boldsymbol{n}\mathcal{D}} \begin{bmatrix} \operatorname{Grad} \widetilde{\boldsymbol{\varphi}} \\ \operatorname{Curl} \widetilde{\boldsymbol{a}} \end{bmatrix} \cdot \begin{bmatrix} \partial^2_{\boldsymbol{F}\boldsymbol{F}}\psi & \partial^2_{\boldsymbol{F}\mathbb{D}}\psi \\ \partial^2_{\mathbb{D}\boldsymbol{F}}\psi & \partial^2_{\mathbb{D}\mathbb{D}}\psi \end{bmatrix} \cdot \begin{bmatrix} \operatorname{Grad} \widetilde{\boldsymbol{\varphi}} \\ \operatorname{Curl} \widetilde{\boldsymbol{a}} \end{bmatrix} \mathrm{d}V \right. \right. \\ \left. \left. \Big/ \int_{\boldsymbol{n}\mathcal{D}} \begin{bmatrix} \operatorname{Grad} \widetilde{\boldsymbol{\varphi}} \\ \operatorname{Curl} \widetilde{\boldsymbol{a}} \end{bmatrix} \cdot \begin{bmatrix} \operatorname{Grad} \widetilde{\boldsymbol{\varphi}} \\ \operatorname{Curl} \widetilde{\boldsymbol{a}} \end{bmatrix} \mathrm{d}V \right\} \right\} \tag{3.58}$$

which constitutes the microscopic coercivity constant.

The relationship $\hat{\psi}^{\boldsymbol{n}}(\overline{\boldsymbol{F}}, \overline{\mathbb{D}}; \overline{\boldsymbol{X}}) \leq \hat{\psi}^{\boldsymbol{1}}(\overline{\boldsymbol{F}}, \overline{\mathbb{D}}; \overline{\boldsymbol{X}})$ between the homogenized macroscopic energy function over an enlarged RVE $\boldsymbol{n}\mathcal{D}$ and over a unit cell RVE $\mathcal{D}$ holds. The equality of them $\hat{\psi}^{\boldsymbol{n}}(\overline{\boldsymbol{F}}, \overline{\mathbb{D}}; \overline{\boldsymbol{X}}) = \hat{\psi}^{\boldsymbol{1}}(\overline{\boldsymbol{F}}, \overline{\mathbb{D}}; \overline{\boldsymbol{X}})$ is only satisfied if the coercivity constant is positive $\hat{\Lambda}_{\boldsymbol{n}\mathcal{D}} > 0$ (see [21, 53] for the purely mechanical case).

The definitions of the above mentioned effective macroscopic energy (3.55) and microscopic coercivity constant (3.58) require the consideration of all possible enlargements of an RVE to find the minimum energy state due to microscopic instabilities and the corresponding critical periodicity. In the numerical setting, the microscopic instability based on (3.58) can be detected as the loss of positive definiteness of the corresponding stiffness matrix which arises the first time along the loading path among the various enlarged RVEs. From a numerical point of view such computations are not feasible. However, Geymonat et al. [21] have shown rigorously for mechanical problems that the microscopic

coercivity constant and thus the critical periodicity still can be determined on a unit cell exploiting the Bloch wave analysis, see also Bertoldi et al. [7], Bertoldi and Gei [9] and Triantafyllidis et al. [89].

The Bloch-Floquet analysis describes testing stability of a unit cell RVE under superimposed periodic perturbations at current incremental deformation state, however with various wavelengths. This could be expressed as

$$\begin{aligned} \mathrm{Div}[\partial^2_{\boldsymbol{FF}}\psi : \mathrm{Grad}\,\mathfrak{v} + \partial^2_{\boldsymbol{F}\mathbb{D}}\psi \cdot \mathrm{Curl}\,\mathfrak{a}] &= \boldsymbol{0} \\ \mathrm{Curl}[\partial^2_{\mathbb{D}\boldsymbol{F}}\psi : \mathrm{Grad}\,\mathfrak{v} + \partial^2_{\mathbb{D}\mathbb{D}}\psi \cdot \mathrm{Curl}\,\mathfrak{a}] &= \boldsymbol{0} \end{aligned} \tag{3.59}$$

with jump conditions on the boundary $\partial\mathcal{D}$ of the unit cell

$$\begin{aligned} \left[\!\left[\partial^2_{\boldsymbol{FF}}\psi : \mathrm{Grad}\,\mathfrak{v} + \partial^2_{\boldsymbol{F}\mathbb{D}}\psi \cdot \mathrm{Curl}\,\mathfrak{a}\right]\!\right] \cdot \boldsymbol{N} &= \boldsymbol{0} \\ \left[\!\left[\partial^2_{\mathbb{D}\boldsymbol{F}}\psi : \mathrm{Grad}\,\mathfrak{v} + \partial^2_{\mathbb{D}\mathbb{D}}\psi \cdot \mathrm{Curl}\,\mathfrak{a}\right]\!\right] \times \boldsymbol{N} &= \boldsymbol{0}\,, \end{aligned} \tag{3.60}$$

where $\boldsymbol{N}$ is the outward normal on the surface of the RVE. $\mathfrak{v}$ and $\mathfrak{a}$ denote the periodic incremental perturbations which can be described in the following forms according to the Bloch-Floquet periodicity condition

$$\mathfrak{v}(\boldsymbol{X}) = \widetilde{\boldsymbol{\varphi}} \exp[\mathrm{i}\boldsymbol{k}\cdot\boldsymbol{X}] \quad \text{and} \quad \mathfrak{a}(\boldsymbol{X}) = \widetilde{\boldsymbol{a}} \exp[\mathrm{i}\boldsymbol{k}\cdot\boldsymbol{X}]\,, \tag{3.61}$$

where $\widetilde{\boldsymbol{\varphi}} \in \mathcal{W}_{\widetilde{\varphi}}$ and $\widetilde{\boldsymbol{a}} \in \mathcal{W}_{\widetilde{a}}$ are $\mathcal{D}$-periodic fluctuations and $\boldsymbol{k} \equiv (k_1, k_2)$ is referred to as Bloch vector which is defined in Fourier domain (see Section 3.3.3). Considering (3.61) results in the following expression for the microscopic coercivity constant

$$\begin{aligned} \hat{\Lambda}_{\boldsymbol{n}\mathcal{D}} = \inf_{\boldsymbol{k}} \Bigg\{ \inf_{\widetilde{\boldsymbol{\varphi}}\in\mathcal{W}_{\widetilde{\varphi}}} \inf_{\widetilde{\boldsymbol{a}}\in\mathcal{W}_{\widetilde{a}}} \Bigg\{ \int_{\mathcal{D}} \begin{bmatrix} \mathrm{Grad}\,\mathfrak{v}^* \\ \mathrm{Curl}\,\mathfrak{a}^* \end{bmatrix} \cdot \begin{bmatrix} \partial^2_{\boldsymbol{FF}}\psi & \partial^2_{\boldsymbol{F}\mathbb{D}}\psi \\ \partial^2_{\mathbb{D}\boldsymbol{F}}\psi & \partial^2_{\mathbb{D}\mathbb{D}}\psi \end{bmatrix} \cdot \begin{bmatrix} \mathrm{Grad}\,\mathfrak{v} \\ \mathrm{Curl}\,\mathfrak{a} \end{bmatrix} \mathrm{d}V \\ \Big/ \int_{\mathcal{D}} \begin{bmatrix} \mathrm{Grad}\,\mathfrak{v}^* \\ \mathrm{Curl}\,\mathfrak{a}^* \end{bmatrix} \cdot \begin{bmatrix} \mathrm{Grad}\,\mathfrak{v} \\ \mathrm{Curl}\,\mathfrak{a} \end{bmatrix} \mathrm{d}V \Bigg\} \Bigg\}\,, \end{aligned} \tag{3.62}$$

where $(\cdot)^*$ denotes the complex conjugate of $(\cdot)$.

Based on this formulation a global instability mode at macroscale, which implies that the wavelength of buckling is much larger than the size of the unit cell, can be detected as the limit case of (3.62). The long-wavelength instability modes based on Bloch-Floquet wave analysis can be given as

$$\hat{\Lambda}_0 = \liminf_{\boldsymbol{k}\to\boldsymbol{0}} \left\{ \inf_{\widetilde{\boldsymbol{\varphi}}\in\mathcal{W}_{\widetilde{\varphi}}} \inf_{\widetilde{\boldsymbol{a}}\in\mathcal{W}_{\widetilde{a}}} \left\{ \int_{\mathcal{D}} \nabla\mathbf{v}^* \cdot \partial^2_{\mathsf{FF}}\psi \cdot \nabla\mathbf{v}\ \mathrm{d}V \Big/ \int_{\mathcal{D}} \nabla\mathbf{v}^* \cdot\ \nabla\mathbf{v}\ \mathrm{d}V \right\} \right\}, \tag{3.63}$$

where $\nabla\mathbf{v} := [\mathrm{Grad}\,\mathfrak{v},\ \mathrm{Curl}\,\mathfrak{a}]^T$ is considered for compactness. Please note that instabilities $\boldsymbol{k} \to \boldsymbol{0}$ can also be analyzed with much less effort by checking the loss of strong ellipticity of homogenized tangent moduli [88, 21, 9]. Additionally, such instabilities should be differentiated from the ones with $\boldsymbol{k} = \boldsymbol{0}$ at the origin of the Bloch vector space. The latter correspond to the unit cell periodic microscopic instabilities, see [21, 9].

3.3.3 Description of reciprocal space of a unit cell

The Bloch vector $\boldsymbol{k}$ for two-dimensional problems is defined in reciprocal space spanned by $\boldsymbol{B}_1$ and $\boldsymbol{B}_2$ (see, e.g., Kittel [32])

$$\boldsymbol{k} = k_1\boldsymbol{B}_1 + k_2\boldsymbol{B}_2 \tag{3.64}$$

with the following definitions of basis vectors

$$\boldsymbol{B}_1 = 2\pi \boldsymbol{L}_2 \times \boldsymbol{L}^{\blacktriangle} \quad \text{and} \quad \boldsymbol{B}_2 = 2\pi \boldsymbol{L}^{\blacktriangle} \times \boldsymbol{L}_1 \,, \tag{3.65}$$

where $\boldsymbol{L}^{\blacktriangle} := \boldsymbol{L}_1 \times \boldsymbol{L}_2 / ||\boldsymbol{L}_1 \times \boldsymbol{L}_2||^2$. The basis vectors $\boldsymbol{B}_1$ and $\boldsymbol{B}_2$ of the reciprocal unit cell satisfy $\boldsymbol{L}_i \cdot \boldsymbol{B}_j = 2\pi\delta_{ij}$ with Kronecker delta δ_{ij}. $\boldsymbol{L}_1$ and $\boldsymbol{L}_2$ are the bases of the unit cell, see Fig. 3.3. The above definition of the basis vectors yield normalized Bloch vector components with respect to 2π. Consequently, the Bloch vector components are defined in the domain $0 \leq k_i < 1,\ i = 1, 2$.

The perturbations $\mathfrak{v}$ and $\mathfrak{a}$ are considered to be periodic with periodicity of the microstructure. This can be expressed as follows

$$\mathfrak{v}(\boldsymbol{X} + \boldsymbol{R}) = \mathfrak{v}(\boldsymbol{X}) \quad \text{and} \quad \mathfrak{a}(\boldsymbol{X} + \boldsymbol{R}) = \mathfrak{a}(\boldsymbol{X}) \,, \tag{3.66}$$

where, $\boldsymbol{R} = n_1\boldsymbol{L}_1 + n_2\boldsymbol{L}_2$ is the lattice vector, and $\boldsymbol{X} \in \mathcal{D}$ are the coordinates of the unit cell.

Considering (3.61), the following expressions are obtained for $\mathfrak{v}(\boldsymbol{X}+\boldsymbol{R})$ and $\mathfrak{a}(\boldsymbol{X}+\boldsymbol{R})$

$$\mathfrak{v}(\boldsymbol{X} + \boldsymbol{R}) = \mathfrak{v}(\boldsymbol{X}) \exp[\mathrm{i}\boldsymbol{k} \cdot \boldsymbol{R}] \quad \text{and} \quad \mathfrak{a}(\boldsymbol{X} + \boldsymbol{R}) = \mathfrak{a}(\boldsymbol{X}) \exp[\mathrm{i}\boldsymbol{k} \cdot \boldsymbol{R}] \,. \tag{3.67}$$

Thus, taking (3.66) into account yields the following condition

$$\boxed{\exp[\mathrm{i}\boldsymbol{k} \cdot \boldsymbol{R}] = 1} \,. \tag{3.68}$$

At an instability point the periodicity of a microstructure may change and a new periodicity can be defined from the above condition as $n_1 = 1/k_1$ and $n_2 = 1/k_2$ in $\boldsymbol{L}_1$ and $\boldsymbol{L}_2$ directions, respectively, as discussed in [8, 7].

3.3.4 Numerical implementation of Bloch-Floquet wave analysis

The numerical implementation is carried out by considering a finite element discretization of the unit cell. The coercivity constant describing the microscopic instability point, as defined in (3.62), can be expressed in two dimensions as

$$\hat{\Lambda}_{\boldsymbol{n}\mathcal{D}} = \inf_{\boldsymbol{k}} \left\{ \inf_{\widetilde{\boldsymbol{\varphi}} \in \mathcal{W}_{\widetilde{\boldsymbol{\varphi}}}} \inf_{\widetilde{\boldsymbol{a}} \in \mathcal{W}_{\widetilde{\boldsymbol{a}}}} \left[a(\gamma, \mathsf{v}) / ||\mathsf{v}||^2_{\mathcal{D}} \right] \right\} \tag{3.69}$$

with the following definitions, cf. (3.62)

$$\begin{aligned} a(\overline{\gamma}, \mathsf{v}) &= \int_{\mathcal{D}} \nabla \mathsf{v}^* \cdot \partial^2_{\mathsf{FF}} \psi(\overline{\boldsymbol{F}} + \nabla\widetilde{\boldsymbol{\varphi}}, \overline{\mathbb{D}} + \operatorname{Curl} \widetilde{\boldsymbol{a}}; \boldsymbol{X}) \cdot \nabla \mathsf{v} \, \mathrm{d}V \\ ||\mathsf{v}||^2_{\mathcal{D}} &= \int_{\mathcal{D}} \nabla \mathsf{v}^* \cdot \nabla \mathsf{v} \, \mathrm{d}V \,, \end{aligned} \tag{3.70}$$

where $\nabla \mathsf{v} := [\operatorname{Grad} \mathfrak{v},\ \operatorname{Curl} \mathfrak{a}]^T$ and $\mathsf{F} := [\boldsymbol{F},\ \mathbb{D}]^T$ are considered. The bilinear form $a(\gamma, \mathsf{v})$ depends on the perturbations v of the unit cell and the macroscopic load parameter γ, which characterizes electro-mechanical loading. An infimum over $\boldsymbol{k}$ requires to

investigate instabilities over the chosen grid of Bloch vector components. Thus, an instability may occur at the critical values of γ_c when $\hat{\Lambda}_{\boldsymbol{n}\mathcal{D}} = 0$ is satisfied. Moreover, $\hat{\Lambda}_{\boldsymbol{n}\mathcal{D}} > 0$ for the loading cases $\gamma < \gamma_c$.

The instability point $\hat{\Lambda}_{\boldsymbol{n}\mathcal{D}} = 0$ in the context of the finite element method is reached when the minimum eigenvalue of the bilinear form $a(\gamma, \mathbf{v})$ vanishes. In $(3.70)_1$, the complex eigenmodes are considered. For convenient numerical implementation, the complex degrees of freedom can be split into real and imaginary parts. Considering $\nabla\mathbf{v} = \nabla\mathbf{v}^{re} + \mathrm{i}\nabla\mathbf{v}^{im}$ and $\nabla\mathbf{v}^{*} = \nabla\mathbf{v}^{re} - \mathrm{i}\nabla\mathbf{v}^{im}$ leading to the real and imaginary split of bilinear form as follows

$$\begin{aligned} a^{re}(\overline{\gamma}, \mathbf{v}^{re}) &:= \int_{\mathcal{D}} \nabla\mathbf{v}^{re} \cdot \partial^2_{\mathbf{FF}}\psi(\overline{\boldsymbol{F}} + \operatorname{Grad}\widetilde{\boldsymbol{\varphi}}, \overline{\mathbb{D}} + \operatorname{Curl}\widetilde{\boldsymbol{a}}; \boldsymbol{X}) \cdot \nabla\mathbf{v}^{re}\, \mathrm{d}V \\ a^{im}(\overline{\gamma}, \mathbf{v}^{im}) &:= \int_{\mathcal{D}} \nabla\mathbf{v}^{im} \cdot \partial^2_{\mathbf{FF}}\psi(\overline{\boldsymbol{F}} + \operatorname{Grad}\widetilde{\boldsymbol{\varphi}}, \overline{\mathbb{D}} + \operatorname{Curl}\widetilde{\boldsymbol{a}}; \boldsymbol{X}) \cdot \nabla\mathbf{v}^{im}\, \mathrm{d}V\,. \end{aligned} \tag{3.71}$$

The latter expressions in the context of the finite element implementation can be written in the following compact form

$$a^h(\overline{\gamma}, \mathbf{d}) = \begin{bmatrix} \mathbf{d}^{re} \\ \mathbf{d}^{im} \end{bmatrix}^T \begin{bmatrix} \mathbf{K} & \boldsymbol{0} \\ \boldsymbol{0} & \mathbf{K} \end{bmatrix} \begin{bmatrix} \mathbf{d}^{re} \\ \mathbf{d}^{im} \end{bmatrix}, \tag{3.72}$$

where $\mathbf{d}^{(\cdot)} := [\mathbf{d}^{(\cdot)}_{AB},\ \mathbf{d}^{(\cdot)}_{AD},\ \mathbf{d}^{(\cdot)}_{A},\ \mathbf{d}^{(\cdot)}_{DC},\ \mathbf{d}^{(\cdot)}_{BC},\ \mathbf{d}^{(\cdot)}_{B},\ \mathbf{d}^{(\cdot)}_{C},\ \mathbf{d}^{(\cdot)}_{D},\ \mathbf{d}^{(\cdot)}_{i}]^T$ are the nodal degrees of freedom (DOFs) and $\mathbf{K}$ is the stiffness matrix of the unit cell, which is given by (3.34). For two-dimensional problems three degrees of freedom per node, i.e., two displacements and one component of electric vector potential are considered. $\mathbf{d}^{(\cdot)}_{AB}$ are DOFs on the boundary AB without containing DOFs at nodes A and B. Likewise $\mathbf{d}^{(\cdot)}_{AD}$, $\mathbf{d}^{(\cdot)}_{DC}$, $\mathbf{d}^{(\cdot)}_{BC}$ are defined on the unit cell boundaries. $\mathbf{d}^{(\cdot)}_{A}$, $\mathbf{d}^{(\cdot)}_{B}$, $\mathbf{d}^{(\cdot)}_{C}$, $\mathbf{d}^{(\cdot)}_{D}$, are the DOFs at the corner nodes of the unit cell, see Fig. 3.3. $\mathbf{d}_i$ denotes the internal DOFs. The real and imaginary parts of the bilinear forms are coupled considering the so-called Bloch-Floquet periodic boundary conditions (3.67). However, before describing the Bloch-Floquet analysis, (3.72) can be further simplified by statically condensing the internal DOFs from algebraic system of equations, see [89]. This allow to improve computational efficiency of the subsequent eigenvalue analysis. Prior to condensation, the stiffness matrix can be expressed as

$$\mathbf{K}(\overline{\gamma}) = \begin{bmatrix} \mathbf{K}_{aa} & \mathbf{K}_{ai} \\ \mathbf{K}_{ia} & \mathbf{K}_{ii} \end{bmatrix}, \tag{3.73}$$

where the subscript 'i' is related to internal DOFs $\mathbf{d}_i$ and the subscript 'a' contains all DOFs other than the internal ones. Applying static condensation yields

$$\mathbf{K}^{\blacktriangledown}(\overline{\gamma}) = \mathbf{K}_{aa} - \mathbf{K}_{ai}\mathbf{K}_{ii}^{-1}\mathbf{K}_{ia}\,. \tag{3.74}$$

Taking (3.74) in (3.72) into account, we obtain

$$a^h(\overline{\gamma}, \mathbf{d}^{\blacktriangledown}) = \begin{bmatrix} \mathbf{d}^{\blacktriangledown re} \\ \mathbf{d}^{\blacktriangledown im} \end{bmatrix}^T \begin{bmatrix} \mathbf{K}^{\blacktriangledown} & \boldsymbol{0} \\ \boldsymbol{0} & \mathbf{K}^{\blacktriangledown} \end{bmatrix} \begin{bmatrix} \mathbf{d}^{\blacktriangledown re} \\ \mathbf{d}^{\blacktriangledown im} \end{bmatrix}, \tag{3.75}$$

where $\mathbf{d}^{\blacktriangledown(\cdot)} := [\mathbf{d}^{(\cdot)}_{AB},\ \mathbf{d}^{(\cdot)}_{AD},\ \mathbf{d}^{(\cdot)}_{A}, \mathbf{d}^{(\cdot)}_{DC},\ \mathbf{d}^{(\cdot)}_{BC},\ \mathbf{d}^{(\cdot)}_{B},\ \mathbf{d}^{(\cdot)}_{C}, \mathbf{d}^{(\cdot)}_{D}]^T$ are DOFs without internal DOFs $\mathbf{d}_i$.

Exploiting the Bloch-Floquet wave analysis (3.67), the following relationship between the opposite boundaries can be written

$$\begin{aligned}
\mathbf{d}_{BC} &= \mathbf{d}_{AD}\exp[\mathrm{i}2\pi k_1] \\
\mathbf{d}_{DC} &= \mathbf{d}_{AB}\exp[\mathrm{i}2\pi k_2] \\
\mathbf{d}_{B} &= \mathbf{d}_{A}\exp[\mathrm{i}2\pi k_1] \\
\mathbf{d}_{C} &= \mathbf{d}_{A}\exp[\mathrm{i}2\pi k_1]\exp[\mathrm{i}2\pi k_2] \\
\mathbf{d}_{D} &= \mathbf{d}_{A}\exp[\mathrm{i}2\pi k_2]\,.
\end{aligned} \tag{3.76}$$

The Bloch-Floquet periodicity condition for the bilinear form, which is split into real and imaginary parts in the context of the finite element discretization, can be reformulated considering the following relationship between the opposite boundaries. It is considered that $\mathbf{d} = \mathbf{d}^{re} + \mathrm{i}\mathbf{d}^{im}$ together with $\exp[\mathrm{i}\boldsymbol{k}\cdot[\![\boldsymbol{X}]\!]] = \cos[\boldsymbol{k}\cdot[\![\boldsymbol{X}]\!]] + \mathrm{i}\sin[\boldsymbol{k}\cdot[\![\boldsymbol{X}]\!]]$ yields (see also [62, 8])

$$\begin{aligned}
\mathbf{d}^{re}(\boldsymbol{X}+[\![\boldsymbol{X}]\!]) &= \mathbf{d}^{re}(\boldsymbol{X})\cos[\boldsymbol{k}\cdot[\![\boldsymbol{X}]\!]] - \mathbf{d}^{im}(\boldsymbol{X})\sin[\boldsymbol{k}\cdot[\![\boldsymbol{X}]\!]] \\
\mathbf{d}^{im}(\boldsymbol{X}+[\![\boldsymbol{X}]\!]) &= \mathbf{d}^{re}(\boldsymbol{X})\sin[\boldsymbol{k}\cdot[\![\boldsymbol{X}]\!]] + \mathbf{d}^{im}(\boldsymbol{X})\cos[\boldsymbol{k}\cdot[\![\boldsymbol{X}]\!]]\,.
\end{aligned} \tag{3.77}$$

Considering (3.77) and (3.76) in (3.75) gives

$$a^h(\overline{\gamma}, \mathbf{d}) = \mathbf{d}_{red}^T \mathfrak{K} \mathbf{d}_{red}\,, \tag{3.78}$$

where

$$\boxed{\mathfrak{K}(\overline{\gamma},\ k_1,\ k_2) = \boldsymbol{Q}^T(k_1,\ k_2)\begin{bmatrix}\mathbf{K}^{\blacktriangledown}(\overline{\gamma}) & \boldsymbol{0} \\ \boldsymbol{0} & \mathbf{K}^{\blacktriangledown}(\overline{\gamma})\end{bmatrix}\boldsymbol{Q}(k_1,\ k_2)} \tag{3.79}$$

is a Hermitian matrix which has real eigenvalues and depends on the macroscopic loading parameter and components of the Bloch vector. It is obtained after condensing the periodic DOFs with $\boldsymbol{Q}$. $\boldsymbol{Q}(k_1,\ k_2)$ can be described by

$$\mathbf{d}^{\blacktriangledown} = \begin{bmatrix}\mathbf{d}^{re}_{AB}\\ \mathbf{d}^{re}_{AD}\\ \mathbf{d}^{re}_{A}\\ \mathbf{d}^{re}_{DC}\\ \mathbf{d}^{re}_{BC}\\ \mathbf{d}^{re}_{B}\\ \mathbf{d}^{re}_{C}\\ \mathbf{d}^{re}_{D}\\ \mathbf{d}^{im}_{AB}\\ \mathbf{d}^{im}_{AD}\\ \mathbf{d}^{im}_{A}\\ \mathbf{d}^{im}_{DC}\\ \mathbf{d}^{im}_{BC}\\ \mathbf{d}^{im}_{B}\\ \mathbf{d}^{im}_{C}\\ \mathbf{d}^{im}_{D}\end{bmatrix} = \begin{bmatrix}\underline{\boldsymbol{1}} & \boldsymbol{0} & \boldsymbol{0} & \boldsymbol{0} & \boldsymbol{0} & \boldsymbol{0}\\ \boldsymbol{0} & \underline{\boldsymbol{1}} & \boldsymbol{0} & \boldsymbol{0} & \boldsymbol{0} & \boldsymbol{0}\\ \boldsymbol{0} & \boldsymbol{0} & \underline{\boldsymbol{1}} & \boldsymbol{0} & \boldsymbol{0} & \boldsymbol{0}\\ \underline{\boldsymbol{c}}_2 & \boldsymbol{0} & \boldsymbol{0} & -\underline{\boldsymbol{s}}_2 & \boldsymbol{0} & \boldsymbol{0}\\ \boldsymbol{0} & \underline{\boldsymbol{c}}_1 & \boldsymbol{0} & \boldsymbol{0} & -\underline{\boldsymbol{s}}_1 & \boldsymbol{0}\\ \boldsymbol{0} & \boldsymbol{0} & \underline{\boldsymbol{c}}_1 & \boldsymbol{0} & \boldsymbol{0} & -\underline{\boldsymbol{s}}_1\\ \boldsymbol{0} & \boldsymbol{0} & \underline{\boldsymbol{c}}_{12} & \boldsymbol{0} & \boldsymbol{0} & -\underline{\boldsymbol{s}}_{12}\\ \boldsymbol{0} & \boldsymbol{0} & \underline{\boldsymbol{c}}_2 & \boldsymbol{0} & \boldsymbol{0} & -\underline{\boldsymbol{s}}_2\\ \boldsymbol{0} & \boldsymbol{0} & \boldsymbol{0} & \underline{\boldsymbol{1}} & \boldsymbol{0} & \boldsymbol{0}\\ \boldsymbol{0} & \boldsymbol{0} & \boldsymbol{0} & \boldsymbol{0} & \underline{\boldsymbol{1}} & \boldsymbol{0}\\ \boldsymbol{0} & \boldsymbol{0} & \boldsymbol{0} & \boldsymbol{0} & \boldsymbol{0} & \underline{\boldsymbol{1}}\\ \underline{\boldsymbol{s}}_2 & \boldsymbol{0} & \boldsymbol{0} & \underline{\boldsymbol{c}}_2 & \boldsymbol{0} & \boldsymbol{0}\\ \boldsymbol{0} & \underline{\boldsymbol{s}}_1 & \boldsymbol{0} & \boldsymbol{0} & \underline{\boldsymbol{c}}_1 & \boldsymbol{0}\\ \boldsymbol{0} & \boldsymbol{0} & \underline{\boldsymbol{s}}_1 & \boldsymbol{0} & \boldsymbol{0} & \underline{\boldsymbol{c}}_1\\ \boldsymbol{0} & \boldsymbol{0} & \underline{\boldsymbol{s}}_{12} & \boldsymbol{0} & \boldsymbol{0} & \underline{\boldsymbol{c}}_{12}\\ \boldsymbol{0} & \boldsymbol{0} & \underline{\boldsymbol{s}}_2 & \boldsymbol{0} & \boldsymbol{0} & \underline{\boldsymbol{c}}_2\end{bmatrix}\begin{bmatrix}\mathbf{d}^{re}_{AB}\\ \mathbf{d}^{re}_{AD}\\ \mathbf{d}^{re}_{A}\\ \mathbf{d}^{im}_{AB}\\ \mathbf{d}^{im}_{AD}\\ \mathbf{d}^{im}_{A}\end{bmatrix} = \boldsymbol{Q}\mathbf{d}_{red}\,, \tag{3.80}$$

where $\underline{\boldsymbol{c}}_i$ and $\underline{\boldsymbol{s}}_i$ are the notations for the diagonal matrices having entries $\cos[\mathrm{i}2\pi k_i]$ and $\sin[\mathrm{i}2\pi k_i]$, respectively. Likewise $\underline{\boldsymbol{c}}_{12}$ and $\underline{\boldsymbol{s}}_{12}$ are diagonal matrices with entries $\cos[\mathrm{i}2\pi(k_1+k_2)]$ and $\sin[\mathrm{i}2\pi(k_1+k_2)]$, respectively. $\underline{\boldsymbol{1}}$ is the identity matrix. The sizes of these matrices are defined according to the respective DOFs to which they are related.

Consequently, the loss of positive definiteness of $\mathfrak{K}$ determines the critical loading points and critical Bloch vector components. The latter could be further exploited to define the new periodicity of the microstructure. To investigate instability points when $k_1 = 0$ and $k_2 = 0$, all three DOFs of $\mathbf{d}_A$ are constrained against rigid-body motions.

Microscopic bifurcation modes are obtained by considering the instability analysis in enlarged RVEs. The mesh of the RVE is perturbed by eigenvectors $\mathbf{d}^\star$ of a critical point

$$\boldsymbol{X} \Leftarrow \boldsymbol{X} + \tau \frac{\mathbf{d}^\star}{\|\mathbf{d}^\star\|}\,, \tag{3.81}$$

where $\boldsymbol{X}$ denotes the undeformed coordinates of the RVE, $\mathbf{d}^\star$ is the total eigenvector of the critical mode and τ is a scaling factor.

3.3.5 Relations between microscopic and macroscopic instability phenomena

Above, three coercivity constants describing macroscopic and microscopic instability phenomena are introduced. The following relationship between these coercivity constants is assumed to hold [88, 21, 47]

$$\boxed{\hat{\Lambda}_{\boldsymbol{n}\mathcal{D}} \leq \hat{\Lambda}_0 \leq \overline{\Lambda}\,.} \tag{3.82}$$

As discussed above $\hat{\Lambda}_0$ and $\overline{\Lambda}$ are vanishing at the same time, meaning that a long-wavelength microscopic instability leads to the loss of strong ellipticity of the homogenized moduli [21]. In other cases, microscopic instabilities are assumed to be constrained by macroscopic instabilities.

3.4 Representative Numerical Examples

The numerical examples consider periodic elastomeric composites with embedded circular as well as elliptical fibers under macroscopic electro-mechanical loading conditions in two dimensions. Plane-strain deformation of microstructures are in focus. Depending on the volume fractions $f_0 = \{0.1,\ \pi/16,\ 0.3\}$ and aspect ratios $\omega = \{1/3,\ 1/2,\ 1,\ 2/1,\ 3/1\}$ of the fibers, the first occurrence of microscopic and macroscopic instabilities are determined. The influence of orientations of the elliptical fibers is considered placing their major axis parallel and perpendicular to the electric loading direction. At a microscopic instability point a change of critical periodicity might be expected. In the given examples, new critical periodicities and bifurcation modes at selected deformations are shown. The macroscopic stability analysis is based on the loss of strong ellipticity of the homogenized moduli at a certain deformation. The Bloch-Floquet wave analysis is used to define the microscopic instabilities. Interactions of the microscopic and macroscopic instabilities are demonstrated.

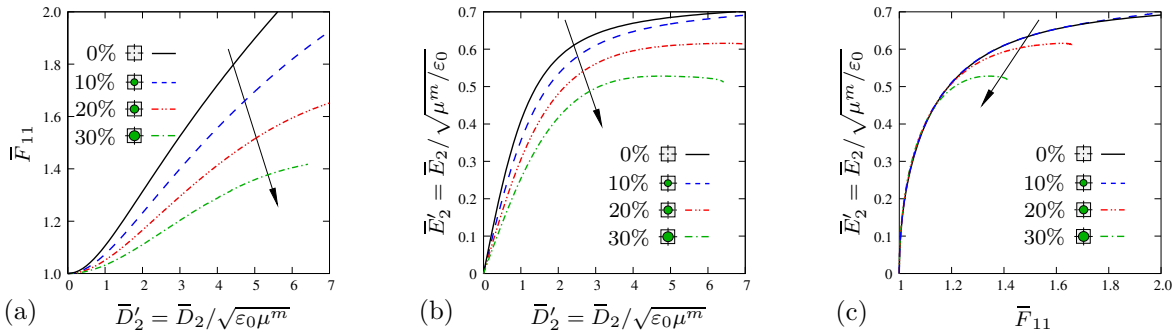

Figure 3.4: *Influence of volume fractions of fibers on the electro-mechanical response of microstructures.* The microstructures are loaded with a vertical electric displacement $\overline{D}'_2$. The resulting macroscopic mechanical deformations are determined from macroscopic equilibrium. The circular fibers have volume fractions $f_0 = \{0,\ 0.1,\ \pi/16,\ 0.3\}$. The plots demonstrate: (**a**) induced macroscopic deformation $\overline{F}_{11}$ depending on $\overline{D}'_2$; (**b**) induced macroscopic electric field $\overline{E}'_2$ as a function of $\overline{D}'_2$; and (**c**) the macroscopic electric field $\overline{E}'_2$ as a function of $\overline{F}_{11}$.

3.4.1 Microscopic constitutive law

We consider the isochoric mechanical energy to be governed by a polyconvex Gent material model [20], while the electric contribution is taken into account in the free-energy function by adding a convex term in the electric displacement $\mathbb{D}$. The volumetric energy $U(\theta)$ has a simple quadratic structure, and the energies for two-dimensional problems are chosen as

$$\begin{aligned} U^m(\theta) &= \frac{\kappa}{2}(\theta-1)^2, \\ \psi^{m,iso}(\boldsymbol{F}^{iso}) &= -\frac{\mu\xi}{2}\ln\left[1-\frac{||\boldsymbol{F}||^2/J-2}{\xi}\right], \\ \psi^e(\boldsymbol{F},\mathbb{D}) &= \frac{1}{2\epsilon_0(J+\chi)}\boldsymbol{C}:(\mathbb{D}\otimes\mathbb{D}) = \frac{J}{2\hat{\epsilon}}||d||^2\,, \end{aligned} \tag{3.83}$$

where θ is the dilatation and κ is the bulk modulus. The isochoric deformation gradient is defined as $\boldsymbol{F}^{iso} = J^{-\frac{1}{2}}\boldsymbol{F}$ in two dimensions. The material parameter ξ is associated with the strain saturation of the microstructure. The second-order tensor $\boldsymbol{C} = \boldsymbol{F}^T\boldsymbol{g}\boldsymbol{F}$ denotes the right Cauchy-Green deformation tensor, $d = J^{-1}\boldsymbol{F}\mathbb{D}$ in $(3.83)_3$ denotes the current electric displacement, $\epsilon_0 = 8.854$ N/MV^2 is the electric permittivity of vacuum and χ is the electric susceptibility in the undeformed configuration. The electric permittivity of the material is defined by $\hat{\epsilon} = \epsilon_0\hat{\epsilon}_r$ with the relative electric permittivity $\hat{\epsilon}_r = \epsilon_0(1+\hat{\chi})$. Based on $(3.83)_3$, we assume a deformation-dependent electric susceptibility $\hat{\chi} = \chi/J$ of the material, see, e.g., McMeeking and Landis [45].

In the following numerical examples, a finite-element formulation with linear interpolations of displacement and electric vector potential fields as well as piecewise constant approximations of pressure and dilatation fields are considered. Due to apparent similarities to the B-bar method, the resulting finite element is denoted as $\overline{B}Q1P0$. For a brief discussion of the numerical stability of the chosen element formulation please refer to Appendix A.

Table 3.1: Material and loading parameters

No.	Parameter	Name	Value
1.	$\Delta\overline{\gamma}$	Macroscopic load increment	$2 \cdot 10^{-3}$
2.	$\Delta\phi$	Path angle increment	1°
3.	κ/μ	Bulk modulus relative to shear modulus	100
4.	μ^f/μ^m	Relative shear modulus of fibers	100
5.	χ^f/χ^m	Relative electric susceptibility of fibers	100
6.	ξ	Strain saturation parameter	100

3.4.2 Electro-mechanical response of microstructures

Before considering instability analysis, the responses of microstructures are demonstrated. Thereby, unit-square RVEs with embedded circular fibers are examined. The macroscopic loading condition

$$\overline{\mathbb{D}}'_2 = \begin{bmatrix} 0 \\ \overline{D}'_2 \end{bmatrix} \tag{3.84}$$

is given in terms of the normalized electric displacement $\overline{\mathbb{D}}' = \overline{\mathbb{D}}/\sqrt{\epsilon_0 \mu^m}$. Here, μ^m is the shear modulus of the elastomeric matrix. The RVE comprises two constituents given by a soft elastomeric matrix and a stiff fiber that points out of plane. Since the longer axis of the fibers is considered to be along the thickness direction, the RVEs are assumed to satisfy the plane-strain deformation.

The response of the microstructures are plotted in Fig. 3.4 for different volume fractions $f_0 = \{0,\ 0.1,\ \pi/16,\ 0.3\}$ of the circular fibers. The shear modulus, the bulk modulus, the strain saturation parameter and the electric susceptibility are taken from Table 3.1. The microstructures are discretized with unstructured meshes (however, the symmetries are considered during meshing) of $\{6748,\ 6500,\ 6748,\ 6940\}$ finite elements according to the volume fractions of fibers $f_0 = \{0,\ 0.1,\ \pi/16,\ 0.3\}$, respectively (see Fig. 3.5 for a representative visualization of a mesh).

The plots in Fig. 3.4**a** and **b** describe the resulting macroscopic mechanical deformation $\overline{F}_{11}$ and normalized electric field $\overline{E}'_2 = \overline{E}_2/\sqrt{\mu^m/\epsilon_0}$ due to the prescribed electric displacement $\overline{D}'_2$. The Fig. 3.4**c** demonstrates the relationship between macroscopic electric field $\overline{E}'_2$ and mechanical stretch $\overline{F}_{11}$. Notice that for the low volume fractions of the fibers the electric field increases monotonically, and stiffening of elastomers is more pronounced. As the volume fraction of the fibers increases, the electric interactions between fibers becomes higher. Consequently, electric actuation is enhanced for composites with higher volume fractions of fibers.

3.4.3 Multiscale stability analysis of microstructures

In the following examples, we consider the influence of geometrical properties of the BVPs on macroscopic and microscopic instabilities under macroscopic loading conditions. The material parameters used in the following examples are motivated from earlier works on multiscale stability analysis [47, 22, 23, 15]. Their normalized values are listed in Table 3.1. In the table, $(\cdot)^f$ and $(\cdot)^m$ denote the fiber and matrix material parameters, respectively.

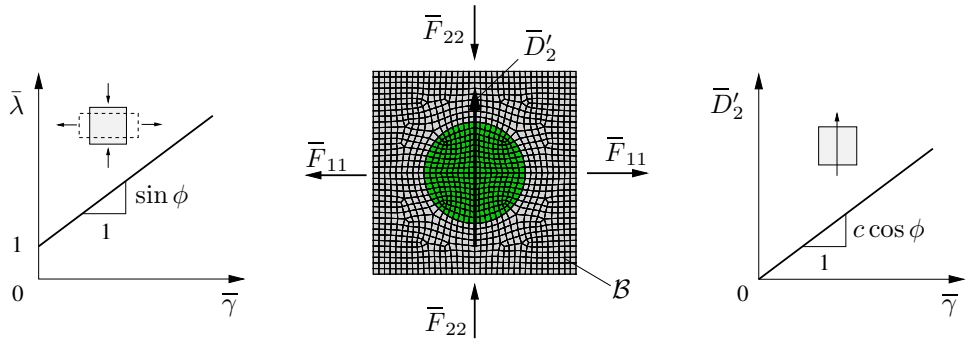

Figure 3.5: *Macroscopic loading of microstructure.* The RVE at the integration point $\overline{\boldsymbol{X}}$ of the macrostructure is under macroscopic isochoric mechanical deformation (i.e., $\det[\overline{\boldsymbol{F}}] = 1$) and electric displacement in vertical direction. Linear loading for the macro-stretch $\overline{\lambda}$ and non-zero component $\overline{D}'_2$ of the electric displacement depending on the loading parameter $\overline{\gamma}$ is considered.

The bulk modulus of the constituents has been chosen 100 times higher than the shear modulus which corresponds to a Poisson ratio $\nu = 0.495$ (for simulations involving a contrast in elastic properties of 1000 please refer to the Appendix A). A microscopic instability corresponds to the loss of positive definiteness of (3.79) at a critical macroscopic deformation state. This can be detected by checking the minimum eigenvalue of $\mathfrak{K}$ over a discrete Bloch vector grid. In the following examples the Bloch vector grid of 72×72 is considered for $0 \leq k_i < 1$. As a result of the symmetries of the condensed stiffness matrix $\mathfrak{K}$ in Bloch vector, the range of Bloch vector components can further be reduced to $0 \leq k_i \leq 0.5$, see Triantafyllidis and Schraad [90].

3.4.3.1 Macroscopic loading of microstructures

The microstructure is loaded by the macroscopic isochoric deformation gradient $\overline{\boldsymbol{F}}$ and electric displacement $\overline{\mathbb{D}}$

$$\overline{\boldsymbol{F}} = \begin{bmatrix} \overline{\lambda} & 0 \\ 0 & \overline{\lambda}^{-1} \end{bmatrix} \quad \text{and} \quad \overline{\mathbb{D}}' = \begin{bmatrix} 0 \\ \overline{D}'_2 \end{bmatrix} \tag{3.85}$$

where $\overline{\lambda} = 1 + \overline{\boldsymbol{\gamma}} \sin\phi$ and $\overline{D}'_2 = c\overline{\boldsymbol{\gamma}} \cos\phi$ have been selected. $\overline{D}'_2 = \overline{D}_2/\sqrt{\epsilon_0 \mu^m}$ is considered to be normalized with respect to the shear modulus μ^m of the elastomeric matrix of the RVE and the electric permittivity ϵ_0 of vacuum. $\overline{\boldsymbol{\gamma}}$ can be understood as pseudo-time to load the microstructure incrementally, see Fig. 3.5. We consider that $\overline{\boldsymbol{\gamma}}$ characterizes both the mechanical and electric loading. In what follows $c = 10$ and $\Delta\overline{\boldsymbol{\gamma}} = 2 \cdot 10^{-3}$ are considered. ϕ is a path angle which allows to determine the instability points at different combinations of the macroscopic stretch $\overline{\lambda}$ and electric displacement $\overline{D}'_2$. In the following, we have considered instability analyses for $\phi = [-90°, 90°]$ with an increment of $\Delta\phi = 1°$. Please note that a change in sign of the electric displacement vector has no influence on the results due to the chosen free-energy function. Therefore, instabilities for other values of $\phi = [90°, 180°]$ will coincide with instabilities in the chosen range. Please also note that the chosen macroscopic deformation state (3.85) implies that $\det[\overline{\boldsymbol{F}}] = 1$ (or, equivalently, $\operatorname{div} \overline{\boldsymbol{v}} = 0$). Thus, macroscopic incompressibility is fulfilled a priori and, consequently, the macroscopic loss of strong ellipticity can be determined with (3.52).

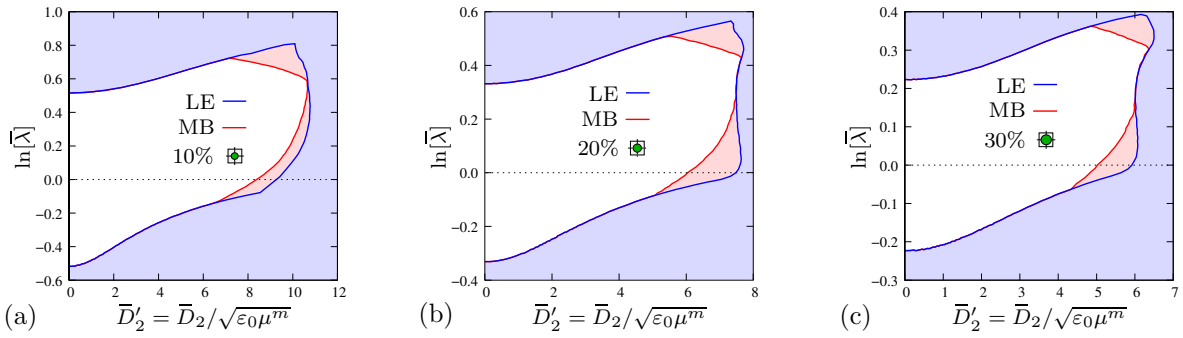

Figure 3.6: *Onset of instability surfaces for periodic microstructures with circular fibers with* $\omega = 1$. The volume fractions of the fibers in (**a**), (**b**) and (**c**) are $f_0 = \{0.1, \pi/16, 0.3\}$, respectively. The discretized microstructures have $\{19,983;\ 20,727;\ 20,820\}$ DOFs in plots (**a**), (**b**) and (**c**), respectively. LE denotes the onset of the macroscopic loss of strong ellipticity, while MB denotes the microscopic buckling points of the RVE. The colored regions in the plots correspond to the unstable loading ranges.

As discussed in Section 3.2.5 the microscopic DOFs are fluctuations of the deformation map and the electric vector potential. Zero fluctuation boundary conditions for all DOFs of the corner nodes of the RVE are applied to avoid rigid-body motions.

3.4.3.2 Stability analysis of microstructures with circular fibers

The first example considers multiscale stability analysis of unit-square RVEs with embedded circular fibers, i.e., with an aspect ratio $\omega = 1$. The plots in Fig. 3.6**a**, **b** and **c** correspond to the fiber volume fractions of $f_0 = \{0.1,\ \pi/16,\ 0.3\}$, respectively. The plots illustrate the first occurrence points of microscopic (red solid lines) and macroscopic

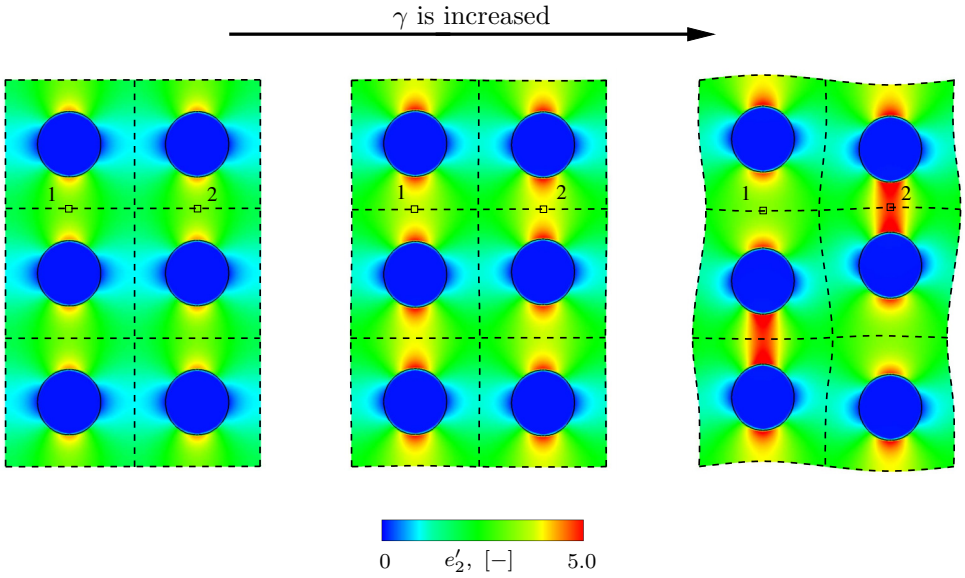

Figure 3.7: *Buckling mode of a microstructure with embedded circular fibers with* $\omega = 1$ *and volume fraction* $f_0 = \pi/16$. The buckling mode corresponds to $\phi = -1°$. The scaling factor $\tau = 1$ in (3.70) is taken. At the bifurcation point the critical periodicity of the microstrucutre alters and the enlarged RVE contains 2×3 unit-cells. The contour plots correspond to the distribution of vertical components e'_2 of the microscopic current electric field $e' = \boldsymbol{F}^{-T} E'$ in the RVE.

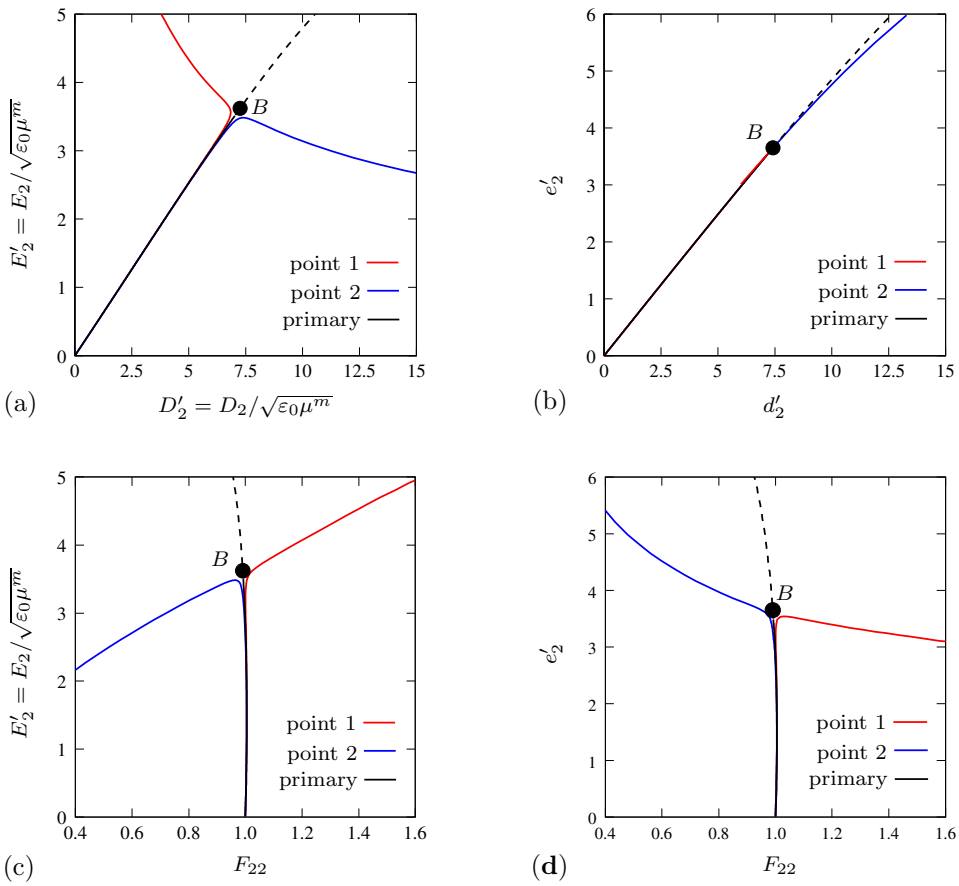

Figure 3.8: *Post-buckling response of the RVE containing* 2×3 *unit-cells.* The plots illustrate the post-buckling behaviors at points '1' and '2' of the enlarged RVE (see Fig. 3.7). 'B' corresponds to the bifurcation point.

(blue solid lines) instabilities in the macroscopic electric displacement $\overline{D}_2'$ and logarithmic stretch $\ln[\overline{\lambda}]$ depending on ϕ. As shown in the figure for all volume fractions in the absence of the electric loading along $\ln[\overline{\lambda}]$ axis ($\phi = -90°$ and $\phi = 90°$) no microscopic instabilities are observed. Furthermore, the macroscopic instability points for $\phi = -90°$ and $\phi = 90°$ occur symmetrically with respect to $\ln[\overline{\lambda}] = 0$ axis. This is due to the symmetric loading conditions and circular shape of the fiber cross sections. The same behavior has also been shown for stiff fibers under mechanical deformations in Michel et al. [47].

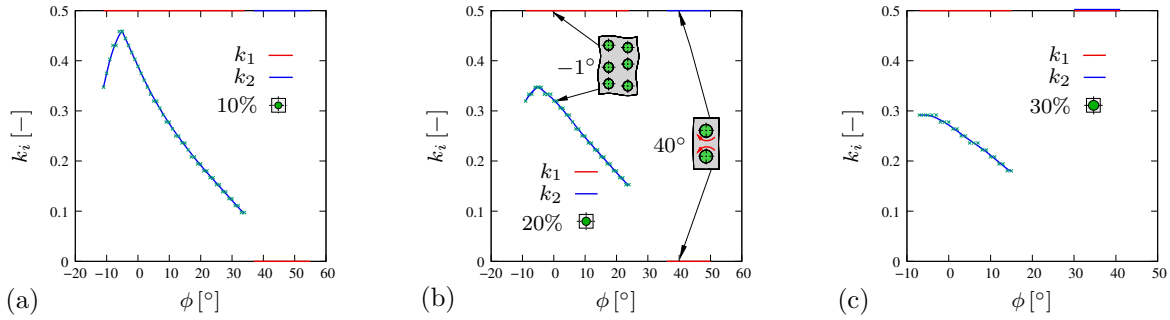

Figure 3.9: *Dimensionless Bloch vector components at microscopic instability points depending on the angle* ϕ *for circular fibers* $\omega = 1$. The plots (**a**), (**b**) and (**c**) correspond to the microstructures with volume fractions $f_0 = \{0.1, \pi/16, 0.3\}$, respectively.

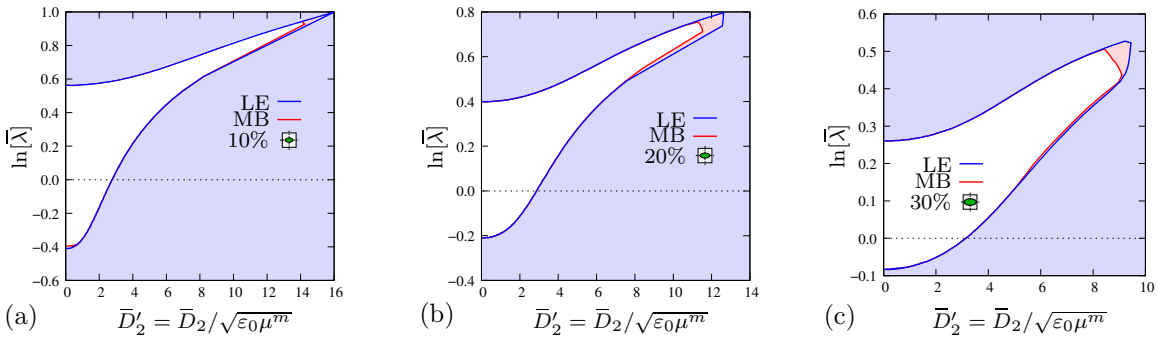

Figure 3.10: *Onset of instability surfaces for periodic microstructures with elliptical fibers with $\omega = 2/1$ (major axis in horizontal direction).* The volume fractions of the fibers in (**a**), (**b**) and (**c**) are $f_0 = \{0.1, \pi/16, 0.3\}$, respectively. The discretized microstructures have $\{19,260; 19,536; 21,063\}$ DOFs in plots (**a**), (**b**) and (**c**), respectively. LE denotes the onset of the macroscopic loss of strong ellipticity, while MB denotes the microscopic buckling points of the RVE. The colored regions in the plots correspond to the unstable loading ranges.

From the plots, it is clear that the macroscopic instabilities are the main instabilities under dominating mechanical deformation. This is in line with the numerical results of Triantafyllidis et al. [89]. When the macroscopic electric displacement $\overline{D}'_2$ is significantly large, the short-wavelength microscopic instabilities occur earlier. The microscopic instabilities in Fig. 3.6**a**, **b** and **c** correspond to $\phi = [-11°, 34°] \cup [37°, 55°]$, $\phi = [-9°, 24°] \cup [36°, 50°]$ and $\phi = [-7°, 15°] \cup [30°, 41°]$, respectively. We observe that as the mechanical deformation increases the microscopic instabilities changes from short-wavelength to long-wavelength instabilities. However, at higher coupled loading (stretching in horizontal direction is considered), the short-wavelength microscopic instabilities are detected once again. The two regions of short-wavelength instabilities in the plots are differentiated. The first region corresponds to $\phi = [-11°, 34°]$, $\phi = [-9°, 24°]$ and $\phi = [-7°, 15°]$ in Fig. 3.6**a**, **b** and **c**, respectively. In this region, the microscopic instabilities are observed due to the high electric interactions of the fibers, which further results in internal rearrangement in the electric field direction, see Fig. 3.7. The reason for this is that the macroscopic electric displacement $\overline{D}'_2$ triggers compression in the vertical direction and extension in the horizontal direction. However, the macroscopic uniform deformation $\overline{\lambda}$ of the RVE has been prescribed by (3.85), too. Therefore, at certain electric loading, buckling of the horizontal ligaments connecting two neighboring fibers occurs. This develops a new periodic pattern in which some fibers displace towards each

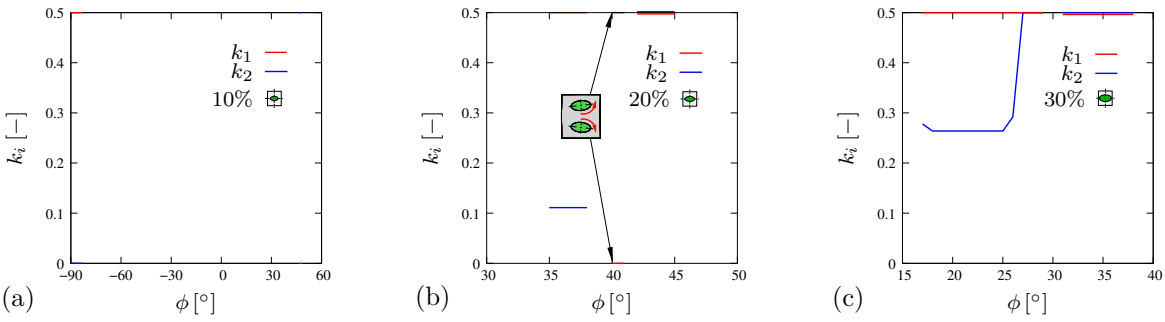

Figure 3.11: *Dimensionless Bloch vector components at microscopic instability points depending on angle ϕ for elliptical fibers with $\omega = 2/1$.* The plots (**a**), (**b**) and (**c**) corresponds to the microstructures with volume fractions $f_0 = \{0.1, \pi/16, 0.3\}$, respectively.

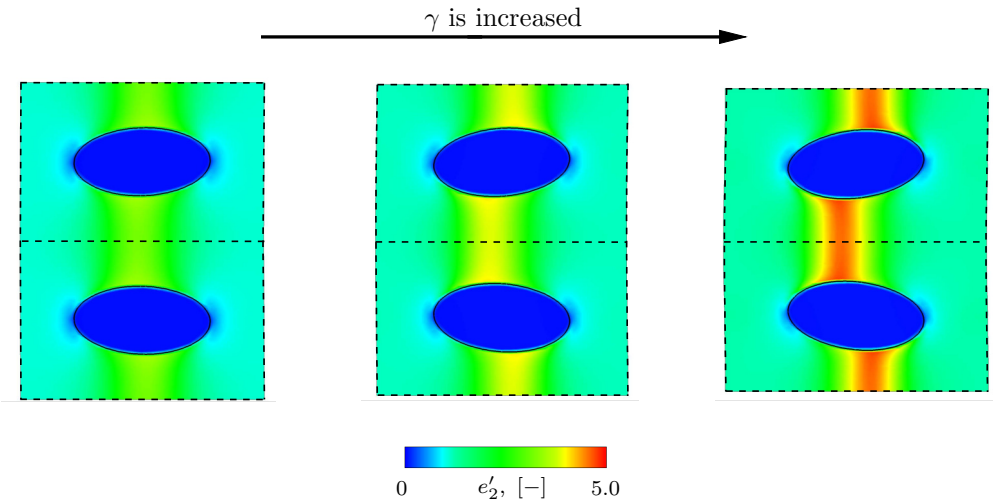

Figure 3.12: *Buckling mode of a microstructure with embedded elliptical fibers* $\omega = 2/1$ *with volume fraction* $f_0 = \pi/16$. The buckling mode corresponds to $\phi = 40°$. The scaling factor $\tau = 1$ in (3.70) is taken. At the bifurcation point the critical periodicity of the microstrucutre alters and the enlarged RVE contains 1×2 unit-cells. The contour plots correspond to the distribution of vertical components e_2' of the microscopic current electric field $\mathscr{e}' = \boldsymbol{F}^{-T}\mathbb{E}'$ in the RVE.

other while others displace apart. Consequently, the most favorable buckling mode is obtained. On the other hand, in the second region, which corresponds to the $\phi = [37°, 55°]$, $\phi = [36°, 50°]$ and $\phi = [30°, 41°]$ in Fig. 3.6**a**, **b** and **c**, respectively, as a result of the high macroscopic electromechanical loading, the buckling occurs due to *rotation* of the fibers. In these cases, the high compressive deformation and electric interaction of the fibers trigger the buckling of the vertical ligaments connecting the neighboring fibers. This buckling, in its turns, results in rotation of the fibers as well, see Fig. 3.9**b** for the sketch of the rotational buckling mode of an enlarged RVE made of 1×2 unit-cells.

In Fig. 3.7, a buckling mode for an enlarged RVE with circular fibers, presented. The plots describe the evolution of the buckling during deformation. The volume fraction of the fibers is $f_0 = \pi/16$. Obviously, at the instability point the periodicity of the

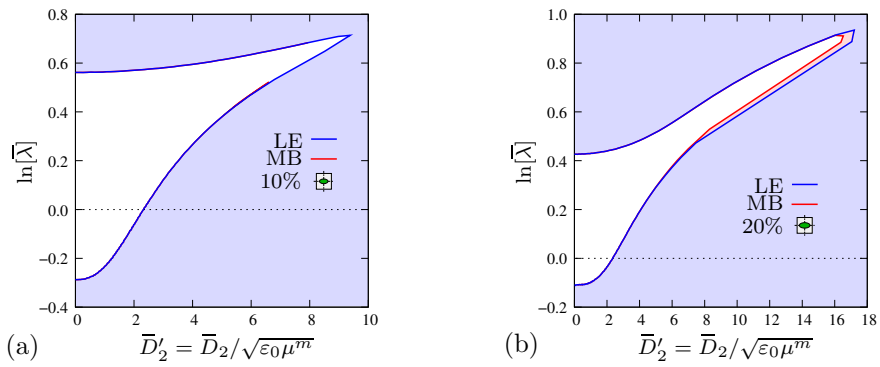

Figure 3.13: *Onset of instability surfaces for periodic microstructures with elliptical fibers with* $\omega = 3/1$ *(major axis in horizontal direction).* The volume fractions of the fibers in (**a**) and (**b**) are $f_0 = \{0.1, \pi/16\}$, respectively. The discretized microstructures have $\{20,052; 20,220\}$ DOFs in plots (**a**) and (**b**), respectively. LE denotes the onset of the macroscopic loss of strong ellipticity, while MB denotes the microscopic buckling points of the RVE. The colored regions in the plots correspond to the unstable loading ranges.

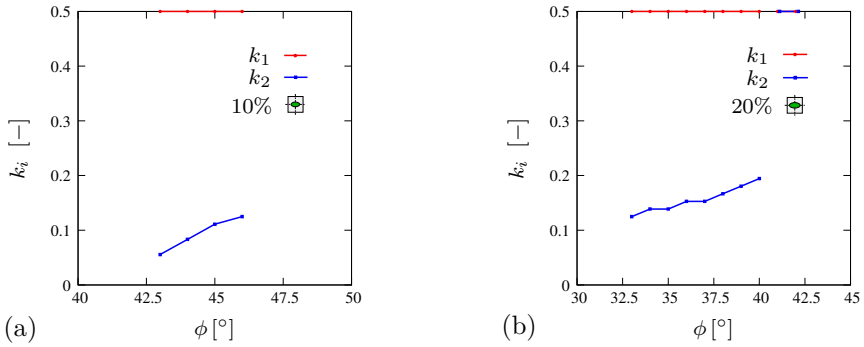

Figure 3.14: *Dimensionless Bloch vector components at microscopic instability points depending on the angle ϕ for elliptical fibers with $\omega = 3/1$.* The plots (**a**) and (**b**) correspond to the microstructures with volume fractions $f_0 = \{0.1, \pi/16\}$, respectively.

microstructure has changed. The new RVE according to the critical periodicity contains 2×3 unit-cells. The enlarged RVE has 122,667 DOFs. The bifurcation point is detected at the macroscopic electromechanical load $\overline{\lambda} \approx 0.99$ and $\overline{D}'_2 \approx 5.96$. The contour plot in the figure displays the distribution of the microscopic current electric field. Notice that, after buckling the electric field increases between attracting fibers, and the opposite effect is observed between repelling fibers. In Fig. 3.8 the local post-buckling behavior associated to two different points of the enlarged RVE in Fig. 3.7 is shown. The plots **a** and **b** describes the dependence of the vertical component of the electric field on the vertical component of the electric displacement in the reference and current configuration, respectively. Furthermore, the plot **c** and **d** illustrate the vertical component of the referential and current electric field versus the vertical microscopic stretch F_{22} at the chosen points of the microstructure, respectively. The current counterparts of the electric displacement $\mathbb{d}' = 1/J\boldsymbol{F}\mathbb{D}'$ and the electric field $\mathbb{e}' = \boldsymbol{F}^{-T}\mathbb{E}'$ are defined as the push-forwards of the referential ones $\mathbb{D}'$ and $\mathbb{E}'$, respectively. Moreover, the primary equilibrium path is also illustrated in the figure.

Please also notice that for higher volume fractions, the ranges of the microscopic instabilities in ϕ decrease, while macroscopic instabilities occur earlier at the same macroscopic deformations. The corresponding dimensionless Bloch vector components at microscopic instabilities depending on ϕ are plotted in Fig. 3.9**a**, **b** and **c**, respectively. In the figures, for some ranges of ϕ non-smooth values of the second component of the Bloch vectors are observed as indicated with green crosses. The non-smooth values are due to the fact that the Bloch vector components stay constant for some small changes of ϕ, which is in turn due to the chosen grid of the Bloch vector. In order to guide the eyes, the Bloch vector components are interpolated using smooth Bezier curves (shown with blue solid lines in the plots).

3.4.3.3 Stability analysis of microstructures with elliptical fibers

In Fig. 3.10 and 3.13, instability surfaces for the microstructures with embedded elliptical fibers are considered. The aspect ratios of ellipses are $\omega = 2/1$ and $\omega = 3/1$, respectively, where the major axis points in horizontal direction, i.e., oriented perpendicular to the electric loading. Fig. 3.10**a**, (b) and (c) present the microstructures with the volume fractions $f_0 = \{0.1, \pi/16, 0.3\}$ of fibers, respectively. Similarly, Fig. 3.13**a** and **b** illustrate

the microstructures with the volume fractions $f_0 = \{0.1, \pi/16\}$ of fibers, respectively. From both figures, it is observed that macroscopic instabilities at $\phi = -90°$ and $\phi = 90°$ are not symmetric, which is due to the differences in the major and minor axes of the ellipses. As expected the microstructure is more stable under macroscopic stretching parallel to the major axis of the ellipses ($\phi = 90°$) than compressing in this direction ($\phi = -90°$). In this example microscopic instabilities (red solid lines) occur only for larger coupled loading scenarios. Additionally, in Fig. 3.10**a** the microscopic instabilities are observed around $\phi = -90°$, which correspond to compression parallel to the major axes. However, for compression perpendicular to the major axes no microscopic instabilities are observed. The microscopic instabilities for $\omega = 2/1$ occur at $\phi = [-90°, -83°] \cup [47°, 48°]$, $\phi = [35°, 38°] \cup [40°, 45°]$ and $\phi = [17°, 29°] \cup [31°, 38°]$ while for $\omega = 3/1$ they occur at $\phi = [43°, 46°]$ and $\phi = [33°, 42°]$.

Comparing the microstructures with embedded fibers having volume fraction of $f_0 = \pi/16$ for aspect ratios $\omega = 1$, $\omega = 2/1$ and $\omega = 3/1$, described in Fig. 3.6**b**, 3.10**b** and 3.13**b**, respectively, it is observed that as the aspect ratio increases the material becomes macroscopically and microscopically more stable for dominating mechanical stretching parallel to the major axes of the ellipses. However, the opposite behavior is observed along the $\overline{D}'_2$ axes. In the figures, as the volume fraction increases the stable loading ranges decreases.

The corresponding approximate values of the dimensionless Bloch vector components are given in Fig. 3.11 ($\omega = 2/1$) and 3.14 ($\omega = 3/1$). As discussed in the previous example, similarly, the non-smooth values of Bloch vector components depending on ϕ are observed here, too, because the chosen Bloch vector grid is slightly coarser for the considered BVPs.

Likewise the previous example, Fig. 3.12 depicts the buckling mode of the deforming composite at $\phi = 40°$. The elliptic fibers have the aspect ratio of $\omega = 2/1$ and volume fraction $f_0 = \pi/16$. The enlarged RVE has 39,795 DOFs. In this example, buckling due to the rotation of the elliptic fibers is noted. The buckling happens at the macroscopic stretch $\overline{\lambda} \approx 1.62$ and electric displacement $\overline{D}'_2 \approx 7.40$. The critical size of periodicity is determined to be 1×2 unit-cells at the instability point.

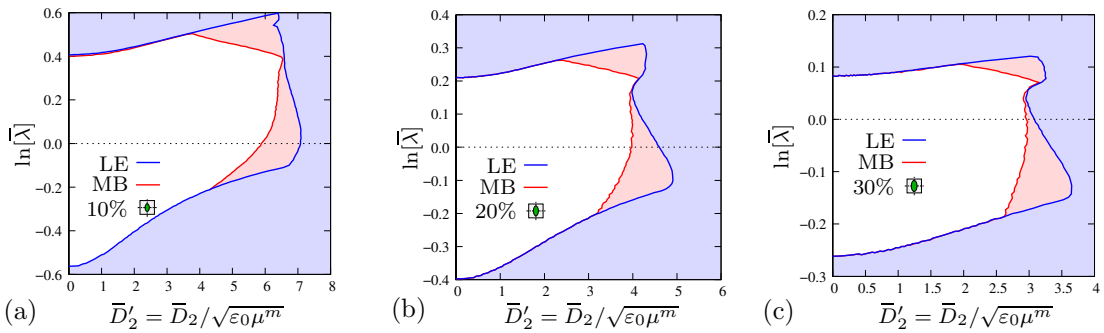

Figure 3.15: *Onset of instability surfaces for periodic microstructures with elliptical fibers with $\omega = 1/2$ (major axis in vertical direction).* The volume fractions of the fibers in (**a**), (**b**) and (**c**) are $f_0 = \{0.1, \pi/16, 0.3\}$, respectively. The discretized microstructures have $\{19,512; 19,764; 20,739\}$ DOFs in plots (**a**), (**b**) and (**c**), respectively. LE denotes the onset of the macroscopic loss of strong ellipticity, while MB denotes the microscopic buckling points of the RVE. The colored regions in the plots correspond to the unstable loading ranges.

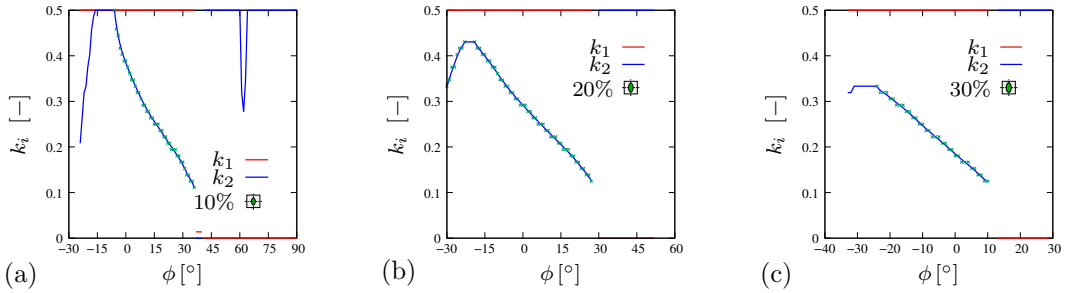

Figure 3.16: *Dimensionless Bloch vector components at microscopic instability points depending on the angle ϕ for elliptical fibers with $\omega = 1/2$.* The plots (**a**), (**b**) and (**c**) correspond to the microstructures with volume fractions $f_0 = \{0.1, \pi/16, 0.3\}$, respectively.

3.4.3.4 Influence of orientation of fibers on instability surfaces

In Fig. 3.15 and 3.17 similar BVPs as described in the previous examples are considered. However, in these cases the major axes of the ellipses are oriented parallel to the electric loading. The corresponding aspect ratios are $\omega = 1/2$ (Fig. 3.15) and $\omega = 1/3$ (Fig. 3.17). In Fig. 3.15**a**, **b** and **c** the onset of macroscopic and microscopic instability surfaces for volume fractions $f_0 = \{0.1,\ \pi/16,\ 0.3\}$ are depicted, respectively. Compared with the previous microstructures, it is observed that the microstructures under electric loading parallel to the major axes are more stable than under loading perpendicular to the major axis (around $\phi = 0°$). Furthermore, Fig. 3.17**a** and **b** correspond to the volume fractions $f_0 = \{0.1,\ \pi/16\}$, respectively. Similar characteristic behaviors can be observed in these examples, too.

As explained in the previous examples, in this case the microscopic instabilities also occur under higher macroscopic electrical as well as electro-mechanical deformations. When the mechanical deformations starts to dominate, the microscopic instabilities coincide with the macroscopic ones developing so-called long-wavelength instabilities. In these examples the short-wavelength microscopic instabilities in Fig. 3.15**a**, **b** and **c** correspond to $\phi = [-24°, 40°] \cup [41°, 90°]$, $\phi = [-30°, 27°] \cup [30°, 52°]$ and $\phi = [-33°, 10°] \cup [13°, 29°]$, respectively, while in Fig. 3.17**a** and **b** they are detected at $\phi = [-30°, 33°] \cup [34°, 68°]$

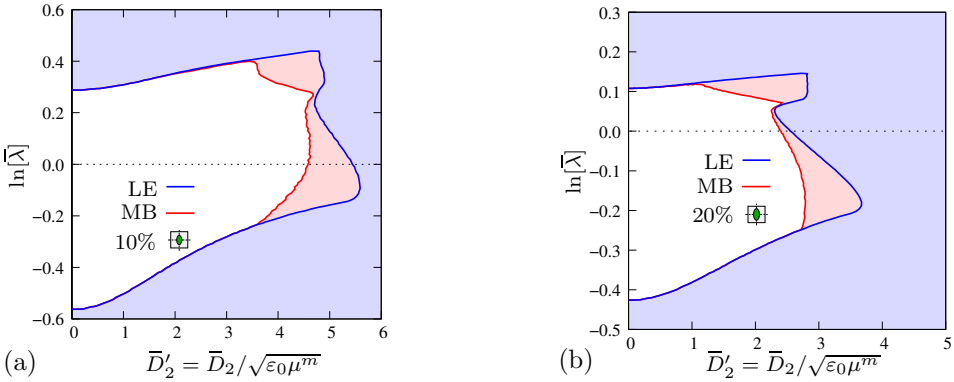

Figure 3.17: *Onset of instability surfaces for periodic microstructures with elliptical fibers with $\omega = 1/3$ (major axis in vertical direction).* The volume fractions of the fibers in (**a**) and (**b**) are $f_0 = \{0.1, \pi/16\}$, respectively. The discretized microstructures have $\{20,172;\ 19,908\}$ DOFs in plots (**a**) and (**b**), respectively. LE denotes the onset of the macroscopic loss of strong ellipticity, while MB denotes the microscopic buckling points of the RVE. The colored regions in the plots correspond to the unstable loading ranges.

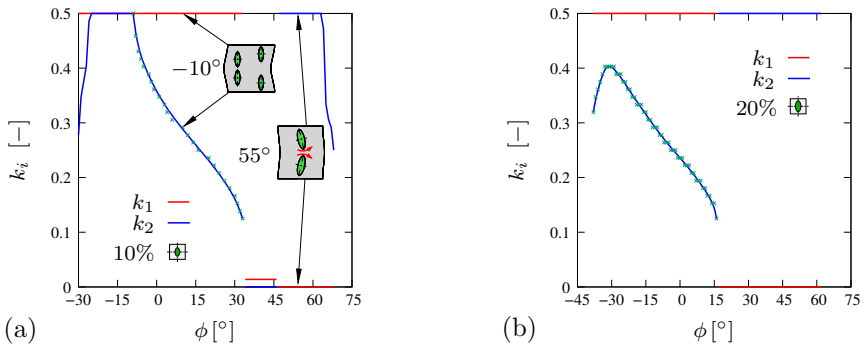

Figure 3.18: *Dimensionless Bloch vector components at microscopic instability points depending on the angle ϕ for elliptical fibers with $\omega = 1/3$.* The plots (**a**) and (**b**) correspond to the microstructures with volume fractions $f_0 = \{0.1, \pi/16\}$, respectively.

and $\phi = [-38°, 16°] \cup [17°, 62°]$, respectively. Similar to the circular fibers in these cases two regions of the short-wavelength microscopic instabilities are also observed. This was not the case for the elliptical fibers with aspect ratios $\omega = \{2/1,\ 3/1\}$ (see, Fig. 3.10 and 3.13). In those examples, the major axis of the fibers was placed perpendicular to the macroscopic electric loading. It seems that when the major axis of the fibers is placed parallel to the macroscopic electric loading the microscopic instabilities along $\overline{D}'_2$ are critical due to the higher electric interactions of the fibers. In the first region the buckling mode corresponds to the internal rearrangement of fibers, however in the second region, where the higher electric loading is distinctly coupled with stretching perpendicular to the major axis, rotational buckling modes are observed.

In Fig. 3.19, a rotational buckling mode is shown at $\phi = 55°$ for the RVE with elliptical fibers having aspect ratio $\omega = 1/3$ and volume fraction $f_0 = 0.1$. The enlarged RVE contains 1×2 unit-cells, which is discretized using $41,067$ DOFs. The bifurcation mode corresponds to the macroscopic coupled deformation of $\overline{\lambda} \approx 1.49$ and $\overline{D}'_2 \approx 3.44$.

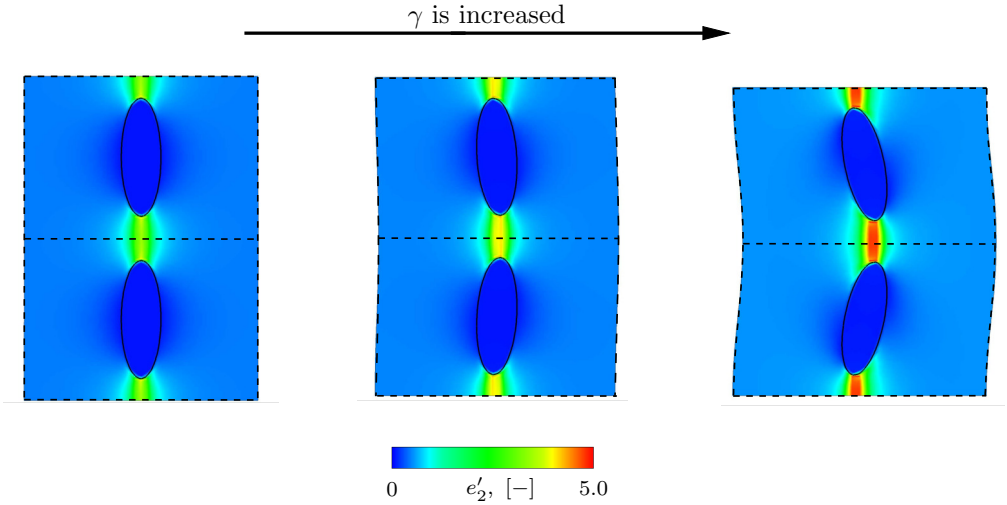

Figure 3.19: *Buckling mode of a microstructure with embedded elliptical fibers with $\omega = 1/3$ and volume fraction $f_0 = 0.1$.* The buckling mode corresponds to $\phi = 55°$. The scaling factor $\tau = 1$ in (3.70) is taken. At the bifurcation point the critical periodicity of the microstrucutre alters and the enlarged RVE contains 1×2 unit-cells. The contour plots correspond to the distribution of vertical components e'_2 of the microscopic current electric field $\mathscr{e}' = \boldsymbol{F}^{-T}\mathbb{E}'$ in the RVE.

3.5 Summary

In this work, we considered the microscopic and macroscopic stability analysis of electroactive polymer composites in the context of computational homogenization. We discussed the implementation of a four-field variational formulation of the microscopic boundary value problem to avoid volumetric locking for nearly incompressible materials. Furthermore, we described in detail the theoretical aspects and numerical implementation to detect the macroscopic loss of strong ellipticity of homogenized moduli and microscopic bifurcation type instabilities. The Bloch-Floquet analysis is applied to primary kinematic fields, i.e., deformation map and electric vector potential, in order to detect the critical periodicity of microstructures and symmetric buckling modes of RVEs. In numerical examples, the multi-scale stability analysis of periodic electroactive polymer composites has been investigated. The considered RVEs comprise a soft elastomeric matrix and stiff fibers with high dielectric constant. The influence of geometric properties of fibers on instability points were studied in detail. It was observed that under electric loading circular fibers lead to higher microscopic and macroscopic stability as compared with elliptical fibers. However, for higher coupled electro-mechanical loading the instability points are first observed at much higher deformation states for the microstructures with embedded elliptical fibers, particularly when the major axes of ellipses are placed perpendicular to the electric field.

To summarize, the formulations and the numerical implementations presented in the paper allow for the definition of critical ensembles of unit cells that constitute suitable RVEs and the determination of associated instability failure loads. All in all, the presented approach provides an access to the design of microstructures that show desired stability properties and the most optimal material response.

Acknowledgements

The financial support of the German Research Foundation (DFG) in the framework of the Research Group 1509 “Ferroic Functional Materials” (project KE 1849/2-2) and the Cluster of Excellence “Simulation Technology” (EXC 310/2) at the University of Stuttgart is gratefully acknowledged.

Appendix

A Computational analysis of the numerical stability of the four-field mean-dilatation finite element formulation

In this appendix, we investigate the numerical stability of the finite element formulation advocated in the present contribution. We analyze its behavior under coupled electro-mechanical loading and compare it with other finite elements frequently used in nearly incompressible elasticity. The considered elements are in detail:

- a *quadrilateral* finite element with *linear* interpolations of the fluctuations of the mechanical displacement and electric vector potential as well as *piecewise constant* interpolations of the pressure and dilatation, in the following denoted as $\overline{B}Q1P0$ (this is the element employed in the present contribution).

- a *quadrilateral* finite element with *quadratic* interpolations of the fluctuations of the mechanical displacement and electric vector potential as well as *piecewise constant* interpolations of the pressure and dilatation, in the following denoted as $\overline{B}Q2P0$.

- a *triangular* finite element with *quadratic* interpolations of the fluctuations of the mechanical displacement and electric vector potential as well as *piecewise constant* interpolations of the pressure and dilatation, in the following denoted as $\overline{B}T2P0$.

Please note that the standard $Q2P0$ and $T2P0$ finite elements are known to be *inf-sup stable* in linear incompressible elasticity [56, 11, 3]. In contrast, the standard $Q1P0$ element is *not inf-sup stable* in the incompressible limit [11]. Regardless of that, the latter is still frequently used for the analysis of nearly incompressible materials, which is mainly due to its robustness and its convenient numerical implementation. In fact, we employ a similar finite element formulation denoted by $\overline{B}Q1P0$ element in the present contribution. This is why we want to study its numerical stability in more detail.

Before starting the study, we mention that even inf-sup stable elements could yield incorrect results in the *nonlinear* elastic regime, see, e.g., Pantuso and Bathe [56], Auricchio et al. [2, 3] amongst others. Thus, we investigate the response of the above mentioned finite elements in consideration of different loading conditions and analyze the results in the spirit of [56]. In order to obtain deeper insights into the behavior of the finite elements, we consider three different loading scenarios given by (i) purely mechanical, (ii) coupled electro-mechanical and (iii) purely electric loading. To be specific, we consider a typical RVE containing circular fibers with volume fraction of $f_0 = \pi/16$ under macroscopic isochoric mechanical stretching $\overline{\lambda}$ in horizontal direction and macroscopic electric displacement $\overline{D}'_2$ in vertical direction, see Fig. 3.20. The underlying material parameters are listed in Table 3.2. Please note that the elastic parameters are chosen in such a way that the Poisson ratio is $\nu = 0.4995$ corresponding to nearly incompressible behavior. To obtain representative insight into the numerical stability of the considered finite elements, we plot the pressure distribution across a cut through the RVE along the X_2 axis in all subsequent studies. Note that the pressure is projected to the nodes.

Purely mechanical loading. In Fig. 3.21 the pressure distribution at the nodes of the various finite elements are depicted under pure macroscopic isochoric mechanical

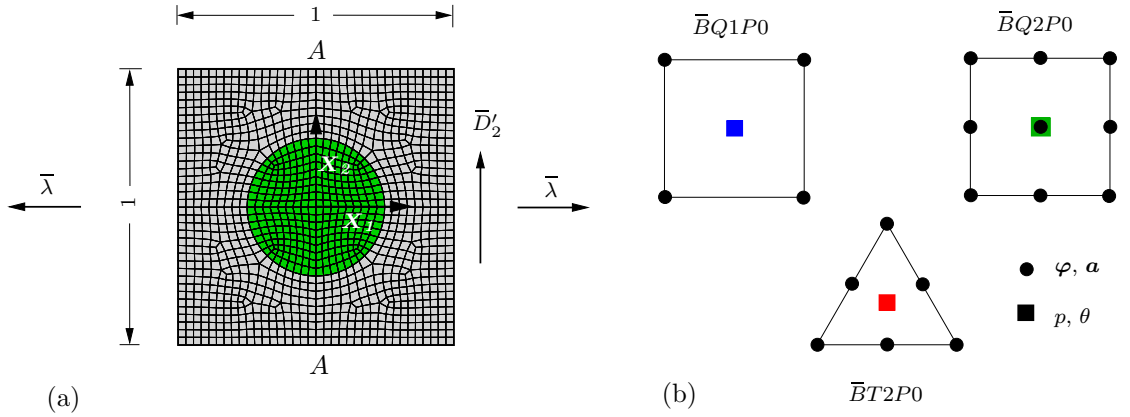

Figure 3.20: *Description of boundary value problem and element types considered in the numerical tests of element stability.* (**a**) The unit-cell RVE is under macroscopic isochoric stretch $\overline{\lambda}$ in horizontal direction (with $\det[\overline{\boldsymbol{F}}] = 1$) and electric displacement $\overline{D}_2'$ in vertical direction. In order to analyze the numerical stability of the element formulations, the pressure distribution across the cut A-A through the RVE along the X_2 axis is plotted under (i) purely mechanical loading ($\overline{\mathbb{D}} = \boldsymbol{0}$), (ii) coupled electro-mechanical loading and (iii) purely electric loading ($\overline{\boldsymbol{F}} = \boldsymbol{1}$); (**b**) Schematic representation of the finite elements considered in the numerical analysis. All of them allow for continuous interpolation of the fluctuations of mechanical displacement and electric vector potential as well as discontinuous interpolation of pressure and dilatation.

Table 3.2: Material parameters

No.	Parameter	Name	Value
1.	κ/μ	Bulk modulus relative to shear modulus	1000
2.	μ^f/μ^m	Relative shear modulus of fibers	100
3.	χ^f/χ^m	Relative electric susceptibility of fibers	100
4.	ξ	Strain saturation parameter	100
5.	f_0	Volume fraction of fibers	$\pi/16$

loading. We observe that for low values of the macroscopic stretch $\overline{\lambda}$ the pressure distribution is nearly identical for all elements. However, at higher stretches the $\overline{B}T2P0$ element shows pressure oscillations, while both the $\overline{B}Q1P0$ and the $\overline{B}Q2P0$ element do not show any oscillations. With increasing loading small discrepancies between the results obtained with the $\overline{B}Q1P0$ and the $\overline{B}Q2P0$ element are observed.

Yet in [56] it has been discussed that in case of $Q2P0$ elements the *ellipticity condition* (which is one of the required conditions for stability of mixed formulations) of the linearized equations around a deformation state is violated "more easily". For more details please refer to [56], Section 3.2 as well as Section 4 for supporting numerical examples. In the letter, Pantuso and Bathe [56] have observed that $Q1P0$ and $Q2P1$ elements do not show any spurious modes and that these elements allow to reach higher strain levels. Moreover, based on a numerical example simulation, they argued that by using a finer discretization with $Q1P0$ elements, a better correspondence to the $Q2P1$ elements can be achieved.

Coupled electro-mechanical loading. In Fig. 3.22 the pressure response under macroscopic coupled electro-mechanical loading is shown. We observe similar behavior as

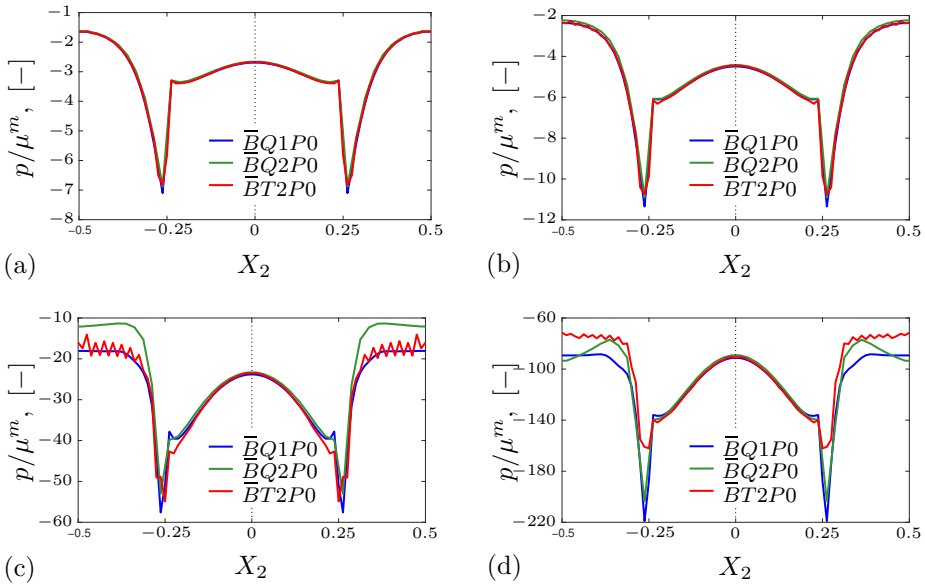

Figure 3.21: *Pressure distribution along X_2 axis at the center of the RVE under isochoric macroscopic loading* $\det[\overline{\boldsymbol{F}}] = 1$. The snapshots correspond to the macroscopic loads: (**a**) $\overline{\lambda} = 1.5$ and $D_2' = 0$; (**b**) $\overline{\lambda} = 1.6$ and $D_2' = 0$; (**c**) $\overline{\lambda} = 2.0$ and $D_2' = 0$; (**d**) $\overline{\lambda} = 2.8$ and $D_2' = 0$.

in the purely mechanical case. Again, oscillations of the $\overline{B}T2P0$ are present and increase with stretch. Moreover, under a macroscopic stretch of $\overline{\lambda} = 1.5$, the pressure at the phase boundaries predicted by the $\overline{B}Q2P0$ element is much higher than the pressure captured by using the $\overline{B}Q1P0$ and $\overline{B}T2P0$ element, respectively. Furthermore, for higher values of stretch, the discretization with $\overline{B}Q2P0$ finite elements loses convergence, which could be due to the reason mentioned above.

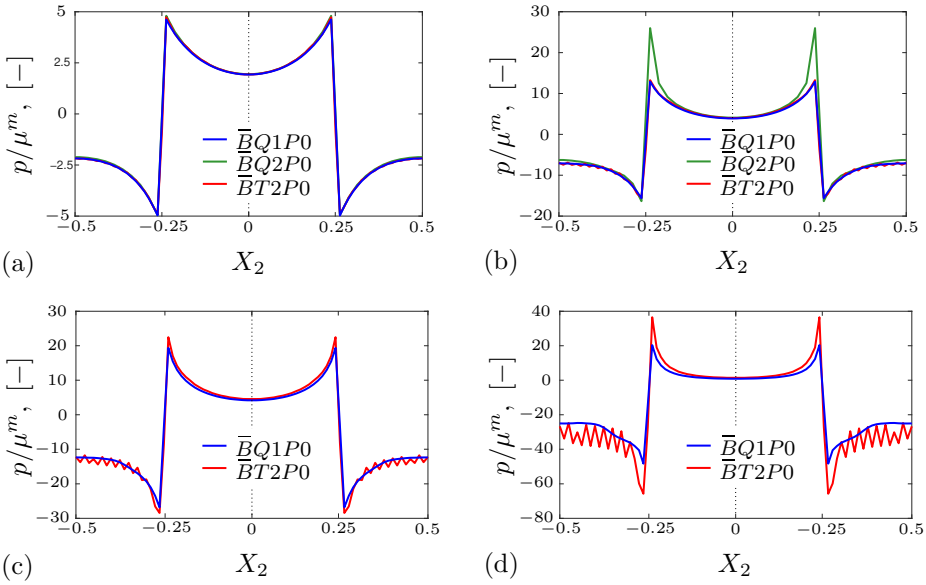

Figure 3.22: *Pressure distribution along X_2 axis at the center of the RVE under isochoric macroscopic loading* $\det[\overline{\boldsymbol{F}}] = 1$. The snapshots correspond to the macroscopic loads: (**a**) $\overline{\lambda} = 1.3$ and $D_2' = 3.0$; (**b**) $\overline{\lambda} = 1.5$ and $D_2' = 5.0$; (**c**) $\overline{\lambda} = 1.6$ and $D_2' = 6.01$; (**d**) $\overline{\lambda} = 1.75$ and $D_2' = 7.52$.

Purely electric loading. In the last example, we analyze the behavior of the RVEs

under purely electric loading. That is, we load the RVE with an electric displacement $\overline{\mathbb{D}}'_2$ while keeping the macroscopic deformation fixed by setting $\overline{\boldsymbol{F}} = \boldsymbol{1}$. As can be seen in Fig. 3.23, the pressure oscillations of the $\overline{B}T2P0$ element are not as pronounced as in the previous examples. Furthermore, the snapshots shown in Fig. 3.23**a**, **b** and **c** indicate that the $\overline{B}Q1P0$ and the $\overline{B}T2P0$ element are in good agreement. Only in **c**, under $\overline{\mathbb{D}} = 8.0$, slight discrepancies are observed at the interface between fiber and matrix. Clearly, these discrepancies become much higher with increasing electric loading, see Fig. 3.23**d**. Under this loading, the RVE discretized with $\overline{B}T2P0$ elements shows unphysical deformations of elements in the region of the interface between matrix and fiber. Furthermore, in **d**, no convergence in case of $\overline{B}Q2P0$ elements could be achieved.

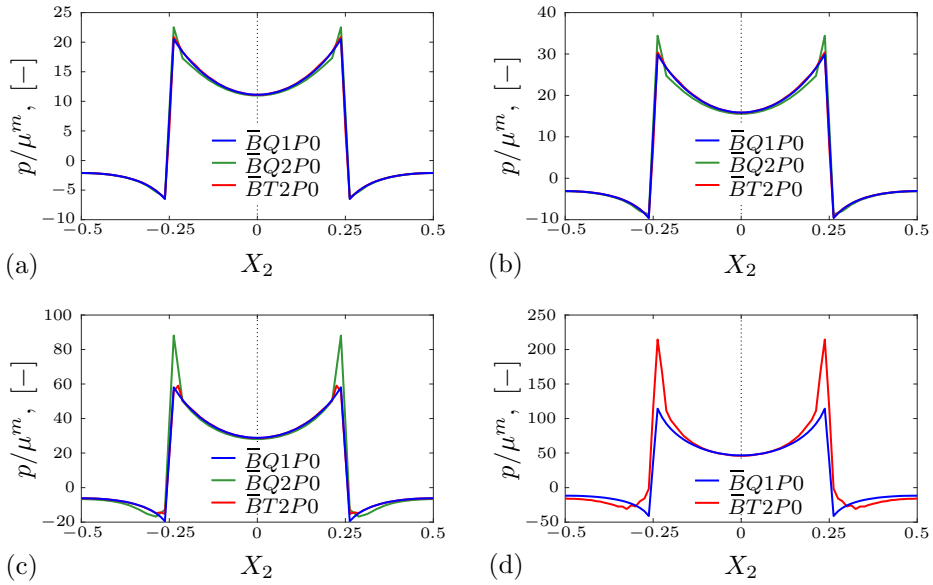

Figure 3.23: *Pressure distribution along X_2 axis at the center of the RVE under isochoric macroscopic loading* $\det[\overline{\boldsymbol{F}}] = 1$. The snapshots correspond to the macroscopic loads: (**a**) $\overline{\lambda} = 1.0$ and $D'_2 = 5.0$; (**b**) $\overline{\lambda} = 1.0$ and $D'_2 = 6.0$; (**c**) $\overline{\lambda} = 1.0$ and $D'_2 = 8.0$; (**d**) $\overline{\lambda} = 1.0$ and $D'_2 = 10.0$.

Conclusion. The numerical studies above indicate that the $\overline{B}Q1P0$ element shows reasonable behaviour under purely mechanical, purely electrical and also coupled electro-mechanical loading. In all considered cases it even outperforms the competing $\overline{B}Q2P0$ and $\overline{B}T2P0$ elements, which are known to be inf-sup stable in the linear elastic regime. We conclude that a dicretization with $\overline{B}Q1P0$ elements as dicussed in Section 3.4 is reasonable for the multi-scale stability analysis of EAP composites considered in this work.

Bibliography: Paper A

[1] Abeyaratne, R., Triantafyllidis, N., [1984]. *An investigation of localization in a porous elastic material using homogenization theory*. ASME Journal of Applied Mechanics 51(3), 481–486. (doi:doi:10.1115/1.3167661)

[2] Auricchio, F., da Veiga, L. B., Lovadina, C., Reali, A., [2005]. *A stability study of some mixed finite elements for large deformation elasticity problems*. Computer Methods in Applied Mechanics and Engineering 194 (9), 1075–1092.

[3] Auricchio, F., da Veiga, L. B., Lovadina, C., Reali, A., Taylor, R. L., Wriggers, P., [2013]. *Approximation of incompressible large deformation elastic problems: some unresolved issues*. Computational Mechanics 52, 1153–1167. (doi:DOI 10.1007/s00466-013-0869-0)

[4] Ball, J., [1977]. *Convexity conditions and existence theorems in nonlinear elasticity*. Archive of Rational Mechanics and Analysis 63, 337–403.

[5] Bar-Cohen, Y., [2002]. *Electro-active polymers: Current capabilities and challenges*. Proceedings of the SPIE Smart Structures and Materials Symposium 4695-02, 1–6.

[6] Bar-Cohen, Y., Zhang, Q., [2008]. *Electro-active polymer actuators and sensors*. MRS Bulletin 33, 173–181.

[7] Bertoldi, K., Boyce, M., Deschanel, S., Prange, S., Mullin, T., [2008]. *Mechanics of deformation-triggered pattern transformations and superelastic behavior in periodic elastomeric structures*. Journal of the Mechanics and Physics of Solids 56, 2642–2668. (doi:doi:10.1016/j.jmps.2008.03.006)

[8] Bertoldi, K., Boyce, M. C., [2008]. *Wave propagation and instabilities in monolithic and periodically structured elastomeric materials undergoing large deformations*. Physical Review B 78 (18), 184107. (doi:10.1103/PhysRevB.78.184107)

[9] Bertoldi, K., Gei, M., [2011]. *Instabilities in multilayered soft dielectrics*. Journal of the Mechanics and Physics of Solids 59, 18–42. (http://www.sciencedirect.com/science/article/pii/S0022509610002036)

[10] Biro, O., Preis, K., [1989]. *On the use of the magnetic vector potential in the finite element analysis of three-dimensional eddy currents*. IEEE Transactions on Magnetics 25 (4), 3145–3159.

[11] Brezzi, F., Fortin, M., [2012]. *Mixed and hybrid finite element methods*. Springer Science & Business Media.

[12] Bustamante, R., Dorfmann, A., Ogden, R. W., [2009]. *On electric body forces and Maxwell stresses in nonlinearly electroelastic solids*. International Journal of Engineering Science 47, 1131–1141.

[13] Carpi, F., [2016]. *Electromechanically Active Polymers*. Springer International Publishing Switzerland. (doi:DOI 10.1007/978-3-319-31530-0)

[14] Coleman, B. D., Noll, W., [1959]. *On the thermostatics of continuous media*. Archive of Rational Mechanics and Analysis 4, 97–128.

[15] Danas, K., [2017]. *Effective response of classical, auxetic and chiral magnetoelastic materials by use of a new variational principle*. Journal of the Mechanics and Physics of Solids 105 (Supplement C), 25 – 53. (doi:https://doi.org/10.1016/j.jmps.2017.04.016)

[16] Dorfmann, A., Ogden, R. W., [2005]. *Nonlinear electroelasticity*. Acta Mechanica 174 (3), 167–183. (doi:10.1007/s00707-004-0202-2)

[17] Dorfmann, A., Ogden, R. W., [2010]. *Electroelastic waves in a finitely deformed electroactive material*. IMA Journal of Applied Mathematics 75(4), 603–636. (doi:doi:10.1093/imamat/hxq022)

[18] Dorfmann, A., Ogden, R. W., [2010]. *Nonlinear electroelastostatics: Incremental equations and stability*. International Journal of Engineering Science 48, 1–14. (http://www.sciencedirect.com/science/article/pii/S0020722508001043)

[19] Feyel, F., Chaboche, J.-L., [2000]. *FE^2 multiscale approach for modelling the elasto-viscoplastic behaviour of long fibre SiC/Ti composite materials*. Computer methods in applied mechanics and engineering 183, 309–330.

[20] Gent, A. N., [1996]. *A new constitutive relation for rubber*. Rubber Chemistry and Technology 69, 59–61.

[21] Geymonat, G., Müller, S., Triantafyllidis, N., [1993]. *Homogenization of nonlinearly elastic materials, microscopic bifurcation and macroscopic loss of rank-one convexity*. Archive for Rational Mechanics and Analysis 122, 231–290. (doi:DOI: 10.1007/BF00380256)

[22] Goshkoderia, A., Rudykh, S., [2017]. *Electromechanical macroscopic instabilities in soft dielectric elastomer composites with periodic microstructures*. European Journal of Mechanics-A/Solids 65, 243–256.

[23] Goshkoderia, A., Rudykh, S., [2017]. *Stability of magnetoactive composites with periodic microstructures undergoing finite strains in the presence of a magnetic field*. Composites Part B: Engineering 128 (Supplement C), 19 – 29. (doi:https://doi.org/10.1016/j.compositesb.2017.06.014)

[24] Hill, R., [1957]. *On uniqueness and stability in the theory of finite elastic strains*. Journal of the Mechanics and Physics of Solids 5, 229–241.

[25] Hill, R., [1963]. *Elastic properties of reinforced solids: Some theoretical principles*. Journal of the Mechanics and Physics of Solids 11, 357–372.

[26] Hill, R., [1965]. *A self-consistent mechanics of composite materials*. Journal of the Mechanics and Physics of Solids 13, 213–222.

[27] Hill, R., [1972]. *On constitutive macro-variables for heterogeneous solids at finite strain*. Proceedings of the Royal Society of London (Series A) 326, 131–147.

[28] Huang, C., Zhang, Q. M., deBotton, G., Bhattacharya, K., [2004]. *All-organic dielectric-percolative three-component composite materials with high electromechanical response*. Applied Physics Letters 84 (22), 4391–4393.

[29] Keip, M.-A., Rambausek, M., [2016]. *A multiscale approach to the computational characterization of magnetorheological elastomers*. International Journal for Numerical Methods in Engineering 107, 338–360.

[30] Keip, M.-A., Rambausek, M., [2017]. *Computational and analytical investigations of shape effects in the experimental characterization of magnetorheological elastomers*. International Journal of Solids and Structures 121, 1–20.

[31] Keip, M.-A., Steinmann, P., Schröder, J., [2014]. *Two-scale computational homogenization of electro-elasticity at finite strains*. Computer Methods in Applied Mechanics and Engineering 278, 62–79.

[32] Kittel, C., [2005]. *Introduction to Solid State Physics*. John Wiley & Sons, Inc.

[33] Kornbluh, R., Pelrine, R., Joseph, J., [1995]. *Elastomeric dielectric artificial muscle actuators for small robots*. Proceedings of the Materials Research Society.

[34] Kornbluh, R., Pelrine, R., Joseph, J., Heydt, R., Pei, Q., Chiba, S., [1999]. *High-field electrostriction of elastomeric polymer dielectrics for actuation*. Proceedings of the SPIE: Smart Structures and Materials 3669, 149–161. (doi:10.1117/12.349672)

[35] Kouznetsova, V. G., Geers, M. G. D., Brekelmans, W. A. M., [2004]. *Multi-scale second-order computational homogenization of multi-phase materials: a nested finite element solution strategy*. Computer Methods in Applied Mechanics and Engineering 193, 5525–5550.

[36] Kovetz, A., [2000]. *Electromagnetic Theory*. Oxford University Press.

[37] Lefèvre, V., Lopez-Pamies, O., [2014]. *The overall elastic dielectric properties of a suspension of spherical particles in rubber: An exact explicit solution in the small-deformation limit*. Journal of Applied Physics 116 (13), 134106. (doi:10.1063/1.4897199)

[38] Lefèvre, V., Lopez-Pamies, O., [2017]. *Nonlinear electroelastic deformations of dielectric elastomer composites: I – Ideal elastic dielectrics*. Journal of the Mechanics and Physics of Solids 99, 409–437.

[39] Lefèvre, V., Lopez-Pamies, O., [2017]. *Nonlinear electroelastic deformations of dielectric elastomer composites: II – Non-Gaussian elastic dielectrics*. Journal of the Mechanics and Physics of Solids 99, 438 – 470. (doi:https://doi.org/10.1016/j.jmps.2016.07.005)

[40] Li, B., Zhou, J., Chen, H., [2011]. *Electromechanical stability in charge-controlled dielectric elastomer actuation*. Applied Physics Letters 99 (24), 244101. (doi:10.1063/1.3670048)

[41] Lopez-Pamies, O., [2014]. *Elastic dielectric composites: Theory and application to particle-filled ideal dielectrics*. Journal of the Mechanics and Physics of Solids 64, 61–82. (doi:http://dx.doi.org/10.1016/j.jmps.2013.10.016)

[42] Mandel, J., [1972]. *Plasticité classique et viscoplasticité*. In: *CISM Courses and Lectures No. 97*. Springer-Verlag.

[43] Marcellini, P., [1978]. *Periodic solutions and homogenization of nonlinear variational problems*. Annali di Matematica Pura ed Applicata 117, 139–152.

[44] Maugin, G. A., [1988]. *Continuum Mechanics of Electromagnetic Solids*. Vol. 33 of *North-Holland Series in Applied Mathematics and Mechanics*. Elsevier Science Publishers, Amsterdam.

[45] McMeeking, R. M., Landis, C. M., [2005]. *Electrostatic forces and stored energy for deformable dielectric materials*. Journal of Applied Physics 72, 581–590.

[46] Michel, J., Lopez-Pamies, O., Ponte Castañeda, P., Triantafyllidis, N., [2007]. *Microscopic and macroscopic instabilities in finitely strained porous elastomers*. Journal of the Mechanics and Physics of Solids 55, 900–938. (doi:doi:10.1016/j.jmps.2006.11.006)

[47] Michel, J., Lopez-Pamies, O., Ponte Castañeda, P., Triantafyllidis, N., [2010]. *Microscopic and macroscopic instabilities in finitely strained fiber-reinforced elastomers*. Journal of the Mechanics and Physics of Solids 58, 1776–1803. (doi:doi:10.1016/j.jmps.2010.08.006)

[48] Miehe, C., [1994]. *Aspects of the formulation and finite element implementation of large strain isotropic elasticity*. International journal of numerical methods in engineering 37, 1981–2004.

[49] Miehe, C., Schotte, J., Schröder, J., [1999]. *Computational micro-macro transitions and overall moduli in the analysis of polycrystals at large strains*. Computational Materials Science 16, 372–382.

[50] Miehe, C., Schröder, J., Becker, M., [2002]. *Computational homogenization analysis in finite elasticity: material and structural instabilities on the micro-and macro-scales of periodic composites and their interaction*. Computer Methods in Applied Mechanics and Engineering 191 (44), 4971–5005.

[51] Miehe, C., Vallicotti, D., Teichtmeister, S., [2016]. *Homogenization and multiscale stability analysis in finite magneto-electro-elasticity. application to soft matter EE, ME and MEE composites*. Computer Methods in Applied Mechanics and Engineering 300, 294–346. (doi:http://dx.doi.org/10.1016/j.cma.2015.10.013)

[52] Miehe, C., Vallicotti, D., Zäh, D., [2015]. *Computational structural and material stability analysis in finite electro-elasto-statics of electro-active materials*.

International Journal for Numerical Methods in Engineering 102, 1605–1637. (doi:DOI: 10.1002/nme.4855)

[53] Müller, S., [1987]. *Homogenization of nonconvex integral functionals and cellular elastic materials*. Archive of Rational Mechanics and Analysis 99, 189–212.

[54] Nagtegaal, J., Parks, D., Rice, J., [1974]. *On numerically accurate finite element solutions in the fully plastic range*. Computer Methods in Applied Mechanics and Engineering 4, 153–177.

[55] Nestorović, M., Triantafyllidis, N., [2004]. *Onset of failure in finitely strained layered composites subjected to combined normal and shear loading*. Journal of the Mechanics and Physics of Solids 52, 941–974. (doi:doi:10.1016/j.jmps.2003.06.001)

[56] Pantuso, D., Bathe, K.-J., [1997]. *On the stability of mixed finite elements in large strain analysis of incompressible solids*. Finite elements in analysis and design 28 (2), 83–104.

[57] Pelrine, R., Kornbluh, R., Joseph, J., Heydt, R., Pei, Q., Chiba, S., [2000]. *High-field deformation of elastomeric dielectrics for actuators*. Materials Science and Engineering: C 11 (2), 89–100. (doi:10.1016/S0928-4931(00)00128-4)

[58] Pelrine, R., Kornbluh, R. D., Joseph, J., [1998]. *Electrostriction of polymer dielectrics with compliant electrodes as a means of actuation*. Sensors and Actuators A: Physical 64, 77–85.

[59] Pelteret, J.-P., Davydov, D., McBride, A., Vu, D. K., Steinmann, P., [2016]. *Computational electro-elasticity and magneto-elasticity for quasi-incompressible media immersed in free space*. International Journal For Numerical Methods in Engineering 108, 1307–1342. (doi:10.1002/nme.5254)

[60] Ponte Castañeda, P., Galipeau, E., [2011]. *Homogenization-based constitutive models for magnetorheological elastomers at finite strain*. Journal of the Mechanics and Physics of Solids 59, 194–215.

[61] Ponte Castañeda, P., Siboni, M. H., [2012]. *A finite-strain constitutive theory for electro-active polymer composites via homogenization*. International Journal of Non-Linear Mechanics 47, 293–306.

[62] Åberg, M., Gudmundson, P., [1997]. *The usage of standard finite element codes for computation of dispersion relations in materials with periodic microstructure*. J. Acoust. Soc. Am. 102 (4).

[63] Rudykh, S., Bertoldi, K., [2013]. *Stability of anisotropic magnetorheological elastomers in finite deformations: A micromechanical approach*. Journal of the Mechanics and Physics of Solids 61, 949–967. (doi:http://dx.doi.org/10.1016/j.jmps.2012.12.008)

[64] Rudykh, S., deBotton, G., [2012]. *Instabilities of hyperelastic fiber composites: Micromechanical versus numerical analyses*. Journal of Elasticity 106, 123–147. (doi:DOI 10.1007/s10659-011-9313-x)

[65] Rudykh, S., deBotton, G., [2012]. *Stability of anisotropic electroactive polymers with application to layered media*. Zeitschrift für angewandte Mathematik und Physik 62, 1131–1142. (doi:DOI 10.1007/s10659-011-9313-x)

[66] Rudykh, S., Lewinstein, A., Uner, G., deBotton, G., [2013]. *Analysis of microstructural induced enhancement of electromechanical coupling in soft dielectrics*. Applied Physics Letters 102 (151905). (doi:doi: 10.1063/1.4801775)

[67] Schröder, J., [2009]. *Derivation of the localization and homogenization conditions for electro-mechanically coupled problems*. Computational Materials Science 46, 595–599.

[68] Schröder, J., Keip, M.-A., [2012]. *Two-scale homogenization of electromechanically coupled boundary value problems*. Computational Mechanics 50 (2), 229–244.

[69] Schröder, J., Neff, P., [2003]. *Invariant formulation of hyperelastic transverse isotropy based on polyconvex free energy functions*. International Journal of Solids and Structures 40, 401–445.

[70] Schröder, J., Neff, P., Ebbing, V., [2008]. *Anisotropic polyconvex energies on the basis of crystallographic motivated structural tensors*. Journal of the Mechanics and Physics of Solids 56, 3486–3506.

[71] Schröder, J., Viebahn, N., Wriggers, P., Auricchio, F., Steeger, K., [2017]. *On the stability analysis of hyperelastic boundary value problems using three- and two-field mixed finite element formulations*. Computational Mechanics, 1–14. (doi:DOI 10.1007/s00466-017-1415-2)

[72] Semenov, A. S., Kessler, H., Liskowsky, A., Balke, H., [2006]. *On a vector potential formulation for 3d electromechanical finite element analysis*. Communication in Numerical Methods in Engineering 22, 357–375.

[73] Semenov, A. S., Liskowsky, A., Balke, H., [2007]. *Vector potential formulation for the three-dimensional finite element analysis of nonlinear electromechanical problems*. In: Dapino, M. J. (Ed.), *Behavior and Mechanics of Multifunctional and Composite Materials 2007*. Proceeding of SPIE Vol. 6526.

[74] Siboni, M. H., Avazmohammadi, R., Ponte Castañeda, P., [2015]. *Electromechanical instabilities in fiber-constrained, dielectric-elastomer composites subjected to all-around dead-loading*. Mathematics and Mechanics of Solids 20 (6), 729–759. (doi:DOI: 10.1177/1081286514551501)

[75] Siboni, M. H., Ponte Castañeda, P., [2014]. *Fiber-constrained, dielectric-elastomer composites: Finite-strain response and stability analysis*. Journal of the Mechanics and Physics of Solids.

[76] Simo, J., Taylor, R., Pister, K., [1985]. *Variational and projection methods for the volume constraint in finite deformation elasto-plasticity*. Computer Methods in Applied Mechanics and Engineering 51, 177–208.

[77] Simo, J. C., Taylor, R. L., [1991]. *Quasi-incompressible finite elasticity in principal stretches. continuum basis and numerical algorithms*. Computer Methods in Applied Mechanics and Engineering 85, 273–310.

[78] Slesarenko, V., Rudykh, S., [2017]. *Microscopic and macroscopic instabilities in hyperelastic fiber composites*. Journal of the Mechanics and Physics of Solids 99, 471–482.

[79] Smit, R., Brekelmans, W., Meijer, H., [1998]. *Prediction of the mechanical behavior of nonlinear heterogeneous systems by multi-level finite element modeling*. Computer Methods in Applied Mechanics and Engineering 155, 181–192.

[80] Spinelli, S. A., Lefèvre, V., Lopez-Pamies, O., [2015]. *Dielectric elastomer composites: A general closed-form solution in the small-deformation limit*. Journal of the Mechanics and Physics of Solids 83, 263 – 284. (doi:https://doi.org/10.1016/j.jmps.2015.06.009)

[81] Spinelli, S. A., Lopez-Pamies, O., [2015]. *Some simple explicit results for the elastic dielectric properties and stability of layered composites*. International Journal of Engineering Science 88, 15 – 28, special Issue on. (doi:https://doi.org/10.1016/j.ijengsci.2014.01.005)

[82] Suo, Z., Zhao, X., Greene, W. H., [2008]. *A nonlinear field theory of deformable dielectrics*. Journal of the Mechanics and Physics of Solids 56, 467–486.

[83] Terada, K., Kikuchi, T., [2001]. *A class of general algorithms for multi-scale analyses of heterogeneous media*. Computer Methods in Applied Mechanics and Engineering 190, 5427–5464.

[84] Tian, L., Tevet-Deree, L., deBotton, G., Bhattacharya, K., [2012]. *Dielectric elastomer composites*. Journal of the Mechanics and Physics of Solids 60 (1), 181–198. (doi:10.1016/j.jmps.2011.08.005)

[85] Tiersten, H. F., [1965]. *Variational principle for saturated magnetoelastic insulators*. Journal of Mathematical Physics 6(5), 779–787.

[86] Toupin, R. A., [1956]. *The elastic dielectric*. Archive for Rational Mechanics and Analysis 5, 849–915.

[87] Triantafyllidis, N., Bardenhagen, S., [1996]. *The influence of scale size on the stability of periodic solids and the role of associated higher order gradient continuum models*. Journal of the Mechanics and Physics of Solids 44, 1891–1928. (doi:doi.org/10.1016/0022-5096(96)00047-6)

[88] Triantafyllidis, N., Maker, B. N., [1985]. *On the comparison between microscopic and macroscopic instability mechanisms in a class of fiber-reinforced composites*. ASME Journal of Applied Mechanics 52, 794–800. (doi:doi:10.1115/1.3169148)

[89] Triantafyllidis, N., Nestorović, M. D., Schraad, M. W., [2006]. *Failure surfaces for finitely strained two-phase periodic solids under general in-plane loading*. ASME Journal of Applied Mechanics 73(3), 505–515. (doi:doi:10.1115/1.2126695)

[90] Triantafyllidis, N., Schraad, M., [1998]. *Onset of failure in aluminum honeycombs under general in-plane loading*. Journal of the Mechanics and Physics of Solids 46 (6), 1089–1124. (doi:doi.org/10.1016/S0022-5096(97)00060-4)

[91] Vogel, F., Bustamante, R., Steinmann, P., [2012]. *On some mixed variational principles in electro-elastostatics*. International Journal of Non-Linear Mechanics 47, 341–354.

[92] Vu, D. K., Steinmann, P., [2012]. *On 3-d coupled bem-fem simulation of nonlinear electro-elastostatics*. Computer Methods in Applied Mechanics and Engineering 201–204, 82–90. (doi:10.1016/j.cma.2011.08.024)

[93] Vu, D. K., Steinmann, P., Possart, G., [2007]. *Numerical modelling of non-linear electroelasticity*. International Journal for Numerical Methods in Engineering 70, 685–704.

[94] Willis, J. R., [1981]. *Variational and related methods for the overall properties of composites*. Advances in Applied Mechanics 21, 1–78.

[95] Yamamoto, M., Hisada, T., [2002]. *A homogenization method for nearly incompressible materials by using characteristic deformation mode superposition*. JSME International Journal 45 (4), 586–602.

[96] Zäh, D., [2014]. *Variational homogenization in electro-mechanics: From micro-electro-elasticity to electroactive polymers*. Ph.D. thesis, University of Stuttgart.

[97] Zäh, D., Miehe, C., [2013]. *Computational homogenization in dissipative electro-mechanics of functional materials*. Computer Methods in Applied Mechanics and Engineering 267, 487–510.

[98] Zhang, Q. M., Li, H., Poh, M., Xia, F., Cheng, Z.-Y., Xu, H., Huang, C., [2002]. *An all-organic composite actuator material with high dielectric constant*. Nature 419, 284–288.

Chapter 4: Paper B

Multiscale Stability Analysis of Periodic Magnetorheological Elastomers

Multiscale Stability Analysis of Periodic Magnetorheological Elastomers

Original publication:

Polukhov, E. & Keip, M.-A. [2021]. *Multiscale Stability Analysis of Periodic Magnetorheological Elastomers.* Mechanics of Materials 159, 103699.

Abstract

We analyze instability phenomena of periodic magnetorheological elastomers in the framework of computational homogenization. Our focus is on two kinds of instabilities given by *macroscopic material* and *microscopic structural* instabilities. While the first are related to the rank-one convexity of an associated homogenized energy density, the latter are related to the coercivity of an associated microscopic boundary value problem. At both scales we detect instabilities of equilibrium states by superimposing wave-like perturbations. At macroscopic scale we consider classical plane waves giving rise to the definition of a generalized acoustic tensor. At microscopic scale we exploit Bloch–Floquet wave analysis, which allows to determine critical buckling modes of microstructures based on computations at unit-cell level. The microscopic material response is governed by a four-field variational principle of magneto-elasticity that is embedded in a framework of first-order computational homogenization. A series of numerical simulations reveals a spectrum of complex pattern transformations that could be triggered by appropriate microstructure design and coupled magneto-mechanical loading.

Keywords: homogenization, magnetorheological elastomers, stability, pattern transformation, Bloch–Floquet wave analysis

4.1 Introduction

Magnetorheological elastomers (MREs) are soft materials that are composed of an elastomer matrix and dispersed magnetizable particles. Due to the presence of the magnetizable particles MREs show pronounced magneto-mechanical coupling. This coupling expresses itself in terms of large magnetically induced deformations and elastic stiffness alterations (Jolly et al. [40], Farshad and Benine [25], Varga et al. [81, 82], Danas et al. [17]). These properties, together with high elastic stretchability, low weight and high durability, make MREs a prototype material for applications as soft actuators, tuned vibration absorbers, stiffness-tunable mounts or suspensions (Ginder et al. [31, 30, 32], Carlson and Jolly [15], Sutrisno et al. [73]).

The steeply advancing developments in experimental testing (Diguet et al. [21], Bodelot et al. [10]) and the recent progresses in manufacturing (Walter et al. [83], Bastola et al. [5]) open the door for new applications of MREs in engineering designs. Associated advancements call for the development of powerful and comprehensive material models. In this context we mention the general continuum theories on the modeling of magneto-mechanical interactions in soft bodies proposed by Dorfmann and Ogden [23], Brigadnov and Dorfmann [11], Dorfmann and Ogden [24], Steigmann [72], Kankanala and Triantafyllidis [42], Bustamante et al. [14]. The continuum-mechanical basis for these approaches was laid down by Truesdell and Toupin [80], Tiersten [74], Brown [13], Maugin and Eringen [48], Pao and Yeh [61], Pao [60] decades ago.

Next to the above phenomenological theories analytical homogenization schemes were developed by Ponte Castañeda and Galipeau [63], Galipeau and Ponte Castañeda [26, 27], providing estimates of the effective material response of MREs. The latter analytical tech-

niques are complemented by computational approaches to homogenization documented in Javili et al. [39], Keip and Rambausek [43, 44], Metsch et al. [49], Kalina et al. [41], Danas [16], Lefèvre et al. [46], Rambausek et al. [64]. Associated homogenization schemes allow for the computation of effective properties based on explicit consideration of physical and topological characteristics of the underlying microstructure.

However, since the related homogenized energy densities are calculated via an averaging process, it is impossible to impose classical stability requirements a priori. In fact, effective energy densities may lose *material stability* (related to ellipticity/rank-one convexity of effective moduli) even when all material models of the microscopic phases are polyconvex [1]. We refer to Triantafyllidis and Maker [77], Geymonat et al. [29], Triantafyllidis and Bardenhagen [76], Miehe et al. [55] for elaborations on microscopic and macroscopic stabilities in the context of homogenization.

Next to material instabilities, a periodic microstructure may suffer *structural instabilities*. These are associated with buckling-type bifurcations at micro-level and result in altered periodicities of the microstructure (Geymonat et al. [29], Triantafyllidis et al. [78], Bertoldi et al. [6], Michel et al. [50]). Depending on the application, it may be intended to prohibit or to trigger related phenomena. In this context, we refer to the recent review article by Kochmann and Bertoldi [45], in which structural instability phenomena of different periodic materials are discussed.

The theoretical stability analysis of heterogeneous materials stands on firm ground. We highlight the work of Geymonat et al. [29] treating a variety of multiscale instability phenomena of composites via rigorous mathematical analysis (see Abeyaratne and Triantafyllidis [1] for a basis). Following these seminal works, various implementations of stability analysis were performed in the field of mechanics by, for example, Miehe et al. [54], Triantafyllidis et al. [78], Bertoldi et al. [6], Michel et al. [50], Rudykh and deBotton [66], Slesarenko and Rudykh [71], Li et al. [47]. Extensions towards coupled problems cover, for example, the fields of electro- and magneto-elasticity, where the focus has mostly been on the analysis of material instabilities. In the field of electro-elasticity we mention the contributions of Bertoldi and Gei [8] on material and structural instabilities of layered media, of Rudykh and deBotton [67] on a general criterion for the onset of material instabilities of layered composites and of Goshkoderia and Rudykh [33] on material instabilities of general periodic media. Furthermore, we mention the work of Polukhov et al. [62] and Jandron and Henann [37] on a unified computational analysis of material and structural instabilities of general periodic electroactive composites. In the field of magneto-elasticity we highlight the contributions of Destrade and Ogden [19] on a general treatment of material stability of magnetoactive solids, of Rudykh and Bertoldi [65] on the material stability analysis of layered composites, and of Goshkoderia and Rudykh [34] on a material stability analysis similar to [33]. We further refer to Miehe et al. [55] for the analysis of material instabilities of fully coupled magneto-electro-mechanical composites.

We observe that in the field of magneto-elasticity a lot of attention has been paid to the analysis of *material instabilities*. A comprehensive framework allowing for the *structural stability analysis* of magnetoactive microstructures is however missing in the literature. While associated treatments are available in the field of electro-elasticity ([62, 37], the field of magneto-mechanical coupling yet remains to be touched. Due to the complex and nonlinear material response of the (ferro)magnetic inclusions and the high practical relevance of MREs, associated studies are expected to reveal important insights into

MRE design and optimization. Next to the applications of MREs mentioned in the first paragraph of the present section we highlight possible applications in devices with tunable acoustic, auxetic, phononic and photonic properties. Associated applications could take advantage of microscopic pattern transformations that can be induced by microscopic structural instabilities. For related studies that exploit mechanically induced microscopic pattern transformations we refer to [22, 7, 38, 9, 2, 84]. As it will be shown in the present work, MREs can be triggered to develop complex pattern transformations that would not be observable in purely mechanically driven scenarios. For example, in case of composites with stiff magnetic inclusions, magnetic loading gives rise to microscopic instabilities even under tension and compression. As was shown by Triantafyllidis et al. [78], Bertoldi and Boyce [7], Michel et al. [50], such an effect is not present under purely mechanical loading. We further show that in case of porous MREs, the range of possible instabilities goes far beyond the well-known instabilities observed under purely mechanical loading conditions. In the latter regard, we also mention the experimental study of [75] on porous magnetoactive structures and the computational study of Danas [16] on auxetic MRE microstructures.

Motivated by that, the present work will provide a unified analysis of macroscopic material and microscopic structural instability phenomena of soft magneto-elastic composites. To be specific, we consider periodic MRE microstructures with soft matrix and embedded inclusions. Point of departure is a microscopic variational formulation of magneto-elasticity embedded in the framework of computational homogenization (Section 4.2). To alleviate locking phenomena related to the quasi-incompressibility of the elastomer matrix, we make use of a four-field variational formulation in terms of displacements, magnetic vector potential, dilatation and pressure as primary variables, resulting in a mixed finite-element formulation. A minimization principle suitable for stability analysis is obtained by condensing out dilatation and pressure at element level. The coupled macroscopic material response is computed by means of periodic first-order computational homogenization. The homogenization approach employed in the present contribution closely follows our previous work [62] on the multiscale stability analysis of electroactive polymer composites. We will thus keep associated discussions short and only comment on the most relevant details that allow for a self-contained presentation. The treatment of macroscopic material and microscopic structural stability analysis is discussed in detail in Section 4.3. Once having established a corresponding numerical implementation, the framework is applied to the multiscale stability analysis of periodic MRE microstructures in Section 4.4. There, we analyze the influence of microscopic topological and material properties on the onset of instabilities under a variety of coupled loading conditions. Finally, the main findings of the present contribution will be summarized in Section 4.5.

4.2 Variational homogenization of magneto-elasticity

In what follows, we present a variational formulation of nonlinear magneto-elasticity in the context of computational homogenization. The homogenization framework allows for the consideration of heterogeneous microstructures, whose constituents could be described with specific constitutive laws. The term “micro” here refers to a length scale that is much smaller than the one of the macroscopic structure so that length scales are separated. Further assuming that the microstructure is periodic, we could identify a rep-

resentative volume element (RVE) that could be used to extract the effective response of the microstructure. In that respect, the macroscopic response is not governed by an effective constitutive law, but is rather defined by homogenization across the RVE. We give a graphical illustration of that procedure in Fig. 4.1.

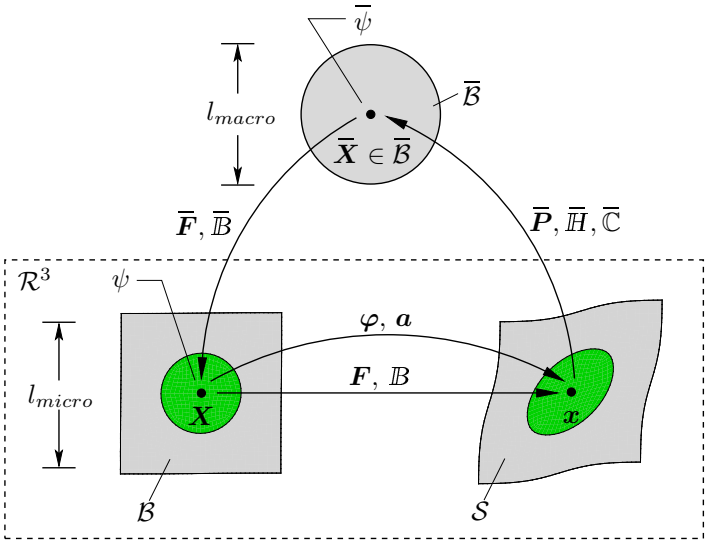

Figure 4.1: *Graphical illustration of computational homogenization in the context of large-strain magneto-elasticity.* At each integration point $\overline{\boldsymbol{X}}$ of the macroscopic structure $\overline{\mathcal{B}}$ with length scale l_{macro} an RVE denoted as $\mathcal{B}$ with length scale $l_{micro} \ll l_{macro}$ is attached. The scale transition from macro- to microscale is carried out by imposing boundary conditions associated with the macroscopic deformation gradient $\overline{\boldsymbol{F}}$ and the macroscopic magnetic induction $\overline{\mathbb{B}}$ on $\mathcal{B}$. After obtaining the solution of the microscopic boundary value problem, which is formulated in terms of the deformation map $\boldsymbol{\varphi}$ and the vector potential $\boldsymbol{a}$ as independent fields, a scale transition from micro- to macroscale is carried out. The scale transition is performed by averaging the microscopic dual fields given by the 1st Piola–Kirchhoff stress $\boldsymbol{P}$ and the magnetic field $\mathbb{H}$. These dual fields are obtained from an energy-density function ψ that is driven by the deformation gradient $\boldsymbol{F}$ and the magnetic induction $\mathbb{B}$. The averaging process results in the effective stresses $\overline{\boldsymbol{P}}$ and effective magnetic field $\overline{\mathbb{H}}$. The effective moduli $\overline{\mathbb{C}}$ are obtained by consistent linearization of the macroscopic field equations. The effective energy $\overline{\psi}$ is defined through an optimization problem on the domain $\mathcal{B}$.

4.2.1 Constitutive state variables at the microscopic level

In the present contribution, we are interested in the stability of magneto-mechanical problems. For this purpose, a variational formulation based on a minimization principle is beneficial. Such a minimization principle could be constructed from a potential that is formulated in terms of the deformation map $\boldsymbol{\varphi}$ and the vector potential $\boldsymbol{a}$. The latter independent fields are defined w.r.t. the reference (undeformed) configuration $\mathcal{B}$ as

$$\boldsymbol{\varphi} : \begin{cases} \mathcal{B} \times \mathcal{T} \to \mathcal{R}^3 \\ (\boldsymbol{X}, t) \mapsto \boldsymbol{\varphi}(\boldsymbol{X}, t) \end{cases} \quad \text{and} \quad \boldsymbol{a} : \begin{cases} \mathcal{B} \times \mathcal{T} \to \mathcal{R}^3 \\ (\boldsymbol{X}, t) \mapsto \boldsymbol{a}(\boldsymbol{X}, t) \,. \end{cases} \tag{4.1}$$

The deformation map $\boldsymbol{\varphi}$ is a bijective map that maps the reference configuration $\mathcal{B}$ onto the current configuration $\mathcal{S}$. The time t will in the following be considered as a loading parameter. Based on the above independent fields, we define the deformation gradient $\boldsymbol{F}$

and the magnetic induction $\mathbb{B}$ as[13]

$$\boldsymbol{F} = \operatorname{Grad} \boldsymbol{\varphi}(\boldsymbol{X}, t) \quad \text{and} \quad \mathbb{B} = \operatorname{Curl} \boldsymbol{a}(\boldsymbol{X}, t) \tag{4.2}$$

and denote them as primary fields. By definition of the latter quantities, we automatically fulfill deformation continuity $\operatorname{Curl} \boldsymbol{F} = \operatorname{Curl}(\operatorname{Grad} \boldsymbol{\varphi}) \equiv \boldsymbol{0}$ and Gauss' law of magnetostatics $\operatorname{Div} \mathbb{B} = \operatorname{Div}(\operatorname{Curl} \boldsymbol{a}) \equiv 0$.

In the context of periodic first-order homogenization, the independent fields can be decomposed into macroscopic and microscopic contributions [55]

$$\boldsymbol{\varphi}(\boldsymbol{X}, t) = \overline{\boldsymbol{F}}(t)\boldsymbol{X} + \widetilde{\boldsymbol{\varphi}}(\boldsymbol{X}, t) \quad \text{and} \quad \boldsymbol{a}(\boldsymbol{X}, t) = \frac{1}{2}\overline{\mathbb{B}}(t) \times \boldsymbol{X} + \widetilde{\boldsymbol{a}}(\boldsymbol{X}, t)\,, \tag{4.3}$$

where $\widetilde{\boldsymbol{\varphi}}$ and $\widetilde{\boldsymbol{a}}$ denote microscopic fluctuations of the deformation map and the vector potential, respectively. The latter are constrained by periodic boundary conditions [35, 52, 68] of the form $[\![\widetilde{\boldsymbol{\varphi}}]\!] = \boldsymbol{0}$ and $[\![\widetilde{\boldsymbol{a}}]\!] = \boldsymbol{0}$, where $[\![(\cdot)]\!] = (\cdot)^+ - (\cdot)^-$ corresponds to the jump of the quantity $(\cdot)$ across opposite boundaries $\partial\mathcal{B}^+$ and $\partial\mathcal{B}^-$ of the RVE, where $\partial\mathcal{B}^+ \cup \partial\mathcal{B}^- = \partial\mathcal{B}$. We refer to Fig. 4.2 for an illustration.

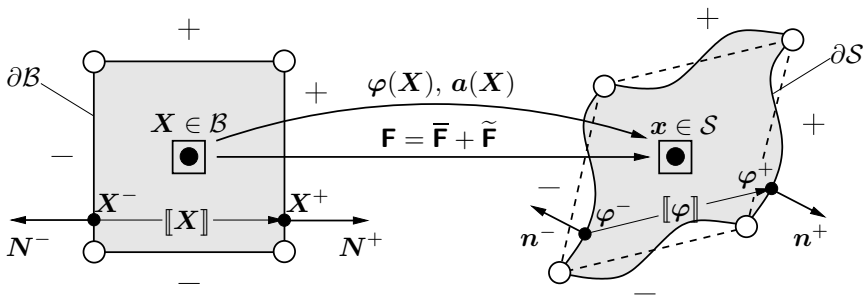

Figure 4.2: *Periodic boundary conditions of a representative volume element.* The RVE is driven by the macroscopic deformation gradient $\overline{\boldsymbol{F}}$ and magnetic induction $\overline{\mathbb{B}}$ under the assumption of periodic boundary conditions for the fluctuations of the deformation map $\widetilde{\boldsymbol{\varphi}}$ and magnetic vector potential $\widetilde{\boldsymbol{a}}$. The symbols '+' and '−' are put in order to indicate pairs of periodic boundaries in the reference configuration $\mathcal{B}$ and current configuration $\mathcal{S}$. We have assembled the deformation gradient and the magnetic induction in the field $\mathsf{F} := [\boldsymbol{F}, \mathbb{B}]^T$ to arrive at a compact illustration.

In (4.3), $\overline{\boldsymbol{F}}$ and $\overline{\mathbb{B}}$ denote the macroscopic deformation gradient and magnetic induction, respectively. By insertion of (4.3) into (4.2) we are able to decompose the corresponding primary fields as

$$\boldsymbol{F} = \overline{\boldsymbol{F}} + \widetilde{\boldsymbol{F}} \quad \text{and} \quad \mathbb{B} = \overline{\mathbb{B}} + \widetilde{\mathbb{B}}\,. \tag{4.4}$$

Further, by integrating both sides of the latter equations over the RVE with volume $|\mathcal{B}|$, we find that

$$\overline{\boldsymbol{F}} = \frac{1}{|\mathcal{B}|}\int_{\mathcal{B}} \boldsymbol{F}\,\mathrm{d}V = \frac{1}{|\mathcal{B}|}\int_{\partial\mathcal{B}} \boldsymbol{\varphi} \otimes \boldsymbol{N}\,\mathrm{d}A \quad \text{and} \quad \overline{\mathbb{B}} = \frac{1}{|\mathcal{B}|}\int_{\mathcal{B}} \mathbb{B}\,\mathrm{d}V = \frac{1}{|\mathcal{B}|}\int_{\partial\mathcal{B}} \boldsymbol{N} \times \boldsymbol{a}\,\mathrm{d}A\,, \tag{4.5}$$

[13] The uppercase operators "Curl", "Div" and "Grad" refer to differentiation with respect to the reference coordinates. Likewise, the lowercase operators "curl", "div" and "grad" refer to differentiation with respect to the current coordinates.

where $\boldsymbol{N}(\boldsymbol{X}^-) =: \boldsymbol{N}^- = -\boldsymbol{N}^+ := -\boldsymbol{N}(\boldsymbol{X}^- + [\![\boldsymbol{X}]\!])$ are outward unit normals of the periodic RVE. In order to arrive at (4.5), we have made use of the periodicity conditions

$$\int_{\mathcal{B}} \widetilde{\boldsymbol{F}} \, \mathrm{d}V = \int_{\partial\mathcal{B}} \widetilde{\boldsymbol{\varphi}} \otimes \boldsymbol{N} \, \mathrm{d}A = \boldsymbol{0} \quad \text{and} \quad \int_{\mathcal{B}} \widetilde{\mathbb{B}} \, \mathrm{d}V = \int_{\partial\mathcal{B}} \boldsymbol{N} \times \tilde{\boldsymbol{a}} \, \mathrm{d}A = \boldsymbol{0} \,, \tag{4.6}$$

where we have further assumed continuity of the independent fields at micro-level.

4.2.2 Constitutive functions at the microscopic level

In order to describe the material behavior at the microscopic level, we follow Dorfmann and Ogden [23] and Steigmann [72] by assuming the existence of an additive energy-density function $\widehat{\psi}$ that is defined per unit volume of the reference configuration and given as

$$\widehat{\psi}(\boldsymbol{F}, \mathbb{B}) = \widehat{\psi}^{mec}(\boldsymbol{F}) + \widehat{\psi}^{mag}(\boldsymbol{F}, \mathbb{B}) \,. \tag{4.7}$$

We further assume that the energy density ψ is polyconvex[14] w.r.t. $\boldsymbol{F}$ and $\mathbb{B}$. Moreover, objectivity of $\widehat{\psi}$ will be automatically satisfied by implicitly defining $\widehat{\psi}$ as a function of the right Cauchy–Green deformation tensor $\boldsymbol{C} = \boldsymbol{F}^T\boldsymbol{F}$. Since we are dealing with elastomeric, that is nearly incompressible, materials we further consider a split of the mechanical energy into volumetric and isochoric parts

$$\widehat{\psi}^{mec}(\boldsymbol{F}, J) = \widehat{\psi}^{mec,vol}(J) + \widehat{\psi}^{mec,iso}(\boldsymbol{F}^{iso}) \,, \tag{4.8}$$

where $\widehat{\psi}^{mec,vol}$ is the volumetric part depending on $J = \det \boldsymbol{F}$ and $\widehat{\psi}^{mec,iso}$ is the isochoric part depending on the isochoric deformation gradient $\boldsymbol{F}^{iso} = J^{-1/3}\boldsymbol{F}$. The magnetic energy function $\widehat{\psi}^{mag}$ is also assumed to have an additive structure, i.e.,

$$\widehat{\psi}^{mag}(\boldsymbol{F}, \mathbb{B}) = \widehat{\psi}^{mag,0}(\boldsymbol{F}, \mathbb{B}) + \widehat{\psi}^{mag,sat}(\boldsymbol{F}, \mathbb{B}) \,, \tag{4.9}$$

where $\widehat{\psi}^{mag,0}$ characterizes the Maxwell contribution for all constituents of an MRE irrespective of their magnetic properties and $\widehat{\psi}^{mag,sat}$ models saturation effects of magnetizable constituents. We will give explicit forms of the above energy densities in Section 4.4.

From the energy-density function (4.7) we determine the 1st Piola-Kirchhoff stress tensor $\boldsymbol{P}$ and the reference magnetic field $\mathbb{H}$ as

$$\boldsymbol{P} = \partial_{\boldsymbol{F}}\widehat{\psi}(\boldsymbol{F}, \mathbb{B}) \quad \text{and} \quad \boldsymbol{P} = \partial_{\mathbb{B}}\widehat{\psi}(\boldsymbol{F}, \mathbb{B}) \,. \tag{4.10}$$

The current magnetic field and magnetic induction can be obtained via push-forward operations, i.e., $\mathbb{h} = \boldsymbol{F}^{-T}\mathbb{H}$ and $\mathbb{b} = \boldsymbol{F}\mathbb{B}/J$ [23]. These fields are related by

$$\mathbb{b} = \mu_0(\mathbb{h} + \mathbb{m}) \,, \tag{4.11}$$

[14] A function $\widehat{\psi}(\boldsymbol{F}, \mathbb{B}) = \widehat{\psi}(\mathbb{F})$ is said to be polyconvex w.r.t. $\boldsymbol{F}$ and $\mathbb{B}$ if there exists a function $\widehat{\psi}(\mathbb{F}) : \mathcal{R}^{25} \to \mathcal{R}$ that is convex w.r.t. each argument of the extended set $\mathbb{F} = \{\boldsymbol{F}, \operatorname{cof}\boldsymbol{F}, \det\boldsymbol{F}, \mathbb{B}, \boldsymbol{F}\mathbb{B}\} \in \mathcal{R}^{25}$, that is [3, 36, 69]

$$\widehat{\psi}(\alpha\mathbb{F}_1 + (1-\alpha)\mathbb{F}_2) \leq \alpha\widehat{\psi}(\mathbb{F}_1) + (1-\alpha)\widehat{\psi}(\mathbb{F}_2) \quad \forall\alpha \in [0,1] \;\text{ and }\; \mathbb{F}_1 \neq \mathbb{F}_2 \,.$$

where m is the magnetization in the current configuration and $\mu_0 = 4\pi \cdot 10^{-7}\,\mathrm{N/A^2}$ is the magnetic permeability of vacuum. The magnetization can also be derived from the underlying energy-density function via

$$\mathit{m} = -\boldsymbol{F}^{-T}\partial_{\mathbb{B}}\widehat{\psi}^{mag,sat}(\boldsymbol{F},\mathbb{B})\,. \tag{4.12}$$

4.2.3 Variational formulation of computational homogenization

In order to alleviate locking phenomena that could arise in the numerical treatment of the nearly incompressible behavior of the elastomeric matrix, we implement a four-field Hu–Washizu-type variational formulation at micro-level. This approach is based on the classical approach to nearly incompressibile elasticity proposed by Simo et al. [70]. The four-field variational formulation takes into account continuous interpolation of the deformation map $\boldsymbol{\varphi}$ and vector potential $\boldsymbol{a}$ as well as discontinuous interpolation of dilatation θ and pressure p. This setting relates our approach closely to the one of Okada and Hisada [59], who employed a Hellinger–Reissner-type mixed formulation to the homogenization of purely mechanical problems.

To arrive at a compact representation of the variational formulation, we only document the central ingredients that may prove helpful for a general understanding. For further information on aspects of numerical implementation and related issues we refer to Miehe [51], Brink and Stein [12], Polukhov et al. [62] and the associated references cited therein.

In the above described setting, the macroscopic energy-density function $\overline{\psi}$ can be defined as the optimum of the homogenized microscopic potential via

$$\overline{\psi}(\overline{\boldsymbol{F}},\overline{\mathbb{B}};\overline{\boldsymbol{X}}) = \inf_{\widetilde{\boldsymbol{\varphi}}\in\mathcal{W}_{\widetilde{\boldsymbol{\varphi}}}}\inf_{\widetilde{\boldsymbol{a}}\in\mathcal{W}_{\widetilde{\boldsymbol{a}}}}\inf_{\theta\in\mathcal{W}_{\theta}}\sup_{p\in\mathcal{W}_{p}}\left\{\frac{1}{|\mathcal{B}|}\int_{\mathcal{B}}\hat{\pi}(\overline{\boldsymbol{F}}+\operatorname{Grad}\widetilde{\boldsymbol{\varphi}},\overline{\mathbb{B}}+\operatorname{Curl}\widetilde{\boldsymbol{a}},\theta,p)\,\mathrm{d}V\right\}, \tag{4.13}$$

where $\hat{\pi}$ is the microscopic potential density per unit volume of $\mathcal{B}$ given by

$$\hat{\pi} = \psi^{mec,vol}(\theta) + p(J-\theta) + \psi^{mec,iso}(\boldsymbol{F}) + \psi^{mag}(\boldsymbol{F},\mathbb{B})\,. \tag{4.14}$$

Thus, the macroscopic energy corresponds to the stationary point of its volume averaged microscopic counterpart in the admissible spaces

$$\begin{aligned}
\widetilde{\boldsymbol{\varphi}} \in \mathcal{W}_{\widetilde{\boldsymbol{\varphi}}} &:= \big\{\widetilde{\boldsymbol{\varphi}} \in H^1(\mathcal{B}) \mid \widetilde{\boldsymbol{\varphi}}^{+} = \widetilde{\boldsymbol{\varphi}}^{-} \text{on } \partial\mathcal{B} = \partial\mathcal{B}^{+} \cup \partial\mathcal{B}^{-}\big\},\\
\widetilde{\boldsymbol{a}} \in \mathcal{W}_{\widetilde{\boldsymbol{a}}} &:= \big\{\widetilde{\boldsymbol{a}} \in H(\operatorname{Curl},\mathcal{B}) \mid \widetilde{\boldsymbol{a}}^{+} = \widetilde{\boldsymbol{a}}^{-} \text{on } \partial\mathcal{B} = \partial\mathcal{B}^{+} \cup \partial\mathcal{B}^{-}\big\},\\
\theta \in \mathcal{W}_{\theta} &:= \big\{\theta \in L^2(\mathcal{B})\big\},\\
p \in \mathcal{W}_{p} &:= \big\{p \in L^2(\mathcal{B})\big\}\,.
\end{aligned} \tag{4.15}$$

The macroscopic dual fields $\overline{\mathbf{P}} := [\overline{\boldsymbol{P}},\overline{\mathbb{H}}]^T$ and coupled moduli $\overline{\mathbb{C}}$ can be obtained from the homogenized energy density (4.13) by

$$\overline{\mathbf{P}} := \partial_{\overline{\mathbf{F}}}\overline{\psi}(\overline{\boldsymbol{F}},\overline{\mathbb{B}};\overline{\boldsymbol{X}}) \quad \text{and} \quad \overline{\mathbb{C}} := \partial^2_{\overline{\mathbf{F}}\,\overline{\mathbf{F}}}\overline{\psi}(\overline{\boldsymbol{F}},\overline{\mathbb{B}};\overline{\boldsymbol{X}})\,, \tag{4.16}$$

where $\overline{\mathbf{F}} := [\overline{\boldsymbol{F}},\overline{\mathbb{B}}]^T$ is a generalized array of the primary fields at macroscale.

4.2.4 Euler–Lagrange equations and linearization

The Euler–Lagrange equations at the microscale follow from the first variation of (4.13) at a macro-state $\{\overline{\boldsymbol{F}}, \overline{\mathbb{B}}\}$ arising as

$$\delta\overline{\psi}(\boldsymbol{F}, \mathbb{B}; \overline{\boldsymbol{F}}, \overline{\mathbb{B}}) = \frac{1}{|\mathcal{B}|}\int_{\mathcal{B}} \begin{bmatrix} \delta\widetilde{\boldsymbol{F}} \\ \delta\widetilde{\mathbb{B}} \\ \delta\theta \\ \delta p \end{bmatrix} \cdot \begin{bmatrix} \partial_{\boldsymbol{F}}(\psi^{mec,iso} + \psi^{mag}) + pJ\boldsymbol{F}^{-T} \\ \partial_{\mathbb{B}}\psi^{mag} \\ \partial_\theta\psi^{mec,vol}(\theta) - p \\ J - \theta \end{bmatrix} \mathrm{d}V = 0\,, \tag{4.17}$$

where $\delta\widetilde{\boldsymbol{\varphi}} \in \mathcal{W}_{\widetilde{\boldsymbol{\varphi}}}$, $\delta\widetilde{\boldsymbol{a}} \in \mathcal{W}_{\widetilde{\boldsymbol{a}}}$, $\delta\theta \in \mathcal{W}_\theta$ and $\delta p \in \mathcal{W}_p$ are admissible variations. Employing standard integral theorems, the Euler–Lagrange equations appear as

1. Balance of linear momentum	$\mathrm{Div}[\partial_{\boldsymbol{F}}\hat{\pi}]$	$= \boldsymbol{0}$	in	$\mathcal{B}$
2. Ampere's law	$\mathrm{Curl}[\partial_{\mathbb{B}}\psi^{mag}]$	$= \boldsymbol{0}$	in	$\mathcal{B}$
3. Continuity of tractions	$[\![\partial_{\boldsymbol{F}}\hat{\pi}]\!] \cdot \boldsymbol{N}$	$= \boldsymbol{0}$	on	$\partial\mathcal{B}$
4. Continuity of tangential magnetic field	$[\![\partial_{\mathbb{B}}\psi^{mag}]\!] \times \boldsymbol{N}$	$= \boldsymbol{0}$	on	$\partial\mathcal{B}$
5. Pressure field	$\partial_\theta\psi^{mec,vol}(\theta) - p$	$= 0$	in	$\mathcal{B}$
6. Dilatation field	$J - \theta$	$= 0$	in	$\mathcal{B}$

(4.18)

4.3 Multiscale stability analysis of periodic MREs

In the following, we apply the above presented variational framework to the stability analysis of magneto-elastic microstructures. We focus on two kinds of instabilities given by *macroscopic material* and *microscopic structural* instabilities. The macroscopic material instabilities are related to the loss of strong ellipticity of macroscopic moduli and are investigated by checking the positive definiteness of a generalized acoustic tensor. Microscopic structural instabilities are associated with buckling phenomena at the micro-level and are investigated by Bloch–Floquet wave analysis. While macroscopic instabilities of MREs have seen a lot of attention [19, 26, 65, 34], the investigation of microscopic instabilities of MREs is still a largely unexplored field.

In what follows we give a compact outline of the theory without discussing details of the associated numerical implementation. The latter closely follows the one documented in our previous work [62]. We further refer to Geymonat et al. [29] for a general treatment of the mentioned instabilities for elastic materials.

4.3.1 Macroscopic material stability analysis

As mentioned above, macroscopic material stability is associated with strongly elliptic material moduli. Usually, strongly elliptic moduli can be enforced by consideration of quasiconvex[15] energy-density functions [3, 69]. In the realm of homogenization we however cannot guarantee quasiconvexity of the macroscopic energy density $\overline{\psi}$. We refer to

[15] Strong ellipticity is related to rank-one convex energy densities and quasiconvexity implies rank-one convexity. A quasiconvex energy density guarantees the existence of solutions of a corresponding boundary value problem, see, for example, Morrey [56] as well as Ball and James [4].

Abeyaratne and Triantafyllidis [1] who have shown that even polyconvex microscopic energies do not imply quasiconvexity at the macroscopic scale. In fact, we may even lose macroscopic rank-one convexity, which is usually associated with the creation of second-order discontinuities or shear bands at the (homogeneous) mesoscale of the equivalent homogenized medium (see, for example, Truesdell and Noll [79, Sec. 68 and 71]).

We follow Destrade and Ogden [18] and analyze the strong ellipticity of the macroscopic coupled moduli $\overline{\mathbb{C}}$ by considering infinitesimal homogeneous plane waves of the form

$$\delta\overline{\boldsymbol{\varphi}} = \overline{\boldsymbol{n}} f(\overline{\boldsymbol{X}} \cdot \overline{\boldsymbol{N}} - \overline{c}\,\overline{t}) \quad \text{and} \quad \delta\overline{\mathcal{B}} = \overline{\boldsymbol{M}} g(\overline{\boldsymbol{X}} \cdot \overline{\boldsymbol{N}} - \overline{c}\,\overline{t})\,, \tag{4.19}$$

where $\overline{\boldsymbol{N}}$ denotes the propagation direction and $\overline{\boldsymbol{n}}$ as well as $\overline{\boldsymbol{M}}$ the corresponding amplitude directions of the waves. Furthermore, $\overline{c}$ signifies the speed of the waves and the functions f as well as g are assumed to have sufficient continuity. Superimposing $\delta\overline{\boldsymbol{\varphi}}$ and $\delta\overline{\mathcal{B}}$ on the current deformation state gives the linearized Euler–Lagrange equations

$$\operatorname{Div}[\overline{\mathbb{A}} : \delta\overline{\boldsymbol{F}} + \overline{\mathbb{G}} \cdot \delta\overline{\mathcal{B}}] = \overline{\rho}_0 \delta\ddot{\overline{\boldsymbol{\varphi}}}(\overline{\boldsymbol{X}}, \overline{t}) \quad \text{and} \quad \operatorname{Curl}[\overline{\mathbb{G}}^T : \delta\overline{\boldsymbol{F}} + \overline{\mathbb{K}} \cdot \delta\overline{\mathcal{B}}] = \boldsymbol{0}\,, \tag{4.20}$$

where $\delta\overline{\boldsymbol{F}}$ and $\delta\overline{\mathcal{B}}$ signify infinitesimal increments of the macroscopic deformation gradient and the magnetic induction, respectively. The individual moduli tensors of the coupled macroscopic modulus $\overline{\mathbb{C}}$ are given by $\overline{\mathbb{A}} = \partial^2_{\overline{\boldsymbol{F}}\,\overline{\boldsymbol{F}}}\overline{\psi}$, $\overline{\mathbb{K}} = \partial^2_{\overline{\mathcal{B}}\,\overline{\mathcal{B}}}\overline{\psi}$, $\overline{\mathbb{G}} = \partial^2_{\overline{\boldsymbol{F}}\,\overline{\mathcal{B}}}\overline{\psi}$ and $\overline{\mathbb{G}}^T = \partial^2_{\overline{\mathcal{B}}\,\overline{\boldsymbol{F}}}\overline{\psi}$.

As we are considering infinitesimal perturbations of the magnetic induction around an equilibrium state, Gauss's law of magnetostatics can be expressed in terms of the infinitesimal perturbations such that

$$\operatorname{Div}\delta\overline{\mathcal{B}} = 0 \quad \overset{(4.19)_2}{\Rightarrow} \quad \overline{\boldsymbol{M}} \cdot \overline{\boldsymbol{N}} = 0\,. \tag{4.21}$$

Considering $(4.21)_2$ in (4.20) and after some manipulations, we obtain the following condition for the strong ellipticity of macroscopic moduli (Destrade and Ogden [19])

$$\overline{\Lambda} = \inf_{\|\overline{\boldsymbol{N}}\|=1} \left\{\overline{\boldsymbol{n}} \cdot \overline{\boldsymbol{\Gamma}}(\overline{\boldsymbol{N}}) \cdot \overline{\boldsymbol{n}}\right\} = \inf_{\|\overline{\boldsymbol{N}}\|=1} \left\{\overline{\rho}_0 \overline{c}^2 \overline{\boldsymbol{n}} \cdot \overline{\boldsymbol{n}}\right\} \geq 0\,, \tag{4.22}$$

where $\overline{\boldsymbol{\Gamma}}(\overline{\boldsymbol{N}})$ is the (Green–)Christoffel tensor or generalized magneto-mechanical acoustic tensor. It can explicitly be given as [19]

$$\overline{\boldsymbol{\Gamma}}(\overline{\boldsymbol{N}}) := \overline{\boldsymbol{Q}}(\overline{\boldsymbol{N}}) - \frac{[\overline{\mathbb{R}}(\overline{\boldsymbol{N}}) \cdot \overline{\boldsymbol{M}}] \otimes [\overline{\mathbb{R}}(\overline{\boldsymbol{N}}) \cdot \overline{\boldsymbol{M}}]}{\overline{\boldsymbol{M}} \cdot \overline{\mathbb{K}} \cdot \overline{\boldsymbol{M}}}\,, \tag{4.23}$$

where $\overline{Q}_{ac} = \overline{\mathbb{A}}_a{}^A{}_c{}^B \overline{N}_A \overline{N}_B$ and $\overline{R}_{aB} = \overline{G}_a{}^A{}_B \overline{N}_A$ (for a representation in two spatial dimensions please refer to Appendix A). Positive definiteness of the Christoffel tensor ensures strong ellipticity of the macroscopic magneto-elastic moduli. We note that in the absence of magnetic loading the second term in (4.23) vanishes and the Christoffel tensor $\overline{\boldsymbol{\Gamma}}$ reduces to the acoustic tensor $\overline{\boldsymbol{Q}}$ of the purely mechanical problem.

By taking a look at (4.22) we observe that a macroscopic instability is associated with a non-positive determinant of the Christoffel tensor $\det\overline{\boldsymbol{\Gamma}}$. Therefore, the condition for the loss of strong ellipticity can alternatively be expressed by

$$\inf_{\|\overline{\boldsymbol{N}}\|=1} \left\{\det\overline{\boldsymbol{\Gamma}}(\overline{\mathbb{C}}, \overline{\boldsymbol{N}})\right\} \begin{cases} > 0 & \text{for strictly elliptic state} \\ \leq 0 & \text{for not strictly elliptic state}\,. \end{cases} \tag{4.24}$$

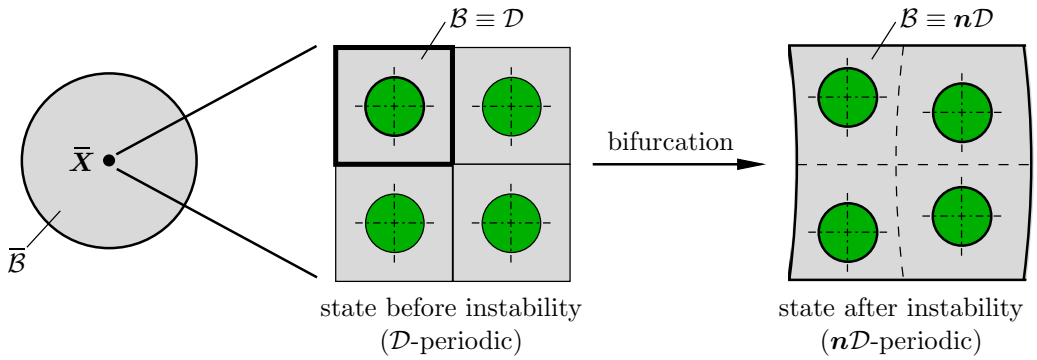

Figure 4.3: *Change of periodicity of a microstructure due to microscopic structural instability.* Before the instability the microstructure is $\mathcal{D}$-periodic, so that its overall response could be computed from a single unit cell. As a result of the instability, the microstructure shifts into an $n\mathcal{D}$-periodic configuration. In the given example, the representative volume element is then composed of 2×2 unit cells.

In a numerical implementation, the above condition of strong ellipticity can be checked either by using an iterative scheme (Miehe and Schröder [53]) or by searching for a non-positive determinant for discrete directions $\overline{\boldsymbol{N}}$.

4.3.2 Microscopic structural stability analysis

Next to the above discussed material instabilities at the macro-level, additional instabilities may occur at the microscopic level. These could be of material or of structural kind. We are focusing on structural instabilities in the following[16]. Such instabilities are associated with bifurcations occurring in RVEs that are composed of several unit cells. At such bifurcation, the microstructure could find an energetically more favorable state having a periodicity that could not be expressed with only a single unit cell (please refer to Fig. 4.3 for a graphical illustration). We express this relationship by (Müller [57])

$$\overline{\psi}(\overline{\boldsymbol{F}}, \overline{\mathbb{B}}; \overline{\boldsymbol{X}}) = \inf_{\boldsymbol{n} \in \mathbb{N}^3} \overline{\psi}^{\boldsymbol{n}}(\overline{\boldsymbol{F}}, \overline{\mathbb{B}}; \overline{\boldsymbol{X}}) \,, \tag{4.25}$$

where $\overline{\psi}^{\boldsymbol{n}}$ is the effective energy density associated with a particular realization of the RVE ($\boldsymbol{n} = [n_1\, n_2\, n_3]^T \in \mathbb{N}^3$ denotes the number of generic unit cells $\mathcal{D}$ in three spatial directions). That energy density follows from a variational principle (Müller [57])

$$\overline{\psi}^{\boldsymbol{n}}(\overline{\boldsymbol{F}}, \overline{\mathbb{B}}; \overline{\boldsymbol{X}}) = \inf_{\widetilde{\boldsymbol{\varphi}}_{\#} \in \mathcal{W}_{\widetilde{\boldsymbol{\varphi}}_{\#}}} \inf_{\widetilde{\boldsymbol{a}}_{\#} \in \mathcal{W}_{\widetilde{\boldsymbol{a}}_{\#}}} \frac{1}{|\boldsymbol{n}\mathcal{D}|} \int_{\boldsymbol{n}\mathcal{D}} \widehat{\psi}(\overline{\boldsymbol{F}} + \operatorname{Grad} \widetilde{\boldsymbol{\varphi}}_{\#}, \overline{\mathbb{B}} + \operatorname{Curl} \widetilde{\boldsymbol{a}}_{\#}) \, \mathrm{d}V \,, \tag{4.26}$$

where fluctuations are now considered to be periodic w.r.t. the enlarged representative volume element $\boldsymbol{n}\mathcal{D}$. This motivates the function spaces

$$\begin{aligned} \widetilde{\boldsymbol{\varphi}}_{\#} \in \mathcal{W}_{\widetilde{\boldsymbol{\varphi}}_{\#}} &:= \big\{ \widetilde{\boldsymbol{\varphi}}_{\#} \in H^1(\mathcal{B}) \quad\;\; | \; \widetilde{\boldsymbol{\varphi}}^{+}_{\#} = \widetilde{\boldsymbol{\varphi}}^{-}_{\#} \text{ on } \partial\boldsymbol{n}\mathcal{D} \big\}, \\ \widetilde{\boldsymbol{a}}_{\#} \in \mathcal{W}_{\widetilde{\boldsymbol{a}}_{\#}} &:= \big\{ \widetilde{\boldsymbol{a}}_{\#} \in H(\operatorname{Curl}, \mathcal{B}) \; | \; \widetilde{\boldsymbol{a}}^{+}_{\#} = \widetilde{\boldsymbol{a}}^{-}_{\#} \;\; \text{on } \partial\boldsymbol{n}\mathcal{D} \big\} \,. \end{aligned} \tag{4.27}$$

Based on this setting, a microscopic structural instability is characterized by a vanishing or negative coercivity constant of the energy functional defined in (4.25) (Geymonat et al.

[16] For the analysis of microscopic material instabilities we refer to Miehe et al. [55].

[29])

$$\Lambda = \inf_{\boldsymbol{n}\in\mathbb{N}^3} \inf_{\widetilde{\boldsymbol{\varphi}}_\#\in\mathcal{W}_{\widetilde{\boldsymbol{\varphi}}_\#}} \inf_{\widetilde{\boldsymbol{a}}_\#\in\mathcal{W}_{\widetilde{\boldsymbol{a}}_\#}} \left\{ \int_{\boldsymbol{n}\mathcal{D}} \begin{bmatrix} \operatorname{Grad}\delta\widetilde{\boldsymbol{\varphi}}_\# \\ \operatorname{Curl}\delta\widetilde{\boldsymbol{a}}_\# \end{bmatrix} \cdot \begin{bmatrix} \partial^2_{\boldsymbol{F}\boldsymbol{F}}\widehat{\psi} & \partial^2_{\boldsymbol{F}\mathbb{B}}\widehat{\psi} \\ \partial^2_{\mathbb{B}\boldsymbol{F}}\widehat{\psi} & \partial^2_{\mathbb{B}\mathbb{B}}\widehat{\psi} \end{bmatrix} \cdot \begin{bmatrix} \operatorname{Grad}\delta\widetilde{\boldsymbol{\varphi}}_\# \\ \operatorname{Curl}\delta\widetilde{\boldsymbol{a}}_\# \end{bmatrix} \mathrm{d}V \right. \\ \left. \Big/ \int_{\boldsymbol{n}\mathcal{D}} \begin{bmatrix} \operatorname{Grad}\delta\widetilde{\boldsymbol{\varphi}}_\# \\ \operatorname{Curl}\delta\widetilde{\boldsymbol{a}}_\# \end{bmatrix} \cdot \begin{bmatrix} \operatorname{Grad}\delta\widetilde{\boldsymbol{\varphi}}_\# \\ \operatorname{Curl}\delta\widetilde{\boldsymbol{a}}_\# \end{bmatrix} \mathrm{d}V \right\}, \tag{4.28}$$

where the expression in the curly brackets is associated with the second variation of (4.26) and evaluated at an equilibrium point. We refer to Miehe et al. [54] for more detailed information.

The stability criterion (4.28) requires the minimization w.r.t. $\boldsymbol{n}$. This necessitates the analysis of different representative volume elements that increase in size with the number of unit cells considered in $\boldsymbol{n}$. Since this is not feasible in most practical situations we follow Triantafyllidis and Maker [77], Geymonat et al. [29], Triantafyllidis et al. [78], Bertoldi et al. [6] and employ Bloch–Floquet wave analysis for the detection of a microscopic structural instability. Based on Bloch–Floquet wave analysis we are able to express the microscopic coercivity Λ in terms of periodic perturbations $(\delta\widetilde{\boldsymbol{\varphi}}_\#, \delta\widetilde{\boldsymbol{a}}_\#) \in \mathcal{W}_{(\widetilde{\boldsymbol{\varphi}}_\#, \widetilde{\boldsymbol{a}}_\#)}$ that are related to unit-cell-periodic perturbations $(\delta\widetilde{\boldsymbol{\varphi}}, \delta\widetilde{\boldsymbol{a}}) \in \mathcal{W}_{(\widetilde{\boldsymbol{\varphi}}, \widetilde{\boldsymbol{a}})}$. They are defined via

$$\delta\widetilde{\boldsymbol{\varphi}}_\#(\boldsymbol{X}, \boldsymbol{k}) := \delta\widetilde{\boldsymbol{\varphi}} \exp[\mathrm{i}\,\boldsymbol{k}\cdot\boldsymbol{X}] \quad \text{and} \quad \delta\widetilde{\boldsymbol{a}}_\#(\boldsymbol{X}, \boldsymbol{k}) := \delta\widetilde{\boldsymbol{a}} \exp[\mathrm{i}\,\boldsymbol{k}\cdot\boldsymbol{X}], \tag{4.29}$$

where $\delta\widetilde{\boldsymbol{\varphi}}$ and $\delta\widetilde{\boldsymbol{a}}$ are $\mathcal{D}$-periodic and $\boldsymbol{k}$ with $[\boldsymbol{k}] = [k_1, k_2, k_3]^T$ is a wave vector[17] characterizing the wavelength of the $\boldsymbol{n}\mathcal{D}$-periodic perturbations. Considering (4.29) in the second variation of (4.26) the microscopic coercivity constant reads

$$\Lambda = \inf_{k_i\in[0,2\pi[} \inf_{\widetilde{\boldsymbol{\varphi}}_\#\in\mathcal{W}_{\widetilde{\boldsymbol{\varphi}}_\#}} \inf_{\widetilde{\boldsymbol{a}}_\#\in\mathcal{W}_{\widetilde{\boldsymbol{a}}_\#}} \left\{ \int_{\mathcal{D}} \begin{bmatrix} \operatorname{Grad}\delta\widetilde{\boldsymbol{\varphi}}^\star_\# \\ \operatorname{Curl}\delta\widetilde{\boldsymbol{a}}^\star_\# \end{bmatrix} \cdot \begin{bmatrix} \partial^2_{\boldsymbol{F}\boldsymbol{F}}\widehat{\psi} & \partial^2_{\boldsymbol{F}\mathbb{B}}\widehat{\psi} \\ \partial^2_{\mathbb{B}\boldsymbol{F}}\widehat{\psi} & \partial^2_{\mathbb{B}\mathbb{B}}\widehat{\psi} \end{bmatrix} \cdot \begin{bmatrix} \operatorname{Grad}\delta\widetilde{\boldsymbol{\varphi}}_\# \\ \operatorname{Curl}\delta\widetilde{\boldsymbol{a}}_\# \end{bmatrix} \mathrm{d}V \right. \\ \left. \Big/ \int_{\mathcal{D}} \begin{bmatrix} \operatorname{Grad}\delta\widetilde{\boldsymbol{\varphi}}^\star_\# \\ \operatorname{Curl}\delta\widetilde{\boldsymbol{a}}^\star_\# \end{bmatrix} \cdot \begin{bmatrix} \operatorname{Grad}\delta\widetilde{\boldsymbol{\varphi}}_\# \\ \operatorname{Curl}\delta\widetilde{\boldsymbol{a}}_\# \end{bmatrix} \mathrm{d}V \right\}, \tag{4.30}$$

where $(\cdot)^\star$ denotes the complex conjugate of $(\cdot)$ and the partial derivatives are computed at an equilibrium state. In contrast to the definition given in (4.28), the coercivity constant in (4.30) allows identifing a microscopic instability from a unit-cell computation.

From (4.29) we observe that for $[k_1, k_2, k_3]^T = [0, 0, 0]^T$ the variations are unit-cell periodic, i.e., $\delta\widetilde{\boldsymbol{\varphi}}_\#(\boldsymbol{X}) = \delta\widetilde{\boldsymbol{\varphi}}(\boldsymbol{X})$ and $\delta\widetilde{\boldsymbol{a}}_\#(\boldsymbol{X}) = \delta\widetilde{\boldsymbol{a}}(\boldsymbol{X})$. Such instability can be captured by a representative volume element that is composed of only one unit cell. However, in the limit case $[k_1, k_2, k_3]^T \to [0, 0, 0]^T$ we observe that the wavelength of the variations becomes infinitely large. This kind of instability is referred to as a global or long-wavelength microscopic instability and formally given by

$$\Lambda_0 = \liminf_{\boldsymbol{k}\to\boldsymbol{0}} \inf_{\widetilde{\boldsymbol{\varphi}}_\#\in\mathcal{W}_{\widetilde{\boldsymbol{\varphi}}_\#}} \inf_{\widetilde{\boldsymbol{a}}_\#\in\mathcal{W}_{\widetilde{\boldsymbol{a}}_\#}} \left\{ \int_{\mathcal{D}} \begin{bmatrix} \operatorname{Grad}\delta\widetilde{\boldsymbol{\varphi}}^\star_\# \\ \operatorname{Curl}\delta\widetilde{\boldsymbol{a}}^\star_\# \end{bmatrix} \cdot \begin{bmatrix} \partial^2_{\boldsymbol{F}\boldsymbol{F}}\widehat{\psi} & \partial^2_{\boldsymbol{F}\mathbb{B}}\widehat{\psi} \\ \partial^2_{\mathbb{B}\boldsymbol{F}}\widehat{\psi} & \partial^2_{\mathbb{B}\mathbb{B}}\widehat{\psi} \end{bmatrix} \cdot \begin{bmatrix} \operatorname{Grad}\delta\widetilde{\boldsymbol{\varphi}}_\# \\ \operatorname{Curl}\delta\widetilde{\boldsymbol{a}}_\# \end{bmatrix} \mathrm{d}V \right. \\ \left. \Big/ \int_{\mathcal{D}} \begin{bmatrix} \operatorname{Grad}\delta\widetilde{\boldsymbol{\varphi}}^\star_\# \\ \operatorname{Curl}\delta\widetilde{\boldsymbol{a}}^\star_\# \end{bmatrix} \cdot \begin{bmatrix} \operatorname{Grad}\delta\widetilde{\boldsymbol{\varphi}}_\# \\ \operatorname{Curl}\delta\widetilde{\boldsymbol{a}}_\# \end{bmatrix} \mathrm{d}V \right\}. \tag{4.31}$$

[17] In the numerical implementation we follow Michel et al. [50] and check coercivity for a uniform grid representing the coefficients of the wave vector. We note that by using such uniform representation, we may leave the function space defined in (4.27), i.e., the perturbations $\delta\widetilde{\boldsymbol{\varphi}}_\#$ and $\delta\widetilde{\boldsymbol{a}}_\#$ will no longer be $\boldsymbol{n}\mathcal{D}$-periodic.

It has been shown rigorously by Geymonat et al. [29] that this instability corresponds to the loss of strong ellipticity of homogenized moduli (see Section 4.3.1).

4.3.3 Relations between the individual coercivity contants

In the latter sections, we have identified three coercivity constants, one of them being related to a macroscopic material instability and two being related to microscopic structural instabilities. According to Geymonat et al. [29] they are related by[18]

$$\Lambda \leq \Lambda_0 = \overline{\Lambda}\,, \tag{4.32}$$

see Triantafyllidis and Maker [77], Michel et al. [50], Bertoldi and Gei [8] for related discussions.

4.4 Numerical analysis of macroscopic and microscopic instabilities in MREs

The above presented framework has been implemented into the finite-element method.[19] Having the numerical implementation at hand, we are able to investigate macroscopic and microscopic instabilities for different geometric and material properties of MRE microstructures. In the following numerical studies, we pay particular attention to volume fractions and shapes of inclusions. Moreover, we study the influence of material parameters on the onset of instabilities. The numerical simulations address two-phase and three-phase MREs, where the two-phase composites are composed of soft elastomer matrix and stiff inclusions with soft-magnetic properties. The three-phase MREs additionally contain voids. The predictive capabilities of the presented framework will be underlined by comparison with experimental data.

Note that in the following multiscale computations, we consider the macroscopic energy density (4.13) at a macroscopic material point to be driven by a given macroscopic state $\{\overline{\boldsymbol{F}}, \overline{\mathbb{B}}\}$. This approach together with consideration of a wide range of loading scenarios provide important insight into the rank-one convexity of the homogenized energy and the microscopic stability for various microscopic topologies of MREs. While such a framework may prove useful for the design of MRE microstructures, it does not address the experimental realization of the considered material states $\{\overline{\boldsymbol{F}}, \overline{\mathbb{B}}\}$. For detailed information on associated challenges please refer to [43, 44, 46, 10].

Before we discuss the instability analysis in detail, we give a brief outline of the employed material models at microscopic scale. Furthermore, we present the homogenized coupled magneto-mechanical response of typical MRE microstructures undergoing stable magneto-mechanical response.

[18] We make use of this relation in the numerical implementation, where we first search for macroscopic instabilities. The associated loading conditions then serve as bounds for the considered microscopic stability analysis.

[19] For detailed comments on the numerical implementation see [62].

4.4.1 Constitutive models of MRE phases

As outlined in (4.8), we model the elastic behavior by an energy-density function of the form $\widehat{\psi}^{mec} = \widehat{\psi}^{mec,vol} + \widehat{\psi}^{mec,iso}$, see also (4.14). In that context, the volumetric energy is assumed to be a convex function of the dilatation θ

$$\widehat{\psi}^{mec,vol}(\theta) = \frac{\kappa}{2}(\theta - 1)^2 \,, \tag{4.33}$$

where κ denotes the bulk modulus at reference configuration. The isochoric mechanical energy is assumed to be governed by a Gent material model [28]

$$\widehat{\psi}^{mec,iso}(\boldsymbol{F}^{iso}) = -\frac{\mu\xi}{2} \ln\left[1 - \frac{||\boldsymbol{F}||^2/J^{2/d} - d}{\xi}\right], \tag{4.34}$$

where ξ is a strain-saturation parameter and μ is the initial shear modulus of the material. Furthermore, $\boldsymbol{F}^{iso} = J^{-1/d}\boldsymbol{F}$ denotes the isochoric part of the microscopic deformation gradient in $d = \{2, 3\}$ spatial dimensions.

The magnetic response is modeled by an additive energy density $\widehat{\psi}^{mag} = \widehat{\psi}^{mag,0} + \widehat{\psi}^{mag,sat}$, where the energy density $\psi^{mag,0}$ is defined as

$$\widehat{\psi}^{mag,0}(\boldsymbol{F}, \mathbb{B}) = \frac{1}{2\mu_0 J}\|\mathbb{B}\|^2_{\boldsymbol{C}} \,. \tag{4.35}$$

In the latter equation, $\|\mathbb{B}\|_{\boldsymbol{C}} := \sqrt{\mathbb{B} \cdot \boldsymbol{C} \cdot \mathbb{B}}$ is short hand for the norm of the referential magnetic induction w.r.t. the right Cauchy–Green tensor $\boldsymbol{C}$. The second part of the energy density is in place to account for magnetic saturation effects. It is modeled by a Langevin-type function

$$\widehat{\psi}^{mag,sat}(\boldsymbol{F}, \mathbb{B}) = \frac{J\mu_0 m_s^2}{3\chi}\left\{\ln\left[\frac{3\chi}{\mu_0 m_s J}\|\mathbb{B}\|_{\boldsymbol{C}}\right] - \ln\left[\sinh\left(\frac{3\chi}{\mu_0 m_s J}\|\mathbb{B}\|_{\boldsymbol{C}}\right)\right]\right\}, \tag{4.36}$$

where $\mu_0 = 4\pi \cdot 10^{-7}\,\mathrm{N/A^2}$ is the magnetic permeability of free space, χ is the magnetic susceptibility and m_s is the saturation magnetization.

4.4.2 Numerical studies on the effective magneto-mechanical response of selected MRE microstructures

In order to provide further insight in the effective response of MREs, we compute the homogenized response of selected two-phase composites under prescribed macroscopic state. This allows us to analyze the typical effective saturation behavior of the magnetic and mechanical response which distinguishes magnetoactive composites from their electroactive counterparts [62].

We perform finite-element simulations on unit-square RVEs with 20% volume fraction of elliptic magnetizable inclusions with aspect ratio $w \in [1/3,\ 1/2,\ 1,\ 2,\ 3]$. The aspect ratio is determined as the ratio of the vertical axes of an inclusion over the horizontal axes. As macroscopic boundary conditions we assume that

$$\overline{\boldsymbol{F}} = \boldsymbol{1} \quad \text{and} \quad \overline{\mathbb{B}} = \begin{bmatrix} \overline{B}_1 \\ \overline{B}_2 \end{bmatrix}, \tag{4.37}$$

where $\overline{B}_1 = \overline{\gamma}\sin\alpha$ and $\overline{B}_2 = \overline{\gamma}\cos\alpha$ with $\overline{\gamma}$ and α being the loading parameter and the orientation angle w.r.t. the vertical direction, respectively. The material parameters used in the present study are listed in Table 4.3, where the magnetic parameters correspond to carbonyl iron [20, 21, 26, 16] .

Table 4.3: Material parameters of two-phase MRE composites considered in numerical examples of Sec. 4.4.2.

No.	Parameter	Name	Matrix	Inclusion
1.	ν	Poisson's ratio	0.495	0.495
2.	μ	Shear modulus / MPa	0.025	25
3.	ξ	Strain saturation	100	100
4.	χ	Magnetic susceptibility	0	0.995
5.	$\mu_0 m_s$	Magnetic saturation / T	–	2.0

In Fig. 4.4, we present the norms of the macroscopic magnetization $\overline{\boldsymbol{m}}$ and the projection $\overline{t}^{\alpha,mec} = \overline{\boldsymbol{\sigma}}^{mec} : (\boldsymbol{n}^\alpha \otimes \boldsymbol{n}^\alpha)$ of the macroscopic mechanical Cauchy stress tensor versus applied macroscopic magnetic induction. Here $\boldsymbol{n}^\alpha = [\sin\alpha,\, \cos\alpha]^T$ refers to the direction of the magnetic loading. $\overline{\boldsymbol{\sigma}}^{mec}$ is the mechanical part of the Cauchy stress tensor under the assumption that the macroscopic Maxwell energy has the form $\hat{\overline{\psi}}^{Maxw} = 1/(2\mu_0\overline{J})\|\overline{\mathbb{B}}\|_{\overline{\boldsymbol{C}}}$.

In Fig. 4.4**a**, we observe that the saturation values of the effective magnetization grow monotonically with the aspect ratio of the inclusions for the magnetic induction applied vertically. However, as the orientation of the magnetic induction deviates from the vertical direction, the evolution of magnetization becomes even more nonlinear, see Fig. 4.4**b** and **c**. For the orientation angle of $\alpha = 45°$ the curves for $w = 1/3$ and $w = 3$ as well as for $w = 1/2$ and $w = 2$ coincide due to the symmetry w.r.t. the magnetic loading.

In Fig. 4.4**e**–**h**, we present the macroscopic Cauchy stress $\overline{t}^{\alpha,mec}$ along the magnetic loading induced by the applied macroscopic magnetic induction. Similar to the magnetization also the Cauchy stress experience saturation. Furthermore, the direction of the magnetic loading has high influence on the stresses. In Fig. 4.4**f**, we observe negative Cauchy stresses for the RVEs contained of elliptic inclusion with aspect ratios $w = 1/3$ and $w = 1/2$. The major axis of these inclusions are oriented in the horizontal direction. Therefore, for the lower values of the orientation angle α, the rotation of them is higher than the elliptic inclusions pointing in the vertical direction. The negative sign of the projected Cauchy stresses also indicates that such microstructures could yield macroscopic extension of the MREs when the deformations are not prescribed, see also [44]. In Fig. 4.4**h**, we again observe identical responses for the aspect ratios $w = 1/3$ and $w = 3$ as well as $w = 1/2$ and $w = 2$ due to the symmetry reasons..

Next to the current study, we present a numerical study under mechanically stress-free conditions for various MRE unit cells in Appendix B.

4.4.3 Stability analysis of two-phase MREs

In the following we investigate the influence of material parameters as well as shape and volume fraction of particles on the buckling-type microscopic and localization-type macroscopic instabilities. The critical macroscopic state leading to microscopic instabilities is

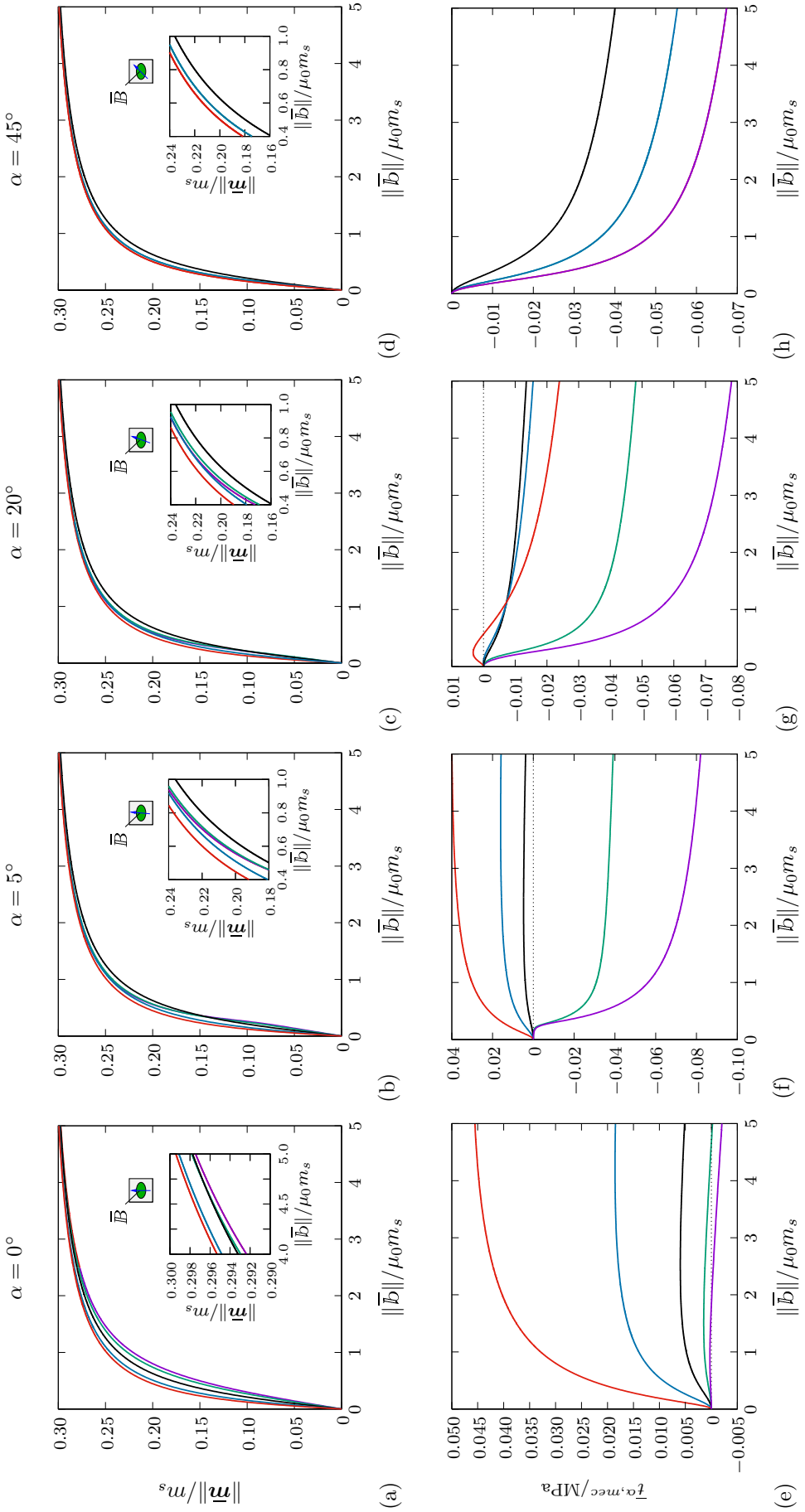

Figure 4.4: *Magneto-mechanical response of periodic MRE unit cells with elliptic inclusions of different aspect ratios.* (**a**)–(**d**) Saturation of the current macroscopic magnetization depending on the orientation angle α of the magnetic induction. (**e**)–(**h**) Mechanical part of the macroscopic traction $\overline{\boldsymbol{t}}^{\alpha,mec} = \overline{\boldsymbol{\sigma}}^{mec} : (\boldsymbol{n}^{\alpha} \otimes \boldsymbol{n}^{\alpha})$ along the applied macroscopic magnetic induction.

associated with the microscopic coercivity constant given in (4.30). We compute it for a discrete set of Bloch vectors $\{k_1, k_2\} \in [0, \pi]$ with 37×37 points in the directions k_1 and k_2, respectively. The loss of macroscopic stability is determined by checking the positive definiteness of the Christoffel tensor $\overline{\boldsymbol{\Gamma}}$ given in (4.24).

4.4.3.1 Stability analysis of stretched MRE microstructures under aligned magnetic loading

As a first loading condition of the microstructure we consider the macroscopic deformation gradient and macroscopic magnetic induction

$$\overline{\boldsymbol{F}} = \begin{bmatrix} \overline{\lambda} & 0 \\ 0 & \overline{\lambda}^{-1} \end{bmatrix} \quad \text{and} \quad \overline{\mathbb{B}} = \begin{bmatrix} 0 \\ \overline{B}_2 \end{bmatrix}, \tag{4.38}$$

where $\overline{\lambda} = 1 + \overline{\gamma} \sin\phi$ and $\overline{B}_2 = c\overline{\gamma} \cos\phi$ are parameterized using a path angle $\phi \in [-90°, 90°]$ and a loading parameter $\overline{\gamma}$. In the present examples, we have set $c = 10$. Such a parameterization allows determining critical loading states for different combinations of macroscopic stretch $\overline{\lambda}$ and magnetic induction $\overline{B}_2$. Please refer to Fig. 4.5 for a graphical illustration.

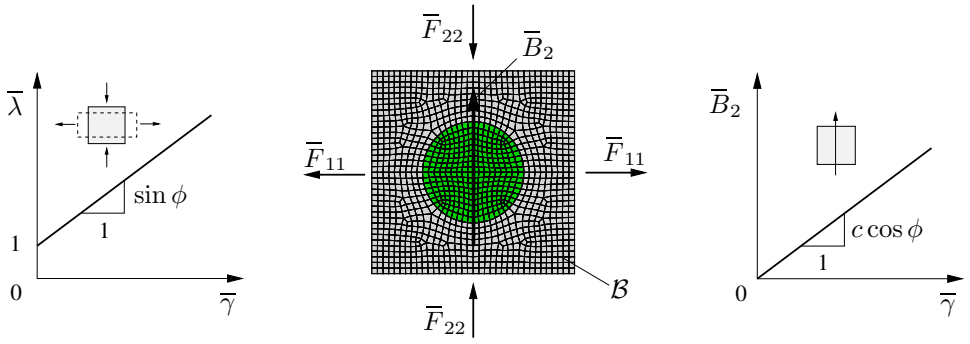

Figure 4.5: *Parameterization of the macroscopic magneto-mechanical boundary conditions.* The RVE is loaded with a macroscopic mechanical deformation $\overline{\boldsymbol{F}} = \overline{\lambda}\,\overline{\boldsymbol{e}}_1 \otimes \overline{\boldsymbol{E}}_1 + \overline{\lambda}^{-1}\,\overline{\boldsymbol{e}}_2 \otimes \overline{\boldsymbol{E}}_2$ and a macroscopic magnetic induction $\overline{\mathbb{B}} = \overline{B}_2\,\overline{\boldsymbol{E}}_2$. The loads in terms of the macro-stretch $\overline{\lambda}$ and the magnetic induction $\overline{B}_2$ are linear functions of the loading parameter $\overline{\gamma}$.

For the spatial discretization of the problem we employ Q_2P_1-type elements with quadratic interpolations of the displacement and magnetic vector potential as well as discontinuous linear interpolations for pressure and dilatation.

Influence of mechanical material parameters on instabilities. In what follows, we investigate the influence of the mechanical properties of the matrix on the occurrence of instabilities in two-phase MREs. The stability is checked for three different shear moduli of the matrix given by $\mu_{matrix} = \{0.01, 0.02, 0.04\}$ MPa. The magnetic inclusions have a volume fraction of $f_0 = 0.2$ and the remaining material parameters are listed in Table 4.3 (in the present example, we set $\mu_{incl} = 1000\ \mu_{matrix}$). The results of our computations are depicted in Fig. 4.6.

In all cases we observe that under purely mechanical loading the composite loses macroscopic material stability before microscopic instabilities could arise. This becomes visible through the blue lines indicating the loss of macroscopic stability. The loss of

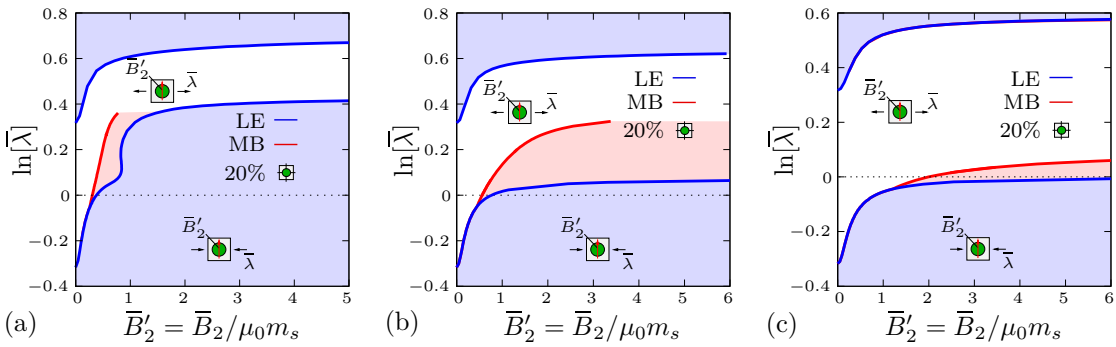

Figure 4.6: *Influence of mechanical stiffness on the stability of unit-square RVEs with circular inclusions.* The plots shown in (**a**), (**b**) and (**c**) refer to shear moduli of the matrix of $\mu_{matrix} = 0.01$ MPa, $\mu_{matrix} = 0.02$ MPa and $\mu_{matrix} = 0.04$ MPa respectively. In all cases, the magnetic inclusions have a volume fraction of $f_0 = 0.2$. Depending on the elastic parameters of the matrix we observe different stability properties. While magnetic loading orthogonal to the applied tension stabilizes the macroscopic material response in case of large stretches, stability is reduced when deformations are moderate. Furthermore, magnetic loading oriented parallel to applied tension reduces macroscopic material stability and may even lead to buckling type micro-instabilities when no macroscopic deformation is applied.

microscopic stability is associated with the red lines. Such an observation is in line with the results of Triantafyllidis et al. [78], Michel et al. [50], who analyzed the stability of soft microstructures with stiff inclusions. It is instructive to note that the stability of the composite under purely mechanical loading is not affected by the magnitude of the shear moduli of matrix and inclusion as long as their ratio $\mu_{incl} = 1000\ \mu_{matrix}$ is fixed. We further observe that the application of magnetic loading orthogonal to tensional stretching stabilizes the composites. On the contrary, when the magnetic induction is applied parallel to tensional stretching it initially destabilizes the material. In both cases we observe a typical saturation behavior associated with the saturation of the magnetization under increasing magnetic loading.

Next to macroscopic material instabilities, we encounter microscopic buckling-type instabilities under the application of magnetic loading, both under compression and tension in the direction of the magnetic loading. Increasing the stiffness of the matrix material effectively delays such instabilities. Again, the saturation of magnetization limits the impact of magnetic loading on microscopic instabilities.

For further illustration, we show snapshots of a microscopic buckling mode at different loading states in Fig. 4.7. The depicted mode corresponds to the microscopic instability point at path angle $\phi = 50°$ of Fig. 4.6**a**. According to the Bloch–Floquet wave analysis this instability is captured by an RVE composed of 2×3 unit cells. As becomes clear from the figure, the instability results in a change of periodicity that is characterized by pairwise vertical attraction of magnetic inclusions and buckling of vertical ligaments of matrix material.

Influence of volume fractions of inclusions on instabilities. We now analyze the stability of microstructures with different volume fractions of inclusions. Corresponding results for volume fractions of $f_0 = \{0.1, 0.2, 0.3\}$ of circular inclusions are depicted in Fig. 4.8.

In the present study, we have selected a shear modulus $\mu_{matrix} = 0.04$ MPa. Again

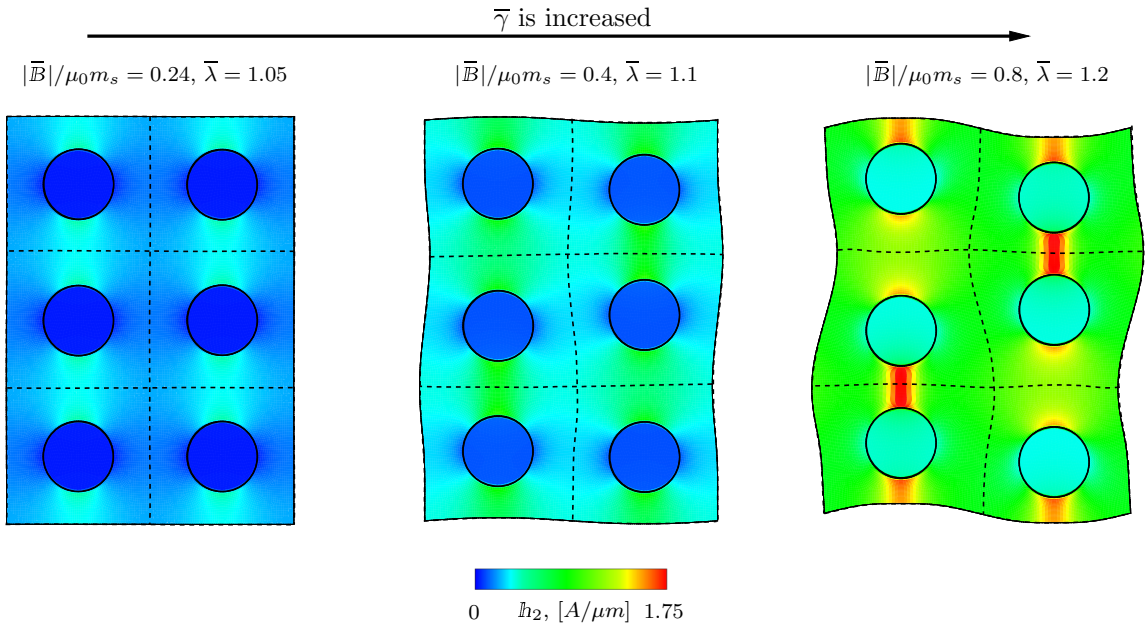

Figure 4.7: *Buckling mode of an MRE microstructure with circular inclusions of volume fraction* $f_0 = 0.2$. The depicted buckling mode is associated with a bifurcation point that is detected under a path angle $\phi = 50°$. At this point, the critical periodicity of the microstructure can be reflected by an RVE composed of 2×3 unit cells.

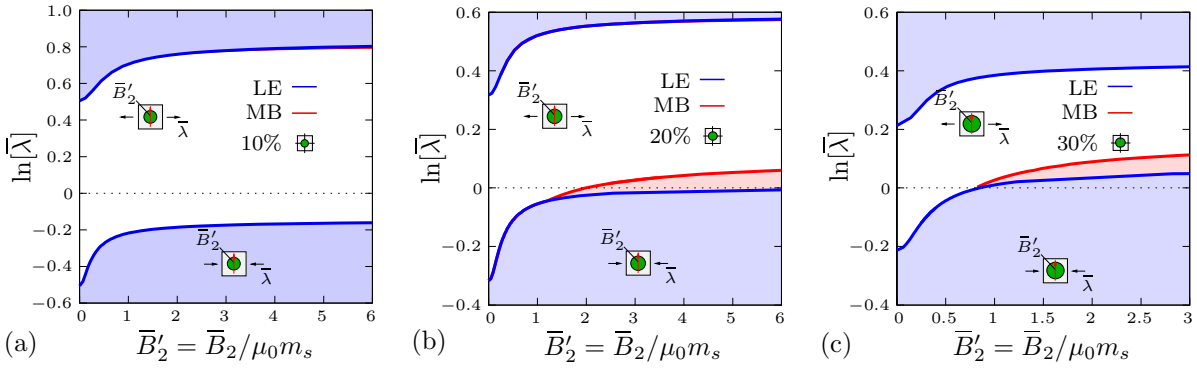

Figure 4.8: *Influence of volume fractions on the stability of unit-square RVEs with circular inclusions.* The plots shown in (**a**), (**b**) and (**c**) refer to volume fractions of the inclusions of $f_0 = 0.1$, $f_0 = 0.2$ and $f_0 = 0.3$ respectively. In all cases, the shear modulus of the matrix is $\mu_{matrix} = 0.04$ MPa. We observe that the range of stable loading paths is narrowed with increasing volume fraction of inclusions. Again, the application of an orthogonal magnetic field gives rise to a stabilizing effect for high values of strech and the oposite is observed for moderate deformations and when magnetic loading is parallel to the applied tension. Like in the previous study, it may however lead to microscopic instabilities when no macroscopic deformation is present.

the shear stiffness of the inclusions is assumed to be 1000 times higher. In Fig. 4.8 we observe that material instabilities are more likely to occur for higher volume fractions of inclusions. Furthermore, it is evident that small volume fractions of inclusions do not lead to buckling-type microscopic instabilities. This can be explained as follows. As we observed in Fig. 4.7, the instability-induced change of periodicity comes along with pairwise attraction of magnetic inclusions in vertical direction and buckling of the matrix material. When the volume fraction of the inclusions reduces, not only the magnetic attraction between the inclusions is lowered, but also the ligaments between the inclusions

become thicker. Both effects hinder microscopic buckling.

We present snapshots of a selected buckling mode for the RVE with $f_0 = 0.2$ in Fig. 4.9. This buckling mode corresponds to the path angle $\phi = 0°$ given in Fig. 4.8**b**.

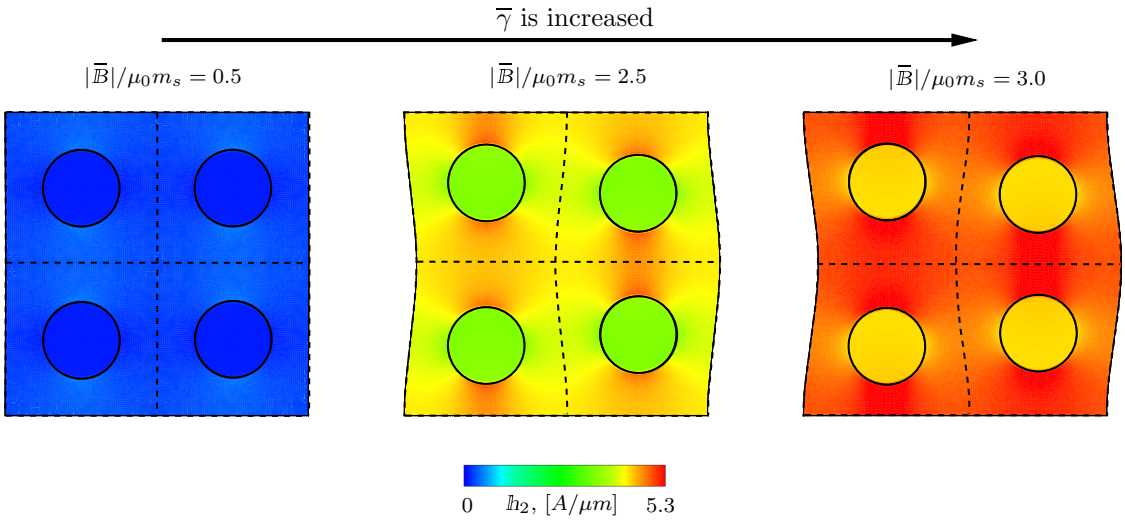

Figure 4.9: *Buckling mode of an MRE microstructure with circular inclusions of volume fraction $f_0 = 0.2$ (purely magnetic loading).* The depicted buckling mode is associated with a bifurcation point that is detected under a path angle $\phi = 0°$, i.e., under purely magnetic loading. At the given instability point, the periodicity of the microstructure is associated with an RVE composed of 2×2 unit cells.

Influence of the shape of inclusions on instabilities. As a final study, we investigate the stability of MREs in consideration of different shapes of inclusions. We compare the behavior of RVEs with circular inclusions with the behavior of RVEs with elliptic inclusions having an aspect ratio of 2 and 1/2, respectively. In all cases, we consider the volume fraction $f_0 = 0.2$. The results of the study are depicted in Fig. 4.10.

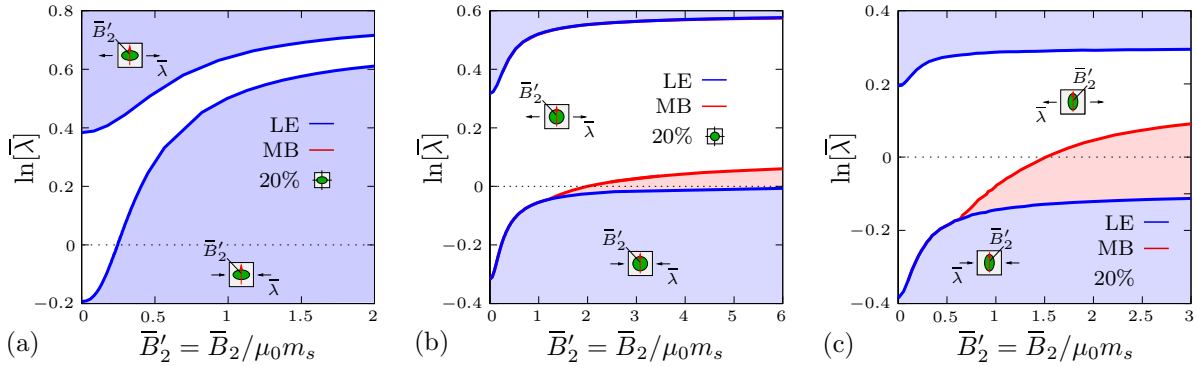

Figure 4.10: *Influence of the aspect ratio of inclusions on the stability of unit-square RVEs.* The plots shown in (**a**), (**b**) and (**c**) refer to aspect ratios of the inclusions of $w = 1/2$, $w = 1$ and $w = 2$ respectively. In all cases, the shear modulus of the matrix is $\mu_{matrix} = 0.04$ MPa. Depending on the aspect ratio, we observe different behavior of the microstructures. In particular, the influence of the magnetic loading on stability is evident.

We observe that the critical loading states are strongly affected by the inclusions' shape and orientation. When the major axis of the inclusions is oriented perpendicular to the macroscopic magnetic loading $\overline{B}_2$ we do not observe any microscopic instability. The range of materially stable loadings is however narrow and firmly bonded by the

saturation of magnetization. When the major axis is oriented parallel to the magnetic loading, microscopic instabilities appear under moderate applied deformations.

In Fig. 4.11, we show a buckling mode of the MRE microstructure with elliptic inclusions oriented parallel to the magnetic loading under purlely magnetic loading.

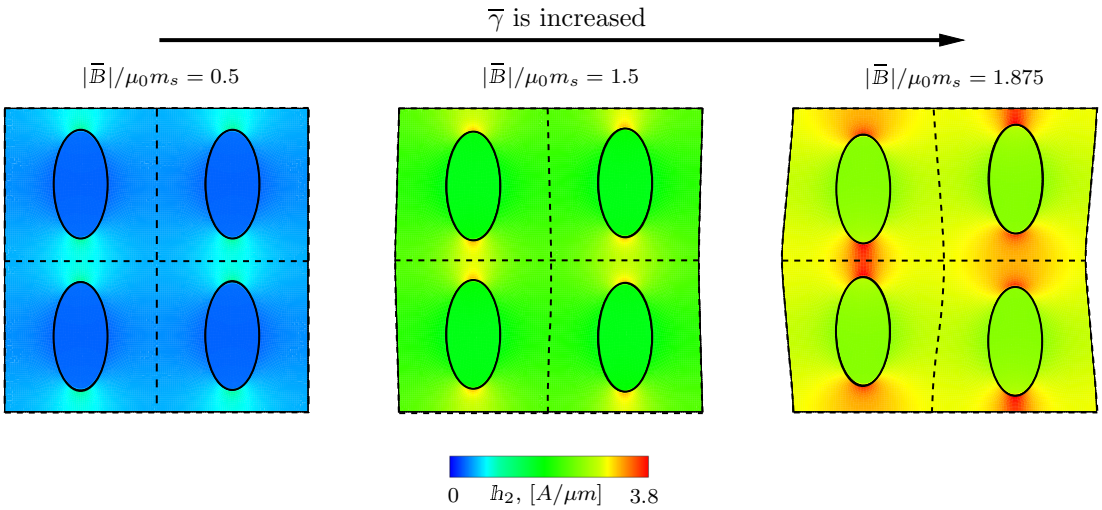

Figure 4.11: *Buckling mode of an MRE microstructure with ellipsoidal inclusions of volume fraction* $f_0 = 0.2$. The depicted mode is associated with a bifurcation point at a path angle of $\phi = 0°$, i.e., purely magnetic loading. At this point, the critical periodicity of the microstructure changes to 2×2 unit cells.

4.4.3.2 Stability analysis of MRE microstructures under purely magnetic loading

In the previous examples we observed that material and structural instabilities may occur even in the absence of mechanical loading. We have however only taken into account a limited set of magnetic loading conditions. Our aim is now to widen the view to a larger variety of loadings of the form

$$\overline{\boldsymbol{F}} = \boldsymbol{1} \quad \text{and} \quad \overline{\mathbb{B}} = \begin{bmatrix} \overline{B}_1 \\ \overline{B}_2 \end{bmatrix}, \tag{4.39}$$

where we parameterize the magnetic loading by $\overline{B}_1 = \overline{\gamma} \sin\phi$ and $\overline{B}_2 = \overline{\gamma} \cos\phi$ with a path angle of $\phi \in [0°, 90°]$. Due to the given symmetry properties of the microstructures under consideration this parameterization captures the full spectrum of magnetic loading.

In Fig. 4.12**a**,**b** the critical macroscopic loading states are illustrated for a microstructure with circular inclusions. Fig. 4.12**c** corresponds to microstructures with elliptic inclusions. In these examples, we have assumed a shear modulus of the inclusions of **a** $\mu_{matrix} = 0.01$ MPa, **b** $\mu_{matrix} = 0.02$ MPa and **c** $\mu_{matrix} = 0.02$ MPa. We further consider the volume fraction of the inclusions $f_0 = 0.2$.

As becomes obvious from the plots, microstructures with circular inclusions lose their microscopic stability when the magnetic loadings points close to the vertical or horizontal direction. However, when the orientation of magnetic loading points surrounds the diagonal of the RVE, macroscopic material instabilities kick in even before micro-bucking

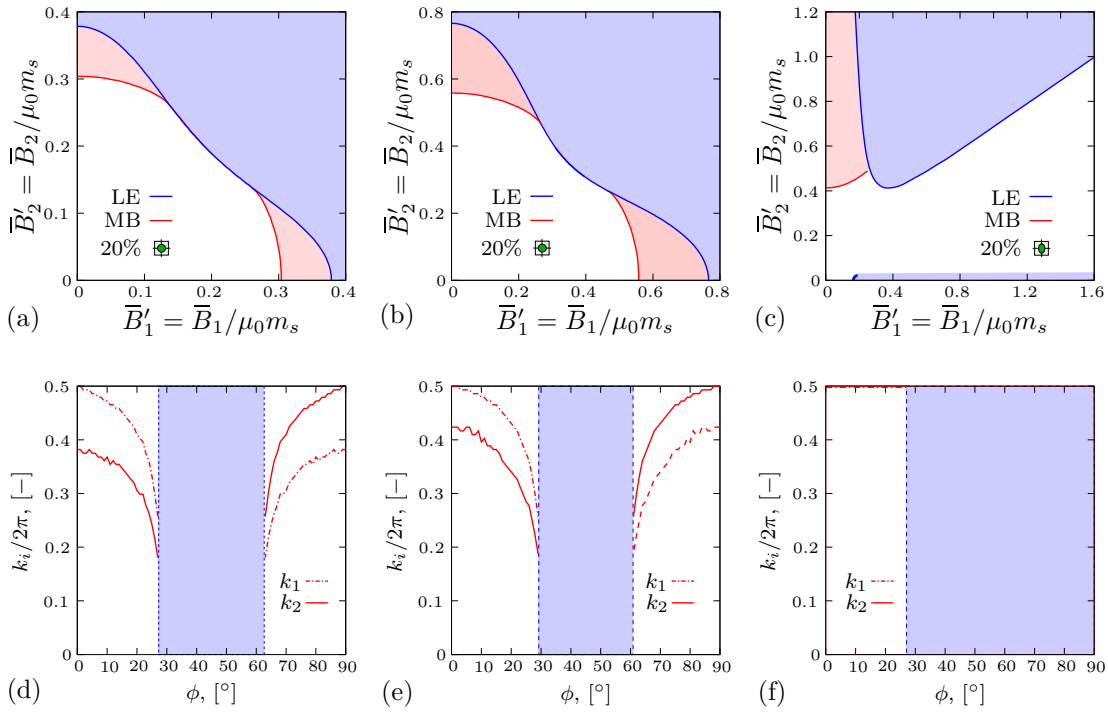

Figure 4.12: *Instabilities of MRE microstructures under purely magnetic loading.* The plots in (**a**) and (**b**) correspond to microstructures with circular inclusions and a shear modulus of the matrix of $\mu_{matrix} = 0.01$ MPa and $\mu_{matrix} = 0.02$ MPa respectively. The plot shown in (**c**) corresponds to a microstructure with elliptic inclusions and a shear modulus of the matrix of $\mu_{matrix} = 0.02$ MPa. The volume fraction of inclusions is $f_0 = 0.2$ in all cases. The graphs shown in (**d**), (**e**) and (**f**) illustrate the Bloch-vector components associated with the microscopic instability points corresponding to the plots (**a**), (**b**) and (**c**) respectively.

could occur. Again, it is evident from the graphs shown in Fig. 4.12**a**,**b** that by increasing the stiffness of the matrix we are able to stabilize the composite. It is further intriguing to note that microstructures with elliptic inclusions do not show any instability in certain loading regimes. For further reference, we depict the components of the Bloch vector corresponding to the latter computations in Fig. 4.12**d**–**f**.

In order to obtain additional insights into the development of macroscopic material instabilities, we plot the determinant of the Christoffel tensor $\det \overline{\boldsymbol{\Gamma}}$ for the path angle $\phi = 90°$ for different magnitudes of macroscopic magnetic loading $\|\mathbb{B}\|$ in Fig. 4.13**a**. The determinant first vanishes at $\overline{\theta} = 90°$ due to a vanishing macroscopic modulus $\overline{A}_1{}^2{}_1{}^2$. In Fig. 4.13**b**, the determinant $\det \overline{\boldsymbol{\Gamma}}$ is plotted for different path angles ϕ, each for a critical loading $\|\mathbb{B}\|$. Macroscopic instabilities are detected for different orientations $\overline{\theta}$.

A typical buckling mode at the path angle $\phi = 63°$ is shown in Fig. 4.14. As a result of the microscopic buckling the periodicity of microstructure corresponds to an RVE composed of 4×3 unit cells.

Influence of magnetic properties on instabilities. In order to get an idea of the influence of the magnetic properties on the occurrence of macroscopic instabilities we perform a corresponding study on an RVE under vertical magnetic loading $\overline{\mathbb{B}} = \overline{B}_2 \overline{\boldsymbol{E}}_2$ and fixed macroscopic deformation $\overline{\boldsymbol{F}} = \boldsymbol{1}$. The considered inclusions have circular shape and volume fractions of $f_0 = 0.2$ and $f_0 = 0.3$, respectively. In Fig. 4.15 we depict macroscopic instability points for various combinations of magnetic saturation $\mu_0 m_s \in [1.5, 3.0]$ T and

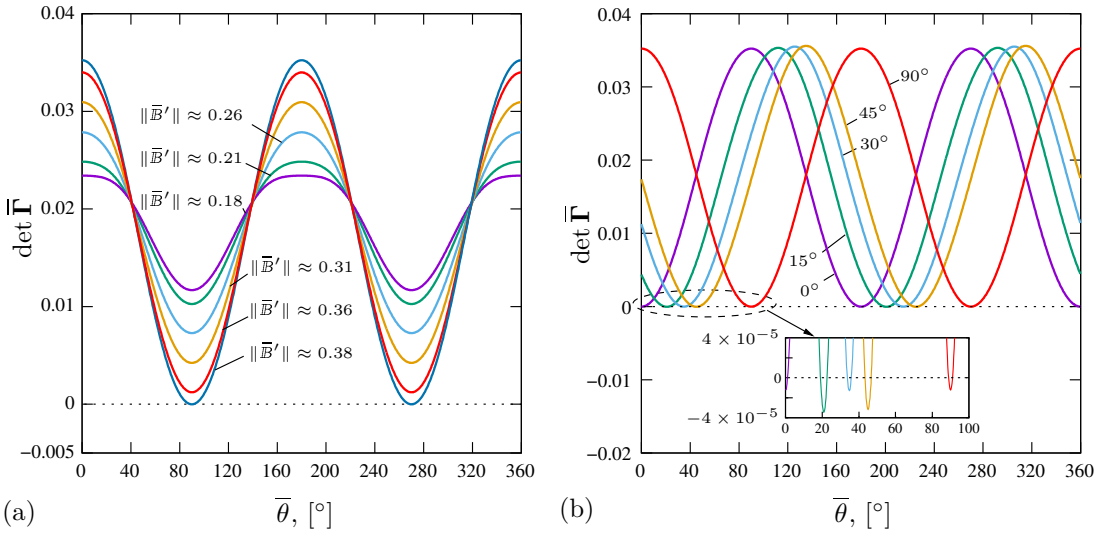

Figure 4.13: *Evolution of the determinant of the Christoffel tensor* $\det \overline{\mathbf{\Gamma}}$ *depending on the orientation* $\overline{\theta}$. The graphs shown in (**a**) depict the determinant of the Christoffel tensor at different macroscopic loading states $\|\overline{\mathbb{B}}'\| = \|\overline{\mathbb{B}}\|/\mu_0 m_s$ at a path angle of $\phi = 0°$, i.e., under purely magnetic loading. At loading $\|\overline{\mathbb{B}}'\| \approx 0.38$ the determinant becomes zero, indicating that the material is macroscopically unstable. In plot (**b**) we show the determinant of the Christoffel tensor under critical loading states for various path angles ϕ. All plots correspond to the scenario illustrated in Fig. 4.12**a**.

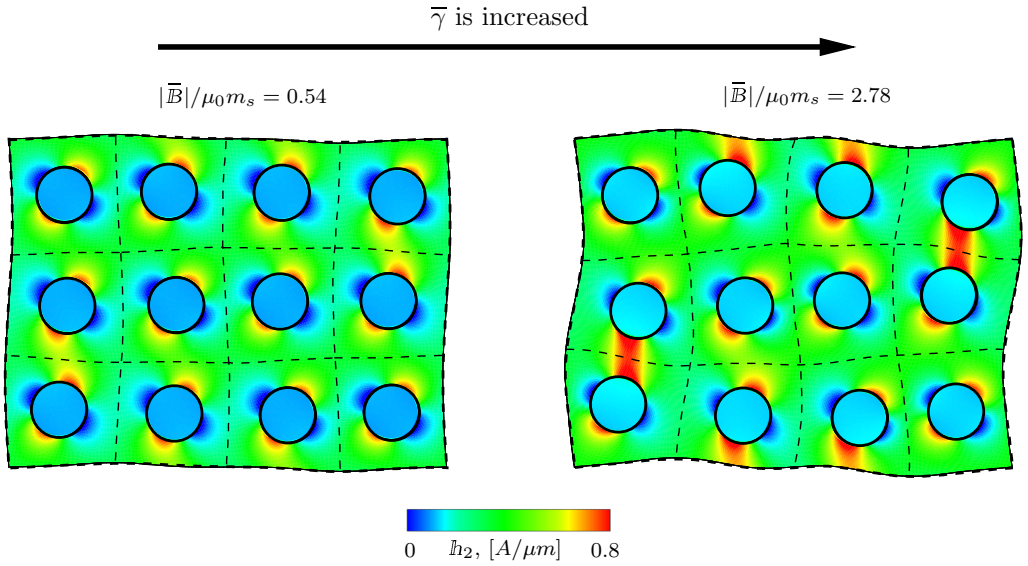

Figure 4.14: *Buckling mode of an MRE microstructure with circular inclusions under purely magnetic loading.* The volume fraction of the inclusions is $f_0 = 0.2$. As becomes obvious the complex bucking mode can only be captured by a microstructure consisting of 4×3 unit cells.

magnetic susceptibility $\chi \in [0.5, 0.995]$. The mechanical material parameters of the matrix and inclusions are given in Table 4.4. In Fig. 4.15 we observe that the critical magnetic loading decreases with increasing magnetic saturation and magnetic susceptibility. All instability points are detected at an orientation angle $\overline{\theta} = 0°$.

Table 4.4: Mechanical material parameters of two-phase MRE composites considered in the numerical example of Sec. 4.4.3.2.

Phase	Poisson's ratio ν	Shear modulus μ, MPa	Strain Saturation ξ
Matrix	0.495	0.01	100
Inclusion	0.495	10.0	100

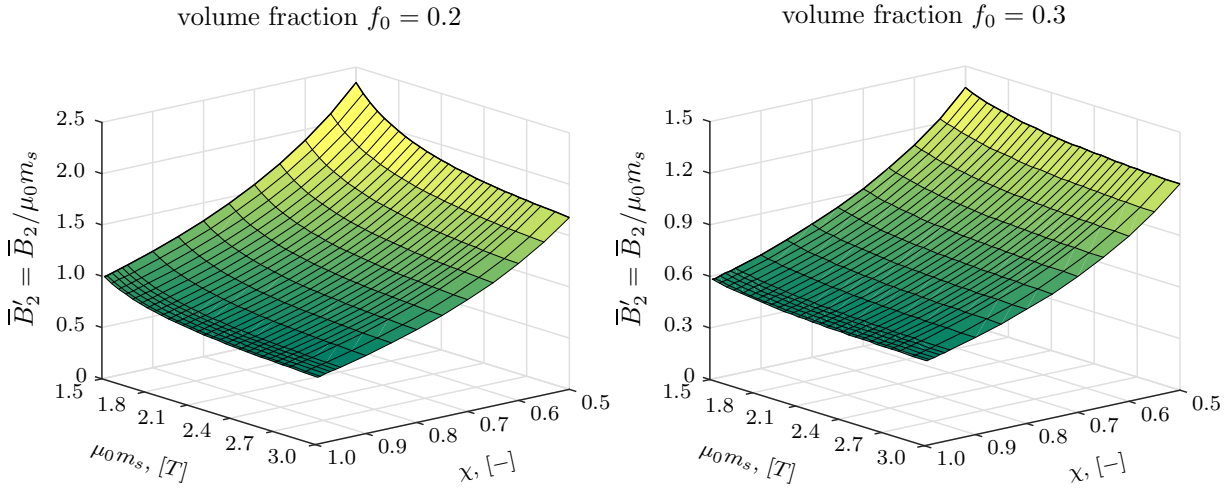

Figure 4.15: *Macroscopic-instability points depending on magnetic material parameters of the inclusions under purely magnetic loading.* The two graphs show the instability points for circular inclusions of volume fraction $f_0 = 0.2$ and $f_0 = 0.3$. We observe that macroscopic material instabilities occur earlier for higher values of material parameters. The influence of the saturation magnetization is however not very pronounced, especially when high values of magnetic susceptibility are present.

4.4.3.3 Stability analysis of stretched MRE microstructures under non-aligned magnetic loading

We now further extend the set of applied macroscopic boundary conditions and study the influence of the direction of the macroscopic magnetic induction w.r.t. the macroscopically applied stretch. For that, we apply the macroscopic loading conditions

$$\overline{\boldsymbol{F}} = \begin{bmatrix} \overline{\lambda} & 0 \\ 0 & \overline{\lambda}^{-1} \end{bmatrix} \quad \text{and} \quad \overline{\mathbb{B}} = \begin{bmatrix} \overline{B}_1 \\ \overline{B}_2 \end{bmatrix}, \tag{4.40}$$

where $\overline{\lambda} = 1 + \overline{\gamma} \sin\phi$, $\overline{B}_1 = c\overline{\gamma} \cos\phi \sin\alpha$ and $\overline{B}_2 = c\overline{\gamma} \cos\phi \cos\alpha$ are parameterized using the path angle $\phi \in [-90°, 90°]$ and the alignment angle $\alpha = \{0°, 5°, 20°, 45°\}$. The latter angle measures the deviation from the vertical direction.

As material parameters for the magnetic inclusions we again assume the ones summarized in Table 4.3. In addition, we select the shear moduli of matrix and inclusions as $\mu_{\text{matrix}} = 0.04\,\text{MPa}$ and $\mu_{\text{incl}} = 1000\ \mu_{\text{matrix}}$, respectively.

In a first study, we consider a square-shaped RVE with circular inclusion of volume fraction $f = 30\%$ and depict corresponding results in Fig. 4.16. In the figure, red lines correspond to the onset of microscopic instabilities and blue lines correspond to the onset of macroscopic instabilities. By comparing Fig. 4.16**a** with Fig. 4.16**b**–**d**, we observe that instabilities are triggered earlier when the RVE is loaded with a magnetic induction that

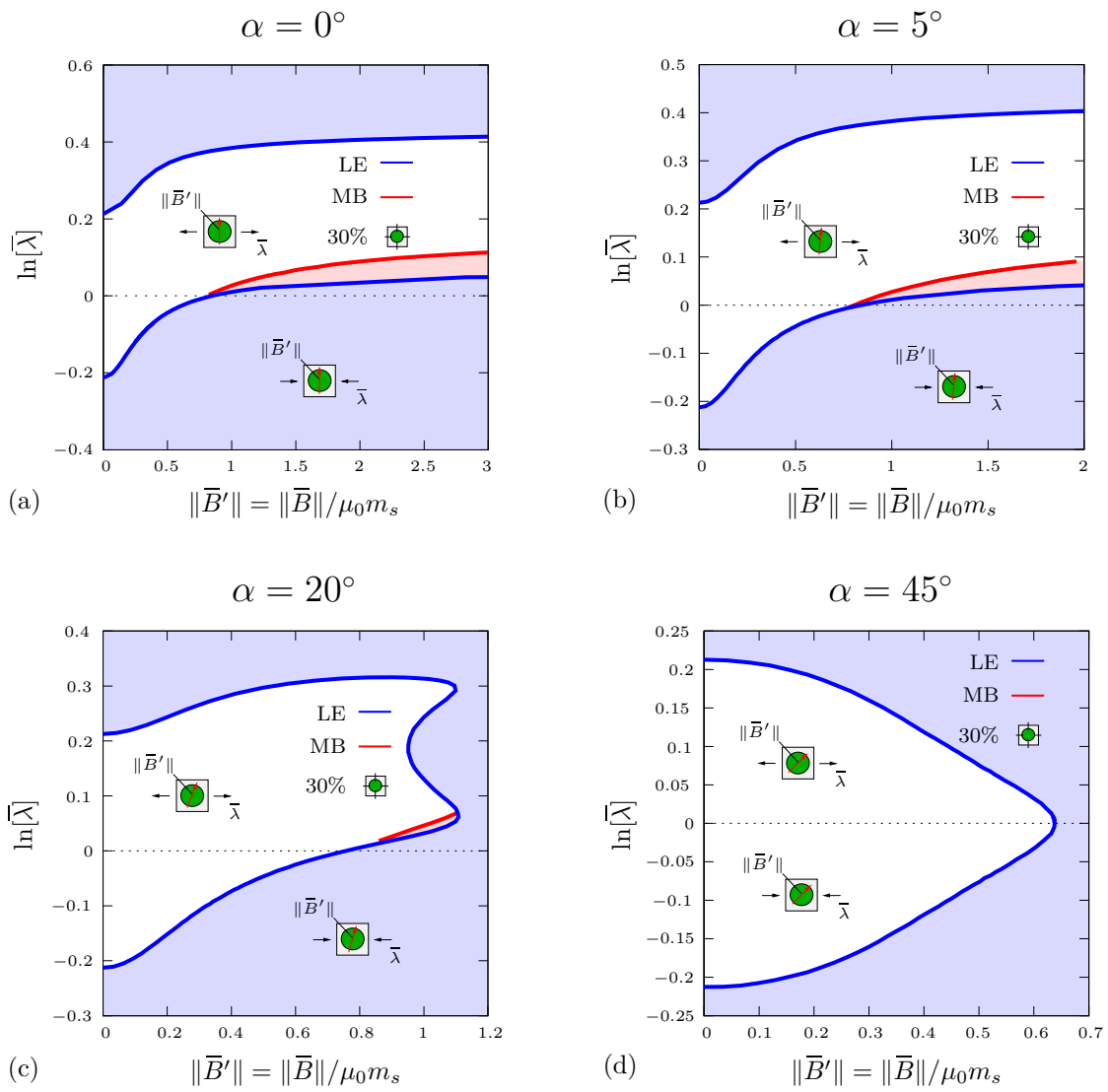

Figure 4.16: *Influence of the alignment of magnetic loading w.r.t. mechanical deformation on the stability of unit-square RVEs with circular inclusions.* The plots shown in (**a**), (**b**), (**c**) and (**d**) refer to alignment angles of magnetic induction of $\alpha = 0°$, $\alpha = 5°$, $\alpha = 20°$ and $\alpha = 45°$, respectively. In all cases, the shear modulus of the matrix is $\mu_{matrix} = 0.04$ MPa. We observe that as the orientation of the magnetic induction deviates from the vertical direction, microscopic instabilities are suppressed and macroscopic instabilities become dominant.

deviates from the vertical direction whenever we account for tension in vertical direction. However, when the RVE is compressed in the vertical direction, an inclined magnetic field delays instabilities. Interestingly, when the alignment angles rises, material instabilities occur even under comparably low magnetic loading (see Fig. 4.16**c**,**d**). In consideration of small alignment angles, this effect is suppressed by the saturation of the magnetization of the inclusions (see Fig. 4.16**a**,**b**).

In a second study, we consider a square-shaped RVE with elliptic inclusion of volume fraction $f = 20\%$ and depict corresponding results in Fig. 4.17. Again, red lines correspond to the onset of microscopic instabilities and blue lines correspond to the onset of macroscopic instabilities. The consideration of elliptical inclusions gives rise to a quite distinct behavior. In particular, we observe that the application of an inclined magnetic loading suppresses the occurrence of microscopic instabilities. A similar phenomenon

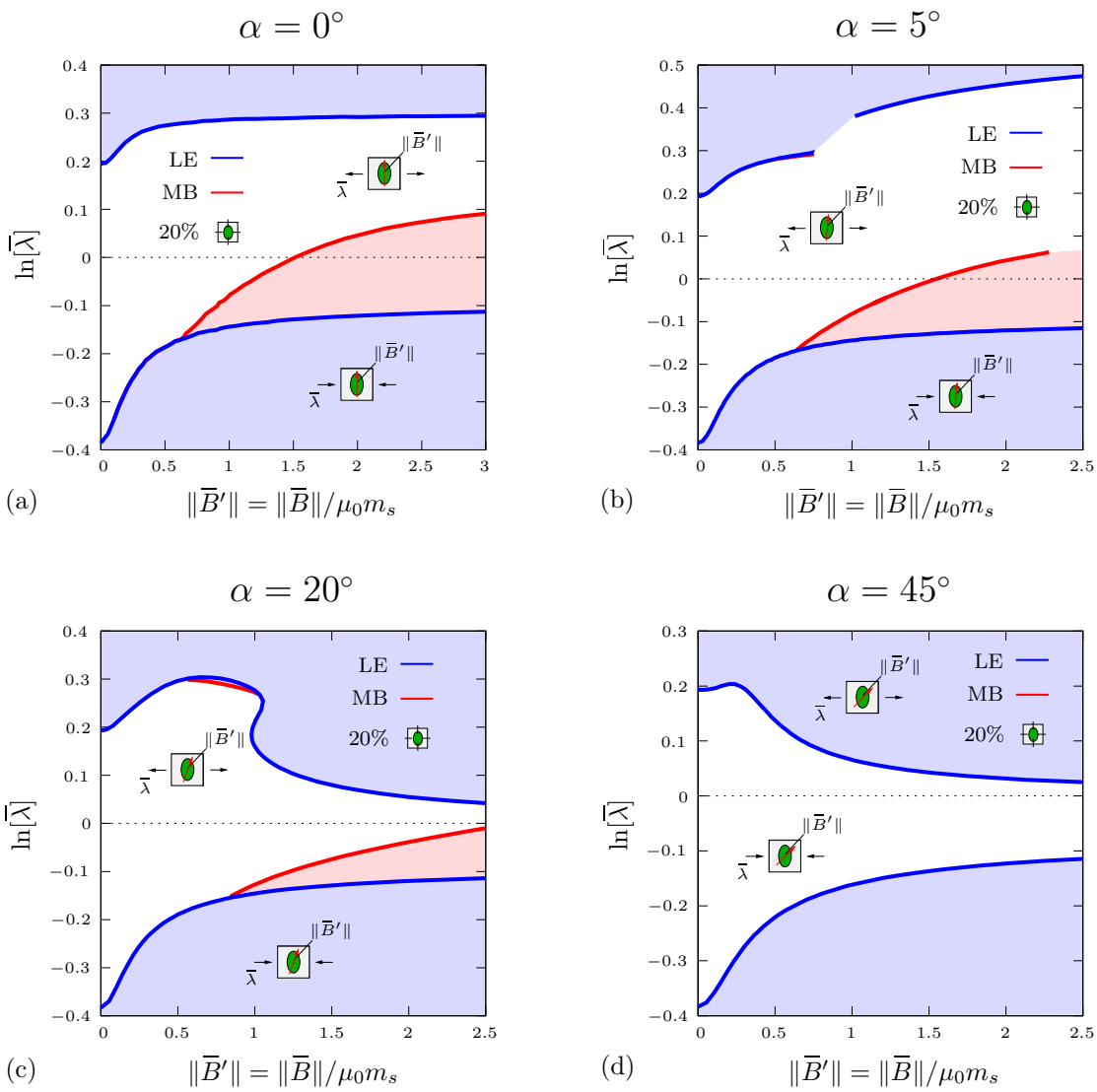

Figure 4.17: *Influence of the alignment of magnetic loading w.r.t. mechanical deformation on the stability of unit-square RVEs with elliptic inclusions.* The plots shown in (**a**), (**b**), (**c**) and (**d**) refer to alignment angles of the magnetic induction of $\alpha = 0°$, $\alpha = 5°$, $\alpha = 20°$ and $\alpha = 45°$, respectively. In all cases, the shear modulus of the matrix is $\mu_{matrix} = 0.04$ MPa. We observe that for elliptic inclusions a non-aligned magnetic field highly influences the instability due to local shearing as a result of the rotation of inclusions.

was detected by [50], who showed that a superimposed shear deformation stabilizes a macroscopically stretched elastic composite. In the present scenario, the stabilization of the composite could be traced back to local shear deformations of the matrix, which are the result of magnetically induced (stable) rotations of the inclusions. When further increasing the alignment angle we observe a decrease of the stable loading ranges.

Some of the above discussed instabilities are related to multi-directional buckling events of the microscopic ligaments, see Fig. 4.18. These again come along with rotations of the elliptical inclusions and are typically observed under moderately applied stretch and large magnetic loading. Please note that under these circumstances we usually detect buckling into microstructures composed of 2×2 unit cells. However, when we apply large stretches and only moderate magnetic loading, we detect a pattern transformation into buckled microstructures composed of 1×2 unit cells (see Fig. 4.19).

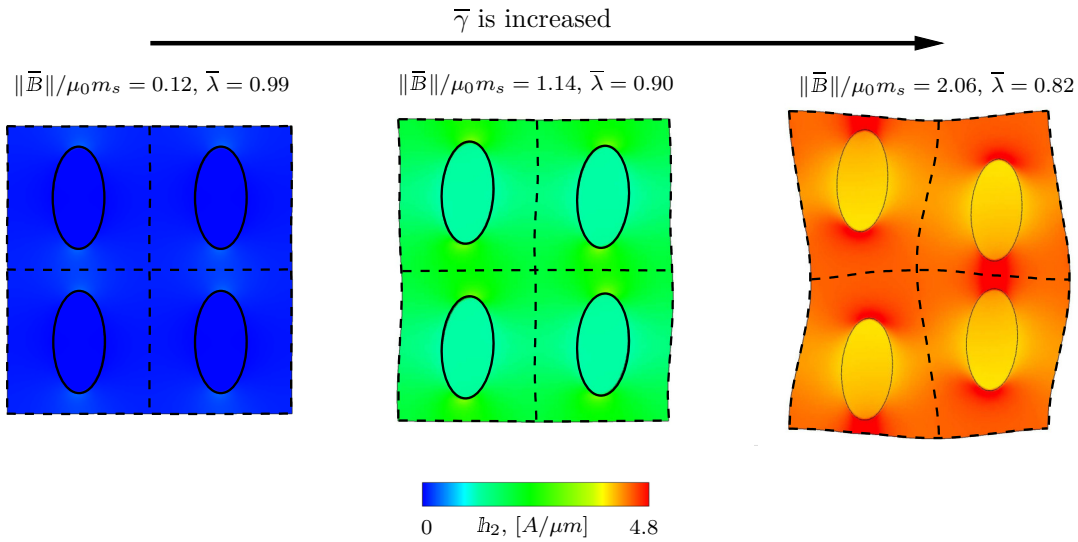

Figure 4.18: *Buckling mode of an MRE microstructure with elliptical inclusions of volume fraction $f_0 = 20\%$ (coupled magneto-mechanical loading).* The depicted buckling mode is associated with a bifurcation point that is detected under a path angle $\phi = -24°$ and an alignment angle $\alpha = 20°$. At the given instability point, the periodicity of the microstructure is associated with an RVE composed of 2×2 unit cells.

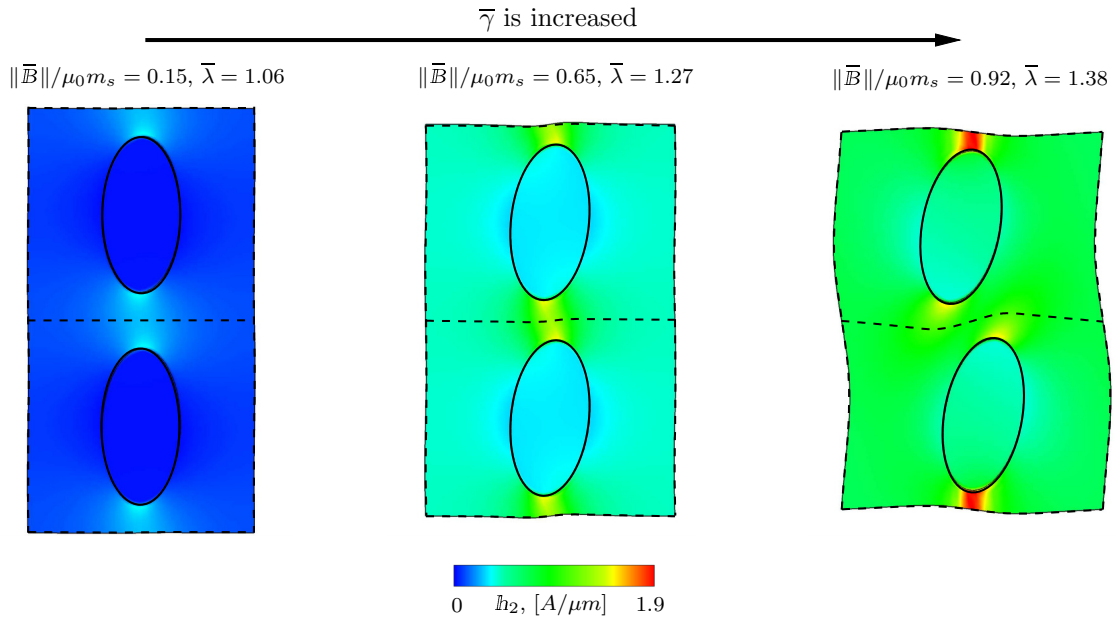

Figure 4.19: *Buckling mode of an MRE microstructure with elliptical inclusions of volume fraction $f_0 = 20\%$ (coupled magneto-mechanical loading).* The depicted buckling mode is associated with a bifurcation point that is detected under a path angle $\phi = 64°$ and an alignment angle $\alpha = 20°$. At the given instability point, the periodicity of the microstructure is associated with an RVE composed of 1×2 unit cells.

4.4.4 Stability analysis of three-phase MREs

As a final example, we consider a three-phase MRE composed of non-magnetic matrix, magnetic inclusions and voids. The volume fraction of voids and inclusions is 40% and 10%, respectively. The material parameters are given in Table 4.5. We have discretized

Table 4.5: Material parameters of the three-phase MRE composite considered in the numerical example of Sec. 4.4.4

No.	Parameter	Name	Matrix	Inclusion	Void
1.	ν	Poisson's ratio	0.495	0.495	0.45
2.	μ	Shear modulus, MPa	0.04	40	10^{-5}
3.	ξ	Strain saturation	100	100	100
4.	χ	Magnetic suscepctibility	0	0.995	0
5.	$\mu_0 m_s$	Magnetic saturation, T	–	2.0	–

the domain with Q_1P_0-type finite elements[20].

The results of the present study are depicted in Fig. 4.20**a**. Here we observe that microscopic buckling does only occur under mechanical tension. An associated instability mode matching the experimental observations documented by Tipton et al. [75] is shown in Fig. 4.20**b**.

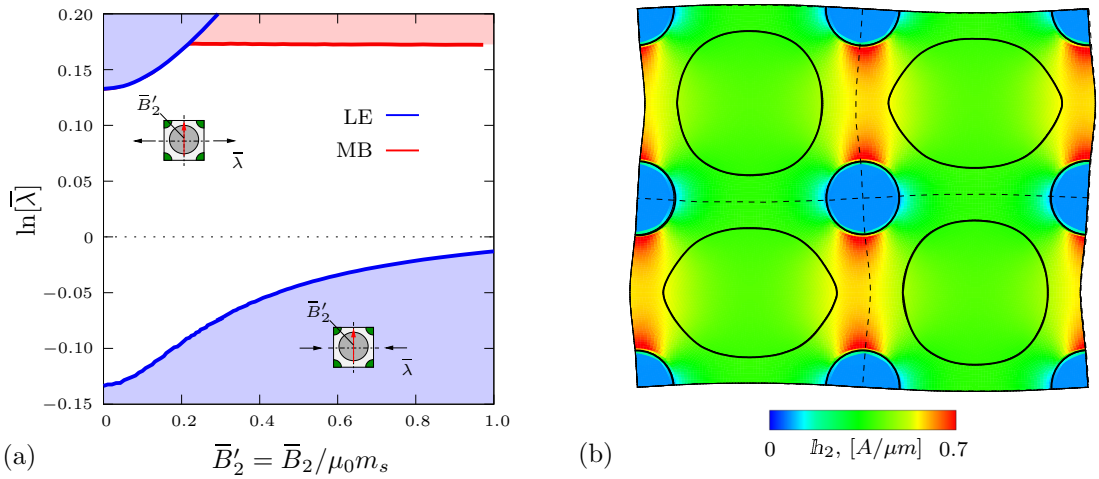

Figure 4.20: *Analysis of microscopic and macroscopic instabilities in a three-phase material.* The three-phase material is given by an elastomer with magnetic inclusions ($f_0^m = 0.1$) and voids ($f_0^v = 0.4$). The picture in (**a**) illustrates the onset of microscopic and macroscopic instabilities under magneto-mechanical loading. The graph in (**b**) shows the altered periodicity of the RVE due to microscopic buckling at a path angle $\phi = 70°$. The given snapshot corresponds to a coupled macroscopic loading state of $\overline{\lambda} \approx 1.2$ and $\overline{B}_2/\mu_0 m_s \approx 0.35$ and is in good qualitative agreement with the experimental findings of Tipton et al. [75].

[20]In case of Q_2P_1-type finite elements we observed zero-energy modes that lead to high distortions of elements. Q_1P_0-type finite elements did not show this behavior.

4.5 Conclusion and Discussion

We investigated the microscopic and macroscopic stability of magnetorheological elastomers under macroscopic magneto-mechanical loading. Starting point was a microscopic four-field variational formulation of magneto-elasticity that we have embedded into a framework of computational homogenization. The variational formulation has a minimization structure based on the mechanical deformation and magnetic vector potential as independent fields. Microscopic buckling-type instabilities were detected by means of Bloch–Floquet wave analysis. Macroscopic instabilities were determined by checking the strong ellipticity of homogenized moduli.

A series of numerical simulations revealed a rich spectrum of instabilities of magnetorheological elastomers. In particular, we have analyzed their overall response in consideration of different material properties, volume fractions and topologies of the individual phases as well as under a large set of coupled loading conditions. As could be shown, instabilities can be prevented or triggered by proper construction of microstructures and adjustment of coupled macroscopic loading. This opens the door to the material design of magnetorheological elastomers with tailored multifunctional properties.

In particular, our studies demonstrate that MREs provide a much richer set of possible pattern transformations than purely elastic materials. In fact, the MREs considered in the present work show complex pattern transformations under tension, compression and even in the absence of mechanical deformation. This goes far beyond the so far known achievable instabilities in elastic composites [78, 7, 50, 58, 7, 38] and may allow the development of MRE-based switches that significantly alter the behavior of composites under magnetic stimuli. In this context we highlight possible applications as tunable periodic (meta-)materials with tailored acoustic, auxetic, phononic and photonic properties.

Acknowledgements

The financial support of the German Research Foundation (DFG) in the framework of the Research Group 1509 “Ferroic Functional Materials” (project KE 1849/2-2) and in the framework of the Cluster of Excellence EXC 2075 (390740016) at the University of Stuttgart is gratefully acknowledged.

Appendix

A (Green-)Christoffel tensor in two-dimensions

Considering two spatial dimensions with $\overline{\boldsymbol{N}} = [\cos\overline{\theta}\ \ \sin\overline{\theta}]^T$ and using (4.21) the Christoffel tensor can be expressed as follows

$$\overline{\boldsymbol{\Gamma}}(\overline{\boldsymbol{N}}) := \overline{\boldsymbol{Q}}(\overline{\boldsymbol{N}}) - \frac{1}{\overline{\mathcal{D}}(\overline{\boldsymbol{N}})}\overline{\boldsymbol{\omega}}(\overline{\boldsymbol{N}}) \otimes \overline{\boldsymbol{\omega}}(\overline{\boldsymbol{N}}) \tag{4.41}$$

with

$$\begin{aligned}
\overline{\boldsymbol{Q}} &= \begin{bmatrix} \overline{A}_1{}^1{}_1{}^1 c^2 + 2\overline{A}_1{}^1{}_1{}^2 cs + \overline{A}_1{}^2{}_1{}^2 s^2 & \overline{A}_1{}^1{}_2{}^1 c^2 + (\overline{A}_1{}^1{}_2{}^2 + \overline{A}_1{}^2{}_2{}^1)cs + \overline{A}_1{}^2{}_2{}^2 s^2 \\ sym. & \overline{A}_2{}^1{}_2{}^1 c^2 + 2\overline{A}_2{}^1{}_2{}^2 cs + \overline{A}_2{}^2{}_2{}^2 s^2 \end{bmatrix} \\
\overline{\boldsymbol{\omega}}(\overline{\boldsymbol{N}}) &= \begin{bmatrix} \overline{G}_1{}^2{}_1 s^2 - \overline{G}_1{}^1{}_2 c^2 + (\overline{G}_1{}^1{}_1 - \overline{G}_1{}^2{}_2)sc \\ \overline{G}_2{}^2{}_1 s^2 - \overline{G}_2{}^1{}_2 c^2 + (\overline{G}_2{}^1{}_1 - \overline{G}_2{}^2{}_2)sc \end{bmatrix} \\
\overline{\mathcal{D}}(\overline{\boldsymbol{N}}) &= \overline{K}_{11} s^2 - (\overline{K}_{12} + \overline{K}_{21})cs + \overline{K}_{22} c^2 \,,
\end{aligned} \tag{4.42}$$

where $c := \cos\overline{\theta}$ and $s := \sin\overline{\theta}$. In the above equation $\overline{\boldsymbol{M}}$ is eliminated using (4.21).

B Numerical studies on the effective magneto-mechanical response of selected MRE microstructures

In order to provide further insight in the macroscopic magnetostriction of MREs, we further compute the homogenized response of selected two-phase composites based on the setting recently proposed by Danas [16].

We perform finite-element simulations on unit-square RVEs with various volume fractions of circular inclusions in the range $[5\% - 40\%]$. As macroscopic boundary conditions we assume that the RVE is mechanically stress-free and loaded with an Eulerian magnetic induction $\overline{\mathbb{b}}_b$ [16], i.e.,

$$\overline{\boldsymbol{P}}_b^{mec} = \boldsymbol{0} \quad \text{and} \quad \overline{\mathbb{b}}_b = \begin{bmatrix} 0 \\ \overline{b}_2 \end{bmatrix} . \tag{4.43}$$

According to Danas [16] the above setting can be accounted for using the macroscopic potential

$$\overline{\Pi}(\overline{\boldsymbol{F}}, \overline{\mathbb{B}}; \overline{\boldsymbol{P}}_b^{mec}, \overline{\mathbb{b}}_b) = \overline{\psi}(\overline{\boldsymbol{F}}, \overline{\mathbb{B}}) - \frac{1}{2\mu_0 \overline{J}}\|\overline{\mathbb{B}}\|^2_{\overline{\boldsymbol{C}}} + \frac{\overline{J}}{2\mu_0\zeta}\|\overline{J}^{-1}\overline{\boldsymbol{F}}\cdot\overline{\mathbb{B}} - \overline{\mathbb{b}}_b\|^2 - \overline{\boldsymbol{P}}_b^{mec} : (\overline{\boldsymbol{F}} - \boldsymbol{1}) \,, \tag{4.44}$$

where $\overline{\psi}$ is defined by (4.13) and ζ is a penalty parameter enforcing the constraint associated with the magnetic-induction fields. This parameter is set to 10^{-7} in the following numerical simulations. The material parameters used in the present study are given in Table 4.3.

In Fig. 4.21 we show the macroscopic magnetization $\overline{m}_2$ and macroscopic deformation gradient $\overline{F}_{22}$ induced by an applied macroscopic magnetic induction $\overline{b}_b = [0, \overline{b}_2]^T$. We observe that the saturation values of the effective magnetization grow with the volume fraction of the magnetic inclusions. Such a behavior is not present for the saturation of the macroscopic deformation $\overline{F}_{22}$, which initially increases with volume fraction, but then starts to decrease for volume fractions greater than 20%, see also Danas [16] for details.

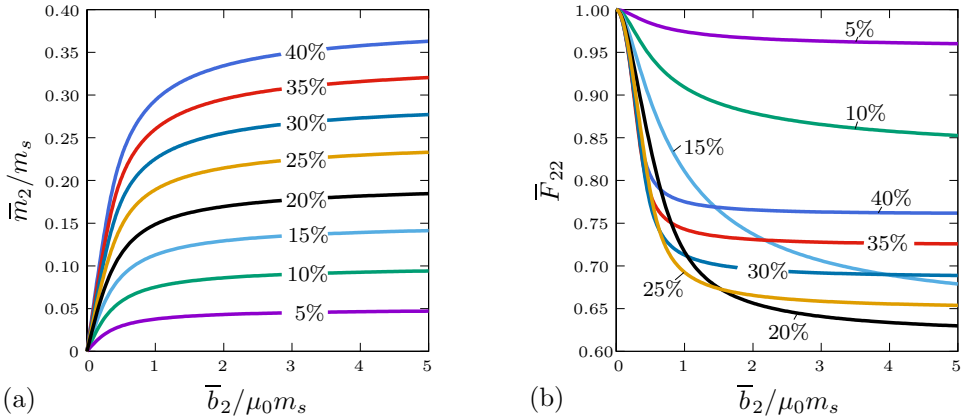

Figure 4.21: *Magneto-mechanical response of periodic MRE unit cells with different volume fractions of circular magnetic inclusions.* In (**a**) we observe that the saturation of the homogenized magnetization $\overline{m}_2$ increases monotonically with the volume fraction of inclusions. In (**b**) we observe that the saturation of deformation $\overline{F}_{22}$ evolves non-monotonically with increasing volume fraction of inclusions.

We note that the setting above is idealized in the sense that usual MRE specimens show a complex macroscopic response which makes it difficult to prescribe the above given fields experimentally. For further discussions, we refer the reader, for example, to to [43, 44, 46, 10].

Bibliography: Paper B

[1] Abeyaratne, R., Triantafyllidis, N., [1984]. *An investigation of localization in a porous elastic material using homogenization theory*. ASME Journal of Applied Mechanics 51(3), 481–486. (doi:doi:10.1115/1.3167661)

[2] Babaee, S., Shim, J., Weaver, J. C., Chen, E. R., Patel, N., Bertoldi, K., [2013]. *3d soft metamaterials with negative poisson's ratio*. Advanced Materials 25 (36), 5044–5049.

[3] Ball, J., [1977]. *Convexity conditions and existence theorems in nonlinear elasticity*. Archive of Rational Mechanics and Analysis 63, 337–403.

[4] Ball, J. M., James, R. D., [1989]. *Fine phase mixtures as minimizers of energy*. In: *Analysis and Continuum Mechanics*. Springer, pp. 647–686.

[5] Bastola, A., Hoang, V., Li, L., [2017]. *A novel hybrid magnetorheological elastomer developed by 3d printing*. Materials & Design 114, 391–397.

[6] Bertoldi, K., Boyce, M., Deschanel, S., Prange, S., Mullin, T., [2008]. *Mechanics of deformation-triggered pattern transformations and superelastic behavior in periodic elastomeric structures*. Journal of the Mechanics and Physics of Solids 56, 2642–2668. (doi:doi:10.1016/j.jmps.2008.03.006)

[7] Bertoldi, K., Boyce, M. C., [2008]. *Wave propagation and instabilities in monolithic and periodically structured elastomeric materials undergoing large deformations*. Physical Review B 78 (18), 184107. (doi:10.1103/PhysRevB.78.184107)

[8] Bertoldi, K., Gei, M., [2011]. *Instabilities in multilayered soft dielectrics*. Journal of the Mechanics and Physics of Solids 59, 18–42. (http://www.sciencedirect.com/science/article/pii/S0022509610002036)

[9] Bertoldi, K., Reis, P. M., Willshaw, S., Mullin, T., [2010]. *Negative poisson's ratio behavior induced by an elastic instability*. Advanced materials 22 (3), 361–366.

[10] Bodelot, L., Voropaieff, J.-P., Pössinger, T., [2018]. *Experimental investigation of the coupled magneto-mechanical response in magnetorheological elastomers*. Experimental Mechanics 58 (2), 207–221.

[11] Brigadnov, I., Dorfmann, A., [2003]. *Mathematical modeling of magneto-sensitive elastomers*. International Journal of Solids and Structures 40 (18), 4659–4674.

[12] Brink, U., Stein, E., [1996]. *On some mixed finite element methods for incompressible and nearly incompressible finite elasticity*. Computational Mechanics 19 (1), 105–119.

[13] Brown, W. F., [1966]. *Magnetoelastic interactions*. Springer.

[14] Bustamante, R., Dorfmann, A., Ogden, R. W., [2008]. *On variational formulations in nonlinear magnetoelastostatics*. Mathematics and Mechanics of Solids 13 (8), 725–745.

[15] Carlson, J. D., Jolly, M. R., [2000]. *MR fluid, foam and elastomer devices*. mechatronics 10 (4), 555–569.

[16] Danas, K., [2017]. *Effective response of classical, auxetic and chiral magnetoelastic materials by use of a new variational principle*. Journal of the Mechanics and Physics of Solids 105 (Supplement C), 25 – 53. (doi:https://doi.org/10.1016/j.jmps.2017.04.016)

[17] Danas, K., Kankanala, S., Triantafyllidis, N., [2012]. *Experiments and modeling of iron-particle-filled magnetorheological elastomers*. Journal of the Mechanics and Physics of Solids 60 (1), 120 – 138. (doi:http://dx.doi.org/10.1016/j.jmps.2011.09.006)

[18] Destrade, M., Ogden, R. W., [2010]. *On the third-and fourth-order constants of incompressible isotropic elasticity*. The Journal of the Acoustical Society of America 128 (6), 3334–3343.

[19] Destrade, M., Ogden, R. W., [2011]. *On magneto-acoustic waves in finitely deformed elastic solids*. Mathematics and Mechanics of Solids 16 (6), 594–604.

[20] Diguet, G., Beaugnon, E., Cavaillé, J., [2009]. *From dipolar interactions of a random distribution of ferromagnetic particles to magnetostriction*. Journal of Magnetism and Magnetic Materials 321 (5), 396 – 401. (doi:https://doi.org/10.1016/j.jmmm.2008.08.112)

[21] Diguet, G., Beaugnon, E., Cavaillé, J., [2010]. *Shape effect in the magnetostriction of ferromagnetic composite*. Journal of Magnetism and Magnetic Materials 322 (21), 3337–3341.

[22] Ding, Y., Liu, Z., Qiu, C., Shi, J., [2007]. *Metamaterial with simultaneously negative bulk modulus and mass density*. Physical review letters 99 (9), 093904.

[23] Dorfmann, A., Ogden, R., [2003]. *Magnetoelastic modelling of elastomers*. European Journal of Mechanics-A/Solids 22 (4), 497–507.

[24] Dorfmann, A., Ogden, R., [2004]. *Nonlinear magnetoelastic deformations of elastomers*. Acta Mechanica 167 (1), 13–28.

[25] Farshad, M., Benine, A., [2004]. *Magnetoactive elastomer composites*. Polymer testing 23 (3), 347–353.

[26] Galipeau, E., Ponte Castañeda, P., [2012]. *The effect of particle shape and distribution on the macroscopic behavior of magnetoelastic composites*. International Journal of Solids and Structures 49 (1), 1–17.

[27] Galipeau, E., Ponte Castañeda, P., [2013]. *A finite-strain constitutive model for magnetorheological elastomers: magnetic torques and fiber rotations*. Journal of the Mechanics and Physics of Solids 61 (4), 1065–1090.

[28] Gent, A. N., [1996]. *A new constitutive relation for rubber*. Rubber Chemistry and Technology 69, 59–61.

[29] Geymonat, G., Müller, S., Triantafyllidis, N., [1993]. *Homogenization of nonlinearly elastic materials, microscopic bifurcation and macroscopic loss of rank-one convexity*. Archive for Rational Mechanics and Analysis 122, 231–290. (doi:DOI: 10.1007/BF00380256)

[30] Ginder, J. M., Nichols, M. E., Elie, L. D., Clark, S. M., [2000]. *Controllable-stiffness components based on magnetorheological elastomers*. In: *Proceedings-SPIE The International Society For Optical Engineering*. International Society for Optical Engineering; 1999, pp. 418–425.

[31] Ginder, J. M., Nichols, M. E., Elie, L. D., Tardiff, J. L., [1999]. *Magnetorheological elastomers: properties and applications*. In: *Proc. SPIE*. Vol. 3675. pp. 131–138.

[32] Ginder, J. M., Schlotter, W. F., Nichols, M. E., [2001]. *Magnetorheological elastomers in tunable vibration absorbers*. In: *Proc. SPIE*. Vol. 4331. pp. 103–110.

[33] Goshkoderia, A., Rudykh, S., [2017]. *Electromechanical macroscopic instabilities in soft dielectric elastomer composites with periodic microstructures*. European Journal of Mechanics-A/Solids 65, 243–256.

[34] Goshkoderia, A., Rudykh, S., [2017]. *Stability of magnetoactive composites with periodic microstructures undergoing finite strains in the presence of a magnetic field*. Composites Part B: Engineering 128 (Supplement C), 19 – 29. (doi:https://doi.org/10.1016/j.compositesb.2017.06.014)

[35] Hill, R., [1963]. *Elastic properties of reinforced solids: Some theoretical principles*. Journal of the Mechanics and Physics of Solids 11, 357–372.

[36] Itskov, M., Khiêm, V. N., [2016]. *A polyconvex anisotropic free energy function for electro- and magneto-rheological elastomers*. Mathematics and Mechanics of Solids 21 (9), 1126–1137. (doi:10.1177/1081286514555140)

[37] Jandron, M., Henann, D. L., [2020]. *Electromechanical instabilities in periodic dielectric elastomer composites*. International Journal of Solids and Structures 191, 220–242.

[38] Jang, J.-H., Koh, C. Y., Bertoldi, K., Boyce, M. C., Thomas, E. L., [2009]. *Combining pattern instability and shape-memory hysteresis for phononic switching*. Nano letters 9 (5), 2113–2119.

[39] Javili, A., Chatzigeorgiou, G., Steinmann, P., [2013]. *Computational homogenization in magneto-mechanics*. International Journal of Solids and Structures 50 (25), 4197–4216.

[40] Jolly, M. R., Carlson, J. D., Munoz, B. C., [1996]. *A model of the behaviour of magnetorheological materials*. Smart Materials and Structures 5 (5), 607.

[41] Kalina, K. A., Metsch, P., Kästner, M., [2016]. *Microscale modeling and simulation of magnetorheological elastomers at finite strains: A study on the influence of mechanical preloads*. International Journal of Solids and Structures 102, 286–296.

[42] Kankanala, S., Triantafyllidis, N., [2004]. *On finitely strained magnetorheological elastomers*. Journal of the Mechanics and Physics of Solids 52 (12), 2869–2908.

[43] Keip, M.-A., Rambausek, M., [2016]. *A multiscale approach to the computational characterization of magnetorheological elastomers*. International Journal for Numerical Methods in Engineering 107 (4), 338–360.

[44] Keip, M.-A., Rambausek, M., [2017]. *Computational and analytical investigations of shape effects in the experimental characterization of magnetorheological elastomers*. International Journal of Solids and Structures 121, 1–20.

[45] Kochmann, D. M., Bertoldi, K., [2017]. *Exploiting microstructural instabilities in solids and structures: From metamaterials to structural transitions*. Applied mechanics reviews 69 (5), 050801.

[46] Lefèvre, V., Danas, K., Lopez-Pamies, O., [2017]. *A general result for the magnetoelastic response of isotropic suspensions of iron and ferrofluid particles in rubber, with applications to spherical and cylindrical specimens*. Journal of the Mechanics and Physics of Solids 107, 343–364.

[47] Li, J., Slesarenko, V., Rudykh, S., [2019]. *Microscopic instabilities and elastic wave propagation in finitely deformed laminates with compressible hyperelastic phases*. European Journal of Mechanics-A/Solids 73, 126–136.

[48] Maugin, G. A., Eringen, A. C., [1972]. *Deformable magnetically saturated media. i. field equations*. Journal of Mathematical Physics 13 (2), 143–155.

[49] Metsch, P., Kalina, K. A., Spieler, C., Kästner, M., [2016]. *A numerical study on magnetostrictive phenomena in magnetorheological elastomers*. Computational Materials Science 124, 364–374.

[50] Michel, J., Lopez-Pamies, O., Ponte Castañeda, P., Triantafyllidis, N., [2010]. *Microscopic and macroscopic instabilities in finitely strained fiber-reinforced elastomers*. Journal of the Mechanics and Physics of Solids 58, 1776–1803. (doi:doi:10.1016/j.jmps.2010.08.006)

[51] Miehe, C., [1994]. *Aspects of the formulation and finite element implementation of large strain isotropic elasticity*. International journal of numerical methods in engineering 37, 1981–2004.

[52] Miehe, C., Schotte, J., Schröder, J., [1999]. *Computational micro-macro transitions and overall moduli in the analysis of polycrystals at large strains*. Computational Materials Science 16, 372–382.

[53] Miehe, C., Schröder, J., [1994]. *Post-critical discontinuous localization analysis of small-strain softening elastoplastic solids*. Archive of Applied Mechanics 64 (4), 267–285.

[54] Miehe, C., Schröder, J., Becker, M., [2002]. *Computational homogenization analysis in finite elasticity: material and structural instabilities on the micro-and macro-scales of periodic composites and their interaction*. Computer Methods in Applied Mechanics and Engineering 191 (44), 4971–5005.

[55] Miehe, C., Vallicotti, D., Teichtmeister, S., [2016]. *Homogenization and multiscale stability analysis in finite magneto-electro-elasticity. application to soft matter EE, ME and MEE composites*. Computer Methods in Applied Mechanics and Engineering 300, 294–346.

[56] Morrey, C. B., [1952]. *Quasi-convexity and the lower semicontinuity of multiple integrals*. Pacific Journal of Mathematics 2 (1), 25–53.

[57] Müller, S., [1987]. *Homogenization of nonconvex integral functionals and cellular elastic materials*. Archive of Rational Mechanics and Analysis 99, 189–212.

[58] Mullin, T., Deschanel, S., Bertoldi, K., Boyce, M. C., [2007]. *Pattern transformation triggered by deformation*. Physical review letters 99 (8), 084301.

[59] Okada, J.-I., Hisada, T., [2009]. *Study on compressibility control of hyperelastic material for homogenization method using mixed finite element analysis*. Journal of Computational Science and Technology 3 (1), 89–100.

[60] Pao, Y.-H., [1978]. *Electromagnetic forces in deformable continua*. In: *In: Mechanics today. Volume 4.(A78-35706 14-70) New York, Pergamon Press, Inc., 1978, p. 209-305. NSF-supported research.* Vol. 4. pp. 209–305.

[61] Pao, Y.-H., Yeh, C.-S., [1973]. *A linear theory for soft ferromagnetic elastic solids*. International Journal of Engineering Science 11 (4), 415–436.

[62] Polukhov, E., Vallicotti, D., Keip, M.-A., [2018]. *Computational stability analysis of periodic electroactive polymer composites across scales*. Computer Methods in Applied Mechanics and Engineering 337, 165–197.

[63] Ponte Castañeda, P., Galipeau, E., [2011]. *Homogenization-based constitutive models for magnetorheological elastomers at finite strain*. Journal of the Mechanics and Physics of Solids 59 (2), 194–215.

[64] Rambausek, M., Göküzüm, F. S., Nguyen, L. T. K., Keip, M.-A., [2019]. *A two-scale FE-FFT approach to nonlinear magneto-elasticity*. International Journal for Numerical Methods in Engineering 117 (11), 1117–1142.

[65] Rudykh, S., Bertoldi, K., [2013]. *Stability of anisotropic magnetorheological elastomers in finite deformations: A micromechanical approach*. Journal of the Mechanics and Physics of Solids 61, 949–967. (doi:http://dx.doi.org/10.1016/j.jmps.2012.12.008)

[66] Rudykh, S., deBotton, G., [2012]. *Instabilities of hyperelastic fiber composites: Micromechanical versus numerical analyses*. Journal of Elasticity 106, 123–147. (doi:DOI 10.1007/s10659-011-9313-x)

[67] Rudykh, S., deBotton, G., [2012]. *Stability of anisotropic electroactive polymers with application to layered media*. Zeitschrift für angewandte Mathematik und Physik 62, 1131–1142. (doi:DOI 10.1007/s10659-011-9313-x)

[68] Schröder, J., Keip, M.-A., [2012]. *Two-scale homogenization of electromechanically coupled boundary value problems*. Computational Mechanics 50 (2), 229–244.

[69] Šilhavỳ, M., [2017]. *Isotropic polyconvex electromagnetoelastic bodies*. Mathematics and Mechanics of Solids, 1081286518754567.

[70] Simo, J., Taylor, R., Pister, K., [1985]. *Variational and projection methods for the volume constraint in finite deformation elasto-plasticity*. Computer Methods in Applied Mechanics and Engineering 51, 177–208.

[71] Slesarenko, V., Rudykh, S., [2017]. *Microscopic and macroscopic instabilities in hyperelastic fiber composites*. Journal of the Mechanics and Physics of Solids 99, 471–482.

[72] Steigmann, D. J., [2004]. *Equilibrium theory for magnetic elastomers and magnetoelastic membranes*. International Journal of Non-Linear Mechanics 39, 1193–1216.

[73] Sutrisno, J., Purwanto, A., Mazlan, S. A., [2015]. *Recent progress on magnetorheological solids: materials, fabrication, testing, and applications*. Advanced Engineering Materials 17 (5), 563–597.

[74] Tiersten, H., [1964]. *Coupled magnetomechanical equations for magnetically saturated insulators*. Journal of Mathematical Physics 5 (9), 1298–1318.

[75] Tipton, C., Han, E., Mullin, T., [2012]. *Magneto-elastic buckling of a soft cellular solid*. Soft Matter 8 (26), 6880–6883.

[76] Triantafyllidis, N., Bardenhagen, S., [1996]. *The influence of scale size on the stability of periodic solids and the role of associated higher order gradient continuum models*. Journal of the Mechanics and Physics of Solids 44, 1891–1928. (doi:doi.org/10.1016/0022-5096(96)00047-6)

[77] Triantafyllidis, N., Maker, B. N., [1985]. *On the comparison between microscopic and macroscopic instability mechanisms in a class of fiber-reinforced composites*. ASME Journal of Applied Mechanics 52, 794–800. (doi:doi:10.1115/1.3169148)

[78] Triantafyllidis, N., Nestorović, M. D., Schraad, M. W., [2006]. *Failure surfaces for finitely strained two-phase periodic solids under general in-plane loading*. ASME Journal of Applied Mechanics 73(3), 505–515. (doi:doi:10.1115/1.2126695)

[79] Truesdell, C., Noll, W., [2004]. *The non-linear field theories of mechanics*. In: *The non-linear field theories of mechanics*. Springer, pp. 1–579.

[80] Truesdell, C., Toupin, R., [1960]. *The classical field theories*. In: *Principles of Classical Mechanics and Field Theory/Prinzipien der Klassischen Mechanik und Feldtheorie*. Springer, pp. 226–858.

[81] Varga, Z., Filipcsei, G., Zrínyi, M., [2005]. *Smart composites with controlled anisotropy*. Polymer 46 (18), 7779 – 7787, stimuli Responsive Polymers. (doi:http://dx.doi.org/10.1016/j.polymer.2005.03.102)

[82] Varga, Z., Filipcsei, G., Zrínyi, M., [2006]. *Magnetic field sensitive functional elastomers with tuneable elastic modulus*. Polymer 47 (1), 227 – 233. (doi:http://dx.doi.org/10.1016/j.polymer.2005.10.139)

[83] Walter, B. L., Pelteret, J.-P., Kaschta, J., Schubert, D. W., Steinmann, P., [2017]. *Preparation of magnetorheological elastomers and their slip-free characterization by means of parallel-plate rotational rheometry*. Smart Materials and Structures 26 (8), 085004.

[84] Wang, P., Casadei, F., Shan, S., Weaver, J. C., Bertoldi, K., [2014]. *Harnessing buckling to design tunable locally resonant acoustic metamaterials*. Physical review letters 113 (1), 014301.

Chapter 5: Paper C

Computational Homogenization of Transient Chemo-Mechanical Processes Based on a Variational Minimization Principle

Computational Homogenization of Transient Chemo-Mechanical Processes Based on a Variational Minimization Principle

Original publication:

Polukhov, E. & Keip, M.-A. [2020]. *Computational homogenization of transient chemo-mechanical processes based on a variational minimization principle.* Advanced Modeling and Simulation in Engineering Sciences 7 (1), 1–26.

Abstract

We present a variational framework for the computational homogenization of chemo-mechanical processes of soft porous materials. The multiscale variational framework is based on a minimization principle with deformation map and solvent flux acting as independent variables. At the microscopic scale we assume the existence of periodic representative volume elements (RVEs) that are linked to the macroscopic scale via first-order scale transition. In this context, the macroscopic problem is considered to be homogeneous in nature and is thus solved at a single macroscopic material point. The microscopic problem is however assumed to be heterogeneous in nature and thus calls for spatial discretization of the underlying RVE. Here, we employ Raviart–Thomas finite elements and thus arrive at a conforming finite-element formulation of the problem. We present a sequence of numerical examples to demonstrate the capabilities of the multiscale formulation and to discuss a number of fundamental effects.

Keywords: computational homogenization, chemo-mechanics, diffusion, hydrogels, porous materials

5.1 Introduction

The continuous advancement of technological innovations in the fields of digitalization and automation leads to increased demands of smart and multifunctional materials. In that context, the design of associated materials with tailor-made properties is paramount. Classical examples cover solids with coupled electro- and magneto-mechanical response such as ferroelectrics or magnetostrictives. More recently, several advanced materials exhibiting chemo-mechanical coupling have entered the scene and experience increased attention since then. Related materials show interactions between fluid flow and deformations and play an important role in emerging applications such as lithium-ion batteries (Wang et al. [40]), heterogeneous concretes (Wang and Ueda [41]), engineered biological tissues (Truskey et al. [38]), or fiber-reinforced superabsorbent hydrogels (Chen and Park [7]).

In order to allow for the theoretical development of related materials and structures, reliable continuum-mechanical models are needed. Related formulations have to take into account the mutual couplings between the fluidic diffusion of some solvent phase and the mechanical deformation of some solid phase in a single multiphase material. In fact, the development of continuum-mechanical models and associated numerical implementations have seen a lot of advancements recently. We refer to the works of Hong et al. [20, 19], Chester and Anand [8], Nilenius et al. [28], Miehe et al. [25], Ehlers and Wagner [11] and Böger et al. [4] among many others.

In addition to that—when targeting the design of materials—the need for multiscale continuum approaches becomes evident. Associated homogenization techniques involving

continuum microstructures trace back to the early works of Voigt [39], Reuss [33], Hill [18]. For the realization of multiscale numerical simulations we refer to Miehe et al. [26], Feyel and Chaboche [12]. A common feature of the above approaches is the identification of a representative volume element (RVE) that reflects the heterogeneity of a given microstructure. Here, one often assumes separation of length scales by postulating that typical length scales of the RVE are much smaller than typical length scales of a corresponding macroscopic problem. This then renders the notion of so-called first-order homogenization schemes.[21]

Extensions of first-order homogenization towards the incorporation of heat conduction have been proposed by Özdemir et al. [29], Temizer and Wriggers [37], Temizer [36] and Chatzigeorgiou et al. [6]. Here, the transient behavior of the material is considered only at the macroscopic level, while at the microscale the problem is assumed to be stationary. In contrast to that, Larsson et al. [24] have proposed the variationally consistent homogenization of heat conduction that takes into account the transient behavior also at the microscopic level.[22] The latter approach leads to size-dependent macroscopic response. As could be shown by the authors, the size dependence vanishes when the size of the RVE approaches zero. While such effect seems in accordance with the idea of scale separation, it does not occur in the first-order homogenization of stationary problems. Related effects and consequences have been discussed by Kaessmair and Steinmann [21] who proposed a transient homogenization framework for coupled chemo-mechanical problems.

Close to the formulations of Larsson et al. [24] and Kaessmair and Steinmann [21] we propose a variationally consistent homogenization approach to the coupled chemo-mechanics of transient diffusion-deformation processes in soft, porous solids. In doing so, we critically revise the influence of the RVE size on the effective macroscopic response of a transient microscopic problem. In contrast to the above-mentioned homogenization schemes of thermo- and chemo-mechanics, we consider the computational homogenization of diffusion-deformation processes within a minimization-based variational formulation. The latter is adopted from the ideas of Miehe et al. [25] and Böger et al. [4].

In the minimization-based formulation, the deformation map and the solvent-volume flux act as the independent fields. Associated formulations have several advantages compared with direct formulations (that are based on balance equations) and standard saddle-point formulations (that usually exploit the chemical potential as independent field next to the displacement):

1. In contrast to direct approaches, variational structures lead to compact representations involving symmetric system matrices [25, 4].

2. For two-dimensional problems it could be shown that the minimization formulation is computationally more efficient than both direct approaches and saddle-point formulations [25, 35].

3. A minimization formulation is not restricted by the inf-sup condition, which is an inherent problem of saddle-point formulations [35, 23].

[21] A higher-order approach has been proposed by Kouznetsova et al. [22].

[22] We refer to Pham et al. [30] for the homogenization of microscopically transient problems in the framework of dynamic metamaterials.

4. A minimization formulation is favorable for the investigation of structural instabilities since the coupled stiffness matrix is positive definite unless an instability occurs [14, 31].

5. In the context of homogenization methods, minimization structures can be embedded into Hashin–Shtrikman variational principles and thus allow the computation of bounds of effective material properties [17, 27].

Next to that, we should however note that the above advantages come at the cost of a more involved spatial discretization of the solvent-volume flux based on $H(\mathrm{Div})$-conforming finite elements. For the latter we refer to Miehe et al. [25], Böger et al. [4], Teichtmeister et al. [35].

The structure of the present contribution is as follows. In Section 5.2, we start with the definition of a rate-type variational principle of homogenization based on the deformation map and the solvent-volume flux as independent field variables. The rate-type principle is then translated into an incremental variational principle of homogenization. The latter comes along with discretization in space and time. For time integration, we employ an implicit Euler scheme. The spatial discretization is realized by means of conforming Raviart–Thomas-type finite elements. Based on the discrete setting, we are able to determine all relevant macroscopic quantities including the algorithmically consistent material moduli. In Section 5.3, we briefly comment on the size dependence of the homogenization problem involving the transient diffusion at microscale. This discussion serves as motivation for the set of numerical examples to be covered in Section 5.4. There we present a sequence of numerical studies of the effective response of two-phase porous composites. A conclusion of the present work will finally be given in Section 5.5.

5.2 Variational homogenization of diffusion-deformation processes

In the present section, we discuss the computational homogenization of diffusion-deformation processes based on a rate-type variational formulation. We consider a variationally consistent approach close to the ideas of Larsson et al. [24]. However, in contrast to the latter work, our goal is to develop a homogenization scheme that is based on a minimization principle. The spatial discretization of the coupled problem will be realized within a conforming finite-element formulation based on Raviart–Thomas-type finite elements. In order not to overload the presentation, we will keep the motivation for the use of certain functionals as concise as possible. For more information on related topics the interested reader is referred to Hong et al. [20, 19] and Böger et al. [4].

5.2.1 Constitutive state variables at the microscopic level

In the context of a minimization formulation, a diffusion-deformation process can be described by two independent fields given by the deformation map $\boldsymbol{\varphi}$ and the solvent-volume flux $\mathbb{H}$ having the following properties (Gurtin et al. [16], Miehe et al. [25], Böger et al. [4])

$$\boldsymbol{\varphi} : \begin{cases} \mathcal{B}_0 \times \mathcal{T} \to \mathcal{B}_t \subset \mathcal{R}^3 \\ (\boldsymbol{X}, t) \mapsto \boldsymbol{\varphi}(\boldsymbol{X}, t) \end{cases} \quad \text{and} \quad \mathbb{H} : \begin{cases} \mathcal{B}_0 \times \mathcal{T} \to \mathcal{R}^3 \\ (\boldsymbol{X}, t) \mapsto \mathbb{H}(\boldsymbol{X}, t)\,, \end{cases} \tag{5.1}$$

where $\boldsymbol{X}$ denotes a material point at the microscopic reference configuration $\mathcal{B}_0$, which is mapped to the current configuration $\mathcal{B}_t$ by the deformation map $\boldsymbol{\varphi}$. The solvent-volume flux $\mathbb{H}$ describes the flow of the solvent volume relative to the solid skeleton. Such interpretation follows Biot's approach to the modeling of porous media [3]. For a detailed derivation of the equations used in the present contribution we refer to Coussy et al. [9].

Furthermore, we introduce the concentration of solvent volume describing the amount of solvent molecules in a referential infinitesimal volume element

$$s : \begin{cases} \mathcal{B}_0 \times \mathcal{T} \to \mathcal{R}^+ \\ (\boldsymbol{X}, t) \mapsto s(\boldsymbol{X}, t) \end{cases} \tag{5.2}$$

with $s = \nu c$. Here ν denotes the volume of a single solvent molecule and c is the number of these molecules. The solvent-volume concentration s can be related to the solvent flux by considering the conservation of solvent-volume concentration (Gurtin et al. [16]). It states that the change of solvent-volume concentration in a given arbitrary domain of a body is equal to the flux of solvent volume across the surface of that domain. Locally, this can be expressed as

$$\dot{s} = -\operatorname{Div} \mathbb{H} \,. \tag{5.3}$$

Considering a first-order approach of homogenization, the independent fields can be decomposed into microscopic and macroscopic contributions

$$\boldsymbol{\varphi}(\boldsymbol{X}, t) := \widetilde{\boldsymbol{\varphi}}(\boldsymbol{X}, t) + \hat{\overline{\boldsymbol{\varphi}}}(\overline{\boldsymbol{X}}, \boldsymbol{X}, t) \quad \text{and} \quad \mathbb{H}(\boldsymbol{X}, t) := \widetilde{\mathbb{H}}(\boldsymbol{X}, t) + \hat{\overline{\mathbb{H}}}(\overline{\boldsymbol{X}}, \boldsymbol{X}, t) \,, \tag{5.4}$$

where $\widetilde{\boldsymbol{\varphi}}$ and $\widetilde{\mathbb{H}}$ denote microscopic fluctuations of the deformation map and the solvent-volume flux, respectively. We refer to Fig. 5.1 for a graphical illustration.

Further considering a Taylor expansion of the macroscopic contributions up to the linear terms yields[23]

$$\begin{aligned} \hat{\overline{\boldsymbol{\varphi}}}(\overline{\boldsymbol{X}}, \boldsymbol{X}, t) &= \overline{\boldsymbol{\varphi}}(\overline{\boldsymbol{X}}, t) + \overline{\boldsymbol{F}}(\overline{\boldsymbol{X}}, t) \cdot \boldsymbol{X} \\ \hat{\overline{\mathbb{H}}}(\overline{\boldsymbol{X}}, \boldsymbol{X}, t) &= \overline{\mathbb{H}}(\overline{\boldsymbol{X}}, t) + \frac{1}{3} \overline{\operatorname{Div}} \overline{\mathbb{H}}(\overline{\boldsymbol{X}}, t) \boldsymbol{X} \,, \end{aligned} \tag{5.5}$$

where $\overline{\boldsymbol{F}} = \overline{\operatorname{Grad}} \overline{\boldsymbol{\varphi}}$ is the macroscopic deformation gradient and $\dot{\overline{s}} = -\overline{\operatorname{Div}} \overline{\mathbb{H}}$ is the rate of the macroscopic solvent-volume concentration. In what follows, we assume that the origin of the coordinate system is located at the geometric center of the RVE, i.e., $\int_{\mathcal{B}_0} \boldsymbol{X} \, \mathrm{d}V = \boldsymbol{0}$.

From (5.4) we obtain the deformation gradient $\boldsymbol{F}$ and the divergence of the solvent flux $\operatorname{Div} \mathbb{H}$ as

$$\boldsymbol{F} = \widetilde{\boldsymbol{F}} + \overline{\boldsymbol{F}} \quad \text{and} \quad \operatorname{Div} \mathbb{H} = \operatorname{Div} \widetilde{\mathbb{H}} + \overline{\operatorname{Div}} \overline{\mathbb{H}} \,. \tag{5.6}$$

The latter equation implies that the solvent-volume concentration can be decomposed into fluctuative microscopic and constant macroscopic parts as $s = \widetilde{s} + \overline{s}$. Integrating the

[23] We note that in $(5.5)_2$, we have assumed macroscopic *isotropic swelling*. Consequently, the linear expansion of the solvent-volume flux is associated with the divergence and not the gradient of $\overline{\mathbb{H}}$. From the following equations, it will become clear that the considered form of the microscopic flux preserves the well-known structure of the diffusion-deformation problem at the micro- and the macroscale.

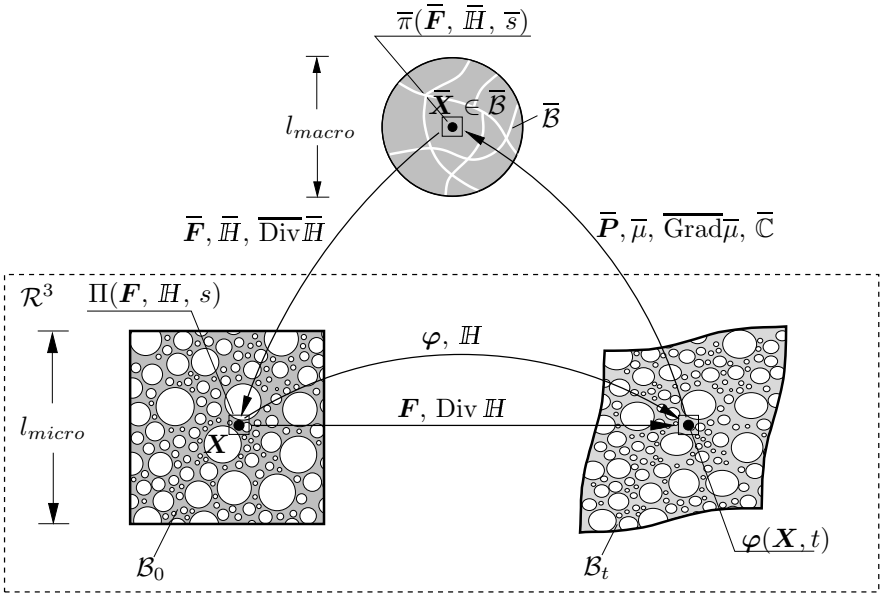

Figure 5.1: *Graphical illustration of the computational homogenization chemo-mechanical processes.* The macroscopic dual fields and moduli at a macroscopic material point $\overline{\boldsymbol{X}}$ are determined by solving a microscopic boundary value problem. The domain of the microscopic problem is chosen such that it represents the heterogeneity of the microstructure in a representative manner and is thus referred to as representative volume element (RVE). In a minimization-based variational formulation the RVE is driven by the deformation gradient $\overline{\boldsymbol{F}}$ as well as the solvent-volume flux $\overline{\mathbb{H}}$ and its divergence $\overline{\mathrm{Div}}\overline{\mathbb{H}}$.

equations in (5.6) over the domain of the RVE with $|\mathcal{B}_0| = vol(\mathcal{B}_0)$ yields

$$\begin{aligned} \overline{\boldsymbol{F}} &= \frac{1}{|\mathcal{B}_0|}\int_{\mathcal{B}_0} \boldsymbol{F}\,\mathrm{d}V = \frac{1}{|\mathcal{B}_0|}\int_{\partial\mathcal{B}_0} \boldsymbol{\varphi}\otimes\boldsymbol{N}\,\mathrm{d}A \quad \text{and} \\ \overline{\mathrm{Div}}\overline{\mathbb{H}} &= \frac{1}{|\mathcal{B}_0|}\int_{\mathcal{B}_0} \mathrm{Div}\,\mathbb{H}\,\mathrm{d}V = \frac{1}{|\mathcal{B}_0|}\int_{\partial\mathcal{B}_0} \mathbb{H}\cdot\boldsymbol{N}\,\mathrm{d}A\,, \end{aligned} \tag{5.7}$$

where we have considered the following relations

$$\int_{\mathcal{B}_0} \widetilde{\boldsymbol{F}}\,\mathrm{d}V = \int_{\partial\mathcal{B}_0} \widetilde{\boldsymbol{\varphi}}\otimes\boldsymbol{N}\,\mathrm{d}A = \boldsymbol{0} \quad \text{and} \quad \int_{\mathcal{B}_0} \mathrm{Div}[\widetilde{\mathbb{H}}]\,\mathrm{d}V = \int_{\partial\mathcal{B}_0} \widetilde{\mathbb{H}}\cdot\boldsymbol{N}\,\mathrm{d}A = 0\,. \tag{5.8}$$

The former equation is satisfied for continuous fluctuations of the deformation map along the whole microstructure, where continuity also relates to the transition across the (arbitrary) boundary of a periodic RVE. The restriction w.r.t. the continuity across an RVE's boundary is usually expressed as $[\![\widetilde{\boldsymbol{\varphi}}]\!] = \boldsymbol{0}$ on $\partial\mathcal{B}_0$, where $[\![(\cdot)]\!] = (\cdot)^+ - (\cdot)^-$ denotes the jump of a quantity $(\cdot)$ across the boundary of an RVE. Analogously equation $(5.8)_2$ is satisfied for continuous normal projections of the solvent-volume flux, i.e., anti-periodic normal projections $[\![\widetilde{\mathbb{H}}]\!]\cdot\boldsymbol{N} = 0$ on $\partial\mathcal{B}_0$. We refer to Fig. 5.2 for a graphical illustration.

5.2.2 Constitutive functions at the microscopic level

As diffusion-deformation processes are dissipative in nature, they can be modeled by a set of two constitutive functions given by an energy-storage function $\hat{\psi}$ and a dissipation-potential function $\hat{\phi}$. The function $\hat{\psi}(\boldsymbol{F}, s)$ models the energy storage due to the deformation of the material and the influx of the solvent molecules. It is assumed to have the

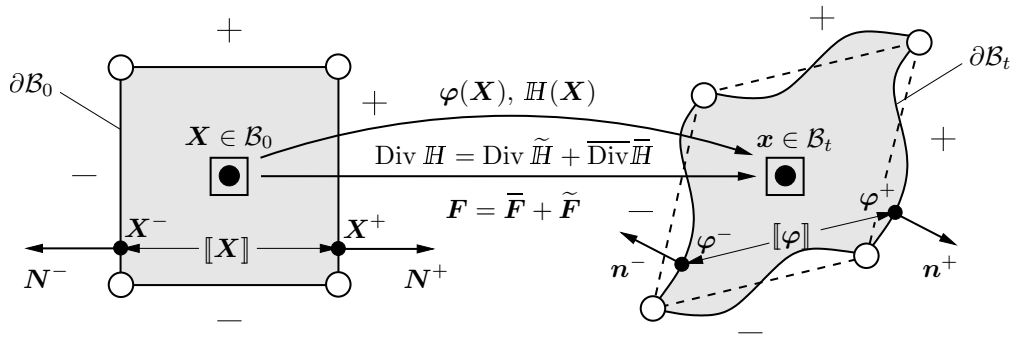

Figure 5.2: *Periodic boundary conditions associated with the minimization-based formulation of chemo-mechanics.* The boundary of the RVE $\mathcal{B}_0$ is split into $\mathcal{B}_0^+$ and $\mathcal{B}_0^-$ with unit outward normals $\boldsymbol{N}^+ = -\boldsymbol{N}^- =: \boldsymbol{N}$. At the respective material points $\boldsymbol{X}^+$ and $\boldsymbol{X}^-$ on these boundaries, the deformation map is considered to be periodic ($\boldsymbol{\varphi}(\boldsymbol{X}^+) = \boldsymbol{\varphi}(\boldsymbol{X}^-)$) and the normal solvent-volume flux $\mathbb{H}$ is considered to be anti-periodic ($\mathbb{H}(\boldsymbol{X}^+) \cdot \boldsymbol{N}^+ = -\mathbb{H}(\boldsymbol{X}^-) \cdot \boldsymbol{N}^-$).

following additive form (Hong et al. [20, 19], Böger et al. [4])

$$\hat{\psi}(\boldsymbol{F}, s) = \hat{\psi}_{mech}(\boldsymbol{F}) + \hat{\psi}_{chem}(s) + \hat{\psi}_{coup}(J, s)\,, \tag{5.9}$$

where $\hat{\psi}_{mech}$, $\hat{\psi}_{chem}$ and $\hat{\psi}_{coup}$ denote the mechanical, chemical and coupled chemo-mechanical contributions. For the modeling of hydrogels, a neo-Hookean material model can be considered for the mechanical energy $\hat{\psi}_{mech}$. The chemical energy $\hat{\psi}_{chem}$ is usually governed by a Flory–Rehner-type constitutive function (Flory and Rehner [13]). The term $\hat{\psi}_{coup}(J, s)$ in the energy-storage function models the coupling between deformation and solvent volume and by relating the volume change of the material to the solvent-volume concentration s. In the variational minimization formulation to be developed below, the dissipation potential $\hat{\phi}(\mathbb{H}; \boldsymbol{F}, s)$ is a convex function of the solvent flux $\mathbb{H}$.[24] The forms of these functions and their relevance for the specific problems at hand will be discussed in the following sections.

5.2.3 Rate-type minimization principle of computational homogenization

The macroscopic potential density $\overline{\pi}(\dot{\widetilde{\boldsymbol{\varphi}}}, \dot{\widetilde{\mathbb{H}}}; \dot{\overline{\boldsymbol{F}}}, \overline{\mathbb{H}})$ of the homogenization problem at a given macroscopic constitutive state $\{\dot{\overline{\boldsymbol{F}}}, \dot{\overline{s}} = -\overline{\operatorname{Div}}[\overline{\mathbb{H}}]\}$ can be described by the minimization principle[25]

$$\overline{\pi}(\dot{\widetilde{\boldsymbol{\varphi}}}^\star, \dot{\widetilde{\mathbb{H}}}^\star; \dot{\overline{\boldsymbol{F}}}, \overline{\mathbb{H}}) = \inf_{\dot{\widetilde{\boldsymbol{\varphi}}} \in \mathcal{W}_{\dot{\widetilde{\boldsymbol{\varphi}}}}} \inf_{\widetilde{\mathbb{H}} \in \mathcal{W}_{\widetilde{\mathbb{H}}}} \frac{1}{|\mathcal{B}_0|} \int_{\mathcal{B}_0} \pi(\dot{\boldsymbol{\varphi}}, \mathbb{H})\, \mathrm{d}V\,. \tag{5.10}$$

This variational principle can be considered as a generalized Hill–Mandel condition and involves the minimization of the volume-averaged microscopic potential density

$$\pi(\dot{\boldsymbol{\varphi}}, \mathbb{H}) := \frac{\mathrm{d}}{\mathrm{d}t}\hat{\psi}(\boldsymbol{F}, s) + \hat{\phi}(\mathbb{H}; \boldsymbol{F}, s) \tag{5.11}$$

[24] Convexity of the dissipation potential function together with vanishing first derivatives at the origin guarantee a priori fulfillment of the second law of thermodynamics.

[25] The index $(\cdot)^\star$ denotes a converged solution. To arrive at a compact notation, we will drop this index in the following whenever there is no danger of confusion.

in the admissible function spaces

$$\begin{aligned}\dot{\widetilde{\boldsymbol{\varphi}}} &\in \mathcal{W}_{\dot{\widetilde{\boldsymbol{\varphi}}}} := \{\dot{\widetilde{\boldsymbol{\varphi}}} \in H^1(\mathcal{B}_0) \mid \dot{\widetilde{\boldsymbol{\varphi}}}^+ = \dot{\widetilde{\boldsymbol{\varphi}}}^- \text{ on } \partial\mathcal{B}_0 = \partial\mathcal{B}_0^+ \cup \partial\mathcal{B}_0^-\},\\ \widetilde{\mathbb{H}} &\in \mathcal{W}_{\widetilde{\mathbb{H}}} := \{\widetilde{\mathbb{H}} \in H(\mathrm{Div}, \mathcal{B}_0) \mid \widetilde{\mathbb{H}}^+ \cdot \boldsymbol{N}^+ = -\widetilde{\mathbb{H}}^- \cdot \boldsymbol{N}^- \text{ on } \partial\mathcal{B}_0 = \partial\mathcal{B}_0^+ \cup \partial\mathcal{B}_0^-\}\,.\end{aligned} \tag{5.12}$$

5.2.4 Incremental variational principle at the microscale

In the numerical setting, the above given rate-type variational principle (5.10) is solved incrementally at discrete times $0 < t_{n+1} \leq T$, where T denotes the ending time of a process. It is assumed that at the beginning of a time interval $[t_n,\, t_{n+1}]$ all variables are known. In the following, we consider the notation $(\cdot)_n$ for discrete variables at time t_n and drop the subscript for the variables at time t_{n+1}, i.e., $(\cdot) := (\cdot)_{n+1}$. Considering an implicit Euler time integration with a time step $\tau = t_{n+1} - t_n$, we replace (5.10) with an alternative incremental macroscopic potential density

$$\overline{\pi}^\tau(\widetilde{\boldsymbol{\varphi}}^\star, \widetilde{\mathbb{H}}^\star; \overline{\boldsymbol{F}}, \overline{\mathbb{H}}) = \inf_{\widetilde{\boldsymbol{\varphi}} \in \mathcal{W}_{\widetilde{\boldsymbol{\varphi}}}} \inf_{\widetilde{\mathbb{H}} \in \mathcal{W}_{\widetilde{\mathbb{H}}}} \frac{1}{|\mathcal{B}_0|} \int_{\mathcal{B}_0} \pi^\tau(\boldsymbol{\varphi}, \mathbb{H})\, \mathrm{d}V \tag{5.13}$$

in terms of the incremental microscopic potential density

$$\pi^\tau(\boldsymbol{\varphi}, \mathbb{H}) := \hat{\psi}(\boldsymbol{F}, s) + \tau\hat{\phi}(\mathbb{H}; \boldsymbol{F}_n, s_n)\,. \tag{5.14}$$

Here, the solvent-volume concentration is determined via implicit Euler integration such that $s = s_n - \tau\,\mathrm{Div}\,\mathbb{H}$. Analogously, we determine $\overline{s} = \overline{s}_n - \tau\overline{\mathrm{Div}}\overline{\mathbb{H}}$ at the macroscale. Note that in (5.14) the dissipation-potential function takes into account known state variables $\{\boldsymbol{F}_n, s_n\}$ at time t_n in order to preserve a variationally consistent structure of the problem (Miehe et al. [25], Böger et al. [4]). The admissible spaces in the incremental setting are defined as

$$\begin{aligned}\widetilde{\boldsymbol{\varphi}} &\in \mathcal{W}_{\widetilde{\boldsymbol{\varphi}}} := \{\widetilde{\boldsymbol{\varphi}} \in H^1(\mathcal{B}_0) \mid \widetilde{\boldsymbol{\varphi}}^+ = \widetilde{\boldsymbol{\varphi}}^- \text{ on } \partial\mathcal{B}_0 = \partial\mathcal{B}_0^+ \cup \partial\mathcal{B}_0^-\}\,,\\ \widetilde{\mathbb{H}} &\in \mathcal{W}_{\widetilde{\mathbb{H}}} := \{\widetilde{\mathbb{H}} \in H(\mathrm{Div}, \mathcal{B}_0) \mid \widetilde{\mathbb{H}}^+ \cdot \boldsymbol{N}^+ = -\widetilde{\mathbb{H}}^- \cdot \boldsymbol{N}^- \text{ on } \partial\mathcal{B}_0 = \partial\mathcal{B}_0^+ \cup \partial\mathcal{B}_0^-\}\,.\end{aligned} \tag{5.15}$$

5.2.5 Euler–Lagrange equations and linearization of the variational formulation

The necessary condition of the incremental variational formulation (5.13) yields

$$\delta\overline{\pi}^\tau(\widetilde{\boldsymbol{\varphi}}, \widetilde{\mathbb{H}}; \overline{\boldsymbol{F}}, \overline{\mathbb{H}}) = \frac{1}{|\mathcal{B}_0|} \int_{\mathcal{B}_0} \begin{bmatrix} \delta\widetilde{\boldsymbol{F}} \\ \mathrm{Div}\,\delta\widetilde{\mathbb{H}} \\ \delta\widetilde{\mathbb{H}} \end{bmatrix} \cdot \begin{bmatrix} \partial_{\boldsymbol{F}}\hat{\psi} \\ -\tau\partial_s\hat{\psi} \\ \tau\partial_{\mathbb{H}}\hat{\phi} \end{bmatrix} \mathrm{d}V = 0\,, \tag{5.16}$$

where $\delta\widetilde{\boldsymbol{\varphi}} \in \mathcal{W}_{\widetilde{\boldsymbol{\varphi}}}$ and $\delta\widetilde{\mathbb{H}} \in \mathcal{W}_{\widetilde{\mathbb{H}}}$. Using integral theorems as well as employing the periodicity conditions (5.15), we arrive at the incremental Euler–Lagrange equations

1. Balance of linear momentum	$\mathrm{Div}[\partial_{\boldsymbol{F}}\hat{\psi}]$	$=$	$\boldsymbol{0}$	in	$\mathcal{B}_0$
2. Inverse Fickian law	$\mathrm{Grad}[\partial_s\hat{\psi}] + \partial_{\mathbb{H}}\hat{\phi}$	$=$	$\boldsymbol{0}$	in	$\mathcal{B}_0$
3. Continuity of tractions	$[\![\partial_{\boldsymbol{F}}\hat{\psi}]\!] \cdot \boldsymbol{N}$	$=$	$\boldsymbol{0}$	on	$\partial\mathcal{B}_0$
4. Continuity of chemical potential	$[\![\partial_s\hat{\psi}]\!]$	$=$	0	on	$\partial\mathcal{B}_0$

(5.17)

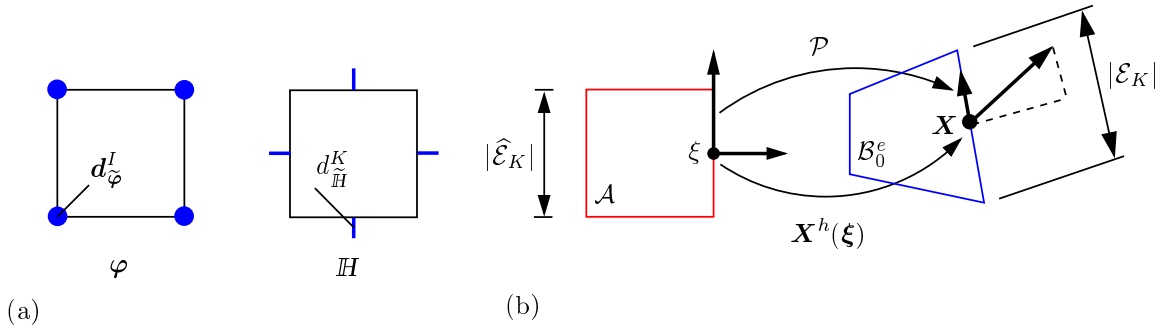

Figure 5.3: *Q_1RT_0 Raviart–Thomas finite element and its mapping from the parametric to the physical space.* a) The deformation map $\boldsymbol{\varphi}$ is continuously interpolated using node-based Q_1 shape functions. The solvent-volume flux $\mathbb{H}$ is approximated using edge-based RT_0 shape functions. b) To obtain the RT_0 shape functions and their derivatives in the physical space, a Piola transformation from the parametric space according to (5.21) is considered.

In (5.17) we identify the constitutive equations for the microscopic dual fields, i.e., the first Piola–Kirchoff stress tensor $\boldsymbol{P} := \partial_{\boldsymbol{F}}\hat{\psi}$ and the chemical potential of the solvent-volume concentration $\mu := \partial_s\hat{\psi}$. The equation $(5.17)_2$ describes an inverse form of Fick's law. The driving force of the diffusion process $\mathbb{M} := -\operatorname{Grad}\mu$ is determined constitutively from the dissipation potential function via $\mathbb{M} = \partial_{\mathbb{H}}\hat{\phi}$.

Linearization of (5.16) leads to the following expression including the incremental microscopic moduli tensor

$$\Delta\delta\overline{\pi}^\tau(\widetilde{\boldsymbol{\varphi}},\widetilde{\mathbb{H}};\overline{\boldsymbol{F}},\overline{\mathbb{H}}) = \frac{1}{|\mathcal{B}_0|}\int_{\mathcal{B}_0}\begin{bmatrix}\delta\widetilde{\boldsymbol{F}}\\ \operatorname{Div}\delta\widetilde{\mathbb{H}}\\ \delta\widetilde{\mathbb{H}}\end{bmatrix}\cdot\begin{bmatrix}\partial^2_{\boldsymbol{F}\boldsymbol{F}}\hat{\psi} & -\tau\partial^2_{\boldsymbol{F}s}\hat{\psi} & \cdot\\ -\tau\partial^2_{s\boldsymbol{F}}\hat{\psi} & \tau^2\partial^2_{ss}\hat{\psi} & \cdot\\ \cdot & \cdot & \tau\partial^2_{\mathbb{H}\mathbb{H}}\hat{\phi}\end{bmatrix}\cdot\begin{bmatrix}\Delta\widetilde{\boldsymbol{F}}\\ \operatorname{Div}\Delta\widetilde{\mathbb{H}}\\ \Delta\widetilde{\mathbb{H}}\end{bmatrix}\mathrm{d}V\,. \tag{5.18}$$

In the following sections, we will take advantage of (5.16) and (5.18) when we consider the finite-element implementation of the homogenization problem.

5.2.6 Finite-element implementation of the homogenization procedure

For the numerical solution of the microscopic diffusion-deformation problem, conforming quadrilateral Q_1RT_0 Raviart–Thomas-type finite elements are implemented [32]. This choice is due to the required function space $H(\operatorname{Div},\mathcal{B}_0)$ of the solvent-volume flux $\mathbb{H}$. An alternative non-conforming discretization on the basis of standard Q_1Q_1 finite elements usually yields non-physical behavior. For recent developments of equivalent minimization principles incorporating a node-based finite-element discretization combined with reduced integration we refer to [35].

In the framework of the Raviart–Thomas-type finite-element discretization, the fluctuations of the deformation map $\widetilde{\boldsymbol{\varphi}}$ are approximated continuously using bilinear Q_1 shape functions, which are related to the nodal degrees of freedom $\underline{\mathbf{d}}^e_{\widetilde{\boldsymbol{\varphi}}}$ of a finite element. The fluctuations of the solvent-volume flux $\widetilde{\mathbb{H}}$ are approximated considering linear RT_0 shape functions, which are related to the fluctuations of the flux degrees of freedom $\underline{\mathbf{d}}^e_{\widetilde{\mathbb{H}}}$ across the edges of the quadrilateral element. We refer to Fig. 5.3a for a qualitative illustration.

Note that only the normal component of the solvent-volume flux $h_K = \int_{\mathcal{E}_K}\mathbb{H}^h\cdot\boldsymbol{N}^e\,\mathrm{d}A$

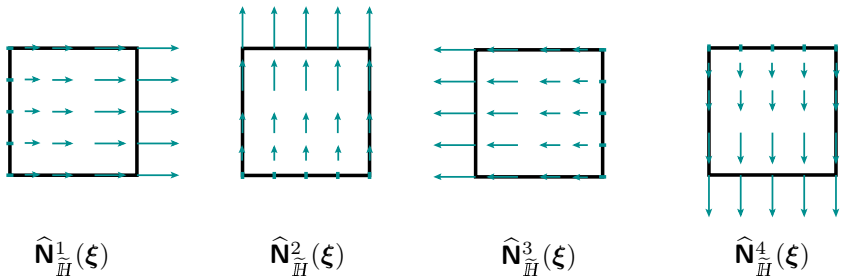

Figure 5.4: *Illustration of the RT_0 shape functions in parametric space.* The normal projections of the RT_0 shape functions are constant along the edge of a finite element in the parametric space $\mathcal{A}$. The projection of the shape function associated with edge K onto the edge $\mathcal{E}_K$ is given by $\underline{\widehat{\mathbf{N}}}^K_{\widetilde{\mathbb{H}}}(\boldsymbol{\xi}) \cdot \widehat{\boldsymbol{N}}^e_0 = 1/2$ and onto all other edges $\widehat{\mathcal{E}}_L$ with $L \neq K$ is $\underline{\widehat{\mathbf{N}}}^K_{\widetilde{\mathbb{H}}}(\boldsymbol{\xi}) \cdot \widehat{\boldsymbol{N}}^e_0 = 0$. The factor $1/2$ is due to the length of the element edge in the parametric space such that $\widehat{\mathsf{d}}^K_{\widetilde{\mathbb{H}}} = \int_{\widehat{\mathcal{E}}_K} \widehat{\mathbb{H}}^h(\boldsymbol{\xi}) \cdot \widehat{\boldsymbol{N}}^e_0 \, \mathrm{d}A$.

at an edge of the element $\mathcal{E}_K$ is considered as degree of freedom. We refer to Raviart and Thomas [32], Brezzi and Fortin [5] for theoretical aspects and to Schwarz et al. [34], Anjam and Valdman [1], Böger et al. [4], Teichtmeister et al. [35] for discussions of the numerical implementation. The interpolation of the independent fields arises as

$$\widetilde{\boldsymbol{\varphi}}^h = \sum_{I=1}^{n_{node}} \mathsf{N}^I_{\widetilde{\boldsymbol{\varphi}}}(\boldsymbol{\xi}) \underline{\mathbf{d}}^I_{\widetilde{\boldsymbol{\varphi}}} =: \underline{\mathbf{N}}^e_{\widetilde{\boldsymbol{\varphi}}} \underline{\mathbf{d}}^e_{\widetilde{\boldsymbol{\varphi}}} \quad \text{and} \quad \widetilde{\mathbb{H}}^h = \sum_{K=1}^{n_{edge}} \underline{\mathbf{N}}^K_{\widetilde{\mathbb{H}}}(\boldsymbol{X}) \mathsf{d}^K_{\widetilde{\mathbb{H}}} =: \underline{\mathbf{N}}^e_{\widetilde{\mathbb{H}}} \underline{\mathbf{d}}^e_{\widetilde{\mathbb{H}}} \,, \tag{5.19}$$

where the scalar shape functions $\mathsf{N}^I_{\widetilde{\boldsymbol{\varphi}}}$ are defined at the node I and the vectorial shape functions $\underline{\mathbf{N}}^K_{\widetilde{\mathbb{H}}}$ correspond to the edge K. While the former can be directly defined in a so-called parametric space $\mathcal{A} = [-1, 1] \times [-1, 1]$, the latter have to be computed via a Piola transformation of the corresponding shape functions $\underline{\widehat{\mathbf{N}}}^K_{\widetilde{\mathbb{H}}}$ in that parametric space(from here on the notation $\widehat{(\cdot)}$ indicates quantities $(\cdot)$ formulated in the parametric space). Similarly, $\underline{\mathbf{d}}^I_{\widetilde{\boldsymbol{\varphi}}}$ denotes the array of the displacement components at the node I and $\mathsf{d}^K_{\widetilde{\mathbb{H}}}$ corresponds to the normal component of the solvent-volume flux at the edge K. An illustration of the Raviart–Thomas shape functions in the parametric space $\mathcal{A}$ is given in Fig. 5.4.

The RT_0 shape functions considered in the present contribution are given in the parametric space as

$$\underline{\widehat{\mathbf{N}}}^1_{\widetilde{\mathbb{H}}} = \begin{bmatrix} \frac{1}{4}(\xi_1 + 1) \\ 0 \end{bmatrix}, \underline{\widehat{\mathbf{N}}}^2_{\widetilde{\mathbb{H}}} = \begin{bmatrix} 0 \\ \frac{1}{4}(\xi_2 + 1) \end{bmatrix}, \underline{\widehat{\mathbf{N}}}^3_{\widetilde{\mathbb{H}}} = \begin{bmatrix} \frac{1}{4}(\xi_1 - 1) \\ 0 \end{bmatrix}, \underline{\widehat{\mathbf{N}}}^4_{\widetilde{\mathbb{H}}} = \begin{bmatrix} 0 \\ \frac{1}{4}(\xi_2 - 1) \end{bmatrix}. \tag{5.20}$$

The degrees of freedom need to be invariant under the change of coordinates from the parametric space to the physical space, i.e., $\widehat{\mathsf{d}}^K_{\widetilde{\mathbb{H}}} = \mathsf{d}^K_{\widetilde{\mathbb{H}}}$. Thus, we apply a Piola transformation to map the vectorial shape functions and their derivatives from the parametric space $\mathcal{A}$ to the reference element $\mathcal{B}^e_0$. We refer to Brezzi and Fortin [5] for more details and to Fig. 5.3b for a graphical illustration. It follows

$$[\cdot](\boldsymbol{X}) := \mathcal{P}\{[\cdot](\boldsymbol{\xi})\} = \frac{1}{\widehat{J}} \widehat{\boldsymbol{J}}(\boldsymbol{\xi})[\cdot](\xi) \quad \text{with} \quad \widehat{\boldsymbol{J}} := \frac{\partial \boldsymbol{X}^h}{\partial \boldsymbol{\xi}} \quad \text{and} \quad \widehat{J} := \det \widehat{\boldsymbol{J}} \,, \tag{5.21}$$

where $\boldsymbol{X}^h : \mathcal{A} \to \mathcal{B}^e_0$ refers to a map from the parametric space to a reference finite element and is determined by $\boldsymbol{X}^h(\boldsymbol{\xi}) = \sum_{I=1}^{n_{node}} \mathsf{N}^I_{\widetilde{\boldsymbol{\varphi}}}(\boldsymbol{\xi}) \boldsymbol{X}^I$ in terms of the nodal coordinates $\boldsymbol{X}^I$ of the considered finite element.

Furthermore, it is important to point out that, in order to have a consistent finite-element implementation for the flux degrees of freedom, we need to make sure that the degrees of freedom on a common edge of two adjacent finite elements are identical. In order to achieve this, we assume a positive orientation for an edge in a finite element $\mathcal{B}^e$ whenever the node numbers of the vertices of that edge increase in counterclockwise direction. In contrast, when the node number decreases, we augment the RT_0 shape function of that edge with a negative sign. As a consequence, an outflux at an edge of a particular finite element will always be associated with influx across the same edge of a neighboring finite element. We refer to Schwarz et al. [34], Anjam and Valdman [1], Böger et al. [4], Teichtmeister et al. [35] for more details on the numerical implementation.

Based on (5.19) we obtain the fluctuations of the deformation gradient and of the divergence of the flux fields as

$$\widetilde{\boldsymbol{F}}^h = \sum_{I=1}^{n_{node}} \underline{\mathbf{d}}^I_{\widetilde{\boldsymbol{\varphi}}} \otimes \operatorname{Grad} \mathsf{N}^I_{\widetilde{\boldsymbol{\varphi}}} =: \underline{\mathbf{B}}^e_{\widetilde{\boldsymbol{\varphi}}} \underline{\mathbf{d}}^e_{\widetilde{\boldsymbol{\varphi}}} \quad \text{and} \quad \operatorname{Div} \widetilde{\mathbb{H}}^h = \sum_{K=1}^{n_{edge}} d^K_{\widetilde{\mathbb{H}}} \operatorname{Div} \underline{\mathbf{N}}^K_{\widetilde{\mathbb{H}}} =: \underline{\mathbf{B}}^e_{\widetilde{\mathbb{H}}} \underline{\mathbf{d}}^e_{\widetilde{\mathbb{H}}} \,. \tag{5.22}$$

Having the above discretization at hand, the necessary condition of the incremental minimization principle (5.16) in the finite-element setting can be written in form of the microscopic residuum vector

$$\begin{aligned} \underline{\mathbf{R}} := \frac{1}{|\mathcal{B}_0|} \mathop{\mathsf{A}}_{e=1}^{n_{elem}} \overline{\pi}^{\tau,e}_{,\underline{\mathbf{d}}^e} = \frac{1}{|\mathcal{B}_0|} \mathop{\mathsf{A}}_{e=1}^{n_{elem}} \int_{\mathcal{B}^e_0} \begin{bmatrix} (\underline{\mathbf{B}}^e_{\widetilde{\boldsymbol{\varphi}}})^T \partial_{\boldsymbol{F}} \hat{\psi}^h \\ (\underline{\mathbf{B}}^e_{\widetilde{\mathbb{H}}})^T (-\tau \partial_s \hat{\psi}^h) + (\underline{\mathbf{N}}^e_{\widetilde{\mathbb{H}}})^T \tau \partial_{\mathbb{H}} \hat{\phi}^h \end{bmatrix} \mathrm{d}V = \boldsymbol{0} \\ \text{with} \quad \underline{\mathbf{d}}^e := \begin{bmatrix} \underline{\mathbf{d}}^e_{\widetilde{\boldsymbol{\varphi}}} \\ \underline{\mathbf{d}}^e_{\widetilde{\mathbb{H}}} \end{bmatrix} , \end{aligned} \tag{5.23}$$

where the first Piola–Kirchhoff stress tensor $\boldsymbol{P}$ is implemented as a vector, i.e., $\underline{\mathbf{P}} = [P_{11},\ P_{22},\ P_{12},\ P_{21}]^T$ in two dimensions. The corresponding mechanical and coupled moduli tensors follow a similar structure. The tangent matrix of the linearized system of equations reads

$$\begin{aligned} \underline{\mathbf{K}} :&= \frac{1}{|\mathcal{B}_0|} \mathop{\mathsf{A}}_{e=1}^{n_{elem}} \overline{\pi}^{\tau,e}_{,\underline{\mathbf{d}}^e \underline{\mathbf{d}}^e} \\ &= \frac{1}{|\mathcal{B}_0|} \mathop{\mathsf{A}}_{e=1}^{n_{elem}} \int_{\mathcal{B}^e_0} \begin{bmatrix} (\underline{\mathbf{B}}^e_{\widetilde{\boldsymbol{\varphi}}})^T \partial^2_{\boldsymbol{F}\boldsymbol{F}} \hat{\psi}^h \underline{\mathbf{B}}^e_{\widetilde{\boldsymbol{\varphi}}} & (\underline{\mathbf{B}}^e_{\widetilde{\boldsymbol{\varphi}}})^T (-\tau \partial^2_{\boldsymbol{F}s} \hat{\psi}^h) \underline{\mathbf{B}}^e_{\widetilde{\mathbb{H}}} \\ (\underline{\mathbf{B}}^e_{\widetilde{\mathbb{H}}})^T (-\tau \partial^2_{s\boldsymbol{F}} \hat{\psi}^h) \underline{\mathbf{B}}^e_{\widetilde{\boldsymbol{\varphi}}} & (\underline{\mathbf{B}}^e_{\widetilde{\mathbb{H}}})^T \tau^2 \partial^2_{ss} \hat{\psi}^h \underline{\mathbf{B}}^e_{\widetilde{\mathbb{H}}} + (\underline{\mathbf{N}}^e_{\widetilde{\mathbb{H}}})^T \tau \partial^2_{\mathbb{H}\mathbb{H}} \hat{\phi}^h \underline{\mathbf{N}}^e_{\widetilde{\mathbb{H}}} \end{bmatrix} \mathrm{d}V \,. \end{aligned} \tag{5.24}$$

A converged microscopic state is obtained by solving the system of equations (5.16) iteratively using, for example, a Newton–Raphson method

$$\underline{\mathbf{d}} \Leftarrow \underline{\mathbf{d}} - \underline{\mathbf{K}}^{-1} \underline{\mathbf{R}} \quad \text{until} \quad ||\underline{\mathbf{R}}|| \leq tol_{micro} \,. \tag{5.25}$$

5.2.7 Effective macroscopic dual fields and moduli tensor

In the numerical setting, taking the variation of $\overline{\pi}^{\tau}$ at the macroscopic material point yields

$$\begin{aligned}\delta\overline{\pi}^{\tau} = \delta\Big\{\frac{1}{|\mathcal{B}_0|}\mathop{\mathsf{A}}_{e=1}^{n_{elem}}\overline{\pi}^{\tau,e}\Big\} &= \frac{1}{|\mathcal{B}_0|}\mathop{\mathsf{A}}_{e=1}^{n_{elem}}\int_{\mathcal{B}_0^e}\begin{bmatrix}\delta\underline{\mathbf{d}}^e\\ \delta\overline{\boldsymbol{F}}\\ \overline{\mathrm{Div}}\delta\overline{\mathbb{H}}\\ \delta\overline{\mathbb{H}}\end{bmatrix}\cdot\begin{bmatrix}\pi^{\tau,e}_{,\underline{\mathbf{d}}^e}\\ \partial_{\boldsymbol{F}}\hat{\psi}^h\\ -\tau\partial_s\hat{\psi}^h+\frac{1}{3}\tau\partial_{\mathbb{H}}\hat{\phi}^h\cdot\boldsymbol{X}\\ \tau\partial_{\mathbb{H}}\hat{\phi}^h\end{bmatrix}\mathrm{d}V\\ &= \frac{1}{|\mathcal{B}_0|}\mathop{\mathsf{A}}_{e=1}^{n_{elem}}\int_{\mathcal{B}_0^e}\begin{bmatrix}\delta\overline{\boldsymbol{F}}\\ \overline{\mathrm{Div}}\delta\overline{\mathbb{H}}\\ \delta\overline{\mathbb{H}}\end{bmatrix}\cdot\begin{bmatrix}\partial_{\boldsymbol{F}}\hat{\psi}^h\\ -\tau\partial_s\hat{\psi}^h+\frac{1}{3}\tau\partial_{\mathbb{H}}\hat{\phi}^h\cdot\boldsymbol{X}\\ \tau\partial_{\mathbb{H}}\hat{\phi}^h\end{bmatrix}\mathrm{d}V\,,\end{aligned} \tag{5.26}$$

where $\underline{\mathbf{R}} := \overline{\pi}^{\tau}_{,\underline{\mathbf{d}}} = \mathsf{A}_{e=1}^{n_{elem}}\overline{\pi}^{\tau,e}_{,\underline{\mathbf{d}}^e}$ vanishes at the solution point of the microscopic boundary-value problem. As a consequence, the macroscopic first Piola–Kirchhoff stress tensor $\overline{\boldsymbol{P}}$ and the negative gradient of the chemical potential $\overline{M}$ (the latter being the driving force of the macroscopic solvent-volume flux) are determined as averages of the corresponding microscopic analogues

$$\overline{\boldsymbol{P}} := \partial_{\overline{\boldsymbol{F}}}\overline{\pi}^{\tau} = \frac{1}{|\mathcal{B}_0|}\mathop{\mathsf{A}}_{e=1}^{n_{elem}}\int_{\mathcal{B}_0^e}\partial_{\boldsymbol{F}}\hat{\psi}^h\,\mathrm{d}V \quad\text{and}\quad \overline{M} := \partial_{\overline{\mathbb{H}}}\overline{\pi}^{\tau} = \frac{1}{|\mathcal{B}_0|}\mathop{\mathsf{A}}_{e=1}^{n_{elem}}\int_{\mathcal{B}_0^e}\partial_{\mathbb{H}}\hat{\phi}^h\,\mathrm{d}V\,. \tag{5.27}$$

However, the macroscopic chemical potential follows from a different averaging process

$$\overline{\mu} := \partial_{\overline{s}}\overline{\pi}^{\tau} = \frac{1}{|\mathcal{B}_0|}\mathop{\mathsf{A}}_{e=1}^{n_{elem}}\int_{\mathcal{B}_0^e}\partial_s\hat{\psi}^h - \frac{1}{3}\partial_{\mathbb{H}}\hat{\phi}^h\cdot\boldsymbol{X}\,\mathrm{d}V\,. \tag{5.28}$$

We observe that $\overline{\mu}$ does not only depend on the average of the microscopic chemical potential but also on its gradient and the spatial dimensions of the RVE. As a consequence, the macroscopic effective response depends on the size of the RVE, which will be discussed in detail in the next section.

Considering a continuous setting and exploiting tensorial manipulations in (5.27) and (5.28), we can express the effective dual fields in terms of the surface integrals over the boundary of the RVE as

$$\begin{aligned}\overline{\boldsymbol{P}} &= \frac{1}{|\mathcal{B}_0|}\int_{\partial\mathcal{B}_0}(\boldsymbol{P}\cdot\boldsymbol{N})\otimes\boldsymbol{X}\,\mathrm{d}A,\\ \overline{M} &= \frac{1}{|\mathcal{B}_0|}\int_{\partial\mathcal{B}_0}\mu\boldsymbol{N}\,\mathrm{d}A,\\ \overline{\mu} &= \frac{1}{3|\mathcal{B}_0|}\int_{\partial\mathcal{B}_0}\mu\boldsymbol{N}\cdot\boldsymbol{X}\,\mathrm{d}A\,.\end{aligned} \tag{5.29}$$

Adopting the notation $\overline{\mathbf{F}} := [\overline{\boldsymbol{F}},\ \overline{\mathrm{Div}}\overline{\mathbb{H}},\ \overline{\mathbb{H}}]^T$, we can write the first-order terms in the

linearization of (5.26) at the macroscale in a compact form as

$$\Delta\delta\overline{\pi}^{\tau} = \delta\overline{\boldsymbol{F}} : \partial^2_{\overline{\boldsymbol{F}}\,\overline{\boldsymbol{F}}}\overline{\pi}^{\tau} : \Delta\overline{\boldsymbol{F}} = \frac{1}{|\mathcal{B}_0|}\mathop{\mathsf{A}}_{e=1}^{n_{elem}} \begin{bmatrix} \delta\underline{\mathbf{d}}^e \\ \delta\overline{\boldsymbol{F}} \end{bmatrix} \cdot \begin{bmatrix} \overline{\pi}^{\tau,e}_{,\underline{\mathbf{d}}^e\underline{\mathbf{d}}^e} & \overline{\pi}^{\tau,e}_{,\underline{\mathbf{d}}^e\overline{\boldsymbol{F}}} \\ \overline{\pi}^{\tau,e}_{,\overline{\boldsymbol{F}}\underline{\mathbf{d}}^e} & \overline{\pi}^{\tau,e}_{,\overline{\boldsymbol{F}}\,\overline{\boldsymbol{F}}} \end{bmatrix} \cdot \begin{bmatrix} \Delta\underline{\mathbf{d}}^e \\ \Delta\overline{\boldsymbol{F}} \end{bmatrix}, \tag{5.30}$$

where

$$\overline{\pi}^{\tau,e}_{,\overline{\boldsymbol{F}}\,\overline{\boldsymbol{F}}} := \int_{\mathcal{B}_0^e} \begin{bmatrix} \partial^2_{\boldsymbol{F}\boldsymbol{F}}\hat{\psi}^h & -\tau\partial^2_{\boldsymbol{F}s}\hat{\psi}^h & \boldsymbol{0} \\ -\tau\partial^2_{s\boldsymbol{F}}\hat{\psi}^h & \tau^2\partial^2_{ss}\hat{\psi}^h + \frac{1}{9}\tau\boldsymbol{X}\cdot\partial^2_{\mathbb{H}\mathbb{H}}\hat{\phi}^h\cdot\boldsymbol{X} & \frac{1}{3}\tau\boldsymbol{X}\cdot\partial^2_{\mathbb{H}\mathbb{H}}\hat{\phi}^h \\ \boldsymbol{0} & \frac{1}{3}\tau\partial^2_{\mathbb{H}\mathbb{H}}\hat{\phi}^h\cdot\boldsymbol{X} & \tau\partial^2_{\mathbb{H}\mathbb{H}}\hat{\phi}^h \end{bmatrix} \mathrm{d}V\,, \tag{5.31}$$

$$\overline{\pi}^{\tau,e}_{,\underline{\mathbf{d}}^e\overline{\boldsymbol{F}}} := \int_{\mathcal{B}_0^e} \begin{bmatrix} (\underline{\mathbf{B}}^e_{\widetilde{\boldsymbol{\varphi}}})^T\partial^2_{\boldsymbol{F}\boldsymbol{F}}\hat{\psi}^h & (\underline{\mathbf{B}}^e_{\widetilde{\boldsymbol{\varphi}}})^T(-\tau\partial^2_{\boldsymbol{F}s}\hat{\psi}^h) & \boldsymbol{0} \\ (\underline{\mathbf{B}}^e_{\widetilde{\mathbb{H}}})^T\tau\partial^2_{s\boldsymbol{F}}\hat{\psi}^h & (\underline{\mathbf{B}}^e_{\widetilde{\mathbb{H}}})^T\tau^2\partial^2_{ss}\hat{\psi}^h + (\underline{\mathbf{N}}^e_{\widetilde{\mathbb{H}}})^T(\frac{1}{3}\tau\partial^2_{\mathbb{H}\mathbb{H}}\hat{\phi}^h\cdot\boldsymbol{X}) & (\underline{\mathbf{N}}^e_{\widetilde{\mathbb{H}}})^T\tau\partial^2_{\mathbb{H}\mathbb{H}}\hat{\phi}^h \end{bmatrix} \mathrm{d}V\,. \tag{5.32}$$

Combining (5.23), (5.26) and (5.30), we obtain an elimination equation at the macroscopic level for the microscopic degrees of freedom, that is

$$\Delta\underline{\mathbf{d}} = \mathop{\mathsf{A}}_{e=1}^{n_{elem}}\Delta\underline{\mathbf{d}}^e = -\left[\frac{1}{|\mathcal{B}_0|}\mathop{\mathsf{A}}_{e=1}^{n_{elem}}\overline{\pi}^{\tau,e}_{,\underline{\mathbf{d}}^e\underline{\mathbf{d}}^e}\right]^{-1}\left[\frac{1}{|\mathcal{B}_0|}\mathop{\mathsf{A}}_{e=1}^{n_{elem}}\overline{\pi}^{\tau,e}_{,\underline{\mathbf{d}}^e\overline{\boldsymbol{F}}}\right] = -\underline{\mathbf{K}}^{-1}\underline{\mathbf{L}} : \Delta\overline{\boldsymbol{F}}\,. \tag{5.33}$$

Considering the results of the latter equation in (5.30), we obtain

$$\Delta\delta\overline{\pi}^{\tau} = \delta\overline{\boldsymbol{F}} : \overline{\mathbb{C}} : \Delta\overline{\boldsymbol{F}} = \delta\overline{\boldsymbol{F}} : \left\{\frac{1}{|\mathcal{B}_0|}\mathop{\mathsf{A}}_{e=1}^{n_{elem}}\overline{\pi}^{\tau,e}_{,\overline{\boldsymbol{F}}\,\overline{\boldsymbol{F}}} - \underline{\mathbf{L}}^T\underline{\mathbf{K}}^{-1}\underline{\mathbf{L}}\right\} : \Delta\overline{\boldsymbol{F}}\,. \tag{5.34}$$

wherein we have identified the macroscopic coupled moduli

$$\boxed{\overline{\mathbb{C}} = \frac{1}{|\mathcal{B}_0|}\mathop{\mathsf{A}}_{e=1}^{n_{elem}}\overline{\pi}^{\tau,e}_{,\overline{\boldsymbol{F}}\,\overline{\boldsymbol{F}}} - \underline{\mathbf{L}}^T\underline{\mathbf{K}}^{-1}\underline{\mathbf{L}}}\,. \tag{5.35}$$

Now having determined the macroscopic dual fields (5.27) and (5.28) as well as the macroscopic moduli (5.35), we could solve a macroscopic boundary value problem under prescribed boundary and initial conditions by using a conforming finite-element discretization analogous to Section 5.2.6.

5.3 Size effects in the homogenization of transient diffusion

In equations (5.28), (5.31) and (5.32), we observe terms that are scaled with the coordinates of the RVE. This gives rise to a size-dependent effective response at the macroscale. To have more insight into the problem, we simplify the above described formulation (5.10) to the diffusion in rigid solids by neglecting any elastic effects. Then, the problem at hand reads

$$\overline{\pi}^{\tau}(\widetilde{\mathbb{H}}^{\star};\overline{\mathbb{H}}) = \inf_{\widetilde{\mathbb{H}}\in\mathcal{W}_{\widetilde{\mathbb{H}}}}\frac{1}{|\mathcal{B}_0|}\int_{\mathcal{B}_0}\hat{\psi}_{chem}(s) + \tau\hat{\phi}(\mathbb{H})\,\mathrm{d}V\,. \tag{5.36}$$

To determine the macroscopic response of the material, we take the variation of (5.36) and arrive at the definition of the macroscopic chemical potential

$$\overline{\mu} = \frac{1}{|\mathcal{B}_0|} \mathop{\mathsf{A}}_{e=1}^{n_{elem}} \int_{\mathcal{B}_0^e} \partial_s \hat{\psi}^h_{chem} - \frac{1}{3} \partial_{\mathbb{H}} \hat{\phi}^h \cdot \boldsymbol{X} \, \mathrm{d}V \,. \tag{5.37}$$

Considering the dissipation-potential function $\hat{\phi}(\mathbb{H}) = \frac{1}{2M} \|\mathbb{H}\|^2$ for the diffusion process in rigid solids with mobility parameter[26] M, we can reformulate the size-dependent term $\overline{\mu}_{\text{size}}$ of the chemical potential $\overline{\mu}$ in (5.37) as

$$\overline{\mu}_{\text{size}} \propto \frac{\tau}{3|\mathcal{B}_0|} \mathop{\mathsf{A}}_{e=1}^{n_{elem}} \int_{\mathcal{B}_0^e} \frac{1}{M} \mathbb{H} \cdot \boldsymbol{X} \, \mathrm{d}V = \frac{\tau}{3|\mathcal{B}_0|} \mathop{\mathsf{A}}_{e=1}^{n_{elem}} \int_{\mathcal{B}_0^e} \frac{1}{M} (\overline{\mathbb{H}} + \widetilde{\mathbb{H}} + \frac{1}{3} \overline{\mathrm{Div}} \overline{\mathbb{H}} \boldsymbol{X}) \cdot \boldsymbol{X} \, \mathrm{d}V \,. \tag{5.38}$$

Furthermore, by considering (5.4) and (5.5), we obtain

$$\overline{\mu}_{\text{size}} \propto \frac{\tau}{3|\mathcal{B}_0|} \mathop{\mathsf{A}}_{e=1}^{n_{elem}} \left(\overline{\mathbb{H}} \cdot \int_{\mathcal{B}_0^e} \frac{1}{M} \boldsymbol{X} \, \mathrm{d}V + \int_{\mathcal{B}_0^e} \frac{1}{M} \widetilde{\mathbb{H}} \cdot \boldsymbol{X} \, \mathrm{d}V + \frac{\overline{\mathrm{Div}} \overline{\mathbb{H}}}{3} \int_{\mathcal{B}_0^e} \frac{1}{M} \|\boldsymbol{X}\|^2 \, \mathrm{d}V \right) . \tag{5.39}$$

We observe that the macroscopic effective response depends on the size of the RVE and the mobility parameter M. Note that the first and second term on the right-hand side of (5.39) vanish for specific realizations of RVEs.[27] In general, however, we expect variations among the effective responses depending on the particular selection of RVEs from periodic microstructures. Due to the size dependence, the effective response of a single unit cell $\mathcal{D}$ differs from the effective response of an ensemble of identical unit cells $\boldsymbol{n}\mathcal{D}$, $\boldsymbol{n} \in \mathbb{N}^3$. In the following, we provide some numerical examples that describe the mentioned size effect for RVEs with different sizes and material parameters.

5.4 Representative numerical examples

In order to demonstrate the capabilities of the variational homogenization procedure discussed above, we present some numerical examples. The first numerical examples consider pure diffusion phenomena and investigate the influence of material parameters, geometry as well as the size of RVEs on the effective, macroscopic response of composite materials (Section 5.4.1). In a second study, we extend the formulation by elastic effects of the solid matrix and couple it to the diffusion processes. In doing so, we will investigate swelling-induced pattern transformations of periodic hydrogels (Section 5.4.2).

In what follows, we assume that the relaxation time of the material is much longer than the solvent's diffusion time. We thus neglect any viscoelastic effects of the material and consider standard Fickian-type diffusion [20, 19, 8]. For an implementation that takes into account the viscoelasticity of the material we refer to Govindjee and Simo [15].

[26] The mobility parameter M can be computed via the Stokes–Einstein relation

$$M = \frac{\nu D}{k_B T} = \frac{\nu}{6\pi R \eta} \,,$$

where ν is the volume of a single solvent molecule, D is the diffusivity, k_B is the Boltzmann constant, T is the absolute temperature, R is the radius of the solvent molecules and η is the viscosity of the solvent [10, 20].

[27] One such realization is given by a symmetric RVE that is parameterized with coordinate axes that originate from the spatial center of the RVE.

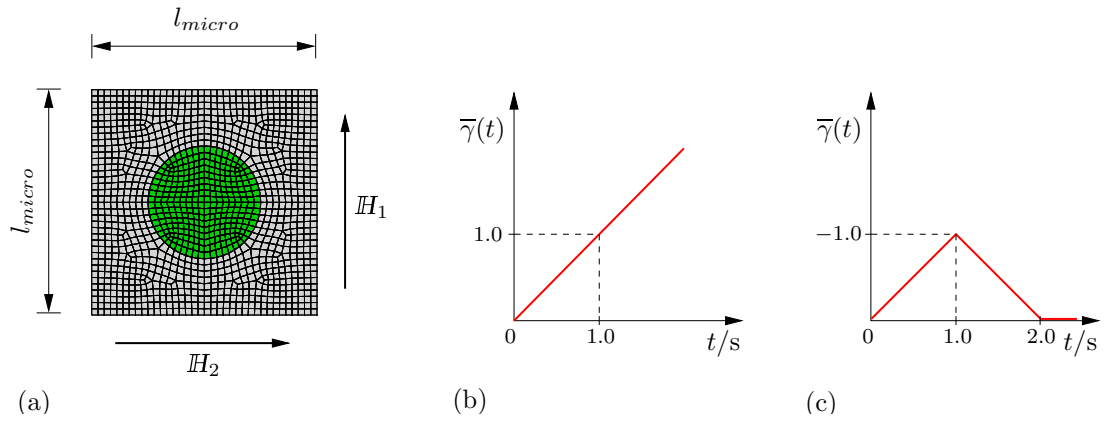

Figure 5.5: *RVE under macroscopic loading conditions.* An RVE with circular inclusion of volume fraction $f_0 = \pi/16$ is attached to a macroscopic material point $\overline{\boldsymbol{X}}$ and driven by the macroscopic fields $\overline{\mathbb{H}} = \boldsymbol{0}$ m/s and $\overline{\mathrm{Div}}\,\overline{\mathbb{H}} = \overline{\gamma}$ s^{-1}.

5.4.1 Investigation of the macroscopic properties of porous rigid solids

In this subsection, we analyze the influence of material parameters and the size of RVEs on the macroscopic response of two-phase materials. We will find that the macroscopic mobility parameter lies within the classical Voigt and Reuss bounds for vanishing RVE size.

5.4.1.1 Microscopic constitutive functions

In Section 5.2.2, we have discussed the basic forms of the energy-storage and dissipation-potential function. In case of a pure diffusion processes (for $\boldsymbol{\varphi} = \text{const.}$ with $\boldsymbol{F} = \boldsymbol{1}$), the energy-storage function reduces to $\hat{\psi}(s) = \hat{\psi}_{chem}(s)$. As our main focus is to investigate fundamental effects, we select the simple quadratic function (Kaessmair and Steinmann [21])

$$\hat{\psi}_{chem}(s) = \frac{A}{2}(s - \frac{1}{2})^2\,, \tag{5.40}$$

where A is a chemical material parameter. As dissipation-potential function we again consider $\hat{\phi}(\mathbb{H}) = \frac{1}{M}\|\mathbb{H}\|^2$ with the mobility parameter M.

5.4.1.2 Description of the problem

In the following, we consider periodic microstructures with circular inclusions. For such microstructures it is straightforward to indentify a periodic unit cell (see Fig. 5.5**a**). In a typical homogenization framework, the effective response of the material could be computed uniquely by considering an RVE that resembles exactly that unit cell. However, as we could see in Section 5.3, the homogenization of transient diffusion processes comes along with well-known size effects in the sense that the physical size of the considered RVE influences its effective response.

In order to analyze this size effect, we will alter the size of associated RVEs in the following way. On the one hand, we will change the size by adjusting the lateral length

of the underlying unit cell. On the other hand, we will change the size by composing an RVE of a certain number of unit cells. In both cases the RVEs will be generated from a primitive square-shaped unit cell having the lateral length of 1 mm. We adopt the following name convention: 'nRVEmm' designates a unique realization of an RVE, where n indicates the scaling of the dimensions of the primitive unit cell and mm indicates a pattern of $m \times m$ primitive unit cells. For example, 2RVE11 and RVE22 both represent an RVE with side length of 2 mm, but while the former is realized by scaling the primitive unit cell by a factor of 2, the latter is made up of 2×2 primitive unit cells. Please refer to Fig. 5.8 for a corresponding visualization. In all following simulations, we consider a volume fraction of the inclusions of $f_0 = \pi/16$.

In a purely diffusive process, the RVEs can be driven by the macroscopic solvent-volume flux $\overline{\mathbb{H}}$ and its divergence $\overline{\mathrm{Div}}\overline{\mathbb{H}}$. As the size effect is due to the linear terms appearing in the solvent flux vector in $(5.5)_2$ (see also (5.39)), we take into account the following macroscopic loading conditions

$$\overline{\mathbb{H}} = \boldsymbol{0} \text{ m/s} \quad \text{and} \quad \overline{\mathrm{Div}}\overline{\mathbb{H}} = \overline{\gamma} \text{ s}^{-1}\,, \tag{5.41}$$

where $\overline{\gamma}$ is a loading parameter. In the current case, we assume that the divergence of the macroscopic solvent-volume flux increases linearly with time, i.e, $\overline{\gamma} \propto t$, see Fig. 5.5**b**. All simulations are carried with the time incrementation $\tau = 0.01$ s. The chemical parameter of the matrix and the inclusion is selected as $A_{mat} = A_{incl} = 10$ N/mm^2. Furthermore, at the beginning of the simulation, the solvent-volume concentration at micro- and macroscale is assumed as $s(t = t_0) = \overline{s}(t = t_0) = 0$. Dirichlet boundary conditions for the normal projections of the fluctuations of the solvent-volume flux are considered, i.e., we set[28] $\widetilde{\mathbb{H}} \cdot \boldsymbol{N} = 0$ on $\partial\mathcal{B}_0$.

5.4.1.3 Influence of mobility parameters on the effective macroscopic response

We now investigate the influence of mobility parameters of the individual constituents on the macroscopic response of the two-phase material.

In a first step, we consider different kinds of square-shaped RVEs with constant mobility parameter $M_{mat} = 0.1$ mm^4/(Ns) of the matrix and altering mobility parameters of the inclusions.

In Fig. 5.6**a** we observe discrepancies in the results depending on the realization of the respective RVE. An increasing size of the RVE leads to a higher magnitude of the effective chemical potential. This effect is due to the last term in (5.39), which arises as the result of the transient nature of the problem. We refer to Larsson et al. [24] for a similar analysis. As expected from (5.39), the discrepancies of the effective responses of different RVEs decrease when we increase the mobility parameter of the inclusions. However, since we keep the mobility parameter of the matrix unchanged at a comparably low level ($M_{mat} = 0.1$ mm^4/(Ns)) the size effect is still pronounced. Further comparing the responses of 2RVE11 and RVE22, we observe that when the mobility parameter of the

[28] We note that in the Raviart–Thomas finite-element implementation anti-periodic boundary conditions need to be considered for the flux degrees of freedom across the boundary of the RVE in order to guarantee a continuous solvent normal flux throughout the microstructure. This can be achieved, for example, by augmenting the shape functions corresponding to the edge-based degrees of freedom at a boundary point $\boldsymbol{X}^+$ on $\partial\mathcal{B}^+$ with a different sign compared with the shape functions at $\boldsymbol{X}^-$ on $\partial\mathcal{B}^-$.

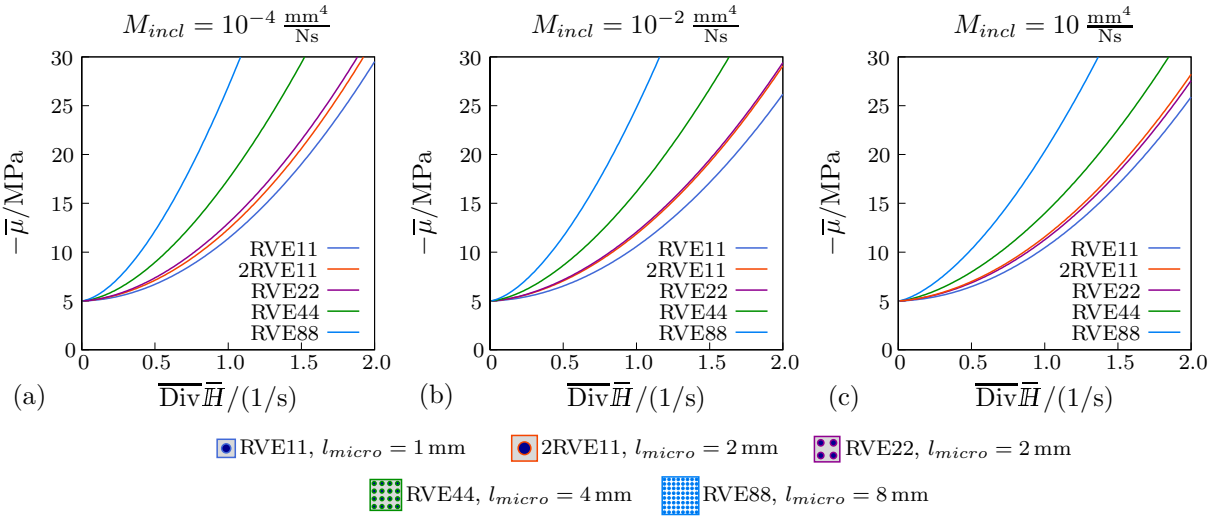

Figure 5.6: *Effective chemical potential depending on the size of the RVE and the mobility parameter of the inclusions.* The evolution of the macroscopic chemical potential $\overline{\mu}$ for different realizations of RVEs is depicted as function of the divergence of the macroscopic solvent-volume flux $\overline{\text{Div}}\,\overline{\mathbb{H}}$ for selected mobility parameters of the inclusions given by (**a**) $M_{incl} = 10^{-4}$ mm^4/(Ns), (**b**) $M_{incl} = 10^{-2}$ mm^4/(Ns) and (**c**) $M_{incl} = 10$ mm^4/(Ns). We observe that the effective chemical potential $\overline{\mu}$ depends strongly on the size of the RVE. Furthermore, the effective response of a single periodic unit cell differs from the effective response of an ensemble of identical periodic unit cells. The observed discrepancies decrease with increasing mobility parameter of the inclusions and vanish when nearly homogeneous microstructures of equal size are considered (e.g., 2RVE11 and RVE22 in b).

matrix and the inclusion have a similar magnitude, the corresponding effective responses nearly coincide (Fig. 5.6**b**). In fact, if we would assume $M_{mat} \equiv M_{incl}$, the responses would be identical since then the RVEs are homogeneous.

In Fig. 5.7, we show the influence of the mobility parameter of the matrix material on the effective response for fixed mobility parameter of the inclusions $M_{incl} = 10^{-4}$ mm^4/(Ns). We observe decreasing discrepancies in the effective responses with increasing mobility parameter of the matrix. This effect can be attributed to the higher volume fraction of the matrix.

Contour plots of the microscopic chemical potential μ for different realizations of RVEs are shown in Fig. 5.8. Remarkable differences in the microscopic response of the RVEs are evident. This confirms that the underlying periodicity cannot be used to reduce computations over an enlarged RVE to computations over a unit-cell RVE.

Above we have demonstrated that the effective chemical potential strongly depends on the mobility parameters of the individual phases as well as on the size and realization of the RVE. We now take a close look at the evolution of the chemical potential for various RVEs over time (Fig. 5.9). In analogy to the previous examples, we consider square RVEs that are either made up of a certain number of equal-sized unit cells or made up of a scaled-up unit cell. The macroscopic loading is again formulated in terms of the loading parameter $\overline{\gamma}$, which will first be linearly decreased to a minimum value and then increased to zero. After that, it will be kept fixed. Please refer to Fig. 5.5**c** for a graphical illustration, in which the negative sign of the loading parameter is related with an influx of the solvent. For time in incrementation we consider the time step $\tau = 0.1\,\text{s}$.

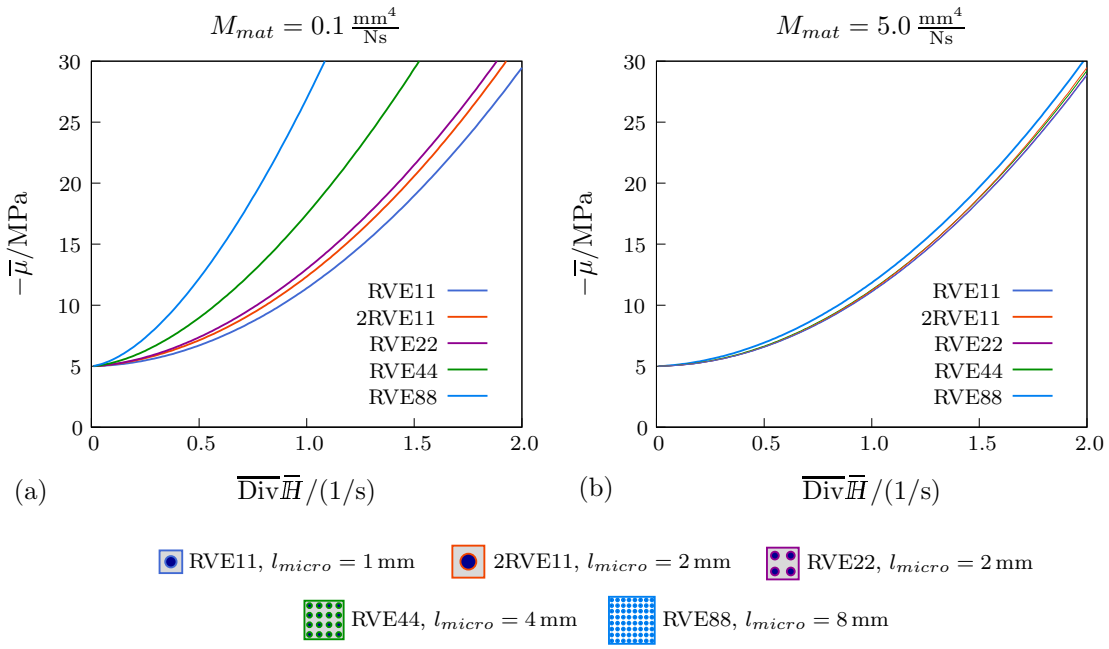

Figure 5.7: *Effective chemical potential depending on the size of the RVE and the mobility parameter of the matrix.* The evolution of the macroscopic chemical potential $\overline{\mu}$ for different realizations of RVEs is depicted as function of the divergence of the macroscopic solvent-volume flux $\overline{\text{Div}}\overline{\mathbb{H}}$ for selected mobility parameters of the matrix given by (**a**) $M_{mat} = 0.1\ \text{mm}^4/(\text{Ns})$ and (**b**) $M_{mat} = 5.0\ \text{mm}^4/(\text{Ns})$. Like in the previous study (Fig. 5.6) we observe that the effective chemical potential $\overline{\mu}$ depends strongly on the size of the RVE. The observed discrepancies decrease with increasing mobility parameter of the matrix.

In Fig. 5.9**a** we observe that the different RVEs show the expected differences in their initial effective response. However, after a certain period of time the responses of all RVEs converge to the same stationary solution, where low mobility parameters of the inclusions lead to longer relaxation times (compare Fig. 5.9**a**,**b**,**c**). We further observe that an increase of the mobility parameter of the inclusions has negligible influence on the behavior under loading, but strongly influences the unloading phase (compare Fig. 5.9**a**,**d** with Fig. 5.9**b**,**e** respectively). In contrast to that, changing the mobility parameter of the matrix strongly influences the loading phase, but shows qualitatively similar trends in the unloading regime (compare Fig. 5.9**a**,**d** with Fig. 5.9**c**,**f** respectively). As a final observation we note that the stationary solutions of different RVEs converge to the same values, even when the material parameters of the individual phases are different. (compare Fig. 5.9**b** with Fig. 5.9**e**). This behavior could be expected from the size-dependent contribution of the effective chemical potential given in (5.39). There, the first term has been assumed zero per definition and the last term of the right-hand side is zero after full unloading. As a consequence, the second term fades out over time due to internal redistributions of the solvent such that finally $\widetilde{\mathbb{H}} \to \boldsymbol{0}$ and thus $\overline{\mu}_{\text{size}} \to 0$. In the stationary state, the size-independent term of the macroscopic chemical potential (5.37) is identical for all considered RVEs since we assume the same chemical parameters for both phases in the microscopic chemical energy (5.40).

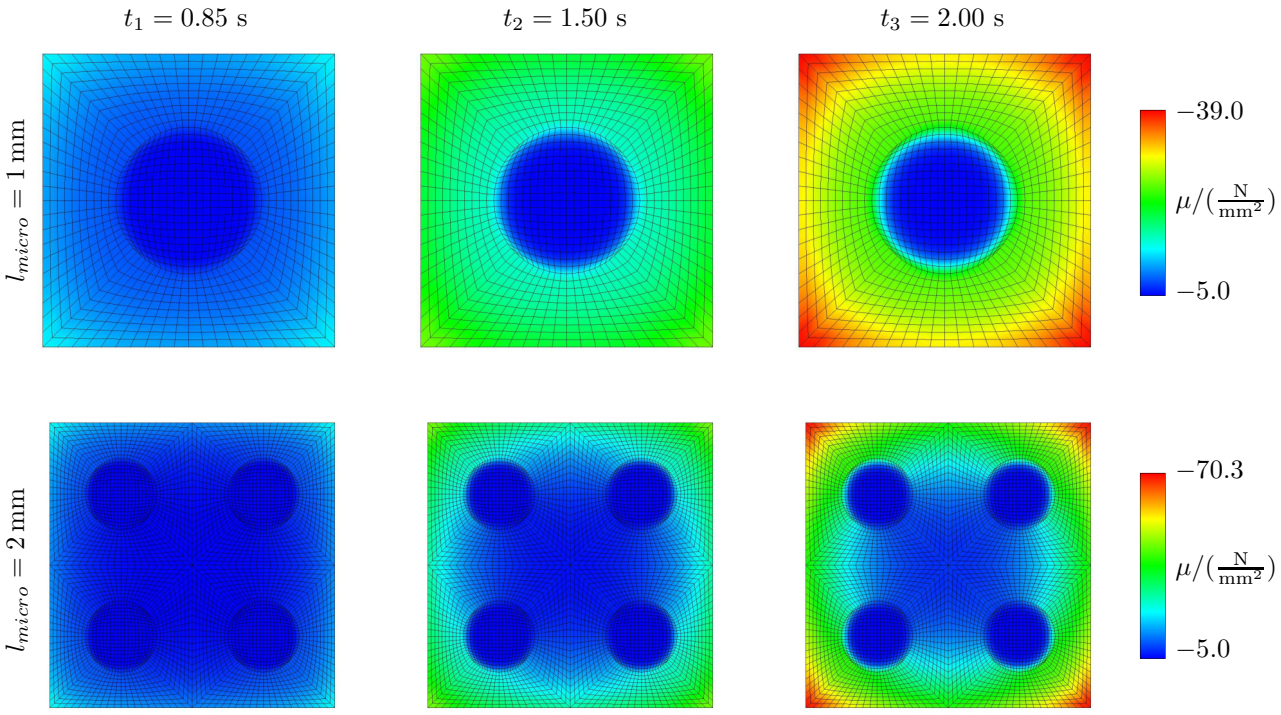

Figure 5.8: *Chemical potential field μ in consideration of two different periodic RVEs at three different instances of time.* Although the considered RVEs are composed of periodic unit cells, we observe remarkable differences in their response. The chemical parameters for the matrix and the inclusions are $A_{mat} = A_{incl} = 10$ N/mm^2. The mobility parameter of the matrix is given by $M_{mat} = 0.01$ mm^4/(Ns) and the mobility parameter of the inclusions is $M_{incl} = 10^{-4}$ mm^4/(Ns).

5.4.1.4 Influence of the size of the RVE on the macroscopic moduli

Next, we study the effect of the size of the RVE on the resulting macroscopic moduli. The influence of the size of the RVE for $M_{mat} = 10^{-1}$ mm^4/(Ns) and $M_{incl} = 10^{-4}$ mm^4/(Ns) on the effective response is shown in Fig. 5.10.

We observe that as the size of the RVE increases the macroscopic chemical parameter $\partial^2_{\overline{s}\,\overline{s}}\overline{\pi}$ as well as the macroscopic mobility parameter $1/(\partial^2_{\overline{\mathbb{H}}_1\overline{\mathbb{H}}_1}\overline{\pi})$ (see (5.35)), increase monotonically although the microscopic material parameters are not changed. However, for $l_{micro} \to 0$, the macroscopic moduli saturate. As becomes visible in Fig. 5.10**a**, the macroscopic chemical parameter approaches the average value of the microscopic chemical parameters, i.e., $\langle \partial^2_{ss}\psi \rangle := \frac{1}{|\mathcal{B}_0|}\int_{\mathcal{B}_0} \partial^2_{ss}\psi \,\mathrm{d}V = 10$ N/mm^2. Analogously, in Fig. 5.10**b**, the macroscopic mobility parameter for $l_{micro} \to 0$ is bounded by the classical Voigt and Reuss bounds (Zohdi and Wriggers [43])

$$\underbrace{\left(\frac{1}{|\mathcal{B}_0|}\int_{\mathcal{B}_0} \partial^2_{\mathbb{H}_1\mathbb{H}_1}\hat{\phi}\,\mathrm{d}V\right)^{-1}}_{\text{Reuss bound}} \leq \frac{1}{(\partial^2_{\overline{\mathbb{H}}_1\overline{\mathbb{H}}_1}\overline{\pi})} \leq \underbrace{\frac{1}{|\mathcal{B}_0|}\int_{\mathcal{B}_0} (\partial^2_{\mathbb{H}_1\mathbb{H}_1}\hat{\phi})^{-1}\,\mathrm{d}V}_{\text{Voigt bound}} . \tag{5.42}$$

To further study the influence of the size of the RVE depending on the mobility parameter of the microstructure, we provide three-dimensional plots for the different mobility parameters of the matrix $M_{mat} = \{0.001, 0.1, 1.0\}$ mm^4/(Ns) in Fig. 5.11.

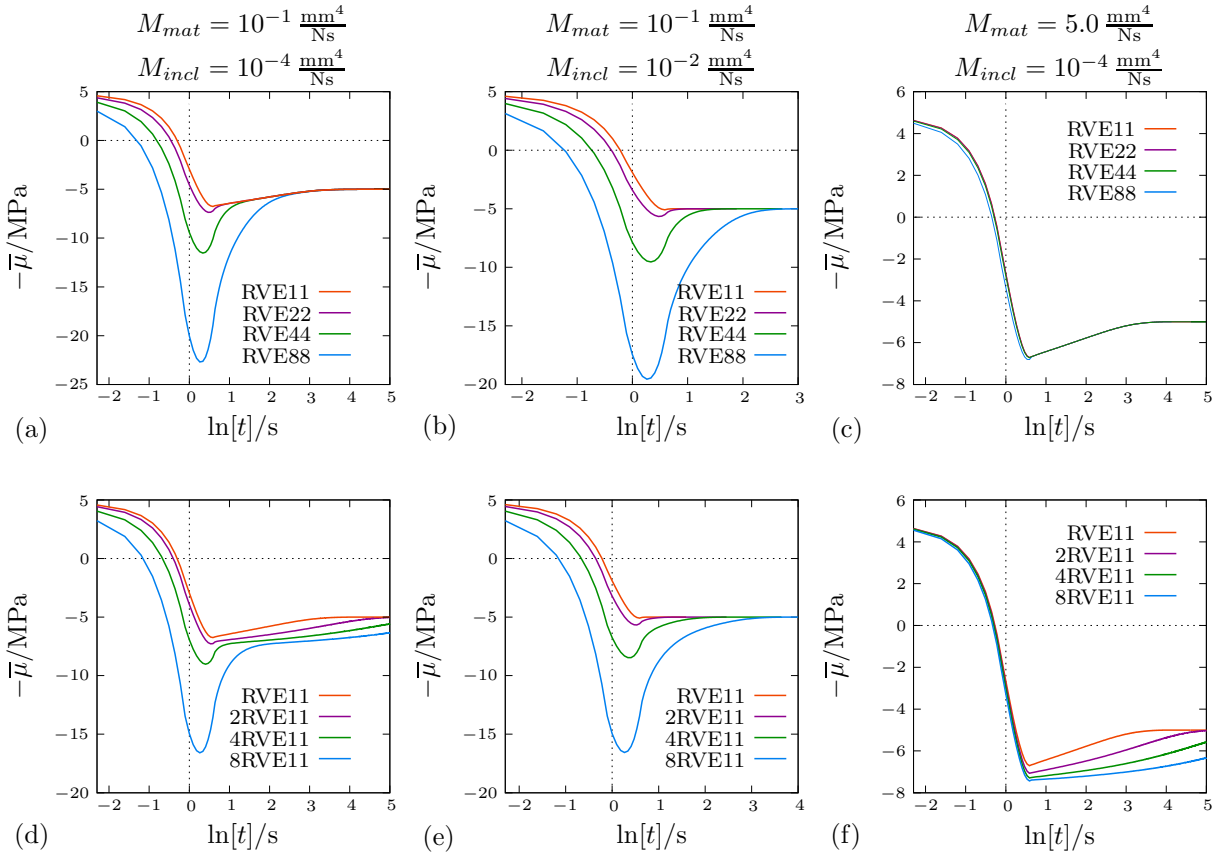

Figure 5.9: *Evolution of the effective chemical potential $\overline{\mu}$ versus loading time t for different microstructures and mobility parameters of the individual phases.* RVEnn denote equal-sized RVEs with lateral length of n mm made up of $n \times n$ unit cells. nRVE11 denotes scaled RVEs made up of one unit cell having a lateral length of n mm. In the plots, the mobility parameter of the matrix and the inclusion is given by (units in mm^4/(Ns)) $M_{mat} = 10^{-1}$ and $M_{incl} = 10^{-4}$ (**a** and **d**), $M_{mat} = 10^{-1}$ and $M_{incl} = 10^{-2}$ (**b** and **e**) and $M_{mat} = 5.0$ and $M_{incl} = 10^{-4}$ (**c** and **f**). We observe that the transient response of the individual RVEs is sensitive with respect to changes of material parameters, but converges to a unique stationary solution.

We plot the macroscopic chemical parameter and the macroscopic mobility parameter against RVE size ($l_{micro} \in [0.002, 2.0]$ m) and mobility parameter of inclusions ($M_{incl} \in [0.001, 10]$ mm^4/(Ns)) in Fig. 5.11**a**–**c** and **d**–**f**, respectively.

In Fig. 5.11**a**–**c**, we observe that the macroscopic chemical parameter is highly dependent on the RVE size l_{micro} as well as the mobility parameter of the matrix material M_{mat}. As M_{mat} increases the macroscopic chemical parameter decreases. However, the influence of the mobility parameter of the inclusions is lower than the one of the matrix material. In Fig. 5.11**c**, we see that as $M_{incl} \to 0$ the effective chemical parameter increases in the given range. In all instances of M_{mat}, M_{incl} and l_{micro}, the macroscopic chemical parameter approaches 10 N/mm^2 when the RVE size approaches zero.

In Fig. 5.11**d**–**f**, we observe that the macroscopic mobility parameter is highly dependent on the size of the RVE and the mobility parameter of the matrix. We also see that for lower values of matrix mobility parameter, the influence of the mobility parameter of the inclusions becomes more pronounced. Additionally, the RVE size becomes more relevant for increasing magnitudes of M_{mat}.

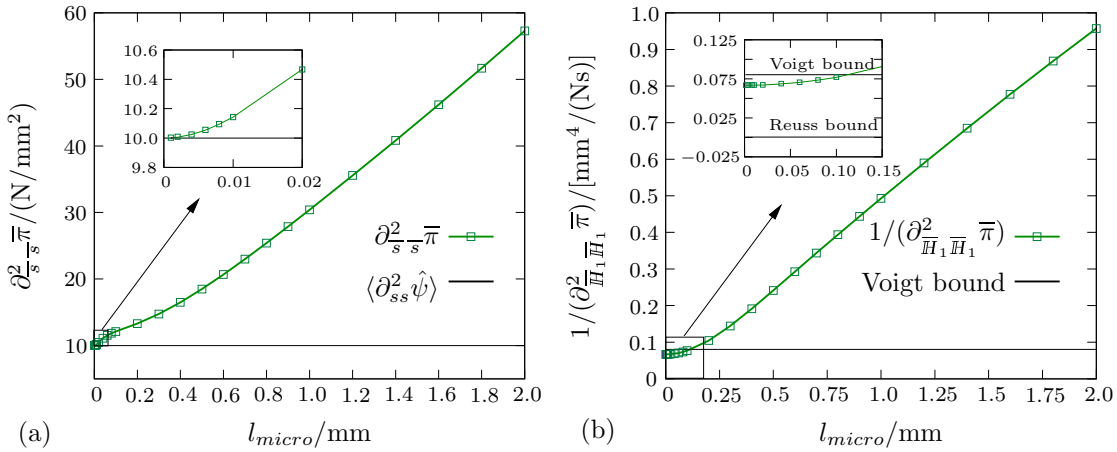

Figure 5.10: *Selected macroscopic moduli depending on the size l_{micro} of square-shaped RVEs with circular inclusions with volume fraction $f_0 = \pi/16$.* The chemical parameter of the matrix and the inclusions are chosen to $A_{mat} = A_{incl} = 10\,\mathrm{N/mm^2}$. The mobility parameter of the matrix and the inclusions is $M_{mat} = 0.1\,\mathrm{mm^4/(Ns)}$ and $M_{incl} = 0.0001\,\mathrm{mm^4/(Ns)}$ respectively. (**a**) We observe that for vanishing size of the RVE $l_{micro} \to 0$, the macroscopic chemical parameter $\partial^2_{\overline{s}\,\overline{s}}\overline{\pi}$ converges to the homogeneous solution $\langle\partial^2_{ss}\hat{\psi}\rangle = \frac{1}{|\mathcal{B}|}\int_{\mathcal{B}}\partial_{ss}\hat{\psi}\,\mathrm{d}V$. (**b**) Furthermore, for vanishing size of the RVE, the macroscopic mobility parameter $\partial^2_{\overline{\mathbb{H}}\,\overline{\mathbb{H}}}\overline{\pi}$ lies firmly within the Voigt and Reuss bound according to (5.42).

Finally, in Fig. 5.11**g**–**i** we illustrate regions of macroscopic mobility parameter that are bound from above by the classical Voigt bound (5.42). It is evident that low magnitudes of matrix mobility parameter lead to larger regions bounded by the Voigt bound. The size of the RVE has a converse influence on this region.

5.4.2 Coupled diffusion-deformation processes in periodic hydrogels

We now present a numerical example that demonstrates the coupled chemo-mechanical response of a two-phase periodic hydrogel microstructure. To be specific, we analyze a pattern transformation due to diffusion-induced swelling phenomena (we refer to Zhu et al. [42] for experimental evidence). In order to model such phenomenon, we need to consider appropriate constitutive equations that take into account the coupled response of hydrogels. The subsequent sections are thus first devoted to the discussion of the used microscopic constitutive functions. Thereafter we analyze the behavior of a periodic hydrogel in consideration of typical geometrical and physical properties under given macroscopic loading conditions.

5.4.2.1 Microscopic constitutive functions

We assume that the mechanical contribution of the energy-storage function in (5.9) can be described by a neo-Hookean function. The chemical energy function is considered to be of the Flory–Rehner-type. These functions are given as

$$\hat{\psi}_{mech}(\boldsymbol{F}) = \frac{\gamma}{2}(\boldsymbol{F}:\boldsymbol{F} - 3 - 2\ln J) \quad \text{and} \quad \hat{\psi}_{chem}(s) = \alpha[s\ln(\frac{s}{1+s}) + \frac{\chi s}{1+s}], \tag{5.43}$$

where α is a mixing modulus and χ is a dimensionless Flory–Huggins interaction parameter. The coupling of the mechanical and the chemical response of the material is modeled

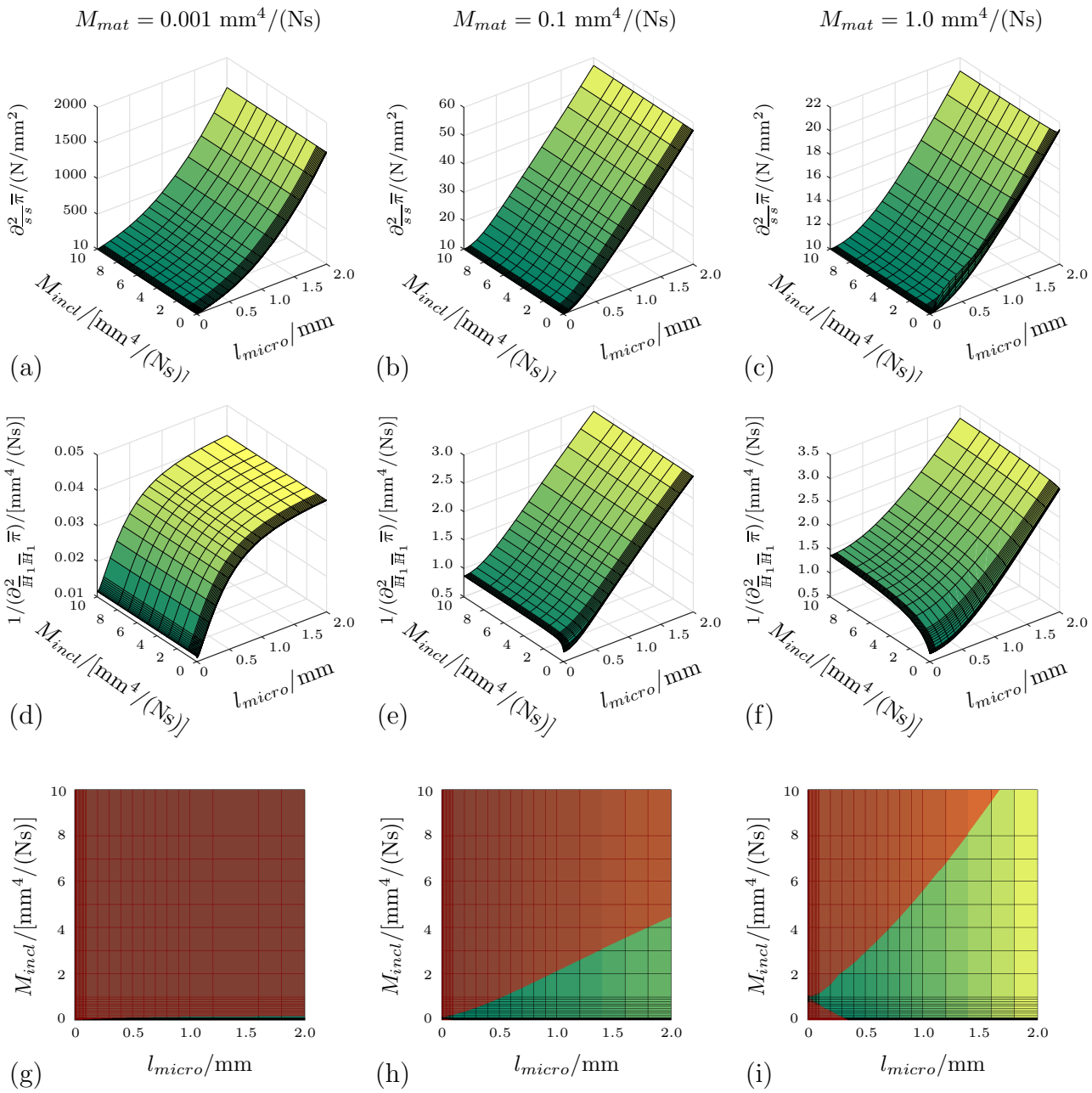

Figure 5.11: *Macroscopic incremental moduli depending on mobility parameters and size of the RVE.* (**a**)–(**c**) Macroscopic chemical parameter and (**d**)–(**f**) selected macroscopic mobility parameter depending on the mobility parameter of the matrix $M_{mat} = \{0.0001, 0.1, 1.0\}$ mm^4/(Ns) and the inclusion $M_{incl} \in [0.001, 10.0]$ mm^4/(Ns) as well as the size of the RVE $l_{micro} \in [0.002, 2.0]$ N/mm^2. (**h**)–(**i**) Red areas indicate regions of the macroscopic mobility parameter that are bounded from above by the Voigt bound.

with the function

$$\hat{\psi}_{coup}(J, s) = \frac{\epsilon}{2}(J - 1 - s)^2 \,, \tag{5.44}$$

where ϵ is a penalty parameter enforcing the volumetric constraint $J = 1 + s$, see Böger et al. [4]. The dissipation-potential function is a convex function of the solvent flux

$$\hat{\phi}(\mathbb{H}; \boldsymbol{F}_n, s_n) = \frac{1}{2Ms_n}\boldsymbol{C}_n : (\mathbb{H} \otimes \mathbb{H}) \,, \tag{5.45}$$

Table 5.6: Material parameters of the two-phase periodic hydrogel composites.

No.	Parameter	Name, unit	Matrix	Inclusion
1.	γ	Shear Modulus, N/mm^2	0.1	10^{-4}
2.	α	Mixing modulus, N/mm^2	24.2	24.2
3.	χ	Mixing parameter, –	0.1	0.1
4.	M	Mobility parameter, mm^4/(Ns)	10^{-4}	10^3
5.	ϵ	Penalty parameter, N/mm^2	10	10^{-3}
6.	J_0	Pre-swollen Jacobian, –	1.01	1.01

where $\boldsymbol{C}$ is the right Cauchy–Green tensor and M is a mobility parameter (Böger et al. [4]).

We note that the swelling-volume concentration $s \geq 0$ is a non-negative quantity and $s = 0$ corresponds to a dry hydrogel polymer network. However, due to the present singularity of $(5.43)_2$ at the dry state we employ a stress-free pre-swollen state as the reference configuration for the Flory–Rehner energy function. We refer to Hong et al. [20, 19], Böger et al. [4] for detailed discussions. Consequently, we write the final forms of the energy-storage function

$$\hat{\psi} = \frac{\gamma}{2J_0}[J_0^{2/3}\boldsymbol{F} : \boldsymbol{F} - 3 - 2\ln(JJ_0)] + \frac{\alpha}{J_0}[s\ln(\frac{s}{1+s}) + \frac{\chi s}{1+s}] + \frac{\epsilon}{2J_0}(JJ_0 - 1 - s)^2\,, \tag{5.46}$$

and the dissipation-potential function

$$\hat{\phi} = \frac{1}{2J_0^{1/3}Ms_n}\boldsymbol{C}_n : (\mathbb{H} \otimes \mathbb{H})\,, \tag{5.47}$$

where J_0 is a Jacobian that characterizes the volume change due to uniform pre-swelling. The initial solvent-volume concentration is determined from the assumption of a stress-free reference configuration as

$$s_0 = \frac{\gamma}{\epsilon}\big(J_0^{-1/3} - \frac{1}{J_0}\big) + J_0 - 1\,. \tag{5.48}$$

The macroscopic solvent concentration $\overline{s}_0$ at the pre-swollen state is defined as the average of the microscopic solvent-volume concentration s_0.

5.4.2.2 Description of the problem

To analyze the effective chemo-mechanical behavior of a hydrogel we consider a two-phase square-shaped RVE with size $l_{micro} = 2$ mm build out of four periodic unit cells (the unit cell is depicted in Fig. 5.5). The volume fraction of the inclusions is $\pi/16$. The inclusions are softer than the matrix and have a higher mobility parameter. The material parameters are listed in Table 5.6.

The RVE is loaded with the macroscopic fields

$$\overline{\boldsymbol{F}} = \boldsymbol{1}\,, \quad \overline{\mathbb{H}} = \boldsymbol{0}\ \text{m/s} \quad \text{and} \quad \overline{\text{Div}}\overline{\mathbb{H}} = -10^{-3}\ \text{s}^{-1}\,. \tag{5.49}$$

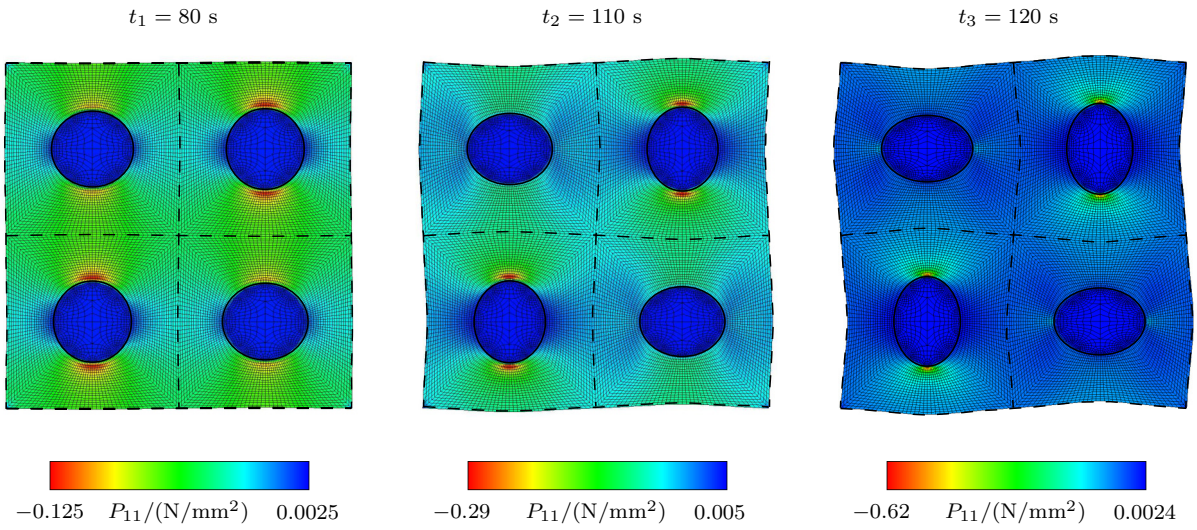

Figure 5.12: *Pattern transformation due to macroscopically driven swelling of a periodic RVE.* Due to swelling of the matrix, the microscopic inclusions initially shrink homogeneously. Then, at a critical loading point, the periodic RVE undergoes a pattern transformation such that the initially circular inclusions deform to non-circular shapes. The contour shows the P_{11} component of the first Piola-Kirchhoff stress tensor $\boldsymbol{P}$ at three different time steps for an RVE build out of four unit cells.

in consideration of periodic boundary conditions for the fluctuations of the deformation map $\widetilde{\boldsymbol{\varphi}}$ and homogeneous Dirichlet boundary conditions for the fluctuations of the outward normal flux $\widetilde{\mathbb{H}} \cdot \boldsymbol{N}$. The computations are performed with a time incrementation of $\tau = 0.1$ s. To ensure that the problem is well-defined, we fix the fluctuations of the deformation map at the corner nodes of the RVE.

5.4.2.3 Swelling-induced pattern transformation of a periodic hydrogel

As a numerical example, we analyze a swelling-induced pattern transformation of a two-phase periodic hydrogel. The periodic RVE is discretized by using $16,000$ $\mathrm{Q_2RT_0}$ finite elements. In Fig. 5.12, we illustrate contour plots of the P_{11}-component of the first Piola–Kirchhoff stress at three different time instances.

We observe that initially the soft inclusions having a volume fraction of $\pi/16$ shrink uniformly until a critical loading point is reached. At critical loading, the RVE undergoes a pattern transformation in the form of a buckling mode. A similar behavior has been observed in experiments by Zhu et al. [42]. When the microstructure buckles the shape of the inclusions becomes non-circular, a state which is typically referred to as the diamond-plate pattern [42]. Such an instability mode has also been observed by Bertoldi et al. [2] for periodic elastic structures with voids or soft inclusions under purely compressive loading. To trigger the buckling mode shown in Fig. 5.12, we have slightly perturbed the finite-element mesh in the given directions.

5.5 Summary

We provided a computational homogenization framework for diffusion-deformation processes within a variationally consistent minimization-based setting that takes into account the deformation map and solvent-volume flux as independent field variables. We have discussed the theoretical aspects as well as the finite-element implementation of the formulation. The latter was realized by means of a conforming Raviart–Thomas-type discretization. By doing so, we were able to compute the macroscopic dual fields and incremental moduli in the numerical setting. Consistent with previous works from the literature, we found that the formulation yields a size-dependent macroscopic response. We confirmed this effect in a number of numerical examples by consideration of different RVEs with different mobility parameters and sizes. We further confirmed that the macroscopic mobility properties are bounded by the classical Reuss and Voigt bounds when the RVE size approaches zero. We also presented a numerical example showing a swelling-induced buckling mode of a soft periodic hydrogel.

Declarations

Availability of data and material. Data will be made available on request.

Competing interests. The authors have no competing interests.

Funding. The financial support of the German Research Foundation (DFG) in the framework of the Collaborative Research Center SFB 1313 (327154368) and within the Cluster of Excellence EXC 2075 (390740016) at the University of Stuttgart is gratefully acknowledged.

Authors' contributions. E.P. and M.-A.K. developed the research idea and designed the study. E.P. performed the numerical implementation and post-processed the simulation data. E.P. and M.-A.K. interpreted the results. Both authors wrote the manuscript and gave their final approval for publication.

Acknowledgements. Not applicable.

Bibliography: Paper C

[1] Anjam, I., Valdman, J., [2015]. *Fast matlab assembly of fem matrices in 2d and 3d: Edge elements*. Applied Mathematics and Computation 267, 252–263.

[2] Bertoldi, K., Boyce, M., Deschanel, S., Prange, S., Mullin, T., [2008]. *Mechanics of deformation-triggered pattern transformations and superelastic behavior in periodic elastomeric structures*. Journal of the Mechanics and Physics of Solids 56, 2642–2668.

[3] Biot, M. A., [1941]. *General theory of three-dimensional consolidation*. Journal of Applied Physics 12 (2), 155–164.

[4] Böger, L., Nateghi, A., Miehe, C., [2016]. *Minimization-and saddle-point-based modeling of diffusion-deformation-processes in hydrogels*. PAMM 16 (1), 307–308.

[5] Brezzi, F., Fortin, M., [1991]. *Mixed and hybrid finite element methods*. Springer-Verlag.

[6] Chatzigeorgiou, G., Charalambakis, N., Chemisky, Y., Meraghni, F., [2016]. *Periodic homogenization for fully coupled thermomechanical modeling of dissipative generalized standard materials*. International Journal of Plasticity 81, 18–39.

[7] Chen, J., Park, K., [2000]. *Synthesis and characterization of superporous hydrogel composites*. Journal of Controlled Release 65 (1-2), 73–82.

[8] Chester, S. A., Anand, L., [2010]. *A coupled theory of fluid permeation and large deformations for elastomeric materials*. Journal of the Mechanics and Physics of Solids 58 (11), 1879–1906.

[9] Coussy, O., Dormieux, L., Detournay, E., [1998]. *From mixture theory to Biot's approach for porous media*. International Journal of Solids and Structures 35 (34-35), 4619–4635.

[10] Edward, J. T., [1970]. *Molecular volumes and the Stokes-Einstein equation*. Journal of Chemical Education 47 (4), 261.

[11] Ehlers, W., Wagner, A., [2015]. *Multi-component modelling of human brain tissue: a contribution to the constitutive and computational description of deformation, flow and diffusion processes with application to the invasive drug-delivery problem*. Computer Methods in Biomechanics and Biomedical Engineering 18 (8), 861–879.

[12] Feyel, F., Chaboche, J.-L., [2000]. *FE^2 multiscale approach for modelling the elasto-viscoplastic behaviour of long fibre SiC/Ti composite materials*. Computer methods in applied mechanics and engineering 183, 309–330.

[13] Flory, P. J., Rehner, J. J., [1943]. *Statistical mechanics of cross-linked polymer networks ii. swelling*. The Journal of Chemical Physics 11 (11), 521–526.

[14] Geymonat, G., Müller, S., Triantafyllidis, N., [1993]. *Homogenization of nonlinearly elastic materials, microscopic bifurcation and macroscopic loss of rank-one convexity*. Archive of Rational Mechanics and Analysis 122, 231–290.

[15] Govindjee, S., Simo, J. C., [1993]. *Coupled stress-diffusion: Case {II}*. Journal of the Mechanics and Physics of Solids 41 (5), 863–887.

[16] Gurtin, M. E., Fried, E., Anand, L., [2010]. *The mechanics and thermodynamics of continua*. Cambridge University Press.

[17] Hashin, Z., Shtrikman, S., [1963]. *A variational approach to the theory of the elastic behaviour of multiphase materials*. Journal of the Mechanics and Physics of Solids 11, 127–140.

[18] Hill, R., [1952]. *The elastic behaviour of a crystalline aggregate*. Proceedings of the Physical Society A 65, 349–354.

[19] Hong, W., Liu, Z., Suo, Z., [2009]. *Inhomogeneous swelling of a gel in equilibrium with a solvent and mechanical load*. International Journal of Solids and Structures 46 (17), 3282–3289.

[20] Hong, W., Zhao, X., Zhou, J., Suo, Z., [2008]. *A theory of coupled diffusion and large deformation in polymeric gels*. Journal of the Mechanics and Physics of Solids 56 (5), 1779–1793.

[21] Kaessmair, S., Steinmann, P., [2018]. *Computational first-order homogenization in chemo-mechanics*. Archive of Applied Mechanics 88 (1-2), 271–286.

[22] Kouznetsova, V. G., Geers, M. G. D., Brekelmans, W. A. M., [2004]. *Multi-scale second-order computational homogenization of multi-phase materials: a nested finite element solution strategy*. Computer Methods in Applied Mechanics and Engineering 193, 5525–5550.

[23] Krischok, A., Linder, C., [2019]. *A generalized inf–sup test for multi-field mixed-variational methods*. Computer Methods in Applied Mechanics and Engineering 357, 112497.

[24] Larsson, F., Runesson, K., Su, F., [2010]. *Variationally consistent computational homogenization of transient heat flow*. International Journal for Numerical Methods in Engineering 81 (13), 1659–1686.

[25] Miehe, C., Mauthe, S., Teichtmeister, S., [2015]. *Minimization principles for the coupled problem of darcy–biot-type fluid transport in porous media linked to phase field modeling of fracture*. Journal of the Mechanics and Physics of Solids 82, 186–217.

[26] Miehe, C., Schotte, J., Schröder, J., [1999]. *Computational micro-macro transitions and overall moduli in the analysis of polycrystals at large strains*. Computational Materials Science 16, 372–382.

[27] Nemat-Nasser, S., Hori, M., [1999]. *Micromechanics: Overall properties of heterogeneous materials*, 2nd Edition. Vol. 36 of *North-Holland series in Applied Mathematics and Mechanics*. Elsevier Science Publisher B. V.

[28] Nilenius, F., Larsson, F., Lundgren, K., Runesson, K., [2014]. *Computational homogenization of diffusion in three-phase mesoscale concrete*. Computational Mechanics 54 (2), 461–472.

[29] Özdemir, I., Brekelmans, W., Geers, M., [2008]. *Computational homogenization for heat conduction in heterogeneous solids*. International journal for numerical methods in engineering 73 (2), 185–204.

[30] Pham, K., Kouznetsova, V. G., Geers, M. G., [2013]. *Transient computational homogenization for heterogeneous materials under dynamic excitation*. Journal of the Mechanics and Physics of Solids 61 (11), 2125–2146.

[31] Polukhov, E., Vallicotti, D., Keip, M.-A., [2018]. *Computational stability analysis of periodic electroactive polymer composites across scales*. Computer Methods in Applied Mechanics and Engineering 337, 165–197.

[32] Raviart, P. A., Thomas, J. M., [1977]. *Primal hybrid finite element methods for 2nd order elliptic equations*. Mathematics of computation 31 (138), 391–413.

[33] Reuss, A., [1929]. *Berechnung der Fließgrenze von Mischkristallen aufgrund der Plastizitätsbedingung für Einkristalle*. Zeitschrift für angewandte Mathematik und Mechanik 9, 49–58.

[34] Schwarz, A., Schröder, J., Starke, G., [2010]. *A modified least-squares mixed finite element with improved momentum balance*. International journal for numerical methods in engineering 81 (3), 286–306.

[35] Teichtmeister, S., Mauthe, S., Miehe, C., [2019]. *Aspects of finite element formulations for the coupled problem of poroelasticity based on a canonical minimization principle*. Computational Mechanics, 1–32.

[36] Temizer, I., [2012]. *On the asymptotic expansion treatment of two-scale finite thermoelasticity*. International Journal of Engineering Science 53, 74–84.

[37] Temizer, I., Wriggers, P., [2011]. *Homogenization in finite thermoelasticity*. Journal of the Mechanics and Physics of Solids 59 (2), 344–372.

[38] Truskey, G. A., Yuan, F., Katz, D. F., [2004]. *Transport phenomena in biological systems*.

[39] Voigt, W., [1887]. *Über die Beziehung zwischen den beiden Elastizitätskonstanten isotroper Körper*. Annalen der Physik 38, 573–587.

[40] Wang, J., Yang, J., Xie, J., Xu, N., [2002]. *A novel conductive polymer–sulfur composite cathode material for rechargeable lithium batteries*. Advanced materials 14 (13-14), 963–965.

[41] Wang, L., Ueda, T., [2011]. *Mesoscale modeling of water penetration into concrete by capillary absorption*. Ocean Engineering 38 (4), 519–528.

[42] Zhu, X., Wu, G., Dong, R., Chen, C.-M., Yang, S., [2012]. *Capillarity induced instability in responsive hydrogel membranes with periodic hole array.* Soft Matter 8 (31), 8088–8093.

[43] Zohdi, T., Wriggers, P., [1999]. *On the effects of microstress on macroscopic diffusion processes.* Acta Mechanica 136 (1-2), 91–107.

Chapter 6: Paper D

Swelling-Induced Pattern Transformations of Periodic Hydrogels – from the Wrinkling of Internal Surfaces to the Buckling of Thin Films

Swelling-Induced Pattern Transformations of Periodic Hydrogels – from the Wrinkling of Internal Surfaces to the Buckling of Thin Films

Original publication:

Polukhov, E., Pytel, L. & Keip, M.-A. [2023]. *Swelling-induced pattern transformations of periodic hydrogels – from the wrinkling of internal surfaces to the buckling of thin films.* Journal of the Mechanics and Physics of Solids 175, 105250.

Abstract

We investigate pattern transformations of periodic hydrogel systems that are triggered by swelling-induced structural instabilities. The types of microstructures considered in the present work include single-phase and two-phase voided hydrogel structures as well as reinforced hydrogel thin films. While the observed transformations of the single-phase structures show good agreement with experimental findings, the two-phase materials provide novel patterns associated with wrinkling of internal surfaces. Furthermore, an extensive parametric study on the reinforced hydrogel thin films reveals new opportunities for the design of complex out-of-plane surface modes caused by swelling-induced instabilities. Next to the mentioned buckling-type instabilities, we encountered the development of micro-creases at the internal surfaces of periodic media.

Keywords: periodic hydrogel structures, pattern transformations, buckling, Bloch-Floquet analysis, swelling-induced instabilities, strong ellipticity

6.1 Introduction

Hydrogels are polymeric, soft and biocompatible materials that undergo large deformations under swelling [32]. At swollen state, their mechanical response depends on both the properties of the polymer and the solvent phase. While the elastic stiffness correlates with the density of cross-links of the polymer network, viscoelasticity is driven by the viscosity of the solvent [1]. Depending on how the polymer network is held together, hydrogels can be categorized as physical (reversible) or chemical (permanent), see [67] and [32] for specific examples related to each category. In the former group, the network is interconnected by polymer-chain entanglements as well as possible additional forces resulting from ionic or hydrophobic interactions and hydrogen bonding [81]. The latter group of hydrogels is based on covalently cross-linked networks. Both physical and chemical hydrogels can be inhomogeneous due to clustered regions of cross-links and swelling, as well as the existence of defects in the polymer network. Furthermore, hydrogels can be classified as conventional or (multi-)stimuli responsive [32]. While both are hydrophilic and undergo swelling in a solvent, (multi-)stimuli responsive hydrogels may also respond to changes in pH, temperature or electric field [31]. In the present work, we will focus on conventional hydrogels and describe their chemo-mechanical response related to the diffusion of a solvent through their polymer network.

6.1.1 Engineering and biomedical applications of hydrogels

Since hydrogels have favorable properties and show tunable, versatile response, they have a wide range of applications, such as fertilizer encapsulaters in agriculture [68], soft actuators [40] in engineering as well as artificial muscles [45], tissue-engineered auricles [3], contact lenses and wound dressings [8] in biomedicine, see also [67, 4, 32] and the references therein. By virtue of intricate fabrication techniques, further applications are being realized not only at macroscopic scale, but also at micro- and nanoscopic scales [53, 69]. Here, we mention in particular the fabrication by means of photolithography, which has attracted increased attention for the manufacturing of patterned and composite hydrogels exhibiting controllable deformations [53, 51]. We refer to [76, 52] for the use of photolithography to fabricate composite periodic hydrogel structures composed of high-swelling and non-swelling regions. By means of the latter, the authors were able to induce out-of-plane buckling in water yielding various periodic buckling patterns. Consequently, by designing associated hydrogel microstructures and by tuning material parameters, a rich set of deformation modes can be activated which increases their potential application as soft devices exploiting chemo-mechanical interactions.

Besides pattern transforming instabilities in periodic systems, surface wrinkling and creasing are observed in hydrogel structures. These instabilities can be exploited to further advance engineering and biomedical applications. In particular, wrinkling of hydrogels can be utilized for controlled formation of microgears [79], generation of multicellular spheroids [84], controlled cell spreading [41] among many other possibilities, see also [49, 25] and the detailed review [14] on instabilities in gels. We further refer to the recent experimental realization of nano-wrinkled architectures by means of laser direct assembly [19].

6.1.2 Continuum-mechanical models for hydrogels

Not least because of the above mentioned favorable properties and applications, hydrogels have gained increased attention in theoretical and computational research. Here, one main goal is to develop versatile and reliable models to simulate their response. Related models can give further insights into underlying features, provide access to the design of pertinent microstructures for specific applications and allow the investigation of the influence of various parameters on the respective behavior. In particular continuum-mechanical models are established and widely used to capture the response of hydrogels at macroscopic as well as microscopic scales. These models take into account chemo-mechanical interactions within the polymer network of a hydrogel, as well as between the polymer network and the diffusing solvent. We refer to [83, 35] for continuum-mechanical models of gels based on Flory–Huggins theory [20, 37], see also the Flory–Rehner type models [21, 22]. Finite-element implementations of the models [83, 35] have been applied to the simulation of transient diffusion processes in [80] and drying-induced instabilities in [34]. We further refer to the continuum approaches addressed in [10, 11, 7].

Note that the finite-element formulation of the above mentioned models has been based on the chemical potential as a primary unknown. In combination with the mechanical deformation map, this corresponds to a saddle-point formulation. Because of the a priori indefiniteness of the underlying system of equations, related implementations could result in numerical challenges associated with *inf-sup instabilities* [73]. Such challenges can be overcome by employing a minimization-based variational formulation as proposed by [6]

for hydrogels; see [56] for a basis rooted in poromechanics.

A further similarity of the above mentioned approaches is the use of Biot's theory [5, 12] relying on a Flory–Rehner-type energy function and Fick's law of diffusion. Alternative continuum-mechanical models have been established on the basis of the so-called Theory of Porous Media [16, 17, 18]. We further refer to recent multiscale modeling approaches to describe the diffusion process in heterogeneous microstructures [50, 44, 64, 63, 43].

6.1.3 Instabilities of hydrogels and their prediction

Continuum-mechanical models of hydrogels have further been exploited to investigate complex instability phenomena such as surface wrinkling, creasing and pattern transformations as a result of deformation-diffusion processes [14] (see Fig. 6.1 for an illustration). Experimental investigations of surface instabilities have been documented, for example, in [71, 75, 27]. In [27], wrinkling and creasing-type instabilities have been studied in pHEMA gels[29], where it has been shown that the resulting surface morphology strongly depends on cross-linker concentration and solvent-polymer interaction. In particular, the authors demonstrated that while a specific hydrogel layer develops wrinkling in water, the same layer shows a transition from wrinkling to creasing when exposed to alcohol and alcohol-water mixture. In [25], surface wrinkling was exploited to control stem-cell morphology and differentiation. Further studies on wrinkling and creasing of hydrogel bilayers have been performed analytically in [47, 46, 78, 39] and computationally in [15, 38, 70]. Although analytical and semi-analytical formulations can be exploited for the efficient instability analysis of hydrogels in the transient setting [39], they can have limitations for the analysis of structures with complex geometries. In the latter case, computational models can be used.

[29]The acronym pHEMA stands for poly(2-hydroxyethyl methacrylate) [27].

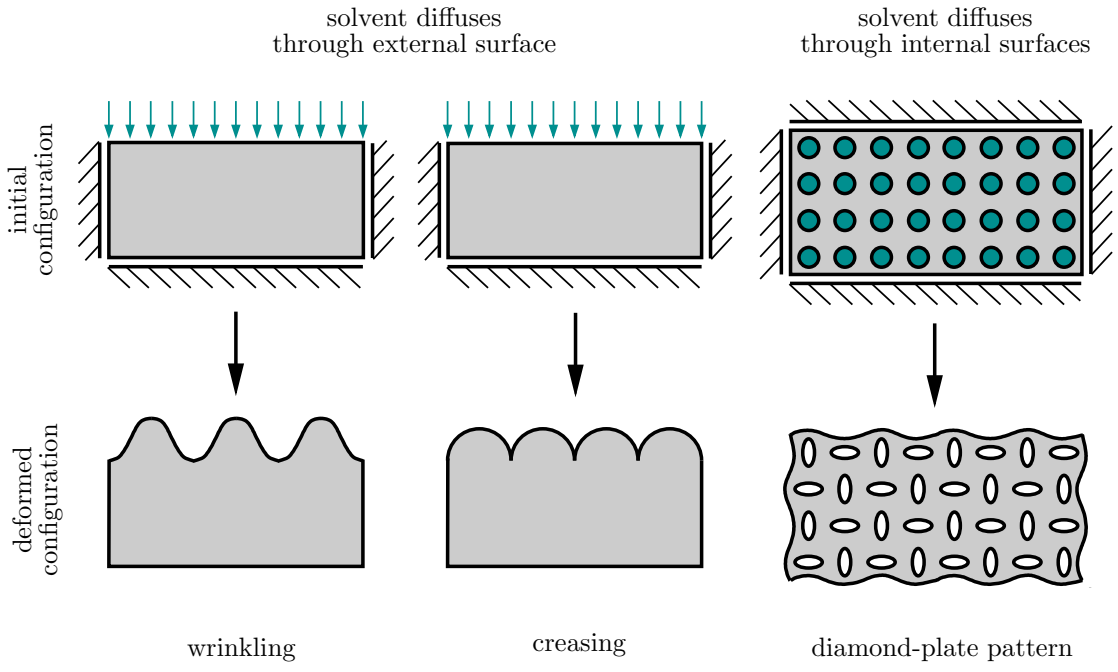

Figure 6.1: *Examples of swelling-induced instabilities in constrained hydrogel structures.*

In addition to surface instabilities, pattern-transforming instabilities in periodic hydrogel structures have been investigated experimentally in [82, 85, 77]. In [82], the authors have shown that when PDMS gels[30] with periodically embedded circular pores of 1 μm diameter are swollen in toluene, an organic solvent, elastic buckling of circular pores into elliptic shapes is observed. In the buckled state, the major axes of the ellipses are mutually orthogonal to one another developing a so-called diamond-plate pattern (see Fig. 6.1). The authors have utilized this instability for the one-step assembly of patterned functional surfaces using superparamagnetic nanoparticles. In [85], similar buckling patterns are exploited to manipulate the optical properties of pHEMA-based periodic hydrogel membranes. In this case, the authors observed diamond-plate patterns during drying of the membrane below a critical temperature after immersing it in deionized water. Further experimental studies on periodic hydrogel films are documented in [76, 52], where microstructures with high-swelling and non-swelling regions developed out-of-plane buckling patterns. It can be shown that the observed patterns depend significantly on the morphological parameters of the microstructure.

Similar to the mentioned experimental studies, [62, 61] deal with the 2D numerical investigation of the effect of prestrain and imperfections on the instability of periodically perforated hydrogels under plane-strain conditions. Their simulations are performed on a larger domain of a periodic structure contained from 2×2 and 10×10 unit-cell representative volume elements. In line with experiments, they have found that the diamond-plate patterns are a dominant instability mode, which are obtained considering random imperfections of the voids without eigenvalue analysis. Following the theoretical and numerical modeling approaches of these works supplemented further with eigenvalue buckling analysis in Abaqus, in [59, 48] 3D pattern transformations on a gel film bonded to a soft substrate are investigated. The authors have studied sequential bifurcations on bifurcated paths considering that the first bifurcation is associated with a hexagonal dimple mode, which led to complex patterns such as herringbone and labyrinth and gave further insight into the nature of the formation of these patterns. We note that in these contributions, the chemical potential is assumed spatially constant within the hydrogel domain, so that transient effects (such as time-dependent diffusion) was not considered. Furthermore, the instability analyses are usually considered on larger domains, which can be reduced to unit-cell computations based on Bloch-Floquet representation theorem as discussed in this work.

All mentioned experimental and numerical studies highlight the wide-ranging opportunities to tune the response of periodic systems by exploiting instabilities and hence to obtain materials with enhanced functionalities that could be considered, for example, in the development of soft and smart devices.

6.1.4 Novel features and objectives of the present contribution

Motivated by the above mentioned works, we study numerically structural as well as material instabilities in periodic hydrogel systems. All considered numerical setups are based on corresponding experimental investigations and the prescription of experimentally motivated boundary conditions. In particular, we study instabilities of perforated composite hydrogel microstructures in two dimensions (cf. [82, 85, 77]) as well as in composite hy-

[30] The acronym PDMS stands for poly(dimethyl siloxane) [82].

drogel thin films in three spatial dimensions (cf. [76, 52]). Here, we do not only observe short-wavelength structural instabilities, which alter the periodicity of the microstructure, but also long-wavelength structural instabilities considering a transient diffusion process.

To model the transient diffusion process in hydrogels, we employ a rate-type variational minimization formulation following [56, 6], see also [64] for an embedding into a multiscale framework. For spatial discretization in two dimensions, we exploit Raviart–Thomas-type finite elements coupled with an implicit Euler scheme for time discretization. In three spatial dimensions, we discretize the domain with (non-conforming) hexahedral finite elements. Within both space-time discrete formulations, we implement Bloch–Floquet wave analysis to determine pattern-transforming instabilities together with the altered periodicity of the microstructure on a unit-cell based computations without considering any imperfections apriori. Furthermore, we derive a condition for the loss of strong ellipticity based on effective moduli of perforated microstructures. The latter is based on an extension of the surface-averaging approach of [55] to the coupled problem of transient chemo-mechanics.

Our studies reveal various experimentally confirmed as well as novel buckling patterns of periodic hydrogel systems depending on their morphology and associated material properties. For example, it will be shown that micro-coated hydrogel microstructures develop complex combinations of the well-known diamond-plate pattern coupled with intricate micro-wrinkling along internal surfaces. To our best knowledge, such pattern transformations have not been recorded yet and could serve for additional applications of periodic hydrogels. Furthermore, our numerical studies in three spatial dimensions indicate new opportunities for the design of complex instability-induced pattern transformations driven by the morphology of the underlying microstructure.

6.1.5 Outline

The present work is structured as follows. As a theoretical basis for the computational analysis of hydrogels, we discuss a variational formulation and its numerical implementation in Section 6.2. Based on that, we address fundamental aspects of structural and material stability analysis as well as the associated numerical implementation in Section 6.3. The developed framework will then be applied to the computational investigation of instabilities of two- and three-dimensional hydrogel microstructures as well as corresponding parametric studies in Section 6.4. Here, we also document a set of newly observed pattern transformations. We close with a discussion of the main contributions and findings in Section 6.5.

6.2 Variational formulation of deformation-diffusion processes

In this section, we discuss the continuum modeling and computational implementation of the coupled chemo-mechanical problem. Opposed to the saddle-point formulations documented in [83, 35, 10, 11, 7], we adopt a variational minimization formulation according to [56, 6]. Such a formulation has proven convenient for the investigation of instabilities [70]. In the underlying variational principle, the deformation map and the solvent-volume flux are chosen as the primary unknowns [56, 6]. The main ingredients of this formulation are an energy-storage functional, a dissipation-potential functional and an external-power

functional, where the latter arises due to applied traction and chemical-potential boundary conditions. For the latter, we propose additional boundary conditions in terms of the jumps of primary fields, which proves useful for the investigation of instabilities in periodic hydrogel structures.

6.2.1 Primary state variables and the second law of thermodynamics

We choose the deformation map $\boldsymbol{\varphi}$ and the solvent-volume flux $\mathbb{H}$ as the primary state variables of the considered minimization principle. If we denote by $\mathcal{B}_0$ and $\mathcal{B}_t$ the reference and the current configuration of the body, respectively, we can describe the mapping of these fields as

$$\boldsymbol{\varphi} : \begin{cases} \mathcal{B}_0 \times \mathcal{T} \to \mathcal{B}_t \subset \mathcal{R}^3 \\ (\boldsymbol{X}, t) \mapsto \boldsymbol{\varphi}(\boldsymbol{X}, t) \end{cases} \quad \text{and} \quad \mathbb{H} : \begin{cases} \mathcal{B}_0 \times \mathcal{T} \to \mathcal{R}^3 \\ (\boldsymbol{X}, t) \mapsto \mathbb{H}(\boldsymbol{X}, t) \end{cases} , \tag{6.1}$$

where the deformation map characterizes the deformed position $\boldsymbol{x} = \boldsymbol{\varphi}(\boldsymbol{X}, t)$ of a material point $\boldsymbol{X} \in \mathcal{B}_0$ at a given time $t \in \mathcal{T}$. The solvent-volume flux is a relative Lagrangian field characterizing local transport of the solvent volume relative to the motion of the polymer[31].

An additional state variable associated with the solvent-volume flux is given by the solvent-volume content $s : \mathcal{B}_0 \times \mathcal{T} \to \mathcal{R}^+$. For an arbitrary subdomain $\mathcal{P}_0 \subseteq \mathcal{B}_0$, the solvent-volume content is determined from the balance of solvent volume [24]

$$\frac{\mathrm{d}}{\mathrm{d}t} \int_{\mathcal{P}_0} s \, \mathrm{d}V = - \int_{\partial \mathcal{P}_0} \mathbb{H} \cdot \boldsymbol{N} \, \mathrm{d}A \quad \Rightarrow \quad \dot{s} = - \operatorname{Div} \mathbb{H} \quad \text{in } \mathcal{P}_0 \, . \tag{6.2}$$

Note that the flux field is defined in the Lagrangian configuration, so that no convective terms related to the spatial change of the solvent-volume content arise.

Based on the second law of thermodynamics, we can write the following inequality for the evolution of the stored-energy density of an arbitrary subdomain $\mathcal{P}_0 \subseteq \mathcal{B}_0$

$$\frac{\mathrm{d}}{\mathrm{d}t} \int_{\mathcal{P}_0} \psi \, \mathrm{d}V \leq \underbrace{\int_{\partial \mathcal{P}_0} \boldsymbol{T} \cdot \dot{\boldsymbol{\varphi}} \, \mathrm{d}A - \int_{\partial \mathcal{P}_0} \mu h \, \mathrm{d}A}_{P_{ext}(\dot{\boldsymbol{\varphi}}, \mathbb{H})} , \tag{6.3}$$

where we have introduced the traction vector $\boldsymbol{T}$ acting on the surface of the deformed subdomain, defined per unit undeformed area $\partial \mathcal{P}_0$, as well as the surface flux $h = \mathbb{H} \cdot \boldsymbol{N}$; μ is the chemical potential of the solvent and characterizes the supplied energy to the system as a result of the influx of solvent volume. We refer to [13] for an analogous interpretation in poromechanics. Localizing the above inequality and distinguishing local and diffusive parts of the dissipation, we obtain

$$\mathcal{D}_{loc} := \boldsymbol{P} : \dot{\boldsymbol{F}} + \mu \dot{s} - \dot{\psi} \geq 0 \quad \text{and} \quad \mathcal{D}_{dif} := \mathbb{H} \cdot \mathbb{M} \geq 0 \, , \tag{6.4}$$

where $\boldsymbol{F} := \operatorname{Grad} \varphi$ is the deformation gradient with $J := \det \boldsymbol{F} > 0$ and $\mathbb{M} := - \operatorname{Grad} \mu$ denotes the negative gradient of the chemical potential. Since we assume diffusion to take place in an otherwise elastic solid, the local part of the dissipation must vanish, i.e.,

[31] We refer to [13] for a micromechanically motivated description of poromechanics.

$\mathcal{D}_{loc} = 0$. Thus, $(6.4)_1$ can be exploited to obtain the constitutive relations for the first Piola-Kirchhoff stress tensor $\boldsymbol{P} = \partial_{\boldsymbol{F}}\hat{\psi}(\boldsymbol{F}, s)$ and for the chemical potential $\mu = \partial_s\hat{\psi}(\boldsymbol{F}, s)$. The inequality $(6.4)_2$ characterizes the dissipation due to the diffusion process, where $\mathbb{M}$ is the driving force for the solvent-volume transport. The latter can be determined from a dissipation-potential density $\hat{\phi}(\mathbb{H}; \boldsymbol{F}, s)$ for a given constitutive state, i.e., $\mathbb{M} = \partial_{\mathbb{H}}\hat{\phi}$.

6.2.2 Constitutive functions: The free-energy and the dissipation-potential density

As we have seen above, the stress tensor, the chemical potential and the negative gradient of the chemical potential are local constitutive fields. They are determined from a free-energy density $\hat{\psi}(\boldsymbol{F}, s)$ and a dissipation-potential density $\hat{\phi}(\mathbb{H}; \boldsymbol{F}, s)$.

In what follows, we consider an additive free-energy function of the form [36, 33, 6, 10]

$$\hat{\psi}(\boldsymbol{F}, s) = \hat{\psi}_{mech}(\boldsymbol{F}) + \hat{\psi}_{chem}(s) + \hat{\psi}(J, s)\,. \tag{6.5}$$

While the mechanical contribution of the free-energy function is assumed to be of Neo-Hookean-type, the chemical contribution is specified as a Flory–Rehner-type function [22]. These contributions together with a coupling term yield the overall free-energy function

$$\hat{\psi}(\boldsymbol{F}, s) = \frac{\gamma}{2}\big[\boldsymbol{F} : \boldsymbol{F} - 3 - 2\ln(\det \boldsymbol{F})\big] + \alpha\big[s\ln\big(\frac{s}{1+s}\big) + \frac{\chi s}{1+s}\big] + \frac{\eta}{2}\big(\det \boldsymbol{F} - 1 - s\big)^2\,, \tag{6.6}$$

where γ is the shear modulus and $\alpha := kT/\nu$ is a mixing modulus with Boltzmann constant k, absolute temperature T and volume of a solvent molecule ν; χ is the Flory–Huggins interaction parameter; η is a penalty parameter to constrain $\det \boldsymbol{F} = 1 + s$ for incompressible hydrogels. We refer to Table 6.7 for further information on the given parameters.

The dissipation-potential function is chosen such that $(6.4)_2$ is satisfied a priori. Therefore, $\hat{\phi}(\mathbb{H}; \boldsymbol{F}, s)$ is assumed to be a convex and normalized function of the solvent-volume flux $\mathbb{H}$ according to $\hat{\phi}(\boldsymbol{0}) = 0$ and $\partial_{\mathbb{H}}\hat{\phi}(\boldsymbol{0}) = \boldsymbol{0}$ at the reference configuration. In the present work, we will consider a dissipation function related to Fickian diffusion given by

$$\hat{\phi}(\mathbb{H}; \boldsymbol{C}, s) = \frac{1}{2Ms}\boldsymbol{C} : (\mathbb{H} \otimes \mathbb{H})\,, \tag{6.7}$$

where M is referred to as a mobility parameter and $\boldsymbol{C} = \boldsymbol{F}^T\boldsymbol{F}$ is the right Cauchy-Green deformation tensor. The dissipation-potential function is formulated in terms of given values $\{\boldsymbol{F}, s\}$ and therefore evaluated numerically at the previous time step $(\cdot)_n$ within an incremental variational formulation [56, 6], see Section 6.2.4 for details.

The above introduced constitutive functions are given with respect to a dry reference configuration. Since (6.6) is singular for the dry state $s(t = 0) = 0$, a pre-swollen state is usually considered as the reference configuration [36, 33, 6]. According to that, the constitutive functions (6.6) and (6.7) defined per unit volume of the pre-swollen reference configuration and appear as

$$\hat{\psi} = \frac{\gamma}{2J_0}[J_0^{2/3}\boldsymbol{F} : \boldsymbol{F} - 3 - 2\ln(JJ_0)] + \frac{\alpha}{J_0}[s\ln(\frac{s}{1+s}) + \frac{\chi s}{1+s}] + \frac{\eta}{2J_0}(JJ_0 - 1 - s)^2 \tag{6.8}$$

and

$$\hat{\phi} = \frac{1}{2J_0^{1/3} M s_n} \boldsymbol{C}_n : (\mathbb{H} \otimes \mathbb{H}) \,, \tag{6.9}$$

where the pre-swollen state is characterized by a Jacobian J_0. The initial condition for the solvent-volume content associated with the pre-swollen reference configuration reads

$$s(t=0) = s_0 = \frac{\gamma}{\eta}\big(J_0^{-1/3} - \frac{1}{J_0}\big) + J_0 - 1 \,. \tag{6.10}$$

The chemical potential at the pre-swollen reference configuration is determined as [6]

$$\mu_0 = -\frac{\eta}{J_0}(J_0 - 1 - s_0) + \frac{\alpha}{J_0}\big[\ln\big(\frac{s_0}{1+s_0}\big) + \frac{1}{1+s_0} + \frac{\chi}{(1+s_0)^2}\big] \,. \tag{6.11}$$

The latter relation is particularly required when applying chemical-potential boundary conditions in the minimization formulation, see Section 6.4.

6.2.3 Boundary conditions for periodic hydrogel structures

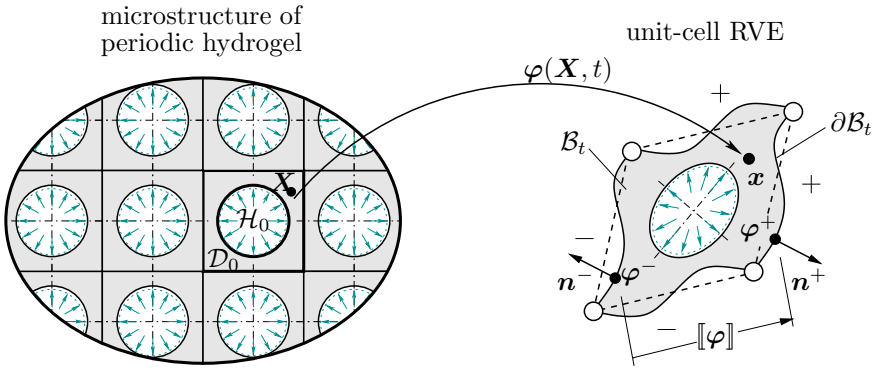

Figure 6.2: *Boundary conditions for a two-dimensional periodic hydrogel microstructure.* The response of periodic materials can be determined by means of unit-cell representative volume elements (unit-cell RVEs) of their microstructure. In the present approach, the unit-cell problem is solved in consideration of the jump conditions for the deformation map $[\![\boldsymbol{\varphi}]\!] = \overline{\boldsymbol{F}}\boldsymbol{X}$ and the solvent-volume flux $[\![\mathcal{H}]\!] \cdot \boldsymbol{N} = 0$ across the external boundary according to (6.12). As can be seen in the figure, the solvent is assumed to enter the RVE through the boundary of the voids. In our computations, this is realized by applying the chemical potential at the void's boundary according to (6.47).

Since our main aim is to investigate instabilities in periodic hydrogels, we will now provide a suitable setup for associated boundary conditions. As we will see, these are partly inspired from homogenization theory such that they allow for the definition of effective quantities, which could be used in the material stability analysis to be discussed later.

For illustration, let us consider the two-dimensional representation of a periodic hydrogel as depicted in Fig. 6.2. Here we assume that any out-of-plane deformation could be neglected and therefore typical plane-strain conditions apply. Since the structure is periodic, any stability analysis could be reduced to the smallest periodic domain, here

given in terms of a square-shaped matrix with a circular void such that $\mathcal{B}_0 = \mathcal{D}_0 \cup \mathcal{H}_0$ with $\mathcal{H}_0$ denoting the domain of the void. In the following, we will refer to such a smallest possible periodic domain as a *unit-cell representative volume element* (unit-cell RVE).

For the chemo-mechanical loading of the unit-cell RVE we prescribe boundary conditions of the generalized form

$$[\![\boldsymbol{\varphi}]\!] = \overline{\boldsymbol{F}}\boldsymbol{X} \quad \text{and} \quad [\![\mathbb{H}]\!] \cdot \boldsymbol{N} = 0 \quad \text{on} \quad \partial\mathcal{B}_0\,, \tag{6.12}$$

where we have introduced an *effective* or *macroscopic* deformation gradient $\overline{\boldsymbol{F}}$ [57, 64]. The dual variable to the effective deformation gradient is the effective first Piola-Kirchhoff stress tensor $\overline{\boldsymbol{P}}$. Both quantities can be determined as the volume averages of their microscopic counterparts as[32]

$$\overline{\boldsymbol{F}} = \frac{1}{|\mathcal{B}_0|}\int_{\partial\mathcal{B}_0} \boldsymbol{\varphi} \otimes \boldsymbol{N}\,\mathrm{d}A \quad \text{and} \quad \overline{\boldsymbol{P}} = \frac{1}{|\mathcal{B}_0|}\int_{\partial\mathcal{B}_0} (\boldsymbol{P}\boldsymbol{N}) \otimes \boldsymbol{X}\,\mathrm{d}A\,, \tag{6.13}$$

where $|\mathcal{B}_0|$ denotes the volume of a unit-cell RVE. Note that according to $(6.12)_2$, we have defined vanishing jump conditions for the solvent-volume flux such that no effective flux is applied on the RVE. This setting is motivated by the assumption that the diffusion process is driven exclusively by suitable chemical-potential boundary conditions acting at the *internal* boundary of unit-cell RVEs. Please refer to Section 6.4 for more details.

6.2.4 Rate-type variational formulation of the deformation-diffusion problem

Above, we have introduced the energy-storage function $\hat{\psi}(\boldsymbol{F}, s)$, the dissipation-potential function $\hat{\phi}(\mathbb{H})$ and the external-loading functional $P_{ext}(\dot{\boldsymbol{\varphi}}, \mathbb{H})$. Having these functions at hand, we define a rate-type potential to characterize the deformation-diffusion response [56]

$$\Pi(\dot{\boldsymbol{\varphi}}, \mathbb{H}) := \int_{\mathcal{B}_0} \pi(\dot{\boldsymbol{\varphi}}, \mathbb{H})\,\mathrm{d}V - P_{ext}(\dot{\boldsymbol{\varphi}}, \mathbb{H}) \quad \text{with} \quad \pi(\dot{\boldsymbol{\varphi}}, \mathbb{H}) := \frac{\mathrm{d}}{\mathrm{d}t}\hat{\psi}(\boldsymbol{F}, s) + \hat{\phi}(\mathbb{H}; \boldsymbol{F}, s)\,, \tag{6.14}$$

where $\pi(\dot{\boldsymbol{\varphi}}, \mathbb{H})$ is the internal-power density. As a result, the variational principle for the considered problem in the continuous setting can be introduced as

$$\{\dot{\boldsymbol{\varphi}}^\star, \mathbb{H}^\star\} = \mathrm{Arg}\left\{\inf_{\dot{\boldsymbol{\varphi}} \in \mathcal{W}_{\dot{\boldsymbol{\varphi}}}} \inf_{\mathbb{H} \in \mathcal{W}_{\mathbb{H}}} \Pi(\dot{\boldsymbol{\varphi}}, \mathbb{H})\right\}, \tag{6.15}$$

where $\mathcal{W}_{\dot{\boldsymbol{\varphi}}}$ and $\mathcal{W}_{\mathbb{H}}$ are the admissible spaces for the rate of the deformation map and the solvent-volume flux

$$\begin{aligned} \mathcal{W}_{\dot{\boldsymbol{\varphi}}} &:= \{\dot{\boldsymbol{\varphi}} \in H^1(\mathcal{B}_0) \,\big|\, \dot{\boldsymbol{\varphi}} = \dot{\boldsymbol{\varphi}}_D \text{ on } \partial\mathcal{B}_0^{\boldsymbol{\varphi}}\} \quad \text{and} \\ \mathcal{W}_{\mathbb{H}} &:= \{\mathbb{H} \in H(\mathrm{Div}, \mathcal{B}_0) \,\big|\, \mathbb{H} = \mathbb{H}_D \text{ on } \partial\mathcal{B}_0^{h}\}\,. \end{aligned} \tag{6.16}$$

[32] We note that when we prescribe the effective deformation $\overline{\boldsymbol{F}}$ via the RVE boundary, the effective stresses can be determined via $(6.13)_2$. Vice versa, it is also possible to apply effective stresses $\overline{\boldsymbol{P}}$ on the RVE. In that case, the effective deformation gradient can be determined via $(6.13)_1$, see [55, 58].

The Euler-Lagrange equations follow as the necessary conditions of the variational formulation as

$$\boxed{\begin{aligned}
&\text{Balance of linear momentum:} && \operatorname{Div}[\partial_{\boldsymbol{F}}\hat{\psi}] &&= \boldsymbol{0} && \text{in} && \mathcal{B}_0 \\
&\text{Inverse Fickian law:} && \nabla[\partial_s\hat{\psi}] + \partial_{\mathbb{H}}\hat{\phi} &&= \boldsymbol{0} && \text{in} && \mathcal{B}_0 \\
&\text{Mechanical traction:} && \partial_{\boldsymbol{F}}\hat{\psi}\cdot\boldsymbol{N} - \boldsymbol{T} &&= \boldsymbol{0} && \text{on} && \partial\mathcal{B}_0^T \\
&\text{Chemical potential:} && -\partial_s\hat{\psi} + \mu &&= 0 && \text{on} && \partial\mathcal{B}_0^\mu
\end{aligned}} \tag{6.17}$$

6.2.5 Space-time discretization of the variational formulation

We solve (6.15) using a conforming finite-element formulation. Before considering the discretization in space, we apply a modified version of the implicit Euler scheme in a time interval $\tau := t - t_n$ with t being the current time step with $0 < t \leq T$ in a considered overall simulation time T. Note that for the variables evaluated at the current time step, we do not use subscripts. Consequently, the time-discrete version of (6.14) reads[33] [56]

$$\Pi^\tau(\boldsymbol{\varphi}, \mathbb{H}) := \int_{\mathcal{B}_0} \hat{\psi}(\boldsymbol{F}, s) + \tau\hat{\phi}(\mathbb{H}; \boldsymbol{F}_n, s_n)\,\mathrm{d}V - P^\tau_{ext}(\boldsymbol{\varphi}, \mathbb{H})\,, \tag{6.18}$$

where the solvent-volume content at the current time step is determined by $s = s_n - \tau\operatorname{Div}[\mathbb{H}]$. The dissipation-potential function $\hat{\phi}(\mathbb{H}; \boldsymbol{F}_n, s_n)$ is evaluated using the deformation gradient and the solvent-volume content from the previous time step t_n in order to stay consistent with the continuous variational setting [56, 6]. For the explicit form of $\hat{\phi}$ we refer to (6.9). The time-discrete external-power functional reads

$$P^\tau_{ext}(\boldsymbol{\varphi}, \mathbb{H}) = \int_{\partial\mathcal{B}_0} \boldsymbol{T}\cdot\boldsymbol{\varphi}\,\mathrm{d}A - \int_{\partial\mathcal{B}_0} \tau\mu h\,\mathrm{d}A\,. \tag{6.19}$$

As a result, we obtain the time-discrete variational formulation with an initial condition for the solvent-volume content as

$$\{\boldsymbol{\varphi}^\star, \mathbb{H}^\star\} = \operatorname{Arg}\{\inf_{\boldsymbol{\varphi}\in\mathcal{W}_{\boldsymbol{\varphi}}} \inf_{\mathbb{H}\in\mathcal{W}_{\mathbb{H}}} \Pi^\tau(\boldsymbol{\varphi}, \mathbb{H})\} \quad \text{with} \quad s(t_0) = s_0\,, \tag{6.20}$$

where Π^τ refers to the time-discretized potential functional. The above formulation is implemented into a conforming finite-element formulation by using a combination of Lagrange- and Raviart–Thomas-type shape functions [6, 64]. This then results in a minimization principle in the space-time discrete form as

$$\underline{\mathbf{d}}^\star = \operatorname{Arg}\{\min_{\underline{\mathbf{d}}} \Pi^{\tau h}(\underline{\mathbf{d}})\}\,, \tag{6.21}$$

where $\Pi^{\tau h}$ denotes the space-time discrete potential functional and $\underline{\mathbf{d}}$ contains all degrees of freedom comprising the node-based displacements and the edge-based normal-projected solvent-volume fluxes.

[33] We remark that the variational formulation (6.18) should also contain the energy-storage function as well as the external-power functional evaluated at the previous time step. However, since these terms are constant they vanish under variation and are therefore omitted from the equations to arrive at a compact representation.

6.3 Stability analysis of periodic hydrogel systems

In this section, we describe methods to investigate the structural and the material stability of periodic hydrogel systems. For the structural stability analysis, we utilize the minimization structure of the underlying incremental system of equations [29, 30, 57]. In doing so, we investigate in particular *short-wavelength* and *long-wavelength* instabilities. The former are usually associated with a change in periodicity of an underlying microstructure, which could arise, for example, due to wrinkling of internal surfaces in perforated systems. We will detect these types of instabilities via Bloch–Floquet analysis. Long-wavelength instabilities are related to the loss of strong ellipticity of a corresponding homogenized continuum. These kinds of instabilities can be detected by checking the positive definiteness of an underlying acoustic tensor. In what follows, we will also present a corresponding numerical method for the analysis of related instabilities.

6.3.1 Minimization-based structural stability analysis

Within a minimization-based approach, hydrogel systems are considered to be structurally stable at an equilibrium state $\underline{\mathbf{d}}^\star$, if all variations of the incremental potential from this equilibrium state under infinitesimally small perturbations are positive, that is [57]

$$\Delta\Pi^{\tau h}(\underline{\mathbf{d}}^\star, \delta\underline{\mathbf{d}}) := \Pi^{\tau h}(\underline{\mathbf{d}}^\star + \epsilon\delta\underline{\mathbf{d}}) - \Pi^{\tau h}(\underline{\mathbf{d}}^\star) > 0\,, \tag{6.22}$$

where ϵ is a small parameter. Considering a Taylor approximation of (6.22) and truncating higher-order terms, we obtain

$$\Delta\Pi^{\tau h}(\underline{\mathbf{d}}^\star, \delta\underline{\mathbf{d}}) \approx \frac{\mathrm{d}}{\mathrm{d}\epsilon}\bigg|_{\epsilon=0} \Pi^{\tau h}(\underline{\mathbf{d}}^\star + \epsilon\delta\underline{\mathbf{d}}) + \frac{1}{2}\frac{\mathrm{d}^2}{\mathrm{d}\epsilon^2}\bigg|_{\epsilon=0} \Pi^{\tau h}(\underline{\mathbf{d}}^\star + \epsilon\delta\underline{\mathbf{d}}) > 0\,. \tag{6.23}$$

Since the first variation vanishes at equilibrium, we arrive at

$$\Delta\Pi^{\tau h}(\underline{\mathbf{d}}^\star, \delta\underline{\mathbf{d}}) \approx \frac{1}{2}\frac{\mathrm{d}^2}{\mathrm{d}\epsilon^2}\bigg|_{\epsilon=0} \Pi^{\tau h}(\underline{\mathbf{d}}^\star + \epsilon\delta\underline{\mathbf{d}}) > 0\,. \tag{6.24}$$

Consequently, structural stability is associated with the second variation of the incremental potential in the sense that

$$\Delta\Pi^{\tau h}(\underline{\mathbf{d}}^\star, \delta\underline{\mathbf{d}}) = \frac{1}{2}\delta\underline{\mathbf{d}}^T\left[\Pi^\tau(\underline{\mathbf{d}})_{,\underline{\mathbf{dd}}}\right]_{\underline{\mathbf{d}}^\star}\delta\underline{\mathbf{d}} = \Lambda\delta\underline{\mathbf{d}}^T\delta\underline{\mathbf{d}} > 0\,. \tag{6.25}$$

The latter results in an eigenvalue problem in terms of the tangent of the underlying system of equations according to

$$\Lambda = \min_{\boldsymbol{n}\in\mathbb{N}^3}\min_{\underline{\mathbf{d}}}\left\{\Delta\Pi^{\tau h}(\underline{\mathbf{d}}, \delta\underline{\mathbf{d}})/\|\delta\underline{\mathbf{d}}\|^2\right\}\begin{cases} > 0 & \text{for stable state } \underline{\mathbf{d}}^\star \\ \leq 0 & \text{for unstable state } \underline{\mathbf{d}}^\star \end{cases}, \tag{6.26}$$

where $\boldsymbol{n} \in \mathbb{N}^3$ denotes the number of unit-cells in RVEs with respect to three spatial directions [60]. The minimization over $\boldsymbol{n}$ allows for the detection of instabilities that would not be describable by means of a unit-cell RVE. However, the above approach is computationally inefficient since it requires the consideration of various realizations of RVEs that grow in size with growing $\boldsymbol{n}$. Therefore, we use Bloch–Floquet analysis to detect such critical structural instabilities on a unit-cell RVE [23].

Based on Bloch–Floquet analysis, the variations $\delta\underline{\mathbf{d}}$ of the degrees of freedom can be represented in terms of unit-cell variations $\delta\underline{\mathbf{d}}_{\mathcal{B}_0}$ as

$$\delta\underline{\mathbf{d}}(\boldsymbol{X}) = \delta\underline{\mathbf{d}}_{\mathcal{B}_0}(\boldsymbol{X}) \exp[\mathrm{i}\boldsymbol{k}\cdot\boldsymbol{X}] \quad \text{with} \quad \delta\underline{\mathbf{d}}^{+}_{\mathcal{B}_0} = \delta\underline{\mathbf{d}}^{-}_{\mathcal{B}_0} \quad \text{on} \quad \partial\mathcal{B}_0 = \partial\mathcal{B}_0^{+} \cup \partial\mathcal{B}_0^{-}\,, \tag{6.27}$$

where $\boldsymbol{k}$ is referred to as Bloch vector, which characterizes the wavelength of the variations. Consequently, this expression leads to the boundary conditions

$$\delta\underline{\mathbf{d}}(\boldsymbol{X}^{+}) = \delta\underline{\mathbf{d}}(\boldsymbol{X}^{-}) \exp[\mathrm{i}\boldsymbol{k}\cdot(\boldsymbol{X}^{+} - \boldsymbol{X}^{-})] \tag{6.28}$$

for a unit-cell RVE. Here, $\boldsymbol{X}^{+}$ and $\boldsymbol{X}^{-}$ denote the reference placement of periodic nodes, which are located at opposite boundaries of the unit-cell RVE, see Fig. 6.2. It follows a stability criterion related to the tangent of a unit-cell RVE according to[34]

$$\boxed{\Lambda = \min_{k_i\in[0,\pi]} \min_{\underline{\mathbf{d}}} \left\{\Delta\Pi^{\tau h}(\underline{\mathbf{d}}, \delta\underline{\mathbf{d}})/\|\delta\underline{\mathbf{d}}\|^2\right\} \begin{cases} > 0 & \text{for stable state } \underline{\mathbf{d}}^{\star} \\ \leq 0 & \text{for unstable state } \underline{\mathbf{d}}^{\star} \end{cases}}\,. \tag{6.29}$$

Depending on the values of the Bloch vector components $k_i \in \mathcal{R}^3$, we distinguish three types of instabilities: (i) unit-cell periodic instabilities for $k_i = 0$; (ii) short-wavelength instabilities for finite values of k_i usually spanning RVEs made of multiple unit cells, where the explicit number of cells can be computed as $n_i = 2\pi/k_i$; (iii) long-wavelength instabilities for $\boldsymbol{k} \to \boldsymbol{0}$. We note that the latter could also be determined from the effective mechanical moduli of periodic hydrogels, see below.

6.3.2 Loss of strong ellipticity: Material stability analysis at macroscale

Having defined macroscopic mechanical boundary conditions in terms of $\overline{\boldsymbol{F}}$, we assume that at macroscale we need to fulfill the balance equation [64]

$$\overline{\mathrm{Div}}[\overline{\boldsymbol{P}}(\overline{\boldsymbol{F}}, \overline{\mathrm{Div}}[\overline{\mathbb{H}}])] = \overline{\rho}_0 \ddot{\overline{\boldsymbol{\varphi}}}\,. \tag{6.30}$$

In order to check if the latter equation satisfies the strong-ellipticity condition, we superimpose a plane wave of the form $\delta\overline{\boldsymbol{\varphi}} = \overline{\boldsymbol{n}} f(\overline{\boldsymbol{X}}\cdot\overline{\boldsymbol{N}} - \overline{c}t)$, such that for infinitesimal $\delta\overline{\boldsymbol{\varphi}}$ it holds that [30, 57]

$$\overline{\mathrm{Div}}[\delta\overline{\boldsymbol{P}}] = \overline{\mathrm{Div}}[\overline{\mathbb{A}} : \delta\overline{\boldsymbol{F}}] = \overline{\rho}_0 \delta\ddot{\overline{\boldsymbol{\varphi}}} \quad \text{with} \quad \delta\overline{\boldsymbol{F}} = \overline{\mathrm{Grad}}\delta\overline{\boldsymbol{\varphi}}\,, \tag{6.31}$$

where $\overline{\mathbb{A}}$ are the effective mechanical moduli of the microstructure. Note that since we do not consider any macroscopic loading in terms of $\overline{\mathrm{Div}}[\overline{\mathbb{H}}]$, we do not have to take into account a corresponding variation in the above equation. After some modifications, (6.31) appears as

$$\overline{\boldsymbol{n}}\cdot\overline{\boldsymbol{Q}}\cdot\overline{\boldsymbol{n}} = \overline{\rho}_0\overline{c}^2\,, \tag{6.32}$$

where $\overline{Q}_{ab} = (\overline{\mathbb{A}})_a{}^A{}_b{}^B \overline{N}_A \overline{N}_B$ is the mechanical acoustic tensor defined in terms of the effective mechanical moduli. It follows the criterion for the material stability at the macroscopic scale

$$\boxed{\overline{\Lambda} = \min_{\|\overline{\boldsymbol{N}}\|=1} \left\{\overline{\boldsymbol{n}}\cdot\overline{\boldsymbol{Q}}\cdot\overline{\boldsymbol{n}}\right\} \begin{cases} > 0 & \text{for materially stable state} \\ \leq 0 & \text{for materially unstable state} \end{cases}}\,. \tag{6.33}$$

[34] For details related to the numerical implementation we refer to [74, 2, 66, 65].

6.3.3 Computation of the effective mechanical moduli of voided hydrogel structures

We now describe the computation of the effective mechanical moduli of voided hydrogel structures following the approach proposed by Miehe and Koch [55]. This approach allows to determine effective moduli based on surface integrals along the external boundary of RVEs. Starting point is the definition of the effective mechanical stresses $(6.13)_2$ and the effective chemical potential [64]

$$\overline{\boldsymbol{P}} = \frac{1}{|\mathcal{B}_0|}\int_{\partial\mathcal{B}_0} (\boldsymbol{P}\boldsymbol{N}) \otimes \boldsymbol{X}\, \mathrm{d}A \quad \text{and} \quad \overline{\mu} = \frac{1}{3|\mathcal{B}_0|}\int_{\partial\mathcal{B}_0} (\mu\boldsymbol{N}) \cdot \boldsymbol{X}\, \mathrm{d}A\,, \tag{6.34}$$

where $\partial\mathcal{B}_0$ denotes the external boundary of an RVE. In the discrete setting, the above equations can be given as follows (see [55] for the purely mechanical case)

$$\overline{\boldsymbol{P}} = \frac{1}{|\mathcal{B}_0|}\sum_{I=1}^{P} \boldsymbol{\lambda}_I^f \otimes [\![\boldsymbol{X}_I^b]\!] \quad \text{and} \quad \overline{\mu} = \frac{1}{3|\mathcal{B}_0|}\sum_{I=1}^{P} \lambda_I^\mu \boldsymbol{N} \cdot [\![\boldsymbol{X}_I^b]\!]\,, \tag{6.35}$$

where $\boldsymbol{\lambda}_I^f$, λ_I^μ and $\boldsymbol{X}_I^b$ denote the nodal forces, the chemical potential and the coordinates associated with the node I on the external boundary of an RVE, respectively. The number $P = M/2$ is defined from the total number of boundary nodes M. Introducing an array of nodal forces and chemical potentials $\boldsymbol{\lambda} := [\boldsymbol{\lambda}_1^f, \lambda_1^\mu, ..., \boldsymbol{\lambda}_P^f, \lambda_P^\mu]^T$ as well as an array containing the effective stresses (in vector notation) and the effective chemical potential $\overline{\mathbf{P}} := [\overline{\boldsymbol{P}}, \overline{\mu}]^T$, we can write (6.35) in a compact form[35]

$$\overline{\mathbf{P}} = \frac{1}{|\mathcal{B}_0|}\sum_{I=1}^{P} \mathbb{Q}_I \boldsymbol{\lambda}_I = \frac{1}{|\mathcal{B}_0|}\mathbb{Q}\boldsymbol{\lambda}\,, \tag{6.36}$$

where $\mathbb{Q} := [\mathbb{Q}_1, ..., \mathbb{Q}_P]$ is the array of projection tensors with

$$\mathbb{Q}_I^T := \begin{bmatrix} [\![(\boldsymbol{X}_I^b)_1]\!] & 0 & [\![(\boldsymbol{X}_I^b)_2]\!] & 0 & 0 \\ 0 & [\![(\boldsymbol{X}_I^b)_2]\!] & 0 & [\![(\boldsymbol{X}_I^b)_1]\!] & 0 \\ 0 & 0 & 0 & 0 & \frac{1}{3}[\![\boldsymbol{X}_I^b]\!] \cdot \boldsymbol{N} \end{bmatrix} \tag{6.37}$$

in two dimensions.

In the following, we are only interested in the effective mechanical moduli. Since these relate the incremental effective stresses to the incremental effective deformation gradient according to $\Delta\overline{\boldsymbol{P}} = \overline{\mathbb{A}} : \Delta\overline{\boldsymbol{F}}$, we first determine the increment of the first Piola-Kirchhoff stress tensor in vector notation from (6.36) as

$$\Delta\overline{\boldsymbol{P}} = \mathbb{L}\Delta\overline{\mathbf{P}} = \frac{1}{|\mathcal{B}_0|}\mathbb{L}\mathbb{Q}\Delta\boldsymbol{\lambda}\,, \tag{6.38}$$

where $\mathbb{L}$ is a projection tensor with entries 0 or 1.

In order to obtain the final expression for the effective-moduli tensor, we need to have a relation between the increment of the generalized nodal forces $\Delta\boldsymbol{\lambda}$ and the effective

[35] $\overline{\mathbf{P}} := [\overline{P}_{11}, \overline{P}_{22}, \overline{P}_{12}, \overline{P}_{21}, \overline{\mu}]^T$ is considered for the corresponding array in two dimensions.

deformation gradient $\overline{\boldsymbol{F}}$. We obtain such a relationship from the following variational principle in the space-time discrete setting

$$\widetilde{\Pi}^{\tau h}(\underline{\mathbf{d}}, \boldsymbol{\lambda}) = \Pi^{\tau h}(\underline{\mathbf{d}}) + \boldsymbol{\lambda} \cdot (\llbracket \underline{\mathbf{d}}^b \rrbracket - \mathbb{Q}^T \overline{\mathbf{F}}) \,, \tag{6.39}$$

where $\overline{\mathbf{F}} := [\overline{\boldsymbol{F}}, \overline{\mathrm{Div}}\overline{H}]^T$ is an array given by $\overline{\mathbf{F}} = [\overline{F}_{11}, \overline{F}_{22}, \overline{F}_{12}, \overline{F}_{21}, \overline{\mathrm{Div}}\overline{H}]^T$ in two dimensions.

The second term on the right-hand side of (6.39) considers the Lagrange multiplier method to enforce the jump boundary conditions for the deformation map and the fluid-volume flux vector of the form

$$\llbracket \boldsymbol{\varphi} \rrbracket = \overline{\boldsymbol{F}} \, \llbracket \boldsymbol{X} \rrbracket \quad \text{and} \quad \llbracket \mathbb{H} \rrbracket \cdot \boldsymbol{N} = \frac{1}{3} \overline{\mathrm{Div}} \overline{H} \, \llbracket \boldsymbol{X} \rrbracket \cdot \boldsymbol{N} \,, \tag{6.40}$$

refer to (6.12) as well as to [64] for more details. Furthermore, $\boldsymbol{X}^b := [\boldsymbol{X}^b_1, ..., \boldsymbol{X}^b_P]^T$ in (6.39) contains the coordinates of the nodes at the external boundary of an RVE. The Lagrange multiplier $\boldsymbol{\lambda}$ can be identified as the array of nodal forces and chemical potentials. Its interpretation follows from the Euler-Lagrange equations of the variational principle. Furthermore, $\underline{\mathbf{d}}^b := [\underline{\mathbf{d}}^b_1, .., \underline{\mathbf{d}}^b_P]^T$ denotes the degrees of freedom at the boundary of the unit-cell RVE. In (6.39), we can express the jump of the degrees of freedom in terms of the latter as

$$\llbracket \underline{\mathbf{d}}^b \rrbracket := \bigwedge_{I=1}^{P} \begin{bmatrix} (\underline{\mathbf{d}}^b_{\boldsymbol{\varphi}})^+_I - (\underline{\mathbf{d}}^b_{\boldsymbol{\varphi}})^-_I \\ (\mathsf{d}^b_h)^+_I + (\mathsf{d}^b_h)^-_I \end{bmatrix} = \mathbb{P} \underline{\mathbf{d}}^b \,, \tag{6.41}$$

where $\mathbb{P}$ is a projection tensor with entries $\{-1, 0, 1\}$. Note that, since we are considering Raviart–Thomas-type elements, the edge-based solvent-volume flux degrees of freedom are anti-periodic at the external boundary [64].

The microscopic problem is usually solved under constant macroscopic deformation gradient for each time step. Therefore, the first variation of (6.39) gives

$$\delta\widetilde{\Pi}^{\tau h} = \begin{bmatrix} \delta\underline{\mathbf{d}}^i \\ \delta\underline{\mathbf{d}}^b \\ \delta\boldsymbol{\lambda} \end{bmatrix} \cdot \begin{bmatrix} \partial_{\underline{\mathbf{d}}^i} \Pi^{\tau h} \\ \partial_{\underline{\mathbf{d}}^b} \Pi^{\tau h} + \mathbb{P}\boldsymbol{\lambda} \\ \mathbb{P}\underline{\mathbf{d}}^b - \mathbb{Q}^T \overline{\mathbf{F}} \end{bmatrix} = \begin{bmatrix} \delta\underline{\mathbf{d}}^i \\ \delta\underline{\mathbf{d}}^b \\ \delta\boldsymbol{\lambda} \end{bmatrix} \cdot \begin{bmatrix} \underline{\mathbf{R}}^i \\ \underline{\mathbf{R}}^b + \mathbb{P}\boldsymbol{\lambda} \\ \mathbb{P}\underline{\mathbf{d}}^b - \mathbb{Q}^T \overline{\mathbf{F}} \end{bmatrix} = \boldsymbol{0} \,, \tag{6.42}$$

where $\underline{\mathbf{d}}^i$ denote the interior degrees of freedom of a unit-cell RVE. Once the above system of equations is solved at the microscale, the sensitivity of the system with respect to the macroscopic deformation gradient can be determined from

$$\Delta\delta\widetilde{\Pi}^{\tau h} = \begin{bmatrix} \delta\underline{\mathbf{d}}^i \\ \delta\underline{\mathbf{d}}^b \\ \delta\boldsymbol{\lambda} \end{bmatrix} \cdot \begin{bmatrix} \underline{\mathbf{K}}^{ii} & \underline{\mathbf{K}}^{ib} & \boldsymbol{0} & \boldsymbol{0} \\ \underline{\mathbf{K}}^{bi} & \underline{\mathbf{K}}^{bb} & \mathbb{P}^T & \boldsymbol{0} \\ \boldsymbol{0} & \mathbb{P} & \boldsymbol{0} & -\mathbb{Q}^T \end{bmatrix} \cdot \begin{bmatrix} \Delta\underline{\mathbf{d}}^i \\ \Delta\underline{\mathbf{d}}^b \\ \Delta\boldsymbol{\lambda} \\ \Delta\overline{\mathbf{F}} \end{bmatrix} = \boldsymbol{0} \,. \tag{6.43}$$

First, from the variations with respect to $\delta\underline{\mathbf{d}}^i$ and $\delta\underline{\mathbf{d}}^b$ in $(6.43)_1$ and $(6.43)_2$, we obtain elimination equations for $\Delta\underline{\mathbf{d}}^i$ and $\Delta\underline{\mathbf{d}}^b$ as

$$\Delta\underline{\mathbf{d}}^i = -(\underline{\mathbf{K}}^{ii})^{-1} \underline{\mathbf{K}}^{ib} \Delta\underline{\mathbf{d}}^b \quad \text{and} \quad \Delta\underline{\mathbf{d}}^b = -(\widetilde{\underline{\mathbf{K}}}^{bb})^{-1} \mathbb{P}^T \Delta\boldsymbol{\lambda} \,, \tag{6.44}$$

where $\widetilde{\underline{\mathbf{K}}}^{bb} = \underline{\mathbf{K}}^{bb} - \underline{\mathbf{K}}^{bi}(\underline{\mathbf{K}}^{ii})^{-1}\underline{\mathbf{K}}^{ib}$. Next, we consider the variation with respect to $\delta\boldsymbol{\lambda}$ in (6.43) and obtain the searched expression of $\Delta\boldsymbol{\lambda}$ given by

$$\Delta\boldsymbol{\lambda} = \left[\mathbb{P}(\widetilde{\underline{\mathbf{K}}}^{bb})^{-1}\mathbb{P}^T\right]^{-1}\mathbb{Q}^T\Delta\overline{\mathbf{F}}\,. \tag{6.45}$$

Finally, we can compute the effective mechanical moduli as

$$\boxed{\Delta\overline{\boldsymbol{P}} = \frac{1}{|\mathcal{B}_0|}\mathbb{L}\mathbb{Q}\left[\mathbb{P}(\widetilde{\underline{\mathbf{K}}}^{bb})^{-1}\mathbb{P}^T\right]^{-1}\mathbb{Q}^T\mathbb{L}^T\Delta\overline{\boldsymbol{F}} \quad \Rightarrow \quad \overline{\mathbb{A}} := \frac{1}{|\mathcal{B}_0|}\mathbb{L}\mathbb{Q}\left[\mathbb{P}(\widetilde{\underline{\mathbf{K}}}^{bb})^{-1}\mathbb{P}^T\right]^{-1}\mathbb{Q}^T\mathbb{L}^T}\,. \tag{6.46}$$

6.4 Numerical investigation of instabilities in hydrogel structures

We now investigate computationally microscopic and macroscopic instabilities in two- and three-dimensional periodic hydrogels, where all considered boundary value problems are motivated from experimental studies (e.g., [82, 85, 77]). The two-dimensional studies of single- and two-phase voided hydrogel microstructures under plane-strain conditions are summarized in Section 6.4.1. Corresponding investigations of structrual instabilities of three-dimensional hydrogel thin films are documented in Section 6.4.2. In all cases, we examine the influence of physical properties and microscopic morphology on the onset and the type of instabilities.

6.4.1 Two-dimensional hydrogel structures

In this section, we study instabilities in single-phase and two-phase voided hydrogel microstructures. While the single-phase hydrogels consist of a hydrogel matrix and voids, the two-phase hydrogels further contain stiff, permeable coatings surrounding the voids as described in Fig. 6.3. The latter structures are motivated from experimental studies on constrained plane bilayer films, which reveal a rich set of wrinkling patterns [28, 26, 27]; see also the analytical and numerical studies [47, 46, 9, 78, 15, 70]. Associated wrinkling phenomena have not only been reported for plane bilayers, but also for bilayer tubes [42, 70] and could be exploited in various engineering and biomedical applications such as controlled formation of micro-gears [79], generation of multi-cellular spheroids [84], controlled cell spreading [41], see also [49, 25]. To the best of our knowledge, *swelling-induced micro-wrinkling at internal surfaces of periodic hydrogels* has not been reported in the literature yet. The sole experimental study coming close to the results reported here is the one recently documented in [19].

In the following, we first discuss suitable boundary conditions and numerical setups of boundary value problems to analyze the given hydrogel microstructures. Next, we provide some numerical studies in order to give further insight into the response of the voided hydrogel microstructures. Eventually, we perform a set of computational investigations demonstrating instabilities in two-dimensional hydrogel microstructures.

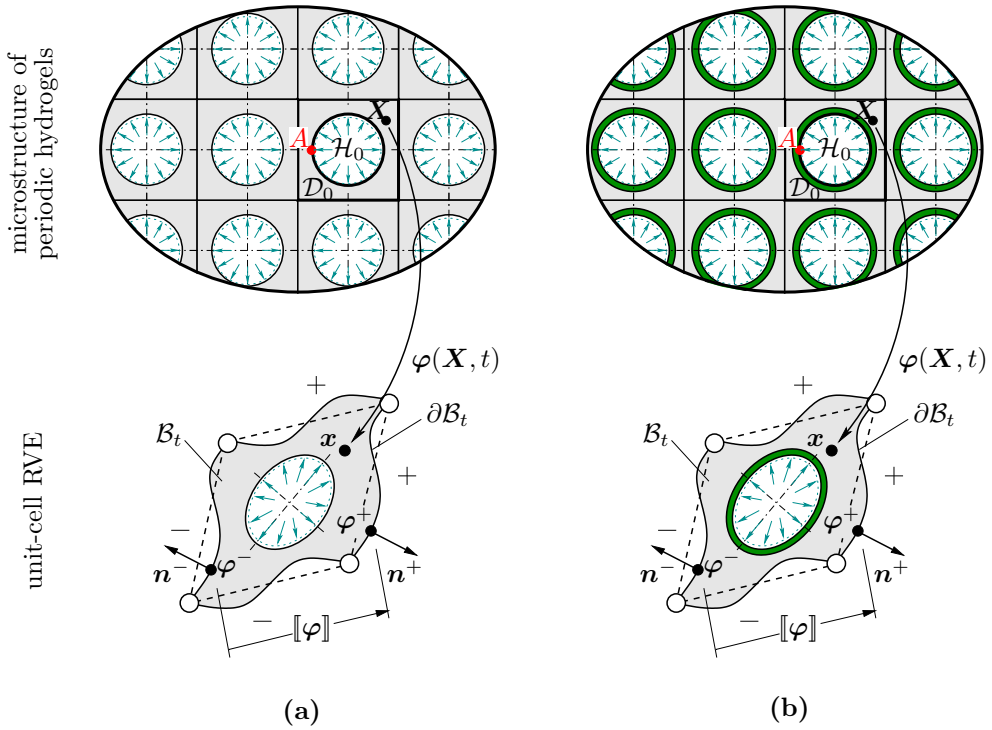

Figure 6.3: *Unit-cell RVEs of two periodic hydrogel microstructures.* We consider (**a**) single-phase hydrogels (consisting of hydrogel matrix and voids) and (**b**) two-phase hydrogels (consisting of hydrogel matrix, hydrogel coatings, and voids). The coating is realized as a stiff film that is perfectly bonded to the matrix (highlighted in green). It is further assumed that the solvent enters the hydrogel through the internal boundary $\partial\mathcal{H}_0$, where we prescribe suitable boundary conditions in terms of the chemical potential. At the external boundary $\partial\mathcal{B}_0$, the jump conditions for the deformation as well as for the solvent-volume flux are applied as described in Section 6.2.3.

6.4.1.1 Boundary conditions in the two-dimensional setting

Since we consider periodic hydrogel microstructures, all computations are reduced to a periodic unit-cell RVE as discussed in Section 6.2.3. Thus, the jump conditions for the deformation map and the solvent-volume flux according to (6.12) are considered at the external boundary of the RVE. In what follows, we set $\overline{\boldsymbol{F}} = \boldsymbol{1}$ to mimic an effectively constrained hydrogel composite. We further assume that a solvent diffuses into the hydrogel solely through the boundary of the voids $\partial\mathcal{H}_0$ and thus consider the mechanical traction and chemical potential on $\partial\mathcal{H}_0$ as

$$\boldsymbol{P}\cdot\boldsymbol{N}=\boldsymbol{0} \quad \text{and} \quad \mu=\lambda(t)\mu_0 \quad \text{on} \quad \partial\mathcal{H}_0 \quad \text{with} \quad \lambda(t)=\begin{cases}1-t & \text{for} \quad t\leq 1\,\text{sec}\\ 0 & \text{for} \quad t>1\,\text{sec}\end{cases}, \tag{6.47}$$

where μ_0 is the chemical potential of the reference state, see (6.11). As can be seen in the latter equation, the chemical potential is linearly increased from μ_0 to zero within one second [6, 15].

In the present work, we consider a time step of $\tau = 4\cdot 10^{-3}\,\text{sec}$ in order to determine instability points accurately. We note that a suitable time-step size is related to the

Table 6.7: Material parameters of the considered hydrogel microstructures.

Parameter	Name, unit	Value	Eq.
γ	Shear modulus, N/mm^2	0.01	(6.8)
α	Mixing modulus, N/mm^2	20.0	(6.8)
χ	Mixing parameter, –	0.1	(6.8)
M	Mobility parameter, mm^4/(Ns)	10^{-4}	(6.9)
η	Penalty parameter, N/mm^2	10γ	(6.8)
J_0	Volumetric pre-swelling, –	1.01	(6.8) & (6.9)

material parameters of the boundary value problem as well as its numerical discretization [73].

In Fig. 6.3, we depict illustrations of microstructures considered in the first part of our studies. The microstructures are discretized using Raviart–Thomas-type finite elements of the type Q_2RT_0, where the displacement field is interpolated using bi-quadratic Lagrangian shape functions associated with node-based degrees of freedom and the solvent-volume flux field is interpolated using linear Raviart–Thomas shape functions associated with edge-based degrees of freedom [6, 64]. Depending on the geometry of the problem, approximately $\geq 9,000$ finite elements (corresponding to approximately $\geq 30,000$ nodes) are used for the discretization of a unit-cell RVE. We refer to Appendix A for further details of the numerical implementation. The used material parameters are summarized in Table 6.7.

6.4.1.2 Response of voided hydrogel microstructures

To obtain a first insight into the behavior of voided hydrogel microstructures, we analyze a sequence of RVEs with the void-volume fractions $f_0 \in [10\% - 50\%]$ and illustrate their response over the simulation time in Fig. 6.4. In Fig. 6.4**a** and **b**, we observe that the radius related to a given void-volume fraction f_0 changes significantly due to the influx of solvent, even after loading $t \geq 1\,\text{sec}$. In Fig. 6.4**c**, we illustrate the solvent volume entering through the boundary of the voids over time according to $h_{void} = -\int_{\partial\mathcal{H}_0} \mathbb{H} \cdot \boldsymbol{N}\, \mathrm{d}A$ with $\boldsymbol{N}$ being a unit normal vector pointing outward the hydrogel matrix. We observe that the influx of the solvent volume increases as we decrease the chemical potential at the void boundary until it finally reaches its maximum at $t = 1\,\text{sec}$ and $\mu^N_{void} = 0.0\,\text{N/mm}^2$. In Fig. 6.4**d**, we have plotted the effective (averaged) first Piola-Kirchhoff stress $\overline{P}_{11} = \overline{P}_{22}$ normalized with respect to the matrix shear modulus γ, see $(6.13)_2$. Notably, the normalized effective stress response is in a similar range for all considered microstructures.

Since the applied chemical potential μ^N_{void} at the void boundary $\partial\mathcal{H}_0$ is zero after $t = 1\,\text{sec}$, it is not suitable for the description of the behavior beyond $t > 1\,\text{sec}$. Therefore, the instability studies documented in the following sections will be discussed with respect to time rather than applied chemical potential.

Creasing instabilities. Before we come to the analysis of structural instabilities, we take a look at two snapshots of the unit-cell RVE with 50% void-volume fraction during its deformation, see Fig. 6.5. There we observe the development of *creases* during the swelling process. When comparing to the results shown in Fig. 6.4, we note that creasing takes

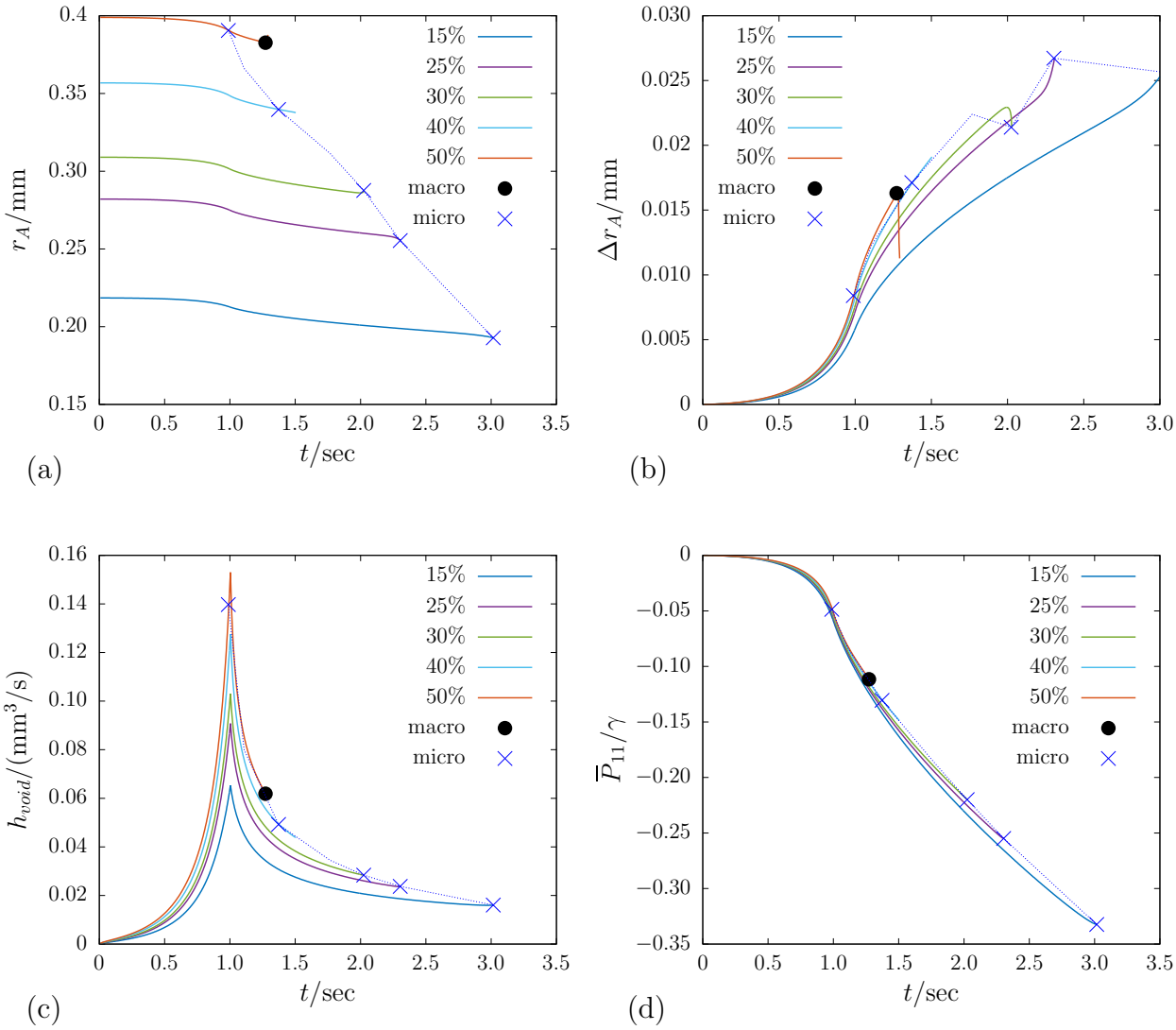

Figure 6.4: *Response of voided hydrogel microstructures versus simulation time.* (**a**) Radius r_A of voids and (**b**) change in the radius Δr_A of voids measured at the point A as depicted in Fig. 6.3 with the initial radius $r_{initial} = \sqrt{f_0/\pi}$; (**c**) Solvent volume entering the hydrogel matrix through the void boundary $h_{void} = -\int_{\partial\mathcal{H}_0} \mathbb{H} \cdot \boldsymbol{N}\, \mathrm{d}A$; (**d**) Effective (averaged) first Piola-Kirchhoff stress $\overline{P}_{11}$ normalized with respect to the shear modulus of the matrix γ.

place after the microscopic instability point and also after the loss of strong ellipticity. Nevertheless, the studies documented in Appendix A indicate that the creasing instability is highly dependent on the finite-element discretization, so that under further refinement of the mesh creasing occurs even earlier than the loss of strong ellipticity. An in-depth study of creasing and its numerical implications is however beyond the scope of the present work.

6.4.1.3 Instabilities in single-phase hydrogels with voids

We now study the onset of instabilities for the voided hydrogel microstructures as described in Fig. 6.3**a**. In particular, we analyze the influence of the void-volume fraction

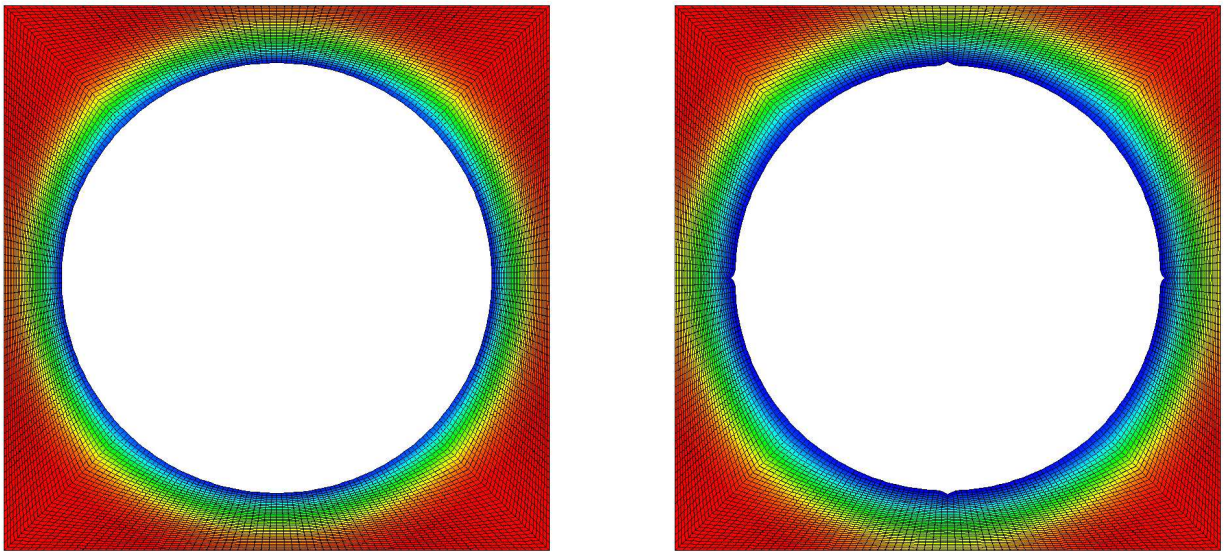

$t = 1.0\,\text{sec}$ $t = 1.284\,\text{sec}$

Figure 6.5: *Snapshots of the deformed hydrogel microstructure with the void-volume fraction* $f_0 = 50\%$. The diffusion of solvent volume takes place through the boundary of the void $\partial\mathcal{H}_0$, where we prescribe the chemical potential according to (6.47). The contour indicates the chemical potential, where blue corresponds to the minimum and red to the maximum value, respectively. We observe that at the time instant $t = 1.284\,\text{sec}$, the void boundary has developed creases.

f_0, the mobility parameter M and the chemical parameter α of the matrix. As in the preceding studies, the remaining material parameters are taken from Table 6.7.

The onset of instabilities for the considered initial boundary value problem is depicted in Fig. 6.6**a**–**d**. In Fig. 6.6**a** and **c**, we plot the critical time versus the void-volume fraction depending on the mobility parameter M and the chemical parameter α, respectively. We observe that both parameters have a significant impact on the time at which a critical instability occurs. As expected, instabilities are initiated earlier for larger M (that is, for faster diffusion through the matrix) and larger α (that is, for an enhanced chemo-mechanical interaction). In Fig. 6.6**b** and **d**, we plot the normalized critical first Piola-Kirchhoff stress $\overline{P}_{11} = \overline{P}_{22}$ at the instability points for different values of the mobility and the chemical parameter. We observe that the critical stresses associated with the various hydrogel microstructures are all in the same range. This indicates that the instability point is strongly correlated with the effective normalized compressive stress state. We further observe that the short-wavelength (microscopic) instabilities are primary for the microstructures with the void-volume fractions $f_0 \in \{20\% - 50\%\}$ and that the long-wavelength (macroscopic) instabilities are primary for the microstructures with the void-volume fractions $f_0 \in \{10\% - 15\%\}$. As a result of the microscopic instabilities, the hydrogel develops the so-called diamond-plate pattern, resulting in a change of periodicity of the microstructure as described in [82, 85, 77] and depicted in Fig. 6.8**f**[36].

We note that the macroscopic instabilities were detected by means of Bloch–Floquet wave analysis with $\boldsymbol{k} \to \boldsymbol{0}$ and coincide with the loss of strong ellipticity of the effective

[36]We note that the buckling modes are derived from the critical eigenvectors (see, e.g., [66]) and are not obtained from a post-buckling analysis.

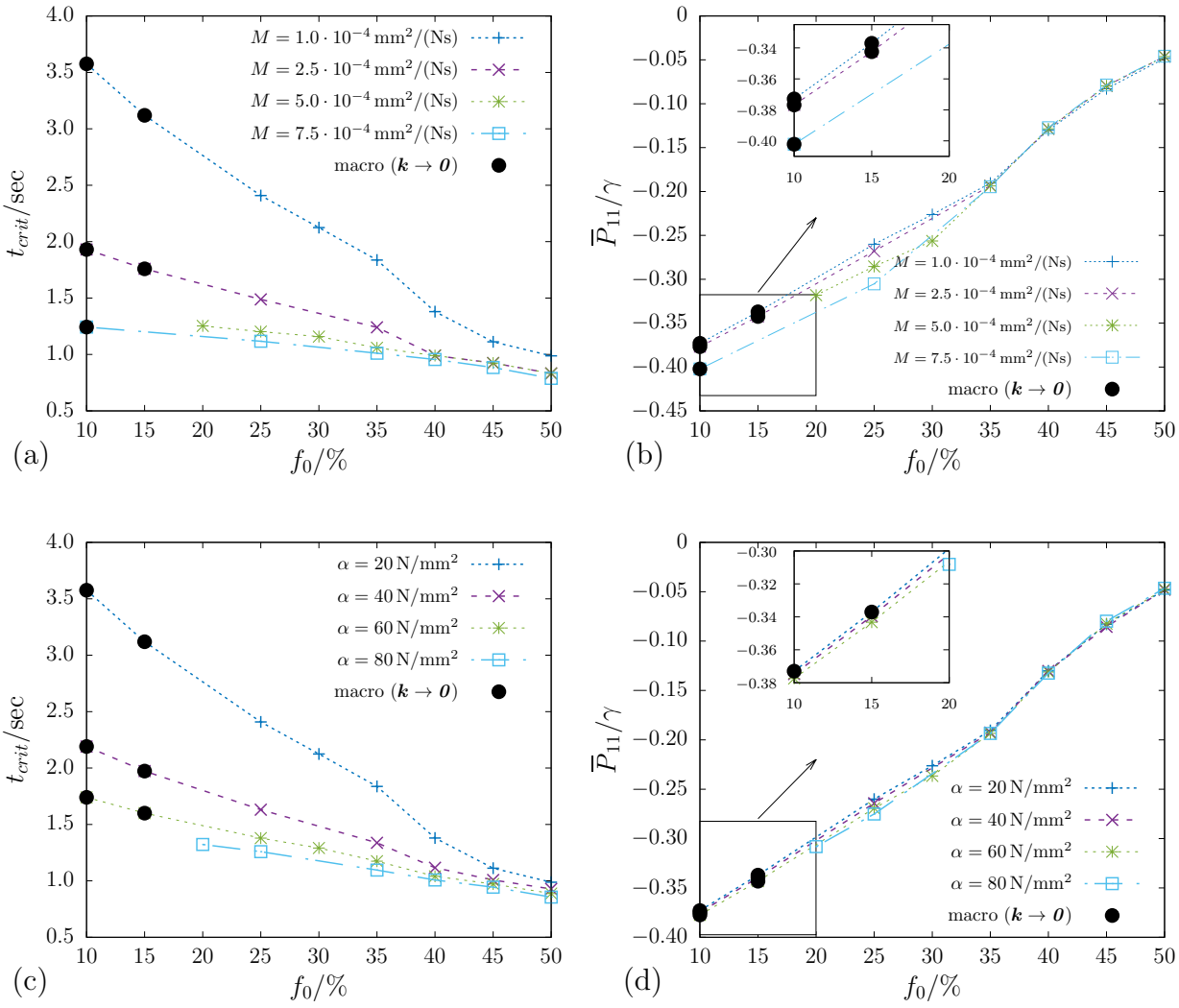

Figure 6.6: *Onset of instabilities depending on the mobility M and the chemical parameter α.* Results are plotted with respect to the critical time t (**a** and **c**) and the normalized effective (averaged) first Piola-Kirchhoff stress $\overline{P}_{11}/\gamma_m$ (**b** and **d**) with γ being the shear modulus of the matrix. We observe that while the mobility and the chemical parameters have significant influence on the critical time, the normalized critical stresses are all in the same range. Note that next to short-wavelength (pattern-transforming) instabilities, we observe long-wavelength instabilities for the void-volume fractions $f_0 = 10\%$ and $f_0 = 15\%$.

mechanical moduli as discussed in Section 6.3.2.

6.4.1.4 Instabilities of two-phase hydrogels with voids

We proceed with analyzing instabilities of two-phase voided hydrogel microstructures as described in Fig. 6.3**b**. As can be seen in this figure, we take into account microstructures composed of hydrogel matrix (m), voids (v) and hydrogel coatings (c) surrounding the voids.

In the following, we investigate the influence of the thickness of the coating as well as of the ratios between the shear moduli and the mobility parameters of the hydrogel

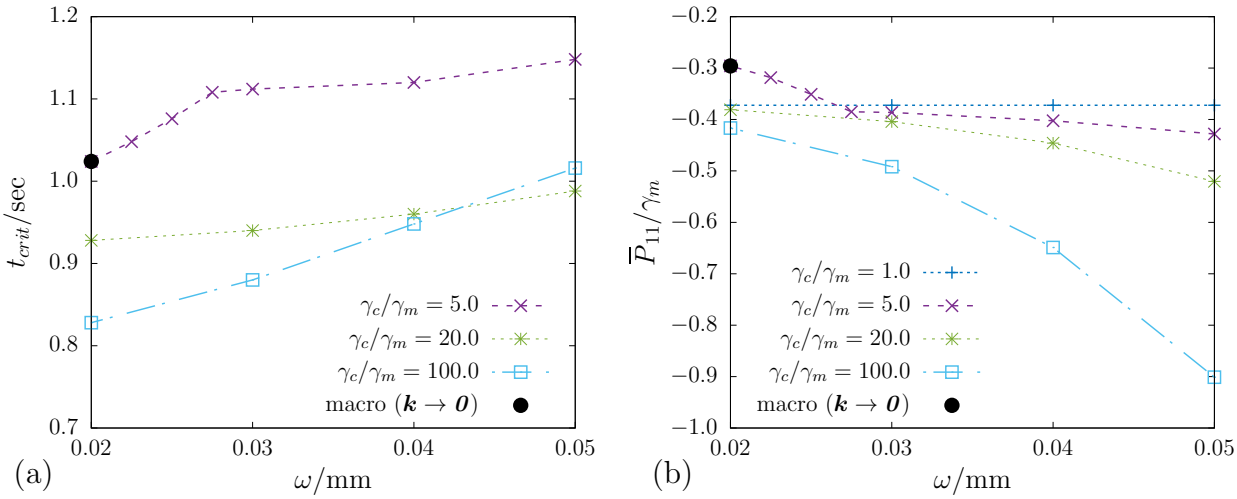

Figure 6.7: *Onset of instabilities for the composite hydrogels with void-volume fraction* $f_0 = 20\%$ *for varying shear-modulus ratios* γ_c/γ_m *of the coating (c) and the matrix (m) as well as coating thickness* ω. The results are plotted with respect to (**a**) the critical time t and (**b**) the normalized effective (averaged) first Piola-Kirchhoff stress $\overline{P}_{11}/\gamma_m$. Again, most instabilities induce pattern transformations from one unit-cell RVE to 2×2 unit-cell RVEs. Furthermore, we observe macroscopic instabilities ($\boldsymbol{k} \to \boldsymbol{0}$).

coating and the hydrogel matrix on the formation of instabilities. Here, we take into account a fixed void-volume fraction $f_0 = 20\%$ and boundary conditions as described in Section 6.4.1. Material parameters for the matrix and the coating are listed in Table 6.7.

In Fig. 6.7, we illustrate the critical time t_{crit} and the effective first Piola-Kirchhoff stress $\overline{P}_{11} = \overline{P}_{22}$ versus the coating thickness ω for various values of shear-modulus ratio γ_c/γ_m of the coating and the matrix. In all studies we assume that the mechanical stiffness of the coating is higher than that of the matrix $\gamma_m = 0.01\,\mathrm{N/mm^2}$. In the present example the mobility parameter of both matrix and coating is set to $M_m = M_c = 10^{-4}\,\mathrm{mm^4/(Ns)}$.

From Fig. 6.7**a**, we observe that the shear-modulus ratio γ_c/γ_m has a significant influence on the critical instability point, such that microscopic instabilities occur much earlier than in case of the corresponding single-phase voided microstructures. Similarly, the critical effective stresses strongly depend on the shear-modulus ratio, see Fig. 6.7**b**. In that context we observe in particular that for $\gamma_c/\gamma_m = 5.0$ and the coating thickness $\omega < 0.025$, instabilities occur much earlier at much lower critical stresses.

We note that while most of the triggered instabilities show a critical periodicity of 2×2 unit cells, the observed microcopic patterns are highly dependent on the thickness of the coating and the ratio of shear moduli, see Fig. 6.8. In particular, two distinct kinds of pattern transformations given by (i) micro-wrinkling and (ii) diamond-plate patterns (mutual deformation of voids into ellipses) are recorded. In the first case, pattern transformations due to wrinkling of the coating are detected for $\gamma_c/\gamma_m < 30$. Here, the number of micro-wrinkles can be tuned by means of the shear moduli of the matrix and the coating. When the shear-modulus ratio exceeds the value of $\gamma_c/\gamma_m = 30$, diamond-plate patterns with smooth internal boundaries as in case of the single-phase hydrogel structures are observed.[37].

[37]We note that while the Bloch–Floquet analysis indicated a long-wavelength instability for the shear-

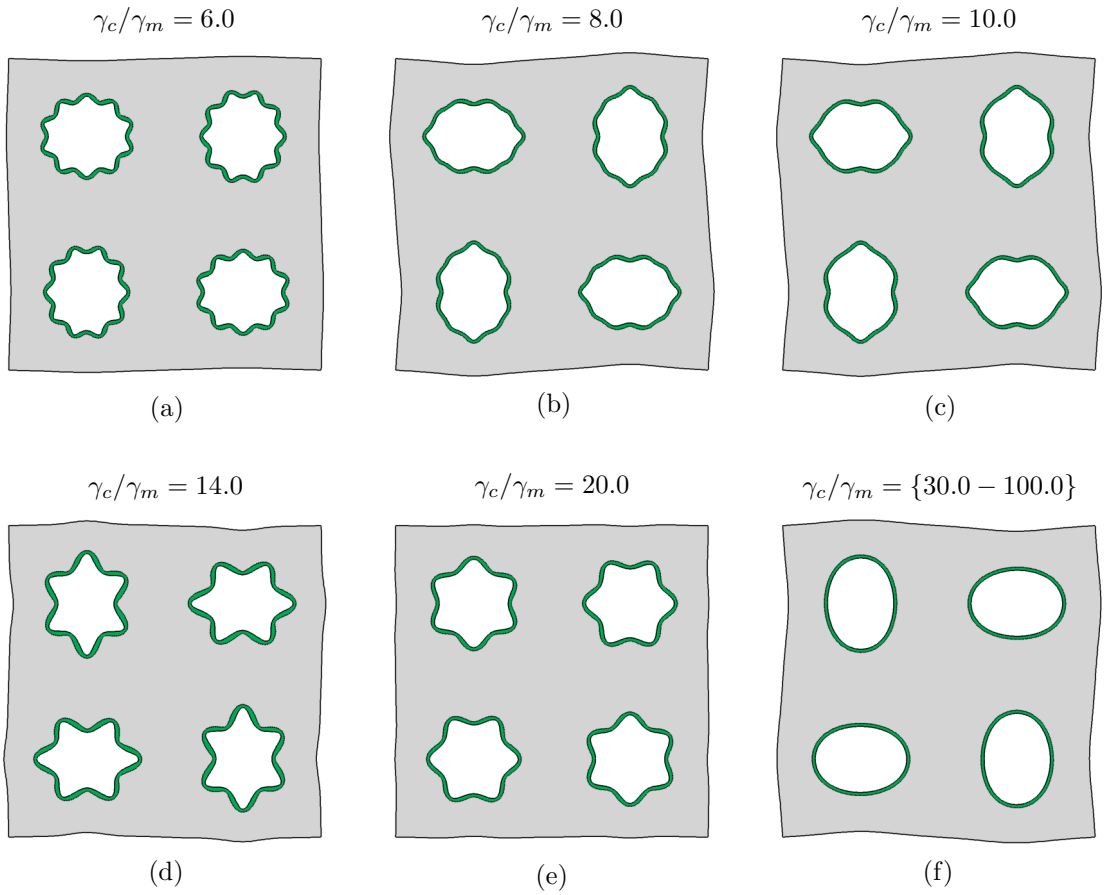

Figure 6.8: *Buckling modes of two-phase hydrogels depending on the shear modulus ratio of the coating (c) and the matrix (m).* The periodic hydrogels are composed of hydrogel matrix, hydrogel coatings with thickness $\omega = 0.02\,\text{mm}$, and voids with volume fraction $f_0 = 20\%$. Depending on the shear-modulus ratio of coating and matrix γ_c/γ_m, pattern-transforming instabilities with and without wrinkling of internal surfaces can be observed.

In Fig. 6.9, we further study instabilities for a wide range of shear-modulus ratios and coating thicknesses $\omega \in \{0.02, 0.03, 0.04, 0.05\}\,\text{mm}$. The graphs describe the critical time t_{crit} and the effective first Piola-Kirchhoff stress $\overline{P}_{11}$ depending on the shear-modulus ratio γ_c/γ_m. Similar to the previous cases, we observe that for small values $\gamma_c/\gamma_m < 10$, the critical instability time increases exponentially. As the stiffness of the coating increases, the corresponding compressive stresses rise and induce earlier buckling. A slightly different response is observed for the thicker and stiffer coatings due to a stabilizing effect, see the intersection of corresponding curves in Fig. 6.7**a**.

In Fig. 6.10, we study the influence of various mobility-parameter ratios M_c/M_m of the coating and the matrix on the onset and the type of instabilities in consideration of a shear-modulus ratio of $\gamma_c/\gamma_m = 5.0$ with $\gamma_m = 0.01\,\text{N/mm}^2$ and a mobility parameter of

modulus ratio $\gamma_c/\gamma_m = 5.0$ (see black bullet in Fig. 6.7), the analysis of effective moduli did not show a loss of strong ellipticity. A further analysis of strong ellipticity beyond the critical point was not possible due to missing convergence. Refining the time-step size did not help to overcome this issue. We refer to [15], who observed a competition between short- and long-wavelength instabilities for small shear-modulus ratios in plane bilayer systems. Their results indicate that for a refined mesh, the long-wavelength instabilities become the primary ones. Further discussions concerning the competition between short- and long-wavelength instabilities can be found, for example, in [39].

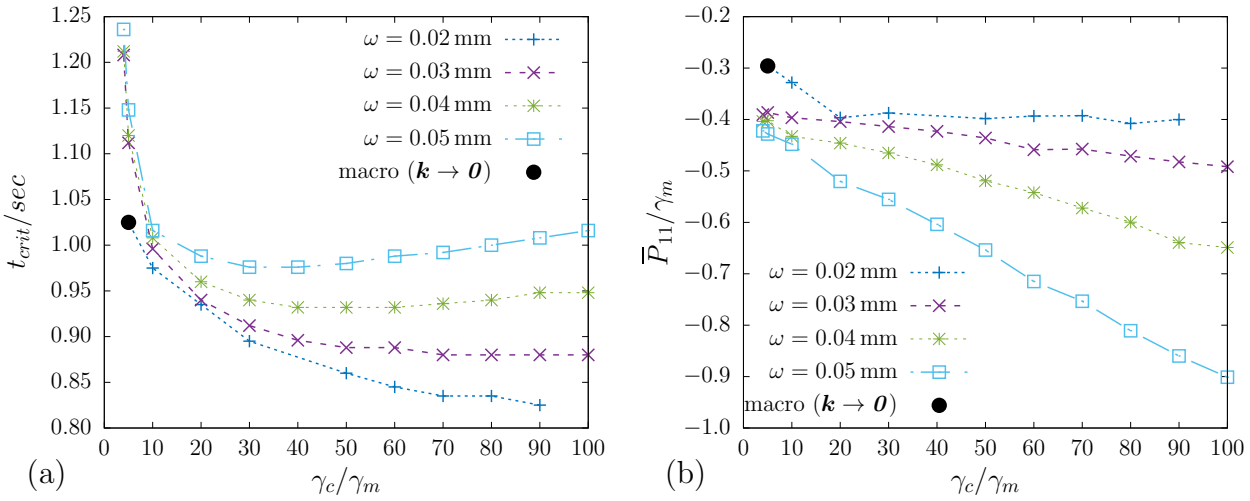

Figure 6.9: *Onset of instabilities for the composite hydrogels with the void-volume fraction $f_0 = 20\%$ depending on the shear modulus ratio γ_c/γ_m of the coating (c) and the matrix (m) as well as the coating thickness ω.* The results are plotted with respect to (**a**) the critical time t and (**b**) the normalized effective (averaged) first Piola-Kirchhoff stress $\overline{P}_{11}/\gamma_m$. The short-wavelength buckling patterns span 2×2 unit-cell RVEs.

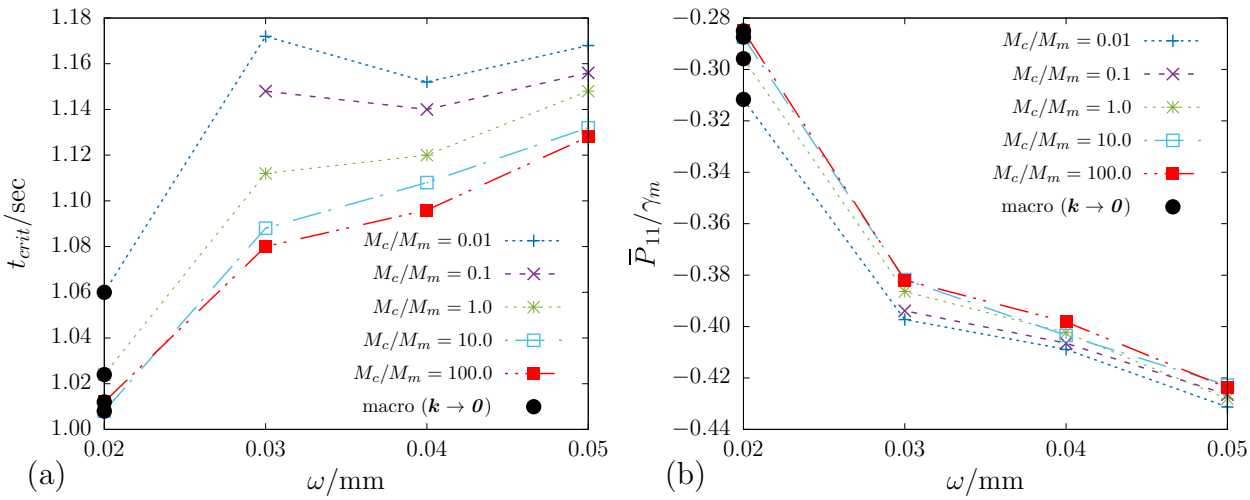

Figure 6.10: *Onset of instabilities for the composite hydrogels with the shear-modulus ratio $\gamma_c/\gamma_m = 5$ and the void-volume fraction $f_0 = 20\%$ depending on the mobility-parameter ratio M_m/M_c of the coating (c) and the matrix (m) as well as the coating thickness ω.* The results are plotted with respect to (**a**) the critical time t and (**b**) the normalized effective (averaged) first Piola-Kirchhoff stress $\overline{P}_{11}/\gamma_m$. The pattern-transforming instabilities span 2×2 unit-cell RVEs.

the coating $M_c = 10^{-4}\,\mathrm{mm}^4/(\mathrm{Ns})$. We illustrate the critical time t_{crit} and the effective first Piola-Kirchhoff stress $\overline{P}_{11} = \overline{P}_{22}$ depending on the thickness ω of the coating. Since the mobility parameter is associated with the diffusivity of the hydrogel, the solvent tends to accumulate in the coating when $M_c/M_m > 1$. As a result, the coating reaches the critical stress faster and the instabilities occur at lower critical time, see Fig. 6.10**a**. In Fig. 6.10**b**, we depict the corresponding effective critical stresses over the coating thickness ω depending on the mobility-parameter ratio. In all considered problems, we observe

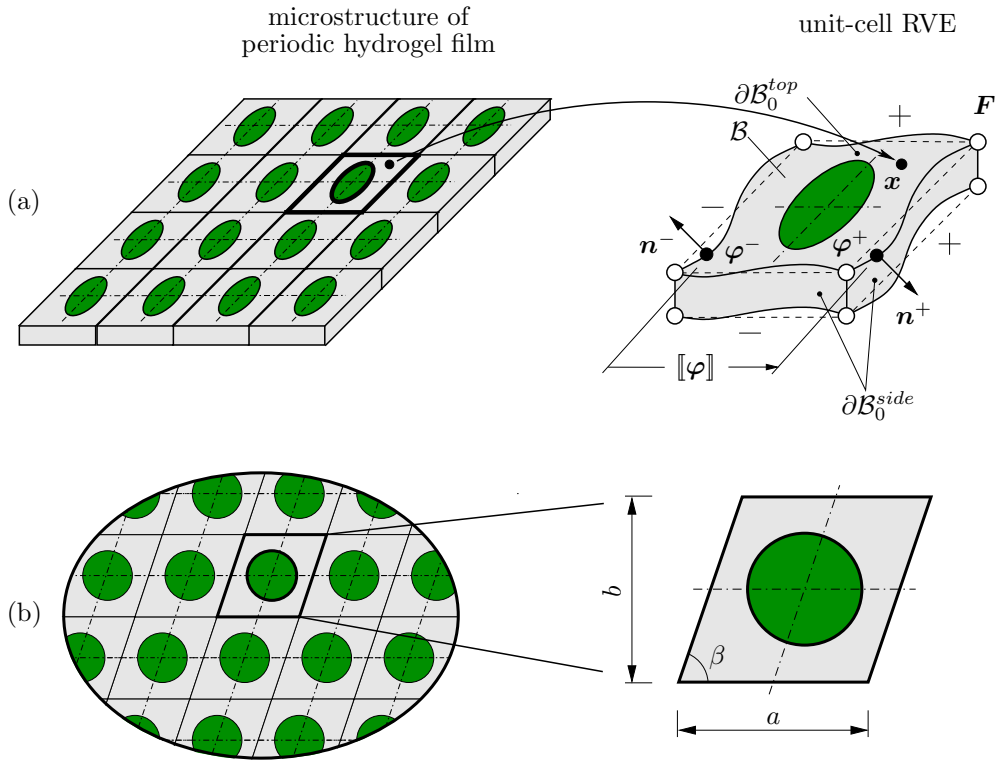

Figure 6.11: *Boundary value problem for the three-dimensional composite hydrogel thin films.* (**a**) The periodic microstructure of a thin film is represented by a unit-cell RVE, where the jump conditions for the deformation map and the solvent-volume flux refer only to the side boundaries, see (6.48). In the three-dimensional setting it is assumed that the solvent diffuses through the top and the bottom surfaces, which is realized by applying associated boundary conditions for the chemical potential. (**b**) A top view of the thin film indicated that the periodic microstructure can be described by means of unit-cell RVEs given by right parallelogrammic prism with cylindrical inclusions. In all considered examples, we assume that the inclusions have lower diffusivity and higher mechanical stiffness than the matrix.

the buckling instabilities resulting in 2×2 unit-cell RVEs. For a coating thickness of $\omega = 0.02\,\mathrm{mm}$, the long-wavelength instabilities are detected again.

6.4.2 Three-dimensional hydrogel films

The previous studies were limited to a two-dimensional plane-strain scenario. We now extend the analysis to the three-dimensional case and investigate structural instabilities in hydrogel thin films. The considered films comprise cylindrical hydrogel inclusions that are embedded into a hydrogel matrix in a periodic manner, see Fig. 6.11. We assume that the diffusivity of the inclusions is low compared with the matrix, so that swelling of the inclusions is not pronounced. The considered setup is motivated from the experimental works [76, 52].

Before we provide the results of a parametric study in consideration of various geometrical properties of microstructures, we discuss suitable boundary conditions for the numerical realization of three-dimensional hydrogel films considering plane periodicity. In that context, we also comment on relevant ingredients of the numerical discretization and

finite-element implementation.

6.4.2.1 Boundary conditions in the three-dimensional setting

Because of the periodic nature of the problem, the following computations can again be reduced to a selected unit-cell RVE. In this connection, we consider the jump boundary conditions across the lateral boundaries of the RVE

$$[\![\boldsymbol{\varphi}]\!] = \widehat{\overline{\boldsymbol{F}}}\,[\![\boldsymbol{X}]\!] \quad \text{and} \quad [\![\mathit{H}]\!] \cdot \boldsymbol{N} = 0 \quad \text{on} \quad \partial\mathcal{B}_0^{\text{side}}\,, \tag{6.48}$$

where $\widehat{\overline{\boldsymbol{F}}}$ is the effective (averaged) deformation gradient in the plane of periodicity, see also Fig. 6.11**a**. We assume that the hydrogel is mechanically constrained in plane and that no stresses arise in out-of-plane direction, that is

$$\widehat{\overline{\boldsymbol{F}}} = \begin{bmatrix} 1 & 0 & 0 \\ 0 & 1 & 0 \\ 0 & 0 & \cdot \end{bmatrix} \quad \text{and} \quad \boldsymbol{P} \cdot \boldsymbol{N} = \boldsymbol{0} \text{ on } \partial\mathcal{B}_0^{top,bottom}\,. \tag{6.49}$$

On the chemical side, the solvent is assumed to enter the hydrogel only through the top and the bottom surfaces of the film, which is reflected by the chemical-potential boundary condition

$$\mu = \lambda(t)\mu_0 \quad \text{on} \quad \partial\mathcal{B}_0^{top,bottom} \quad \text{with} \quad \lambda(t) = \begin{cases} 1-t & \text{for} \quad t \leq 1\,\text{sec} \\ 0 & \text{for} \quad t > 1\,\text{sec} \end{cases}, \tag{6.50}$$

where μ_0 is the chemical potential of the reference state, refer to (6.11). In what follows, we consider a time-step size of $\tau = 4 \cdot 10^{-3}\,\text{sec}$.

The geometry of the boundary value problem and the corresponding unit-cell RVE are described in Fig. 6.11**b**. Here, the film has the thickness $\omega = 0.02\,\text{mm}$ and plane dimensions of $a \times b$ with a fixed length of $a = 1.0\,\text{mm}$. The inclusions with radius $r = 0.25\,\text{mm}$ have lower diffusivity and higher elastic stiffness than the matrix ($M_i/M_m = 0.01$, $\gamma_i/\gamma_m = 10$). The remaining material parameters of both phases are taken from Table 6.7.

The microstructures described in Fig. 6.11**b** are discretized using hexahedral finite elements of the type H_1H_1. Here, the displacement field and the solvent-volume flux are assumed as nodal degrees of freedom resulting in six degrees of freedom per node. Depending on the morphology, $5,500$ to $9,000$ finite elements ($8,500$ to $14,000$ nodes) are needed for the discretization of a unit-cell RVE.

6.4.2.2 Instabilities of three-dimensional two-phase hydrogel thin films

In Fig. 6.12, we illustrate the onset of instabilities depending on the morphological parameters of the RVE. We observe that both the width of the unit cell b as well as the angle β have a significant influence on the critical time and the critical stress. Since the volume fraction of the stiff inclusions (for fixed radii) decreases with increasing b, the composite effectively becomes softer and instabilities occur earlier. A similar behavior can be observed for decreasing angle β, which results in an effectively larger distance

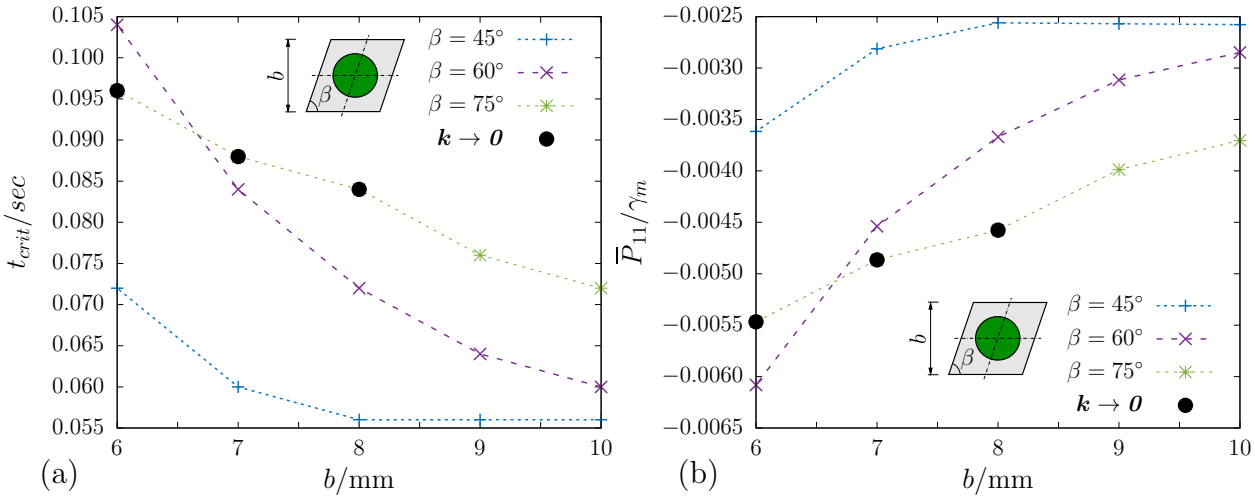

Figure 6.12: *Onset of instabilities for the three-dimensional composite hydrogel films depending on their morphology.* A shear-modulus ratio of $\gamma_i/\gamma_m = 10$ between inclusions and matrix as well as a morphology with $a = 1.0\,\text{mm}$ and $r = 0.25\,\text{mm}$ are considered. Instabilities are depicted with respect to (**a**) the critical time t and (**b**) the normalized effective (averaged) first Piola-Kirchhoff stress $\overline{P}_{11}/\gamma_m$.

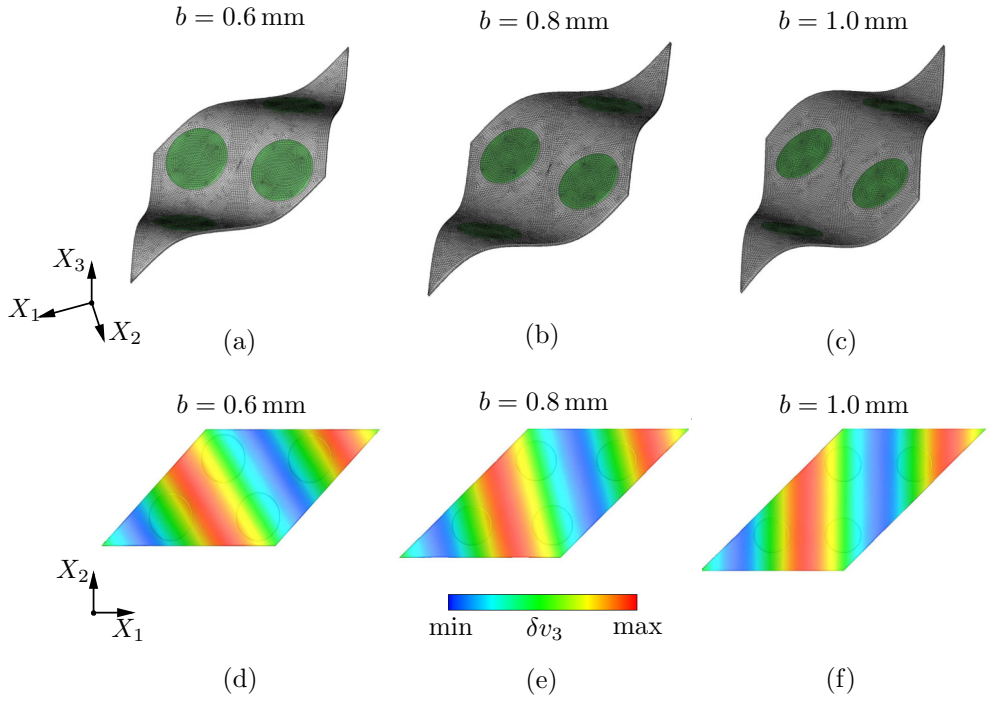

Figure 6.13: *Buckling modes of composite hydrogels with $\beta = 45°$ depending on the width b of the unit-cell RVE.* (**a**)–(**c**) Different buckling patterns spanning 2×2 unit-cell RVEs; (**d**)–(**e**) Contour plots of the critical eigenvectors (δv_3; top view) reveal the change in the direction of the buckling depending on the width of the unit-cell RVE.

between inclusions in the X_2-direction for a fixed value of b. While in most cases we observe buckling into a configuration described by 2×2 unit-cell RVEs, some computations indicate a transition from short-wavelength to long-wavelength instabilities. These points are indicated by black bullets in Fig. 6.12.

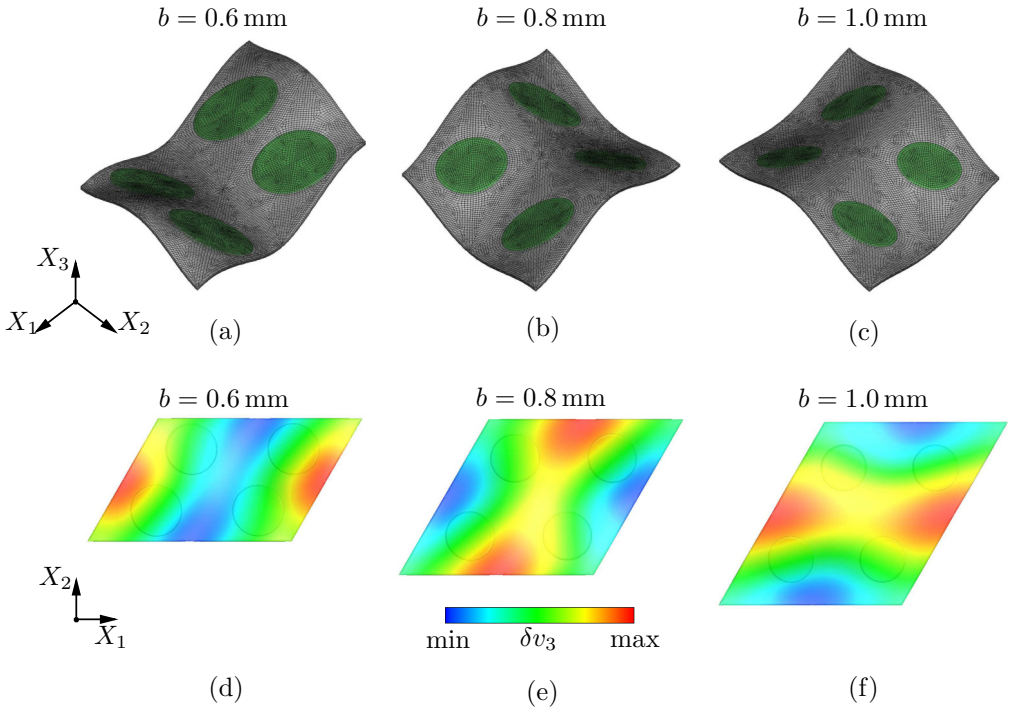

Figure 6.14: *Buckling modes of composite hydrogels with $\beta = 60°$ depending on the width b of the unit-cell RVE.* (**a**)–(**c**) Different buckling patterns spanning 2×2 unit-cell RVEs; (**d**)–(**e**) Contour plots of the critical eigenvectors (δv_3; top view) reveal the change in the direction of the buckling depending on the width of the unit-cell RVE.

In Fig. 6.13, we illustrate representative buckling patterns for different widths b of the film for an angle $\beta = 45°$ (see Fig. 6.14 for $\beta = 60°$). In case of $\beta = 45°$, we observe *wrinkling* of the microstructure, see Fig. 6.13**a**–**c**, where the direction of the wrinkling pattern can be influenced by adjusting the width b of the unit-cell RVE (see Fig. 6.13**d**–**f**). For $\beta = 60°$, we observe a different buckling pattern in the form of cooperative saddle-point shapes, see Fig. 6.14. Similar patterns can be observed for films with $\beta = 75°$, see Fig. 6.15. For better insight into the overall buckling patterns, we refer to Fig. 6.16, where we plot larger domains of representative buckled films.

6.5 Conclusion

In the present work, we studied instabilities in two-dimensional and three-dimensional composite hydrogels with periodic microstructures. In two dimensions, we investigated the onset of instabilities for single-phase voided microstructures as well as two-phase coated microstructures. We observed that in case of single-phase hydrogels, the periodicity of the microstructure may change from a unit-cell RVE to a larger RVE containing 2×2 unit cells, forming the well-known diamond-plate pattern frequently observed in experiments. For two-phase composites with thin coating surrounding the voids, we observed that the buckling modes can be substantially different from those of the single-phase hydrogel microstructures. Here, the change in periodicity and the development of patterns can be attributed either to wrinkling of the coating or to cooperative deformation of voids into ellipses. A detailed parametric study revealed that the observed patterns depend on the thickness of the coating as well as on the material parameters of coating and matrix.

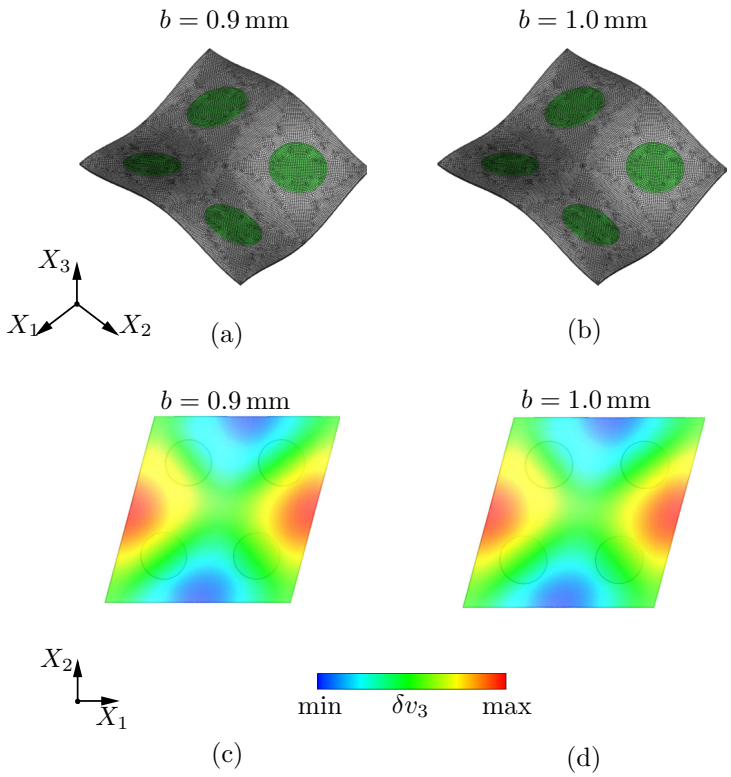

Figure 6.15: *Buckling modes of the composite hydrogels with $\beta = 75°$ depending on the width b of the unit-cell RVE.* (**a**)–(**c**) Buckling patterns span 2×2 unit-cells of the hydrogel films. (**d**)–(**e**) contour plots of the critical eigenvectors (δv_3) from top view reveal the change in the direction of buckling region depending on the width of the unit-cell.

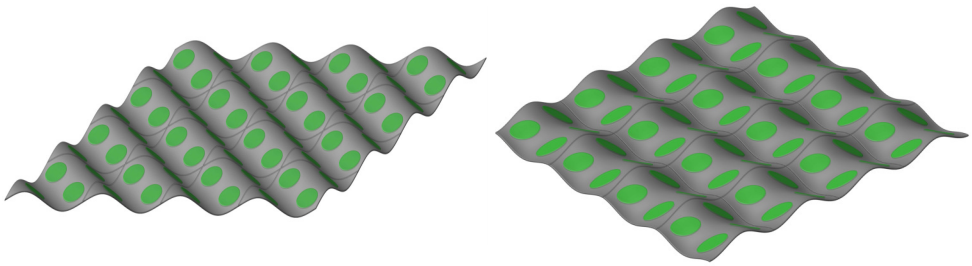

Figure 6.16: *Buckling modes of composite hydrogel microstructures composed of unit-cell RVEs with width $b = 0.8\,mm$.* (**a**) We observe wrinkling of the microstructure for $\beta = 45°$ and (**b**) cooperative buckling for $\beta = 60°$.

Our simulations of three-dimensional composite hydrogel films revealed various buckling patterns depending on the arrangement of small reinforcing particles within the hydrogel matrix of the microstructure. These findings could provide access to the design of complex out-of-plane buckling patterns to be tuned by adjustment of microstructures.

Acknowledgements

Funded by Deutsche Forschungsgemeinschaft (DFG, German Research Foundation) under Germany's Excellence Strategy – EXC 2075 – 390740016. This funding is gratefully acknowledged.

Appendix

A Numerical implementation and mesh convergence study for single-phase voided hydrogel microstructures

In this appendix, we provide relevant details on the numerical implementation of the given model and study the influence of the finite-element discretization on simulation results.

Numerical implementation. The coupled deformation-diffusion initial boundary value problem is implemented in FEAP [72] exploiting self-coded user element and material routines. Furthermore, user macros are implemented to extract the effective properties of the microstructure considering surface-based integration as discussed in Section 6.3 as well as to extract the global tangent matrix for stability analysis. The stability analysis based on the Bloch-Floquet theory and the strong ellipticity condition documented in Section 6.3 are implemented in MATLAB® [54].

Convergence study. In the following study, we investigate the convergence of the numerical solutions w.r.t. the time at which an instability can be observed and the corresponding critical effective stress. For that, several mesh-refinement steps are considered, resulting in a sequence of six different discretizations with {800; 1 800; 3 200; 5 000; 7 200; 9 800} Q_2RT_0 finite elements (corresponding to {3 360; 7 440; 13 120; 20 400; 29 800; 39 760} nodes). We refer to Fig. 6.17 for visualizations of selected meshes of a representative hydrogel microstructure. The corresponding material parameters are summarized in Table 6.7.

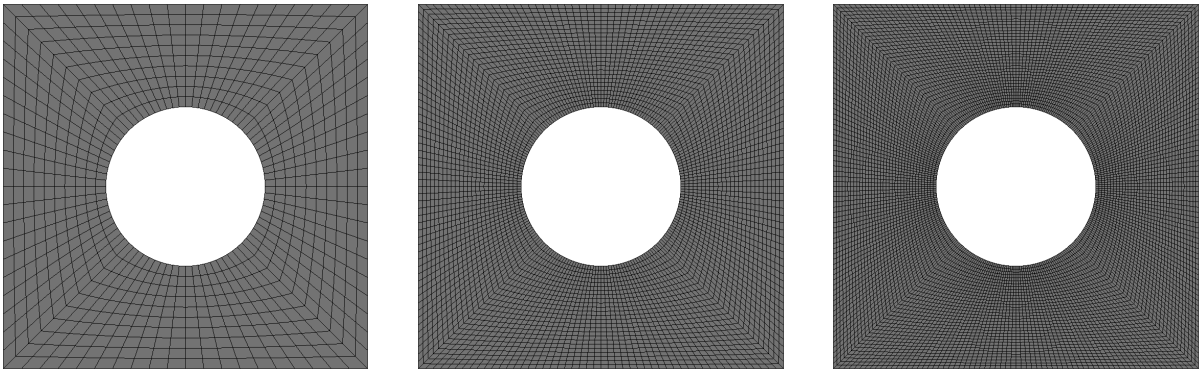

800 finite elements 5 000 finite elements 9 800 finite elements

Figure 6.17: *Finite-element meshes of the convergence study.* Representative discretizations of the hydrogel microstructure with void-volume fraction $f_0 = 15\%$.

Results of the convergence study are plotted in Fig. 6.18. To overcome convergence issues in case of the microstructures with the void-volume fractions $f_0 \leq 20$ % and the discretizations with $\{7,200; 9,800\}$ finite elements, we reduced the applied chemical potential at the internal boundary to $10^{-3}\,\mathrm{N/mm^2}$ instead of zero and employed adaptive time stepping with maximum and minimum time steps given by $\tau_{max} = 4 \cdot 10^{-3}\,\mathrm{sec}$ and $\tau_{min} = 10^{-3}\,\mathrm{sec}$, respectively. For the remaining volume fractions $\{30, 40, 50\}$ %, a time-step size of $\tau = 4 \cdot 10^{-3}\,\mathrm{sec}$ has been used. We note that each time step usually requires three or four Newton iterations to converge.

In Fig. 6.18, the critical instability points are shown for the microstructures with void-volume fractions $f_0 = \{15\%, 30\%, 40\%, 50\%\}$. We observe that the discretization has a notable impact on the detection of the instability points, especially for the lower void-

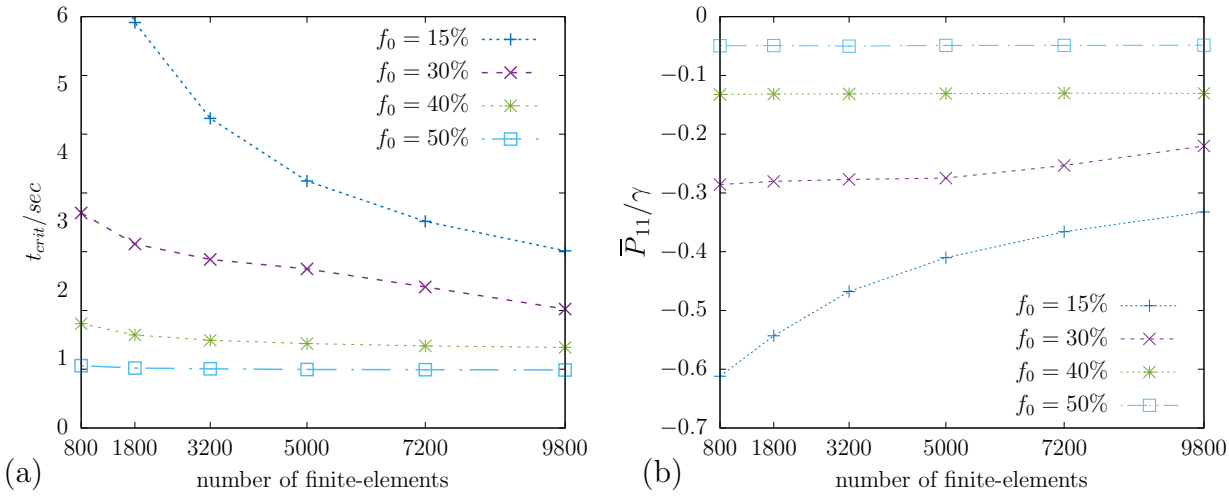

Figure 6.18: *Results of the convergence study with Q_2RT_0-type finite elements.* (**a**) Critical time t_{crit} and (**b**) effective stress $\overline{P}_{11}$ for voided hydrogel microstructures with different volume fractions.

volume fractions. Nevertheless, both buckling mode and type of instability are identical for all discretizations considered.

In Fig 6.19**a**, we plot data points related to the loss of strong ellipticity and the development of creases at the internal boundary of the microstructure with void-volume fraction $f_0 = 50\%$. While we observe fast convergence for the critical time at which strong ellipticity is lost, the critical time for creasing does not seem to have fully converged yet for the finest mesh discretization. We further did not encounter any creases in case of the discretization with 800 finite elements. We refer to Fig. 6.19**b**, where we have illustrated a creased microstructure with a discretization of 9 800 finite elements.

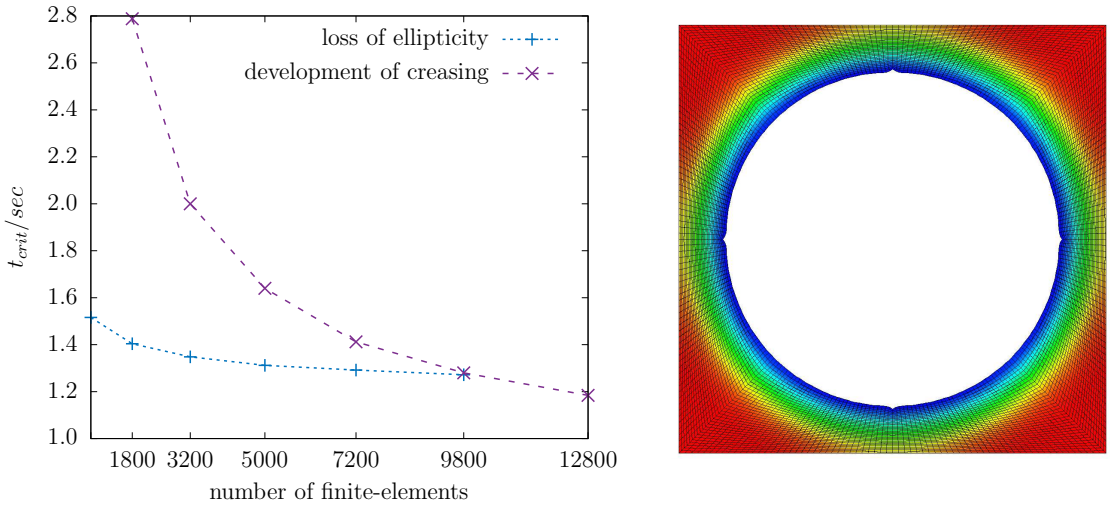

(a) convergence study (b) creasing at time $t = 1.288\,\text{sec}$

Figure 6.19: *Results of the convergence study with Q_2RT_0-type finite elements.* (**a**) Loss of the strong ellipticity of the effective moduli and (**b**) development of creases within the hydrogel microstructure with a void-volume fraction of $f_0 = 50\%$.

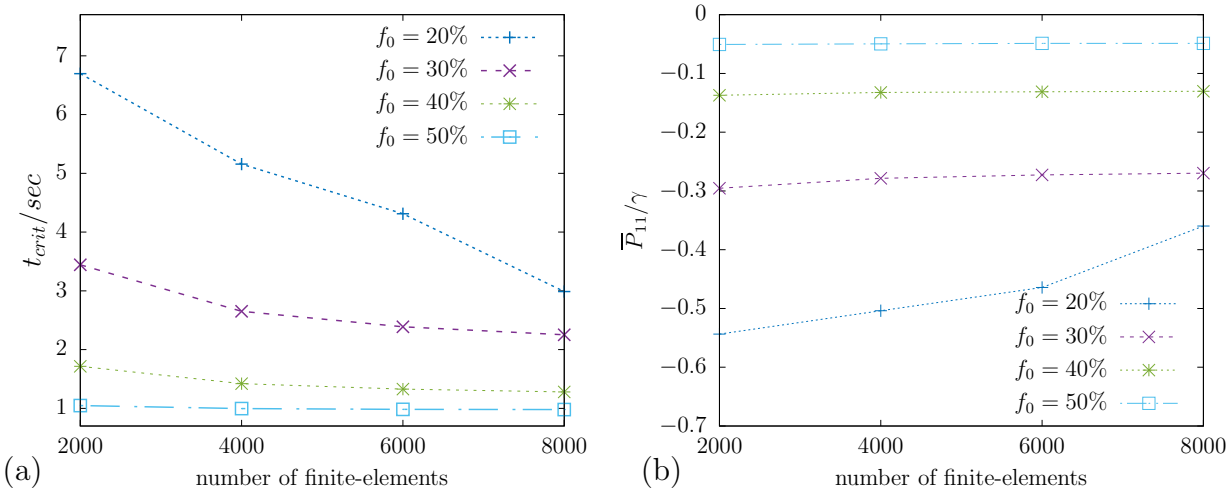

Figure 6.20: *Results of the convergence study with Q_1RT_0-type finite elements.* (**a**) Critical time t_{crit} and (**b**) effective stress $\overline{P}_{11}$ for voided hydrogel microstructures with different volume fractions.

In Fig. 6.20, we further show the results of a convergence study based on $\mathrm{Q_1RT_0}$ finite elements. This study shows a similar behavior as in case of quadratic elements. However, for some microstructures with small void-volume fraction ($f_0 \leq 20\%$) the discretization with $\mathrm{Q_1RT_0}$ elements gives rise to short-wavelength instabilities, while the the discretizations with quadratic finite elements yield long-wavelength instabilities.

As a compromise between accuracy and efficiency, we consider a discretization with 9 800 finite elements for the stability analysis of single-phase voided hydrogel microstructures in Section 6.4.1.3.

Bibliography: Paper D

[1] Bai, R., Yang, J., Suo, Z., [2019]. *Fatigue of hydrogels*. European Journal of Mechanics - A/Solids 74, 337–370. (doi:https://doi.org/10.1016/j.euromechsol.2018.12.001)

[2] Bertoldi, K., Boyce, M., Deschanel, S., Prange, S., Mullin, T., [2008]. *Mechanics of deformation-triggered pattern transformations and superelastic behavior in periodic elastomeric structures*. Journal of the Mechanics and Physics of Solids 56, 2642–2668.

[3] Bichara, D. A., O'Sullivan, N.-A., Pomerantseva, I., Zhao, X., Sundback, C. A., Vacanti, J. P., Randolph, M. A., [2012]. *The tissue-engineered auricle: past, present, and future*. Tissue Engineering Part B: Reviews 18 (1), 51–61.

[4] Bichara, D. A., Zhao, X., Hwang, N. S., Bodugoz-Senturk, H., Yaremchuk, M. J., Randolph, M. A., Muratoglu, O. K., [2010]. *Porous poly (vinyl alcohol)-alginate gel hybrid construct for neocartilage formation using human nasoseptal cells*. Journal of Surgical Research 163 (2), 331–336.

[5] Biot, M. A., [1941]. *General theory of three-dimensional consolidation*. Journal of Applied Physics 12 (2), 155–164.

[6] Böger, L., Nateghi, A., Miehe, C., [2017]. *A minimization principle for deformation-diffusion processes in polymeric hydrogels: constitutive modeling and fe implementation*. International Journal of Solids and Structures 121, 257–274.

[7] Bouklas, N., Landis, C. M., Huang, R., [2015]. *A nonlinear, transient finite element method for coupled solvent diffusion and large deformation of hydrogels*. Journal of the Mechanics and Physics of Solids 79, 21–43.

[8] Caló, E., Khutoryanskiy, V. V., [2015]. *Biomedical applications of hydrogels: A review of patents and commercial products*. European polymer journal 65, 252–267.

[9] Cao, Y., Hutchinson, J. W., [2012]. *Wrinkling phenomena in neo-hookean film/substrate bilayers*. Journal of applied mechanics 79 (3).

[10] Chester, S. A., Anand, L., [2010]. *A coupled theory of fluid permeation and large deformations for elastomeric materials*. Journal of the Mechanics and Physics of Solids 58 (11), 1879–1906.

[11] Chester, S. A., Di Leo, C. V., Anand, L., [2015]. *A finite element implementation of a coupled diffusion-deformation theory for elastomeric gels*. International Journal of Solids and Structures 52, 1–18.

[12] Coussy, O., [2004]. *Poromechanics*. John Wiley & Sons.

[13] Coussy, O., Dormieux, L., Detournay, E., [1998]. *From mixture theory to Biot's approach for porous media*. International Journal of Solids and Structures 35 (34-35), 4619–4635.

[14] Dervaux, J., Amar, M. B., [2012]. *Mechanical instabilities of gels*. Annu. Rev. Condens. Matter Phys. 3 (1), 311–332.

[15] Dortdivanlioglu, B., Linder, C., [2019]. *Diffusion-driven swelling-induced instabilities of hydrogels*. Journal of the Mechanics and Physics of Solids 125, 38–52.

[16] Ehlers, W., Acartürk, A., [2009]. *The role of weakly imposed dirichlet boundary conditions for numerically stable computations of swelling phenomena*. Computational Mechanics 43 (4), 545–557.

[17] Ehlers, W., Acartürk, A., Karajan, N., [2010]. *Advances in modelling saturated soft biological tissues and chemically active gels*. Archive of Applied Mechanics 80 (5), 467–478.

[18] Ehlers, W., Wagner, A., [2019]. *Modelling and simulation methods applied to coupled problems in porous-media mechanics*. Archive of Applied Mechanics 89 (4), 609–628.

[19] Fan, X., Deng, C., Gao, H., Jiao, B., Liu, Y., Chen, F., Deng, L., Xiong, W., [2022]. *3d printing of nanowrinkled architectures via laser direct assembly*. Science Advances 8 (31), eabn9942.

[20] Flory, P. J., [1953]. *Principles of polymer chemistry*. George Banta Publishing Company.

[21] Flory, P. J., Rehner, J. J., [1943]. *Statistical mechanics of cross-linked polymer networks i. rubberlike elasticity*. The Journal of Chemical Physics 11 (11), 512–520.

[22] Flory, P. J., Rehner, J. J., [1943]. *Statistical mechanics of cross-linked polymer networks ii. swelling*. The Journal of Chemical Physics 11 (11), 521–526.

[23] Geymonat, G., Müller, S., Triantafyllidis, N., [1993]. *Homogenization of nonlinearly elastic materials, microscopic bifurcation and macroscopic loss of rank-one convexity*. Archive of Rational Mechanics and Analysis 122, 231–290.

[24] Gurtin, M. E., Fried, E., Anand, L., [2010]. *The mechanics and thermodynamics of continua*. Cambridge University Press.

[25] Guvendiren, M., Burdick, J. A., [2010]. *The control of stem cell morphology and differentiation by hydrogel surface wrinkles*. Biomaterials 31 (25), 6511–6518.

[26] Guvendiren, M., Burdick, J. A., Yang, S., [2010]. *Kinetic study of swelling-induced surface pattern formation and ordering in hydrogel films with depth-wise crosslinking gradient*. Soft Matter 6 (9), 2044–2049.

[27] Guvendiren, M., Burdick, J. A., Yang, S., [2010]. *Solvent induced transition from wrinkles to creases in thin film gels with depth-wise crosslinking gradients*. Soft Matter 6 (22), 5795–5801.

[28] Guvendiren, M., Yang, S., Burdick, J. A., [2009]. *Swelling-induced surface patterns in hydrogels with gradient crosslinking density.* Advanced Functional Materials 19 (19), 3038–3045.

[29] Hill, R., [1957]. *On uniqueness and stability in the theory of finite elastic strains.* Journal of the Mechanics and Physics of Solids 5, 229–241.

[30] Hill, R., [1962]. *Acceleration waves in solids.* Journal of the Mechanics and Physics of Solids 10 (1), 1–16.

[31] Hoffman, A. S., [1995]. *"intelligent" polymers in medicine and biotechnology.* Artificial organs 19 (5), 458–467.

[32] Hoffman, A. S., [2012]. *Hydrogels for biomedical applications.* Advanced drug delivery reviews 64, 18–23.

[33] Hong, W., Liu, Z., Suo, Z., [2009]. *Inhomogeneous swelling of a gel in equilibrium with a solvent and mechanical load.* International Journal of Solids and Structures 46 (17), 3282–3289.

[34] Hong, W., Zhao, X., Suo, Z., [2008]. *Drying-induced bifurcation in a hydrogel-actuated nanostructure.* Journal of Applied Physics 104 (8), 1–4.

[35] Hong, W., Zhao, X., Zhou, J., Suo, Z., [2008]. *A theory of coupled diffusion and large deformation in polymeric gels.* Journal of the Mechanics and Physics of Solids 56 (5), 1779–1793.

[36] Hong, W., Zhao, X., Zhou, J., Suo, Z., [2008]. *A theory of coupled diffusion and large deformation in polymeric gels.* Journal of the Mechanics and Physics of Solids 56 (5), 1779–1793.

[37] Huggins, M. L., [1941]. *Solutions of long chain compounds.* The Journal of Chemical Physics 9 (5), 440.

[38] Ilseng, A., Prot, V., Skallerud, B. H., Stokke, n. B. T., [2019]. *Buckling initiation in layered hydrogels during transient swelling.* Journal of the Mechanics and Physics of Solids 128, 219–238.

[39] Ilseng, A., Skallerud, B. H., Stokke, B. T., Prot, V., [2021]. *A perturbation analysis approach for studying the effect of swelling kinetics on instabilities in hydrogel plates.* Journal of Applied Mechanics 88 (5).

[40] Ionov, L., [2014]. *Hydrogel-based actuators: possibilities and limitations.* Materials Today 17 (10), 494–503.

[41] Jiang, X., Takayama, S., Qian, X., Ostuni, E., Wu, H., Bowden, N., LeDuc, P., Ingber, D. E., Whitesides, G. M., [2002]. *Controlling mammalian cell spreading and cytoskeletal arrangement with conveniently fabricated continuous wavy features on poly (dimethylsiloxane).* Langmuir 18 (8), 3273–3280.

[42] Jin, L., Liu, Y., Cai, Z., [2018]. *Asymptotic solutions on the circumferential wrinkling of growing tubular tissues.* International Journal of Engineering Science 128, 31–43.

[43] Kaessmair, S., Runesson, K., Steinmann, P., Jänicke, R., Larsson, F., [2021]. *Variationally consistent computational homogenization of chemomechanical problems with stabilized weakly periodic boundary conditions*. International Journal for Numerical Methods in Engineering 122 (22), 6429–6454.

[44] Kaessmair, S., Steinmann, P., [2018]. *Computational first-order homogenization in chemo-mechanics*. Archive of Applied Mechanics 88 (1-2), 271–286.

[45] Kaneko, D., Gong, J. P., Osada, Y., [2002]. *Polymer gels as soft and wet chemomechanical systems–an approach to artificial muscles*. Journal of Materials Chemistry 12 (8), 2169–2177.

[46] Kang, M. K., Huang, R., [2010]. *Effect of surface tension on swell-induced surface instability of substrate-confined hydrogel layers*. Soft Matter 6 (22), 5736–5742.

[47] Kang, M. K., Huang, R., [2010]. *Swell-induced surface instability of confined hydrogel layers on substrates*. Journal of the Mechanics and Physics of Solids 58 (10), 1582–1598.

[48] Kikuchi, S., Matsubara, S., Nagashima, S., Okumura, D., [2022]. *Diversity of the bifurcations and deformations on films bonded to soft substrates: Robustness of the herringbone pattern and its cognate patterns*. Journal of the Mechanics and Physics of Solids 159, 104757.

[49] Lam, M. T., Sim, S., Zhu, X., Takayama, S., [2006]. *The effect of continuous wavy micropatterns on silicone substrates on the alignment of skeletal muscle myoblasts and myotubes*. Biomaterials 27 (24), 4340–4347.

[50] Larsson, F., Runesson, K., Su, F., [2010]. *Variationally consistent computational homogenization of transient heat flow*. International Journal for Numerical Methods in Engineering 81 (13), 1659–1686.

[51] Li, C. Y., Hao, X. P., Wu, Z. L., Zheng, Q., [2019]. *Photolithographically patterned hydrogels with programmed deformations*. Chemistry–An Asian Journal 14 (1), 94–104.

[52] Ma, P., Niu, B., Lin, J., Kang, T., Qian, J., Wu, Z. L., Zheng, Q., [2019]. *Sequentially controlled deformations of patterned hydrogels into 3d configurations with multilevel structures*. Macromolecular Rapid Communications 40 (3), 1800681.

[53] Ma, S., Yu, B., Pei, X., Zhou, F., [2016]. *Structural hydrogels*. Polymer 98, 516–535.

[54] MATLAB, [2017]. *MATLAB version 9.3.0.713579 (R2017b)*. Natick, Massachusetts.

[55] Miehe, C., Koch, A., [2002]. *Computational micro-to-macro transitions of discretized microstructures undergoing small strains*. Archive of Applied Mechanics 72 (4), 300–317.

[56] Miehe, C., Mauthe, S., Teichtmeister, S., [2015]. *Minimization principles for the coupled problem of darcy–biot-type fluid transport in porous media linked to phase field modeling of fracture*. Journal of the Mechanics and Physics of Solids 82, 186–217.

[57] Miehe, C., Schotte, J., Schröder, J., [1999]. *Computational micro-macro transitions and overall moduli in the analysis of polycrystals at large strains*. Computational Materials Science 16, 372–382.

[58] Miehe, C., Vallicotti, D., Teichtmeister, S., [2016]. *Homogenization and multiscale stability analysis in finite magneto-electro-elasticity. application to soft matter EE, ME and MEE composites*. Computer Methods in Applied Mechanics and Engineering 300, 294–346. (doi:http://dx.doi.org/10.1016/j.cma.2015.10.013)

[59] Miyoshi, H., Matsubara, S., Okumura, D., [2021]. *Bifurcation and deformation during the evolution of periodic patterns on a gel film bonded to a soft substrate*. Journal of the Mechanics and Physics of Solids 148, 104272.

[60] Müller, S., [1987]. *Homogenization of nonconvex integral functionals and cellular elastic materials*. Archive of Rational Mechanics and Analysis 99, 189–212.

[61] Okumura, D., Inagaki, T., Ohno, N., [2015]. *Effect of prestrains on swelling-induced buckling patterns in gel films with a square lattice of holes*. International Journal of Solids and Structures 58, 288–300. (doi:https://doi.org/10.1016/j.ijsolstr.2015.01.015)

[62] Okumura, D., Kuwayama, T., Ohno, N., [2014]. *Effect of geometrical imperfections on swelling-induced buckling patterns in gel films with a square lattice of holes*. International Journal of Solids and Structures 51 (1), 154–163. (doi:https://doi.org/10.1016/j.ijsolstr.2013.09.018)

[63] Pollmann, N., Larsson, F., Runesson, K., Lundgren, K., Zandi, K., Jänicke, R., [2021]. *Modeling and computational homogenization of chloride diffusion in three-phase meso-scale concrete*. Construction and Building Materials 271, 121558.

[64] Polukhov, E., Keip, M.-A., [2020]. *Computational homogenization of transient chemo-mechanical processes based on a variational minimization principle*. Advanced Modeling and Simulation in Engineering Sciences 7 (1), 1–26.

[65] Polukhov, E., Keip, M.-A., [2021]. *Multiscale stability analysis of periodic magnetorheological elastomers*. Mechanics of Materials 159, 103699.

[66] Polukhov, E., Vallicotti, D., Keip, M.-A., [2018]. *Computational stability analysis of periodic electroactive polymer composites across scales*. Computer Methods in Applied Mechanics and Engineering 337, 165–197.

[67] Rosiak, J. M., Yoshii, F., [1999]. *Hydrogels and their medical applications*. Nuclear Instruments and Methods in Physics Research Section B: Beam Interactions with Materials and Atoms 151 (1-4), 56–64.

[68] Rudzinski, W. E., Dave, A. M., Vaishnav, U. H., Kumbar, S. G., Kulkarni, A. R., Aminabhavi, T. M., [2002]. *Hydrogels as controlled release devices in agriculture*. Designed Monomers and Polymers 5 (1), 39–65. (doi:10.1163/156855502760151580)

[69] Savina, I. N., Ingavle, G. C., Cundy, A. B., Mikhalovsky, S. V., [2016]. *A simple method for the production of large volume 3d macroporous hydrogels for advanced*

biotechnological, medical and environmental applications. Scientific reports 6 (1), 1–9.

[70] Sriram, S., Polukhov, E., Keip, M.-A., [2021]. *Transient stability analysis of composite hydrogel structures based on a minimization-type variational formulation*. International Journal of Solids and Structures 230-231, 111080. (doi:https://doi.org/10.1016/j.ijsolstr.2021.111080)

[71] Tanaka, T., Sun, S.-T., Hirokawa, Y., Katayama, S., Kucera, J., Hirose, Y., Amiya, T., [1987]. *Mechanical instability of gels at the phase transition*. Nature 325 (6107), 796–798.

[72] Taylor, R. L., Govindjee, S., [2021]. *FEAP – A finite element analysis program*.

[73] Teichtmeister, S., Mauthe, S., Miehe, C., [2019]. *Aspects of finite element formulations for the coupled problem of poroelasticity based on a canonical minimization principle*. Computational Mechanics, 1–32.

[74] Triantafyllidis, N., Nestorović, M. D., Schraad, M. W., [2006]. *Failure surfaces for finitely strained two-phase periodic solids under general in-plane loading*. ASME Journal of Applied Mechanics 73(3), 505–515. (doi:doi:10.1115/1.2126695)

[75] Trujillo, V., Kim, J., Hayward, R. C., [2008]. *Creasing instability of surface-attached hydrogels*. Soft Matter 4 (3), 564–569.

[76] Wang, Z. J., Zhu, C. N., Hong, W., Wu, Z. L., Zheng, Q., [2017]. *Cooperative deformations of periodically patterned hydrogels*. Science Advances 3 (9), e1700348.

[77] Wu, G., Xia, Y., Yang, S., [2014]. *Buckling, symmetry breaking, and cavitation in periodically micro-structured hydrogel membranes*. Soft Matter 10 (9), 1392–1399.

[78] Wu, Z., Bouklas, N., Huang, R., [2013]. *Swell-induced surface instability of hydrogel layers with material properties varying in thickness direction*. International Journal of Solids and Structures 50 (3-4), 578–587.

[79] Yin, J., Bar-Kochba, E., Chen, X., [2009]. *Mechanical self-assembly fabrication of gears*. Soft Matter 5 (18), 3469–3474.

[80] Zhang, J., Zhao, X., Suo, Z., Jiang, H., [2009]. *A finite element method for transient analysis of concurrent large deformation and mass transport in gels*. Journal of Applied Physics 105 (9), 1–9.

[81] Zhang, X. N., Wang, Y. J., Sun, S., Hou, L., Wu, P., Wu, Z. L., Zheng, Q., [2018]. *A tough and stiff hydrogel with tunable water content and mechanical properties based on the synergistic effect of hydrogen bonding and hydrophobic interaction*. Macromolecules 51 (20), 8136–8146.

[82] Zhang, Y., Matsumoto, E. A., Peter, A., Lin, P.-C., Kamien, R. D., Yang, S., [2008]. *One-step nanoscale assembly of complex structures via harnessing of an elastic instability*. Nano letters 8 (4), 1192–1196.

[83] Zhao, X., Hong, W., Suo, Z., [2008]. *Stretching and polarizing a dielectric gel immersed in a solvent*. International Journal of Solids and Structures 45 (14–15), 4021–4031.

[84] Zhao, Z., Gu, J., Zhao, Y., Guan, Y., Zhu, X., Zhang, Y., [2014]. *Hydrogel thin film with swelling-induced wrinkling patterns for high-throughput generation of multicellular spheroids*. Biomacromolecules 15 (9), 3306–3312.

[85] Zhu, X., Wu, G., Dong, R., Chen, C.-M., Yang, S., [2012]. *Capillarity induced instability in responsive hydrogel membranes with periodic hole array*. Soft Matter 8 (31), 8088–8093.

Presently published contributions in this report series

IAM 1 Matthias Leuschner: *Numerically Efficient Computational Homogenization : Fourier-Accelerated Nodal Solvers and Reduced Basis Model Order Reduction*, 2018.

IAM 2 Daniel Vallicotti: *Magneto-Electro-Mechanical Coupling Phenomena Across Multiple Length Scales : Variational Framework and Stability Analysis*, 2019.

IAM 3 Lukas Böger: *Saddle-Point and Minimization Principles for Diffusion in Solids : Phase Separation, Swelling and Fracture*, 2020.

IAM 4 Matthias Rambausek: *Magneto-Electro-Elasticity of Soft Bodies Across Scales*, 2020.

IAM 5 Ashish Sridhar: *Phase-Field Modeling of Microstructure and Fracture Evolution in Magneto-Electro-Mechanics*, 2020.

IAM 6 Osorno Tejada, Maria Camila: *Multiscale Modelling of Hydro-Mechanical Coupling in Porous Media*, 2021.

IAM 7 Malte Sauerwein: *Simulation of Coupled Transfer and Transport Phenomena in Multi-Phase Materials with Application to Polymer Gels*, 2021.

IAM 8 Stephan Teichtmeister: *Variational Methods for Dissipative Multifield Problems in Solid Mechanics*, 2021.

IAM 9 Oliver Kunc: *Finite Strain Hyperelastic Multiscale Homogenization via Projection, Efficient Sampling and Concentric Interpolation*, 2021.

IAM 10 Patrick Schmidt: *Hydro-Mechanical Coupling of Flow in Deformable High-Aspect Ratio Fractures*, 2022.

IAM 11 Daniel Kienle: *Phase-Field Modeling of Multi-Field Problems with Applications to Hydraulic-Elastic-Plastic Fracturing*, 2022.

IAM 12 Felix Selim Göküzüm: *Fast Solvers for Homogenization Problems : Fast Fourier Transform- and Neural Network-Based Approaches*, 2022.

IAM 13 Aref Nateghi: *A View of the Interplay Between Chemistry and Mechanics : Strain-Induced Crystallization in Rubbers and Thermo-Chemo-Mechanical Modeling of Electrode Particles in Lithium-Ion Batteries*, 2023.

IAM 14 Matthias Ruf: *Experimental Multi-Scale Characterization Using Micro X-Ray Computed Tomography*, 2023.

IAM 15 Elten Polukhov: *Multiscale Modeling and Stability Analysis of Soft Active Materials – from Electro- and Magneto-Active Elastomers to Polymeric Hydrogels*, 2023.

Institute of Applied Mechanics (IAM)
Chair of Materials Theory

Investigation of the stability of materials and structures has always been among the important tasks of mechanics. Since instabilities can induce sudden changes in the response of materials, they have often been treated as failure points and avoided during the designing processes. Ever since complex materials in the form of composites and metamaterials started emerging, instabilities have become paramount for smart applications. Material and structural instabilities are exploited not only to harvest and dissipate energy but also to tune the mechanical, acoustical, and optical properties of composites.

This work aims to investigate the stability of the response of composites and metamaterials that exhibit electro-, magneto-, and chemo-mechanical coupling phenomena. To model these materials and to analyze the associated multiscale stability, minimization-type variational formulations are developed and implemented. At the microscale, pattern-transforming structural instabilities are studied for a rich set of material and geometrical parameters. Similarly, at the macroscale, localization-type material instabilities are investigated.

ISBN 978-3-937399-63-8